Numerical Simulations of Stationary and Transient Spray Combustion for Aircraft Gas Turbine Applications

Thèse

Alain Athanase Fossi

Doctorat en génie mécanique
Philosophiæ doctor (Ph. D.)

Québec, Canada

Résumé

Le développement des turbines à gaz d'aviation actuelles et futures est principalement axé sur la sécurité, la performance, la minimisation de la consommation de l'énergie, et de plus en plus sur la réduction des émissions d'espèces polluantes. Ainsi, les phases de design de moteurs sont soumises aux améliorations continues par des études expérimentales et numériques. La présente thèse se consacre à l'étude numérique des phases transitoires et stationnaires de la combustion au sein d'une turbine à gaz d'aviation opérant à divers modes de combustion. Une attention particulière est accordée à la précision des résultats, aux coûts de calcul, et à la facilité de manipulation de l'outil numérique d'un point de vue industriel. Un code de calcul commercial largement utilisé en industrie est donc choisi comme outil numérique. Une méthodologie de Mécanique des Fluides Numériques (MFN) constituée de modèles avancés de turbulence et de combustion jumelés avec un modèle d'allumage sous-maille, est formulé pour prédire les différentes phases de la séquence d'allumage sous différentes conditions d'allumage par temps froid et de rallumage en altitude, ainsi que les propriétés de la flamme en régime stationnaire.

Dans un premier temps, l'attention est focalisée sur le régime de combustion stationnaire. Trois méthodologies MFN sont formulées en exploitant trois modèles de turbulence, notamment, le modèle basé sur les équations moyennées de Navier-Stokes instationnaires (URANS), l'adaptation aux échelles de l'écoulement (SAS), et sur la simulation aux grandes échelles (LES). Pour évaluer la pertinence de l'incorporation d'un modèle de chimie détaillée ainsi que celle des effets de chimie hors-équilibre, deux différentes hypothèses sont considérées : l'hypothèse de chimie-infiniment-rapide à travers le modèle d'équilibre-partiel, et l'hypothèse de chimie-finie via le modèle de flammelettes de diffusion. Pour chacune des deux hypothèses, un carburant à une composante, et un autre à deux composantes sont utilisés comme substituts du kérosène (Jet A-1). Les méthodologies MFN résultantes sont appliquées à une chambre de combustion dont l'écoulement est stabilisé par l'effet swirl afin d'évaluer l'aptitude de chacune d'elle à prédire les propriétés de combustion en régime stationnaire. Par la suite, les rapports entre le coût de calcul et la précision des résultats pour les trois méthodologies MFN formulées sont explicitement comparés.

La deuxième étude intermédiaire est dédiée au régime de combustion transitoire, notamment à la séquence d'allumage précédant le régime de combustion stationnaire. Un brûleur de combustibles gazeux, muni d'une bougie d'allumage, et dont la flamme est stabilisée par un accroche-flamme, est

utilisé pour calibrer le modèle MFN formulé. Ce brûleur, de géométrie relativement simple, peut aider à la compréhension des caractéristiques d'écoulements réactifs complexes, en l'occurrence l'allumabilité et la stabilité. La méthodologie MFN la plus robuste issue de la précédente étude est reconsidérée. Puisque le brûleur fonctionne en mode partiellement pré-mélangé, le modèle de combustion paramétré par la fraction de mélange et la variable de progrès est adopté avec les hypothèses de chimie-infiniment-rapide et de chimie-finie, respectivement à travers le modèle de Bray-Moss-Libby (BML) et un modèle de flammelettes multidimensionnel (FGM). Le modèle d'allumage sous-maille est préalablement ajusté via l'implémentation des propriétés de la flamme considérée. Par la suite, le modèle d'allumage est couplé au solveur LES, puis successivement aux modèles BML et FGM. Pour évaluer les capacités prédictives des méthodologies résultantes, ces dernières sont utilisées pour prédire les évènements d'allumage résultant d'un dépôt d'énergie par étincelles à diverses positions du brûleur, et les résultats sont qualitativement et quantitativement validés en comparant ceux-ci à leurs homologues expérimentaux.

Finalement, la méthodologie MFN validée en configuration gazeuse est étendue à la combustion diphasique en la couplant au module de la phase liquide, et en incorporant les propriétés de la flamme de kérosène dans le modèle d'allumage. La méthodologie MFN résultant de cette adaptation, est préalablement appliquée à la chambre de combustion étudiée antérieurement, pour prédire la séquence d'allumage et améliorer les prédictions antérieures des propriétés de la flamme en régime stationnaire. Par la suite, elle est appliquée à une chambre de combustion plus réaliste pour prédire des évènements d'allumage sous différentes conditions d'allumage par temps froid, et de rallumage en altitude. L'aptitude de la nouvelle méthodologie MFN à prédire les deux types d'allumage considérés est mesurée quantitativement et qualitativement en confrontant les résultats des simulations numériques avec les enveloppes d'allumage expérimentales et les images d'une séquence d'allumage enregistrée avec une caméra infrarouge.

Abstract

The development of current and future aero gas turbine engines is mainly focused on the safety, the performance, the energy consumption, and increasingly on the reduction of pollutants and noise level. To this end, the engine's design phases are subjected to improving processes continuously through experimental and numerical investigations. The present thesis is concerned with the simulation of transient and steady combustion regimes in an aircraft gas turbine operating under various combustion modes. Particular attention is paid to the accuracy of the results, the computational cost, and the ease of handling the numerical tool from an industrial standpoint. Thus, a commercial Computational Fluid Dynamics (CFD) code widely used in industry is selected as the numerical tool. A CFD methodology consisting of its advanced turbulence and combustion models, coupled with a subgrid spark-based ignition model, is formulated with the final goal of predicting the whole ignition sequence under cold start and altitude relight conditions, and the main flame trends in the steady combustion regime.

At first, attention is focused on the steady combustion regime. Various CFD methodologies are formulated using three turbulence models, namely, the Unsteady Reynolds-Averaged Navier-Stokes (URANS), the Scale-Adaptive Simulation (SAS), and the Large Eddy Simulation (LES) models. To appraise the relevance of incorporating a realistic chemistry model and chemical non-equilibrium effects, two different assumptions are considered, namely, the infinitely-fast chemistry through the partial equilibrium model, and the finite-rate chemistry through the diffusion flamelet model. For each of the two assumptions, both one-component and two-component fuels are considered as surrogates for kerosene (Jet A-1). The resulting CFD models are applied to a swirl-stabilized combustion chamber to assess their ability to retrieve the spray flow and combustion properties in the steady combustion regime. Subsequently, the ratios between the accuracy of the results and the computational cost of the three CFD methodologies are explicitly compared.

The second intermediate study is devoted to the ignition sequence preceding the steady combustion regime. A bluff-body stabilized burner based on gaseous fuel, and employing a spark-based igniter, is considered to calibrate the CFD model formulated. This burner of relatively simple geometry can provide greater understanding of complex reactive flow features, especially with regard to ignitability and stability. The most robust of the CFD methodologies formulated in the previous configuration is reconsidered. As this burner involves a partially-premixed combustion mode, a combustion

model based on the mixture fraction-progress variable formulation is adopted with the assumptions of infinitely-fast chemistry and finite-rate chemistry through the Bray-Moss-Libby (BML) and Flamelet Generated Manifold (FGM) models, respectively. The ignition model is first customized by implementing the properties of the flame considered. Thereafter, the customized ignition model is coupled to the LES solver and combustion models based on the two above-listed assumptions. To assess the predictive capabilities of the resulting CFD methodologies, the latter are used to predict ignition events resulting from the spark deposition at various locations of the burner, and the results are quantitatively and qualitatively validated by comparing the latter to their experimental counterparts.

Finally, the CFD methodology validated in the gaseous configuration is extended to spray combustion by first coupling the latter to the spray module, and by implementing the flame properties of kerosene in the ignition model. The resulting CFD model is first applied to the swirl-stabilized combustor investigated previously, with the aim of predicting the whole ignition sequence and improving the previous predictions of the combustion properties in the resulting steady regime. Subsequently, the CFD methodology is applied to a scaled can combustor with the aim of predicting ignition events under cold start and altitude relight operating conditions. The ability of the CFD methodology to predict ignition events under the two operating conditions is assessed by contrasting the numerical predictions to the corresponding experimental ignition envelopes. A qualitative validation of the ignition sequence is also done by comparing the numerical ignition sequence to the high-speed camera images of the corresponding ignition event.

Contents

List of Tables

List of Figures

To the Holy Trinity
To the memory of my late father,
Jean
To my mother, Marie
To my siblings
To all other members of my family

«Les Hommes de génie sont des météores destinés à brûler pour éclairer leur siècle.»

Napoléon Bonaparte (1769-1821)

Acknowledgments

The achievement of this work has been made possible through the contributions of many people, funding agencies and an industrial partner, and I would like to express my deepest gratitude to all of them.

The work described in the present thesis was carried out in the Combustion Laboratory of the Department of Mechanical Engineering at Université Laval, where I conducted my PhD project, with the financial support from FQRNT and the seed funding initially provided by P&WC, CRIAQ & MDEIE. I am extremely grateful to each of these agencies, and to P&WC for the support during the project.

Firstly, I would like to express my thanks to my supervisor Prof. Alain DeChamplain for giving me the opportunity to discover the challenging world of numerical combustion and especially its application to aircraft gas turbines. I am extremely grateful for his support, invaluable guidance and for his continuing help even before I came to Quebec city. I also wish to thank him for his availability and for providing a pleasant work atmosphere and good work tools. I would also like to thank Prof. Jeffrey Bergthorson at McGill University for his continuing support throughout this project. I appreciate the invaluable advice and the positive attitude of both of them, along with their trust and the freedom they provided me to work independently.

I am deeply grateful to my MSc supervisor Prof. Marcel Obounou at the University of Yaoundé 1 (Cameroon) for introducing me in the world of combustion, for all the advice he gave me regarding the combustion science, and for his assistance during the admission process at Université Laval.

I would also like to thank Dr. Benjamin Akih-Kumgeh at Syracuse University for his advice and helpful discussions regarding the Jet A-1 surrogates, their chemical kinetic mechanisms, and the reduction techniques. I thank him also for the time he devoted to our numerous scientific and non scientific discussions, and for the suitable references he provided me regarding some specific topics throughout this research project.

A special thanks to Dr. Salvador Navarro-Martinez at Imperial College London for the helpful discussions regarding one of the experimental configurations used in the present work, and for the references he provided me for more detailed explanations. This assistance has been particularly useful to initiate the work described in the present thesis.

I would also like to thank Dr. Samer Ahmed (Cambridge University) for the helpful discussions regarding the second experimental configuration used in the current study. This second configuration and the related explanations have been an invaluable validation tool to move forward this research project.

A special thank to Prof. Amsini Sadiki at Darmstadt University for helpful discussions regarding the Large Eddy Simulation theory.

I am grateful to Prof. Heinz Pitsch at RWTH Aachen University for providing me with his FlameMaster code and all the related documentation including his Master's thesis for more detailed explanations. These documents have been of invaluable support for me at the beginning of my thesis.

A special thank to Prof. Mathias Ihme at Stanford University for addressing some of my misunderstandings related to the prediction of pollutants in turbulent combustion.

A special thank to Prof. Sébastien Candel at École centrale Paris for helpful discussions we had on combustion science during the summer school on clean combustion at the University of Toronto Institute of Aerospace Studies (UTIAS).

I would like to thank Prof. Thierry Poinsot at CERFACS Toulouse for addressing some of my concerns regarding the turbulent combustion modelling, and for all the advice he provided me during the combustion summer school at Princeton University.

I am grateful to our research associate, M. Bernard Paquet, who helped me to address some of my various misunderstandings related to gas turbine engines at the beginning of this research project.

I would also like to thank Dr. Linassier Guillaume for the helpful discussions regarding ignition modelling, for all the references he provided me when I started my research project. I deeply appreciated his availability and advice.

During my PhD program, I received the exemption scholarship and some financial assistance from Université Laval through its various support plans. I am therefore indebted to Université Laval for this support.

I would like to thank the manager of the graduate studies program of the Department of Mechanical Engineering at Université Laval, Prof. Claire DesChênes, for the welcome and all the invaluable advice she gave me at the beginning and throughout my PhD program.

I am grateful to the teaching staff of the department of Mechanical Engineering at Université Laval, and especially, to Prof. Ivan Marciel and Prof. Guy Dumas for helpful discussions on fluid mechanics, namely, the fundamental assumptions in CFD and the boundary layer theory. Also, I would particularly like to thank both of them for allowing me to use their Tecplot licences throughout my PhD project.

I am grateful to Prof. Michael Pfitzner at the University of Federal Armed Forces Munich for the

helpful discussions we had on the Large Eddy Simulation theory and its numerical implementation during the ASME Turbo Expo 2014 conference in Germany.

I am grateful to the teaching staff of the International Institute for Water and Environmental Engineering, especially to Prof. Yezouma Coulibaly, Dr. Maryam Sido and Mr. Francis Semporé for the training I received from them, and for their assistance during the admission process at Université Laval.

Finally, I would like to thank all the members of the Combustion Laboratory at Université Laval (CLUL) for the helpful scientific and non scientific discussions we had, as well as the wonderful moments we spent together. I am particularly grateful to most of them for their moral assistance when my father passed away only few months after I joined the CLUL group. I cannot find words to thank them enough for that, and I will be forever grateful to them for this particular support.

Avant-propos

Deux déclarations de deux célèbres personnalités au cours des deux siècles qui ont précédé le nôtre peuvent être exploitées pour mieux comprendre le rôle de l'Homme de génie en combustion au quotidien: La première et la plus ancienne est celle de Napoléon Bonaparte (1769-1821) qui se formule comme suit: «*Les Hommes de génie sont des météores destinés à brûler pour éclairer leur siècle*». La deuxième, relativement plus récente, est celle de Thomas Edison (1847-1931) qui dit ceci: «*Le génie est fait d'un pour cent seulement d'inspiration et de quatre vingt dix neuf pour cent de transpiration*.»

Contrairement aux mots «BRÛLER» et «ÉCLAIRER» qui sont utilisé au sens connotatif dans la déclaration de Napoléon Bonaparte, le mot génie est employé au sens dénotatif et renvoie aux dispositions ou aptitudes qui font qu'un être humain est capable de réaliser des choses extraordinaires et nouvelles. Faisant allusion à cette aptitude humaine qu'est le génie, Thomas Edison fait remarquer qu'il s'acquiert majoritairement au terme de travaux de longue haleine.

L'INSPIRATION au sens de Thomas Edison, peut être assimilée au talent reçu de la providence; l'action de «BRÛLER» au sens de Napoléon Bonaparte, peut être assimilée à la TRANSPIRATION au sens de Thomas Edison, et chacune des deux terminologies peut être considérée comme l'effort de fructification du ou des talent(s) reçu(s).

En s'appuyant sur les bienfaits de la combustion dans la vie au quotidien, la pensée de Napoléon Bonaparte transposée dans le monde de la combustion peut de façon évidente se formuler de la manière suivante: «*Les combustibles sont des météores qui doivent brûler pour éclairer le chemin des avancées technologiques*.»

En revanche, comme on l'observe au quotidien, lorsque les combustibles brûlent mal, ils peuvent plutôt obscurcir le chemin des avancées technologiques. Avec les termes de Thomas Edison, on dira que l'Homme de génie en combustion trouve du plaisir à TRANSPIRER pour rendre son INSPIRATION (i.e. le talent reçu de la providence) utile la société. Avec les termes de Napoléon Bonaparte, on dira que l'Homme de génie en combustion prend plaisir à «BRÛLER» pour qu'une fois les combustibles brûlés, ils ne servent qu'à éclairer le chemin des avancées technologiques, jamais à leur obscurcissement! Contrôler la combustion et la rendre exclusivement utile c'est ça la finalité des efforts de l'Homme de génie en combustion!

Nomenclature

Roman letters, Uppercase:

B_T: Spalding transfer number

C_p: Specific heat at constant pressure

C_D: Drag coefficient

D: Diffusion coefficient

Da:Damköhler number

D_T: Thermal diffusion coefficient

G: Group number

Ka: Karlovitz number

Le: Lewis number

Ma: Mach number

N_s: Number of species Nu: Nusselt number

Pe: Péclet number

P_3: Total pressure at the combustor inlet

Re: Reynolds number

Re_t: Reynolds number

R_{sw}: Swirler Radius

St_v: Vaporization Stokes number

Sc_t: Turbulent Schmidt number

$\dot{S}_m$: mass source term due to the fuel evaporation

$\dot{S}_h$: Energy source term due to interaction with liquid phase

$\dot{S}_{mU_i}$: Source term of the i^{th} momentum component

T_d: Droplet temperature

T_3: Air temperature at the combustion inlet

U_i: i^{th} flow velocity component

Y_{O_2}: Oxidizer mass fraction

W_e: Weber number

W_{ec}: Critical Weber number

W_3: Air mass flow rate at the combustor inlet

$\widetilde{Z''^2}$: Mixture fraction variance

Roman letters, Lowercase:

a_c: Cloud radius

a_F: Radius of flame surrounding a spherical droplet

a_q: Quenching value of the strain rate

k: Turbulent kinetic energy

l_D: Diffusion length scale

m_d: mass of the droplet (mass of the stochastic droplet)

s_L: Laminar burning velocity

s: Stoichiometric air-to-fuel ratio

t_c: Diffusion time of heat into the cloud

Greek letters, Uppercase:

$(\Delta Z)_F$: Flame thickness in the mixture fraction space

Φ: Spray function

Greek letters, Lowercase:

α: Mass loading ratio

α_F: Critical mass loading ratio

δ_d: Droplet interspace distance

ε: Dissipation rate

λ: Thermal conductivity

ρ: Density

ρ_l: Liquid phase density

ξ_ϕ:Phase indicator function

σ_{ij}: Stress tensor

ϕ:Phase index

ϕ_{TS}: Vector of tracking scalars

χ: scalar dissipation rate

χ_q: Quenching value of the scalar dissipation rate

χ_{st}: Stoichiometric scalar dissipation rate

ω: Eddy frequency

$\dot{\omega}_h$: Energy source term due to chemical reactions

Acronyms:

AFL: Alternative Fuels Laboratory McGill University
AFR: Air-to-Fuel Ratio
API: American Petroleum Institute
ASTM: American Society for Testing and Materials
BML: Bray-Moss-Libby Model
BR: Blockage Ratio
CFD: Computational Fluid Dynamics
CKM: Chemical Kinetics Mechanism
CLUL: Combustion Laboratory Université Laval
CMC: Conditional Moment Closure
UHF: Unburned Hydrocarbon Fuel
CPU: Central Processing Unit
CSP: Computational Singular Perturbation
CRZ: Central Recirculation Zone
DCKM: Detailed Chemical Kinetics Mechanism
DDES: Delayed Detached Eddy Simulation
DES: Detached Eddy Simulation
DFT: Diffusion Flamelet Tabulation
DPIK: Discrete Particle Ignition Kernel
DPM: Discrete Phase Model
DRW: Discrete Random Walk
EDC: Eddy Dissipation Concept
EE: Eulerian-Eulerian formulation
EL: Eulerian-Lagrangian formulation
EQ: Equilibrium
FAR:Fuel-to-Air Ratio
FDM: Finite Difference Method
FGM: Flamelet Generated Manifold
FPI: Flamelet Prolongation of ILDM
FVM: Finite Volume Method
ILDM: Intrinsic Low Dimensional Manifold
JetSurF: Jet Surrogate Fuel
JSR: Jet-Stirred Reactors
KHRT: Kelvin-Helmholtz Rayleigh-Taylor
LDA: Laser Doppler anemometry
LDV: Laser Doppler Velocimetry
LES: Large Eddy Simulation
LOI: Level Of Importance

MFGM: Multi-dimensional Flamelet Generated Manifold
MFM: Multi-regime Flamelet Model
MFN: Mécanique des Fluides Numérique
MMD: Mass Median Diameter
MPI: Message Parallel Interface
MUSCL: Monotonic Upstream-Centered Scheme for Conservation Law
PDE: Partial Differential Equation
PDF: Probability Density Function
PEQ: Partial Equilibrium
PIV: Particle Image Velocimetry
PLIF: Planar Laser Induced Fluorescence
PRESTO: PRessure STaggered Option
P&WC: Pratt and Whitney Canada
QSSA: Quasi Steady State Assumption
QUICK: Quadratic Upstream Interpolation for Conservative Kinematics
RAM: Random Access Memory
RANS: Reynolds-Averaged Navier-Stokes
RCCE: Rate Controlled Constraints Equilibria
RCKM: Reduced Chemical Kinetics Mechanism
RFL: Rich Flammability Limit
RMS: Root Mean Square
RNG: Renormalization Group Theory
RSM: Reynolds Stress Model
RST: Reynolds Stress Transport
S-A Spalart-Allmaras model
SAS: Scale-adaptive simulation
SGS: Sub-Grid Scale
SIMPLE: Semi-Implicit Method for Pressure Linked Equations
SIMPLEC: Semi-Implicit Method for Pressure Linked Equations-Consistent
SMD: Sauter Mean Diameter
SRS: Scale Resolved Simulation
SRZ: Secondary Recirculation Zone
SSD: Stochastic Secondary Droplet
SST: Shear-Stress Transport
TAB: Taylor Analogy Break-up
UFPV: Unsteady Flamelet Progress Variable
URANS: Unsteady Reynolds-Averaged Navier-Stokes
USB: University of Southern California
VOF: Volume Of Fluid

WALE: Wall-Adapting Local Eddy
WMLES: Wall-Modelled LES

Introduction

Background

The need to address energy challenges of the 21st century (the rapid growth in energy needs, the gradual depletion of fossil fuels, and the reduction of greenhouse gas emissions) has drawn attention to the development of new energy sources and conversion technologies, and to the optimization of existing energy systems. These two approaches are respectively devoted to secure the energy supply and improve the efficiency so as to rationalize the consumption of the available energy resources and minimize the ecological footprint. Due to the substantial contribution of combustion in energy production, the optimization of combustion systems appears today and for a foreseeable future as an intermediate and reliable solution for the above-mentioned energy challenges. Specifically, in advanced combustion systems like those of the aerospace industry, the use of new energy sources such as biomass-derived fuels remains at a relatively early stage of research while optimization has so far been at the basis of numerous design and operating criteria. The development of current and future aero gas turbine engines is mainly focused on safety, performance, minimization of the energy consumption, and increasingly on the reduction of pollutant emissions and noise levels. In order to meet all these requirements, engines design phases are subjected to continuous improvements in engine processes through experimental and numerical investigations. However, some phenomena related to each of these design and operating criteria are often too expensive to investigate experimentally. Due to significant progress in combustion modelling and in numerical methods along with the exponential increase in computing resources, numerical simulation e.g. Computational Fluid Dynamics (CFD) is an alternate choice to closely study the behaviour of combustion systems. As operating mode, the CFD uses mathematical models to describe physical phenomena in such a way as to predict the dynamic behaviour of a given physical system. The reliability of a CFD model as a whole is heavily dependent on that of the mathematical models used to describe the investigated physical system. The latter are calibrated by comparing the CFD predictions against experimental data generated using specific parameters, and the resulting well-adjusted CFD model can be further used to predict other complicated phenomena which are difficult to assess experimentally. From an operational standpoint, even considering this additional asset, CFD should not be viewed as a way of eliminating the need for experiments. Instead, CFD provides additional information that can help in understanding the system thoroughly, and also in giving more insight to experimental data. Thus, CFD and experiments are complementary. Depending on the accuracy of a CFD model, it can significantly reduce the experimental testing

needed for a novel design of aero-engines by providing engine manufacturers with a wide database of virtual simulations and parametric investigations in a reasonable time-frame. This complementarity is further necessary for combustion systems involving heterogeneous combustion such as liquid-fueled engines, which involve strong interactions between the gaseous and liquid phases.

Motivation

Due to the relatively high energy density of liquid fuels and the need to reduce storage volumes in aircraft gas turbines, liquid fuels are mainly used, and are introduced in the form of a disperse spray of small droplets. The optimization of such combustion systems requires a proper understanding of two phase combustion, which involves several complex phenomena mutually and continuously interacting. These are phenomena involved in the gas phase (e.g. molecular and turbulent mixing, chemical reactions, etc.), liquid phase (e.g. fuel atomization, evaporation, droplet dynamics, etc.) and interactions between the gas and liquid phases. These interactions include turbulence-chemistry, turbulence-spray and spray-chemistry interactions, which are intrinsically unsteady in a turbulent environment. Further, the need for flame stabilization and high combustion efficiency leads to complicated flow patterns in combustors such as swirling flows, breakdown of large-scale vortex structures and recirculation zones. Thus, optimizing such combustion systems, along with elaborating some of their operating criteria, require a careful investigation of transient phenomena that feature very small time scales, such as those related to safety (e.g. cold start and altitude relight after possible flameout that may occur at high altitude due to severe atmospheric conditions) and environmental regulations (e.g. reduction of pollutant and noise emissions). These two concerns are currently among the most challenging issues faced by the combustion community in general, and by the aero-engine manufacturers in particular. This work is of direct interest to P&WC, an aero engine company. Accurately predicting these safety and environmental criteria depends strongly on the turbulence and chemistry models implemented as well as turbulence-chemistry interaction modelling [Poinsot and Veynante, 2005].

In this respect, several research papers and combustion textbooks have so far highlighted the relevance of a detailed chemistry model in the prediction of the critical transient phenomena mentioned earlier. However, the full exploitation of assets provided by a detailed chemistry model faces the limitations of the current computing resources. Detailed chemistry models can involve far beyond hundreds of species and thousands of elementary reactions, and these numbers become larger for heavy hydrocarbons such as those found in jet fuels. This large number of species leads to several transport equations that need to be solved, in addition to those governing the non-reacting two phase flow, resulting in prohibitive computing time. Considering such computing resource requirements, and especially the need to resort to supercomputers when investigating phenomena involved in most practical configurations, it is necessary to develop simulation approaches that can help in investigating the above mentioned phenomena while providing the best trade-off between accuracy and computing costs. As attempts to address computational cost issues, various advanced turbulence and combustion models have so far been formulated and successfully validated in some academic and industrial configurations. There are still some drawbacks related to investigating some other critical combus-

tion phenomena. These drawbacks include the assumptions done in model formulations and/or the prohibitive computing costs incurred when these models are customized to accurately capture some combustion phenomena. For instance, when implemented with a realistic chemistry model, the transport PDF formulation provides an efficient way of predicting various combustion processes. Unfortunately, it incurs high computing costs for large size reaction mechanisms, while tabulated chemistry approaches such as flamelet-based models and conditional moment closure circumvent such an issue. However, in spite of the abilities of these tabulated-chemistry-based combustion models to operate with detailed reaction mechanisms, their application to a given combustion device is subjected to some technical requirements, namely, rapid mixing and short combustion times (i.e. separation between chemistry and mixing time scales) which allows decoupling chemistry calculations from those of mixing. Fortunately, these requirements are also those of a stable and efficient combustion in the majority of practical combustion systems [Bray et al., 2005].

The present study lies in an optimization context governed by the above mentioned concerns, and is based on a promising alternative consisting of using advanced turbulence models coupled to advanced combustion models based on the tabulated-chemistry concept to investigate steady and transient phases of combustion in an aero gas turbine combustion chamber. More specifically, a CFD model based on tabulated flamelet-based chemistry approaches is first formulated in order to predict the aero-thermo-chemical state (aerodynamics, temperature and chemical species fields) in an aero gas turbine combustion chamber operating in the steady regime. Subsequently, the approach is extended to transitional regimes to predict two critical phenomena which are essential to maintain a reliable operation of an aircraft engine, namely, cold start and altitude relight. These two combustion processes are critical in an aircraft engine since they ensure easy and efficient light-up during ground starting, and a rapid relight of engines after flameout in flight. The latter may occur because of the adverse climatic conditions and/or a take-off from a wet runway where there is a risk of ingestion of excessive amount of water and ice.

Experimental configurations

The target model of combustion chamber used in the current study (scaled can combustor) was provided by P&WC, and was used in the Combustion Laboratory at Université Laval (CLUL) to investigate the effects of biofuels on the engine operability limits for the cold start (ground starting) and altitude relight regimes [Jean, 2017]. However, a realistic validation of a CFD model intended to assist the design of new gas turbine combustors requires well-characterized and focused experiments on the investigated phenomena. Due to the lack of relevant detailed experimental data for both steady combustion and ignition phase, two additional experimental configurations are selected from the literature in order to calibrate the two new formulated CFD models. These are the steady combustion regime-based experiments conducted at Imperial College London using a liquid-fueled swirl-stabilized can combustor [Sheen, 1993], which is similar to the P&WC scaled can combustor, and the spark-ignition-based experiments conducted at Cambridge University using a bluff-body stabilized burner [Ahmed, 2007a]. The main reasons for choosing these two models are the following:

in the former case, the combustor geometry is quite similar to the target model, and the flow patterns are as complex as in the P&WC scaled model combustor. But, instead of introducing air through the liner holes in both primary/secondary and dilution zones of the combustion chamber to achieve high mixing rates, a highly swirling motion is imposed to the main air flow. Furthermore, detailed experimental data including pollutant concentrations are available. In the second case, the burner can produce flames of varying stability, efficiency, pollutant formation and heat transfer through the variation in design and operating conditions. For example, the ability of this burner to mimic complex flow patterns close to those found in real combustion chambers, can provide a greater understanding of complex flows, and ignition requirements such as stability and ignitability. The stability aspect lies in the fact that, the burner involved a radial fuel injection in co-flowing to avoid the fuel penetration in the recirculation zone. Consequently, combustion occurs in a partially premixed mode because of the partial premixing of fuel with air, and consequently, at some locations of the reacting flow field, triple flames may develop and contribute to the overall flame stabilization [Puri et al., 2001a, Qin et al., 2004]. Finally, detailed experimental data are available for this burner so as to allow a step-by-step validation of the formulated ignition-based CFD model.

Based on these preliminary investigations, the suitable parameters for each of the formulated CFD models are used to investigate steady combustion and ignition events in the P&WC scaled can combustor, with particular attention paid to the ease of handling the numerical tool and to the reduction of computational costs. All the simulations in the present study are conducted using a surrogate model of the liquid fossil fuel commonly used in commercial aviation (Jet A-1 surrogate), except for one of the intermediate simulations which is conducted with a gaseous fuel in order to calibrate the formulated CFD model and assess ignition performance. The two formulated CFD models enable assessment of safety standards and inexpensive prediction of emissions and ignition parameters. The robustness of these approaches lies in their extensibility, and therefore in their ability to also cover some relevant issues such as the security of energy supply along with the safety and environmental challenges. Indeed, there are globally two possible ways of securing the energy supply by means of conventional fuel replacement (through biomass-derived fuels for example). These are the engine-adaptation and the fuel-adaptation. The first approach would consist of modifying the engines technology to allow using the new fuels without any fuel modification, while the second approach aims to change the properties of new fuels and/or to manufacture new fuels through chemical processes (e.g. Fischer-Tropsch synthesis and transesterification of vegetable oils) so as to achieve the properties of conventional fuels. For the time being, the second approach seems more appropriate and is widely used to produce new biomass-derived fuels for the existing combustion systems. Based on this observation, and considering the fact that alternative fuels differ from conventional fuels mainly by their properties and reaction mechanisms, the CFD methodology developed in the present study can be used for investigations of attractive biofuels to combust in aero gas turbines.

Outline of the thesis

The present introduction discussed the background for the research objectives and motivation obtained from previous studies devoted to address some energy challenges of the 21st century through the optimization of combustion technical devices. This discussion is also based on some of the current concerns for P&WC which are among the most challenging issues faced by all engine manufacturers. The remaining part of the thesis are organized as follows:

Chapter 1: A brief description of the physical phenomena involved in turbulent spray combustion along with their interactions is first presented. This summarized description is followed by a literature review of the turbulent spray combustion modelling. The remaining part of the chapter focuses on the various modelling approaches used in the current study for turbulence and combustion as well as their interactions with the spray, with special emphasis placed on the tabulated chemistry concept.

Chapter 2: The fuel properties obtained from experiments and empirical correlations are first presented, followed by a brief literature review of jet fuel surrogates and their detailed reaction mechanisms. Thereafter, the choice of the fuel surrogates is discussed, and the technique used to reduce the size of their corresponding detailed reaction mechanisms is explained.

Chapter 3: The experimental configurations used to calibrate and validate the two formulated CFD models are described in terms of combustor designs, practical interests and combustion diagnostic techniques.

Chapter 4: The state-of-the art of mesh generators and CFD codes is first briefly presented, followed by the choice of the numerical tools to be used in all simulations. Thereafter, the relevant points regarding the mesh are discussed, and the numerical schemes are selected depending on the turbulence models used. The penultimate part of this chapter focuses on the numerical implementation of turbulence, spray and combustion models, along with their mutual interactions. A detailed description of the spark-based ignition model used to capture the early stage of the ignition events is also provided. This chapter ends with a summary of the boundary conditions and the allocated computing resources for each of the three investigated configurations, and the elaboration of the simulation flowchart.

Chapter 5: The results and discussions related to the numerical simulation of a steady turbulent swirl-stabilized spray flame are first presented with the aim of calibrating and validating the first CFD model formulated. Thereafter, this CFD model is applied to the P&WC combustor to assess the main flame trends. In the second part of the chapter, the results pertaining to the numerical simulation of ignition events resulting from the forced ignition of a bluff-body stabilized burner are discussed, the ultimate goal being the calibration of the spark-ignition-based CFD model, which is subsequently used to predict ignition events in the P&WC scaled combustor. The predictive capabilities of the ignition-based CFD model is appraised by comparing sequences of the numerical ignition events against their

experimental counterparts recorded by means of a high-speed camera.

Conclusions and suggestions for further research: The main outcomes of the present work and the suggestions for future research are summarized. This section is followed by an appendix consisting of a list and copies of recent publications of this work. The thesis ends with a list of all the references used in this study.

Chapter 1

Literature review

Due to their higher power-to-weight ratio and fuel flexibility, gas turbine engines are best suited for aerospace propulsion. Since their beginning in the years 1930-1940, gas turbine engines have been experiencing improvements in terms of overall performance, power-to-weight ratio, volume and cross-sectional area, lifetime, endurance, reliability, reduction of pollutant emissions and noise level. These continuous improvements are mainly due to the optimization of main engine components (e.g. compressor, combustion chamber, etc.), and to the progress in thermal limits of materials used to manufacture critical engine components such as turbines and combustion chambers. In this work, attention is focused on the combustion chamber which is the engine component where the investigated phenomena occur. The ignition and the resulting steady combustion that may happen within a liquid-fuelled combustion chamber are both phenomena involved in spray combustion. Thus, in order to accurately simulate these technical phenomena, all the basic processes of spray combustion, their interactions, as well as their mathematical modelling must be known in detail. This chapter provides an overview of various phenomena involved in turbulent combustion along with their interactions, with special attention on spray combustion. In the following sections, the set of processes involved in turbulent spray combustion as well as their interactions are first described. Thereafter, the modelling techniques used in spray combustion are outlined with a particular emphasis on those used in the present study.

1.1 Physical phenomena in spray combustion

From a global standpoint, spray combustion involves a liquid phase and a gaseous phase. However, the chemical reactions of combustion are generally assumed to occur in the gas phase, far enough from the liquid interface. Therefore, the liquid fuel must be evaporated and mixed with air in order to burn. The combustion efficiency is then strongly related to the evaporation rate which depends on the surface-to-volume ratio of the liquid fuel. Practically, to achieve high evaporation rates, the fuel surface-to-volume ratio is increased by injecting the liquid fuel in the form of a fine spray of small droplets through the process known as atomization [Lefebvre, 1983, 1989]. Consequently, spray

combustion involves all processes governing the spray generation, its evaporation, the mixing of the evaporated fuel with the oxidizer by means of turbulence, the chemical reactions of combustion as well as the spray-turbulence-chemistry interactions. These physical processes and the related interactions are illustrated in the following Figure 1.1. Considering the relevance and the contribution of these interactions [Williams, 1965, Sirignano, 1999], it becomes necessary to assess the features of each of them in order to better identify the assumptions applicable to the investigated configurations.

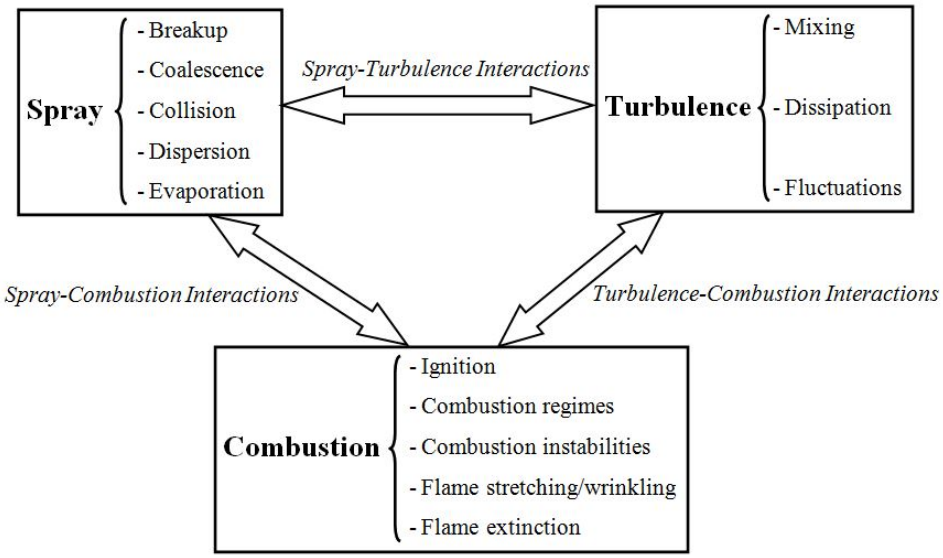

Figure 1.1: Interactions governing turbulent spray combustion

– *Turbulence-Combustion interactions*

The coupling strategy between turbulence and combustion phenomena is based on the time and length scales analysis. The comparison of these scales allows distinguishing the interaction regimes as elaborated by Damköhler [Damköhler, 1940]. More explicitly, the interaction between turbulence and the flame may lead to turbulence modification through flow-acceleration, and an increase in viscosity within the flame front. Depending on the order of magnitudes for chemistry and turbulence times scales, the interactions may generate turbulence through the so called "*flame-generated turbulence*" illustrated by Karlovitz [Karlovitz et al., 1953], or may mitigate the turbulence through a process termed "*flow-relaminarization by combustion*". On the other hand, it is established that spray combustion occurs in non-premixed, or more realistically, in partially premixed mode depending on the injector design. In order to appraise the potential effects of turbulence on each of these combustion modes, it is necessary to first identify the parameters that may affect the flame structure. In an heterogeneous mixture, the reaction zone is attached to the high temperature region close to stoichiometric condition, and is convected and diffused with the mixing field. Unlike the premixed combustion mode, there is no flame speed, which would move the combustion front relative to its previous position.

However, there is a chemical time scale that can be related to the inverse of the quenching value of the scalar dissipation rate, χ_q. This latter value corresponds to the condition where heat loss by diffusion out of the reaction zone cannot be balanced by the heat release within the region of chemical reactions, so that, all mixing zones featuring this value are quenched. Viewed in this way, the scalar dissipation rate, χ_q, is then an eigenvalue of the laminar diffusion flame problem analogous to the laminar flame speed, s_L, that is an eigenvalue for the premixed laminar flame. It has the dimension of s^{-1}, and may then be considered as the inverse of a characteristic mixing time.

Since there is no physical velocity scale (e.g. propagation speed) in diffusion flames, no meaningful length scale (e.g. flame front thickness) can rigorously be defined. To mimic these physical quantities in diffusion flames, parameters such as diffusive layer thickness and diffusivity are generally used. Because the flame position is fixed by the mixing field, mixture fraction space rather than physical space should be considered to define the physical parameters that are used to set the dimensionless quantities of the turbulent combustion diagram. Thus, two dimensionless quantities are first defined, namely, the ratio of the mixture fraction fluctuations to the diffusion thickness, $\tilde{Z''^2}/(\Delta Z)_F^2$, and the time scale ratio, $\chi_q/\tilde{\chi}$. The flame thickness in the mixture fraction space, $(\Delta Z)_F$, may be defined using the stoichiometric mixture fraction gradient and a diffusion length scale, l_D. The latter is defined using a diffusion coefficient, D, and the strain rate, a, which corresponds to a velocity gradient, and may physically be interpreted as the inverse of the characteristic flow time. The diffusion thickness appearing in $\tilde{Z''^2}/(\Delta Z)_F^2$ (i.e. $(\Delta Z)_F^2$) covers all the diffusive layers surrounding the reaction zone, and therefore, corresponds to the preheat zone thickness in premixed flames. For hydrocarbon-air mixtures, Z_{st} is small enough so that $(\Delta Z)_F = (\chi_{st}/2a)^{1/2} \sim 2Z_{st}$.

By plotting the ratio $\tilde{Z''^2}/(\Delta Z)_F^2$ over the time scale ratio, $\chi_q/\tilde{\chi}$, the following combustion diagram shown in Figure 1.2 was established by Peters [1997]. One can notice that, for large mixture fraction variances (i.e. $\tilde{Z''^2} > (\Delta Z)_F^2$), mixture fraction fluctuations extend to sufficiently lean and rich mixtures so that the diffusion layers surrounding the reaction zones are separated. For small mixture fraction variances (i.e. $\tilde{Z''^2} < (\Delta Z)_F^2$), which may either be due to intense mixing or to partial premixing, a situation arises where diffusion layers surrounding the reaction zones are connected. The two regimes (i.e. connected and separated flame zones) are delimited by the states for which $\tilde{Z''^2}$ equals $(\Delta Z)_F^2$. According to the ratio of the scalar dissipation rates, if $\tilde{\chi}_{st} > \chi_q$, which means an excessive turbulence level, laminar flamelets cannot exist in the diffusion flame; this situation is denoted as flame extinction zone in Figure 1.2.

– *Turbulence-Spray interactions*

The spray properties are strongly related to the atomization mechanisms, the latter being determined by the design of the atomizer used to generate the spray. In the region of the primary atomization which is close to injector exit, under the effect of aerodynamic forces, the liquid sheet generated by the fuel injector becomes unstable and disintegrates into ligaments and

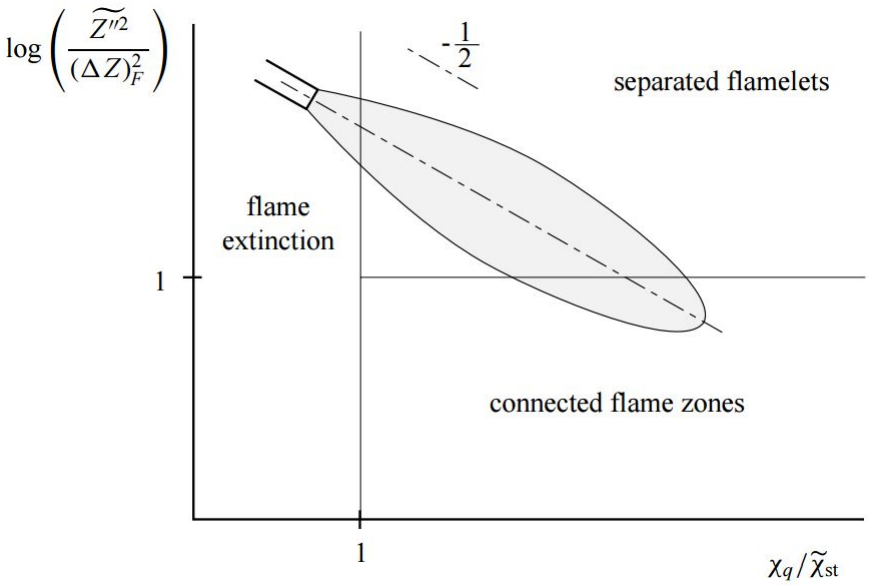

Figure 1.2: Regimes in non-premixed and partially premixed combustion (Peters, 2000)

large drops. The primary breakup occurs mainly through the Kelvin-Helmholtz instability at the droplet surface that results from the relative velocity between the gas and the liquid phases [Som and Aggarwal, 2010]. Once the droplets are detached from the intact liquid sheet, secondary breakup follows through Rayleigh-Taylor instabilities resulting from the denser, heavier fluid being accelerated by the lighter fluid [Baele and Reitz, 1999, Som and Aggarwal, 2010]. This process further leads to small spherical droplets stabilized by their surface tension. During this ensuing process, turbulence plays an essential role in altering the spray characteristics through shape change, breakup, collision, and agglomeration of the droplets. An overview of the main phases of an atomization process is provided in Figure 1.3.

The dynamics of the resulting spray is partly determined by its density. Physical phenomena related to the spray dynamics such as droplet breakup, droplet coalescence and the other interactions between the spray and turbulence are more difficult to capture in dense sprays (typically dispersed sprays having a fuel volume ratio, or fuel volume fraction, larger than 1%) than in a dilute spray (i.e. a dispersed spray having a liquid fuel volume fraction less than 1%). Their proper resolution requires the implementation of more elaborate models, which still constitute a challenging task as it is commonly assumed that the structure of a dense spray consists of an intact liquid core and a multiphase mixing layer surrounding the core [Faeth et al., 1995, Turner et al., 2012]. For example, depending on the fuel volume fraction (ratio between the volume of the fuel and that of the gas in the combustion chamber), two kinds of assumptions may be made when modelling turbulence/spray interactions: these are the “one-way coupling” and the “two-way coupling” approaches. The former assumption (also termed “direct coupling”) can account for the effects of turbulence on the droplets dispersion whilst neglecting any turbulence generated by droplet motion. The “one-way coupling” is applicable to dilute sprays since the

liquid phase has negligible effect on the properties of the gaseous phase. For the second assumption (also termed "reciprocal coupling"), the effects of turbulence on droplets dispersion along with those of droplet dynamics on turbulence are accounted for.

Depending on the operating conditions and the spray features, the effects of the spray on turbulence can be either an increase or a damping of the turbulence level. The detailed modelling of fuel atomization and the dynamics of the resulting spray is a challenging issue, inasmuch as it requires numerous intermediate models for the various physical phenomena involved. In the present study, the liquid fuel is assumed to be entirely atomized, and the initial droplet distributions are obtained from both experimental data and empirical correlations based on the configuration of the fuel injectors used. The fuel injection is simulated and modelling efforts are mainly devoted to a proper modelling of the spray dynamics along with its interactions with turbulence.

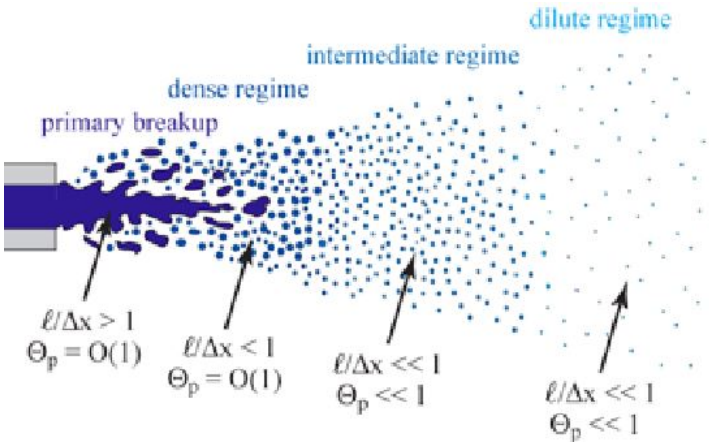

Figure 1.3: Phenomenological description of an atomization process (APTE, 2015)

– *Spray-Combustion interactions*

With the exception of liquid monopropellants which may directly burn in liquid phase owing to the combination of both fuel and oxidiser in the same chemical molecule, chemical reactions of combustion for most technical devices occur in the gaseous phase, far enough from the liquid interface. The spray evaporation is therefore an essential step before combustion can occur. However, considering the sizes and range of droplets in a given spray configuration as depicted in Figure 1.3, it is obvious that several spray burning regimes are likely to occur depending on the sizes of droplets, their number density, and their rate of heat exchange with the gaseous phase. In order to identify the various spray burning regimes that may take place, many research teams have so far conducted theoretical works to set a spray combustion diagram that can help distinguishing the main burning regimes. In this vein, by considering a quasi-stationary spherical monodisperse cloud of radius a_c carrying a uniform distribution of n droplets per unit volume in which each droplet has a radius, a, and a density, ρ_d, Chiu et al. [1982] developed a

combustion diagram illustrating various burning regimes under the fast-chemistry assumption.

The strategy used by these authors is based on a non-dimensional quantity termed as combustion group number, G. The latter is defined using a set of physical parameters, namely, the heat diffusive time into the cloud, $t_c = a_c^2/D_T$, the evaporation time, $t_e = (\rho_d/\rho)(a^2/D_T)$ of each droplet, and the characteristic time scale of variation of mass and thermal energy in the surrounding gas produced by the evaporation process, $t_g = (4\pi D_T a n/3)^{-1}$. In this diagram fully described in [Chiu et al., 1982, Urzay, 2011], the combustion-regimes are solely delimited by the lines corresponding to constant values of the combustion group number, $G = t_c/t_g = (a_c/a_g)^2$. Based on the definition of the number of droplets in the cloud, $N = 4\pi a_c^3 n/3$, and that of the droplets interspace distance, $\delta_d = (4\pi n/3)^{-1/3}$, the combustion group number may be related to the number of droplets and the dimensionless droplet interspace distance, δ_d, as follows: $G \sim N^{2/3} a/\delta_d$. This leads to the diagram in the $(\delta_d/a, N)$ space as shown in [Chiu et al., 1982]. For $G \gg 1$ an external sheath-combustion regime occurs, in which the heat does not have enough time to diffuse in the cloud and initiate the droplet evaporation, thereby restraining combustion and evaporation to occur only in thin superficial layers of thickness $\mathscr{O}(G^{-1/2})$ with respect to the cloud radius. For a sufficiently large Damköhler number, the fuel evaporate in the outer shell of the cloud burns in a diffusion flame that envelops the cloud. This regime is encountered only in large and dense spray clouds, where $(a_c/\delta_d \gg (\delta_d/a)^{1/2}$; for such spray configurations, a decrease of the droplet-number density, or of the cloud radius lead to a wider evaporation zone that can penetrate the central region of the cloud.

For $G = \mathscr{O}(1)$, the burning spray exhibits an external group-combustion regime, in which the time needed for heat diffusion in the cloud is sufficiently long to evaporate the droplets inside. The liquid in the central region of the cloud is at the boiling temperature and, as for the large-G case, the fuel vapour burns in a diffusion flame that envelops the cloud. For $G \leq \mathscr{O}(1)$ an internal group-combustion regime occurs as an intermediate limit between external sheath-combustion and single-droplet combustion; in this regime, the droplets evaporate without combustion in the central region of the cloud, which is surrounded by a diffusion flame and by an outer region of a similar size in which individual droplet burning occurs.

In the last configuration defined by $G \ll \mathscr{O}(1)$, the heat-diffusion time in the cloud is much shorter than the spray-gas interaction time, and each droplet burns individually with a surrounding flame. Realistically, this latter combustion regime cannot occur, unless the droplet interspace distance, δ_d, is larger than the flame diameter, $2a_F$.

In order to cope with some drawbacks of this combustion diagram such as its inability to predict the single-droplet burning regime, as well as the various combustion regimes that may occur for the same value of the combustion group number as a result of different values of the mass-loading ratio, $\alpha = t_v/t_g = (\rho_d/\rho)(a/\delta_d)^3$, the diagram was subsequently improved by Urzay [2011]. In the revised-diagram as shown in Figure 1.4, two different dimensionless quantities are introduced. These are the dimensionless mass-loading ratio, α/α_F, α_F being the critical mass-loading ratio, and the ratio between the vaporization Stokes number and the critical mass-

loading, St_v/α_F. The critical mass-loading ratio, α_F represents the value of α for which the droplet interspace distance is equal to the flame diameter (i.e. $\delta_d = 2a_F$). α_F is calculated using the large-activation-energy analyses for unity Lewis number [Williams, 1965] for sufficiently small Péclet numbers, $Pe = |\mathbf{v} - \mathbf{v}_d|\, a/D_T$ (i.e. when the flame lies within the Stokes region where relative advection is not important; $\mathbf{v}$ and $\mathbf{v}_d$ being respectively the gas and the droplet velocity vectors):

$$\alpha_F = (\frac{\rho_d}{8\rho}) = \{\ln\left(\frac{1+S_L}{S_L}\right) / \ln\left[1 + \frac{c_p\,(T - T_B) + q_r/S_L}{Lv}\right]\}^3 \tag{1.1}$$

where q_r is the chemical heat released per unit mass; $S_L = s/Y_{O_2}$ is a local stoichiometric coefficient in which s and Y_{O_2} stand for the stoichiometric air-to-fuel ratio and the oxidizer mass fraction in the vicinity of the fuel droplet, respectively.

The second physical parameter used to define the other new dimensionless quantities, St_v/α_F, namely, the vaporization Stokes number, St_v, represents the ratio of the single droplet evaporation time, t_e, to the diffusion time of heat into the cloud, t_c. Thus, the revised diagram describing the spray-combustion interactions is drawn in the $(\alpha/\alpha_F, St_v/\alpha_F)$ space instead of the $(\delta_d/a, N)$ space. This choice avoids dealing with the fuel dependency related to the presence of α_F which depends on the stoichiometric characteristics.

By contrasting this new diagram with the one described previously [Chiu et al., 1982], one can notice the following features: For $G \gg 1$, the external sheath-combustion regime discussed previously still takes place; for $G = \mathcal{O}(1)$ the evaporation layer thickness widens inward over a distance comparable to the radius of the cloud, and a transition occurs from external sheath-combustion to either external group-combustion or internal group-combustion regimes, depending on the liquid mass-loading, α. Especially, for $G = \mathcal{O}(1)$ and $\alpha/\alpha_F \gg 1$, or equivalently, for $\delta_d \ll 2a_F$, external group-combustion occurs. In this regime, all droplets in the cloud undergo evaporation, and since the droplet interspace distance is smaller than the flame radius of a single droplet, a single diffusion flame envelops the cloud. However, for $G = \mathcal{O}(1)$ and $\alpha/\alpha_F \gg 1$, or equivalently, for $\delta_d \gg 2a_F$, internal group-combustion occurs. This regime corresponds to an intermediate and transient regime toward incipient single-droplet combustion regimes, in which all droplets in the cloud undergo evaporation. However, since the droplet interspacing is larger than the flame radius of a single droplet, diffusion flames surrounding each droplet on the outer region of the cloud can be found, and a diffusion flame which envelops the spray core where external group-combustion is taking place, moves towards the center of the cloud to burn zones featuring a stoichiometric mixture. For $G \ll 1$, the time needed for the ambient thermal energy to diffuse inside the cloud is much faster than the spray-gas interaction time, and all droplets undergo evaporation. However, unless $\alpha/\alpha_F < 1$, a diffusion flame around a single droplet cannot be sustained. Therefore, for small group number, single-droplet combustion takes place for $\alpha/\alpha_F < 1$, while external group-combustion occurs for $\alpha/\alpha_F > 1$. Although, the two combustion diagrams are based on the assumptions of negligible droplet-kinematic effects (since the gaseous phase surrounding the fuel-cloud is considered at rest), they allow accessing some

relevant features of spray-combustion interactions. These two investigations, along with that by Reveillon and Vervisch [2005] show that it is challenging to establish universal diagrams if these effects are included, although they are very important in many technical devices. Depending on the ratio between the evaporation and combustion time scales, which can be measured using an evaporation-based Damköhler number, the combustion processes may occur either in homogeneous or in heterogeneous phase. In the first case, the reaction rate depends only on the distribution of the fuel vapour resulting from the spray dispersion and evaporation, while in the second case, the spray and flame are strongly coupled. Therefore, in addition to chemical reactions, the flame structure is also dependent on the spray parameters.

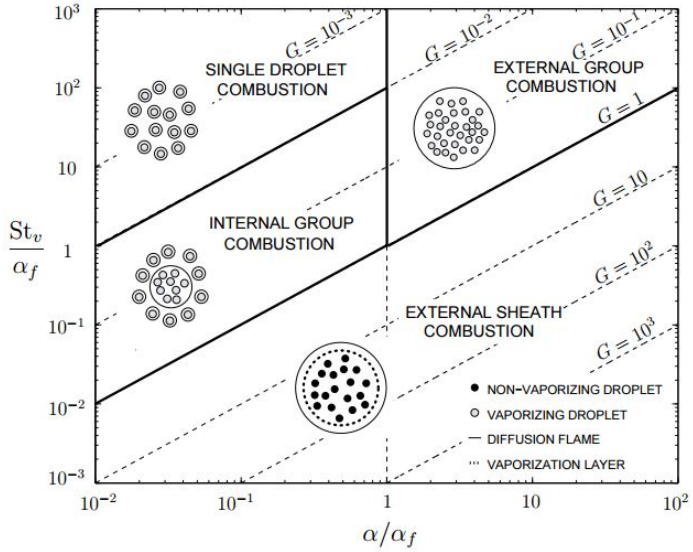

Figure 1.4: Burning regimes in spray combustion (Urzay, 2011).

1.2 Spray combustion theory and modelling approaches

Spray combustion is one type of two-phase reacting flows which are also referred as multiphase flows. This class of flow consists roughly of any moving mixture of substances having phases which are initially separated (e.g. mixture of gas with either liquid or solid), and involving exothermic chemical reactions. As mentioned earlier, the need to increase the surface-to-volume ratio leads to the fuel atomization, and consequently, to its injection in the form of a spray of small droplets. The size of droplets formed depends on the injector design as well as the fuel properties; but typically, they fall within the size range of 10-100μm diameter. The velocities of the resulting droplets depend on the injection conditions (e.g. injection pressure), droplet sizes, as well as the injector position. The droplets are dispersed under the influence of turbulence in the surrounding gas; they evaporate as a result of heat transfer from the surrounding hot gas, and the resulting fuel vapour mixes with air prior to combustion. Spray combustion involves therefore the liquid as the dispersed (or discrete) phase, and the surrounding gas as the continuous (or carrier) phase, all together with chemical reactions.

Each droplet (or particle) of the spray can then be viewed as an unattached body whose motion is primarily controlled by convection and gravity forces and consequently, one of the most challenging issues regarding the spray combustion modelling lies in the theoretical description of the liquid phase.

Considering the determining role of the dynamics of each phase in spray combustion as a whole, and the differences between the features of each phase, it is clear that conservation equations for each phase along with the modelling for the coupling between the two phases are needed. In this regard, there are globally three different approaches that can be used to simulate turbulent spray flames; these are the Eulerian-Eulerian(EE), the Eulerian-Lagrangian(EL), and the PDF formulations. All the three approaches are based on an Eulerian modelling of the gaseous phase, and they differ by their spray modelling techniques. Comprehensive reviews of spray combustion modelling and simulation can be found for instance in [Subramaniam, 2013, Jaegle et al., 2011, Senoner et al., 2009, Ge and Gutheil, 2006, Jones and Sheen, 1999, Vié et al., 2013, Kaufmann, 2004]. One can succinctly note here that, for the EE approach, both liquid and gas properties exist simultaneously at any given point in space, and they represent an average of the properties over the vicinity of that point, the size of that neighbouring zone being much larger than the average spacing between the droplets. The equations governing this formulation are then obtained by the standard control volume approach that accounts for the fluxes of mass, momentum, and energy conservation for the gas and the liquid phases entering and exiting the control volume. However, due to the averaging approach, such an approach (also termed as two-continua formalism) cannot provide a high resolution of phenomena featuring scales as small as (or smaller than) the average distance between the droplets. These drawbacks of the two-continua formalism, along with its inability to capture some relevant spray features such as the spray polydispersity and droplet crossing trajectories, have led to the development of advanced Eulerian spray models. Sample of these models and the related assumptions may be found in [Fevrier et al., 2005, Kaufmann et al., 2008]. The latter are based on a probabilistic formalism and addresses the main drawbacks of the two-continua formalism, while providing high resolution for very small scales. The probabilistic formulation leads to a mesoscopic Eulerian modelling, which is generally classified in the group of PDF approaches. In the EL approach, each droplet in the spray is viewed as a particle on which various transfers of mass, momentum and heat are applied during the calculation of its trajectory. As the dynamics of each particle is calculated in the EL approach, it is obvious that for sprays containing a very high number of droplets (e.g. several millions and more as it is generally the case for dense sprays), the calculation of the trajectories of all droplets requires computational resources very much higher than the capabilities of current computers unless the particles are clustered into small groups known as "stochastic particles" (i.e. groups of particles with neighbouring properties) which reduce considerably their number, and thereby the computing cost.

In this work, the liquid volume fraction, α is small enough (i.e. α<10%) thus justifying the dilute spray assumption. As this study aims also to formulate a CFD model that can be used to simulate a forced ignition of liquid-fuelled combustion chambers, the EL approach is retained not only for its ability to account for the polydispersity of the spray, but also because of its ability to offer resolution

on scales smaller than the average distance between the droplets [Williams, 1965, Sirignano, 1999]. Plus, the choice of the EL approach in the present study limits complex intermediate tasks that would be needed in a customized Eulerian-based spray model likely to account for realistic chemistry along with the chemical non-equilibrium effects due to turbulence.

Whatever the implemented approach, the global accuracy of results depends not only upon the proper inclusion of various interactions between the two phases, but also on the ability of the spray model to cope with the wide range of scales involved in the investigated phenomena. The equations governing the gaseous and the liquid phases are respectively presented in the following subsections.

1.2.1 Mathematical formulation of the EE and PDF approaches

The two-continua and the probabilistic formalisms may conceptually be viewed as two Eulerian modelling approaches of the spray. In fact, the two approaches do not deal with the dynamics of each droplet in the spray; the liquid phase is assumed to be a continuum, and their operating modes differ solely by the filtering procedure: a volumetric filtering is used in the former approach, while the statistical-type filtering is used in the second approach. Detailed explanations and assumptions regarding the two-continua formalism are provided in [Kaufmann, 2004, Kaufmann et al., 2008]. The intermediate steps used to derive the liquid phase equations according to the two-continua formalism can be summarized as follows: (i) the equations for each phase are first multiplied by a phase indicator function, ξ_ϕ defined so as to equal 1 in the ϕ phase and 0 elsewhere; (ii) the commutativity relations are thereafter applied between the derivative operators and ξ_ϕ; (iii) the operator for the volumetric filtering is applied on the control volume, and the resulting unclosed terms are modelled. According to the PDF formulation, a detailed description of the derivation procedure and the related assumptions are provided in [Fevrier et al., 2005, Kaufmann et al., 2008].

One can succinctly note that the approach is based on the gas-kinetic theory, and involves the following main steps: (i) A probability density function (PDF) is defined based on a conditional ensemble average of the particle properties for a given turbulent flow field realization; (ii) A transport equation is derived for this PDF, and the resulting PDF is used to define a local statistical averaging of the fuel properties; (iii) the transport for the PDF is thereafter multiplied by a given function of the spray, Ψ, and the statistical filtering described earlier is applied to the resulting equation with the aim of obtaining the Enskog's equation; (iv) the conservation equations governing the mean (also termed as mesoscopic) motion are obtained by replacing the spray function, Ψ, by the appropriate spray quantities; (v) Finally, the uncorrelated motions and the terms governing the exchange with the carrier phase are modelled. As this second approach is relatively more robust compared to the two-continua formalism (in its ability to deal with the whole range of scales, while enabling modelling of unresolved motions), only the equations governing the PDF is provided in the present chapter.

Gaseous phase equations

The conservation equations governing the dynamics of the gaseous phase in the Eulerian formu-

lation are derived by applying the mass, momentum, energy and species balance on a control volume selected in the flow field. Based on the two-way coupling assumption, these equations may be written as follows:

$$\frac{\partial \rho}{\partial t} + \frac{\partial \rho U_i}{\partial x_i} = \dot{S}_m \tag{1.2}$$

$$\frac{\partial \rho U_i}{\partial t} + \frac{\partial \rho U_i U_j}{\partial x_j} = -\frac{\partial P}{\partial x_i} + \frac{1}{R_e}\frac{\partial \sigma_{ij}}{\partial x_j} + \dot{S}_{mU_i} \tag{1.3}$$

$$\frac{\partial \rho h}{\partial t} + \frac{\partial (\rho h + P) U_j}{\partial x_j} = \frac{\partial}{\partial x_i}\left(\frac{\mu C_p}{R_e Pr}\frac{\partial T}{\partial x_i}\right) + \frac{1}{R_e}\frac{\partial \sigma_{ij} U_j}{\partial x_i} + \dot{\omega}_h + \dot{S}_h \tag{1.4}$$

$$\frac{\partial \rho Y_k}{\partial t} + \frac{\partial \rho Y_k U_j}{\partial x_j} = \frac{\partial}{\partial x_i}\left(\frac{\mu}{R_e Sc}\frac{\partial Y_k}{\partial x_i}\right) + \dot{\omega}_{Y_F} + \delta_{kF}\dot{S}_m \tag{1.5}$$

where the viscous stress tensor, σ_{ij} is defined by

$$\sigma_{ij} = \mu\left(\frac{\partial U_i}{\partial x_j} + \frac{\partial U_j}{\partial x_i}\right) - \frac{2}{3}\mu\frac{\partial U_k}{\partial x_k}\delta_{ij},$$

and the mechanical pressure which allows accounting for the normal stresses in the momentum equation, P, is calculated using the equation of state for perfect gases,

$$P = \rho RT. \tag{1.6}$$

In these equations, $j = 1,2,3$, while $j = 1,...N$; ρ and u_j stands respectively for the density, and the velocity component in the j^{th} direction; Y_k is the mass fraction of the k^{th} species, while E_t stands for the sensible enthalpy. Re, Pr and Sc are respectively the Reynolds, the Prandtl and the Schmidt numbers. The coupling between discrete and continuous phases is achieved through the source terms, $\dot{S}_m$, $\dot{S}_{mU_i}$, and $\dot{S}_h$ accounting respectively for the transfer of mass, momentum and energy between the two phases. The source term of mass may be written as:

$$\dot{S}_m = \rho_d \frac{\pi}{4}\frac{1}{V}\sum_l a^{l^3}/t_v^l \tag{1.7}$$

$$\dot{S}_{mU_i} = -\frac{1}{V}\sum_l -\frac{dm_d^l \mathbf{V}_d^l}{dt} \tag{1.8}$$

where m_d^l is the mass of the $l-th$ droplet. Also, the energy variation of the gaseous flow induced by the droplets inside the cell volume V is defined by:

$$\dot{S}_h = -\frac{1}{V}\sum_l -\frac{dm_d^l C_p^s T_d^l}{dt} \tag{1.9}$$

Liquid phase equations

In order to apply the derivation steps listed above for the spray-PDF formulation, a function, W_p describing the time history of a given particle in the phase space is first defined. Considering that each particle is characterized by its position, $\mathbf{x}_p$, velocity, $\mathbf{u}_p$, temperature, T_p and mass, m_p, this function

may be expressed as $W_p = F_p(\alpha_p, \beta_p, \gamma_p, \mathbf{x}, t)$, where α_p, β_p, γ_p, and $\mathbf{x}$ are respectively the velocity, temperature, mass, and position at the time t. Thereafter, an ensemble average over dispersed phase realization $\langle . \rangle$ conditioned by any given carrier phase realization, H_F, is applied to define the following conditional particle PDF:

$$\begin{aligned} f_p(\alpha_p, \beta_p, \gamma_p; \mathbf{x}, t | H_f) &= \langle W_p^{(m)}(\alpha_p, \beta_p, \gamma_p; \mathbf{x}, t) | H_f \rangle \\ &= \lim_{\mathscr{N}_p \to +\infty} \left[\frac{1}{\mathscr{N}_p} \sum_{m=1}^{\mathscr{N}_p} W_p^{(m)}(\alpha_p, \beta_p, \gamma_p; \mathbf{x}, t) \right] \end{aligned} \tag{1.10}$$

where $W_p^{(m)}$ is the fine grid PDF of the realizations of position, velocity, mass and temperature in time of any given particle, and H_f stands for a given carrier fluid flow realization. Physically, this function represents the local instantaneous probable number density of particles with a translation velocity $u_p = \alpha_p$, a temperature $T_p = \beta_p$ and a $m_p = \gamma_p$ at a location, $\mathbf{x}$, for a given time, t [Kaufmann, 2004, Boileau et al., 2008]. The conditional PDF obeys a Boltzmann-type equation, which accounts for momentum exchange with the carrier phase, gravity force, and particle–particle collisions:

$$\begin{aligned} \frac{\partial}{\partial t} f_p + \frac{\partial}{\partial x^j} \alpha_{p,j} f_p = \left(\frac{\partial f_p}{\partial t} \right)_{coll} - \frac{\partial}{\partial \alpha_{p,j}} \langle \frac{du_{p,j}}{dt} | \alpha_p, \beta_p, \gamma \rangle f_p - \frac{\partial}{\partial \beta_p} \langle \frac{dT_p}{dt} | \alpha_p, \beta_p, \gamma \rangle f_p \\ - \frac{\partial}{\partial \beta_p} \langle \frac{dm_p}{dt} | \gamma_p, \beta_p, \gamma \rangle f_p \end{aligned} \tag{1.11}$$

where $\left(\frac{\partial f_p}{\partial t} \right)_{coll}$ stands for the temporal change of the PDF due to particles interactions such as collisions, coalescence and breakage; the $\frac{d}{dt}$ term represents the Lagrangian variation of the PDF due to momentum, heat and mass exchanges with the carrier phase, or to the volumic effects (e.g. gravity, radiation, etc.). By multiplying the Boltzmann-type PDF-transport equation by any particle function, Φ, an Enskog-type equation is derived for the corresponding particle function as follows:

$$\begin{aligned} \frac{\partial}{\partial t} \rho_l \breve{\alpha}_l \langle \Phi \rangle_l + \frac{\partial}{\partial x_j} \rho_l \breve{\alpha}_l \langle u_{p,j} \Phi \rangle_l = \mathbb{C} + (m_p \Phi) + \rho_l \breve{\alpha}_l \langle \frac{du_{p,j}}{dt} \frac{\partial \Phi}{\partial u_{p,j}} \rangle_l + \rho_l \breve{\alpha}_l \langle \frac{dT_p}{dt} \frac{\partial \Phi}{\partial T_p} \rangle_l \\ + \rho_l \breve{\alpha}_l \langle \frac{dm_p}{dt} \left(\frac{\partial \Phi}{\partial m_p} + \frac{\Phi}{m_p} \right) \rangle_l . \end{aligned} \tag{1.12}$$

Considering that the velocity of each particle located at x, at a given time t, $u_p(x,t)$ can be divided into two parts according to the following relation:

$$u_p(x,t) = \breve{u}_l + u_l'' \tag{1.13}$$

where $\breve{u}_l$ is the velocity of the mesoscopic motion also termed as *mesoscopic velocity*, while u_l'' stands for the velocity of the random uncorrelated motion also termed as *uncorrelated velocity*. Based on this decomposition, the set of equations governing the mesoscopic motion of the liquid phase can be deduced by replacing the various particle functions in the general form of the Enskog equation written earlier. The conservative equation for the particle density (i.e. $\Phi = 1/m_p$), the volume fraction

($\Phi = 1$), the momentum (i.e. $\Phi = \mathbf{u}_p$), the uncorrelated energy ($\phi = 1/2(u_{p,j} - \breve{u}_{l,j})(u_{p,j} - \breve{u}_{l,j}) = 1/2u''_{p,j}u''_{p,j}$) and the enthalpy ($\Phi = h_{s,p}$) are respectively given by the following equations:

$$\frac{\partial \breve{n}_l}{\partial t} + \frac{\partial}{\partial x_i}\breve{n}_l \breve{u}_{l,i} = \mathbf{T}(m_p^{-1}) + \mathbf{C}(1) \tag{1.14}$$

where $\mathbf{T}(\Phi) = -\frac{\partial}{\partial x_i}\rho_l \breve{\alpha}_l \langle u''_{p,i}\Phi \rangle_l$ is the operator of uncorrelated fluxes.

$$\frac{\partial \rho_l \breve{\alpha}_l}{\partial t} + \frac{\partial}{\partial x_i}\rho_l \breve{\alpha}_l \breve{u}_{l,i} = \mathbf{T}(1) + \mathbf{C}(m_p) + \Gamma_l \tag{1.15}$$

where $\mathbf{T}(1) = 0$; Γ_l is the rate of mass change due to evaporation, which can be expressed by $\Gamma = -\rho_l \breve{\alpha}_l \langle \frac{1}{m_p}\frac{dm_p}{dt} \rangle_l$

$$\frac{\partial \rho_l \breve{\alpha}_l \breve{u}_{l,j}}{\partial t} + \frac{\partial}{\partial x_j}\rho_l \breve{\alpha}_l \breve{u}_{l,i} \breve{u}_{l,j} = \mathbf{T}(u''_{p,i}) + \mathbf{C}(m_p \mathbf{u}_p) + F_{d,i} + \Gamma_{u,i} \tag{1.16}$$

where $\mathbf{T}(u''_{p,i})$ is the momentum carried by the uncorrelated motion; $\mathbf{C}(m_p\mathbf{u}_p)$ is the momentum exchange between the particles through collisions, breakage and coalescence; $F_{d,i} = \rho_l \breve{\alpha}_l \langle \frac{F_{p,i}}{m_p} \rangle_l = \breve{n}_l F_{p,i_l}$ is the momentum exchange with the gaseous phase as a result of the drag force acting on each particle; $\Gamma_{u,i} = \rho_l \breve{\alpha}_l \langle \frac{u_{p,i}}{m_p} + \frac{dm_p}{dt} \rangle_l = \rho_l \breve{n}_l \{u_{p,i}\frac{dm_p}{dt}\}_l$ stands for the momentum exchange due to evaporation.

$$\frac{\partial \rho_l \breve{\alpha}_l \breve{h}_{s,l}}{\partial t} + \frac{\partial}{\partial x_j}\rho_l \breve{\alpha}_l \breve{u}_{l,j} \breve{h}_{s,l} = \mathbf{T}(h''_p) + \mathbf{C}(m_p h_{s,p}) + \Lambda_l + \Phi_l \tag{1.17}$$

where $\mathbf{T}(h''_p)$ is the enthalpy carried by the uncorrelated motion, while $\mathbf{C}(m_p h_{s,p})$ represents the enthalpy exchange between particles.

$\Lambda_l = \rho_l \breve{\alpha}_l \langle \frac{h_{s,p}}{m_p} + \frac{dm_p}{dt} \rangle_l$ is the enthalpy change due to the mass exchange with the gaseous phase; $\Phi_l = \rho_l \breve{\alpha}_l \langle \frac{dh_{s,p}}{dt} \rangle_l$ is the enthalpy change due to heat transfer by conduction in the liquid phase.

$$\frac{\partial \rho_l \breve{\alpha}_l \delta\breve{\theta}_l}{\partial t} + \frac{\partial}{\partial x_j}\rho_l \breve{\alpha}_l \delta\breve{\theta}_l = \mathbf{T}(\frac{1}{2}1/2u''_{p,j}u''_{p,j}) + \mathbf{C}(\frac{1}{2}1/2m_p u''_{p,j}u''_{p,j}) + W_\theta + \Gamma_\theta + \mathbf{U}_\theta \tag{1.18}$$

where $\mathbf{T}(\frac{1}{2}1/2u''_{p,j}u''_{p,j})$ represents the uncorrelated energy carried by the uncorrelated motion;

$\mathbf{C}(\frac{1}{2}m_p u''_{p,j}u''_{p,j})$ is exchange of uncorrelated energy between the particles;

$W_\theta = \rho_l \breve{\alpha}_l \langle u''_{p,j}\frac{F_{p,i}}{m_p} \rangle_l = \breve{\alpha}_l \langle u''_{p,j}\frac{F_{p,i}}{m_p} \rangle_l$ stands for the change in energy due to the drag;

$\Gamma_\theta = \rho_l \breve{\alpha}_l \langle \frac{1}{2}\frac{u''_{p,j}u''_{p,j}}{m_p}\frac{dm_p}{dt} \rangle_l = \breve{n}_l \{1/2u''_{p,j}u''_{p,j}\frac{dm_p}{dt}\}_l$ is the change in uncorrelated energy due to the mass transfer;

and $\mathbf{U}_\theta = -\rho_l \breve{\alpha}_l \delta\breve{R}_{l,ij}\frac{\partial \breve{u}_{l,j}}{\partial x_j}$ account for the effects of the uncorrelated tensor on the uncorrelated energy, $\delta\breve{R}_{l,ij}$.

These equations derived for the mesoscopic motion can be further simplified, depending on the features of the investigated configurations (e.g. dilute or dense spray). For instance, for a dilute monodisperse spray, such simplifying assumptions based on a dilute spray along with the resulting equations and the modelling approaches for the unclosed terms may be found in [Boileau et al., 2008].

1.2.2 Mathematical formulation of the EL approach

As mentioned earlier, the two-continua formalism is not able to resolve phenomena on the scale of the order of droplet spacing since averaging occurs over a distance larger than the droplet spacing. In order to cope with such drawbacks, the Eulerian-Lagrangian approach has so far been applied to various spray configurations [Hollmann and Gutheil, 1998, Sanjosé et al., 2011, Chrigui et al., 2012, Jones et al., 2012, Fossi et al., 2015a,c]. In this approach, the set of equations governing the dynamics for gaseous phase remains the same as those of the EE approach. The droplet properties are no longer governed by the equations of two-continua formalism or those of the mesoscopic motion presented earlier. Instead, ordinary differential equations are written that describe the change in droplet properties along the droplet trajectory. Depending on the spray configuration, namely, the number of droplets and their properties, the droplets can be followed individually, or clustered into groups of representative particles gathering a fixed number of droplets with neighbouring properties. It is assumed that the initial conditions are continuous, so that any droplet that begins in the neighbourhood of some given droplet remains in the neighbourhood of that droplet as they both move. Because such a calculation approach involves a fixed number of droplets, the droplet numbers are automatically conserved and consequently, there is no need to develop an equation for the conservation of droplet numbers. The droplets (or representative particles) need to be tracked, and their trajectories are determined by solving the following equations [Sanchez et al., 2015, Chrigui et al., 2012]:

$$\frac{dx_{li}^{(k)}}{dt} = u_{li}^{(k)} \tag{1.19}$$

where $x_{li}^{(k)}$ is the position of the center of the particle (or representative particle) in the $k-th$ size group. The motion of any Lagrangian particle, moving in an Eulerian framework is governed by the Newton's second law:

$$\frac{du_{li}^{(k)}}{dt} = \sum_j \left(F_i^{(k)}\right)_j \tag{1.20}$$

where $\left(F_i^{(k)}\right)_j$ is a given force, j acting of the droplet. Unfortunately, this equation cannot be solved without knowing the forces acting on each droplet. For the full spray equation, $\left(F_i^{(k)}\right)_j$ includes many types of forces, and those relevant to combustion are the drag force, the thermophoretic force [1], the Saffmann Lift force [2], the Brownian force [3], the Faxen force [4], and some additional effects such as

1. Force experienced by a small particle suspended in a gas that has a temperature gradient
2. Lift force experienced by a sub-micron particle because of the shear effects
3. Force experienced by a sub-micron particle due to the Brownian motion
4. Force due to the curvature of the flow

those related to the Magnus (or rotation) effects, to the gravity, and to the particle radiation interaction. Most of these forces can be neglected depending on the spray feature, namely, the high density ratio between the two phases, and the droplet size which are not generally sub-microns for current atomizers. These include Saffmann and Brownian forces; Magnus effects can also be neglected considering that droplets rotation are not very important. The remaining forces to be considered in the previous equations are those due to the drag, the temperature gradient, and the gravity. Based on these simplifying assumptions, the following equation can be derived for the droplets motion:

$$\frac{du_{li}^{(k)}}{dt} = F_D^{(k)}\left(u_i - u_{li}^{(k)}\right) + \frac{g_i(\rho_l - \rho)}{\rho_l} + F_{Th} \tag{1.21}$$

Where F_{Th} is the themophoretic force per unit particle mass expressed as follows:

$$F_{Th} = -D_{T,l}\frac{1}{m_p T}\frac{\partial T}{\partial x_j}, \tag{1.22}$$

where the thermophoretic coefficient, $D_{T,l}$, is either defined as a constant or calculated using the correlation by Talbot et al. [1980]. $F_D^{(k)}(u_i - u_{li}^{(k)})$ is the drag force per unit particle mass, and F_D is defined by:

$$F_D = \frac{18\mu}{\rho_l d_l^2}\frac{C_D R_e}{24} \tag{1.23}$$

where u_i is the fluid flow velocity; u_{li} is the particle velocity; μ is the molecular viscosity of the fluid; ρ is the fluid density; ρ_l is the density of the particle; and d_l is the particle diameter. The relative Reynolds number, R_e is defined as

$$R_e = \frac{\rho d_l |u_{li}^{(k)} - u_i|}{\mu} \tag{1.24}$$

The C_D term appearing in drag force expression is the drag coefficient, which may be calculated using various laws such as the spherical drag law, the non-spherical drag law, Stokes Cunningham drag law, the High-Mach-Number drag law, and the dynamics drag model. The suitable drag coefficient law is determined by the features of the investigated spray. For instance, in some configurations of turbulent spray flow, the Weber number, $W_e = \rho {u_i}^2 d_l/\sigma$, (i.e. ratio of the inertial forces to the surface tension) is larger than the critical value, $W_{ec} \sim 12$, and therefore, the spray undergoes substantial fluctuations. In such configurations, the dynamic drag model is more suitable, considering the dependency of the droplet coefficient upon the droplet shape, and the ability of the dynamic drag model to take into account the droplet shape distortion that occurs at large Weber number. In the model formulation, the shape of the droplet is assumed to change from spherical shape to a disk shape. The effects of the corresponding distortion are accounted for by linearly varying the drag between that of the sphere, and a value of 1.54 corresponding to a disk according to Liu et al. [1993]. The drag coefficient is then expressed by following equation:

$$C_d = C_{d,sphere}(1 + 2.63y), \tag{1.25}$$

where the drag of the sphere, C_{sphere} is calculated according to the following relationship:

$$C_{d,sphere} = \begin{cases} 0.424 & R_e > 1000 \\ \frac{24}{Re}\left(1 - \frac{1}{6}R_e^{2/3}\right) & R_e \leq 1000 \end{cases} \tag{1.26}$$

The droplet distortion y is obtained by solving the following differential equation, which is derived from the Taylor Analogy Breakup model (also termed as TAB model) as described in [O'Rourke and Amsden, 1987].

$$\frac{d^2y}{dt^2} = \frac{C_F}{C_b}\frac{\rho}{\rho_l}\frac{u_i^2}{r^2} - \frac{C_k}{\rho_l}\frac{\sigma}{r^3}y - \frac{C_d}{\rho_l}\frac{u_l}{r^2}\frac{dy}{dt} \tag{1.27}$$

1.3 Spray dynamics

As discussed in the previous section, the suitability of the modelling approaches used in spray combustion is strongly related to the spray features. The latter is determined by the injector design and pressure difference as well as the sub-models used to describe droplet evaporation and their interactions. This section provides an overview of the mechanisms involved in spray generation along with the models used to describe phenomena occurring in the spray until its complete conversion into vapour.

1.3.1 Fuel Atomization

Phenomenologically, atomization can be defined as a physical process whereby a volume of liquid is converted into a multiplicity of small droplets, the main goal being the production of high ratios of surface-to-mass (or volume) in the liquid phase, which is propitious to a high evaporation rate. In gas turbine combustion chambers, atomization is generally accomplished by spreading the fuel into a thin sheet to induce instability and promote disintegration of the sheet into droplets. This thin sheet may be obtained by discharging the liquid fuel through orifices with specially shaped passageways, by forcing it through narrow slots, by spreading it over a metal surface, or by feeding it to the centre of a rotating disk or cup. Whatever the means by which atomization is achieved (hydraulic, pneumatic, or mechanical) the primary function of an atomizer is always to attenuate the fuel into a fine jet or thin sheet from which ligaments and ultimately droplets will be produced, and to distribute resulting droplets throughout the combustion zone in a controlled pattern and direction. In the gas turbine industry, injectors design has been subjected to continuous improvements, with ultimate goal of achieving the characteristics of an ideal fuel injector. A detailed discussion of these injector characteristics are provided in [Lefebvre, 1983]; the most relevant ones include: (i) the good atomization over the entire range of fuel flows; (ii) the rapid response to throttle changes; (iii) the freedom from flows instabilities; (iv) the low susceptibility to gum formation by heat effects; (v) the low susceptibility to blockage by contaminants and to carbon buildup on the nozzle face; (vi) the capability for scaling, to provide design flexibility; (vii) the low cost, the light weight, the ease of manufacture, and the ease of removal for servicing; (viii) low susceptibility to damage during manufacture and installation. In addition to these criteria, an ideal injector should also provide an easily ignitable mixture, a ratio of maximum to minimum fuel flow that exceeds the ratio of maximum to minimum airflow, the controlled dispersion of the fuel throughout the primary combustion zone, and an exit gas temperature distribution that is insensitive to variations in fuel flow rate. The main types of atomizers found in gas turbine indus-

try include pressure-swirl atomizers, fan-spray atomizers, rotary atomizers, air-assist atomizers, and air-blast atomizers.

Pressure-swirl atomizers

The simplest form of pressure-swirl atomizer is the so-called *Simplex* atomizer where fuel is fed into a swirl chamber through tangential ports that give the fuel a high angular velocity, thereby creating an air-cored vortex. The swirl chamber exit is the final orifice, and the rotating liquid flows through its orifice under both axial and radial forces to emerge from the atomizer in the form of a hollow conical sheet, the cone angle being determined by the relative magnitude of the radial and axial velocities at the injector exit. For such an atomizer, the fuel properties (e.g. viscosity), the ambient pressure, and the fuel-injection pressure influence the global properties of the resulting spray, namely, the spray-cone angle, the spray penetration, and the mean diameter of the spray (e.g. the Sauter Mean Diameter, SMD). For instance, an increase in the fuel-injection pressure differential causes the fuel to be discharged from the atomizer at a higher velocity. This raises the Weber number, thereby promoting a finer atomization.

Despite the ability of *Simplex* atomizers to produce spray with much wider spray-cone angles compared to that exhibited by plain-orifice atomizers which are rather narrow (precluding therefore their use for most practical gas turbine applications), they feature some drawbacks which are mainly related to the fact that, the flow rate varies as the square root of the pressure differential across the injector. Consequently, doubling the fuel flow rate requires a fourfold increase in fuel-injection pressure. This basic drawback of the simplex atomizer has led to the development of various *wide-range* pressure swirl atomizers, such as *duplex*, *dual-orifice* and *spill* atomizers, in which ratios of maximum to minimum fuel output in excess of 20 can readily be achieved with fuel-injection pressures not exceeding 7 MPa.

The design procedure for *duplex* atomizers is almost similar to that for *simplex* atomizers. The main difference between the two configurations lies in the fact that its swirl number employs two sets of tangential swirl ports. The first set is the primary port for the flows encountered when the engine is idling or operates at high altitude, while the other set consists of the main passage for the large flows required under normal operating conditions. Such a design leads to a superior performance of the duplex nozzle, especially at low fuel flows. However, the *duplex* atomizer still features some drawbacks, namely, the tendency of the spray cone angle to be about 20^o smaller in the combined flow range than in the pilot flow range. According to the *dual-orifice* atomizer, it consists of two simplex nozzles that are fitted concentrically, one inside another. The pilot nozzle is mounted on the inside, and the arrangements of pilot and main nozzles are done in such a way that the pilot spray does not interfere with either the main orifice or the main fuel within the orifice. At low fuel flows all the fuel is supplied from the pilot nozzle, which features a low flow number. Once the fuel pressure reaches a predetermined value located between 1.4 and 3 MPa (depending on the engines), the pressurizing value opens and admits fuel to the main nozzle, which has a higher flow number. This new design

allowing all the fuel to flow through the pilot nozzle leads to an atomization quality that tends to be high, since a high fuel pressure is needed to force the fuel through the small ports in the pilot swirl chamber.

Although providing high spray quality for low flow rates, the performance of *dual-orifice* atomizers are precluded in some regimes. In fact, when the pressurising valve opens and admits fuel in the main nozzle, the atomization quality becomes poorer as a result of low main fuel pressure. Even if the atomization quality can be improved with a further increase in fuel flow, there is inevitably a range of fuel flows, starting from the point at which the pressurizing valve opens. The adverse effects of this particular drawback of the *dual-orifice* atomizer can be mitigated when designing the injector, by ensuring that the opening of the pressurized valve does not occur at the same time with an engine operating point at which high combustion efficiency and low pollutant emissions are essential. The last type of the wide-range pressure-swirl atomizers listed earlier, namely, the *spill* atomizer is basically designed as the *simplex* atomizer, and provides some improvements over the *duplex* and the *dual-orifice* atomizers. In fact, instead of being solid as for *simplex* atomizers, the rear wall of the swirl chamber contains an annular passage through which fuel can be "spelled" away from the atomizer. Fuel is supplied to the swirl chamber at high pressure and high flow rate, and the fraction of fuel injected into the combustion zone is varied and controlled by a valve located in the spill return line. Because of this constant use of a relatively high pressure, the *spill-return* atomizer is capable of producing an efficient fuel atomization, even at extremely low fuel flows. Therefore, a most useful characteristic of the *spill-return* atomizer is the wide range of fuel flows over which atomization quality is high. Other relevant features include the absence of moving parts and, because the flow passages are designed to handle large flows freedom from blockage by contaminants in the fuel (e.g. gum formation due to the fuel aromatic content). This latter aspect is relevant, especially when considering eventual increase of gas turbine fuels in aromatic contents. In spite of these assets, the *spill-atomizer* features some drawbacks that limit its use, namely, the large variation in spray cone angle with changes in fuel flow rate. The effect of a reduction in flow rate is a spray cone widening, since the axial component of velocity is lowered without affecting the swirl component. From a combustion viewpoint, a spray angle that narrows with a reduction in fuel flow rate is much more desirable. Other drawbacks of the *spill-return* atomizer include the need of large capacity pumps to handle the large recirculating flows, and the fact that the fuel metering is more complicated than with other types of atomizers.

Fan-spray atomizers

Fan-spray atomizers are used to generate flat sprays. They consist of shaped orifices; each orifice forces the liquid into two opposing streams within itself, so that a flat spray issues from the orifice and spreads out in the shape of an annular sector. Although there are some configurations of fan-spray atomizers that can produce very fine sprays (SMD <25 μm), it is generally found that drop sizes from fan-spray atomizers are larger than those from swirl-spray atomizers of equal flow rate. Fan-spray atomizers are more suitable for small annular combustion chambers, as they provide a good lateral spread of fuel, and allow therefore minimizing the number of injection points.

Rotary atomizers

In the rotary atomizer, liquid is fed onto a rotating surface, where it spreads out fairly uniformly under the action of a centrifugal force. The rotating surface may take the form of a flat disk, vaned disk, cup, or slotted wheel, with diameters varying from 25 to 450 mm. This atomizer configuration provides some improvements such as its extreme versatility, its ability to atomize successfully liquids that vary widely in viscosity, and its ability to control the thickness and uniformity of the liquid sheet by regulating the liquid flow rate and the rotational speed. Several mechanisms of atomization are observed with a rotating flat disk, depending on the fuel flow rate and the rotational speed of the disk. At low flow rates for instance, the liquid spreads out across the surface, and is centrifuged off as discrete drops of uniform size, each drop drawing behind it a fine ligament. The drops finally separate from the ligaments, which are themselves converted into a series of fine drops of fairly uniform size. A further increase in flow rate leads to a condition in which the ligaments can no longer accommodate the flow of liquid. A thin continuous sheet is formed that extends from the lip until the contraction force at the free edge due to surface tension is just equal to the kinetic energy of the advancing sheet. A thick rim is produced, which again disintegrates into ligaments and drops. From this brief description of the *rotary atomizer*, it is expected the mean droplet size to diminish with an increase in rotational speed, and to increase with flow rate and fuel viscosity. This expectation is validated by various theoretical and experimental investigations of the factors governing the atomization properties of rotary atomizers, which have resulted in a number of drop-size relationships [Lefebvre, 1989, Bayvel and Orzechowski, 1993].

Air-assist atomizers

This group of atomizers are used to circumvent some drawbacks of pressure-swirl atomizers, namely, the *simplex* atomizer. In fact, a basic drawback of *simplex* atomizers lies in the fact that, if the swirl ports are sized to pass the maximum fuel flow at the maximum fuel-injection pressure, then the fuel pressure differential is too low to give good atomization at the lowest fuel flow. This problem is generally overcome by using dual-orifice or duplex nozzles; another alternative approach consists of employing the simplex swirl-atomizer, which always gives good atomization at high fuel flows, and using air or stream to strengthen the atomization process at low fuel flows. A wide variety of designs of this type have been produced for use in industrial gas turbines and oil-fired furnaces [Ashgriz, 2011]. In the internal-mixing type, the spray cone angle is minimum for maximum airflow, and the spray widens as the airflow is reduced. This type of atomizer is very suitable for highly viscous fuels, and good atomization can be obtained even for very low fuel flow rates. External-mixing types can be designed to give a constant spray angle at all fuel flows. They have the advantage that there is no danger of fuel finding its way into the air line. However, their utilization of air is less efficient, and consequently their power requirements are higher. In spite of all these good features, there is a main drawback from a gas turbine standpoint, namely, the need for an external supply of high-pressure air. This drawback makes air-assist atomizers not suitable for aircraft applications. They are instead more attractive for large industrial engines, especially as the high-pressure air is needed only during engine

light-up and acceleration.

Airblast atomizers

Air-assist and *airblast* atomizers have the same operating mode, since both use kinetic energy of a flow airstream to shatter the fuel jet or sheet into ligaments and then droplets. The main difference between the two configurations lies in the quantity of air employed and its atomizing velocity. With air-assist nozzles, where air is supplied from a compressor or a high-pressure cylinder, it is important to keep the air flow rate down to a minimum. However, as there is no special restriction on air pressure, the atomizing air velocity can be made very high. Air-assist atomizers are characterized by their use of a relatively small quantity of very high-velocity air. However, because the air velocity through an atomizer is limited to a maximum value (typically around 120 m/s) corresponding to the pressure differential across the liner wall, a larger amount of air is required to achieve good atomization. Hence, this air is not wasted, since after atomizing the fuel, it flows into the primary zone, where it provides part of the air required for primary combustion.

Airblast atomizers have many advantages over pressure atomizers, especially in their application to gas turbine engines with high pressure ratios. They require lower fuel pressures and produce a finer spray. Moreover, because the *airblast* atomization process ensures thorough mixing of air and fuel, the resulting combustion process generates very low soot formation and a blue flame of low luminosity, resulting in relatively cool liner walls with minimal exhaust smoke. A further asset of the *airblast* atomizer is that it provides a sensibly constant fuel distribution over the entire range of fuel flows. This offers an important practical advantage in terms of exit temperature distribution. The latter, which is determinant for turbine blade life at high pressures, may adequately be predicted from temperature surveys carried out at lower and more convenient levels of pressure. These advantages of *airblast* atomizers have led in recent years to their installation in a wide range of industrial and aircraft engines.

1.3.2 Droplet interactions

For aircraft gas turbines and many other combustion systems, the spray of droplets generated by the atomization devices described above are generally discharged in a turbulent air flow. Prior to the total evaporation of droplets, strong interactions occur. These are spray-turbulence interactions, mutual interactions between droplets, droplet-wall interactions, and droplet heating. This subsection focuses on the first three types of interactions as they play a relevant role on both droplet-heating and droplet-evaporation phenomena, which are discussed in the next subsection. Many investigators have shown that it is convenient to characterize the droplet collision process in terms of Weber number, We, and the impact parameter, Ip. The former is the ratio of inertial force to the surface force, and is defined as $We = \rho_d U^2 d_{ds}/\sigma_l$, where d_{ds} is the diameter of the smaller droplet, σ_l is the surface tension of the droplet fluid, and ρ_d is the droplet density. The second is the distance from the center of one droplet to the relative velocity vector placed on the center of the other droplet. From

fluid-mechanics-based analysis, it is established that each droplet travelling into a moving fluid experiences a drag force. In a turbulent flow, the droplet shapes are significantly impacted and so do the droplet trajectories. These effects are generally accounted for in the droplet calculations through a dynamic drag coefficient as mentioned earlier. According to the droplet-wall interactions, there are several approaches available in the literature depending of the investigated configurations (operating conditions) and the desired accuracy. The simpler modelling approaches assumed that the droplets are either reflected or trapped when they reach the wall of the combustion chamber. In the former case, the droplets are rebounded off the boundary with changes in their momentum defined by a restitution coefficient; detailed information regarding this approach are provided in [Tabakoff and Wakeman, 1982]. In the second approach, the droplets are completely vaporized instantaneously, and the computation accounts for the resulting fuel vapours. For more accurate treatment, wall-jet and wall-film models are also available. The wall-jet model is suitable for configuration involving very hot walls, while the wall-film model is a good assumption for in-cylinder diesel computations at typical operating conditions. The wall-film model consists of four regimes: sticking, rebounding, spreading, and splashing, which are all based on the impact energy and the wall temperature. Detailed explanations regarding the wall-film model are provided in [Stanton and Rutland, 1996, 1998, O'Rourke and Amsden, 2000]. In addition to the interactions with the gaseous phase and the walls of the combustion chamber, the droplets interact mutually. The strength of this latter type of interaction is determined by the Weber number and the impact distance, Ip, introduced earlier. According to Orme [1997], the interaction between two droplets travelling in a moving fluid may generally result in bounce, stable coalescence, temporary coalescence followed by disruption, or temporary coalescence followed by fragmentation, depending on the value of the We and Ip and the fluid property. These possible droplet collision phenomena are illustrated in Figure 1.5.

Droplet bounce will occur if the surfaces of the droplets do not make contact due to the presence of a thin intervening gas film. The colliding droplets will coalesce when the air film thickness reaches a critical value, which is of the order of $10^{-2}\mu m$ as established by Mackay and Mason [1963]. The droplets may coalesce temporary or permanently, depending on the collisional kinetic energy and the impact parameter. Temporary coalescence occurs when the collisional kinetic energy exceeds the value for stable coalescence, and will result in either disruption or fragmentation. In disruption, the droplet surfaces have made contact and the droplets temporarily coalesce; the increase in collisional kinetic energy is too severe so that the coalescence is followed by disruption. Disruption corresponds to the case where the collision product separates into the same number of droplets which existed prior to the collision.

The fourth type of collision, the fragmentation, occurs when the kinetic energy is excessive. In this type, the coalesced droplets undergo catastrophic break-up into numerous small droplets. The relevance of the inclusion of the break-up phenomenon along with the other collision phenomena is strongly determined by the spray characteristics (e.g. the liquid volume fraction of the spray) and the Weber number. For spray configuration characterised by high Weber numbers (i.e. a Weber number

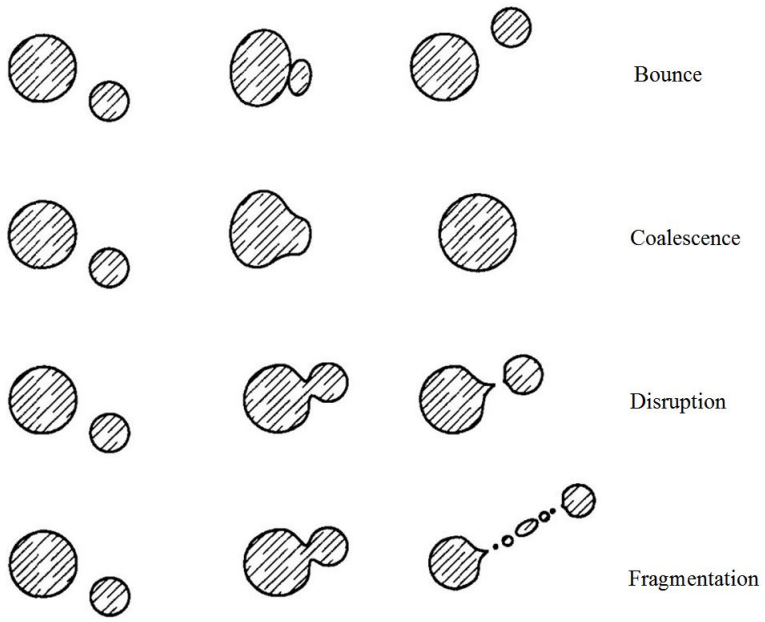

Figure 1.5: Illustration of possible droplet collision phenomena (Orme, 1997)

larger than the critical Weber number which is around 12), the break-up phenomenon needs to be taken into account. In this regard, there are several modelling approaches; the most classical of them is the Taylor Analogy Break-up (TAB) model, which is derived using the Taylor's analogy between an oscillating and distorting droplet, and a spring mass system. Detailed explanations regarding the derivation of this model which is applicable to many engineering sprays exhibiting moderate-Weber number are provided in [O'Rourke and Amsden, 1987].

For high-Weber-number spray flows however (typically We>100), there are other modelling approaches which are more suitable; these are the WAVE breakup model, the Kelvin-Helmholtz Rayleigh-Taylor (KHRT) model, and the Stochastic Secondary Droplet (SSD) break-up model. The WAVE model considers the break-up of the injected liquid to be induced by the relative velocity between the gas and the liquid phases; detailed information regarding this model derivation may be found in [Reitz, 1993]. The second of these break-up models for high-Weber number flows, the KHRT, was formulated by Patterson and Reitz [1998] and Beale and Reitz [1999], and considers the competing effects of aerodynamic break-up and instabilities due to droplet acceleration. However, the performance of the model is hampered when it is applied to low pressure spray. In both TAB and WAVE break-up models, the droplet break-up is determined using a single diameter scale. In contrast, the SSD model formulated by Apte et al. [2003] treats the break-up phenomena as a discrete random event resulting in a distribution of diameter scales over a range. The probability of beak-up is independent of the parent droplet size and the secondary droplet size is sampled from an analytical solution of the Fokker-Planck equation for the probability distribution; the parameter for the distribution being based on the local conditions.

1.3.3 Droplet heating and evaporation models

The spray of droplets generated by the atomization devices needs to be evaporated and efficiently mixed with air for combustion to proceed. The droplet evaporation and mixing rates are therefore the key aspects for the combustion efficiency, and thereby to control pollutant emissions. This subsection focuses on the former aspect which is prior to the second: the droplet heating and evaporation models, which are used to simulate spray combustion when designing and/or optimizing engines, are briefly reviewed with a particular emphasise on the modelling approach applied in the current study, which is rather similar for many in-house and commercial CFD codes.

The heat and mass exchange between droplets and the gaseous phase are governed by droplet heating and evaporation laws. According to Sirignano [1999], these laws can be subdivided into the following groups in order of ascending complexity: (i) models based on the assumption that the droplet surface temperature is uniform and does not change with time; (ii) models based on the assumption that there is no temperature gradient inside droplets (i.e. the assumption of infinite thermal conductivity of liquid); (iii) models allowing to account for the finite liquid thermal conductivity while neglecting the re-circulation inside droplets; (iv) models including both finite liquid thermal conductivity and the re-circulation inside droplets through the introduction of a correction factor to the liquid thermal conductivity; (v) models describing the re-circulation inside droplets in terms of vortex dynamics; and (vi) models based on the full resolution of the Navier-Stokes equation. The first group is particularly attractive for analytical studies of droplet evaporation and thermal ignition of fuel/air mixture [Goldfarb et al., 1999, Bykov et al., 2002] since the dimension of the system is reduced through the complete elimination of the equation for droplet temperature. Due to this latter assumption of the model, it appears to be too simplistic for application in most CFD codes. The two last groups are not used in most CFD codes, and are not expected to be used in a foreseeable future due to their complexity; they are however widely used for validation of more basic models of droplet heating for in-depth understanding of the underlying physics [Sirignano, 1999, Abramzon and Sirignano, 1989, Chiang et al., 1992, Polynin et al., 2002]. The models (ii)-(iv) are implemented in many in-house and commercial CFD codes; the second group of models in particular is widely applied in design- and optimization-oriented engine simulations. The inert heating and evaporation of a spray of droplets in most practical combustion systems, and especially in the combustion chambers of aircraft gas turbines, are inherently transient and occur with radiative effects in turbulent environment which is known to promote high heat and mass transfer rates as well as high mixing rates between the evaporated fuel and air. It is then obvious that a proper modelling approach must account for transient, convective and radiation effects.

In the current simulations, the infinite liquid conductivity model which belongs to this second group is adopted as a zeroth approximation to model heat and mass transfers between the two phases. The droplet surface temperature is then assumed to be uniform, time-varying, and equal to the temperature inside the droplet, while finite liquid thermal conductivity and droplet internal recirculation are neglected [Sirignano, 1999]. The heat exchange between the droplets and the gaseous phase takes

place in three different regimes, namely, the inert heating, evaporation and boiling regimes. This regimes are subsequent and are delimited by the vaporization temperature, t_v, and the boiling temperature, t_b. The inert heating increases the temperature of the droplets up to the vaporization temperature which corresponds to the "flash point" of the fuel. In this regime (i.e. $t_d \leq t_v$), there is no exchange of mass between the gaseous and liquid phases, and the following equation is used to determine the change in temperature.

$$m_{dj} C_{pdj} \frac{dT_{dj}}{dt} = hS_d(T_g - T_{dj}) + \varepsilon_d S_d \sigma(\theta_R^4 - T_d^4) \tag{1.28}$$

where "j" stands for the fuel component index, m_{dj} is the mass of the "j" species in the droplet, C_{pdj} is the heat capacity of the "j" species in the droplet, S_d is the surface area of the droplet, T_g is the local temperature of the gaseous phase, h is the convective heat transfer coefficient, ε_d is the droplet emissivity, σ is the Stephan-Boltzmann constant, and θ_R is the radiation temperature. The fuel component index "j" allows implementing multicomponent fuel properties. For an one-component fuel, $j = 1$, while for the two-component fuel, $j \in \{1;2\}$. To better capture the early stage of heating, the heat convection coefficient needs to be corrected through the implementation of a time-dependent gas thermal conductivity [Sazhin et al., 2001] or a time-dependent heat convection coefficient [Cooper, 1977]. However, for a time-varying droplet surface temperature, the range of applicability of these equations is still unclear.

The second regime is characterized by a droplet temperature exceeding the vaporization temperature. The heat gained by the droplets contributes not only to raise their temperature as in the first regime, but also to vaporize the moving droplets. The resulting fuel vapour is transferred to the gaseous phase through convection and diffusion processes. The evaporation rate generated by convection and diffusion phenomena is calculated using the following equation:

$$\dot{m}_{d,j} = \frac{dm_{d,j}}{dt} = S_{dj} k_{m,j} \rho_g ln(1 + B_{m,j}) \tag{1.29}$$

where $k_{m,j}$ is the mass transfer coefficient for the fuel component "j", $B_{m,j}$ is the Spalding mass number for species "j", and ρ_g is the density of bulk gas.

In the third regime, the fuel is in the burning regime as the droplet temperature exceeds the boiling temperature. The rate of mass transfer in this regime is calculated using the following equation:

$$\dot{m}_{d,j} = \frac{dm_{d,j}}{dt} = \frac{x_j \pi d_d k_g}{C_{pg}} \left(2.0 + Re_d^{1/2} Sc^{1/3}\right) ln(1 + B_{T,j}) \tag{1.30}$$

where x_j stands for the volume fraction for the component "j" in the droplet and k_g is the thermal conductivity of the gas. $B_{T,j}$ is the Spalding heat transfer number for component "j" computed as: $B_{T,j} = C_{pg}(T_g - T_d)/h_{evap,j}$, where $h_{evap,j}$ is the latent heat of evaporation for the component "j". When the mass is transferred from the droplet to the gas phase, the change in droplet temperature is affected since a part of the heat received from the gaseous phase is used for the fuel evaporation. The change in droplet temperature is therefore calculated as follows:

$$m_{d,j} C_{pd,j} \frac{dT_{d,j}}{dt} = hS_d(T_g - T_{d,j}) + \varepsilon_d S_d \sigma(\theta_R^4 - T_d^4) - \dot{m}_{d,j} h_{fg} \tag{1.31}$$

where h_{fg} is the latent heat, h is the heat convection coefficient calculated using the modified Nusselt number defined by: $Nu = hd_d/k_g = \left(2.0 + Re_d^{1/2} Pr^{1/3}\right) ln(1+B_T)/B_T$, in which $Pr = c_g \mu / k_g$ is the Prandtl number. In each of the two regimes, the mass transfer rate for a multicomponent fuel is calculated by summing the mass transfer rates of the individual components.

1.4 Combustion models

The spray dynamics discussed above shows that combustion in the majority of liquid-fuelled combustion systems occurs in a non-premixed mode or more realistically in a partially-premixed mode, depending on the atomizer configuration. The non-premixed combustion mode leads to diffusion flames, the latter being related to the fact that the continuous combustion requires the diffusion of air and the fuel in the reaction zone.

From a safety point of view, diffusion flames are of practical interest; however, sophisticated mixing devices are necessary to achieve high mixing rates which are propitious to low pollutants emissions. In the partially-premixed combustion mode, the partial premixing refers to any premixing of fuel with air that may occur prior to combustion. This combustion mode involves both non-premixed and premixed combustion modes. Plus, depending on the operating condition, triple flames may develop and contribute to global flame stabilization [Puri et al., 2001b, Qin et al., 2004]. This combustion mode is then of particular interest from a flame stabilization standpoint, and is expected to minimize pollutants emissions in comparison to diffusion flames. In particular, this stabilization effect can be related to the self-induced propagation mechanism of premixed flames (i.e. the lean and rich branches of the triple flame), which promotes a relatively lower sensitivity to turbulence perturbations. The most common models used for spray combustion simulations can be classified into two main groups depending on the assumption made on the rate of chemical reactions.

The first group relies under the assumption that the chemical reactions are faster compared to the smallest scales of turbulence; this hypothesis is also termed as infinitely-fast chemistry assumption. In contrast, the second group assumes that chemistry time scales can be of the same order as those of turbulence; this is also termed as the finite-rate chemistry assumption. Considering the outcomes from investigations carried out by several research teams on the relevance of a detailed fuel-oxidation mechanism and a proper modelling of turbulence-chemistry interactions when simulating some critical combustion phenomena related to safety and environmental concerns (e.g. local extinction, re-ignition, and pollutant emissions), this second group is suitable for most practical configurations [Peters, 2000, Hilbert et al., 2004b, Poinsot and Veynante, 2005]. Various approaches have been developed in the combustion community to implement the finite-rate chemistry assumption in CFD codes. The robustness of each of these approaches is strongly related to its ability to circumvent some issues imposed by the size of a detailed fuel-oxidation mechanism, namely, the requirements in terms of dynamic memory (RAM) and CPU usage. A realistic fuel-oxidation mechanism generally consists of large number of species and elementary reactions; this number becomes even larger

for heavy hydrocarbons such as those found in jet fuels. A straightforward combustion model would consist of solving transport equations for all the species involved in the reaction mechanism. However, considering the large number of species involved in detailed chemistry models, it is clear that their implementation in a given CFD code would lead to more than a hundred additional transport equations to solve, and therefore to additional needs in computing resources. Furthermore, depending on the turbulence models used, the species reaction rates that would result from the spatial filtering (for LES-based simulations) or time-averaging (for RANS simulations) of species transport need to be modelled.

Globally, three main approaches have so far been used in the combustion community to implement the finite-rate chemistry assumption. These are the tabulated flamelet-based chemistry approaches (e.g. the laminar diffusion flamelet, and the flamelet generated manifold), the Conditional Moment Closure (CMC) models, and the PDF transport models. All of these combustion models, including those based on the infinitely-fast chemistry assumption, are formulated with some flexibilities which allow them to handle configurations exhibiting the two combustion modes that are likely to be involved in spray combustion. However, the accuracy of the prediction generated by each of them depends on the gap that exists between the mixing and the chemistry time scales, which is measured by the Damköhler number (Da). The common feature of these combustion models lies in the fact that all of them allow circumventing the issue related to the modelling of the reaction rates of numerous species. In addition to this advantage, some of them circumvent also the prohibitive computing time that occurs when dealing with detailed chemistry.

The commonly-used approach consists of replacing all the species transport equations by those of a very few number of representative scalars (also termed as "tracking scalars") which can be either reactive or non-reactive, but are non-conserved in spray combustion as shown in the following equation:

$$\frac{\partial \rho \phi_{TS,j}}{\partial t} + \frac{\partial \rho \phi_{TS,j} U_i}{\partial x_i} = \frac{\partial}{\partial x_i}\left(D_{\phi_{TS,j}} \frac{\partial \phi_{TS,j}}{\partial x_i} \right) + \dot{\omega}_{\left(\phi_{TS,j}\right)_{reaction}} + \dot{S}_{\left(\phi_{TS,j}\right)_{evaporation}} \tag{1.32}$$

where $\phi_{TS,j}$ is the set of "tracking scalars". The species index appearing in the species transport equation,"k", and the "tracking scalars" index, "j" are respectively defined in such a way that $k \in [1, N_s]$, and $j \in [1, N_{TS}]$ with $N_{TS} \ll N_s$; N_{TS} and N_s being respectively the Number of "Tracking Scalars" considered, and the Number of Species involved in the fuel-oxidation mechanism. For instance, in the mixture fraction-progress variable formulation, $\phi_{TS,j} \in \{Z, Y_c\}$, where the mixture fraction, Z, is the non-reactive scalar, while the progress variable, Y_c, is the reactive scalar. For the non-reactive scalar, the source term due to reaction, $\dot{\omega}_{Zreaction}$, is obviously zero, while the source term due to evaporation, $\dot{S}_{Zevaporation}$ is non-zero, and is equal to the mass source term, since the changes in mixture fraction are due to convection, diffusion and evaporation, but not reaction. For the reactive scalar, Y_C, these two source terms are non-zero; the source term of the progress variable due to reaction is generally modelled, while the second source term due to evaporation is generally neglected, assuming that chemical reactions of combustion occur in the gaseous phase, far enough from the liquid interface [Chrigui

et al., 2012]. In others words, the chemistry calculations are decoupled from those of mixing, and the chemistry effects are included through a map with a pre-calculated chemistry. The relevance of such an approach which is based on the separated time scales concept lies in the fact that stable and efficient combustion in most practical combustion systems are achieved when the chemical time scales are short compared to those of the mixing [Bray et al., 2005]. In this section, a brief description of the methods used to implement the infinitely-fast chemistry assumption is first provided along with their drawbacks. Subsequently, the modelling background for each of the three approaches widely used to implement the finite-rate chemistry assumption is discussed.

1.4.1 Infinitely-fast chemistry assumption and incorporation approaches

In the full equilibrium assumption, chemistry is rapid enough for chemical equilibrium to always exist at the molecular level. An algorithm based on the minimization of Gibbs free energy is used to perform the chemical equilibrium calculations. The latter consisting of establishing a relationship between the representative scalars (the mixture fraction) and the generic scalars (e.g. species mass fraction and temperature). Such an approach is sturdy for some practical configurations since it allows including the effects of intermediate species and dissociation reactions. It can therefore produce a more realistic prediction of flame temperatures than the eddy-dissipation model for which the reaction rates are assumed to be controlled by turbulence only. However, as advocated by Peters [2010], a combustion model based on the equilibrium calculations over the whole range of the mixture fraction (i.e. $Z \in [0,1]$), features some drawbacks such as a zero-prediction and an over-prediction of slow species concentrations in the fuel-lean and fuel-rich regions of the combustion chamber, respectively. In an attempt to address this issue of the full equilibrium approach (EQ), a partial equilibrium approach (PEQ) was formulated. This approach avoids complex tasks related to equilibrium calculations in the fuel-rich regions, while improving the prediction of the main flame trends and the slow species. The entire range of the mixture fraction is then divided into two parts using a cut-off value of the mixture fraction, Z_{RFL}, which is physically a Rich Flammability Limit (RFL). Thereafter, chemical equilibrium calculations are performed over a restricted range of the mixture fraction (i.e. $Z \in [0, Z_{RFL}]$), while the remaining range is treated with mixing calculations. Physically, this means that, in the remaining range of the mixture fraction, the combustion reactions are extinguished and unburned fuel coexists with reacted material. In such fuel-rich zones, the composition at a given value of the mixture fraction is computed from the composition at the limiting mixture fraction (i.e $Z = Z_{RFL}$), and that corresponding to the fuel inlet stream (i.e $Z = 1$) is based on a known stoichiometry.

Even provided with this refinement strategy, the partial equilibrium approach may lead to unrealistic results when it is applied to some configurations. In fact, in most practical combustion systems involving turbulent reacting flows, chemical non-equilibrium effects due to turbulence such as flame stretching and/or flame wrinkling are present and should be taken into account for a proper modelling of turbulence-chemistry interactions, and for an accurate prediction of the main flame trends in the fuel-rich side of hydrocarbon flames, including species characterized by low reaction rates such as

carbon monoxide (CO), Nitrogen oxides (NOx), and others pollutants. The implementation of the finite-rate chemistry assumption has been proven to be a efficient way of addressing this issue. As an adequate approach to implement this assumption, flamelet models have so far been formulated, and they provide efficient ways to account for chemical non-equilibrium effects in configurations exhibiting large or moderate Damköhler numbers. The flamelet models and the derivation assumptions are discussed in the following subsection.

1.4.2 Finite rate chemistry assumption: Flamelet models

The formulations of most flamelet models are based on a common characteristic of some practical combustion systems mentioned earlier, namely the fact that, a stable and efficient combustion in these systems exhibits large or moderate Damköhler numbers [Bray et al., 2005, Pitsch, 2006]. Consequently, chemical reactions of combustion occur in a narrow regions called "thin reaction zone" or flamelets. Generally, the structures of these thin reaction zones are quite similar to that of a laminar flame, and the thickness is small compared to the majority or all the flow length scales. From a simulation point of view, the main advantage of this physical characteristic is that the chemistry calculations can be decoupled from those of the mixing, through the tabulated chemistry concept. In addition, configurations exhibiting a wide separation between the time scales of the chemistry and those of turbulence (i.e. large Damköhler number) provide two additional benefits: the flame structure remains laminar, and the diffusive transports occur essentially in the direction normal to flame surface, the latter corresponding to the surface of a stoichiometric mixture. The laminar one-dimensional structure of the flame, and the wide separation between chemical and mixing time scales can then be viewed as the fundamental assumption of tabulated flamelet-based chemistry approaches. In non-premixed combustion, the classical form of these models is the laminar diffusion flamelet. In this model, turbulent flames are viewed as an ensemble of locally one-dimensional thin structures (or flamelets) embedded in the turbulent flow, with each flamelet being subjected to the local properties of the turbulent flow [Peters, 2000, Claramunt et al., 2006]. This classical version of flamelet models can be considered as an extension of the "flame sheet" model, which assumes infinitely fast chemistry assumption, so that the reaction zone is an infinitely thin interface. As discussed in the previous subsection, such an approach cannot capture relevant non-equilibrium phenomena such as extinction, re-ignition, lift-off and blow-off. The laminar diffusion flamelet relaxes (at least partly) the infinitely-fast chemistry assumption by introducing a new parameter, the scalar dissipation rate, which allows modelling the local effects of turbulence on the flamelet structure, and consequently, on the global flame structure. The equations for the laminar diffusion flamelet can be expressed either in physical or in mixture fraction space. Especially in the mixture fraction space, they are derived by performing a Crocco-type coordinate transformation on the conservative equations for species and energy, the new coordinate system being attached to the flame surface. The resulting unrefined form of the flamelet equations are the following:

$$\rho\frac{\partial Y_i}{\partial \tau} = \frac{\rho\chi}{2Le_i}\frac{\partial^2 Y_i}{\partial Z^2} + \frac{1}{4}\left(\frac{1}{Le_i}-1\right)\left[\frac{\partial(\rho\chi)}{\partial Z} + \rho\chi\frac{C_p}{\lambda}\frac{\partial}{\partial Z}\left(\frac{\lambda}{C_p}\right)\right]\frac{\partial Y_i}{\partial Z} + \dot{\omega}_i \tag{1.33}$$

$$\rho\frac{\partial T}{\partial \tau}=\frac{\rho\chi}{2}\frac{\partial^2 T}{\partial Z^2}+\frac{\rho\chi}{2C_p}\frac{\partial C_p}{\partial Z}\frac{\partial T}{\partial Z}+\frac{\rho\chi}{2C_p}\sum_{i=1}^{N}\left(\frac{C_{pi}}{Le_i}\frac{\partial Y_i}{\partial Z}\right)\frac{\partial T}{\partial Z}-\frac{1}{C_p}\sum_{i=1}^{N}h_i\dot{\omega}_i+\frac{Q_R}{C_p} \tag{1.34}$$

In these equations, T and C_p are respectively the temperature and the mixture-averaged specific heat; Y_i and C_{pi} are the mass fraction and the specific heat of the ith species respectively, while h_i and $\dot{\omega}_i$ are the enthalpy and the rate of production of the ith species; Le_i is the Lewis number of the ith species, defined by $Le_i=\lambda/(\rho D_i mc_p)$, D_{im} being the multicomponent ordinary diffusion coefficients. The instantaneous scalar dissipation rate, χ, is defined by:

$$\chi\equiv\chi_Z=2D_Z(\nabla Z.\nabla Z). \tag{1.35}$$

It allows measuring the degree of departure from the equilibrium state, and needs to be modelled to close the flamelet equations. In this regard, various modelling approaches have been proposed. Some of them include the use of analytical approximations based on the laminar diffusion flame structure or on the one-dimensional laminar mixing layer as reported in [Peters, 2000, Claramunt et al., 2006]; the use of a constant scalar dissipation rate under stoichiometric conditions (e.g. [Chan et al., 1998]); and the use of an iterative strategy incorporating the local profile of the scalar dissipation rate at each location of the flame (e.g. [Claramunt et al., 2006]).

In all the simulations carried out in the current study, the first modelling approach based on the analytical expression for the scalar dissipation is used, $\chi(Z)=a_s/\pi exp\{-2\left[erfc^{-1}(2Z)\right]^2\}$, where a_s is the strain rate, indicating the maximum velocity gradient, and $erfc^{-1}$ is the inverse of the complementary error function. Commonly, the physical space parameter, a_s, is eliminated, and the scalar dissipation rate is expressed as a function of the scalar dissipation rate at stoichiometric conditions, χ_{st}. This approach allows parameterizing the scalar dissipation rate in terms of χ_{st} as: $\chi(Z)=\chi_{st}exp\{2\left[erfc^{-1}(2Z_{st})\right]^2-2\left[erfc^{-1}(2Z)\right]^2\}$. Some assumptions are commonly made to simplify the flamelet equations: (i) the preferential and differential diffusion are generally neglected through the unity-Lewis number assumption; (ii) the unsteady terms are neglected, which physically means that, the flamelet structure is assumed to be controlled by only a balance between the steady diffusion and chemical reaction processes; (iii) finally, the radiative heat lost is generally neglected. These assumptions lead to the following simplified form of the flamelet equations which is implemented in the majority of diffusion flamelet solvers:

$$\frac{\rho\chi}{2}\frac{\partial^2 Y_i}{\partial Z^2}+\dot{\omega}_i=0 \tag{1.36}$$

$$\frac{\rho\chi}{2}\frac{\partial^2 T}{\partial Z^2}+\frac{\rho\chi}{2C_p}\frac{\partial C_p}{\partial Z}\frac{\partial T}{\partial Z}+\frac{\rho\chi}{2C_p}\sum_{i=1}^{N}\left(\frac{C_{pi}}{Le_i}\frac{\partial Y_i}{\partial Z}\right)\frac{\partial T}{\partial Z}-\frac{1}{C_p}\sum_{i=1}^{N}h_i\dot{\omega}_i=0 \tag{1.37}$$

Considering the relevance of these assumptions, it is obvious that the suitability of such a reduced model in retrieving some critical combustion properties in many configurations is not guaranteed. In fact, in the widespread approximation which consists of neglecting the unsteady term in the flamelet equations and also termed as *steady laminar diffusion flamelet*, it is physically assumed that the flamelet lifetime is much longer than the characteristic time scale of phenomena involved in the

flamelet equation. However, such an assumption does not take into account rapid changes of the scalar dissipation profiles at the flame front and the processes such as radiation heat transfer and pollutant formation. Furthermore, when differential diffusion is considered, it is shown that the transient effect is important to balance the term in the flamelet equation responsible for super-equilibrium ($\partial\rho\chi/\partial Z$). Depending on the available computing resources and the combustion properties of interest, the implementation of these unsteady terms (i.e. the *unsteady laminar diffusion model*) along with the non-unity Lewis number assumption is likely to outperform the *steady laminar diffusion flamelet model* (SLDFM), provided a careful choice of the mixture fraction diffusion coefficient. In this vein, according to Pitsch and Peters [1998], the use of equal thermal and mixture fraction diffusivity leads to a well description of the flame structure.

For some flame configurations, the laminar diffusion flamelet equations, even in their non-refined form, feature some relevant limitations with respect to the regime of validity of the model. Most of these limitations are inherent to the fundamental assumption of the model, namely, the assumption of laminar thin burning regime made in the model formulation. In other words, as illustrated in the turbulent combustion diagrams, the flamelet model can be applied only for combustion regimes characterized by large Damköhler numbers (i.e. $Da \gg 1$) and low Karlovitz number (i.e. $Ka < 1$). The former non-dimensional number is the ratio between the mixing and the chemistry time scales, while the latter is the ratio between the time of chemistry and those of the smallest structures of the turbulence (i.e. Kolmogorov structures). When the turbulence intensity increases (i.e. when the mixing time scales and therefore the Damköhler number decreases, typically $Da < 1$), the performance of the model begins to be impeded. In fact, for high turbulence intensities, the turbulent eddies can not only wrinkle or corrugate the flame front, but can also penetrate the flame and thicken the flame so that the local flame structure can no longer remain laminar and mono-dimensional. With an intense turbulence, the eddy can even tear the inner reaction zone thereby leading to flame quenching. The laminar flamelet model cannot capture such a flame regime. In order to address this issue, some alternative approaches have been formulated. The most popular ones are the transported Probability Density Function (PDF) developed by Pope [1985] and the Conditional Moment Closure (CMC) developed independently by Bilger and Klimenko [Bilger, 1993, Klimenko, 1993, Klimenko and Bilger, 1999, Klimenko, 2001]. These combustion models are subsequently discussed in two following subsections.

1.4.3 Finite rate chemistry assumption: Transported probability density function

The combustion models based on transported probability density function (PDF) proceed by solving the composition joint PDF equations, through a method initially developed by Pope [1985], to predict the properties of the turbulent reactive flow fields. This approach shows promising results, even when applied to configurations exhibiting low Damköhler number (typically, $Da < 1$). From a numerical standpoint, the transported PDF approach involves large dimensionality for which the usual numerical techniques such as finite difference and finite volume are not very attractive due to the memory constraints. This concern was circumvented by Pope using a Monte-Carlo simulation

technique. Such an approach helped to combine the velocity-PDF and the composition-PDF to obtain the advantages of both, namely, the fact that both convection and reaction rates appear in a closed form as they do in velocity-PDF and composition-PDF, respectively. From a physical standpoint, the operating mode of the PDF model consists of treating the turbulent reacting flow as an ensemble of particles so that each particle has its own position and composition, and travels in the flow with an instantaneous velocity. The particle state is described by its position, velocity, and reactive scalars; and the particle properties are described by stochastic Lagrangian models. Nonetheless, it is worth noting that the PDF equations can be derived, modelled and solved by the Eulerian method (i.e. PDF of fluid properties at a fixed spatial location). The main asset of the PDF-based combustion models is that it allows to cope with large density variations and the non-linear reaction source term involved in turbulent reactive flows. These two assets are justified by the fact that, in variable density flows, the effects of convection, reaction, body forces, and the mean pressure gradient term can be treated without approximation. For a turbulent reacting flow whose aerodynamics and thermochemical states are respectively defined by $\underline{U}$ and $\underline{\Phi}$, where $\underline{U}$ represents the three velocity components, while $\underline{\Phi}$ stands for σ composition variables (i.e. species mass fraction and enthalpy), the mean of each physical quantity, $Q = Q(\underline{U},\underline{\Phi})$, of the reacting system is calculated by convolving the latter with the joint PDF, f_{PDF}, according to the following equation:

$$\langle Q(\underline{U},\underline{\Phi})\rangle = \iint Q(\underline{U},\underline{\Phi}) f_{PDF}(\underline{U},\underline{\Phi}) d\underline{U} d\underline{\Phi}). \tag{1.38}$$

For instance, the mean reaction reaction rate is calculated using the following equation:

$$\overline{\dot{\omega}_R} = \int_{Y_1}\int_{Y_2}\ldots\int_{Y_N}\int_T \dot{\omega}_k(Y_1,Y_2\ldots Y_N,T) dY_1 dY_2\ldots dY_N dT \tag{1.39}$$

From this example, it is clear that the classical issue of modelling the mean reaction rate is simply transferred to the calculation of the joint PDF, f_{PDF}. In practice, it is not obvious to presume the shape of such a joint PDF so that balance equations are derived to close the problem. The derivation of the transported equation for the joint PDF is based on the conservative equations for momentum and composition scalars expressed in a compact form as follows:

$$\frac{D\underline{U}}{Dt} = \underline{A} \text{ and } \frac{\underline{\Phi}}{Dt} = \underline{\Theta} \tag{1.40}$$

where $\underline{A}\equiv A_j$ is the total force (i.e. volume and surface forces) per unit mass, and $\underline{\Theta}\equiv\Theta_\alpha$ is the net source of Φ, with $\alpha\in\{1,2,\ldots\sigma\}$. By using the continuity equation and a PDF derivation approach based on the balance of two independent expressions for $\langle\rho DQ/Dt\rangle$, Pope [1985] derived the following transport equation for the velocity-scalar joint PDF, $f_{PDF} = f_{PDF}(\underline{U},\underline{\Phi};\underline{x},t)$

$$\rho(\underline{\Phi})\frac{\partial f_{PDF}}{\partial t} = \rho\underline{\Phi}U_j\frac{\partial f_{PDF}}{\partial x_j} = -\frac{\partial}{\partial U_j}\left[\rho(\underline{\Phi})\langle A_j|\underline{U},\underline{\Phi}\rangle f_{PDF}\right] - \frac{\partial}{\partial\Phi_\alpha}\left[\rho(\underline{\Phi})\langle\Theta_\alpha|\underline{U},\underline{\Phi}\rangle f_{PDF}\right] \tag{1.41}$$

In spite of the fact that the reaction and convection transports can be treated without approximation, even in variable density flows, and the fact that the assumption regarding the flame structure is no longer needed in the transported PDF approaches, there are some challenges: the turbulent transport

and molecular mixing terms in the PDF transport need to be modelled, and the performance of the model depends on the closure model adopted. In addition, the model involves high computing resources when dealing with detailed chemistry models, and its performance in the LES context is not clearly established.

1.4.4 Finite rate chemistry assumption: Conditional Moment Closure

As for the equilibrium-chemistry and laminar flamelet models discussed above, the basic idea governing the development of the conditional moment closure (CMC) methods consists of finding how the reactive scalars (e.g. temperature, species mass fraction, etc.) are related to a conserved scalar. In the context of non-premixed combustion, such a relationship generally relies on the mixture fraction, the turbulent fluctuations of the latter being modelled with a PDF whose shape can be either presumed or obtained by solving a transport equation as discussed in the previous section. In the same vein, Klimenko [1993] and Bilger [1993] developed independently the CMC technique using two different mathematical procedures: the Bilger's derivation consists of decomposing the scalars into its conditional mean and fluctuations in their transport equation, while the Klimenko's approach considers the joint PDF evolution of the reactive and conserved scalars. The two derivation techniques are based on non-premixed unsteady flames, and lead to the same form of the CMC equation, namely, the species and enthalpy equations which are conditionally averaged on a sample space variable, ζ. The identical form yielded by the two formulations provides substantial reliability to the model. In CMC methods, equations are derived and modelled for the conditional moments of the reactive scalars (or shortly, the conditionally averaged scalars), $\langle \phi_i | \zeta \rangle$. For instance, using the Klimenko's joint PDF method as established in [Klimenko and Bilger, 1999], the transport equation for the conditionally averaged mass fractions can be expressed as follows:

$$\frac{\partial \langle \rho Y_i | \zeta \rangle P_\zeta}{\partial t} + \nabla.(\langle \rho Y_i \underline{U} | \zeta \rangle P_\zeta) = \langle \rho \omega_i | \zeta \rangle P_\zeta - \frac{\partial^2 (\langle \rho \chi_\zeta Y_i | \zeta \rangle P_\zeta)}{\partial \zeta^2} + \frac{\partial (\langle 2\rho \chi_{\zeta, Y_i} Y_i | \zeta \rangle P_\zeta)}{\partial \zeta}, \quad (1.42)$$

where t is time; $\underline{U}$ is the velocity vector, ω_i is the rate of formation of species, i, per unit mass of the mixture; χ is the scalar dissipation rate defined by $\chi_\zeta = D_\zeta \nabla\xi \nabla\xi$, and $\chi_{\zeta,Y_i} = D_\zeta \nabla\xi \nabla Y_i$ is a cross-scalar dissipation rate between ζ and Y_i; ξ is the mixture fraction; D_ξ is the diffusion coefficient of the mixture fraction, and P_ζ is the mixture fraction PDF. $\langle | \zeta \rangle$ denotes the conditional averaging in ζ space. A similar equation is derived for the conditional average enthalpy. These equations have unclosed terms involving the conditional average of the species reaction rate and of the net radiative heat transfer.

The CMC model based on the first-order approximation assumes that the conditional fluctuations are negligible, and that the conditional chemical source term is only a function of the first-order moments. In some configurations of non-premixed turbulent flames involving small fluctuations of reactive scalars at a given mixture fraction value, such an assumption may lead to inaccurate prediction of the investigated phenomena; for configurations involving large fluctuations of the reactive scalars at a given mixture fraction value, the CMC model based on the first assumption is no longer applicable.

A possible way to address the limitations introduced by the first order assumption would be to close the conditional chemical source term using a second-order approximation [Kronenburg et al., 1998]. In addition to the need of closure approximations for the chemical source term, the above CMC equation (based on the species mass fraction) contains additional unclosed terms that need to be modelled for its complete closure. These are the conditional averaged velocity, $\langle \underline{U}|\zeta\rangle$, and the conditional averaged scalar dissipation, $\langle \chi|\zeta\rangle$. This is usually done using information already existing on the velocity and mixing fields. Finally, the mapping operation is achieved by convolving the conditional averaged scalars with the PDF according to the following two equations:

$$\tilde{Y}_i = \frac{1}{\bar{\rho}} \int_0^1 \langle \rho Y_i|\zeta\rangle P_\zeta d\zeta \text{ and } \tilde{\omega}_i = \frac{1}{\bar{\rho}} \int_0^1 \langle \rho \omega_i|\zeta\rangle P_\zeta d\zeta \tag{1.43}$$

Since the formulation of its classical form, the CMC method has been subjected to some improvements with respect to computational resource requirements, and inclusion of relevant phenomena such as the preferential diffusion of species. According to the former type of improvements, a computationally less expensive approach was formulated by Bushe and Steiner [1999] to circumvent the additional computing expenses incurred by the resolution of the transport equation for the conditional averages in mixture fraction space. The second type of improvements was recently achieved by Ma and Devaud [2015] who proposed a CMC formulation including a differential diffusion; they applied this new formulation to simulate a non-premixed flame investigated experimentally by Barlow and Carter [1994, 1996], and its prominent effect on NO predictions was noted. Similar to the PDF approach discussed earlier, in spite of the fact that CMC methods deal with more realistic assumptions, they are not often used in the combustion industry due to the high computational costs involved. For most practical combustion systems, and especially, those fed by liquid fuels such as aero gas turbines, these computational costs become so critical that flamelet models are usually preferred. However, as briefly mentioned in the previous section devoted to the classical flamelet model, the majority of the limitations for the classical flamelet model are due to the formulating assumptions. The most detrimental assumptions to the model performance with respect to spray combustion modelling include the single burning regime assumption and the non-inclusion of the spray evaporation effects. The development of improved flamelet models discussed in the next section are mainly guided by the need to address such limitations.

1.4.5 Finite rate chemistry assumption: Improved flamelet models

The classical flamelet model relies on the assumption of a single-burning regime; furthermore, the flamelet state is not always correctly identified in the whole flamelet solution space provided by the unsteady laminar diffusion flamelet model (ULDFM) as depicted by the corresponding S-shaped curve. It is worth recalling that the latter consists of three branches with different physical meanings. These are the upper branch which corresponds to the stable burning regime, the middle branch which represents the unstable (alternate burning and extinguishing regimes), and the lower branch which corresponds to the mixing (or extinguished) regime. To address these first drawbacks, a reactive "tracking" scalar, also termed progress variable, was first introduced to identify the change in

regime of each single flamelet. This strategy led to the mixture fraction-progress variable formulation, and more explicitly to an improved flamelet model which is widely known as the *unsteady flamelet/progress variable* (UFPV) model.

Considering the fact that spray combustion in most liquid-fuelled combustors involves a fuel injection into a high-temperature chamber, the fuel droplets are partially vaporized and the resulting vapour is mixed with oxidizer prior to combustion, the progress variable introduced in the UFPV model captures premixing effects and other flame characteristics such as flame lift-off and flame front propagation. The second drawback is mainly due to the fact that the model does not include effects of the spray dynamics on the flamelet structure. In other words, when the model is applied to spray combustion, it is assumed that all the droplets are entirely vaporized at once so that chemical reactions of combustion occur exclusively in the gaseous phase without any interaction with the droplets.

Although the discrepancies introduced by such an assumption are likely to be mitigated in some practical configurations exhibiting dilute sprays of small droplets, it is worth mentioning that the model does not hold for many other configurations in which the spray involves large droplet sizes that are not completely vaporized before starting to burn. As an alternative approach to address this second drawback, Hollman and Gutheil [1998] formulated a spray flamelet model allowing to directly include the effects of the spray dynamics on the flamelet structure. Their strategy is consistent since it led to a reasonable prediction of the thermochemical state and especially the temperature field in the cold zone around the injector orifice. However, this spray-based flamelet model involves a very high-dimensional library, and the pre-processing task is still demanding in terms of computing resources since all physical spray parameters such as droplet diameter, liquid volume fraction, liquid injection velocity, and others have to be varied when generating the flamelet library. As an alternative approach to this constraint of the spray flamelet model, some research teams found a more efficient approach in tabulating only the chemical subspace accessed by spray combustion, and a possible way to do this is to identify this subspace from the gaseous flamelets. This new approach was validated by Baba and Kurose [2008] who showed the need of combustion model for partially-premixed flames to guarantee an accurate prediction of spray flames.

Among the drawbacks of the laminar diffusion flamelet model with respect to its unsuitability to reacting flows with multi-burning regimes, the single-burning regime is by far the most impairing feature. An efficient way to cope with this particular limitation consists in tabulating only the chemical subspace accessed by spray combustion using multi-regime flamelet models. This potential solution leads to the investigation of the new chemical reduction and tabulation approaches. When the prediction of intermediate species and pollutant emissions is of interest, two chemistry treatments can be applied. The first approach consists of using skeletal chemistry schemes derived from the detailed schemes, while the second consists of implementing full detailed chemistry models to accurately describe the overall reaction. Although each of these two approaches can provide a reasonable description of the chemical processes involved in the reacting system, it is worth noting that both of them are subject to some constraints which may preclude their application to some configurations. In

the first approach for instance, the optimal choice of the number of reduced reactions and species so as to reasonably describe the overall reaction rate is a tedious process. Furthermore, this choice is not always unique as it can be more or less problem dependent. The second method guarantees a reasonable level of accuracy, but huge amounts of memory and computing time are most often necessary, especially for heavy hydrocarbon fuels whose detailed oxidation mechanisms involved more than a thousand elementary reactions among hundreds of species.

The improved flamelet models discussed in this subsection are formulated to address the drawbacks of this second approach. In some configurations where detailed chemistry models become cumbersome, a reduced chemical scheme is proposed to model the chemistry effects. The strategy used for the chemical model reduction is mainly based on an order of magnitude analysis of the chemical time scales involved, namely, the fact the reacting system involves fast and slow reactions. The classical reduction techniques proceed by applying partial equilibrium and steady state assumptions for all the reactions characterized by small time scales (i.e. fast reactions). The species involved in the reacting system are assumed to be created and consumed at a very high rate and thus remain almost in equilibrium. However, when dealing with heavy hydrocarbon fuels, the choice of fast time scales results in a tedious process since it is generally done by hand, and requires a prior knowledge of the chemical kinetics of the reacting system. Plus, the validity of the steady state assumption commonly done in the second model is quite narrow in the band of thermodynamic states since species which are considered to be at steady state in some low temperature ranges are not necessarily in that state when the temperature raises. As an attempt to address this issue, two mathematical formulations have been first developed to automatically differentiate and select the fast time scales that can be used for the equilibrium assumption. These are Computational Singular Perturbation (CSP) by Valorani et al. [2006], and Intrinsic Low Dimensional Manifold (ILDM) by Mass and Pope [1992]. In the CSP method, the fast time scales are obtained from the detailed chemical source term, whereas the ILDM method proceeds by separating fast and slow chemical processes using an eigenvalue analysis of the Jacobian of the chemical source term.

Although these two reduction techniques overcome some limitations of the classical reduction methods, it is worth mentioning that in some cases the steady state assumption for fast time scales is less efficient and not always suitable. In the range of low temperatures for instance, the number of species remaining in quasi-equilibrium is less, and neither of the two approaches (CSP and ILDM) is applicable. This is because only time scales of reaction rates are considered for time scale separation by neglecting convection and diffusion, while reaction rate terms are not very dominating in the low temperature range, and the convection and diffusion are then non-negligible. In order to overcome this limitations of ILDM at low temperature, two new tabulation techniques have been developed. These are Flamelet Prolongation of ILDM (FPI) by Gicquel et al. [2000], and the Flamelet Generated Manifold (FGM) by Oijen and de Goey [2000, 2004]. The two tabulation techniques are based on the projection of laminar partially premixed flame solution in a reduced sub-space. The sub-space is populated using freely propagating laminar premixed flamelets calculated with the inclusion of

convection and diffusion effects for various equivalence ratios, ϕ, within the whole flammability range $[\phi_L, \phi_R]$, where ϕ_L and ϕ_R are the lean and rich flammability limits, respectively. These two tabulation techniques combine the advantage of flamelet formulation with the dimensional reduction techniques, and are based on a 2-D subspace ((Y_C, Z)), where Y_C and Z are respectively the reaction progress variable and the mixture fraction. The progress variable evolves monotonically between fresh and burnt gases; and for hydrocarbon combustion, it is generally defined as the normalized sum (for the normalized reaction progress variable, C) or the un-normalized sum (for the un-normalized progress variable, Y_C) of products mass fraction in different ways using the following general equation:

$$C = \frac{Y_C}{Y_C^{eq}} = \frac{\sum_k a_k (Y_k - Y_k^u)}{\sum_k a_k Y_k^{eq}} \tag{1.44}$$

For instance, The definitions used by Fiorina et al. [2005] and Ihme and Pitsch [2008] are respectively shown in the following equations:

$$Y_C = Y_{CO_2} + Y_{H_2O} + Y_{CO} + Y_{H_2} \tag{1.45}$$

$$Y_C = Y_{CO_2} + Y_{CO} \tag{1.46}$$

In their basic forms, FPI and FGM can be viewed as premixed flamelet tabulation (PFT) methods since each of them maps the chemical sub-space accessed by a flame through a collection of gaseous laminar premixed flames. Such flamelet structures can be generated by projecting the species and energy conservative equations in the progress variable space. Through an approach similar to that used in the laminar diffusion flamelet model discussed earlier, the following equations are derived to generate the premixed flamelets over the whole range of equivalence ratios.

$$\rho \frac{\partial Y_i}{\partial \tau} + \frac{\partial Y_i}{\partial Y_C} \dot{\omega}_C = \frac{\rho \chi_{Y_C}}{Le_i} \frac{\partial^2 Y_i}{\partial Y_C^2} + \frac{\rho \chi_Z}{Le_i} \frac{\partial^2 Y_i}{\partial Z^2} + \frac{2\rho \chi_{Z,Y_C}}{Le_i} \frac{\partial^2 Y_i}{\partial Z \partial Y_C} + \dot{\omega}_i \tag{1.47}$$

$$\begin{aligned} \rho \frac{\partial T}{\partial \tau} + \frac{\partial T}{\partial Y_C} \dot{\omega}_C - \frac{1}{C_p} \left(\frac{\partial C_p}{\partial Y_C} + \sum_{i=1}^{N} \frac{C_{p_i}}{Le_i} \frac{\partial Y_i}{\partial Y_C} \right) \left(\frac{\partial T}{\partial Y_C} \rho \chi_{Y_C} + \frac{\partial T}{\partial Z} \rho \chi_{Z,Y_C} \right) \\ - \frac{1}{C_p} \left(\frac{\partial C_p}{\partial Z} + \sum_{i=1}^{N} \frac{C_{p_i}}{Le_i} \frac{\partial Y_i}{\partial Z} \right) \left(\frac{\partial T}{\partial Z} \rho \chi_Z + \frac{\partial T}{\partial Y_C} \rho \chi_{Z,Y_C} \right) \\ = \rho \chi_{Y_C} \frac{\partial^2 T}{\partial Y_C^2} + \rho \chi_Z \frac{\partial^2 T}{\partial Z^2} + 2\rho \chi_{Z,Y_C} \frac{\partial^2 T}{\partial Z \partial Y_C} - \frac{1}{C_p} \sum_{i=1}^{N} h_i \dot{\omega}_i \end{aligned} \tag{1.48}$$

A careful observation of these equations shows that, the premixed flamelet equations expressed in the Y_C-space involve six dimensions. These are the time, τ; the mixture fraction, Z; the reaction progress variable, Y_C; the scalar dissipation rate of the mixture fraction, $\chi_Z = (\lambda/\rho C_p)\nabla Z \nabla Z$; the scalar dissipation rate of the progress variable, $\chi_{Y_C} = (\lambda/\rho C_p)\nabla Y_C \nabla Y_C$; and the cross-scalar dissipation rate defined between the mixture fraction and the progress variable, $\chi_{Z,Y_C} = (\lambda/\rho C_p)\nabla Z \nabla Y_C$. For tabulations based on pure premixed flamelets, the two scalar dissipation rates related to the mixture fraction gradient, χ_Z and χ_{Z,Y_C} are neglected, which physically means zero-diffusion fluxes across iso-mixture

fraction surfaces. This assumption leads to a more simplified form of the flamelet equations, which is used in the majority of premixed flamelet solvers:

$$\rho\frac{\partial Y_i}{\partial \tau}+\frac{\partial Y_i}{\partial Y_C}\dot{\omega}_C=\frac{\rho\chi_{Y_C}}{Le_i}\frac{\partial^2 Y_i}{\partial Y_C^2}+\dot{\omega}_i \tag{1.49}$$

$$\rho\frac{\partial T}{\partial \tau}+\frac{\partial T}{\partial Y_C}\dot{\omega}_C=\frac{1}{C_p}\left(\frac{\partial C_p}{\partial Y_C}+\sum_{i=1}^{N}\frac{C_{p_i}}{Le_i}\frac{\partial Y_i}{\partial Y_C}\right)\frac{\partial T}{\partial Y_C}\rho\chi_{Y_C}+\rho\chi_{Y_C}\frac{\partial^2 T}{\partial Y_C^2}-\frac{1}{C_p}\sum_{i=1}^{N}h_i\dot{\omega}_i \tag{1.50}$$

As established by Fiorina et al. [2005], even in its form including the two scalar dissipation rates (i.e. $\chi_{Y_C}\neq 0$, $\chi_{Z,Y_C}\neq 0$, and $\chi_Z=0$), the tabulation based on premixed flamelets for a range of equivalence ratios is accurate only when the modelled flame structure remains close to the structure of a premixed flame front. When the diffusion of mass across iso-equivalence ratio surfaces dominates, it leads to some discrepancies. An alternative method to address this issue would be to base the chemistry tabulation on diffusion flamelets as it is done in the laminar diffusion or in the flamelet-progress variable formulation (FPV) discussed in the previous subsection. However, such a tabulation technique (also termed as Diffusion Flamelet Tabulation, DFT) which is based on a 2D-subspace defined by the mixture fraction and its scalar dissipation rate, is likely to properly model the structure of a given flame if the latter is predominantly diffusion-controlled since it cannot capture the structure and consequently the propagation of premixed flame front. Considering the critical drawbacks of these two tabulation techniques which are based on the single burning regime, it is clear that, they cannot accurately capture the structure of spray flames as spray flames are known to exhibit both premixed-like and diffusion-like reaction zones due to partial premixing of the evaporated liquid fuel with the oxidizer [Franzelli et al., 2013]. To address the limitations of these single regime models with respect to spray combustion, the multi-regime flamelet model (MFM) was formulated to capture all the reaction zones involved in spray flames. The two single regime models are, to some extent, the starting points of the multi-regime flamelet models inasmuch as they are the limit states of this improved tabulation technique. In fact, in the multi-regime flamelet model, the chemical structure of complex flames is mapped by a collection of one-dimensional gaseous partially-premixed counterflow flamelets characterized by an injection of pure air against a fuel/air mixture for different values of equivalence ratio, ϕ, and strain rate, a.

The tabulation is then built by first varying the fuel/air stream equivalence ratio between, $\phi=\phi_{sl}$ and $\phi=+\infty$, ϕ_{sl} being the smallest value of the fuel air stream equivalence ratio for which the counterflow flame is stabilized. Thereafter, each flamelet is solved for different strain rate values, $a\in\,]0,a_q[$, where a_q stands for the quenching value of the strain rate. On the one hand, when $\phi=+\infty$ and $a\in\,]0;a_q[$, the table is filled by diffusion flamelets as in the diffusion flamelet tabulation. On the other hand, when $a=a$ and $\phi\in\,]\phi_L,\phi_R[$ (ϕ_L and ϕ_R being respectively the lean and rich flammability limits), the table is filled with unstrained laminar premixed flamelets as in the premixed flamelet tabulation. This procedure allows mapping the chemical subspace with premixed, non-premixed and partially premixed flamelets, and consequently leads to an improved modelling of the global flame structure, as all the reaction zones are pretty well captured. This subspace, which is the solution space

used by current improved FGM models, is identified by three parameters: the progress variable, Y_C, the mixture fraction, Z, and the scalar dissipation rate of the mixture fraction, χ_Z.

1.5 Turbulence models

The discussions conducted in the previous sections allowed determining the transport equations that govern turbulent reactive flows when dealing with either an Eulerian-Eulerian or an Eulerian-Lagrangian formulation. These equations consist of the continuity, momentum, and scalars transport equations, and can be solved using various approaches depending on the desired level of accuracy and the available computing resources. With respect to these two latter criteria, there are globally three different approaches. These are the direct numerical simulation (DNS), the Reynolds-Averaged Navier-Stokes (RANS), and the Scale Resolved Simulation (SRS) approaches. The third group of simulation approaches includes Large Eddy Simulation (LES) and all its variants, as well as hybrid RANS/LES approaches such as the Scale Adaptive Simulation (SAS) and the Detached Eddy Simulation (DES) approaches. The following section discusses the characteristics of these turbulence models, namely, their formulation and the related assumptions along with the trade-off between the computational cost and the accuracy of the results.

1.5.1 Direct Numerical Simulation (DNS)

A DNS of a given flow field consists of solving a complete three dimensional and time-dependent conservative and transport equations governing that flow field without any turbulence model; this implies that, in a turbulent environment, the whole turbulence spectrum is resolved. To this end, the grid spacing and the time step in the computation are usually defined smaller than those of the smallest turbulence scales (i.e. the Kolmogorov scales). Obviously, such a simulation approach leads, in principle, to numerically-accurate solutions of the exact equations of motion, and a proper solution of the investigated flow field, provided that high accurate numerical schemes are implemented. With this potential retrieval capabilities, from a practical standpoint, the statistics computed from DNS results can be used to test proposed closure approximations in engineering modelling.

At the most fundamental level, the DNS offers a new way to investigate some critical processes such as those related to flame/turbulence interactions [Poinsot and Veynante, 2005], and can also be used to obtain information about essentially-unmeasurable properties like pressure fluctuations [Wilcox, 2006]. Based on these latter assets, DNS can also be viewed as an additional source of "experimental data" (i.e. data for model validation), recorded with unobtrusive (or non-intrusive) measuring techniques. Considering the operating mode of DNS (the resolution of the whole turbulence spectrum), it is clear that the DNS of practical configurations would lead to prohibitive computing costs. As discussed in [Wilcox, 2006, Poinsot and Veynante, 2005, Swaminthan and Bray, 2011], for a simple case of non-reacting flows, the range of length scales increases as $Re_t^{3/4}$, while that of time scales increases as $Re_t^{1/2}$, where Re_t is a turbulence Reynolds number defined using the root-

mean-square turbulence viscosity, u_t, the turbulence length scale, Λ, and the kinematic viscosity, ν. The consequence of such a flow-Reynolds-number dependence is that the DNS of even turbulent non-reactive flows at practical Reynolds numbers is still too computationally expensive. The computing resource requirements becomes even larger in combustion problems since chemical reactions introduce their own time scales, which may sometimes be smaller than those of the Kolmogorov scales, thus extending the range of scales to be resolved; furthermore, additional non-linear transport equations need to be solved for species and enthalpy. Considering that the accurate description of some combustion phenomena requires a realistic fuel-oxidation mechanism, and that the most reliable fuel-oxidation mechanism often involves hundreds of species and elementary reactions, it is clear that the implementation of detailed chemical processes in a DNS computation is still a difficult task with the current computational capabilities. Nevertheless, some DNS computations of turbulent combustion in simplified geometries with either single global reaction or a relatively reduced set of elementary reactions have so far been conducted, and have proved to be an invaluable research tool for exploring the basis physics and testing the validity of modelling assumptions. In the particular case of configurations involving spray combustion, a part of the computing resources has to be allocated to the spray dynamics calculations, and some simplifying assumptions are generally made, which impede the potential performance of the DNS. First, it is assumed that the liquid is in the form of spherical droplets with evaporation occurring at the droplet surface, and that equilibrium prevails between the two phases. Furthermore, in order to reduce the computing costs, the transports of mass, momentum and energy occurring in the thin layer surrounding the droplet are not solved, and instead, theoretical models combined with experimental correlations are employed. In spite of the exponential growth in computing power, a DNS of a practical gas turbine combustion chamber is not expected to be achievable in the near future, the main cause being the prohibitive requirements of DNS in terms of computing resources. As a temporary solution, the combustion community has so far exploited alternative approaches to retrieve (at least partly) macroscopic structure of turbulent reacting flows. These are the RANS and the SRS approaches respectively discussed in the two following subsections.

1.5.2 Reynolds Averaged Navier-Stokes approaches (RANS)

The RANS simulation technique is a classical solution to the problem of a wide range of length and time scales in turbulent flows. It consists of solving the ensemble-averaged (for unsteady RANS) or time-averaged (for RANS) form of the conservative equations governing the investigated flow. The statistical averaging process can be either Reynolds-based or Favre-based (i.e. mass-weighted) depending on whether the flow is incompressible or compressible. In both cases, a substantial part of the turbulent spectrum is filtered out, and the minimum scales of the averaged variables are much larger than the smallest scales of the turbulent fluctuations. However, because of the non-linear nature of the original equations, their averaged forms contain additional terms such as Reynolds stresses which involves co-variances of turbulent fluctuations about the mean flow. To further elaborate this brief discussion based on the RANS simulation technique, the following Favre-averaged equations of

continuity, momentum and scalars are considered:

$$\frac{\partial \bar{\rho}}{\partial t} + \frac{\partial \bar{\rho}\tilde{u}_j}{\partial x_j} = \bar{\dot{S}}_m \tag{1.51}$$

$$\frac{\partial \bar{\rho}\tilde{u}_j}{\partial t} + \frac{\partial}{\partial x_j}\left(\bar{\rho}\tilde{u}_i\tilde{u}_j\right) = -\frac{\partial \bar{p}}{\partial x_i} + \frac{\partial}{\partial x_j}\left(\bar{\sigma}_{ij} - \bar{\rho}\widetilde{u_i'' u_j''}\right) + \bar{\dot{S}}_{u_j} \tag{1.52}$$

$$\frac{\partial \bar{\rho}\tilde{\phi}_k}{\partial t} + \frac{\partial}{\partial x_j}\left(\bar{\rho}\tilde{u}_j\tilde{\phi}_k\right) = \frac{\partial}{\partial x_j}\left(\bar{J}_{\phi_k} - \bar{\rho}\widetilde{u_j'' \phi_k''}\right) + \tilde{\dot{\omega}}_{\phi_{k\_Averaged}} + \bar{\dot{S}}_{\phi_k} \tag{1.53}$$

where $\sigma_{ij} = \mu\left(\frac{\partial u_i}{\partial x_j} + \frac{\partial u_j}{\partial x_i} - \frac{2}{3}\delta_{ij}\frac{\partial u_l}{\partial x_l}\right)$ is the strain-rate tensor, while J_{ϕ_k} are the laminar diffusion fluxes of scalars such as enthalpy and representative scalars (depending on the combustion models considered for the investigation). The laminar diffusion fluxes are commonly calculated using Fick's law, or more explicitly, using the gradient diffusion assumption with the molecular diffusion coefficient of the applicable scalars, D_{ϕ_k}, as follows: $J_k = D_{\phi_k}\frac{\partial \phi_k}{\partial x_j}$. The source terms $\dot{S}_m$, $\dot{S}_{u_j}$ and $\dot{S}_{\phi_k}$ account for the interactions with the liquid phase, while the other scalar source term, $\dot{\omega}_{\phi_k}$ takes into account the effects of all heat releases including those from the chemical reactions on the thermochemical state. Depending on the approach adopted to investigate the combustion phenomenon as a whole, these terms may require closure models. The remaining terms, the Reynolds stresses, $\bar{\rho}\widetilde{u_i'' u_j''}$, and the turbulent diffusion fluxes of scalars, $\bar{\rho}\widetilde{u_j'' \phi_k''}$, are the unclosed terms generated by the statistical averaging. The development of closure approaches for these terms is the essence of the RANS simulation techniques. Indeed, to circumvent the so-called *closure problem* that the derivation of transport equations for these co-variances using the original equations would have generated, two different formulations are commonly adopted in the RANS simulation technique, and lead to a reasonable accuracy of predictions for a wide range of turbulent flows. These are the Reynolds stress modelling, and the Reynolds Stress Transport (RST).

The Reynolds stress approach is based on the Boussinesq assumption (also termed as gradient diffusion assumption), and consists of relating the Reynolds stresses to the velocity gradient through a turbulence parameter, the turbulent viscosity. The latter is chosen in analogy to the molecular viscosity which is a fluid physical property, and is computed using turbulence quantities such as the turbulence kinetic energy and its dissipation rate among others. The turbulence quantities are obtained by solving either one transport equation (for one-equation-based RANS) or two transport equations (for two-equations-based RANS). The formulation of such transport equations has been the focus of extensive investigations over many decades, and depending of the flow configuration and the investigated phenomena, significant progress have been achieved, justifying therefore the widespread use of RANS approaches in industries. For internal flows especially, the most robust and the most popular are the two-equation RANS methods such as $k-\varepsilon$ and $k-\omega$, together with all their variants (e.g. RNG $k-\varepsilon$, Realizable $k-\varepsilon$, SST $k-\omega$, etc.). Detailed reviews of these RANS approaches can be found in [Wilcox, 2006]; only the RANS model used to conduct preliminary simulations in the current study is discussed in the chapter devoted to the numerical implementation.

Similarly, the turbulent diffusion fluxes of scalars are computed using the gradient diffusion assumption based on the turbulent viscosity, μ_t, and the turbulent Schmidt number, Sc_t. The turbulent Schmidt number is defined as $Sc_t = \frac{\mu_t}{\rho D_t}$, where D_t is the turbulent diffusivity of the scalar considered. Although this first class of RANS techniques is worthwhile from an industrial standpoint (due to its simplicity and the reduced computational cost involved), it is important noting that they assume an isotropic eddy-viscosity. Unfortunately, the range of validity of such an assumption is too narrow, especially when dealing with some internal flow configurations such as highly swirled combustion chamber. For instance, RANS approaches based on the assumption of isotropic viscosity cannot capture flow features resulting from anisotropy in the Reynolds stresses. Furthermore, the turbulent viscosity is always overestimated, leading to an excessive dissipation of the turbulent structures [Menter and Egorov, 2010].

The second group of RANS approaches, the RST model, has a potential to circumvent the isotropic assumption, as it proceeds by solving transport equations for the Reynolds stresses, together with an equation for the dissipation rate. This means that, in addition to the standard flow equations, seven additional transport equations need to be solved to determine the structure of a 3D flow field. The RST model accounts for streamline curvature, swirl, rotation, and rapid changes in strain rate in a more rigorous manner than the first group of RANS approaches, it therefore has a potential to predict more reasonably complex flow fields. However, the accuracy of prediction is strongly determined by the closure assumptions adopted to model various terms in the transport equations for the Reynolds stresses. The modelling of the pressure-strain and the dissipation-rate terms is particularly challenging, and is often considered to be responsible for hampering the accuracy of RST predictions. Considering the additional computing expenses incurred in RST simulations, the model is attractive only when dealing with configurations whose flow features of interest are the result of anisotropy in the Reynolds stresses. Such configurations include highly swirling flows in combustion chambers, rotating flow passages, and the stress-induced secondary flows in ducts. In addition, most technical combustion devices often require rapid mixing and short combustion times to ensure high combustion efficiency and proper flame stabilization [Bray et al., 2005]. These latter conflicting requirements lead to devices characterized by very complicated flow patterns, such as swirling flows, breakdowns of large-scale vortex structures, and recirculating regions. In combustion chambers exhibiting such flow patterns, an accurate prediction of some critical combustion phenomena like pollutants emissions cannot be achieved using RANS approaches since such critical phenomena are inherently unsteady and involves very small time scales.

In order to cope with these potential RANS drawbacks which are mainly related to the lost of flow details induced by the averaging process, Scales-Resolved Simulation (SRS) consisting of a partial resolution of the turbulence spectrum have so far been formulated, and are increasingly popular. A more robust form of SRS approaches is the Large Eddy Simulation (LES) technique, which has already been applied to a variety of combustion problems of technical interest including predictions of pollutants [Eggenspieler and Menon, 2004]; aircraft engine combustion [Kim et al., 1999, Moin,

2002, 2004]; reciprocating engine combustion [Haworth and Jansen, 2000]; combustion, flashback, and blowoff in premixed stationary power-generation gas turbine combustor [Selle et al., 2004, Stone and Menon, 2003]; and combustion instabilities [Shinjo et al., 2003, Wall and Moin, 2005]. In the next subsection, the LES-equations and assumptions from their derivation are presented.

1.5.3 Large Eddy Simulation (LES)

The Large Eddy Simulation technique consists of resolving large-scale motions, while modelling small-scale motions as well as their interactions with the large ones. The separation between the large and the small scales motions is achieved using a cut-off length scale also termed as filter width. This threshold length scale represents the size of the smallest turbulence structures captured by the computational mesh size. The robustness of the LES is mainly due to the fact that, most of the energy of turbulence is contained in large eddy motions, whereas small scales are in the inertial and viscous subrange and thus are much more isotropic (due to the turbulence cascade) than the large scales that are more controlled by the overall geometry [Lesieur and Metais, 1996, Lesieur et al., 2005, Poinsot and Veynante, 2005, Pitsch, 2006]. The partial resolution of the turbulent spectrum provides an accuracy and computing costs for LES that fall between those of DNS and RANS. By applying a time-invariant spatial filter to the conservation equations governing the chemically reacting flow as described previously for both Eulerian-Eulerian and Eulerian-Lagrangian formulation, the following Favre-filtered conservation equations are derived for large scale motions:

$$\frac{\partial \bar{\rho}}{\partial t} + \frac{\partial \bar{\rho}\tilde{u}_j}{\partial x_j} = \bar{\dot{S}}_m \tag{1.54}$$

$$\frac{\partial \bar{\rho}\tilde{u}_j}{\partial t} + \frac{\partial}{\partial x_j}\left(\bar{\rho}\tilde{u}_i\tilde{u}_j\right) = -\frac{\partial \bar{p}}{\partial x_i} + \frac{\partial}{\partial x_j}\left[\bar{\sigma}_{ij} - \bar{\rho}\left(\widetilde{u_i u_j} - \tilde{u}_i\tilde{u}_j\right)\right] + \bar{\dot{S}}_{u_j} \tag{1.55}$$

$$\frac{\partial \bar{\rho}\tilde{\phi}_k}{\partial t} + \frac{\partial}{\partial x_j}\left(\bar{\rho}\tilde{u}_j\tilde{\phi}_k\right) = \frac{\partial}{\partial x_j}\left(\bar{J}_{\phi_k} - \bar{\rho}\left(\widetilde{u_j\phi_k} - \bar{\rho}\tilde{u}_j\tilde{\phi}_k\right)\right] + \tilde{\dot{\omega}}_{\phi_k\_Filtered} + \bar{\dot{S}}_{\phi_k} \tag{1.56}$$

with

$$\tilde{\Phi} = \frac{1}{\bar{\rho}}\int \Phi(\mathbf{x}_i^{'})F(\mathbf{x}_i - \mathbf{x}_i^{'})d\mathbf{x}_i^{'} \tag{1.57}$$

where Φ stands for the investigated physical quantities, namely, the velocity and scalars (i.e. $\Phi \equiv \Phi(u_i, \phi_k)$); $F(\mathbf{x}_i)$ is the time-invariant filter function whose shape is defined in such a way that it approaches zero when $\mathbf{x}_i^{'}$ exceeds the filter width, and it obeys the following normalization law: $\int F(x_i^{'})dx_i^{'}) = 1$. Filter shapes exhibiting such a trend include cut-off filters in the spectral space, box filters in the physical space, and Gaussian filters in the physical space. A detailed description of these filter shapes can be found in [Poinsot and Veynante, 2005]. In all these equations, the bar and tilde accents stand for Reynolds and Favre-filtered quantities, respectively, unlike RANS equations in which they stand for Reynolds and Favre-averaged quantities, respectively. As noticed for RANS equations, these LES equations involve unclosed quantities that need to be modelled. These are the subgrid-scale stresses (SGS), $\tau_{SGS} = \bar{\rho}\left(\widetilde{u_i u_j} - \tilde{u}_i\tilde{u}_j\right)$ in the momentum equations, and the subgrid-scale scalars fluxes, $\bar{\rho}\tilde{u_j}\tilde{\phi}_k$, in the scalars equations. The former is modelled using an eddy viscosity

assumption, while the second is modelled using the eddy diffusivity. In most LES codes, the SGS term is often split into its isotropic (first term on the right hand side) and deviatoric (second term on the right hand side) parts as follows:

$$\tau_{SGS} = \underbrace{\tau_i j - 1/3\tau_k k\delta_i j} + \underbrace{1/3\tau_k k\delta_i j}; \tag{1.58}$$

the isotropic part is embedded with the pressure term, while the anisotropic (or deviatoric) part is modelled.

As modelling approaches, various SGS models have been formulated depending on the flow complexity. These are the classical Smagorinsky model originally formulated by Smagorinsky [1963] through an extension of the Boussinesq turbulent viscosity approach, and its improved versions such as the Dynamic Smagorinsky-Lilly Model [Germano et al., 1991], the Smagorinsky-Lilly [Lilly, 1992], the Wall-Adapting Local Eddy-viscosity (WALE) model [Nicoud and Ducros, 1999], the Algebraic Wall-Modelled LES (WMLES) model [Shur et al., 2008], and the Dynamic Kinetic Energy Subgrid-Scale Model [Kim and Menon, 1997]. From this brief description of the LES approach, it can easily be seen that the potential ability of the LES to capture flow details is related to the cut-off length scale (i.e. the width of the filter function). In other words, the accuracy of LES predictions based on its classical formulation is inherently mesh dependent, and increases when the size of the local computational cell decreases. However, that LES mesh dependency can be mitigated by implementing other filtering techniques such as the explicit filtering which allows a separation of the filter size and the mesh spacing. Whatever the filtering technique adopted, it is proved that, a well-conducted LES of practical configurations is still computationally expensive so that it is not obvious to predict if the LES simulation technique will soon be widely applied in gas turbines research development. This uncertainty is further powered by constraints related to the investigation of some critical combustion phenomena, namely, those allowing to meet the safety requirements and to cope with the surge in environmental regulations such as ignition and pollutant emissions. Indeed, as mentioned so far, an accurate prediction of these latter combustion processes asks for sophisticated chemistry models, which involve high number of species and elementary reactions for heavy hydrocarbon fuels such as jet fuels. Furthermore, a part of the computing resources needs to be allocated to the spray treatment. Thus, depending on the flow patterns exhibited by the simulated configuration, the investigated phenomena, and the global requirements in terms of computing resources, it may often be necessary to first locate the flow regions requiring more elaborate treatment techniques (e.g. unstable regions) so as to perform LES-like analysis in these regions only, the remaining flow regions being treated with the conventional RANS approaches. Such approaches have been formulated to provide a reasonable accuracy, while keeping the computational cost at a moderate level (compared to a full LES simulation). The most popular of these approaches are Scale-Adaptive Simulation (SAS), and Detached Eddy Simulation (DES) and its variants. The theory behind each of these two models is briefly discussed in the two following subsections.

1.5.4 Scale-Adaptive Simulation (SAS)

Due to the LES-like treatment it provides in some flow regions, SAS has a potential to partially resolve the turbulence spectrum and thus belongs to the group of Scales Resolved Simulation (SRS) techniques. However, the method should be viewed as a second generation of Unsteady RANS method rather than a sub-grid scale modelling. In fact, the SAS method does not contain any parameter related to the grid used for the resolution of the conservative equations as it is the case for LES and the DES model discussed in the next subsection. SAS was developed by Menter and Egorov [2010] by modifying the $k-kL$ model initially developed by Rotta. In the modification made to the Rotta model, a second length scale, the Von Karman length-scale LvK, was introduced to take into account the length-scale of the resolved eddies. Thus, unlike the standard RANS models which provide a length scale proportional to the thickness of the shear layer, SAS dynamically adjusts to the length-scales of the resolved structures depending on the flow situation. More explicitly, the new length-scale, LvK, allows the SAS model to operate in RANS-like mode in the stable regions of the flow and to exhibit LES-like resolution in the unstable flow regions. The transition from RANS to LES is initiated by the level of flow instabilities. For flow involving weak instabilities, the SAS model is expected to produce results close to those of unsteady RANS.

The mathematical formulation of the SAS approach is quite similar to that of the Unsteady RANS approaches based on the turbulent viscosity modelling, in the sense that, the Reynolds stresses are also modelled as in unsteady RANS approaches, but using the following modified equations for the turbulence kinetic energy, k and the eddy frequency, ω.

$$\frac{\partial \bar{\rho}\tilde{k}}{\partial t}+\frac{\partial}{\partial x_j}\left(\bar{\rho}\tilde{k}\tilde{u}_j\right)=\frac{\partial}{\partial x_j}\left[\left(\mu+\frac{\mu_t}{\sigma_k}\right)\frac{\partial \tilde{k}}{\partial x_j}\right]-D_k+G_k+S_k \tag{1.59}$$

$$\frac{\partial \bar{\rho}\tilde{\omega}}{\partial t}+\frac{\partial}{\partial x_j}\left(\bar{\rho}\tilde{\omega}\tilde{u}_j\right)=\frac{\partial}{\partial x_j}\left[\left(\mu+\frac{\mu_t}{\sigma_\omega}\right)\frac{\partial \tilde{\omega}}{\partial x_j}\right]-D_\omega+G_\omega+S_\omega+Q_{SAS}+(1-F_1)F_2 \tag{1.60}$$

where the D_k and D_ω terms are respectively the dissipation of the turbulence kinetic energy and the eddy frequency, while the P_k and P_ω terms are their production rates; the S_k and S_ω terms are the source terms defined as in the classical RANS approaches; the F_1 and F_2 terms are defined as follows:

$$F_1=\frac{1}{\tilde{\omega}}\frac{\partial \tilde{\omega}}{\partial x_j}\Big/\frac{1}{\tilde{k}}\frac{\partial \tilde{k}}{\partial x_j},\ \text{and}\ F_2=\frac{2\bar{\rho}}{\sigma_{\omega,2}}\frac{1}{\tilde{\omega}}\frac{\partial \tilde{k}}{\partial x_j}\frac{\partial \tilde{\omega}}{\partial x_j}. \tag{1.61}$$

The Q_{SAS} term is defined using the Von Karman length scale, L_{vK}, as shown in the following equation:

$$Q_{SAS}=max\left[\bar{\rho}\eta_2 kS^2\left(\frac{L}{L_{vK}}\right)^2-C\frac{2\bar{\rho}\tilde{k}}{\sigma_\Phi}max\left(\frac{1}{\tilde{\omega}^2}\frac{\partial \tilde{\omega}}{\partial x_j}\frac{\partial \tilde{\omega}}{\partial x_j},\frac{1}{\tilde{k}^2}\frac{\partial \tilde{k}}{\partial x_j}\frac{\partial \tilde{k}}{\partial x_j}\right),0\right], \tag{1.62}$$

where $\eta_2=3.51$, $\sigma_{Phi}=2/3$, $C=2$, $L=\sqrt{k}/\left(C_\mu^{1/4}\tilde{\omega}\right)$, and $L_{vK}=k\left(\frac{\partial \tilde{u}_j}{\partial y}\right)/\left(\frac{\partial^2 \tilde{u}_j}{\partial y^2}\right)$ The ω-equation source term provides SAS with ability to retrieve important flow structures compared to steady and unsteady Reynolds-averaged Navier Stokes simulation approaches (i.e. RANS and URANS). This turbulence-resolving capability of the SAS method has been validated through a set of representative

test cases, covering both underlying generic flows along with practical engineering applications. These include purely aerodynamics flows with massive separation and heat transfer as well as more complex flows such as gaseous and spray combustion [Egorov et al., 2010, Fossi et al., 2015a]. Such validation cases show the ability of the SAS method to overcome some RANS weaknesses (e.g. overestimation of the turbulent viscosity which leads to an excessive dissipation of the turbulent flow structures) and thus its suitability for some configurations of industrial flows. In addition to SAS method whose ability to capture some flow details due to the Von Karman length scale introduced in the ω-equation as mentioned earlier, there is another group of hybrid RANS/LES approaches, the Detached-Eddy Simulation (DES), which provides refinements similar to those of the SAS method, and which are based on a cut-off length scale concept as the LES method.

1.5.5 Detached-Eddy Simulation (DES)

The main motivation behind the formulation of the Detached-Eddy Simulation (DES) approach is the same as for the SAS method, namely, the estimates which indicate that the computational costs of applying Large-Eddy Simulation (LES) to complete typical configurations such as an airplane, submarine, or road vehicle are prohibitive. These high costs incurred with LES for complete configurations at high Reynolds numbers are due to the highly refined resolution needed in some critical computation domains such as the boundary layers, an issue that remains difficult to overcome, even with a fully successful wall-layer model. Based on these constraints, the DES method aims to combine the most favourable aspects of the two techniques, namely, the application of the RANS models for predicting the attached boundary layers, and the LES for the resolution of time-dependent, three dimensional large eddies. The overall computing resource requirements is then significantly reduced, since LES is no longer applied to capture relatively small structures that populate the boundary layer, and which is known to be very thin for high-Reynolds-number flows. The base model employed in the majority of DES methods is the Spalart-Allmaras (S-A) one-equation model [Spalart and Allmaras, 1992]. This model consists of solving the following transport equation for a representative variable, "$\tilde{\nu}$", which is identical to the kinematic viscosity except in the near-wall (viscosity-affected) region [Shur et al., 1999].

$$\frac{\partial \bar{\rho}\tilde{\nu}}{\partial t} + \frac{\partial}{\partial x_j}(\bar{\rho}\tilde{\nu}\tilde{u}_j) = \frac{1}{\sigma_{\tilde{\nu}}}\left[\frac{\partial}{\partial x_j}\{(\mu+\rho\tilde{\nu})\frac{\partial \tilde{\nu}}{\partial x_j}\} + G_{b2}\rho\left(\frac{\partial \tilde{\nu}}{\partial x_j}\right)^2\right] + G_\nu - D_\nu + S_\nu \tag{1.63}$$

where G_ν is the generation of the turbulent viscosity, and D_ν is the destruction of the turbulent viscosity that occurs in the near-wall region due to the wall blocking and viscous damping, $\sigma_{\tilde{\nu}}$ and G_{b2} are the model constants, and ν is the molecular viscosity. The destruction term for the eddy viscosity, D_ν, is proportional to $(\tilde{\nu}/d))^2$, where d is the distance to the wall. When balanced with the production term, G_ν, this term adjusts the eddy viscosity to scale with the local deformation strain, S, and d (i.e. $\tilde{\nu} \propto Sd^2$). Subgrid-eddy (SGS) viscosities, ν_{SGS}, scale with S, and the grid spacing, Δ (i.e. $\nu_{SGS} \propto S\Delta^2$). This analogy allows obtaining a subgrid-scale model within the S-A formulation by simply replacing d with the length scale Δ directly proportional to the grid spacing. The model used in

the S-A-based DES formulation is obtained by modifying the length scale of the S-A destruction term to be the minimum distance to the closest wall and a length scale proportional to the local grid spacing (i.e. $\tilde{d} = min(d, C_{DES}\Delta)$. In RANS predictions of high Reynolds number flows the wall-parallel (streamwise and spanwise) spacings are usually of the order of the boundary layer thickness, and are larger than the wall-normal spacing. Choosing the length scale, Δ, for DES based on the largest local grid spacing (i.e. one of the wall-parallel directions) then ensures that RANS treatment is retained within the boundary layer. Near the solid walls, $d \ll \Delta$ and the model acts as the S-A model, while away from the walls where $\Delta \ll d$, a subgrid model is obtained. This incorporation of the grid spacing into the model is compatible with the existence of a filter width in LES that determines the resolved fraction of the turbulence spectrum. The grid refinement provides a way to increase the range of resolved scales, and consequently the accuracy of the simulation.

Depending on the flow complexity, more refinement could be necessary to achieve a higher level of accuracy. In this vein, several other versions of the DES approach have been formulated using RANS turbulence models based on two-equations such as Realizable $k-\varepsilon$, SST $k-\omega$, and SST transitional model. Each of these two-equation DES methods is based on the modification of the transport equation for the kinetic energy, k, through its dissipation term, D_k. This modification consists of expressing the dissipation term, D_k, as a function of a grid-space-based parameter, with the same aim of combining the advantages of both RANS and LES methods. Detailed explanations regarding the DES approach along with the visual and quantitative success can be found in [Spalart, 2009]. In addition to these two-equation DES methods, other improved DES methods have been formulated; these are the Delayed Eddy Simulation (DDES) and the Improved Delayed Eddy Simulation methods. These two latter DES versions are also based on the modification of the k-equation so as to include information on the local grid spacing. They have a similar operating mode in the sense that, they both attempt to keep the boundary layer in the steady RANS mode even with more grid refinement. Detailed explanations regarding the derivation of these models as well as the related assumptions are provided in [Spalart et al., 2006, Shur et al., 2008].

1.6 Turbulence-combustion interactions

In turbulent combustion, it would be unrealistic to discuss chemical reactions and turbulence separately without considering their strong coupling and continuous interactions at the same time. Various modelling approaches are available to capture these interactions depending on whether the chemistry and mixing are simultaneously or separately treated. When a transport equation is solved for each species (i.e. species-transport-based combustion model) involved in the reacting system, the modelling of turbulent-chemistry interactions reduces to that of the mean (for RANS approaches) or filtered (for LES approaches) species reaction rates. The commonly-used modelling techniques include the eddy-dissipation model formulated by Magnussen and Hjertager [1976] and the eddy-dissipation-concept formulated by Magnussen [1981]. In the former technique, the reaction rates are assumed to be controlled by turbulence only, and consequently, the expensive Arrhenius chemical

calculations are avoided. The second approach is an extension of the former approach to incorporate detailed chemical kinetics effects. For the reasons discussed earlier (i.e. the separation between the time scales of chemistry and those of mixing in the majority of combustion systems involving efficient and stable combustion), the thermochemical state is determined by solving the transport equations for the first and the second moments of representative (or "tracking") scalars, and by mapping the latter with a pre-calculated chemistry. The main benefit for such an approach is that it drastically reduces the computational cost, especially when dealing with detailed mechanisms for heavy hydrocarbon jet fuels. By proceeding this way, the turbulence-combustion interactions are captured by modelling the turbulent fluctuations for the "tracking" scalars using a joint probability density function (PDF). In the transported PDF approach discussed above, a transport equation is solved to determine the PDF, the main limitations being the prohibitive computing costs incurred when dealing with detailed chemistry. To cope with these limitations, the shape of the PDF is generally presumed using analytical functions such as *delta* and *beta* functions. In all simulations conducted in the current study, the PDF shapes of the representative scalars are presumed. To simplify the pre-integration, the assumption of statistical independence between the representative scalars is adopted. Detailed comments on the PDF shapes and the related simplifying assumptions is provided in the chapter devoted to the numerical implementation.

This chapter described phenomena involved in turbulent spray combustion, while presenting the various approaches used to model each of them. From a global point of view, it can be noticed that spray combustion consists mainly of heat and mass transfers through convective and diffusive transports as well as chemical reactions which are responsible for the entire heat released. Especially, diffusive transports are mainly governed by transport properties, and the latter have to be considered with a particular care for a more accurate modelling of diffusive transports. In addition to transport properties, accurate chemistry modelling is relevant when predicting ignition and the main flame properties in the steady combustion regime. Further, jet fuels such as kerosene (Jet A-1) are mixtures of several heavy hydrocarbon fuels whose accurate oxidation mechanisms consist of thousand of reactions among hundreds of species. Thus, the chemistry modelling in spray combustion involving jet fuels has to be conducted with robust strategies so as to keep the computational cost at an affordable level. The next chapter focuses on the transport properties of jet fuels, the various surrogates of jet fuels, and their oxidation mechanisms.

Chapter 2

Fuel properties and reaction mechanisms

Aircraft gas turbine engines generate power by converting chemical energy stored in the fuel into a combination of mechanical energy and heat; securing the fuel supply is then essential to the continuous exploitation of this energy conversion technology. As mentioned in the introduction, the fuel-adaptation technique has so far been adopted in this regard, and consists of modifying the properties of new fuels and/or manufacturing new fuels through chemical processes (e.g. crude oil refining combined with additives, Fischer-Tropsch synthesis, transesterification of vegetable oils, etc.) so as to achieve the properties of conventional fuels. An appropriate understanding of the thermophysical properties of these conventional fuels is therefore necessary to anticipate the exploitation of new fuels in the existing combustion systems. Furthermore, even with conventional fuels, the combustion efficiency and the pollutant emissions are strongly guided by the spray characteristics. The latter depends upon the fuel injection system whose effective design requires a proper understanding of the thermophysical properties of fuels over the range of conditions that engines may experience. On the other hand, jet fuels are mixtures of several hydrocarbons that vary depending on the crude oil source and the manufacturing process. Thus, from a modelling point of view, surrogate fuels and the corresponding oxidation mechanisms are necessary to model the combustion of jet fuels. The present chapter discusses the thermophysical properties of fuels and their effect on both atomization and combustion processes. Subsequently, fuel surrogates used to model jet fuels are discussed and finally, the chemical kinetic mechanisms used to describe their combustion are presented, with a particular emphasis placed on aircraft gas turbine fuels.

2.1 Fuel properties

Fuels that can be used in aircraft gas turbines and other advanced air-breathing combustion systems are characterized and controlled by specifications. For aircraft applications in particular, the optimal fuel is a compromise solution to the various requirements faced by every link in the global fuel production-consumption chain. Some of the most relevant requirements include the fuel availability that must be guaranteed by fuel manufacturers, the aircraft's reliability which is to be guaranteed

by both engine and aircraft manufacturers, and some requirements from aircraft's users such as safety, low cost, ease of handling, among others. The primacy of one requirement relative to the others depends on whether the exploitation is civil or military. For military aircraft for instance, the fuel cost is a secondary issue compared to availability, supply logistics, and capability of operating over a wide range of conditions. In both military and civilian applications, a common composition requirement to all aviation fuels is that they shall form a blend of only hydrocarbon compounds except for specified additives. More specifically, the following usage requirements should be met: high energy content; good combustion quality; good fuel stability for safe storage and distribution; good fuel fluidity, lubricity, and volatility; and non-corrosivity. In addition, other requirements such as contaminant limits, cleanliness, additives for various purposes, and other miscellaneous properties should be met depending on the applications considered [Lefebvre, 1983, CRC, 1983]. All these fuel characteristics can be classified into two main groups: their physical properties, and their combustion properties. While combustion properties are mainly concerned with the amount of energy that can be extracted from fuel molecules, the physical properties are also relevant to non-combustion applications since fuels can also be used as hydraulic fluids in engine control systems, and as coolants for certain fuel system components.

2.1.1 Physical properties

In order for combustion to take place in the combustion chamber, the spray supplied by the injector must be vaporized and mixed with air. The mixing of fuel and air is governed by molecular diffusion, and predominantly by turbulent transport (convection or bulk motion) since the flow is generally highly turbulent in most practical combustion systems. As pointed out in the previous chapter, stable and efficient combustion in most applications requires shorter chemical time scales than those of mixing. Especially for combustion systems featuring time scales that are shorter than those of the smallest scales of turbulence (i.e. Kolmogorov scales), chemical reactions of combustion occur mostly at the molecular level so that flame fronts are torn by turbulence scales, but are not destroyed. It can then be deduced that the physical properties of the fuel have relevant effects on the whole combustion process, and should be considered with a particular care. This subsection provides a brief review of some of the most relevant physical properties of jet fuels.

Flash point and fuel volatility

The flash point of a given fuel corresponds to the lowest temperature at which it gives off sufficient vapour to form a flammable mixture with air. It can therefore provide a measure of the flammability and volatility of heavier fuels, and is also useful for classifying fuels from the fire risk viewpoint. The volatility of a fuel may be assessed from a knowledge of its distillation range, vapor pressure, and flash point. A high fuel volatility has a beneficial effect on the global combustion performance by providing easier light-up, improved stability, and higher combustion efficiency. These advantages are most apparent in configurations with poor fuel atomization, since large droplets can still evaporate completely. The disadvantages of high volatility include excessive fuel evaporation losses at high

altitude as well as increased fire hazard.

Freezing point

One of the most relevant motivations that governed the development of aircraft gas turbines is connecting safely two destinations across the globe in a reasonable time with affordable costs. Thus, both civil and military aircraft engines are expected to operate over a wide range of environmental conditions for economical purposes (e.g. flight at high altitude allows reducing fuel consumption) and weather constraints. Harsh environmental conditions have remarkable detrimental effects on the aircraft's exploitation. For instance, the ground cold-start of aircraft engines must endure low temperatures in winter, and similar conditions for high altitude flights with ambient temperatures as low as 193 K, highly increasing thereby the fuel viscosity, which in turn causes problems for pumping the fuel. Another problem at low temperatures arises when solid hydrocarbon crystals start to form in heavier fuel components, which are liable to restrict the flow of fuel through filters in the fuel system. Based on these usage constraints, the freezing point becomes a critical parameter for a given fuel, and corresponds physically to the temperature at which a given fuel first shows the presence of solid crystals. The freezing point is commonly improved by means of additives, and is the main difference between the two commercial jet fuels, namely, Jet A and Jet A-1. The former has a freezing point of -40^oC, and is used in the United States, while the rest of the world uses Jet A-1. The lower freezing point of Jet A-1 (-47^oC) makes it more suitable for long international flights, especially on polar routes during winter. Aircraft fuel specifications stipulate a maximum freezing point of -46^oC (-51^oF)or -58^oC (-73^oF) depending on the applications [CRC, 1983].

Critical properties

The critical properties of a given fuel are of practical interest as they are used to estimate other properties of that fuel (e.g. liquid density, viscosity, surface tension, heat capacity, diffusion coefficient, heat of vaporization and thermal conductivity). Furthermore, as seen in the past, any future advanced aircraft operating under supercritical conditions will experience an increased in thermal management requirements [Edwards and Zabarnick, 1993], and such a condition coupled to high temperature promotes fuel decomposition to eventually form detrimental solid carbon deposits. Critical properties of the fuel are necessary to define the supercritical regions necessary to study specifically the effects of supercritical conditions on the potential for carbon deposits on fuel wetted surfaces. The critical properties of substances can be either measured experimentally or estimated using other related properties. In this regard, various experimental methods and correlations have been developed to determine the critical temperature, density, and pressure of pure hydrocarbons and complex mixtures. The experimental approaches include for instance, the sealed tube method used to measure the critical temperature of the jet fuel [Lyons, 1985], the rapid sealed tube technique used to measure critical temperature and density, and the low residence time flow method used to measure the critical temperature and pressure of thermally unstable fluids [Teja et al., 1989]. On the other hand, empirical correlations can be used to estimate the critical properties of complex mixtures, namely, the

critical temperature and the critical pressure. The former corresponds physically to the temperature above which fuel vapour cannot be liquefied regardless of pressure, while the second corresponds to the pressure required to liquefy the gas at its critical temperature. The most accurate of these correlations includes the one described in the API Technical Data Book [Daubert and Danner, 1997] and also described in [Odgers and Kretschmer, 1986]. The former reference recommends the following correlation to determine the critical temperature:

$$T_c = 186.16 + 1.6667\Delta - 0.7127\times10^{-3}\Delta^2 \tag{2.1}$$

$$\Delta = SG(VABP + 100.0), \tag{2.2}$$

where T_c is expressed in degrees Fahrenheit, SG is the specific gravity, and VABP is the volumetric average in degrees Fahrenheit boiling point which is the average of the STMD86 distillation temperatures at 10, 30, 50, 70 and 90 vol. % for the ASTM distillation points. According to Odgers and Kretschmer [1986], the following correlations can be respectively used to estimate the critical temperature with an accuracy of $\pm 15K$, the critical pressure with an accuracy of $\pm 10\%$, and the critical volume with an accuracy of $\pm 15\%$:

$$T_c = 1.045\times10^{-3}T_{50}.\rho_{288} + 259, K \tag{2.3}$$

$$logP_c = 3.70 - 1.50M_f \tag{2.4}$$

$$V_c = 25.35\times10^{-21}\rho_{288}^{5.667}, m^3/mol \tag{2.5}$$

where T_{50} is the ASTM D86 distillation temperature at 50 vol. % distilled points (i.e. the temperature at which 50% of the fuel is distilled), while ρ_{288} is the density at 288 K. The ASTM D86 distillation temperatures are obtained from ASTM D2887 simulated distillation (SD) by gas chromatography, using the method described in API Technical Data Book [Daubert and Danner, 1997]. The ASTM D86 temperatures of the jet fuels at different volume percent points converted from the simulated distillation temperatures at the corresponding weight percent points are provided in Table 2.1. The critical

Fuel	vol % distilled						
	0	10	30	50	70	90	100
Jet A	300	352	374	401	438	486	546
Jet A-1	351	367	373	386	403	433	499

Table 2.1: ASTM D86 Temperature (^oF) of jet fuels at different volume percent points (converted from simulated distillation temperatures at the corresponding weight percent points)

pressure of jet fuels is determined using the procedure described in the API Technical Data Book (see Figure 4D 2.1 in [Daubert and Danner, 1997]), using the SG, VABP, API gravity, and ASTM slope as parameters. The values of these parameters, and the corresponding critical temperature and pressure are respectively given in the following two tables for both Jet A and Jet A-1.

Fuel	SG	VABP, ^oF	API gravity	ASTM slope, $^oF/\%$
Jet A	0.803	410	44.7	1.68
Jet A-1	0.799	392	45.6	0.83

Table 2.2: Relevant properties of Jet A and Jet A-1 in determining their critical properties

Fuel	$T_c, ^oF$	$T_c, ^oC$	$P_c, psia$	P_c, atm
Jet A	749	398	345	23.5
Jet A-1	731	388	340	23.1

Table 2.3: Estimated critical temperatures and pressures of Jet A and Jet A-1 using API methods

Boiling point

The boiling point is defined as the temperature at which the saturated vapour pressure of a liquid is equal to the surrounding atmospheric pressure. As noted earlier, both Jet A and Jet A-1 are mixtures of several hydrocarbon fuels, and each of them is therefore characterized by a boiling point range, unlike single-component-fuels for which the boiling point corresponds to a single temperature value. Experimental investigations on Jet A showed that the boiling point range spans from approximately 149 to 290^{o}C. An adequate knowledge of the range of boiling point temperature allows minimizing evaporation loss and avoid vapour lock. In fact, until the minimum temperature of this range is reached, the loss of fuel by evaporation is negligible, but once the fuel temperature exceeds this value, boiling occurs and the fuel loss due to evaporation becomes appreciable; the resulting vapour may disrupt the supply of fuel to the engine. If the boiling point temperature range is known, such issues can be avoided by pressurizing the fuel tank. Plus, from a modelling standpoint, the boiling temperature (or more realistically, the boiling point range) plays an essential role in formulating the models that can be applied to capture all the relevant phenomena experienced by a given spray of droplets (e.g. droplets heating and evaporation). For modelling purposes, an average boiling temperature is usually considered, and is commonly defined using either volume average boiling point, $T_{av,vol}$, or molar average boiling point, $T_{av,mol}$. The former definition is by far the most useful. It can be used to retrieve the second, and is given by the following relationship:

$$T_{av,vol} = \frac{T_{10} + T_{30} + T_{50} + T_{70} + T_{90}}{5}, \tag{2.6}$$

where the temperatures T_{10}, T_{30}, T_{50}, T_{70} and T_{90} are defined as reported earlier.

Vapour pressure

The vapour pressure of a liquid fuel corresponds to the pressure exerted by its vapour above its surface at a given temperature. High vapour pressure ensures rapid evaporation of fuel in the combustion chamber, and is therefore desirable from a combustion standpoint. However, as pointed out earlier, low vapour pressures have advantages in terms of lower fuel losses due to evaporation at high altitudes in vented tanks, and reduced fire hazard. In general, the vapor pressure of a fuel consisting of either a pure compound or a complex mixture increases with temperature. The temperature

dependency of the vapour pressure is provided by empirical correlations which are expressed using Antoine constants that are determined by experimental measurements. Such correlations are provided in [Wichterie and Linek, 1971] for pure compounds. For complex mixtures such as Jet A and Jet A-1, the determination of the true vapour pressure of fuels is complicated by dissolved air; furthermore, the presence of additives may also seriously affect the value. In the present work, the Antoine constants are determined by using a set of experimental data collected in the Alternative Fuels Laboratory (AFL) at McGill University. As these constants are empirically determined for a restricted temperature range, the vapour pressures for an extended temperature range are obtained through extrapolation using the empirical constants found in the restricted temperature range, with the Antoine's correlation:

$$log_{10}P = A - \frac{B}{C+T} \tag{2.7}$$

where the Antoine parameters are respectively defined as: $A = 7.563$, $B = 2179.00$, and $C = 0$ over the temperature range $T \in [358.5; 365.4]$, and the corresponding profile is shown in Figure 2.1

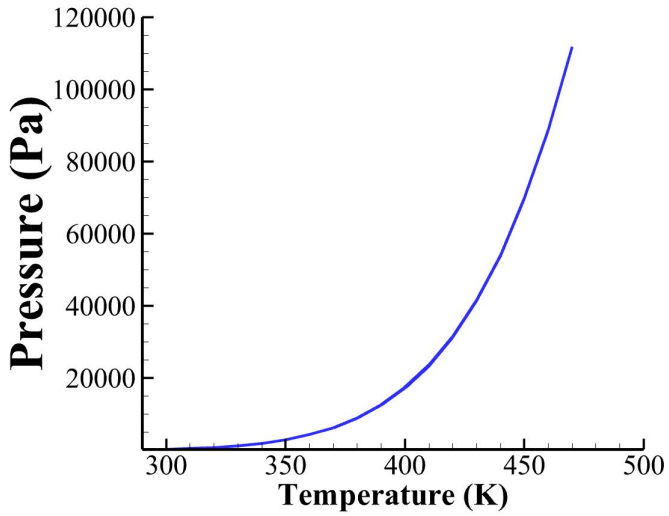

Figure 2.1: Vapour pressure for Jet A-1

Density

The density of a substance is the mass contained in a unit volume of that substance. In practice, the relative density (also called specific gravity) is commonly used. For a given fuel, the relative density at T_1/T_2 is conventionally defined as the ratio of the mass of a given volume of fuel at a temperature T_1 to the mass of an equal volume of pure water at a temperature T_2. A reference temperature of $T_1 = 288\ K$ is often used, with T_2 set at $277\ K$, where the density of water is the highest. The relative density of a fuel is related to its average boiling point and chemical composition and is fairly easy to determine; it provides a useful indication of hydrocarbon/carbon ratio, calorific value, and tendency toward carbon formation. In general, aromatics and paraffins have higher and lower densities, respectively, with naphthalenes and olefins lying in between. For small ranges of temperature, the density of

fuel decreases as the temperature increases as shown in the following correlation:

$$\rho_T = \rho_{REF}[1 + C(288 - T)] \tag{2.8}$$

where ρ_T is the fuel density at T, ρ_{REF} is the density at the reference temperature ($T_{REF} = 288K$), T is the temperature (K) and C is the mean coefficient of expansion. The values of C and the corresponding reference density and relative density are provided in Table 2.4. For some purposes, such as correlation

d_{REF}	0.70	0.75	0.80	0.85	0.90	0.95	1.00
$10^3 C$	1.251	1.066	0.932	0.819	0.733	0.684	0.653
ρ_{REF}	700	750	800	850	900	950	1000

Table 2.4: Value of the mean expansion coefficient, C, and the corresponding references density and relative density (Odgers and Kretschmer, 1986)

development, it is deemed more convenient to specify the density in terms of the API gravity. Such a specification is provided by the following expression:

$$API_{gravity} = \frac{141.5}{d_r(at 288K/289K)} - 131.5, [degrees] \tag{2.9}$$

Viscosity

The viscosity of a liquid represents the frictional force between adjacent layers of the liquid, and allows therefore quantifying its resistance to flow (gradual deformation by shear stress and tensile stress). This latter role is of practical interest, since it strongly determines the power required to pump the fuel through the fuel system. The viscosity of a complex mixture depends mainly on the chemical composition of the hydrocarbons contained in the fuel, and has a marked effect on the formation of a well-atomized spray and hence on the rate of atomization [Lefebvre and Ballal, 2010]. Most fuel-injection systems are capable of providing satisfactory pressure atomization with a viscosity up to around $15 \times 10^{-6} m^2/s$, depending on the design of the atomizer and the available fuel-injection pressure [Lefebvre, 1983]. For instance, as pointed out when describing the types of injectors in the previous chapter, the performance of airblast atomizers is fairly insensitive to fuel viscosity compared to that of pressure atomizers. The viscosity of gas turbine fuels depends greatly on temperature. Thus, fuels that have to operate at low temperatures require a low viscosity since at normal temperature, such fuels may be difficult to pump due to a loss of lubricity. It is then obvious that heavy oils and residual fuels must usually be heated before being introduced in the atomizer. Also, viscosity provides relevant information on the operating range: in the case of aviation fuels for instance, the high viscosity featured at low temperatures dictates the minimum operating temperature at which a satisfactory spray can be obtained. The limiting acceptable ambient-temperature viscosity of the fuel which is currently 12×10^{-6} for starting is indirectly dictated by this minimum operating temperature. To model these viscosity variations that liquid fuels, such as jet fuels, experience due to the change in temperature as a result of preheating and/or chemical reactions, it is necessary to correlate the dynamic

(or absolute) viscosity to the temperature. In this regard, Viswanath and his co-workers [Viswanath et al., 2007] have proposed the following empirical correlation for the dynamic viscosity:

$$ln(\mu) = A + \frac{B}{T}, [cP] \tag{2.10}$$

where the values of the constants A and B were evaluated based on aviation jet fuel viscosity measurement data from the experimental investigation conducted by Atkins and Ervin [2005]. For Jet A, these constants are respectively equal to -8.45 and 2489.9. This correlation is quite similar to the following correlation formulated by Fitzgerald and Daubert (see chapter 11 of [Daubert and Danner, 1997]) for the liquid viscosity of pure compounds at low temperature:

$$\mu = 1000exp(A + B/T + ClnT + DT^E), [cP] \tag{2.11}$$

where T is the temperature, in degrees Rankine; and A through E are the correlation coefficients provided in Table 11A2.2 of the same reference (i.e. [Daubert and Danner, 1997]). This correlation for pure compounds is also of practical interest, namely, from a modelling standpoint since complex fuels are generally replaced by surrogate fuels which consist of a set of pure compounds carefully selected. This operation will be discussed in the next section. For many engineering purposes, the so-called kinematic viscosity, ν, is more convenient: $\nu = \mu/\rho$, measured in m^2/s.

Surface tension

Surface tension is the elastic tendency of liquids that make them acquire the least surface area possible. The force governing this elastic tendency is due to molecular interactions within the liquid, and leads to an increase of the energy at the liquid surface, which in turn increases the cohesion between fluid elements (i.e. the net force consisting of the strength interaction, the electromagnetic interaction, and the gravitational interaction). The surface tension has a significant effect on fuel atomization since for both pressure and airblast atomizers, the mean diameter of the resulting spray depends on the surface tension according to the following relationship: $SMD \propto \sigma_F^{0.6}$ [Lefebvre, 1989]. The surface tension is sensitive to the temperature change, and this sensitivity can be quantified through the following relationship:

$$\sigma \left[\frac{M_f}{\rho_l}\right]^{2/3} = k(T_c - T - 6), [N/m] \tag{2.12}$$

where σ is the surface tension; ρ_l is the density; T is the actual temperature; k is a constant, which is equal to 2.21×10^{-7} for many liquids; M_F is the fuel molar mass; and T_c is the critical temperature. The surface tension at a given temperature, T, can also be calculated using the following relationship:

$$\sigma = C(\rho_l - \rho_v)^4, \tag{2.13}$$

where C is constant for any liquid; the effects of temperature change can implicitly be accounted for using the correlations of the temperature dependency on density for both ρ_l and ρ_v, the latter being evaluated at the same temperature. From a spray dynamics point of view, the droplet surface tension allows quantifying the intensity of the secondary breakup phenomenon. In fact, in a given spray

flow configuration, the inertial forces may be divided by the surface tension to yield a dimensionless number termed as Weber number, $We = \rho U^2 L/\sigma$, where U and L are respectively the velocity of the fluid and the characteristic length. The secondary breakup phenomena is deemed relevant when the Weber number exceeds the critical value (which is approximately equal to 12) [Lefebvre, 1983, Helenbrook, 2001].

Thermal conductivity

The thermal conductivity of a substance is a property that quantifies the ability of heat to flow by conduction through a quiescent solid, liquid, or gaseous layer of that substance; it is defined as the proportionality constant, λ, in the Fourier's law of heat conduction. The thermal conductivity of liquid fuels is sensitive to temperature change. For pure liquid hydrocarbons for instance, two different correlations are proposed depending on the range of the operating pressures and temperatures. For pressure below 3.447 MPa absolute, and at reduced temperatures, $T_r = T/T_c$, between 0.25 and 0.80, the following correlation can be used:

$$\lambda = \frac{CM^n}{V_m}\left[\frac{3+20(1-T_r)^{2/3}}{3+20(1-527.67/T_c)^{2/3}}\right] \tag{2.14}$$

where λ is the thermal conductivity; M is the molecular weight; V_m is the molecular volume at 68^oF; T_r is the reduced temperature; T_c is the critical temperature; T is the temperature; C and n are coefficients obtained from Table 2.5. Above the boiling point, and at all pressures, the following correlation can

Hydrocarbon structure	n	C
For unbranched, straight chain hydrocarbon	1.001	1.676×10^{-3}
For branched and cyclic hydrocarbons	0.7717	4.079×10^{-3}

Table 2.5: Values of constants n and C for each type of hydrocarbon structure

be used to calculate the thermal conductivity of pure liquid hydrocarbons:

$$\lambda = \frac{-1.884 \times 10^{-6} P_r^2 + 1.442 \times 10^{-6} P_r + \alpha exp(\beta \rho_r)}{\gamma} \tag{2.15}$$

The parameters α, β and γ are respectively defined by the following relationships:

$$\alpha = \frac{7.137 \times 10^{-3}}{\beta^{3.322}} \tag{2.16}$$

$$\beta = 0.40 + \frac{0.986}{exp(0.58\lambda)} \tag{2.17}$$

$$\gamma = \frac{T_c^{1/6} M^{1/2}}{(P_c/14.696)^{2/3}} \tag{2.18}$$

where λ is the thermal conductivity; ρ and $\rho_r = \rho/\rho_c$ are the density and the reduced density respectively; ρ_c, V_c, P_c, and T_c are the critical density, volume, pressure, and temperature respectively; M is the molecular weight; P and $P_r = P/P_c$ are the pressure and the reduced pressure. For fuels involving

a complex mixture of pure liquid hydrocarbons (e.g. jet fuels), if the composition and thermal conductivities of these pure components are known, the thermal conductivity can be calculated using the following relationship:

$$\lambda_m = \sum_i \sum_j \phi_i \phi_j \lambda_{ij} \tag{2.19}$$

with

$$\lambda_{ij} = 2\left(\frac{1}{\lambda_i} + \frac{1}{\lambda_j}\right)^{-1} \tag{2.20}$$

and

$$\phi_i = \frac{x_i V_i}{\sum_j x_j V_j} \tag{2.21}$$

In these expressions, $k_{ij} = k_{ji}$, $k_{ii} = k_i$ and $\sum_i \phi_i = 1$; λ_j is the thermal conductivity of the mixture; ϕ_i and ϕ_j are the volume fractions of pure components i and j; λ_i and λ_j are the thermal conductivities of the pure compounds i and j; V_i and V_j are the molar volumes of pure components i and j, while x_i and x_j are the molar fractions of the pure components i and j. In practice, the thermal conductivity of liquid fuels may be estimated using the following correlation [Odgers and Kretschmer, 1986]:

$$\lambda = \frac{7}{\rho_{288}}\left(0.132 - 6.33 \times 10^{-4} T\right), [W/mK] \tag{2.22}$$

where T is the absolute temperature.

Specific heat and the related thermodynamic properties

The specific heat of the fuel is the amount of energy transferred into or out of a unit mass of the fuel when increasing or decreasing its temperature. In some systems such as very high speed aircraft, the fuel may be used as a coolant or as a heat sink to absorb heat from the airframe and engines. The specific heat is needed in many calculations, including heat transfer and chemical equilibrium calculations. For the second type of application in particular, the specific heat appears as an important fuel property since it can be used to derive the other thermodynamic properties such as enthalpy and entropy which are necessary for chemical equilibrium calculations. The enthalpy is the energy required to bring a fuel from one reference state to another state, while the entropy is a measure of irreversibility in a thermodynamic system during a change of state. The specific heat, the enthalpy, and the entropy are all functions of state, and are sensitive to temperature change. Their temperature dependence follows a polynomial expression. For the Jet A-1 for instance, the following polynomial correlations with coefficient shown in Table 2.6 can be used for the specific heat, enthalpy, and entropy, depending on the phase of fuel and the temperature range:

$$\frac{C_p^o}{R} = a_1 + a_2 T + a_3 T^2 + a_4 T^3 + a_5 T^4 \tag{2.23}$$

$$\frac{H_T^o}{R} = a_1 T + \frac{a_2}{2} T^2 + \frac{a_3}{3} T^3 + \frac{a_4}{4} T^5 + \frac{a_5}{5} T^5 + a_6 \tag{2.24}$$

$$\frac{S_T^o}{R} = a_1 lnT + a_2 T + \frac{a_3}{2} T^2 + \frac{a_4}{3} T^3 + \frac{a_5}{4} T^4 + a_7 \tag{2.25}$$

$Liquid : 298K \leq T \leq 650K$	$Gas : 298K \leq T \leq 1000K$	$Gas : 1000K \leq T \leq 5000K$
$a_1 = 0.13993639E04$	$a_1 = 0.19935137E01$	$a_1 = 0.24875975E02$
$a_2 = -0.13440366E02$	$a_2 = 0.13383918E00$	$a_2 = 0.78259103E-01$
$a_3 = 0.48492245E-01$	$a_3 = -0.82891249E-04$	$a_3 = -0.31556353E-04$
$a_4 = -0.75524882E-04$	$a_4 = 0.31180914E-07$	$a_4 = 0.57891394E-08$
$a_5 = 0.43166687E-07$	$a_5 = -0.71528712E-11$	$a_5 = -0.39838032E-12$
$a_6 = -0.15588486E06$	$a_6 = -0.35903496E05$	$a_6 = -0.43110507E05$
$a_7 = -0.54852414E04$	$a_7 = 0.27744570E02$	$a_7 = -0.93633944E02$

Table 2.6: Coefficients for specific heat of Jet A-1 in the liquid and gas phases

Thermal and species diffusion coefficients

As discussed in the previous chapter, combustion processes are simulated by solving a set of conservative equations (continuity, momentum, energy, and species equations). For the direct approach consisting of solving the transport equations for all the species, some physical parameters such as thermal diffusivity (D_T) and species diffusivity (D_{km}) are respectively needed in the energy transport equation and those of species. The former is defined using the thermal conductivity, the density and the specific heat at constant pressure ($D_T = \frac{\lambda}{\rho C_p}$), and is a measure of the ability of a substance to conduct thermal energy relative to its ability to store thermal energy. The second, the species diffusion coefficient, is used for multispecies gases, and has a physical meaning quite similar to that of the binary diffusion coefficient (D_{pk}). However, instead of measuring the diffusion of species p into species k as does the binary diffusion coefficient, it measures the diffusion of species k into the rest of the mixture. For combustion models consisting of solving the transport equations for a reduced set of representative scalars which are thereafter mapped with a pre-calculated chemistry, the thermal diffusion coefficient is most often used to replace the mixture fraction diffusivity [Pitsch and Peters, 1998, Peters, 2000]. In combustion analysis, the thermal and the species diffusion coefficients are usually combined to define the Lewis number, $Le = D_T / D_{km}$, which is another relevant dimensionless number for flows involving a simultaneous transfer of heat and mass. The Lewis number allows quantifying both differential and preferential diffusion, since on the one hand, it captures indirectly the rate of diffusion of a given species relative to another species, and on the other hand, it captures directly the rate of diffusion of a given species relative to that of heat. For n-paraffins and especially for linear alkanes which are among the major components of jet fuels, the diffusion coefficient into nitrogen decreases as the molecular weight increases, and the difference in diffusion coefficients among mixtures becomes larger as the temperature increases [Chae, 2010, Chae and Violi, 2011]. This trend is also observed for cycloalkanes and aromatics, and also expected for Jet A-1 since paraffins and aromatics are among the major components of Jet A-1.

Latent heat of vaporization

The latent heat of vaporization is the amount of heat required to vaporize a unit weight of a liquid at a constant pressure. The latent heat of vaporization decreases with an increase in pressure, and becomes zero at the critical point. The latent heat of evaporation at the average boiling point of a jet fuel may be related to the relative density and the fuel temperature by the following expression:

$$h_{fg} = \frac{360 - 0.39T_F}{d_r}, [kJ/kg] \tag{2.26}$$

where d_r and T_F are respectively the relative density and the fuel temperature.

2.1.2 Combustion properties

In addition to the physical properties described above, fuels are also characterized by thermal properties. The latter are concerned with fuel properties which are involved in heat energy transfer to and from the fuel, and the heat released by the fuel combustion. Such properties include specific heat, enthalpy, heat of vaporization, and net heat of combustion. Just as the physical properties, these properties play an important role in the design of aircraft engines, and are essential to engine performance [Lefebvre, 1983].

Specific energy

The specific energy of a given fuel, also termed as calorific value (or heat of combustion), is the amount of energy released as heat when a unit weight of that fuel is burned to completion under standard conditions. In practice, and especially for gas turbine fuels, the lower calorific value is most relevant as it is easier to measure. For most hydrocarbon fuels, the specific energy can be related to the relative density: the lightest fuels have the highest specific energy, whilst the heaviest fuels have the highest energy density. The specific energy of a fuel depends entirely on its chemical composition and, in particular, on the hydrogen/carbon ratio. If the chemical composition of the flow is known, the following correlation derived by Ragozin [1961] can be used to obtain a good estimation of the specific energy:

$$Q_{comb} = 0.339C + 1.03H - 0.109(O - S) - 0.025W \tag{2.27}$$

where C, H, O, S and W are the mass percentages of carbon, hydrogen, oxygen, sulphur, and water, respectively, in the fuel. If the chemical composition is unknown, the specific energy can be estimated with less precision using only the relative density as follows:

$$Q_{comb} = 51.5 - \frac{5.95}{1.53 - d_r}, [MJ/kg] \tag{2.28}$$

2.2 Effects of fuel properties on the atomization and combustion processes

The combustion of liquid fuels is rendered possible through an atomization device. As mentioned in the previous chapter, such devices increase the surface to volume ratio of the fuel by converting the

latter into small droplets through a process known as atomization. The resulting spray needs to be vaporized and mixed with air to allow the combustion process to take place. In practice, the spray is polydisperse due to the presence of droplets having various sizes; it is then obvious that, depending on the size of the droplets, combustion may occur with some droplets which are not completely vaporized, and consequently, the combustion quality is strongly affected. In fact, from an environmental standpoint, it is better that the combustion process occurs in a premixed combustion regime. In the context of spray combustion, such a combustion regime is promoted by a total evaporation of the droplet, followed by the perfect mixing of the resulting fuel vapour with air. However, depending upon the performance of the injector used, along with the limitations of the mixing devices (e.g. swirler, bluff-body, and brewing through the liner holes perforated in the combustor walls), such a homogeneous mixture is not always easy to achieve. An illustration of this effect is provided by two research teams: [Burgoyne and Cohen, 1954] showed that, for spray consisting of droplets having a diameter less or equal to $7\mu m$, the combustion process occurs in a nearly premixed mode provided that the mixing is effectively done. In the same vein, Rink and Lefebvre [1986] investigated the effect of droplet size on the pollutant formation. Their investigation shows that, when the mean diameter of droplets in a given mixture is successively decreased from $110\mu m$ to $70\mu m$ and to $30\mu m$, the emissions of CO, UHF, NOx, and soot decrease. The reason behind this observation is that small droplets have short evaporation times, and consequently, they have enough time to mix with air before igniting, leading to partial premixing which is known to burn more efficiently compared to mixtures found in pure non-premixed configurations. Based on this effect of atomization on the combustion process, it is clear that most of the physical parameters affecting atomization are liable to affect the combustion process. In addition to the physical properties influencing the atomization quality, the combustion process is also affected by other fuel properties, namely, the thermal properties discussed in the previous section.

2.2.1 Effects of fuel properties on the atomization

The atomization quality is assessed through the spray characteristics. The latter include the spray dispersion, the spray penetration, the spray cone angle, the spray patternation, the mean diameter of the droplets contained in the spray (e.g. Sauter Mean diameter, SMD), and the radial and circumferential liquid distributions. In addition to the injector geometry (e.g. fuel and air passages, discharge orifice diameter, etc.) and the atomization conditions (e.g. injection pressure measured by the liquid pressure differential, fuel mass flow rate), spray characteristics are influenced by the fuel properties described earlier. The relevance of the influence of these fuel properties is strongly determined by the injector configuration, the latter corresponding to various types of injectors described in the previous chapter (i.e. plain-orifice, pressure-swirl, rotary, air-assist, airblast, etc.).

Effect of fuel physical properties on the SMD

In general, for the above-listed injector types, the SMD of a given spray increases as the viscosity increases, and decreases with an increase in density. According to the outcomes of many experimental

investigations [Simmons and Harding, 1980, Jones, 1985, Kennedy, 1985, Lefebvre, 1983, Wang and Lefebvre, 1987], the SMD increases as the surface tension increases. The sensitivity of the SMD to the changes in surface tension, for practical configurations involving a Weber number less than unity, can be captured using the following correlation: $SMD \propto \sigma^a$, where a is equal to 0.19. According to Kennedy [1985], for simplex nozzles featuring much higher flow number (i.e. ratio of the fuel flow rate to the square root of the differential pressure), the dependence of SMD on surface tension is far stronger ($a = 1$). However, the value of 0.25 is used in many correlations since investigations by Jones [1985] on nozzles featuring high flow numbers led to that value, which is fairly close to those of the other investigators [Simmons and Harding, 1980, Lefebvre, 1983, Wang and Lefebvre, 1987]. There are many correlations which allow determining the sensitivity of the SMD and the mass median diameter (MMD) to the fuel physical properties, for various injector configurations. The SMD being physically the diameter of a representative drop whose ratio of volume to surface area is the same as that of the entire spray, while the MMD (also denoted by $D_{0.5}$) represents the droplet diameter so that 50% of total liquid is in the droplets of smaller diameter. An extensive discussion of such correlations for various injector configurations are provided in [Lefebvre, 1989]; some of them extracted from the references [Harmon, 1955, Fraser et al., 1962, Kayano and Kamiya, 1978, Simmons, 1979, Elkotb, 1982, Jones, 1985, Lefebvre, 1989] are summarized in the following Table 2.7 to emphasize the SMD sensitivity to fuel properties, atomization conditions (i.e. operating variables), and to the atomizer geometry.

Atomizer	SMD correlation	Investigators
Plain-orifice	$SMD = 3330 d_o^{0.3} \mu_L^{0.07} \rho_L^{-0.648} \sigma^{-0.15} U_L^{-0.15} \mu_G^{0.78} \rho_G^{-0.052}$	Harmon (1955)
	$SMD = 3.08 \mu_L^{0.385} (\sigma \rho_L)^{0.737} \rho_A^{0.06} \Delta P_L^{-0.54}$	Elkotb (1982)
Pressure-swirl	$SMD = 2.25 \sigma^{0.25} \mu_L^{0.25} \dot{m}_L^{0.25} \Delta P_L^{-0.5} \rho_A^{-0.25}$	Lefebvre (1989)
	$MMD = 2.47 \dot{m}_L^{0.315} \Delta P_L^{-0.47} \mu_L^{0.16} \mu_A^{-0.04} \sigma^{0.25} \rho_L^{-0.22} \times \left(\frac{l_o}{d_o}\right)^{0.03} \left(\frac{L_s}{D_s}\right)^{0.07} \left(\frac{A_p}{D_s d_o}\right)^{-0.13} \left(\frac{D_s}{d_o}\right)^{0.21}$	Jones (1982)
Rotary	$SMD = 0.26 N^{-0.79} Q^{0.32} d^{-0.69} \rho_L^{-0.29} (1 + 1.027 \mu_L^{0.65})$	Kayano (1978)
	$SMD = 0.483 N^{-0.6} \rho_L^{-0.5} \left(\frac{\mu_L \dot{m}_L}{d}\right)^{0.2} \left(\frac{\sigma}{nh}\right)^{0.1}$	Fraser et al. (1962)
Air-assist	$SMD = C \left(\frac{\rho_L^{0.25} \mu_L^{0.06} \sigma^{0.375}}{\rho_A^{0.375}}\right) \left(\frac{\dot{m}_L}{\dot{m}_L U_L + \dot{m}_A U_A}\right)^{0.55}$	Simmons (1979)
Airblast	$SMD = 0.48 d_o \left(\frac{\sigma}{\rho_A U_A d_o}\right)^{0.4} \left(1 + \frac{1}{ALR}\right)^{0.4} + 0.15 \left(\frac{\mu_L^2}{\sigma \rho_L d_o}\right)^{0.5} \left(1 + \frac{1}{ALR}\right)$	Rizk (1984)

Table 2.7: Some SMD correlations for various injector types

Effect of fuel physical properties on the spray cone angle

In addition to geometrical parameters of the atomizer (e.g. orifice diameter, d_o) and its operating

variables (e.g. fuel pressure differential, ΔP_L), some fuel properties have an effect on the spray cone angle. For instance, the spray cone angle widens slightly with an increase in density, while an increase in viscosity leads to a decrease of the spray cone angle. According to [Rizk and Lefebvre, 1985], the sensitivity of the spray cone angle to fuel properties can be appraised using the following correlation:

$$2\theta_m = 6K^{-0.15}\left(\frac{\Delta P_L d_o^2 \rho_L}{\mu_L^2}\right)^{0.11}. \tag{2.29}$$

From this correlation, it can be seen that, unlike the other fuel physical properties, the surface tension has no effect on spray cone angle; this is generally confirmed experimentally.

2.2.2 Effects of fuel properties on the combustion process

As briefly discussed earlier, the combustion characteristics are impacted by the physical properties of liquid fuels; these effects occur either directly through processes governed by physical properties (e.g. molecular diffusion), or indirectly through fuel atomization. For the first case, if the flow regime is laminar, the effects of the fuel physical properties are relevant since all the transport phenomena such as heat, momentum and mass transfers are mainly governed by the fuel physical properties in the gaseous phase (e.g. viscosity, thermal diffusivity, and mass diffusion coefficient). In addition to the direct effect of these properties on combustion, other fuel properties such as specific energy (or calorific value) and heat of vaporization have significant effects on combustion, since, they determine the maximum amount of heat that can be extracted from a given fuel, and the energy needed to vaporize the spray, respectively. In turbulent environments, turbulent mixing overwhelms molecular mixing, and is therefore of significant contribution to the combustion efficiency. The indirect effect of the fuel properties on combustion is related to the atomization quality: with an effective mixing device, a good atomization improves the combustion efficiency, and minimizes pollutant emissions.

2.3 Jet fuel surrogates

As are gasoline and diesel fuels, jet fuels used in modern aircraft applications (e.g. Jet A and Jet A-1) are mixtures of large numbers of different hydrocarbons from different molecular classes whose composition varies depending on crude source and manufacturing process [Wang, 2001]. Several experimental investigations from the literature show that the most prevalent components belong to the group of straight chain paraffins (i.e n-paraffins such as n-decane, n-dodecane, etc.), branched chain paraffins (i.e. i-paraffins and cyclo-paraffins such as iso-octane, iso-cetane, etc.), aromatics (e.g. benzene, toluene, etc.), and naphtalenes (e.g. cycloliphatic, methylcyclohexane, etc.). For instance, from the experimental investigation conducted by Violi and his co-workers [Violi et al., 2002], the composition of military aviation fuel, JP-8, on a molar basis may be approximated as follows: n-paraffins-28%, iso-paraffins-29%, cycloparaffins-20%, alkylbenzenes-18%, naphtalenes-2% and misc-3%. More specifically, this empirical composition states that jet fuels are composed of alkanes (such as dodecane, tetradecane and isoctane) which are the most abundant components and

account for 50-60% by volume, cycloalkanes (such as methylcyclohexane, tetralin, and decalin) and aromatics (such as toluene, xylene, and naphthalenes) which are the second most predominant components and represent 20-30% by volume, and finally alkenes whose percentage is less than 5% in volume. For the same fuel and other similar jet fuels such as Jet A and Jet A-1, the outcomes of other investigators [Mayfield, 1996, Edwards and Maurice, 2001, Humer et al., 2007b, Honnet et al., 2009, Dagaut and Cathonnet, 2006] show large variations in composition. This disparity in investigation outcomes allows noticing the ambiguity in defining a universal composition for jet fuels so as to directly simulate its combustion behaviour. A promising approach to overcome this difficulty consists of developing a surrogate fuel that can emulate the combustion characteristics of the target fuel. In general, a surrogate fuel is defined as a mixture of a limited number of hydrocarbons whose composition can be formulated in order to better match fuel physical and chemistry properties [Edwards and Maurice, 2001], and is intended to provide a baseline for performance and emissions, and a tool that could facilitate modelling. It is then clear that the starting point for surrogates development should be based upon the chemical composition and the combustion performance of a typical or average jet fuel. In order to supply literature with a representative composition of jet fuels so as to allows concentrating efforts on both fuel surrogates development and their oxidation mechanisms, a recent "World Fuel Survey" was conducted by Colket et al. [2007] under the auspices of the Coordinating Research Council, where 55 jet fuels samples consisting of Jet A, Jet A-1, JP-8, and JP-5 were obtained from locations world-wide. The common characteristics of these jet fuels and the composition of resulting representative composition are summarized in two following Table 2.8 and Table 2.9:

Jet fuels	Specification	Description	Flash point (^oC)	Freezing point (^oC)
Jet A-1	ASTM D1655, (UK DefStan 91-91)	Standard commercial jet fuel	>38	<-47
Jet A	ASTM D1655	U.S. domestic jet fuel	>38	<-40
JP-8	MIL-DTL-83133	U.S. military jet fuel (Jet A-1 + 3 additives)	>38	<-47
JP-5	MIL-DTL-5624	U.S. Navy high flash jet fuel	>60	<-46

Table 2.8: Common characteristics of jet fuels

Based on the outcomes of extensive works carried out on the authentic jet fuels and their reference components over the past decades, various surrogate definitions have so far been proposed for both JP-8 and Jet A; these include single component and multi-component surrogates, the composition being mainly based on the major components of real jet fuels as discussed earlier. In an early study, a 12-component surrogate fuel for JP-8 was first proposed by Schulz [1991]; the reliability of the surrogate fuel was assessed by comparing its oxidative stability to that of the real fuel. In the same vein, a three-component surrogate consisting of 79% n-undecane, 10% n-propylcyclohexane, and 11% 1,2,4-trimethylbenzene on a molar basis, was formulated by Gueret and his co-workers [Gueret et al., 2007]; their formulation was based on data obtained from a jet stirred reactor, and was mainly motivated by the need to emulate the high-temperature oxidation process of the real kerosene fuel. With a sim-

Jet fuel components	World survey average, vol%	Composite Jet A blend
Paraffins(n- + i-)	58.78	55.2
Monocycloparaffins	10.89	17.2
Dicycloparaffins	9.25	7.2
Tricycloparaffins	1.08	0.6
Alkyl benzenes	13.36	12.7
indans tetralins	4.9	4.9
Naphthalene	0.13	<0.2
Substitued naphthalenes	1.55	1.3

Table 2.9: Composition results for 55 “World survey” fuels

pler approach consisting of using n-decane as single component surrogate, Dagaut and his co-workers [Dagaut et al., 1994] reproduced successfully experimental data of Jet A-1 in a stirred reactor, and their results showed a strong analogy between n-decane and kerosene oxidation kinetics. Following this study, another surrogate fuel was formulated by Violi et al. [2002], Cooke et al. [2005], and its performance was thereafter assessed by Humer et al. [2007a]. They first defined three surrogate fuels composed of n-decane, n-dodecane, methylcyclohexane, toluene, and o-xylene, and they compared their extinction and autoignition with JP-8, Jet A and the other surrogate proposed by Violi and his co-workers. Recently, the Aachen Jet A surrogate was proposed by Honnet et al. [2009]; the latter is made up of 80% of n-decane and 20% of 1,2,4-trimethylbenzene. Later, Dooley et al. [2010] proposed a three-component Jet A surrogate composed of n-decane, iso-octane, and toluene, and compared the surrogate with Jet A for a variety of experimental data, and a good agreement was noted between the surrogate and the target real fuel. As further analysis suggested the need for large molecular weight hydrocarbons to match the typical threshold sooting index and molecular weight of Jet A, Dooley et al. [2012] subsequently formulated a four-component surrogate, consisting of n-dodecane, iso-octane, 1,3,5-trimethylbenzene, and n-propylbenzene. The appropriateness of this four component surrogate formulation was demonstrated through the experimental measurements of various gas phase combustion kinetic phenomena of the surrogate mixture and the target Jet A fuel. This brief discussion on jet fuel surrogates allows noticing that the most prevalent components often include a long straight chain paraffin, namely, n-decane or/and n-dodecane [Schulz, 1991, Gueret et al., 2007, Dagaut et al., 1994, Lindstedt and Maurice, 2000, Violi et al., 2002, Dagaut and Cathonnet, 2006, Humer et al., 2007b, Dooley et al., 2010, 2012, Akih-Kumgeh and Bergthorson, 2013] as well as aromatics such as toluene and trimethylbenzene [Gueret et al., 2007, Lindstedt and Maurice, 2000, Dooley et al., 2012, Akih-Kumgeh and Bergthorson, 2013, Munzar et al., 2013a], and the highly branched iso-octane to represent the branched components in jet fuels [Schulz, 1991, Violi et al., 2002, Dooley et al., 2012].

Due to their relatively reduced number of components (compared to that of typical jet fuels), detailed chemical kinetics and transport properties of surrogates can be developed to predict combustion performance of the target fuels such as ignition, flame stability, extinction and emission characteristics, as long as the formulated kinetic models are validated against reliable fundamental combustion

properties. The kinetic models of jet fuel surrogates, along with their implementation in CFD simulations, are discussed in the next section.

2.4 Chemical kinetic models for jet fuel surrogates

Experiments allow establishing that chemical reactions of combustion are naturally triggered whenever elements of the "fire triangle" (fuel, heat and oxidizing agent) are present and combined in the right mixture; the combustion process can then be stopped by removing any one of these elements. In a generic manner, combustion is defined as a rapid exothermic reaction in which reactants (fuel and oxidizer) are converted into new species (combustion products) with substantial release of energy, usually in the form of heat and light [Destriau and Borghi, 1995]. The fuel and oxidizer molecules interact at the molecular level during the oxidation process to produce new species. Thermodynamics allow determining the final state of such a reaction process with global reaction assumptions, but it does not describe the actual physical process since it does not provide any information on how fast the reaction proceeds and whether under a particular reaction condition, the reaction can proceed to the equilibrium state. Furthermore, it is often necessary to describe the main (if not all) oxidation steps involved in the formation and depletion of both major species and some intermediate species, to be able to properly match some combustion properties. Such a description is provided by the chemical kinetics, and for jet fuels in particular, the oxidation mechanisms are obtained through the oxidation kinetics of pure compounds involved in the jet fuel surrogates described in the previous section [Dagaut and Cathonnet, 2006, Bergthorson and Thomson, 2015]. Thus, to better understand the concept that governs the development of chemical kinetic mechanisms for jet fuel surrogates, it is essential to rely on the theory behind the kinetic mechanisms of pure compounds, namely, simpler hydrocarbon fuels. In a combustion process, combustion properties such as heat released (or flame temperature) and pollutant emissions are mainly determined by the reaction rate. In other words, the ability of a kinetic model to match such combustion properties is strongly related to its ability to retrieve the empirical reaction rates for various operating conditions (e.g. temperature and pressure ranges); such an ability depends on the number of species (major, minor and intermediate species) and reaction steps involved in the kinetic mechanism. From a global point of view, the oxidation of a given hydrocarbon occurs through a chain reaction mechanism; the latter consists of a set of elementary reactions that can be unimolecular, bimolecular or trimolecular depending on the number of molecules that collide simultaneously [Wang, 2015]. A chain reaction mechanism can be divided into three main consecutive steps, namely, the *chain initiation*, the *chain propagation*, and the *chain termination*. The first step leads to the production of free radical species which are extremely reactive, and can therefore readily attack one of the reactants; such attacks correspond to the beginning of the *chain propagation*, they produce new reactive free radical species, and occur reversibly so that the back reaction step can proceed at a rapid rate to compete with the forward reaction steps. From a kinetic standpoint, there is therefore no net production or destruction of the chain carriers. This second step of the oxidation mechanism ends with the *chain termination*, during which, product species are

formed; the chain termination can be due to radical-radical recombination, radical-molecule reactions that produce less-reactive radicals, and/or radical quenching by the wall of the reactor.

As pointed out earlier, the oxidation kinetics of jet fuel surrogates can roughly be viewed as a concatenation of the oxidation mechanisms of pure components involved in their surrogate models. Several kinetic models have so far been formulated and validated for various range of operating conditions. Among the available detailed mechanisms, some of them were developed and extended by hand (e.g. GRI-Mech 3.0 mechanism [Bowman et al., 2004]), while others are obtained through an automatic generation process carried out by computer software; a way to automatically generate detailed mechanisms is described in [Blurock, 1995, 2000]. Detailed chemical kinetic mechanisms including species larger than C12-hydrocarbons are generated by the use of *reaction classes* associated with the reacting substructure in the species and a set of reaction constants. In both cases, the validation of the kinetic mechanism for a given fuel (or fuel surrogates) is generally done by means of chemical kinetic codes such as the PREMIX [Kee et al., 1985] and CANTERA [Goodwin, 2003] codes, or the CHEMKIN package [Kee et al., 1985, 1986, Design], which are used together with the newly developed kinetic models to compute essential combustion properties such as ignition delays, laminar burning velocity, flame extinction limits, combustion emissions, and other main features of the flame structure. The numerical predictions are thereafter compared to their experimental counterparts to assess the reliability of the newly developed kinetic models for the operating conditions considered in the numerical and experimental investigations.

Extensive investigations have so far been conducted by various research teams based on this procedure; the earlier versions of these investigations were mainly concerned with pure hydrocarbon fuels, and were conducted in jet-stirred reactors (JSR) over various ranges of operating conditions. Each of these investigations led to detailed kinetic models for the investigated pure hydrocarbon fuel; some of them, namely, those dealing with heavy hydrocarbon fuels are summarized in Table 2.10 along with the proposed detailed kinetic models [Dagaut et al., 1994, Ristori et al., 2001, Dagaut et al., 2002].

The samples of kinetics models shown in Table 2.10 allow noticing that realistic oxidation schemes involve large number of species and elementary reactions. Furthermore, these mechanisms are relatively simple compared to other kinetic mechanisms of pure compounds. In fact, according to Westbrook et al. [2009], the size of some of the heavy hydrocarbon detailed mechanisms from C_{10} through C_{16} when species and reactions for larger fuels have been removed are the following: $C_{10}H_{22}$ (940 species, 3 878 reactions); $C_{12}H_{26}$ (1 282 species, 5 030 reactions); $C_{14}H_{30}$(1 668 species, 6 449 reactions); and $C_{16}H_{34}$ (2 116 species, 8 130 reactions). The size of these mechanisms as well as those found in an early paper by Simmie [2003] reviewing the detailed chemical kinetic models for the combustion of hydrocarbon fuels, provide an idea on the size of detailed kinetic models for typical jet fuel surrogates, considering the categories of major constituents of real jet fuels as presented earlier (alkanes, cycloalkanes, aromatics, and alkenes). In this regard, it is obvious that a detailed mechanism of a jet fuel surrogate built with fully detailed mechanisms of pure compounds would lead to a ki-

Pure compounds (Investigators)	Size of the detailed kinetic model	Performance	test conditions
n-decane (Dagaut et al., 1994)	573 elementary reactions, most of of them being reversible among 90 species	Good prediction of major species over the whole range of pressure, temperature, and equivalence ratios	JSR at pressures extending from 10 to 40 atm in the temperature range 750-1 150 K
n-hexadecane (Ristori et al., 2001)	242 species and 1801 reactions	Prediction of species mole fractions (reactants, intermediate and final products)	JSR at 1 atm, from 1 000 to 1250 K and for equivalence ratios of 0.5, 1 and 1.5
toluene (Dagaut et al., 2002)	120 species and 920 reactions	Prediction of the benzene oxidation at 0.46 to 10 atm, the ignition-oxygen-argon mixtures and the combustion of benzene in flames	JSR at 1 atm, from 1 000 to 1 375 K and for equivalence ratios ranging from 0.5 to 1.5

Table 2.10: Sample of detailed kinetic models for pure compounds (heavy hydrocarbons)

netic model whose size does not facilitate efficient and inexpensive kinetic simulations. To overcome this difficulty, some features of jet-engines in terms of operating conditions are generally exploited. For instance, recognizing that jet-engine combustion only requires temperatures above 1 000 K, Naik and his co-workers [Naik et al., 2011] have reduced the full n-dodecane developed by Westbrook et al. [2009], by removing the low temperature kinetics. The resulting high temperature reduced mechanism (3 556 elementary reactions among 348 species) includes also the high-temperature iso-octane mechanism derived by Curran et al. [2002] in order to simulate their S-8 (S-8 is a synthetic jet fuel produced by the Fischer-Tropsch process from synthesis gas derived from natural gas) surrogate consisting of n-decane, n-dodecane, and iso-octane. Thereafter, this reduced version was successfully used by [Hui and Sung, 2013] to simulate the laminar flame speeds of n-decane, n-dodecane, iso-octane and S-8. Such approaches are used to develop chemical kinetic models for jet fuel surrogates, and the resulting kinetic models are thereafter validated by assessing their ability to retrieve relevant combustion properties of various pure components of jet fuels, as well as those of the real jet fuels, for various ranges of operating conditions (e.g. temperature, pressure, and equivalence ratios). Depending on the range of operating conditions and the large number of combustion properties to be matched, a continuous improving process may be necessary to improve the reliability of a kinetic model for a given jet-fuel surrogate.

A typical illustration of such a continuously improving process is provided by the various releases of the Jet Surrogate Fuel (JetSurF) model: The first interim version of the JetSurF model (JetSurF 0.2) was released in september 2008, and was developed from a base model termed as USC-Mech II [Wang et al., 2007 (accessed April 19, 2016]. The latter was developed at the University of Southern California, and consists of 111 species and 784 reactions to describe the oxidation of H_2 and CO and the high-temperature chemistry of $C_1 - C_4$ hydrocarbons. The base model considers the pressure depen-

dence for unimolecular and bimolecular chemically activated reactions involved in the mechanism, and was validated against experimental data ranging from laminar flame speeds, ignition delay times behind shock waves, to species profiles in flow reactors and burner stabilized flames. The development of the JetSurF 0.2 model consisted of appending the base model with 83 additional species and 675 reactions to describe high temperature pyrolysis of normal alkanes from heptane through dodecane, leading to the JetSurF 0.2 model composed of 194 species and 1 459 reactions. This first version was validated for larger-hydrocarbons by many research teams in terms of laminar flame speeds, ignition delays, species profiles behind reflected shock waves, and species concentration profiles in jet-stirred and flow reactors. A summary of these extensive validations may be found in [Sirjean et al., 2008 (accessed April 19, 2016]. This first version of JetSurF model was thereafter slightly improved to yield the second version, JetSurF 1.0, almost identical to the first model and consisting of the same number of species and reactions, but featuring a preliminary determination of the model uncertainty and its quantitative impact on predicted combustion properties. A summary of the validation tests conducted with this JetSurF version are provided in [Sirjean et al., 2009 (accessed April 19, 2016]. Subsequently, the JetSurF 1.0 was appended with a set of reactions (158 species and 624 reactions) to describe the high-temperature pyrolysis and oxidation of cyclohexane and its derivatives such as n-butylcyclohexane, n-propylcyclohexane, ethylcyclohexane and methylcyclohexane, leading to a third version of the JetSurF model, JetSurF 1.1, consisting of 2083 reactions among 352 species. The validation tests conducted with this version are provided in [Sirjean et al., 2009 (accessed April 19, 2016]. The latest release of the JetSurF model, JetSurF 2.0, consists of 348 species and 2 163 reactions, and includes all the prediction capabilities of JetSurF 1.1; it also includes limited low-temperature chemistry for cyclohexane and the alkylated cyclohexane compounds, though further work is necessary to improve the reliability of this part of the model. The current performances of this latest version can be found in [Wang et al., 2010 (accessed April 19, 2016].

Based on the brief description of these two samples of kinetic models for jet fuel surrogates, one can notice that, even with rough approximations in formulating the jet fuel surrogates (i.e. with a number of components as few as possible), the corresponding detailed kinetic model involves high number of species and reactions. Consequently, their implementation into simulation of the combustion chamber of practical aircraft engines is rendered difficult by the high computational costs and stiffness problems, so that it is often necessary to resort to a reduction step. Such an approach and the resulting mechanisms are discussed in the following subsection.

2.5 Reduced chemical kinetic models and the reduction techniques

Reduced chemical kinetic models are deemed a good compromise between the need for improved combustion chemistry description in simulations and the high computational costs of detailed chemistry models. Developing these reduced chemistry models, while retaining the ability to predict essential combustion properties is a challenging task since sophisticated reduction techniques are required. As for the development of detailed chemical kinetic models, the reduced mechanism can be

worked out by hand on the basis of the total sum of the experience and knowledge available, and can result in compact and accurate mechanisms, as the resulting mechanisms are subsequently validated by the experimental data. Considering that oxidation mechanisms are generally restricted to a narrow range of operating conditions, it is therefore advantageous to find general procedures that can reduce mechanisms automatically by using physical quantities or other parameters associated with different reactions and species involved in the detailed kinetic model. Thus, based on a set of selected criteria identified beforehand, it is possible to detect species that play a minor role in the overall reaction process so as to exclude them from the kinetic mechanism. Such a reduction technique can be implemented by the use of *reaction flow* and *sensitivity analysis*, or by using *Directed Relation Graph* (DRG) methods. Furthermore, as mentioned in the previous chapter, mathematical procedures can be applied to further reduce the computing time associated to a given fuel oxidation mechanism. Such mathematical procedures do not exclude species, but rather the species concentrations are calculated by simpler and less time-consuming algebraic equations, or they are tabulated as functions of a few representative variables. The portion of the mechanism that is left for detailed calculations is substantially smaller than the original mechanism. These methods often make use of the wide range of time scales and are thus termed as *time scale separation methods*. The most popular of these methods include those of *Computational Singular Perturbation* (CSP), the *Intrinsic Low Dimensional Manifolds* (ILDM), and the *Level Of Importance* (LOI) analysis in which the Quasi Steady State Assumption (QSSA) or partial equilibrium approximation (e.g. Rate-Controlled Constraints Equilibria, RCCE) is used to treat the steady state or equilibrated species. In the current study, a detailed kinetic model, JetSurF 2.0, is used as the base detailed kinetic model, and a sensitivity analysis termed as Alternate Species Elimination (ASE) method is used to reduce the size of the mechanism so as to facilitate its incorporation into simulations. In this approach, a characteristic combustion property is first used to define a normalized change, *NC*, induced by the alternate suppression of each species in the model. Thereafter, a threshold value of this, *NC*, is defined, and all chemical species whose *NCs* are below the user-defined threshold value are directly eliminated. Detailed explanations regarding this approach and some validations can be found in [Akih-Kumgeh and Bergthorson, 2013, Peters et al., 2014]. By applying this approach to the initial size of JetSurF 2.0 (348 species and 2 163 reactions), a reduced version consisting of 139 species and 1 045 reactions is obtained and validated against experimental data for flame speed and extinction rates [Munzar et al., 2013b,a, 2014]. The reduced kinetic model is also verified to predict other combustion properties in agreement with the detailed model and its validation targets.

The present chapter discussed the transport properties and the various fuel surrogates used for Jet A-1 as well as their oxidation mechanisms. These transport and chemical properties are implemented in the CFD models described in Chapter 1, and the latter are applied to some experimental configurations. The next chapter presents each of these configurations, while highlighting the practical interests of each of them.

Chapter 3

Experimental configurations

Numerical simulations are deemed to significantly contribute to the design and optimisation of technical devices involving flow and chemical reactions. The latter include advanced combustion systems such as aero gas turbines, and the main task of numerical simulations consists of describing the technical processes using mathematical models to understand the dynamic behaviour of the investigated system and make a reliable prediction of its future evolution. In general, the reliability and the prediction capabilities of a given computational model are assessed by comparing the numerical prediction against the experimental results carefully conducted with well-defined parameters. This validation step is essential to the full exploitation of the relevant advantages of numerical simulations, namely, the prediction of complicated processes which are difficult to access experimentally. Furthermore, when provided with accurate empirical correlations, advanced numerical simulation approaches such as DNS may become attractive compared to experimental approaches due to the level of detail of its predictions. The main reasons behind this attraction being the intricate tasks and high expenses involved in experimental investigations on the one hand, and the ease of handling, the ability to quickly change the operating conditions, the high repeatability, and the relatively low costs of incurred in the numerical approaches on the other hand. It is then clear that, in spite of the exponential increase in computing resources and other potential benefits of numerical simulations, the latter rely on experimental studies which are almost essential to the significant progress in combustion modelling which in turn contribute to the reliability of numerical approaches. From this perspective, numerical simulations are not considered to eliminate the need of experiments; instead, it is a complementary approach to experimental investigations as it helps understanding the system thoroughly, while giving more insight to the experimental data to reach some logical conclusions. As the aim of the current study consists of setting simulation approaches that can be used to retrieve the structure of a chemically reacting spray flow in both steady and transient regimes, some experimental configurations are first selected from the literature to calibrate the computational models and to assess their predictive capabilities. The choice of the experimental configurations is mainly guided by their ability to mimic complex flow patterns close to those encountered in real combustion chambers, and the availability of detailed experimental data so as to allow a step-by-step validation of both turbulence and combustion

models. A highly swirl-stabilized tubular combustion chamber is first selected to assess the predictive capabilities of the computational model to retrieve the structure of spray reacting flow in the steady combustion regime. Subsequently, a bluff-body stabilized burner is used to calibrate the computational model formulated beforehand with the aim of retrieving the flow characteristics in the transient combustion regime. In addition, the effect of the spark location on the ignition success is investigated with the ultimate goal of determining the locations of the mixing zone which are more likely to yield a successful ignition event. The well-turned computational model is thereafter extended to spray combustion, with the aim of predicting both transient and steady combustion regimes, namely, the ignition sequence and the resulting steady combustion regime in two different configurations of can combustors, the first being the swirl-stabilized combustion chamber and the second being the scaled combustion chamber equipped with liner holes. Detailed descriptions of each of these experimental configurations, along with the measurement techniques, are sequentially presented in the following two subsections.

3.1 Highly swirl-stabilized combustion chamber

Swirling flows are widely used in many combustion devices. In gas-turbine engines especially, the flow patterns involved in the primary-zone of the combustion chamber are of prime importance to mixing and flame stability. Various flow patterns are employed, and one of the features common to all is the generation of swirling motions that creates vortices which in turn entrain and recirculate a portion of the hot combustion products to mix with the incoming air and fuel. These vortices are continually renewed by air flowing through holes pierced on the combustor liner, supplemented in most cases by air flowing through swirlers and cooling slots and, depending on the injector configuration, by air employed in the atomization and/or sudden expansion experienced by the flow [Lefebvre, 1983]. The stabilization and mixing effects of the swirling motions are due to the dynamics of the resulting recirculation zones; the latter behave as pairs of counter-rotating vortices, and from fluid mechanics analysis, the resulting effect of such vortical flow dynamics leads to a velocity reversal increasing residence and mixing time for better flame stability [Kundu et al., 2012]. The characteristics of swirling motions involved in a given combustion device can then be used to control stability and intensity of combustion, along with the size and shape of the flame region. In this regard, numerous experimental investigations, serving for years as benchmarks for computational methods and turbulence models, have been conducted in the past with the aim of determining the effect of swirler design parameters such as vane type, vane angle, vane aspect ratio and space/chord ratio (defined by the number of vanes) on the aerodynamics of the downstream recirculation region on one hand, and the quantification of the amount of rotation imparted to the axial flow on the other hand. According the effect of swirler design parameters, the type of swirler needs to be first identified. Globally, there are two main configurations, namely, the radial and axial-flow types; most conventional combustors are equipped with axial swirlers with curved vanes for better aerodynamics properties. An extensive description of various types of single air swirlers for combustors is provided in [Kilik, 1976]. The

same reference shows that the size of the recirculation zone is increased by (i) an increase in vane angle, (ii) an increase in the number of vanes (i.e. a decrease in space to chord ratio), (iii) a decrease in vane aspect ratio, and (iv) a change in vane shape (e.g. a change from flat to curved vanes). For the quantification of the amount of rotation imparted to the axial flow, Beer and Chigier [1972] defined a nondimensional parameter termed as *Swirl Number* to quantify the amount of rotation imparted to the flow. The swirl number, S_N, is mathematically defined as the ratio of the axial flux of tangential momentum, G_{tm}, to the axial flux of axial momentum (i.e. axial thrust), G_{am}:

$$S_N = \frac{G_{tm}}{R_{sw} G_{am}} \tag{3.1}$$

In this equation, R_{sw} stands for the outer radius of the swirler, and the axial fluxes of tangential and radial momentum are respectively defined by

$$G_{tm} = \int_0^{R_{sw}} 2\pi r^2 WU dr \tag{3.2}$$

and

$$G_{am} = \int_0^{R_{sw}} 2\pi r U^2 dr + \int_0^{R_{sw}} 2\pi r p dr, \tag{3.3}$$

where U, W, and p are the axial and tangential components of the velocity and the static pressure, respectively, in any cross section of the jet. In practice, a simplified form of the swirl number relationship is most often used; the latter was proposed by Sheen et al. [1996], and is expressed as follows:

$$S_N = \frac{\int_0^{R_{sw}} r^2 WU dr}{R_{sw} \int_0^{R_{sw}} rU^2 dr} \tag{3.4}$$

The strength of a given swirling motion is defined by the value of the swirl number. For values of swirl number less than around 0.4, no flow recirculation is generated by the swirler, and the swirling motion is described as weak. However, when the streamlines diverge considerably and there is still no recirculation (typically, configurations exhibiting a swirl number between 0.4 and 0.6), the swirling motion is considered as moderate. For configurations exhibiting a swirl number of $S_N \geq 0.6$, the flow is considered as highly swirled; most practical configurations belong to this regime.

In the current study, a reduced model of a swirl-stabilized tubular combustion chamber is used (see Figure 3.1). The main feature of this combustor model lies in the fact that high mixing rates are achieved by using high swirl intensity which results in an intense rotating motion imparted to the flow. Such a configuration differs from that of conventional combustion chambers in which high mixing rates are achieved by means of both swirlers and holes pierced in the combustor liner (i.e. by combining swirling motion imparted to the flow, and the stirring generated by air issued from the holes located on the wall of the combustion chamber). As illustrated by the schematic representation of the second model of can combustors considered in the current study (see Figure 3.7), the holes located on the combustor liner are of various sizes and consist of several rows. These holes play two main roles depending on their configurations and locations; some of them are used to supply air for combustion initiation and termination, while the others supply air for walls cooling and the

reduction of flame temperature. Especially, the reduction of the flame temperature is ensured by holes known as *dilution holes*, while wall cooling is ensured by *cooling slots*. Thus, attention is not paid to the wall cooling when dealing with the aforementioned swirl-stabilized can combustor. An overview of the first combustor geometry, and the swirl-induced flow patterns, are respectively shown in Figure 3.1 and Figure 3.2. This combustion chamber was used by Sheen [1993] in an experimental

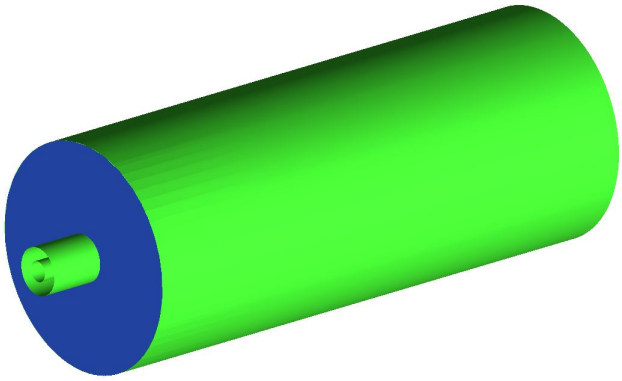

Figure 3.1: 3D view of the scaled swirl-stabilized combustion chamber

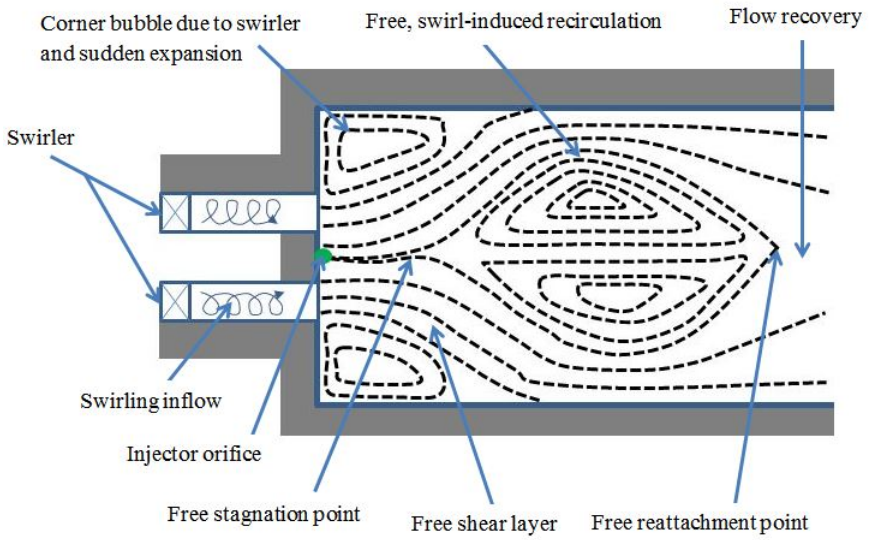

Figure 3.2: Flow patterns involved in the swirl-stabilized combustion chamber

setup at Imperial College London to investigate the steady combustion regime, with the main aim of determining the structure of a swirl-stabilized spray flame.

3.1.1 Practical interests

The surge in environmental regulations makes combustion properties such as pollutant emissions critical in both steady and transient combustion regimes. The investigated configuration features a swirl number of 0.91, which physically implies that a high swirl motion is imparted to the flow. Thus, with this initial swirling motion and the sudden expansion experienced by the annular air flow, along with the spray dynamics, the combustion chamber exhibits complex flow patterns close to those encountered in real combustion chambers. As mentioned earlier, such flow patterns include recirculating regions, swirling flows and breakdown of large-scale vortical structures which interact mutually and continually, leading to a challenging flow behaviour. Plus, the central recirculation zone formed by the swirling jet is strongly affected by the cylindrical centre body (see Figure 3.2) which acts as a bluff-body, and the flow exhibits coherent structures such as Precessing Vortex Cores (PVC), which create regions with high velocity fluctuations (PVCs improve the mixing because of the creation of larger turbulent scales which translate through into the dissipation range of the energy cascade). The main interest of such a configuration lies in the fact that, detailed experimental data on combustor aerodynamics (velocity components and the corresponding fluctuations) are available, and can help assessing the reliability and the robustness of turbulence models. The configuration provides additional tools for the validation of turbulence models, namely, detailed experimental data on both major and slow species. The prediction of some species are to some extent, more sensitive to the choice turbulence model than to the chemistry model (e.g. LES coupled to a simple chemistry model may outperform URANS coupled to a detailed chemistry model [Pierce and Moin, 2004]), and a sophisticated chemistry model is needed for an accurate prediction of slow species [Hilbert et al., 2004a, Poinsot and Veynante, 2005, Peters, 2000]. It is then clear that this configuration can provide not only further insight on the predictive capabilities of turbulence models, but also, it can help assessing the capabilities of combustion models in terms of prediction of pollutants which are known to feature low reaction rates. Finally, the configuration is concerned with a fuel-lean combustion mode (equivalence ratio, $\phi \approx 0.53$), which is gradually used by aircraft engine manufacturers as an alternative solution to improve fuel economy and to adapt to stringent emission standards [Dunn-Rankin, 2008].

3.1.2 Combustor dimensions and operating conditions

A sketch of the combustion chamber is shown in Figure 3.3. It consists of a 500-mm long cylindrical combustion chamber with an internal diameter of 200 mm, and is mounted with a swirler that has 20 equally spaced vanes at a discharge angle of 30^o to the axis. The swirler is installed in an annular duct located 50 mm upstream of the front plate of the combustor. In the non-reacting experiment, an annular swirling air jet flows into a cylindrical combustion chamber where it mixes with air which is initially at rest. The injector orifice, located in the middle of the combustor front plate, has a diameter of 0.25 mm, and in the reacting experiments, injects liquid Jet A-1 in the form of a fine hollow conical spray. The air flow and the liquid spray are not preheated and the exit of the combustor is open to the atmosphere. The co-flowing air enters the combustion chamber axially

with a tangential velocity component generated by the swirler. The annular pipe has an outer radius, $R = 21$ mm. The spray flow is turbulent and highly swirled, since the swirl number $S_N = 0.91 > 0.6$, and the Reynolds number (based on the annular duct radius) is approximately 21 300. The fuel mass flow rate is 0.951 g/s, and the air-to-fuel ratio is 27.88.

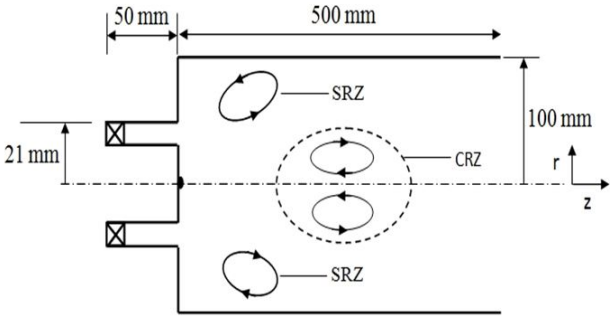

Figure 3.3: Dimensions of the Imperial College London scaled swirl-stabilized combustor

3.1.3 Measurement techniques

In general, the aerodynamic of a given combustion chamber is provided by instantaneous velocity at each point of the combustor. For turbulent flows, in particular, the velocity measurements consist of determining local values of the first and the second moment of the velocity components. There are several approaches that can be used in this regard depending on the flow configuration. These include Pitot-tube, Hot-wire Anemometry, Laser Doppler Anemometry (LDA) also termed as Laser Doppler Velocimetry (LDV) and the Particle Image Velocimetry (PIV).

Pitot-tube measurement technique

The operating mode of the Pitot-tube measurement technique is similar to that of a restriction flow meter: the tip brings the approaching fluid to a stop, allowing measurement of the stagnation pressure at the tip, and an approximative value of the static pressure in the free stream at the side of the tube. Bernoulli's equation is thereafter used to deduce the velocity.

Hot-wire Anemometry

The hot-wire anemometry technique consists of putting a very fine short wire in the flow and heating it up. When the fluid flow crosses the wire, the wire is cooled by the fluid. In order to keep the wire temperature constant, a current is supplied proportionally to the rate at which the wire is being cooled, which is related to the flow velocity. Although this approach leads to good measurements, it may not be appropriate for all applications, so that more refined measurement techniques are necessary.

Laser Doppler Anemometry (LDA)

The LDA approach is suitable for a wider range of flow configurations; it requires a laser and some optics, and is thus a relatively complicated and quite expensive measurement technique. The LDA measurement technique consists of focusing the laser beam into the flow on a small volume; the flow is seeded with tracer particles, and a photomultiplier is used to detect the Doppler shift caused by the flow of particles through the target volume. The velocity is thereafter deduced from the output of the photomultiplier. Although this approach leads to excellent spatial and temporal resolutions, it is worth noting that it features some drawbacks, namely, the need of an optical access and additional equipments for two- and three-component measurements. The basic LDA setup allows measuring one velocity component, and additional beams and probes are necessary to measure the three velocity components.

Particle Image Velocimetry(PIV)

The main difference between PIV (i.e. classical PIV and its variants) and the aforementioned measurement techniques is that PIV produces two-dimensional or even three-dimensional vector fields, while the others techniques measure the velocity at one point. A typical PIV system consists of a camera, a laser with an optical lens to generate a thin light sheet to limit and illuminate the physical region, and a synchronizer to act as an external trigger to control the camera and laser to capture a displacement of seeding particles and map the velocity field for the fluid flow under investigation. The fluid flow is first seeded with tracer particles so as to achieve a small Stokes number (i.e. with particles sufficiently small so as to faithfully follow the flow dynamics: typically, $S_{tk} \ll 1$ and ideally, $Stk \ll 0.1$). The fluid, with the entrained particles, is illuminated so that particles are visible; the motions of the seeding particles are used to deduce the velocity field of the flow being investigated. The variants of the PIV approaches include particle tracking velocimetry (i.e. PIV with low particle concentration so each individual particle is followed) and laser speckle velocimetry (i.e. PIV with a particle concentration so high that it is not possible to distinguish between the individual particles in an image).

For the configuration considered in the present study, the measurements were obtained using Laser Doppler Anemometry (LDA). The reported experimental data include first and second order moments of the three velocity components and temperature, as well as the species mole fractions at some cross sections of the combustion chamber. The experiments do not provide any measurement of the flow upstream of the combustion chamber inlet, and no measurements of the spray properties are reported. Thus, the specification of accurate spray and air inflow boundary conditions for the simulation is essential, but unfortunately lacking from this data set.

3.2 Bluff-body stabilized burner

In addition to swirlers, bluff-bodies are used in many advanced combustion systems such as ramjet and turbojet after-burner systems to improve flame stabilization, and are undoubtedly the most important configurations in this regard [Lefebvre, 1983]. Due to this flame stabilization effect for dif-

ferent bluff-body configurations, they are also termed as flame-holders, and the flame-holding mechanism is mainly governed by the recirculation zones generated in the wake behind the bluff-body; the downstream wake being formed as a result of flow separation occurring at the trailing edge of the stabilizer. In addition, the near-wake region supports a recirculating flow, and as the velocity in this region is much lower than the main-stream velocity, a shear layer is formed in which heat- and mass-transfer processes (and thus global mixing) are enhanced by turbulent diffusion. The blockage caused by the bluff-body in the flowing mixture stream increases the turbulence level due to the vortex shedding and flow separation. Another relevant characteristic of such a flow configuration lies in the fact that the combustion products trapped inside the recirculation zone may serve as a burning source by continuously igniting the incoming fresh fuel-air mixture.

From this brief description of the bluff-body-induced flow dynamics, it can be noticed that bluff-body and the swirler devices play a relevant role in improving fuel-air mixing and flame stabilization. There are various bluff-body shapes (e.g. disk, cylindrical, conical), and the corresponding induced-aerodynamics have been experimentally analysed and reported by many investigators for both non-reacting and reacting flow configurations, with the aim of determining the influence of the geometric parameters of a given bluff-body (i.e. shape, blockage ratio, etc.) on the flow dynamics, namely, the velocity fields, the eddy shedding frequency, the size of the recirculation zone, among others. For instance, in an earlier investigation, Taylor and Whitelaw [1984] observed that the effect of increasing the blockage ratio (BR) on the recirculation zone in an open flow is opposite to that in a confined flow, as the length and the width of the recirculation zone tended to increase with an increase in BR. They related this difference to the confining wall which prevents the generation of large streamline curvature towards the stagnation point, and maintain large axial velocities at all downstream stations. Also, they investigated the influence of the bluff-body shape using two different shapes with the same BR=25%: a disk and a 45^o cone. By replacing a disk bluff-body by a 45^o cone-shaped one, they found that: (i) the recirculation zone is shortened and narrowed by 10%; (ii) the recirculation mass flow rate is decreased by 40%; and (iii) the largest value of the turbulent kinetic energy is reduced by 40%. By using two disk bluff-bodies with different blockage ratios, namely, 25% and 50%; the same authors found that for a 25% blockage ratio, the maximum turbulent kinetic energy lies near the stagnation point, whereas for the 50% blockage ratio, it is far from the centreline in the shear layer. In the same vein, the influence of bluff-body geometry on flame stabilization process was investigated by [Esquiva-Dano et al., 2001]; the investigation was based on a non-premixed burner featuring central fuel injection with disk- and conical-shaped bluff-bodies. They investigated the mechanism of flame stabilization, with an increasing air velocity up to the fuel jet velocities. The blockage ratios of the two flame-holders were the same except that, the conical-shaped flame-holder was more streamlined than that of disk shaped and therefore led to an expansion of boundary layer. Their results converged to those of the first research group, and show that the dimensions of the resulting recirculation zone behind the bluff-body wake differ both in height and width, due to the difference in flow divergence produced. The conical bluff-body produces a wider range of regimes for flame stabilization than the disk shaped one, due to the difference in the aerodynamics which also influence the fuel-air mixing. As portrayed

earlier to illustrate the flow pattern involved in the swirl-stabilized combustor (see Figure 3.2), an experimental attempt of flow field visualization made by Balachandran [2005] allows noticing two distinct recirculation zones downstream of the conical shaped bluff-body burner (see Figure 3.4(b)). These are the central recirculation zone (CRZ) at the wake of the bluff-body, and a side recirculation zone (SRZ) formed between the burner confinement and the core jet region. Through experimental measurements, the height and the width of the central recirculation zone was found to be 1.5 and 1 times the diameter of bluff-body respectively. This empirical result is of particular interest, especially when investigating ignition with a closer look at the effect of spark location on ignition success. Once the decision is made to spark inside or outside the recirculation regions, the traversing mechanism used for the spark deposition can be better positioned.

Considering the twofold objectives of the current study, namely, the formulation of a CFD model that can retrieve the structure of reacting spray flow in both steady and transient combustion regimes, a relatively simple configuration consisting of spark ignition of a bluff-body stabilized burner is used in an intermediate step to calibrate the basic form of the formulated CFD model. As the configuration is based on a gaseous fuel (methane), the CFD model is first formulated for homogeneous combustion, and is thereafter extended to spray combustion with the aim of predicting the whole ignition sequence and the resulting steady combustion regime in a liquid-fuelled combustion chamber. It is worth noting that the numerical simulations based on the bluff-body stabilized burner were substantially facilitated by the outcomes of the first investigation, namely, the previous simulations based on the steady combustion regime in the highly swirl-stabilized tubular combustor. In fact, the first simulations based on the steady combustion regime allowed comparing various turbulence and combustion models in terms of trade-off between computational costs and the accuracy of the results, and suggested therefore robust and reliable turbulence and combustion models for subsequent simulations (at least in terms of the aerodynamics of the combustion chamber and main flame trends).

In general, phenomena such as the ignition sequence of a burner (or in a combustion chamber) and other transient combustion phenomena are relatively more difficult to investigate compared to the steady combustion regime due to the wide range of size and time scales involved. Indeed, in spark-based ignition engines, the flame kernel ignition resulting from the spark discharge, and its subsequent propagation until the full ignition, is governed by complex mechanisms due to the interaction of various physical phenomena that feature very small characteristic length and time scales. The bluff-body stabilized burner considered in the present study was built and used by Ahmed [2007b] in an experimental setup at Cambridge University to investigate the spark ignition of turbulent non-premixed flames, with the main goal of determining the effect of the spark location on the ignition success. The design of this burner was partially based on a previous model designed by Balachandran [2005] for premixed bluff-body flame investigations: both bluff-bodies have the same outside dimensions in order to keep the same flow patterns. A 3D view of the combustion chamber and the corresponding flow pattern are shown in Figure 3.4(a) and Figure 3.4(b).

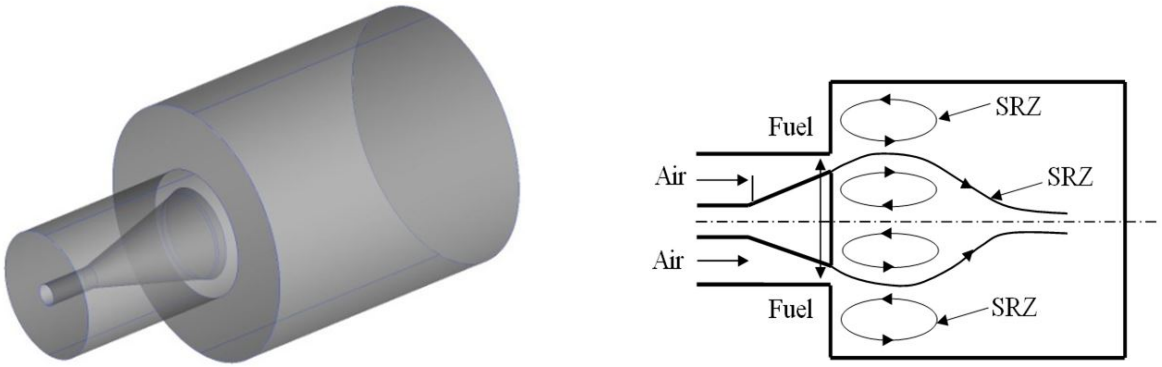

(a) 3D view of the Cambridge University's bluff-body stabilized burner.

(b) Flow pattern.

Figure 3.4: An overview of the Ahmed's bluff-body stabilized burner and the corresponding flow pattern

3.2.1 Practical interest

The bluff-body stabilized burner considered in the current study represents an important class of practical burners, and was specifically designed for fundamental investigations. Its main advantages include the following: (i) through variation in design and operating conditions, this burner can produce flames of varying stability, efficiency, pollutant formation and heat transfer rates; (ii) due to the ability of this burner to mimic complex flows as those existing in real configurations, it can provide a greater understanding of complex flow fields, and ignition requirements such as stability and ignitability; (iii) the radial fuel injection of the fuel avoids penetration of the recirculation zone, and allows combustion to occur in partially-premixed mode and therefore, at some locations within the combustion chamber, triple flames may develop and contribute to the overall flame stabilization; and (iv) finally, detailed experimental data along with the corresponding boundary conditions are available so as to facilitate a step-by-step validation of the CFD model. These data include the velocity and mixing fields and high-speed camera images of the ignition sequence. The experimental data for the first and second moments of the velocity components and those of the mixture fraction recorded in the cold flow experiments allow assessing the prediction capabilities of the turbulence model and the associated submodels, while high-speed camera images of the ignition sequence recorded at various time frames help appraising the performance of the other models employed in the reacting flow experiment.

3.2.2 Experimental burner description

A more detailed description of target experiment is shown in Figure 3.5. It is composed of two main parts: the inlet part and the flame zone. The inlet part consists of two concentric circular ducts of length 400 mm. The inner diameter of the outer duct, D_s, is 35 mm, while the inlet duct is a 6-mm-internal diameter tube, and has a wall thickness of 0.5 mm. The inner duct diverges out near the flame zone to form a conical shaped bluff-body of diameter D_b=25 mm, leading to a blockage ratio, $BR = D_b^2/D_s^2$, of 50%. The bluff body is designed with a 0.7 mm slot just 2 mm below the flame zone.

The aim of such a design is to allow a radial fuel injection that achieves a non-premixed flame without a penetration of the recirculation zone. The reactants are fed from the bottom of the burner by the two concentric cylindrical ducts; the annulus between the outer and the inner ducts serves as the passage for the air, which flows through a 200 mm long plenum of inner diameter 100 mm. The plenum has divergent and convergent cross-sections at the inlet and the exit, respectively, which helps to avoid flow separation during expansion and contraction. The fuel (methane having 99.96% of purity) is supplied by the inner duct, which is closed at the top. The fuel is diverted and injected radially on the axially flowing air stream through the 0.7 mm slot located 2 mm below the flame zone inlet. The flame zone is enclosed using an 80-mm-long fused quartz cylinder of inner diameter 70 mm, which provides optical access for imaging, and also avoids air entrainment from the surroundings. As the experiments are also concerned with a swirler on both flame stability and ignitability, a 60^o swirl vane was introduced in the flow 50 mm upstream of the bluff-body surface. However, since the results provided for non-swirling case include detailed measurements of the flow and the mixing fields, only the non-swirling case is considered for the CFD model calibration. Also, to minimize the requirements in computing resources, only the two parts of the burner described earlier are considered in the computing model; these two parts are delimited by the dashed lines in the schematic representation of the experimental apparatus (see Figure 3.5).

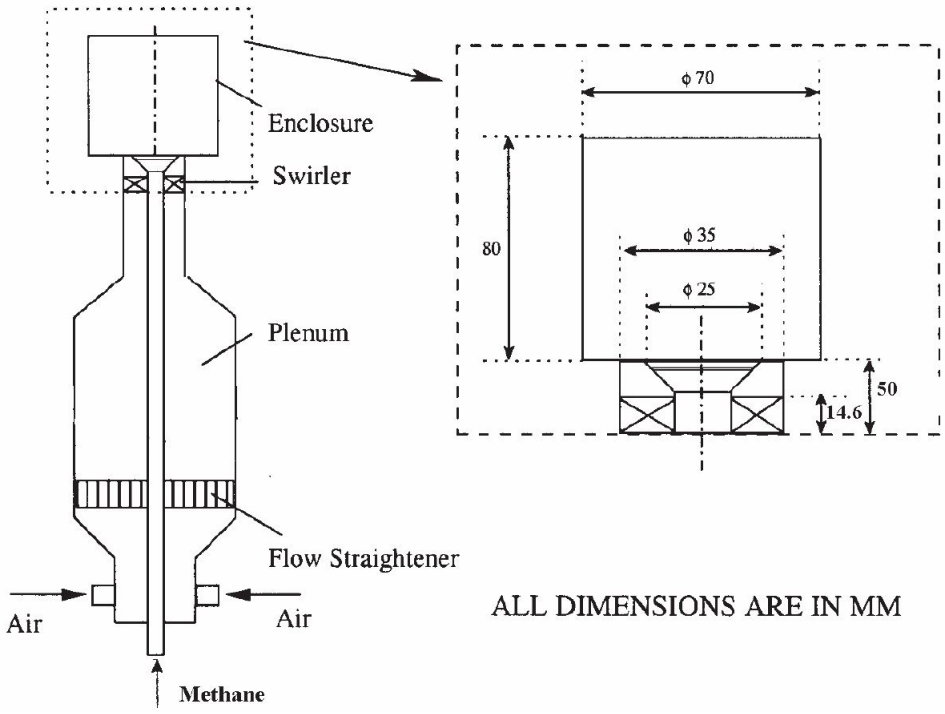

Figure 3.5: Schematic representation of the Cambridge University experimental apparatus [Ahmed et al., 2007]

An inductive ignition system was specially designed to produce repeatable sparks whose energy

and duration could be varied independently. The spark was created between two tungsten electrodes with a diameter of 1 mm, which were placed to ensure minimum disturbance to the flow. The spark gap was set to be 2 mm for all experiments. For most conditions, the igniter generated a 500 μs spark with an energy of 200 mJ, but only approximately 30% of this energy is transferred from the spark to the mixture. In the other conditions for which the standard spark parameters did not lead to a successful ignition, the energy and/or the spark duration were increased to quantify the local ignitability and thus determine the flammability limits. To allow the generation of sparks at various specific locations of the flow field, two electrodes were attached to a two-dimensional traversing mechanism by a ceramic tube so as to allow the igniter to be traversed axially and radially to cover the whole flow field with a 0.1 mm resolution.

3.2.3 Operating conditions and measurement techniques

Various operating conditions were adopted depending on the type of measurements of interest. At first, the velocity measurements were carried out on only one flow condition consisting of a turbulent air inflow having a velocity $U_{air} = 10$ m/s (i.e. $Re = 1.67\times10^4$) without swirl or fuel injection. Based on this first operating conditions, a LDV system was used to measure the radial profiles of the velocity components (axial and radial velocities) at various cross sections of the burner. This first series of measurements allows determining the size (length and width) of the recirculation zone and the global flow dynamics of the burner, and provides of idea on the stability limits (i.e. flow conditions which are suitable to stabilize the flame). Subsequently, the mixture fraction distribution was measured using an acetone-based PLIF technique. In this second series of measurements, the fuel was replaced by air, and the resulting substitute of the fuel stream was seeded with acetone for visualization purposes. A 45×50 mm area of the flow field was first selected and covered by the ICCD camera to image the corresponding acetone distribution. The resulting images were then postprocessed to deduce the mixture fraction distribution; the detailed explanations in this regard are provided in [Ahmed, 2007b]. The measurements were carried out using two different operating conditions based on the same air fuel velocity (i.e. $U_{air} = 10$ m/s), and two different fuel velocities, namely $U_f = 5$ and $U_f = 8$; the two conditions were mimicked by $U_{act} = 2.5$ and 4 m/s when replacing fuel with seeded air in the acetone-based PLIF experiments. When replacing the fuel by the seeded air, the mass flow rate of the air issued from the fuel stream was set equal to the fuel mass flow rate. As reported by the experimenter, this option, compared to the two other options tested (seeded air having momentum equal to the fuel momentum, $\rho_f U^2$, and seeded air having velocity equal to the fuel velocity), leads to reasonable and realistic results although it is not sufficiently representative of the fuel distribution. The mixture fraction field extracted from this second measurement phase allows measuring the local flammability and can help estimate roughly the ignitability limits. The third group of measurements was concerned with reacting flow experiments: the investigation of the ignition process and the flame stability limits. As mentioned earlier, various spark scenarios defined by the amount of spark energy and the spark duration were considered at different locations of the burner mixing field with the aim of determining the effect of the spark location and the spark parameters on the ignition success. The

corresponding ignition events, from the moment of spark discharge to the global flame stabilization were visualized by using a high-speed camera.

3.3 Scaled can combustor including liner holes and cooling slots

The swirl-stabilized combustion chamber presented earlier is used to assess the capabilities of various CFD models in terms of retrieving the structure of a spray flow and the combustion properties in the steady combustion regime. All the CFD models tested are formulated in the environment of a CFD code providing a easy handling from an industrial stand point, and the ultimate goal of the study is to isolate the CFD model leading to the best trade-off between the computational cost and the accuracy of the results. The assets of the resulting CFD model are thereafter used to formulate a CFD model capable of retrieving the structure of reacting flows in the transient regime, namely, an ignition sequence in a liquid-fuelled can combustor. To this end, a part of the multi-physics phenomena is temporarily excluded from the study: the spray dynamics and its interactions with gaseous phase are first omitted. Thus, a basic version of such a CFD model is formulated to predict the ignition sequence in a gaseous fuel configuration; this basic CFD model is validated by using the bluff-body burner as described earlier. Subsequently, the basic CFD model is extended to the spray combustion with the aim of improving the prediction of the main flame trends in the steady combustion regime, and especially to capture the ignition sequence that precedes the steady combustion regime (i.e. flame kernel initiated by the spark deposit, flame kernel propagation until the full ignition of the combustion chamber, and the global flame stabilization). The new CFD model is first applied to the swirl-stabilized combustor described earlier, and to a scaled can combustor (with a simplex nozzle) provided by P&WC. As mentioned earlier, the main difference between the two combustion chamber lies in the fact that, instead of using the high swirl number to achieve high mixing rates, the fuel-air mixing is enhanced by air issued from the holes pierced in the combustor liner, and the added cooling slots. Furthermore, the temperature of the exhaust gases can be controlled (i.e. reduced to avoid burning turbine blades) by the air issued from the dilution holes, and the walls of the combustion chamber are cooled; this configuration is therefore more representative of practical configurations. Through these features, the scaled can combustor allows emphasizing the relevance of cooling, mixing and dilution processes in improving engine safety and engine performance (e.g. efficiency and pollutant reduction). These safety and performance criteria are strongly influenced by aerodynamic parameters such as pressure losses and the flow through the combustor liner. The overall pressure loss across the combustion chamber is defined as the ratio of the total pressure drop to the total pressure at the combustor inlet (i.e. $\Delta P_{3-4} = (P_{int} - P_{out})/P_{int} = (P_3 - P_4)/P_3$). It can also be determined using the velocity loss, which is another dimensionless quantity defined as the ratio of the total pressure drop to the reference dynamic pressure (i.e. $\Delta P_{3-4}/q_{ref}$). The overall pressure loss and the velocity loss are related through the Mach number according to the following relationship:

$$\frac{\Delta P_{3-4}}{P_3} = \frac{\Delta P_{3-4}}{q_{ref}} \frac{R}{2} Ma^2 \tag{3.5}$$

where the Mach number, Ma, is defined by:

$$Ma = \left(\frac{W_3\sqrt{T_3}}{A_{ref}P_3}\right)^2 \tag{3.6}$$

In this relation, the reference area, A_{ref}, corresponds to the reference cross section of the combustion chamber. From this definition, it can be seen that, unlike the pressure loss which depends on the operating conditions, the velocity loss depends on the combustion chamber geometry only. Similarly, the flow through the liner holes is mainly determined by geometrical parameters such as the area of the liner holes. The mass flow rate through a single liner hole can be calculated using the following expression:

$$\dot{m}_h = C_D A_h \sqrt{2\rho_3(P_3 - p_{4,j)}} \tag{3.7}$$

where P_3 is the total pressure upstream of the hole, $p_{4,j}$ is the static pressure downstream of the hole, and C_D is the discharge coefficient. For an incompressible non-swirling flow, the discharge coefficient for a jet flowing across the liner wall through a plain circular hole is defined by:

$$C_D = \frac{1.25(K-1)}{\sqrt{4K^2 - K(2-\alpha)^2}} \tag{3.8}$$

where α is the ratio of the hole mass flow rate to the annulus mass flow rate ($\alpha = \dot{m}_h/\dot{m}_{an}$, and K is the ratio of the jet dynamic pressure to the annulus dynamic upstream pressure of the hole station considered.

The reduced can combustor is represented in Figure 3.6 and Figure 3.7. It has a diameter of 65 mm and length of 170 mm, and was used in the Combustion Laboratory at Université Laval to investigate two main physical phenomena, namely, the ignition and post-shutdown heat soak-back phenomena. The former type of the study was mainly concerned with the assessment of the flight envelope for aircraft operation with new jet biofuels in comparison with Jet A-1 performance [Jean, 2017], while the second was mainly devoted to investigate the thermal behaviour and magnitude of heat soak-back occurring in a gas turbine combustor along with its potential consequence on the fuel delivery system [Ghazlani et al., 2015]. The experiment based on Jet A-1 was concerned with both cold start and altitude relight, and the ignition sequence corresponding to one of the operating conditions was recorded using a high-speed camera [Marcotte et al., 2013]. Some of these experimental results are used to appraise the predictive capabilities of the CFD model in predicting each of these ignition events under various operating conditions.

The present chapter described all the three experimental configurations considered in this study. The reasons for choosing each of them were also discussed as well as the various measurement techniques employed in the corresponding experiments. The models discussed in Chapter 1 allow formulating a global CFD methodology that can be used to predict phenomena of interest in each of these configurations. As mentioned in the introduction, the global CFD methodology is formulated in a commercial CFD code environment. The majority of the sub-models used to build the global CFD model are available in the CFD code, and when predicting some phenomena, some models are customized to strengthen the robustness of the CFD code. The next chapter is devoted to the CFD code

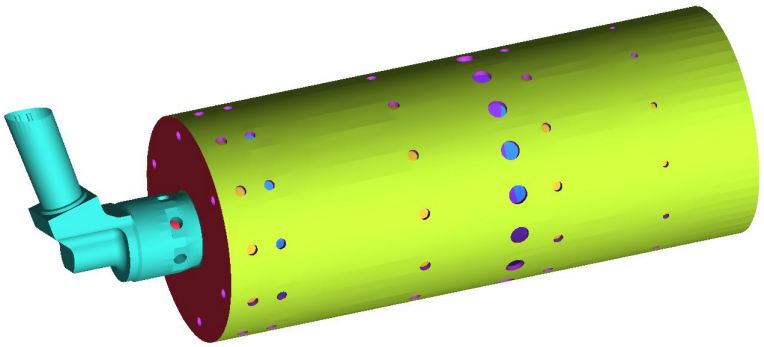

Figure 3.6: Schematic representation of the reduced can combustor [Gratton and Sampath, 1983]

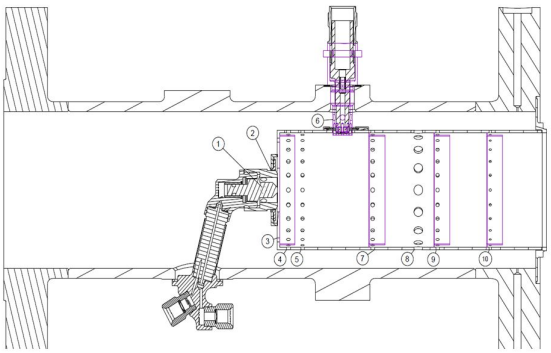

Figure 3.7: Longitudinal cross section of the reduced can combustor [Gratton and Sampath, 1983]

description, the implementation of the newly developed CFD methodology, the boundary conditions used in the three configurations, and finally, the flowchart adopted for the simulations.

Chapter 4

Numerical implementation

Turbulent chemically reacting flows are governed by a set of conservative and transport equations that need to be solved to simulate the various physical processes involved. As discussed in the first chapter, this set includes the classical Navier-Stokes equations and the other similar convection-diffusion equations such as those of turbulence parameters and scalars. To cope with the non-linear nature of these equations that makes it difficult to apply analytical methods, numerical methods have been used since the early days of computers, and they are applied in the field widely known as Computational Fluid Dynamics (CFD). The process of CFD consists globally of five main steps: (i) the portion of the physical geometry which involves the investigated phenomena, as well as the related boundary conditions, are first defined; (ii) the numerical discretization methods such as Finite Differences, Finite Elements, and Finite Volumes methods are applied to transform the analytical form of the conservative equations into their discretized form; (iii) since the discretized form is based on elementary domains, the whole computational flow field is divided into discrete small domains (also termed as computational cells) which are thereafter combined to the conservative equations to build algebraic equations for the discrete variables (e.g. velocities, pressure, enthalpy and other scalars, etc.); (iv) the discretized equations are first linearized, and the resulting linear system of equations is translated into machine language using programming tools; (v) finally, the computer code is run to iteratively solve the linear system, and the calculation process yields updated values of the discrete variables that meet some convergence criteria set beforehand. All these steps are summarized by the flowchart shown in Figure 4.1.

Based on this brief description, it is clear that mesh generators and CFD codes are essential tools to the numerical implementation of a given flow field problem, and their robustness determines the accuracy of the numerical results. Indeed, these two tools are used to submit physical problems to computers so as to leverage their computing capabilities. The former provides a grid of the physical domain, while the latter uses the grid to solve the flow field of interest. In particular, CFD codes are built by applying numerical methods to the mathematical formulation of the investigated flow field. The solver accounts for all the physical phenomena involved in the physical system (e.g. fluid and spray dynamics, heat and mass transfers, chemical reactions, and their various interactions), while

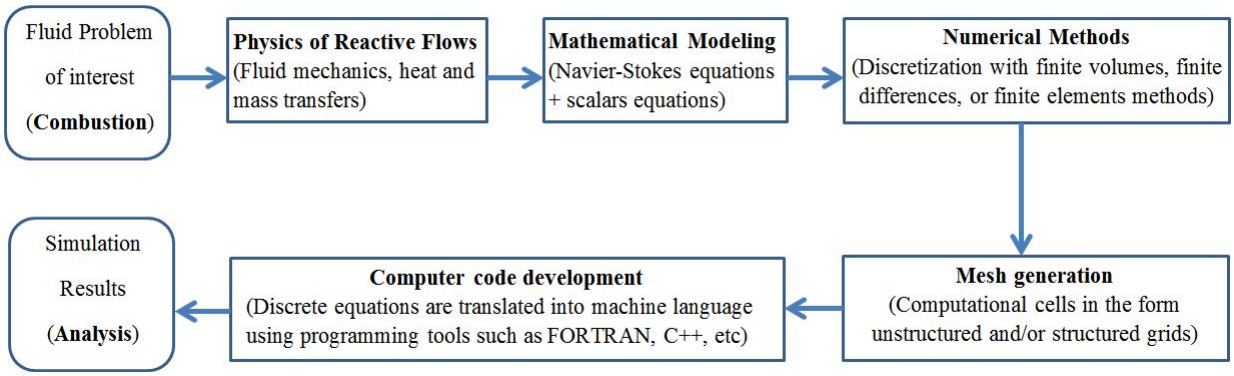

Figure 4.1: Main steps in applying Computational Fluid Dynamics

the numerical methods are mainly concerned with the types and various schemes used to discretize the analytical form of the conservative equations. This chapter discusses the numerical methods, and provides a brief review of the various numerical tools used in CFD. Finally, the numerical tools and the models used in the current study are discussed and supported at the end with a global flowchart of the current simulations.

4.1 Numerical methods in fluids

The three classical numerical methods used to solve various flow field problems described by partial differential equations (PDEs) include the finite difference method (FDM), the finite element method (FEM) and the finite volume method (FVM). The FDM is the oldest approach, and is based on the application of a local Taylor expansion series to approximate the differential equations. The FDM uses a topologically square network of lines to discretize PDEs, and is therefore relatively simple to program. This operating mode leads to some limitations in terms of accuracy and flexibility, especially when handling complex geometries in multiple dimensions [Smith, 1985, Morton and Mayers, 1994, Thomas, 1995, Joaquim and Spencer, 2005]. The FDM is currently used in few specialized codes that can handle complex geometries with high accuracy and efficiency by using embedded boundaries conditions or overlapping grids (with the solution interpolated across each grid). As another attempt to cope with this issue related to handling complex geometries, other techniques based on the integral form of PDEs (instead of differential form as in FDM) have been developed; these techniques include the FEM and the FVM. The use of the integral formulations is advantageous as they provide a more natural treatment of Neumann boundary conditions as well as that of discontinuous source terms due to their relatively reduced requirements on the regularity or smoothness of the solution [Hirsch, 1988, Zienkievicz and Taylor, 2000]. Another asset of the integral formulations lies in their abilities to dealt with complex geometries in multidimensional problems since the integral formulations do not rely on any special mesh structure [Hirsch, 1988, Joaquim and Spencer, 2005]. The FEM is widely used in structural analysis of solids, but can also be applied to fluids if it is carefully formulated so

as to ensure a conservative solution. As an attempt in this vein, an adapted version of FEM for fluid dynamics application was formulated; detailed information regarding this FEM version are provided in [Karniadarkis and Sherwin, 1999]. However, although such an adapted version is much more stable compared to the FVM, it is worth mentioning that it may require more memory and slower solution time than the FVM. When the finite difference and finite element methods are used to discretize the Navier-Stokes equations, the values of variables are stored at the nodes, and the conservation of mass, momentum and energy need to be controlled manually. In contrast, with the finite volume method, if the Navier-Stokes equations are satisfied in every control volume, it will automatically be satisfied for the whole fluid domain. The flux entering a given volume is identical to that leaving the adjacent volumes and for this reason, the finite volume method is a conservative method. Plus, the finite volume is formulated to allow both structured and unstructured meshes. Due to all these benefits, it is preferred and implemented in most CFD codes.

4.2 Mesh generators and CFD codes

Extensive work in numerical methods, along with the exponential growth in computing resources, have led to the development of algorithms to automate the various tasks involved in the CFD process, namely, the mesh generation and the resolution of discrete equations. These algorithms are now implemented in numerical codes, and the latter are available in the form of in-house and commercial codes. Each of these categories features advantages and drawbacks: for instance, in-house CFD codes provide great flexibility in terms of model implementation, and allow therefore to test and to validate newly developed models. However, they are not easy to handle from an industrial standpoint, especially when dealing with complex grids and multi-physics problem, and when considering some programming paradigms requiring advanced knowledge in technical computing such as message parallel interface (MPI) algorithms in parallel computation. This latter aspect is of practical interest since it allows taking the full advantage of the available computing resources. In contrast, commercial CFD codes are often devoid of the models at the cutting edge of research, they offer a relatively little extensibility (i.e. implementation of new models), but they are very convivial. Therefore, commercial CFD codes are being increasingly used to address complex engineering problems. Several mesh generators and CFD codes have so far been proposed by the research community, and they are extensively used in both academic research and industrial applications. For mesh generators in particular, they are two main groups with respect to the type of discretization considered. In finite volume discretization for instance, the most popular mesh generation codes include GAMBIT, ANSYS meshing, ICEM CFD (owned by ANSYS) and STAR-CD+ (owned by CD-Adapco); in finite element discretization CUBIT (owned by SANDIA) and T-grid (owned by ANSYS) are among the most popular. In addition to these commercial mesh generators, several other non-commercial mesh generators are available in various research laboratories. According to the CFD codes used in reactive flow simulations, both in-house and commercial CFD codes are widely used in academic and industrial environments, although the commercial type tends to supplant the former in industry. Among the in-house CFD codes,

some of the most famous include CDP developed by the Center for Integrated Turbulence Simulations (CITS) [1] at Stanford University [CITS], AVBP developed at CERFACS [CERFACS], OpenFOAM [OpenFOAM], the RAPTOR code (owned by SANDIA), the CEDRE code (owned by ONERA) etc. CDP is a CFD code devoted to multiphysics phenomena, and is in gradual improvement with the final goal of full engine simulations. Its current version has the following capabilities: (i) unstructured collocated finite volume discretization of low Mach number variable density Navier-Stokes equations, Lagrangian particle tracking for liquid fuel sprays, a steady flamelet/progress variable combustion model, Dynamics Smagorinsky subgrid scale closures, parallel preprocessing, and particle-mesh load balancing; detailed information regarding the performance of the CDP code can be found on the CITS website [CITS]. AVBP is an unstructured LES code dedicated to complex geometries such as those found in practical applications. It can be used to simulate complex flows such as non-reactive and reactive turbulent compressible multi-phase flows, and can combine the advantages of unstructured and structured grid technologies in terms of meshing flexibility and solution accuracy. As with the CDP code, the AVBP CFD code is used in many bilateral industrial/academic research projects; the latter includes pollutant reduction in both gas turbines and piston engines, fluid/structure interaction in liners, and fuel-staged combustion instabilities. A summary of the extensive performance of this CFD code are provided on the CERFACS website [CERFACS]. The third CFD code, OpenFOAM, is a free open source CFD software developed by OpenCFD Ltd at ESI Group, and distributed by the OpenFOAM foundation [OpenFOAM]. OpenFOAM is used in many areas of engineering and science from both commercial and academic organizations, and it has an extensive range of features to solve various complex flows field involving turbulence, heat and mass transfers, and chemical reactions. A list of other in-house CFD codes used by the research community may be found in [Gicquel et al., 2012]. According to commercial CFD codes, there are also many variants and their reliability may vary from one application to another. For instance, depending on the models implemented and the accuracy of the numerical schemes used to discretize the governing equations, some of them may perform well for gaseous combustion, and feature large discrepancies in spray combustion. Some of the most popular commercial CFD codes used in combustion include CFX, Fluent, and STAR-CD; both CFX and Fluent codes, and the ANSYS mesh generators presented earlier, are currently embedded into a single software package. In the current work, ANSYS FLUENT^{TM} is selected as the CFD code, the choice being partly guided by the needs of the industrial partner of the present study, as well as the extensibility offered by this CFD code with respect to the combustion processes being investigated. The following subsection provides a brief description of the mesh generator, ICEM-CFD, followed by that of the ANSYS FLUENT solvers. The remaining sections of this chapter are mainly concerned with the description of the models applied to simulate each of the configurations presented in the previous chapter. ANSYS FLUENT^{TM} is continually being improved, so all the comments regarding the drawbacks of the implemented models are based on the version used in this work (Version 15.0); it may then be possible to notice some improvements with respect to these drawbacks in future releases.

1. CITS became the Center for Turbulence Research (CTR) after 2005

4.3 An overview of ANSYS ICEM-CFD and geometry meshing

ANSYS ICEM-CFD is a commercial software dedicated to mesh geometries for a wide variety of CFD and FEA codes. For CFD analysis especially, various meshing modules are available and can be used to generate various mesh topologies. These are the Tetra, the Hexa, and the Prism modules. The Tetra mesher is an automated meshing module based on unstructured meshing technology. It works directly from the geometry's surfaces, and operates by filling the volume with tetrahedral elements using the Octree approach. The Tetra mesher is easier to handle, and provides options to automatically refine and/or coarsen the mesh both on geometry's surfaces and within the enclosed volume. Furthermore, other algorithms such as the Delaunay algorithm and the Advancing Front algorithm are available to create tetrahedral elements from an existing surface mesh, and to give a smoother transition in the volume element size. Unlike the Tetra mesher, the Hexa mesher is a semi-automated meshing module that can be used to generate multi-block structured or unstructured hexahedral volume meshes, and requires therefore some expertise since blocks need to be built and iteratively adjusted to the underlying geometry for a good mesh quality. The resulting blocking can be used for other similar geometries for full parametric capabilities. The Prism mesher is available to mesh geometries whose near-wall physics of the flow field are of interest: it consists of inserting layers of prisms near the boundary surface and tetrahedral elements in the remaining computational domain, and can therefore be viewed as an improved version of the Tetra mesher. ICEM-CFD also provides options to build hybrid meshes; the latter can be achieved by merging Tetra and Hexa meshes at their common interfaces through generation of a layer of pyramids at those interfaces. This hybrid mesh strategy allows to deal with complex geometries while taking the full advantage of the structured mesh technology. The other hybrid meshing strategy available in ICEM-CFD is Hexa-core. For this case also, the new mesh is connected to the remainder of Prism/Tetra hybrid through an automatic generation of pyramids. The main advantage of the Hexa-core mesh technology lies in its ability to reduce the number of elements for a quicker solver run time and better convergence. For the first two configurations considered in the current simulations, namely, the swirl-stabilized combustion chamber and the bluff-body stabilized burner, the structured meshing technology is adopted. This choice is partly motivated by the fact that, the two geometries are relatively simple and allow a good geometry blocking. Furthermore, the structured mesh technology is known to help taking the full advantages of the computing algorithm capabilities. However, due to the more complex nature of the geometry involved in the third configuration (i.e. the combustion chamber equipped with liner holes), the unstructured mesh technology is applied. In each case, various mesh resolutions are considered for the purpose of the required mesh sensitivity study, and each of them is built so as to meet the general mesh requirements consisting of smoothing and refining the grid near the solid wall to capture boundary layer effects, and in particular around the orifice of the fuel jet to capture the fuel-air shear layers. The mesh densities investigated in each of the three configurations are summarized in Table 4.1:

Experimental Configuration	Meshing technology	Mesh density
Swirl-stabilized combustor	Structured meshing (hexahedral elements)	0.8 Million
		1.2 Million
		2.16 Million
Bluff-body stabilized burner	Structured meshing (hexahedral elements)	0.7 Million
		1.5 Million
		2.2 Million
		3.2 Million
Scaled can combustor (with liner walls and cooling slots)	Unstructured meshing (tetra and prism elements)	4.5 Million (0.7 M nodes)
		9.5 Million (1.7 M nodes)
		16.5 Million (2.6 M nodes)

Table 4.1: Meshing technology and mesh density for each investigated configuration

4.4 An overview of ANSYS FLUENT^{TM}

ANSYS FLUENT^{TM} is a commercial finite volume-based CFD code consisting of two main solver technologies: a pressure-based solver and a density-based solver. The two solvers can be used for a broad class of flows ranging from incompressible to highly compressible flows. However, one formulation may yield solution more quickly or resolve certain flow features better than the other, depending on the flow configuration. Although the two approaches use the momentum equations to obtain the velocity field, there are some differences in the way of solving the transport equations (continuity, momentum, energies, species, and/or other scalars). For the density-based approach, the continuity equation is used to obtain the density field, while the pressure field is determined from the equation of state. In addition, all the conservative equations are solved simultaneously except for those of turbulence and other scalars which are solved sequentially. In contrast, in the pressure-based approach, the pressure field is extracted by solving a pressure-correction equation (i.e. the equation derived from the continuity and the momentum equations), and the conservative equations (including those of turbulence and other scalars) are solved either simultaneously and/or sequentially depending on the sub-algorithm adopted. In both cases, two formulations are available with respect to the way the coupled equations are linearised: these are the implicit and explicit formulations. The former formulation offers a broader stability and a converged steady-state solution can be obtained faster than with the explicit formulation, although requiring more memory. In the pressure-based solver, there are two ways to achieve pressure-velocity coupling: the segregated and coupled algorithms. In the segregated algorithms, the governing equations are solved sequentially, separated from each other, while in the coupled algorithm, the momentum equations and the pressure-based continuity equation are solved simultaneously with an implicit formulation. The coupled algorithm provides better convergence speed, but the associated memory requirements are larger than those of the segregated algorithms. In the current work, the pressured-based solver is used, and various segregated algorithms are considered to achieve the pressure-velocity coupling. These are the Semi-IMplicit Pressure Link Equations (SIMPLE), the SIMPLE-Consistent (SIMPLEC), and the Pressure-Implicit with Splitting of Operators (PISO).

4.4.1 Discretization in ANSYS FLUENT^{TM}

The discretization of the Navier-Stokes equations and the other transport equations governing reactive flows consists of the temporal discretization of the unsteady terms, and the spatial discretization of the convective and diffusive terms. With respect to these two types of discretization, ANSYS FLUENT provides several discretization schemes of various accuracies, depending on the selected turbulence model. Also, discretization schemes are necessary for the new pressure equation introduced by the pressure-based solver technology. Due to the cell-centered nature of the finite volume technique and thus of the CFD code, all the discretization schemes lead to the values of variables at the cell centers, and such informations are not sufficient to achieve the final solution of the investigated flow field. In addition to the fact that the values of the variables at each point throughout the physical domain need to be known, the calculation of convective terms, and more generally, all the volume integrals containing a divergence term require values of variables at the cell-faces since the integral volumes of divergence terms are converted to surface integrals through the Green-Ostrogradski theorem (also termed the divergence theorem). These cell-face values can be obtained by interpolation using the values of these variables taken at the centers of two adjacent cells. Thus, interpolation schemes are also required, as well as methods for computing all the gradients necessary to determine values of scalars at the cell faces and computing secondary diffusion terms and velocity derivatives.

Spatial discretization schemes

For the pressure, the current version of ANSYS FLUENT^{TM} (V15) provides five different interpolation schemes: these are the standard, the PRessure STaggered Option (PRESTO), the linear, the second order, and the body force weighted interpolation schemes. In the current simulations, both PRESTO and second-order interpolation schemes are used to solve the pressure equation. This choice is mainly due to the complex flow patterns exhibited by the investigated flow field, namely, the swirling motions and the recirculation zones generated by devices such as swirlers and bluff-bodies. According to the density, there are four different interpolation schemes: these are the first-order and the second-order upwind schemes, the power law scheme, the Monotonic Upstream-Centered Scheme for Conservation Laws (MUSCL scheme) which is finite volume-based, and the Quadratic Upstream Interpolation for Convective Kinematics (QUICK) scheme which is a high-order differencing scheme. As the second-order upwind scheme provides stability for the discretization of the pressure-correction equation, it is applied in the current simulations. With respect to the gradient computation, the CFD code provides three approaches: the Green-Gauss Cell-based, the Green-Gauss Node-based and the Least Squares Cell-based approaches. As it can be deduced from the designation of the two first approaches, they are based on the Green-Gauss theorem summarized by the following equation:

$$(\nabla \phi)_{ci} = \frac{1}{V} \sum_{f} \bar{\phi}_f \vec{A}_f \tag{4.1}$$

where ϕ_f is the value of ϕ at the cell face centroid, and the summation is over all the faces enclosing the cell. The ϕ_f is calculated differently in the cell-based and node-based approaches: in the cell-based approach, ϕ_f is calculated as the average of the values at the neighbouring cell centers, ϕ_{ci}

and ϕ_{ci+1} (i.e. $\bar{\phi}_f = (\phi_{ci} + \phi_{ci+1})/2$), while in the node-based approach, the face value is defined as the arithmetic average of the nodal values on the face (i.e. $\bar{\phi}_f = \frac{1}{N_f}\sum_n^{N_f} \bar{\phi}_n$, where N_f is the number of nodes on the face, and $\bar{\phi}_n$ are the nodal values constructed from the weighted average of the cell values surrounding the nodes). The node-based gradient is known to be more accurate than the cell-based gradient particularly on skewed and distorted unstructured meshes. However, it is relatively more expensive to compute than the cell-based gradient scheme. In the least squares cell-based gradient calculation, the solution is assumed to vary linearly so that, the change in cell values between ϕ_{ci} and ϕ_{ci+1} along the vector δr_j from the centroid of cell ci to cell $ci+1$ can be expressed as follows:

$$(\nabla\phi)_{ci}.\Delta r_j = (\phi_{ci} + \phi_{ci+1}) \tag{4.2}$$

On skewed and distorted unstructured meshes, the accuracy of the least-square gradient method is comparable to that of the node-based gradient, and both are much more superior to that of the cell-based approach. Furthermore, the least-square gradient approach is less expensive in computation than the two other approaches. Thus, in the current simulations, the least-squares gradient approach is applied. For the discretization of momentum, energy and other scalar transport equations, the various numerical schemes mentioned earlier can be used (i.e. first-order and second-order upwind schemes, power law, QUICK and third order MUSCL). For turbulence flows in particular, the CFD code provides more elaborated numerical schemes to conduct simulation with advanced turbulence models; these include the Boundary Central Differencing and the Central Differencing Schemes. In all the SAS and LES simulations performed in the current study, these advanced numerical schemes are applied.

Temporal discretization schemes

Temporal discretization involves the integration of every unsteady term in the differential equations governing the fluid flow over a time step δt. Reacting fluid flows may involve a single phase only (e.g. gaseous combustion) or two phases (e.g. spray combustion), and as discussed in the first chapter, Eulerian modelling approach is always used for the gaseous phase, while the liquid phase can be modelled using either Eulerian or Lagrangian approach. The two modelling approaches are available in the CFD code, and especially for the Eulerian modelling approach, first-order and second-order accurate schemes are available for the temporal discretization of the unsteady terms appearing in the gaseous phase equations. The latter can be used under either implicit or explicit time stepping formulation. For most transient phenomena, the explicit formulation is known to be more accurate and less expensive compared to the implicit formulation, but it does not guarantee an unconditional stability with respect to the time step size. As pointed out earlier, the pressure-based solver is used in the current simulations because of the relatively large number of models associated and therefore its applicability to the simulation of a wider range of physical phenomena. The second-order accurate implicit time stepping formulation is retained for the transient terms.

For the Lagrangian analysis of the liquid phase, both low-order and high-order schemes are available to discretize the unsteady terms involved in the spray equations (e.g. droplet position, droplet

velocity, etc.). The low-order schemes includes implicit and analytical schemes, while the high order schemes consist of trapezoidal and Runge-Kutta methods. The preliminary simulations in the present study are first conducted using the trapezoidal method, and subsequently, the Runge-Kutta approach is applied to refine the predictions.

4.4.2 Turbulence models in ANSYS FLUENT^{TM}

Most of the turbulence models discussed in the first chapter are available in the ANSYS FLUENT^{TM}. Several RANS approaches consisting of modelling the turbulent viscosity with the gradient diffusion assumption are also available in the CFD code. These include the one-equation-based RANS (the Spalart-Allmaras model), and RANS models based on two equations such as the classical $k-\varepsilon$ model and all its variants (e.g. the *RNG* $k-\varepsilon$ and *Realizable* $k-\varepsilon$ models), and the standard $k-\omega$ model with its variants (e.g. the *SST* $k-\omega$ and the $k-kl-\omega$ models). The accuracy of each of these RANS approaches is mainly determined by the suitability of the corresponding assumptions to the flow configuration. For instance, as discussed in the first chapter, with its swirl-dominated-flow option, the *RNG* $k-\varepsilon$ is suitable for highly swirling flows, but it does not capture properly phenomena involved in the near wall regions. Thus, for an efficient use of this model, it is often necessary to resort to robust near-wall treatment approaches (e.g. the use of wall functions). On the other side, the modifications incorporated in the $k-\omega$ approach to account for low-Reynolds number effects and shear flow spreading make the $k-\omega$ models suitable for the investigation of phenomena involving shear layers (e.g. fluid-wall interactions). However, in the standard $k-\omega$ model, the solutions are sensitive to the values of k and ω outside the shear layer regions and, consequently, such an approach is not suitable for internal flow simulations. Its variant, the *SST* $k-\omega$ model which is formulated so as to combine the advantages of the standard $k-\omega$ in the near-wall region, and those of the $k-\varepsilon$ in the free stream regions, may realistically predict some internal flows.

As all the RANS approaches based on one or two-equations assume an isotropic eddy-viscosity, they may not capture flow features properly if the flow features are the result of anisotropy in the Reynolds stress. Such anisotropic flow configurations include highly swirling flows in combustion chambers and internal stress-induced secondary flows. For such cases, ANSYS FLUENT^{TM} provides a more elaborate RANS model termed the Reynolds Stress Model (RSM). As described in the first chapter, the RSM model accounts for the effects of streamline curvature, swirl, rotation, and rapid changes in strain rate by solving transport equations for each Reynolds stress term. In some preliminary simulations carried out in this study, both isotropic and anisotropic eddy-viscosity-based RANS models, the *RNG* $k-\varepsilon$ and the *RSM* models, respectively, were tested. Although some improvements were obtained using the *RSM* model, large discrepancies still exist with respect to the experimental data. The results pertaining to the *RSM* model is then not presented in the current thesis to only focus on models providing significant improvements.

In spite of the improvements provided by some advanced RANS approaches as briefly discussed above, it is worth recalling that most practical combustion systems lead to complex flow patterns

in combustion chambers to deliver stable and efficient combustion. In addition, some critical time-dependent phenomena such as pollutant formation, extinction and ignition feature very small time scales. It is then clear that an accurate prediction of such flow patterns and thus the combustion processes involved in the combustion chamber cannot be achieved using RANS approaches. For such phenomena, the CFD code provides advanced turbulence models such as SAS, DES and LES to cope with the limitations of the DNS and RANS approaches in terms of computing resource requirements and accuracy respectively; such advanced turbulence models are used in the current study. Especially, two LES formulations based on two different modelling approaches of the eddy viscosity, the Smagorinsky-Lilly and the WALE models, are adopted.

4.4.3 Two-phase models in ANSYS FLUENT^{TM}

As discussed in the first chapter, there are globally two approaches of modelling two-phase flow: the Euler-Euler and the Euler-Lagrange methods. According to the former approach, ANSYS FLUENT^{TM} provides three different Eulerian models. These are the *Volume of Fluid (VOF)*, the *Mixture* and the *Eulerian* models. The VOF model is a free surface technique that can be used to model two or more immiscible fluids in both steady and unsteady regimes. It consists of solving a continuity equation for the volume fraction of each phase of the fluids throughout the domain, and a single set of momentum equations that depends on the volume fractions of all phases through physical properties such as the density and the viscosity. For the unsteady analysis, both implicit and explicit schemes are available for the temporal discretization. The implicit scheme includes numerical schemes of various accuracies (e.g. QUICK, first order upwind, second order upwind, etc.), while the explicit scheme consists of applying the standard finite-difference interpolation schemes to the volume fraction values computed at the previous time step. Typical applications of the VOF model include the prediction of jet breakup, the steady and transient tracking of any liquid-gas interface, the motion of large bubbles in a liquid, and the motion of liquid after a dam break. However, in the current version of ANSYS FLUENT^{TM} (version 15) and the older versions, these potential capabilities are hampered by some limitations: the VOF model can only be used with the pressure-based solver; the model does not allow for void regions where no fluid of any type is present and thus all control volumes need to be filled with either a single phase or a combination of phases; and some temporal discretization schemes such as the second-order implicit time-stepping formulation cannot be used with the VOF explicit numerical scheme. The *Mixture model* is a simplified multiphase model that can be used as a substitute of the full Eulerian multiphase model in many applications. In fact, the application of the full multiphase model may not be feasible in some situations, for instance, when the multiphase flow involves a wide distribution of the particulate phase or when the interphase laws are unknown or are not proved to be reliable. The *Mixture* model is computationally less expensive than the full multiphase model as a relatively small number of variables is solved. Plus, it allows modelling some more complex multiphase phenomena such as phase interpenetration and the difference in velocity of all phases involved in the multiphase flow. The *Mixture* model solves the continuity, momentum, and energy equations for the mixture, as well as the volume fraction equation for the secondary phases.

If the phases are moving at different velocities, algebraic expressions for the relative density are also considered. Typical applications of the *Mixture* model includes the modelling of multiphase flows where the phases move at different velocities (although a local equilibrium is assumed over a short spatial length scales), homogeneous multiphase flows with very strong coupling and phases moving at the same velocity, and the calculation of non-Newtonian viscosity. The third category of the Eulerian model provided by the current version of ANSYS FLUENT^{TM}, the *Eulerian* model is intended for the modelling of multiphase phases initially separated, but interacting during the flow. The phases can be liquids, gases, or solids in nearly any combination. In the *Eulerian* model, a single pressure is shared by all phases, and the continuity and momentum equations are solved for each phase. In addition to these limitations, the VOF and the two other Eulerian models are not currently compatible with some advanced combustion models implemented in ANSYS FLUENT^{TM} (V 15); these include the Eddy Dissipation Concept in the *Species Transport* model, the *Non-Premixed* model, the *Premixed* model, the *Partially-Premixed* model with all the related sub-models (e.g. *Partial Equilibrium*, *Diffusion Flamelet*, and *Flamelet Generated Manifold*) and the *Composition PDF Transport* model. Furthermore, the two other Eulerian modelling approaches (i.e. the Eulerian and the Mixture models) are not implemented in the LES solver. In addition to these Eulerian modelling approaches for the liquid phase, ANSYS FLUENT^{TM} provides a Lagrangian modelling approach through a module termed *Discrete Phase Model (DPM)*. In this Lagrangian modelling of the liquid phase, a large number of particles (which correspond to droplets in the current study) are tracked individually or in the form of stochastic particles (i.e. particles having neighbouring properties). As discussed in the first chapter, such an approach is appropriate for dilute sprays such as those of the investigated configurations because of a relatively reduced number of droplet trajectories to be calculated. In addition, some spray interaction phenomena such as droplet collision, coalescence and agglomeration can be neglected [Elghobashi, 1994]. Thus, in all simulations including spray combustion, the spray is described in terms of droplet position, velocity, size and thermodynamic state. All the sprays investigated are dilute and are generated by pressure-swirl-atomizers (simplex atomizers). Due to the absence of experimental data for the spray, the detailed characterization of simplex atomizers done by Lefebvre [1989] are used to specify some spray boundary conditions. The effects of convection on each droplet are, however, taken into account as well as the droplet secondary break-up phenomenon. The change in droplet shape is taken into account in the droplet trajectory calculation through the implementation of a dynamic drag coefficient in the drag force expression. In addition to the drag force, the effect of the gravity and that of the temperature gradient are accounted for using the gravitational force and the thermophoretic force, respectively. Although the DPM module can include other spray interaction forces such Brownian and Saffman lift forces, these two forces are neglected in the current simulations because of the droplet sizes involved in the spray ($d_d > 10^{-6}m$). For heat and mass transfer, it is assumed that the heat exchanged between the droplets and the gaseous phase are governed by inert heating, evaporation and droplet boiling. These processes are assumed to be sequential, and are initiated by the vaporization and the boiling temperatures. The infinite liquid-conductivity model is used to model heat and mass transfer caused by convective and diffusive transports. The droplet

surface temperature is thus assumed uniform, time-varying, and equal to the temperature inside the droplet, while both the finite liquid thermal conductivity and the droplet internal recirculation are neglected. The inert heating increases the temperature of the droplets up to the vaporization temperature (i.e. "flash point"); during this step, there is no exchange of mass between gaseous and liquid phases. During the second step, when the droplet temperature exceeds the vaporization temperature, some fuel mass are transferred from the droplet to the gaseous phase. The rates of mass and heat transfer, and the change in droplet temperature are calculated using the set of equations presented in the first chapter.

According to the turbulent dispersion of droplets, two main methods are available for the simulation approaches based on Reynolds averaged equations. These are the *stochastic tracking* and the *particle cloud tracking* methods. The first approach is epitomized by the Discrete Random Walk (DRW) model whereby the turbulent dispersion of particles is obtained by integrating the equations governing the trajectory of each individual particle using the instantaneous fluid velocity which can be decomposed into mean velocity and fluctuating velocity components along the particle path during the integration. In the DRW model, the fluctuating velocity component is a discrete piecewise function that is a constant function of time. By computing the trajectory in this manner for a sufficiently large number of representative particles, the random effects of turbulence on the particle dispersion can be accounted for. In the second approach, the turbulent dispersion of particles about a mean trajectory is calculated using statistical methods: the concentration of particles about the mean trajectory is represented by a Gaussian probability density function (PDF) whose variance is based on the level of particle dispersion due to turbulent fluctuations. The mean trajectory is obtained by solving the ensemble-averaged equations of motions for all particles represented by the cloud. Finally, in all simulations based on the Reynolds averaged approach (URANS and SAS) the turbulent dispersion of droplets are taken into account using the DRW model.

In LES, the approach is different since LES is concerned with the subgrid-scales (SGS) induced by the filtering operation. The dispersion of the spray droplets could be less relevant in the current simulations since the mesh resolution allows capturing at least 85% of the instantaneous carrier phase turbulence level. However, it is worth noting that reports from the literature highlighted the effects of the SGS fluctuations in the prediction of the properties for the dispersed phase. For instance, through an asymptotic analysis, Shotroban et al. [2007] demonstrated that LES may not be able to predict the particle concentration when the effects of SGS fluctuations on particles are neglected in an anisotropic turbulent flow. This result was subsequently supported by Bini and Jones [2008] through a numerical investigation which showed that the SGS dispersion plays a crucial role in determining the spreading and properties of the discrete phase. In the same vein, another investigation conducted by Dianat et al. [2009] showed that the incorporation of a SGS dispersion model tends to improve the predictions of the droplets concentration. The SGS dispersion is more relevant for evaporating droplets which tend, at the end of their life time, to follow the continuous phase and act as tracer particles, by promptly responding to SGS fluctuations. Based on the outcomes of these investigators,

it appears that the SGS-induced dispersion is relevant for the prediction of spray combustion. In all LES-based simulations of spray combustion conducted in this work, the dispersion of droplets are neglected; this first approximation is adopted for simplification purposes.

4.4.4 Combustion models in ANSYS FLUENT^{TM}

Various combustion models are available in ANSYS FLUENT^{TM}. These include the *Species Transport* model, the *composition PDF* model, and the combustion models based on the tabulated chemistry with representative scalars such as the mixture fraction and/or the reaction progress variable. The *Species Transport* model is available through various classical sub-models such as the Laminar Finite-Rate, the Eddy-Dissipation, and through an advanced Eddy-Dissipation model (the Eddy-Dissipation Concept). In spite of the potential capabilities of the Species Transport model, it features some drawbacks in turbulent environment. These drawbacks discussed in the first chapter preclude the application of Species Transport model to practical configurations, especially when dealing with pollutant prediction, as the latter requires implementation of a sophisticated chemistry model. In addition to the requirements in terms of computational costs, it is not obvious to properly model the mean reaction rates and the filtered reaction rates appearing in the RANS and LES formulations of the species transport equations, respectively. Similarly, the implementation of a detailed chemistry model in simulations based on the *composition PDF* model is still computationally expensive although this approach has proven capable of reproducing the structure of spray flow and combustion properties in configurations involving complex flow patterns (e.g. see [Jones et al., 2012]). Due to these limitations and the characteristics of the investigated configurations along with the need to keep the computing resources at a reasonable level, particular attention is given to the tabulated chemistry models. The second group of combustion models implemented in ANSYS FLUENT^{TM}, and based on representative scalars includes the *premixed combustion*, the *partially-premixed combustion* and the *non-premixed combustion* models. The *premixed combustion* model is based on the reaction progress variable and is suitable for configurations involving homogeneous mixtures of fuel and air prior to combustion. As discussed in the first chapter, spray flames belong to the group of non-premixed flames, and more realistically to the group of partially-premixed flames, depending on the fuel atomizer configuration. In the two investigated spray-based configurations, the liquid fuel is supplied by simplex atomizers. Thus, potentially, both non-premixed and partially-premixed combustion models are capable of reasonably predicting the main combustion properties. The difference between the two models is mainly based on the number of representative scalars used to capture the flame structure. In the non-premixed model, all the species transport equations are replaced by a single transport equation for a non-reactive scalar; the latter is conservative for gaseous combustion, and non-conservative for spray combustion because of the mass transfer to the gaseous phase due to spray evaporation. The non-premixed combustion model in ANSYS FLUENT^{TM} can be used either under the infinitely fast chemistry (the full equilibrium and the partial equilibrium approaches) or under the finite-rate chemistry assumption through the steady diffusion flamelet and the unsteady diffusion flamelet models. Similarly, the partially-premixed combustion model allows making the infinitely-fast chemistry as-

sumption through the two above mentioned equilibrium models. In addition to the diffusion flamelet model, the finite-rate chemistry assumption can be achieved through the Flamelet Generated Manifold (FGM) based on both premixed or diffusion flamelet structures. The mixture fraction/progress variable formulation adopted in the FGM model, together with the other assets of FGM as described in the first chapter, makes the partially-premixed combustion model suitable for both homogeneous and spray combustion, especially when dealing with configurations exhibiting high Damköhler numbers, and when predicting species characterized by low reaction rates such as pollutants. Thus, after performing simulation of a spray flame in a swirl-stabilized combustion chamber using a tabulated chemistry based on both partial equilibrium and diffusion flamelet models, the FGM is first applied to the same configuration, and thereafter, to the two other configurations in order to investigate the ignition event and the resulting steady combustion regime. It is worth recalling that the presence of two tracking scalars in the FGM model allows simultaneously capturing changes in equivalence ratio and the flame front propagation.

4.4.5 Turbulence-Chemistry interactions in ANSYS FLUENT^{TM}

When dealing with the tabulated chemistry concept in ANSYS FLUENT^{TM}, the turbulence-chemistry interactions are taken into account by modelling the turbulent fluctuations of the "tracking parameters", namely, the representative scalars (reaction progress variable and mixture fraction), the enthalpy, and the scalar dissipation rate. For the simulations based on both the non-premixed and the partially-premixed combustion models, a joint Probability Density Function (PDF) approach is applied. The joint PDF accounts for the SGS fluctuations (or the turbulent fluctuations in the RANS context) of all the "tracking" scalars, and its shape is presumed as discussed in the first chapter. When performing the pre-integration, some simplifying assumptions are done. First, all the representative scalars are assumed to be statistically independent. This assumption is commonly used in the literature, and allows expressing the joint PDF as a product of independent PDFs corresponding to each of the "tracking" scalars [Oijen and de Goey, 2000, Pierce and Moin, 2004]. Secondly, the SGS fluctuations of the mixture fraction are modelled using a presumed subgrid-PDF. A previous study carried out by Gutheil [2010], and based on a comparison between the Monte-Carlo PDF and the standard beta-PDF, demonstrates that the beta function describes a different PDF shape. The standard beta-PDF, as established by Cook and Riley [1994, 1998], is used as a first approximation for the mixture fraction. For the simulations based on the *non-premixed combustion* model in particular, the delta-PDF shape is used for the enthalpy and the scalar dissipation rate, which physically means that the turbulent fluctuations of the enthalpy and those of the scalar dissipation rate are neglected. According to the simulations based on the *partially-premixed combustion* model, the turbulent fluctuations of the mixture fractions are captured with the beta-PDF as described in the non-premixed case, while those of the progress variables are modelled using two different approaches depending on the assumption done for the reaction rate. Under the infinitely-fast chemistry assumption, the turbulent fluctuations of the progress variables are captured using a bimodal-PDF as described in the Bray-Moss-Libby (BML) model, and when dealing with the finite rate chemistry assumption, they are captured using

the beta-PDF.

4.4.6 Spark-based ignition model in ANSYS FLUENT^{TM}

Previous investigations based on spark-ignition of liquid-fuelled combustors, and especially those of aircraft gas turbines, have shown that successful spark-based ignition consists of three main consecutive steps. These are the flame kernel initiation, its propagation to ignite the nearest regions of the flame kernel and the whole combustion chamber, followed by the global flame stabilization reaching ultimately the stable combustion regime [Herweg and Maly, 1996, Eichenberger and Roberts, 1999, Eisazadeh-Far et al., 2010]. When simulating such an ignition sequence with a particular attention paid to the early stage of the flame kernel growth, the CFD model should be able to capture phenomena featuring small scales comparable to the spark plug gap of the igniter which is generally less than a millimeter [Tan and Reitz, 2006]. A straightforward approach, in this regard, would consist of refining the mesh of the combustion chamber. Although such an approach appears potentially more realistic compared to the other approaches in which the mechanisms governing the early stage of the kernel growth are totally ignored (e.g. [Boileau et al., 2008]), it features some drawbacks such as drastic increases in computing resources requirements, and the non-inclusion of the effects of turbulence on the early stage of the spark kernel growth (unless the DNS is applied, the filter width defined for LES will not allow a full inclusion of the turbulence effects on the early stage of the kernel growth). Because of these two relevant limitations, alternative approaches are necessary. As an attempt to circumvent these limitations, subgrid approaches have so far been proposed to capture the dynamics of the flame kernel initiated by the spark deposition [Tan and Reitz, 2006, Liang and Reitz, 2006, Garcia et al., 2011, Triantafyllidis et al., 2009, Subramanian et al., 2010]. Among these approaches, the discrete particle ignition kernel (DPIK) model seems one of the most robust since it accounts for the spark discharge energy, and for the effects of the flow turbulence on the kernel growth. The robustness of the DPIK model was validated in three different complex configurations based on gaseous combustion, namely, the ignition of an homogeneous charge constant volume vessel, the ignition of an homogeneous charge pancake-shaped-combustion-chamber engine, and finally the homogeneous charge Caterpillar-converted propane-fuelled engine [Tan and Reitz, 2006]. In this approach, the flame kernel location is marked by particles, while the flame surface density is obtained from the number density of particles in each computational cell. Thus, the flame kernel growth can still be accurately tracked although the flame kernel features scales that are generally smaller than the computational size. In the present work, the DPIK model, in its original form, is first validated on another complex configuration: a bluff-body stabilized burner. Subsequently, the model is slightly modified and adapted to the liquid fuel under investigation. The modification consists of implementing a correlation for the kerosene laminar flame speed as a function of temperature, pressure and equivalence ratio. The modified DPIK model relies on the same basic assumptions as the original version: (i) the phenomena involved in the pre-breakdown and the breakdown phases are neglected, and only those involved in the arc and glow discharge phases are accounted for; (ii) the kernel flame structure is not resolved, and the temperature and all reactive scalars jump from their values in the unburned mixture to the

corresponding equilibrium values in the burned gas; (iii) the ignition kernel surface is assumed to be located just in front of the flame so that the heat transfer between the kernel and the unburned gas is negligible; (iv) the pressure is uniform inside and outside the ignition kernel, and the temperature inside the kernel is uniform. In addition, as a first approximation, the effects of the droplet dynamics on the spark kernel are also neglected during the arc and the glow discharge phases. By expressing the increase in flame kernel mass (i.e. the ignition kernel mass burning rate) for a spherical-shape ignition kernel using an effective kernel growth speed, S_{eff}, defined as the sum of turbulent flame speed, S_{TFS}, and the plasma velocity, S_{plasma}, the following equation is derived to describe the volume expansion of the ignition kernel. The step-by-step derivation of the model can be found in [Tan and Reitz, 2006]:

$$\frac{dr_k}{dt} = \frac{\rho_u}{\rho_k}\left(S_{TFS} + S_{plasma}\right) + \frac{V_k}{A_k}\left(\frac{1}{T_k}\frac{dT_k}{dt} - \frac{1}{p}\frac{dp}{dt}\right) \tag{4.3}$$

where ρ_u is the unburnt gas velocity, A_k and V_k are respectively the surface area and the volume of the ignition kernel, ρ_k is the gas density, and subscript k refers to the kernel. To reduce the model's complexity, additional assumptions are made: the pressure increase due to combustion is neglected; the temperature inside the kernel is assumed to be spatially uniform and equal to the adiabatic flame temperature of the air-fuel mixture; and the plasma contribution in the kernel growth speed is neglected. The second assumption is realistic because of the short duration of the breakdown phase (a few nanoseconds) compared to both arc and glow discharge phases which last longer (of the order of milliseconds). However, considering the outcomes of many investigators [Thiele et al., 2000, Ferguson and Kirkpatrick, 2000], it is clear that the plasma phase is present in all the three consecutive steps of a spark-based ignition sequence. Thus, the negligible plasma velocity assumption is theoretically expected to affect the prediction of the ignition kernel development, but this effect is mitigated by the deceleration experienced by the flow due to the presence of droplets. Such deceleration effects of the droplets on the flame speed were elucidated by Neophytou et al. [2011]. Considering the fact that the ignition kernel size in the early stage of the ignition sequence (i.e. flame kernel formation and its initial growth) is typically small compared to the turbulent integral length, the ignition flame kernel is only sensitive to the small turbulent scales. Therefore, to properly model the spark kernel expansion, the effects of the small scales of turbulence must be taken into account. In this vein, Herweg and Maly [1996] have proposed a model for the turbulent flame speed, S_{TFS}, to include the effects of the strain on the kernel development. This model was included in the DPIK model, and is mathematically represented by the following equation:

$$\frac{S_{TFS}}{S_L} = I_0 + {I_0}^{1/2}\left(\frac{u^{'}}{u^{'}+S_L}\right)^{1/2}\left(1-exp(\frac{r_k}{l})\right)^{1/2}\left[1-exp(-\frac{t}{T_{0G}})\right]^{1/2}\left(\frac{u^{'}}{S_L}\right)^{5/6} \tag{4.4}$$

where S_L is the laminar burning velocity of the kerosene surrogate; $u^{'}$ is the turbulence intensity, l is the turbulence integral length scale; T_{0G} is a characteristic time scale defined by $T_{0G} = l/(u^{'}+S_L)$, and I_0 is the stretch factor that allows accounting for the effects of strain on the flame kernel development. The stretch factor is expressed as follows:

$$I_0 = 1 - \left(\frac{l_F}{15l}\right)^{(1/2)}\left(\frac{u^{'}}{S_L}\right)^{(3/2)} - 2\frac{l_F}{r_k}\frac{\rho_u}{\rho_k} \tag{4.5}$$

where l_F is the thickness of laminar flame which is calculated using the transport properties and the laminar burning velocity: $l_F = (\lambda/c_p)_0/(\rho S_L^0)$. The heat conductivity, λ, and the heat capacity, c_p, are determined at the inner layer temperature, while the density and the laminar burning velocity are evaluated in the unburned region. The laminar burning velocity S_L is calculated using the following correlation derived by Metghalchi and Keck [1982]:

$$S_L = [s_1 - s_2(\Phi - s_3)^2]\left(\frac{T}{298}\right)^{(\alpha_1-\alpha_2(\Phi-1))} \times \left(\frac{p_k}{101.3}\right)^{(-\beta_1-\beta_2(\Phi-1)} (1-2.1R) \tag{4.6}$$

where R is the residual gas fraction. This burning velocity modelling approach is more realistic as it accounts for variations of the equivalence ratio, Φ, burnt gas pressure, p_k, and the local unburned temperature, T, effects. The quantities s_1, s_2, s_3, α_1, α_2, β_1 and β_2 are the model parameters which are empirically determined. Although experimental investigations by Hui and Sung [2013] have shown some slight differences between the laminar flame speed for kerosene and those of its major components named in the second chapter (i.e. n-paraffins, iso-paraffins, cycloparaffins, and alkylbenzenes), a correlation for the laminar flame speed of an iso-paraffin, namely, that of iso-octane, is used as a rough approximation. The choice is mainly guided by the fact that the correlation was validated for a wide range of pressure (0.5-40 atm) and temperature (298-700 K) with a 10% uncertainty (see [Metghalchi and Keck, 1982]). Further, a review paper by Bergthorson and Thomson [2015] and earlier investigations by Munzar et al. [2013b,a] show that the flame speeds and combustion dependence of the Jet A-1 components are not so different. Although experimental data for the laminar flame speeds of Jet A-1 along with those of its major components have so far been published in the literature, it is worth noting that these data are generally recorded under restricted operating conditions which do not cover the range of operating conditions that engines may experience. For the CFD code releases older than version 15.0, the implementation of this correlation can be achieved through a User Defined Function (UDF).

At each time step, the kernel size is calculated using the DPIK model, and compared to a critical radius, r_{kc}, which is related to the integral turbulent length scale, l. Once the size of the ignition kernel reaches this critical radius (i.e. $r_k \geq r_{kc}$), the ignition model switches to the combustion model described in the previous section.

4.5 Boundary conditions and computational setup

4.5.1 Boundary conditions

Highly-swirl stabilized combustor

For the air inflow, top-hat profiles based on the experimental equivalence ratio and swirl number are imposed for the axial and tangential air velocity components. The turbulent inlet conditions are specified through the hydraulic diameter and the turbulent intensity; the latter being estimated by using a correlation for a fully developed pipe flow at the core, $I = 0.16(Re_{D_H})^{(-1/8)}$, where Re_{D_H}

is the Reynolds number based on the hydraulic diameter, D_H. Impermeability and no-slip boundary conditions are applied for the velocity at the walls of the combustion chamber. The values of the velocity components at the combustor inlet, and the corresponding equivalence ratio, are summarized in Table 4.2:

Axial velocity (m/s)	Tangential velocity (m/s)	Swirl number (S)	Air temperature (K)	Air-to-Fuel ratio	Global equivalence ratio (Φ)	Reynolds number (Re)
19.2	17.5	0.91	300	27.88	0.53	≈ 21350

Table 4.2: Boundary conditions: velocity components and equivalence ratio

The pressure-swirl atomization of the fuel is simulated using a hollow cone-type injection model. The resulting droplet size distribution is assumed to follow the classical Rosin-Rammler correlation: the mass fraction of droplets of diameter greater than d, $f(d)$ is defined by $f(d) = exp[-(d/d_m)^n]$, where n and d_m are the spread parameter and the mean diameter of droplets, respectively. Due to the lack of data on the spray characteristics, a parametric investigation is first conducted based on the features of a "Simplex" atomizer as described in [Lefebvre, 1989]. This parametric study is conducted in both URANS and SAS simulations of the steady combustion regime, and is used to calibrate the injection model through the determination of suitable parameters for the Rosin-Rammler correlation (i.e. mean diameter, d_m and spread parameter, n) and the spray cone angle, α. The secondary droplet breakup is taken into account using the classical Taylor Analogy Break-up (TAB) model, while the droplet turbulent dispersion is accounted for in URANS and SAS simulations using a statistical approach, namely, the Discrete Random Walk (DRK) model. However, for the LES simulations, the effects of the SGS fluctuations on the droplet dispersion are neglected in a first approximation since the mesh resolution allows capturing at least 85% of the turbulence spectrum. According to the droplet-wall interaction, it is assumed that droplets rebound off the walls with a change in their momentum, and the resulting change of momentum is quantified by a restitution coefficient as described in [Tabakoff and Wakeman, 1982]. The spray parameters tested and those retained for the subsequent simulations are reported in Table 4.3, while a sample of the fuel distribution corresponding to these selected spray parameters is shown in Figure 4.2 through some spray features such as droplet mass, droplet diameter, and droplet Weber number. It is worth mentioning that on these pictures, the droplet density is significantly decreased, while the droplet sizes are increased to improve the visibility. Particularly, it can be noticed that, as a result of the secondary break-up and droplet evaporation, droplet diameters and droplet mass decrease with increasing distance from the injector exit. The remaining parameters essential to the injection model, are provided by the experimental measurements and are summarized in the section devoted to the experimental configuration.

Set of parameters tested/ Spray parameters	Cone angle (α)	Mean droplet diameter (d_m)	Spread parameter (n)
Set of spray cone angles	$\alpha \in \{70^o; 80^o; 90^o\}$	$d_m = 60\mu m$	$n = 10$
Set of mean droplet sizes	$\alpha = 80^o$	$d_m \in \{40\mu m; 50\mu m; 70\mu m\}$	$n = 10$
Set of spread parameters	$\alpha = 80^o$	$d_m = 50\mu m$	$n = \{3.5; 10\}$
Spray parameters retained	$\alpha = 80^o$	$d_m = 50\mu m$	$n = 3.5$

Table 4.3: Spray parameters investigated to calibrate the injection model

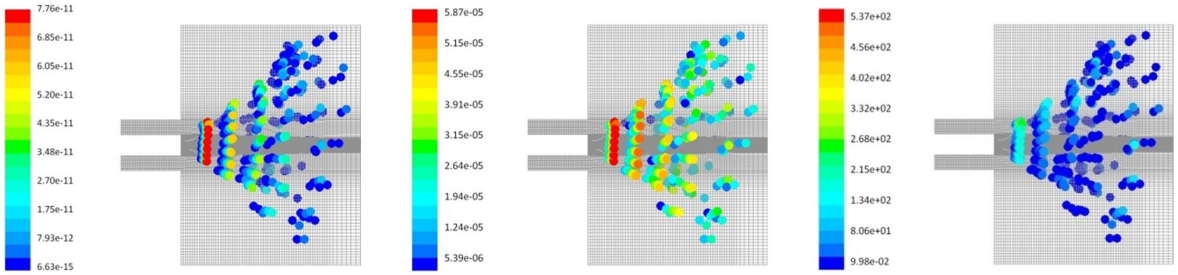

(a) Droplet mass (b) Droplet diameter (c) Droplet Weber number

Figure 4.2: Spray distribution for the selected spray parameters

Chemistry tabulation based on the partial equilibrium model:

As a first approximation, the steady combustion regime in the swirl-stabilized combustor was simulated using a partial equilibrium approach. This approach, denoted as EQ for sake of brevity, is preferred over the full equilibrium approach for the reasons discussed in the first chapter. The entire range of the mixture fraction is divided into two parts using a cut-off value of the mixture fraction (i.e. a rich limit, Z_{limit}), thereafter, chemical equilibrium calculations are performed over a restricted range of Z ($Z \in [0, Z_{limit}]$) while the remaining range is treated with mixing calculations. Physically, this means that in the remaining range, the combustion reaction is extinguished and that unburned fuel coexists with reacted material. In such fuel-rich zones, the composition at a given value of the mixture fraction is computed from the composition at the limiting mixture fraction (set here as $Z_{limit} \sim 1.3 Z_{stoichiometric}$) and that corresponding to the fuel inlet stream ($Z = 1$) based on a known stoichiometry. However, as stated previously, in practical combustion systems where flame stretching and/or flame wrinkling are relevant, the assumption of local chemical equilibrium may lead to unrealistic results. Among these cases one can denote the modelling of the rich side of hydrocarbon flames, the prediction of the intermediate species that governs the NOx formation, the prediction of some species characterized by low reaction rate (e.g. CO and other pollutants), and the modelling of lift-off and blow-off phenomena in jet flames. For an accurate simulation of such phenomena, chemical non-equilibrium effects need to be properly accounted for. As a first attempt in this regard, two other tabulated chemistry approaches are subsequently used; these are the classical diffusion flamelet and the FGM models.

Chemistry tabulation based on the diffusion flamelet model:

Theoretically, although some spray flames may be viewed in some extent as non-premixed flames depending on the atomizer configuration, it is relevant mentioning that tabulated chemistry based on the gaseous diffusion flamelets is suited for some spray combustion configurations because of the droplet evaporation and the subsequent premixing of the resulting fuel vapour with air. In the current simulations, the adoption of this approach as a rough approximation, is motivated by the spray characteristics, and an earlier investigation by Hollmann and Gutheil [1998] comparing the performance of two tabulation strategies, namely, a tabulation based on gaseous diffusion flamelets and a tabulation based on spray flamelets which allows accounting for the effects of the spray on the flame structure. The outcomes of this study show that the two tabulation methods lead to results almost identical except in the cold zone around the injector exit where the tabulation based on gaseous diffusion flamelets needs a cut-off temperature to predict the low temperature region (around the injector exit). For dilute sprays with relatively small droplet sizes like those of the current investigation, the effect of these cold zones is likely to be mitigated. For this first tabulation method, one and two-component fuels are used as Jet A-1 surrogates. Their oxidation mechanism is described by a reduced chemical model consisting of 1 024 reactions among 139 species, derived from the detailed model, JetSurF 2.0, by applying the alternate species elimination (ASE) method as described in Chapter 2. After verifying the ability of the reduced model to reproduce the prediction of combustion properties by the detailed version (DCKM), the reduced model (RCKM) is used to solve the flamelet equations. In addition to the extensive validation reported in the second chapter, an example of validation for the reduced model with respect to the prediction of the structure of a diffusion flame is shown in Figure 4.3.

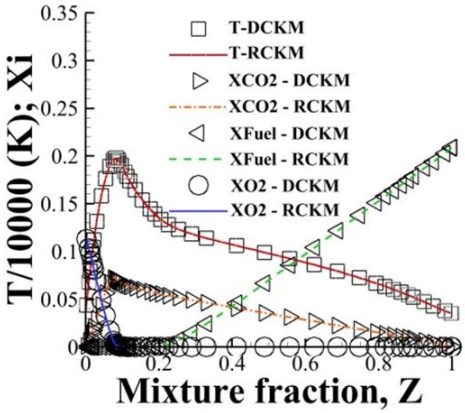

Figure 4.3: A sample of validation of the reduced chemical kinetic model (RCKM)

The flamelet solutions for both one and two-component surrogate fuels are generated over the entire range of the flow conditions, the latter being captured by turbulent strain due to fuel-air mix-

ing. The turbulent strain is quantified by the scalar dissipation rate (χ), and allows measuring the degree of departure from the equilibrium. Samples of the flamelet solutions corresponding to some selected values of the scalar dissipation rates, along with the corresponding S-shaped curve, are shown in Figure 4.4. It is seen that, due to chemical non-equilibrium effects caused by turbulent strain (e.g.

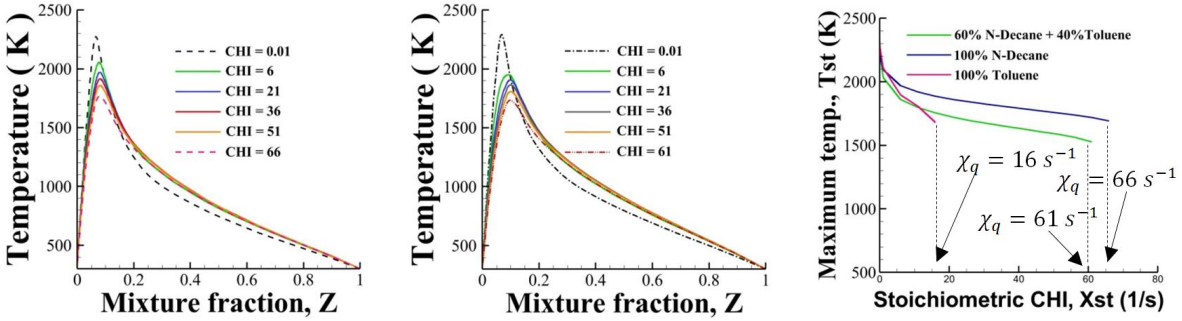

(a) Pure n-decane (b) n-decane + toluene (c) S-shaped curves

Figure 4.4: Flamelet solutions and the corresponding S-shaped curves

flame stretching), the maximum temperature decreases progressively from the near-equilibrium state corresponding here to $\chi = 0.01s^{-1}$, towards the quenching state (i.e. $\chi = \chi_q$), passing through intermediate states that feature finite rate chemistry with low and high strain rates. On the S-shaped curve corresponding to each surrogate fuel, only the upper branch is reproduced because of the restrictiveness of the solution space under the steady state assumption. One can notice that the quenching limit of the two-component Jet A-1 surrogate lies between toluene and n-decane (i.e. $\chi_{q_{N-decane}} > \chi_{q_{N-decane+toluene}} > \chi_{q_{Toluene}}$); such a trend may be explained by their difference in reactivity.

Chemistry tabulation based on the FGM model:

In spite of the ability of the diffusion flamelet model to capture moderate chemical non-equilibrium effects, it does not allow realistic prediction of some combustion properties even when dealing with gaseous combustion. These drawbacks are partly related to the restrictiveness of the solution space, which originates from the steady state assumption generally applied to the model. With this assumption, the steady diffusion processes are assumed to be balanced by the steady chemical reactions, which is not always valid in practice. Even with the relaxation of this assumption, the diffusion flamelet model still features some drawbacks with respect to the selection of the proper state of flamelet solutions. In fact, the S-shaped curve describing the complete flamelet solution space consists of three branches: an upper branch representing the steady burning regime, a middle branch corresponding the an unstable regime (i.e. alternate burning and extinguished regimes), and a lower branch also knows as mixing branch, which corresponds to the extinguished regime. As these branches overlap for some ranges of the scalar dissipation rate (or Damköhler number), it is obvious that there is a need of a parameter to properly identify the suitable branch and thus the exact state of each flamelet solution. Furthermore, as discussed in the first chapter, the single burning regime exhibited by the

diffusion flamelet model does not allow capturing multi-burning regimes occurring in spray flames. Especially, when simulating some transient phenomena such as ignition sequences (e.g. cold start or altitude relight), there is a need of a scalar to track the flame front propagation. Thus, as a first attempt to cope with all these issues, a mixture fraction-progress variable formulation, in the line of the FGM is subsequently applied to the same configuration with the aim of predicting both the transient and the steady combustion regimes. As the FGM used for this configuration is based on diffusion flamelets, the classical diffusion flamelet equations are solved, and the flamelet species reaction fields are converted to the reaction progress variable, Y_C. As the strain rate increases, the flamelet chemistry departs further from the chemical equilibrium, and the progress variable decreases from the unity (value at the equilibrium state) towards its extinction value, Y_{C_q}. The FGM between Y_{C_q}, and the unburnt state, $Y_C = 0$, is determined from the thermochemical state of the final extinguishing flamelet by switching to unsteady flamelets. To capture the early stage of the ignition, each of these chemistry tabulation approaches is coupled to the ignition model described earlier. A sample of the FGM solutions is shown in Figure 4.5:

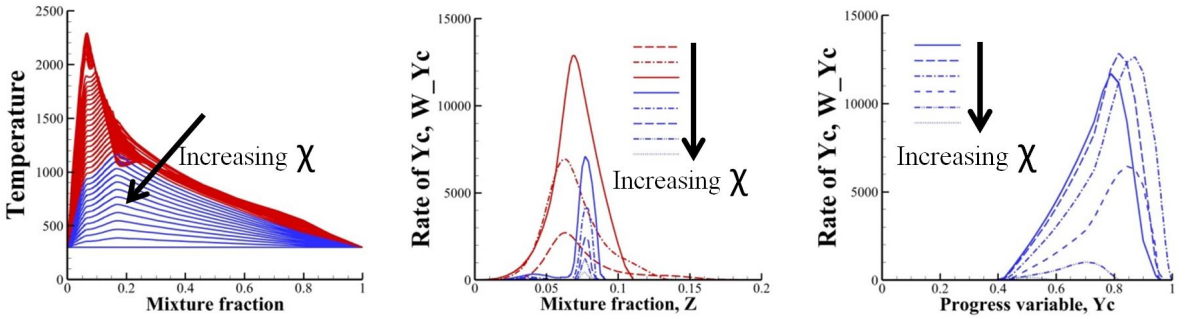

(a) FGM solutions

(b) Reaction rates around the stoichiometric mixture fraction (Z_{st})

(c) Reaction rates between the equilibrium ($Y_C = 1$) and the extinction limit ($Y_C = 0.4$)

Figure 4.5: Structure of the Diffusion-FGM solutions (for Jet A-1)

Figure 4.5 (a), presents the FGM structure with a progressive evolution of the burning regime (red curves) towards the extinguished regime (blue curves) as the scalar dissipation rate increases. Figure 4.5 (b), showing the range of values of the reaction rate, allows noticing the intensity of chemical reactions around the stoichiometry. The effects of the strain rate are also noticeable; the maximum reaction rate is significantly reduced by large strain rates, while the sensitivity of the reaction rate to the change in mixture fraction is significantly increased. This latter result is obtained by contrasting the slopes of the red curves and those of the blue curves in Figure 4.5 (b). Finally, in Figure 4.5 (c), it can be seen that chemical reactions occur in the region bounded by $Y_C = 1$ (i.e. equilibrium) and $Y_C = 0.4$, the latter being the extinction limit of the reaction progress variable.

Bluff-body stabilized burner

Top-hat profiles based on the experimental bulk air velocity are imposed for axial and radial air

velocity components. The oscillations that may arise from this approach are mitigated by carefully setting the under-relaxation parameters. The turbulent inlet conditions are specified through the turbulent intensity and the hydraulic diameter of the annular duct, D_H. The turbulence intensity is estimated by using a correlation for a fully developed pipe flow at the core ($I = 0.16(Re_{D_H})^{(-1/8)}$) where Re_{D_H} is the Reynolds number based on D_H. Impermeability and no-slip boundary conditions are applied at the walls bounding the flame zone. Due to the fact that the experimental value of the fuel velocity was measured at the exit of the circular gap which is located 2 mm just before the burner exit, a substantial part of the upstream geometry (50 mm in length) is considered, along with the flame zone as reported in the previous chapter. This approach is adopted to capture the partial premixing of the fuel with air in its early stage prior to combustion. The axial and radial air velocities at the inlet of the burner are selected in such a way to match the experimental values for the equivalence ratio. To this end, several values are tested, and the most promising results are obtained by imposing top-hat profiles of 6 m/s for both axial and radial velocities at this cross section of the burner inlet, which is located 50 mm upstream. According to the spark parameters, the three different scenarios mentioned previously are considered. As for the previous configuration, a combustion model based on both infinitely fast chemistry, namely, the classical BML model, and another combustion model based on the finite rate chemistry assumption through the FGM model are subsequently used. When applying the classical BML model, the chemistry tabulation is based on the equilibrium approach. For the FGM-based simulations, two different tabulation approaches are adopted: a tabulation based on premixed flamelets and another tabulation based on diffusion flamelets. In each case, the flamelet solutions are generated by solving the premixed-FGM and the diffusion-FGM equations. For this purpose, the reaction mechanism describing the combustion kinetics and the corresponding thermodynamic data for the fuel under investigation are used to calculate the reaction rate of each species, while models for the mixture fraction and the progress variable scalar dissipation rates are used to close the flamelet equations as discussed earlier. When parameterizing the FGM using laminar premixed flamelets, the latter is generated over a range of mixture fractions using 64 points to discretize each dimension of the mixture fraction-progress variable space (Z, Y_C). For the FGM based on diffusion flamelets, steady diffusion flamelets are first generated over a range of scalar dissipation rates, first by starting from a condition featuring nearly zero-straining due to fuel-air mixing (i.e.$\chi_Z = 0.01s^{-1}$), and next by increasing this value in increments of ($2s^{-1}$) until the condition for which the flamelet extinguishes because of an excessive straining (i.e. $\chi_Z = \chi_q$). The diffusion FGM solutions are thereafter deduced from the diffusion laminar flamelets as described above. A sample of the structure of each type of the FGM solutions generated at the same conditions is shown in Figure 4.6 and Figure 4.7. As the fuel burned in the burner is methane having a 99.96% purity [Ahmed, 2007b], the GRI 3.0 mechanism is used to generate these flamelet solutions. One can see that for the two FGM tabulation approaches, chemical reactions are hampered with an increase in scalar dissipation rate, χ.

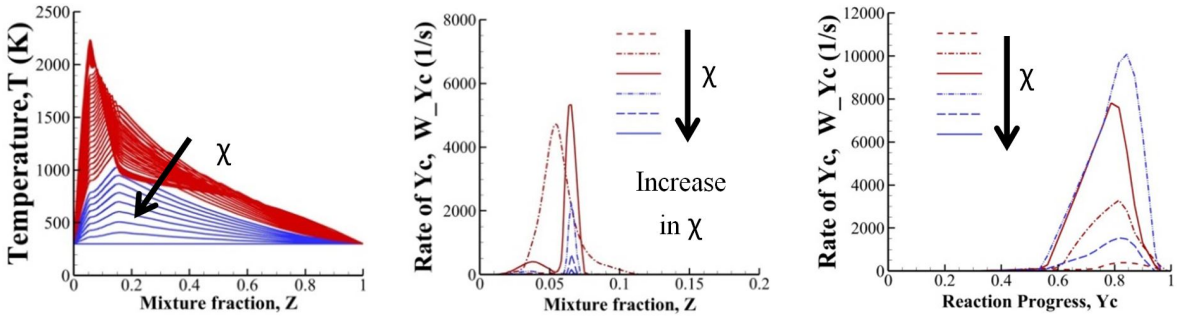

(a) FGM solutions (b) Reaction rates (c) Reaction rates

Figure 4.6: Structure of the Diffusion-FGM solutions (for methane)

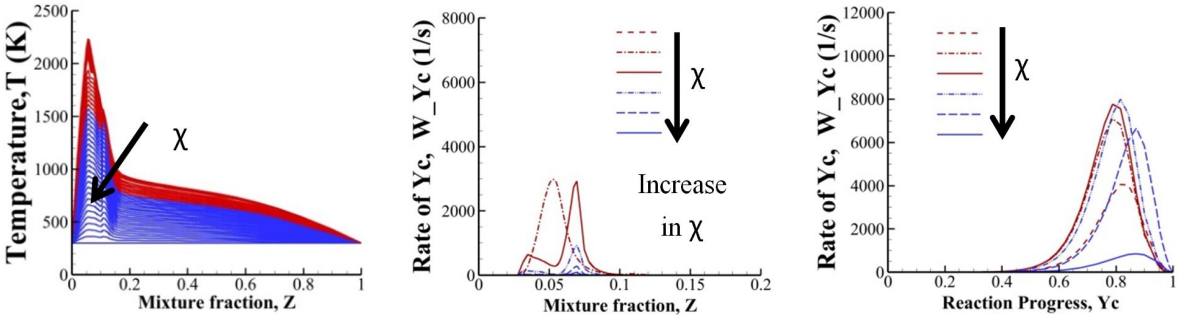

(a) FGM solutions (b) Reaction rates (c) Reaction rates

Figure 4.7: Structure of the Premixed-FGM solutions (for methane)

Scaled can combustor with liner holes

As mentioned earlier, the CFD model formulated to capture the ignition event is extended to spray combustion. The model is first applied to the highly swirl-stabilized combustion chamber to predict the ignition sequence and the combustion properties in the steady combustion regime. Thereafter, the model is applied to the P&WC scaled can combustor with two injector configurations: the simplex and duplex atomizers. For the simplex atomizer, simulations are conducted for twenty different operating conditions of cold start and altitude relight. According to the duplex nozzle, only one test condition is

simulated though detailed experiments were also conducted for this nozzle. This restriction is mainly related to the fact that, all the tests based on the duplex nozzle were conducted assuming a fuel supply through one orifice only, the ultimate goal of using that second atomizer being the investigation of the effect of the injector flow number on ignition properties. Although the experimental results with the simplex nozzle are based on one orifice only, they can provide information regarding the effect of the injector Flow number on the ignition performance. The simulation based on the duplex nozzle is mainly devoted to provide a qualitative validation of the CFD model with respect to the prediction of the whole ignition sequence, by using the high speed infrared camera images of the ignition event. The test conditions considered are summarized in Table 4.4 and Table 4.5.

Injection system	Operating conditions				
	ID.T.	Air mass flow rate $W_3(g/s)$	total pressure drop $(\Delta P_{3-4})/P_3(\%)$	FAR	Air temperature $T_3(K)$
duplex nozzle	A	37.23	0.25	1.23	283
	B	25.15	1.81	0.47	233

Table 4.4: Cold start test conditions with the duplex nozzle; ID.T is the identification of the test condition. FAR stands for Fuel-to-Air Ratio

Injection system	Operating conditions				
	ID.T.	Air mass flow rate $W_3(g/s)$	total pressure drop $(\Delta P_{3-4})/P_3(\%)$	FAR	Air temperature $T_3(K)$
Simplex nozzle: for the test conditions $T_3 = 283K$ and $T_3 = 233K$	A	22.95	0.53	0.04	283
	B	22.95	0.53	0.02	283
	C	32.19	1.68	0.06	283
	D	32.19	1.68	0.12	283
	E	41.87	2.53	0.04	283
	F	42.85	1.91	0.061	233
	G	23.52	0.66	0.061	233
	H	23.52	0.66	0.10	233
	I	23.52	0.66	0.08	233
	J	32.27	1.02	0.057	233

Table 4.5: Cold start test conditions with the simplex nozzle; ID.T is the identification of the test condition.

The majority of the test conditions simulated and reported in Table 4.5, are selected on the experimental ignition envelope, while the remaining conditions are selected outside the experimental ignition limits. This choice allows assessing the ability of the CFD model to predict conditions propitious to successful and unsuccessful cold starts. In addition to the operating temperature, T_3, the conditions considered for the cold start tests and simulations differ in terms of the total pressure drop, ΔP_{3-4}; air mass flow rate, $\dot{m}_{Air}$; and Fuel-to-Air Ratio (FAR).

For the altitude relight simulations, two operating altitudes are considered as shown in Table 4.6:

35 kft and 15 kft. For these two flight altitudes eleven operating conditions are simulated with respect to five conditions for the altitude of 15 kft, and six operating conditions for the altitude of 35 kft. As done for the cold start simulations, the conditions simulated are selected on the experimental ignition envelope and outside the corresponding experimental ignition limits. In addition to the operating altitude, H_{al}, the test conditions considered differ in terms of the air pressure, P_3; the air temperature, T_3; and the total pressure drop across the combustion chamber.

In both cold start and altitude relight simulations, the conditions are selected so as to investigate the effect of certain operating parameters on the ignition success. These parameters include the equivalence ratio, the operating temperature, and the operating pressure, the total pressure drop across the combustion chamber. The outcomes of the investigation are thereafter discussed by contrasting the latter with the empirical correlation established in the literature with respect to the effect of the operating pressure, temperature, equivalence ratio on the ignition timing.

Injection system	Operating conditions				
	ID.T	Air mass flow rate $W_3(g/s)$	total pressure drop $(\Delta P_{3-4})/P_3(\%)$	FAR	Altitude $H_{al}(kft)$
simplex nozzle: for the operating altitudes $H_{al} = 15kft$ and $H_{al} = 35kft$	A	23.52	0.94 ($P_3 = 67964Pa$)	0.14	15 ($T_3 = 271K$)
	B	23.52	($P_3 = 101325Pa$)	0.14	15 ($T_3 = 271K$)
	C	23.52	0.98 ($P_3 = 67964Pa$)	0.10	15 ($T_3 = 271K$)
	D	24.03	1.08 ($P_3 = 67964Pa$)	0.061	15 ($T_3 = 271K$)
	E	20.96	0.89 ($P_3 = 67964Pa$)	0.037	15 ($T_3 = 271K$)
	F	8.36	0.37 ($P_3 = 34630Pa$)	0.069	35 ($T_3 = 245K$)
	G	24.82	($P_3 = 101325Pa$)	0.05	35 ($T_3 = 245K$)
	H	11.66	0.44 ($P_3 = 101325Pa$)	0.02	35 ($T_3 = 245K$)
	I	8.36	0.37 ($P_3 = 34630Pa$)	0.095	35 ($T_3 = 245K$)
	J	11.66	0.44 ($P_3 = 101325Pa$)	0.078	35 ($T_3 = 245K$)
	K	24.0	0.49($P_3 = 101325Pa$)	0.05	35 ($T_3 = 245K$)

Table 4.6: Altitude relight test conditions with the simplex nozzle

4.5.2 Computational setup

Configurations based on the gaseous flame: Bluff-body stabilized burner

As mentioned so far, the use of the bluff-body stabilized burner is essentially devoted to the calibration of the ignition model, considering all the assets the configuration provides from a fundamental investigation point of view. As the investigated flow is turbulent, inertial phenomena dominate diffusive phenomena. Thus, a time scale based on a representative convective time scale is used to define the simulation time step. The outer radius of the annular duct is selected as the reference length ($L_{REF} = D_s/2$), while the air bulk velocity is used as a reference velocity ($U_{REF} = U_{air}$). These two parameters are used to define a reference time scale, $t_{REF} = L_{REF}/U_{REF} = D_s/(2U_{air})$, and based on this reference time scale, the time step of the simulation is thereafter defined as $\Delta t = 0.003 t_{REF}$ (i.e.

$\Delta t = 10^{-5}$s). The simulations are performed in two distinct stages: the first stage is based on air flow only with no fuel injection, and is mainly devoted to the mesh sensitivity study, while allowing the prediction of velocity profiles which are validated with experimental data since the latter were recorded using the air flow only [Ahmed, 2007b, Ahmed et al., 2007]. The second simulation stage is based on the flow of a methane-air mixture, and is conducted to retrieve the mixture fraction distribution within the combustion zone. In both cases, the simulations are initialized with a constant field for air and fuel, and are first performed over a time period equal to 10 000 time steps (i.e. $\sim 125 t_{REF}$), which is approximately equal to 12 times the characteristic computational time (i.e. the time used by the flow to cross the computational domain in the stream direction with the velocity equal to the bulk velocity). This first step of the simulation conducted over 10 000 time steps is devoted to eliminate the adverse effects of flow initialization, and to obtain an initial flow evolving naturally from the initialization with the imposed boundary conditions. Subsequently, for the cold flow investigation, the simulations are continued for 10 000 more time steps in sampling statistics mode, and this additional number of time steps is deemed sufficient to yield the statistical convergence. For the reactive flow study, the simulations are also continued for 10 000 additional time steps but after injecting fuel radially into the annular co-flowing air. As for the cold flow simulations, this additional number of time steps is necessary to eliminate the artificial influence of the fuel stream initialization. At the end of this simulation stage, simulations are continued for 10 000 further time step under the sampling statistics mode to collect mean value of the mixture fraction and the corresponding fluctuations. Once a reasonable field of mixture fraction is obtained, the ignition model is paired with a combustion model, and applied to investigate the ignition, with a particular attention paid to the effect of spark location on the ignition event.

Configurations based on spray flames: Scaled can combustion chambers

As in the previous configuration, the investigated two-phase reactive flows are turbulent. Because every droplet features its own time scale, a time scale based on both a representative convection time scale and a representative droplet residence time are used to define the simulation time step. For instance, when simulating the highly-swirl stabilized spray flame, the outer diameter of the annular duct is selected as reference length, $L_{REF} = R$, while the air bulk velocity is chosen as a reference velocity, $U_{REF} = U_{air}$. These two parameters are used to define a reference time, $t_{REF} = L_{REF}/U_{REF} = R/U_{air}$. Based on a representative droplet residence time and ignition-based characteristic time scales, the time step of the LES simulations is thereafter defined as $\Delta t = 0.1 t_{REF}$; such a definition based on parameters that are homologous to those cited above, is also adopted for the scaled can combustor involving liner holes. In each case, the cold flow simulation is started with an initialized field, and is first performed over a time period equal to 1 500 time steps, which is approximately equal to 6 times the characteristic computation time defined earlier. The cold flow simulation is conducted with respect to two intermediate steps, namely, the unsteady non-reacting flow simulation without coupling with the liquid phase until convergence, and thereafter, the simulation with the inclusion of the liquid phase. This first simulation stage is performed until some convergence criteria set beforehand are

satisfied, and is devoted to eliminate the artificial effects of the flow initialization, and to obtain an initial spray flow evolving naturally with the imposed boundary conditions, while becoming statistically steady. Subsequently, the subgrid ignition model is paired with the FGM model, and the two models are coupled to the LES-spray-solver; the resulting CFD model is used to continuous simulations for 4 000 additional time steps ($\sim 400\ t_{REF}$). During this second phase, the ignition sequence is recorded by monitoring the evolution of reactive scalars (e.g. the changes in progress variable and/or temperature). Two sparks are deposited at two different locations in the shear layer between the cone of fuel and air. The choice of these spark locations in the swirl-stabilized combustion chamber is guided by the outcomes of the previous investigation conducted using the bluff-body stabilized burner. For the P&WC scaled can combustor, the determination of the spark locations is mainly based on the position of the spark plug, although some spark locations are also tested. The energy and the duration of each spark are respectively set to 500 mJ and 100 ms, and the initial spark kernel size is set equal to the gap between the spark plugs (i.e. 2 mm). At the end of this second phase which is characterized by the full ignition of the combustion chamber and a global flame stabilization, simulations are continued for 3 500 additional time steps under the statistical sampling mode to retrieve the spray flow and combustion properties governing the steady combustion regime. This additional number of time steps is sufficient to yield the statistical convergence. When investigating the steady combustion regime, particular attention is paid to the prediction of species characterized by low reaction rates such as carbon monoxide (CO), since an accurate prediction of such species may guarantee a reasonable prediction of other pollutants which are known to feature low reaction rates.

4.5.3 Computing resources and simulation flowcharts

The mathematical models and numerical schemes described in this chapter are used to simulate each of the three experimental configurations presented in Chapter 3. All the 3D unsteady simulations are run in parallel mode using 16 Quad-core Intel Xeon X5560 processors of the Compute Canada/Calcul Québec network supercomputer, and the flowchart adopted for the simulations are shown in Figure 4.8. The numerical results corresponding to each configuration are sequentially discussed in the next chapter.

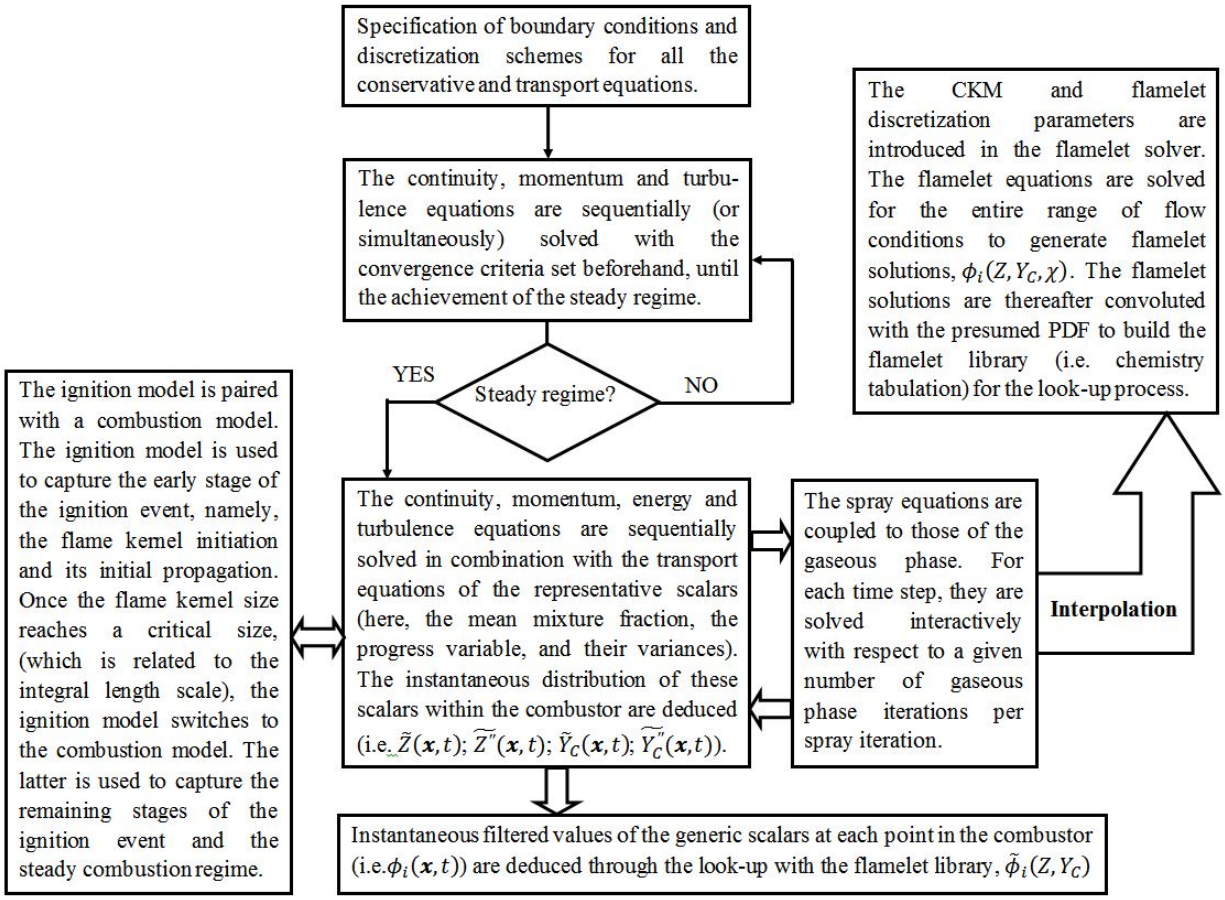

Figure 4.8: Flowchart of the simulations

Chapter 5

Results and discussions

As pointed out in the introduction, the main goal of the current study is to formulate a CFD methodology to accurately predict some combustion phenomena in both steady and transient spray combustion regimes. To this end, two major concerns faced by the combustion community, and especially by gas turbine manufacturers are considered, namely, safety and environmental regulations. For the former concern, attention is paid to the ground cold start and the altitude relight which are respectively essential to engine start-up prior to plane take-off, and for in-flight flameout that may occur at high altitude due to severe atmospheric conditions. The second concern is mainly oriented towards an accurate prediction of pollutants. The three configurations described in the chapter devoted to experimental configurations are considered. However, considering the fact that detailed experimental data are not available for the third configuration (i.e. tubular combustion chamber involving a liner designed with a specific pattern of holes) in the two combustion regimes, the capability of the newly formulated CFD methodology to accurately predict the spray flow structure and combustion properties in the steady combustion regime is first assessed by comparing the predictions to the experimental results collected from a swirl-stabilized spray flame (i.e. using the first configuration described in Chapter 3). Based on these predictions, the CFD methodology is optimized through advanced turbulence and combustion models for the subsequent simulations. For the transient combustion regime, the computational requirements due the size of scales involved are circumvented by resorting to a subgrid spark-based ignition model. The latter is coupled to the CFD methodology that was previously used for the prediction of the steady combustion regime, and is newly validated using an experimental configuration for which detailed experimental data are available, namely, the bluff-body stabilized burner. As this latter configuration is based on a gaseous fuel, the CFD model is subsequently extended to spray combustion by coupling a spray module to the CFD model used in the gaseous case, and especially, by adjusting the ignition model so as to match the flame speed of heavy hydrocarbon fuels such as Jet A-1. This adjustment leads to a more realistic modelling of the effective velocity to better capture the rate of the flame kernel expansion in its early stage of growth. The new formulated CFD model is reapplied to the swirl-stabilized combustion chamber with the aim of predicting the ignition sequence and the resulting steady combustion regime. Finally, the same CFD model is applied

to the third configuration (i.e. the tubular combustion chamber involving liner holes) with the aim of predicting cold start and altitude relight for two different operating conditions as described in the previous chapter devoted to the computational setup and boundary conditions. This chapter presents and discusses the results of each of the above listed investigations, and is thus divided into four different parts: the prediction of the steady combustion regime in a swirl-stabilized combustion chamber; the prediction of the spark ignition of the bluff-body stabilized burner; the extension of the CFD model to predict both the ignition sequence and the resulting steady combustion regime; and finally, the prediction of ignition events under various conditions of cold-start and altitude relight in a scaled can combustion chamber including an annular section with liner and holes to modulate incoming air for adequate combustion and wall cooling.

5.1 Prediction of the steady combustion regime in a swirl-stabilized tubular combustion chamber

As mentioned in the previous chapter, the combustion chamber sketched in Figures 3.1 and 3.2 (see Chapter 3, Section 3.1) is discretized using three different densities of structured meshes, namely, 0.8, 1.2 and 2.16 million hexahedral elements. By performing a mesh sensitivity study, the following observations are noted: for the URANS simulations, the grid consisting of 1.2 million elements provides results almost identical to those generated by the grid consisting of 2.16 million elements, and any further grid refinements do not improve the URANS predictions. According to the simulations based on the SAS model, the grid consisting of 2.16 million elements is found sufficient to reach the best accuracy since further mesh refinements through the mesh adaptation algorithm of the CFD code do not lead to more accurate results. However, because of the intrinsic mesh dependency for LES (i.e. the decrease in filter width which leads to an increase in the prediction accuracy), the densest of the three grids (i.e. 2.16 million) is retained for LES simulations, and some mesh adaptations are performed in some specific zones of the combustion chamber so as to properly capture the spray dynamics, the mixing process in the first instant of the evaporation phase, and both the shear layer and boundary layer effects. The grid is then refined near the solid boundaries, and particularly around the combustor axis and the injector exit, leading to approximately 60% of elements localized in these zones of the combustor. An illustration of the mesh features is provided through a coarse grid shown in Figure 5.1, where the grid is presented coarser to allow seeing its characteristics. Thus, although the final mesh density is used for the three turbulence models to assess the intrinsic prediction capability of each of them regardless of the mesh density, it is worth emphasizing that, for this first investigated configuration, the URANS results can also be achieved using the mesh density consisting of 1.2 million hexahedral elements, while the SAS results can be obtained using the mesh of 2.16 million elements with no need of grid refinements. For these reasons, in the current study, the comparison of the trade-off between the computing resources and the accuracy of the results for each turbulence model is done based on the minimum computing resources necessary to achieve the maximum accuracy in URANS and SAS simulations. The comparison of the three turbulence models is done using

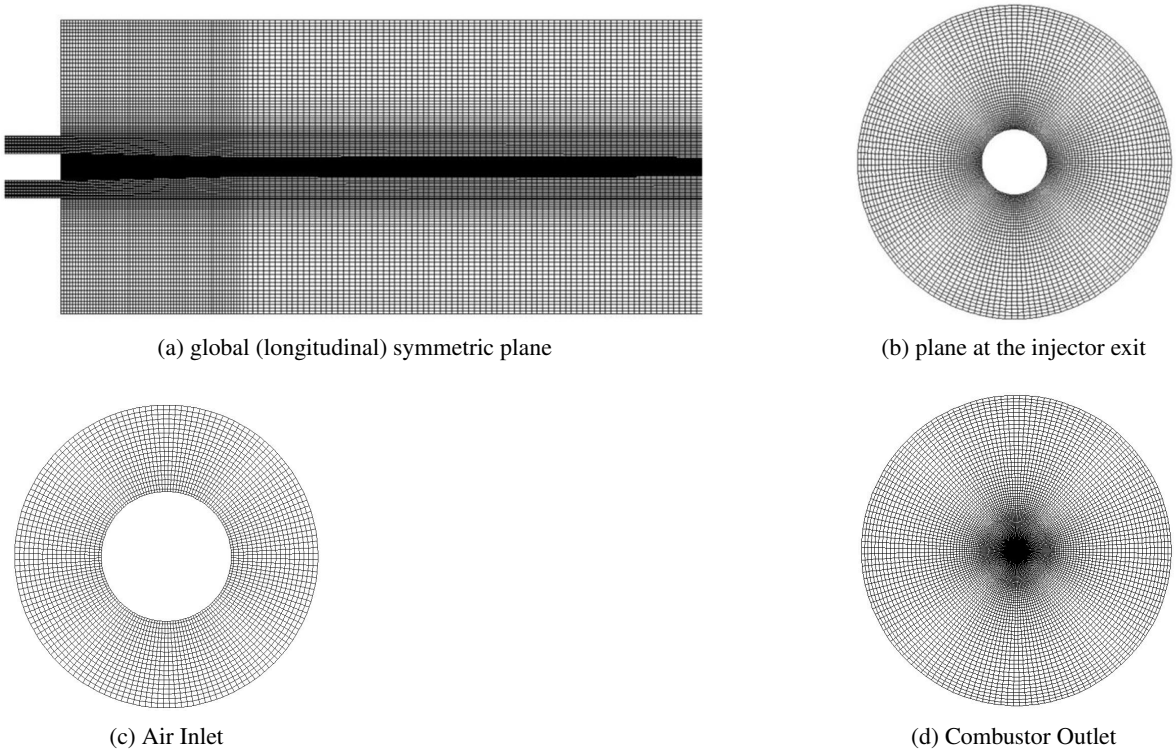

(a) global (longitudinal) symmetric plane

(b) plane at the injector exit

(c) Air Inlet

(d) Combustor Outlet

Figure 5.1: Sample of the combustor grid used for the three turbulence models

two different assumptions for the rate of chemical reactions, namely, the infinitely fast and the finite rate chemistry assumptions. Subsequently, the relevance of the implementation of a two-component fuel as the surrogate for Jet A-1 is investigated. In the present thesis, only the comparison of the three turbulence models based on the infinitely fast chemistry assumption through the partial equilibrium approach is presented. An explicit comparison of URANS and SAS using a finite rate chemistry assumption with one and two-component fuel surrogates may be found in [Fossi et al., 2015a] (see the Appendices), while an explicit comparison of SAS and LES based on the finite rate chemistry assumption is provided in [Fossi et al., 2015c] (see the Appendices). The three turbulence models presented earlier are available in the CFD code, and all the simulations are performed using the double precision mode. A segregated solver, the Semi-Implicit Method for Pressure Linked Equations (SIMPLE) algorithm, is used for the pressure-velocity coupling. Second-order schemes are used to discretize the pressure correction equation [1], momentum equation, the equations for turbulent quantities such as the turbulent kinetic energy, k, and its dissipation rate, ε, and the equations of thermochemical variables (e.g. representative scalars, energy, etc.). The temporal discretization of transient derivatives is done using an implicit second-order scheme, which is based on an iterative time-advancement algorithm. Thus, all the transport equations are solved iteratively, for a given time-step, until the convergence criteria are meet before moving on to the next time step. For both SAS and LES simulations, transient derivatives are discretized using bounded second-order implicit scheme. The bounded central

1. The pressure correction equation is used to enforce the mass conservation and obtain the pressure field

differencing scheme is used for the momentum equation, while second-order schemes are used to discretize the transport equations of the remaining variables. As mentioned in the previous chapter, the Lagrangian analysis of the spray is performed using the discrete phase model (DPM). For the URANS and SAS simulations, the Discrete Random Walk (DRW) model is used to take into account the effect of turbulence on droplet dispersion. However, for LES simulations, the effect of turbulence on the droplets dispersion is neglected for the reasons discussed in the previous chapter. With the simulation time step defined as described in the previous chapter (i.e. based on a representative droplet residence time and a convective time scale), the simulations are started with initialized fields, and are first performed over a time period equal to 8 000 time steps, which is approximately equal to 30 times the characteristic computation time (i.e. the time used by the flow to cross the computational domain in the main stream direction with the velocity equal to the bulk velocity). It is worth noting here, that for URANS simulations in particular, the time step can be taken longer than that of the LES simulations without affecting the accuracy of the URANS results; such a choice allows reducing the number of time steps that need to be simulated to reach the steady regime. This first stage of simulations is devoted to eliminating the influence of initialization, and to obtain an initial flow evolving naturally with the imposed boundary conditions, while becoming statistically steady. Subsequently, simulations are continued for 4 000 further time steps under sample statistics mode. This additional number of time steps is deemed sufficient to yield the statistical convergence. As, announced at the end of the previous chapter, all 3D unsteady calculations are sequentially run in parallel mode using 16 Quad-core Intel Xeon X5560 processors on the Compute Canada/Calcul Québec network supercomputer. The residual criteria are set to 10^{-6} for the energy equation and 10^{-4} for the remaining transport equations. In order to mitigate eventual issues with convergence, the first stage of each simulation is conducted according to two main intermediate steps. The first is the simulation of the unsteady non-reacting flow without any coupling with the liquid phase to convergence, and the second is the simulation until convergence with the inclusion of the liquid phase and chemical reactions.

5.1.1 Aerodynamics of the combustion chamber

The prediction of the combustion chamber aerodynamics using the three turbulence models is shown in Figure 5.2, Figure 5.3, and Figure 5.4. Specifically, in Figure 5.2 and Figure 5.3, the abilities of the three turbulence models to capture vortical structures of the flow are compared. The vortical structures are colored by the mean temperature (see Figure 5.2) and the mean mixture fraction (see Figure 5.3), and are extracted using a vortex detection method based on the isosurfaces corresponding to a given value of the second real eigenvalue of the symmetric matrix, $S^2 + \Omega^2$ (i.e. the parameter "λ_2"), where S is the strain tensor and Ω is the vorticity tensor. The λ_2 parameter as well as the Ukubo-Weiss criterion, $Q = \Omega^2 - S^2$, are related to the Navier Stokes equations and reflect the amount of strain and vortical motions in the flow field [Sahner, 2008]. One can first notice the better performance of LES, and thereafter that of SAS, for capturing the smaller turbulence structures compared to URANS where they are almost inexistent. Although this result is obviously expected considering the assumptions governing the derivation of each of the three turbulence models, it is of particular interest

for the current investigation since it provides an illustration of the need of solving flow structures to predict accurately both the aerodynamics and thermochemical states. This illustration is better understood when it is contrasted with the predictions of the velocity field as well as the thermochemical state within the combustion chamber.

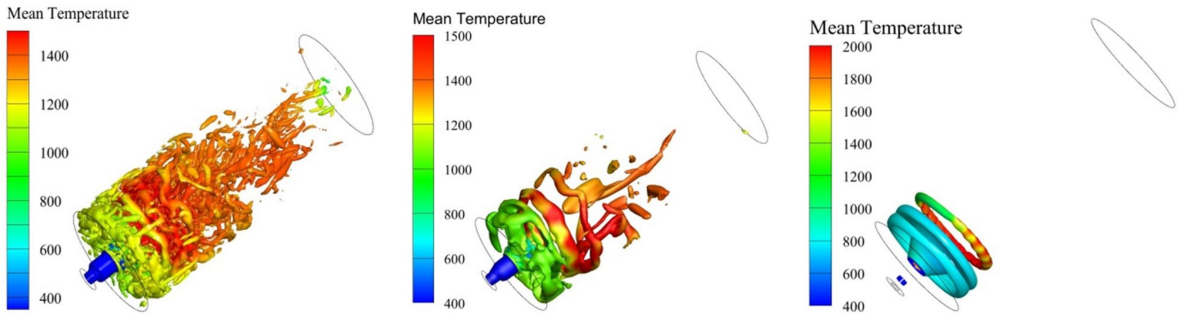

(a) LES (b) SAS (c) URANS

Figure 5.2: Turbulence resolved structures colored by the mean temperature

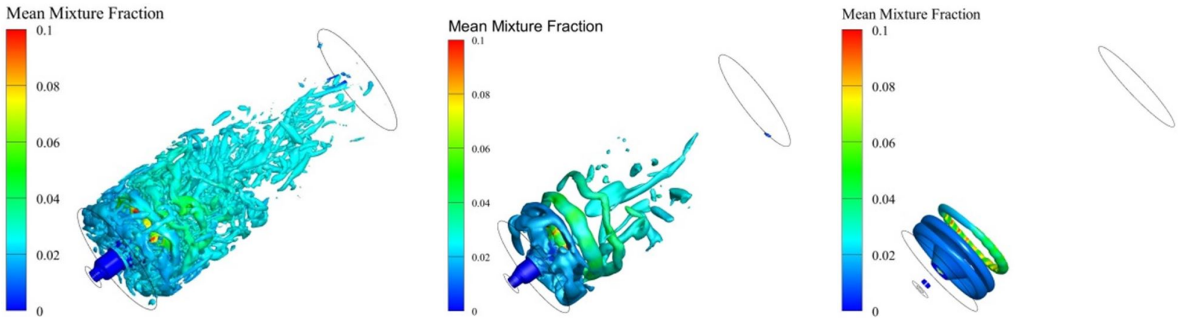

(a) LES (b) SAS (c) URANS

Figure 5.3: Turbulence resolved structures colored by the mean mixture fraction

In Figure 5.4, recirculation zones are shown using contours of velocity vectors colored by the axial velocity; one can see the side and central recirculation zones (SRZ and CRZ) generated by the combined effects of both the sudden expansion and the swirler. The vortical structures generated in these recirculation zones help to stabilize the flame with a lower bulk velocity. In fact, they behave as two counter-rotating vortices and, considering the dynamics of each pair of counter-rotating vortices, their resulting effect leads to a velocity reversal for an increase in residence time and for an improved mixing with better flame stability.

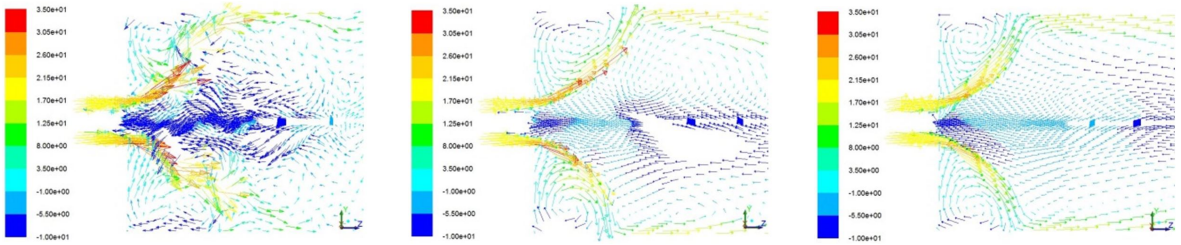

(a) LES (b) SAS (c) URANS

Figure 5.4: Recirculation zones captured through velocity vectors colored by axial velocity (m/s)

The radial profiles of the three velocity components and the corresponding fluctuations at several axial positions along the axis of the combustor are shown in Figure 5.5 and Figure 5.6. It can be globally noticed that, the three turbulence models predict reasonably well the aerodynamics state. For the axial and radial profiles (see Figure 5.5), some discrepancies are noted in the zone close to the injector exit near the combustor axis ($z/R \leq 1.0$). This may be related to the dynamics of the spray which is particularly dense in this zone due partly to the secondary break-up phenomenon as shown by the particle Weber number distribution (see Figure 4.2(c) in Chapter 4). Such a zone requires a more elaborate model to accurately solve both the spray dynamics and its interaction with turbulence, but that would result in a much higher computational cost. Apart from this zone, reasonable agreements with experimental velocity components are obtained at each cross section of the combustion chamber. In all the represented cross sections of the combustor, negative values of the axial velocity are noted, evidencing the presence of recirculation zones. The fluctuations corresponding to each velocity component are shown in Figure 5.6. Although significant differences are globally found between experimental results and the predictions, one can at least notice that both LES and SAS yield improved predictions compared to URANS.

5.1.2 Thermochemical state based on the infinitely fast chemistry assumption

In order to compare the predictive capabilities of the three turbulence models with respect to the thermochemical state of spray flames, the swirl-stabilized spray flame produced in the first configuration is simulated using the three turbulence models paired with a combustion model based on the equilibrium assumption. For this first approximation study, a one-component fuel, n-decane, is used as the surrogate for Jet A-1. The radial profiles of temperature and molar fraction for the major species (carbon dioxide and oxygen) corresponding to each of the simulations using the partial equilibrium assumption and the one-component fuel surrogate, are shown in Figure 5.7 and Figure 5.8, respectively. The part of the combustion chamber for which experimental data are available corresponds approximately to the first one-fifth of the total combustor length. This part, which is relatively close to the injector, can be divided into two main zones: a peripheral zone ($r \in]-0.1, 0.01[$ and $r \in]0.01, 0.1[$) and a central zone directly close to the injector exit ($r \in [-0.1, 0.01]$ and $z/R \leq 1.5$). In the first part, the

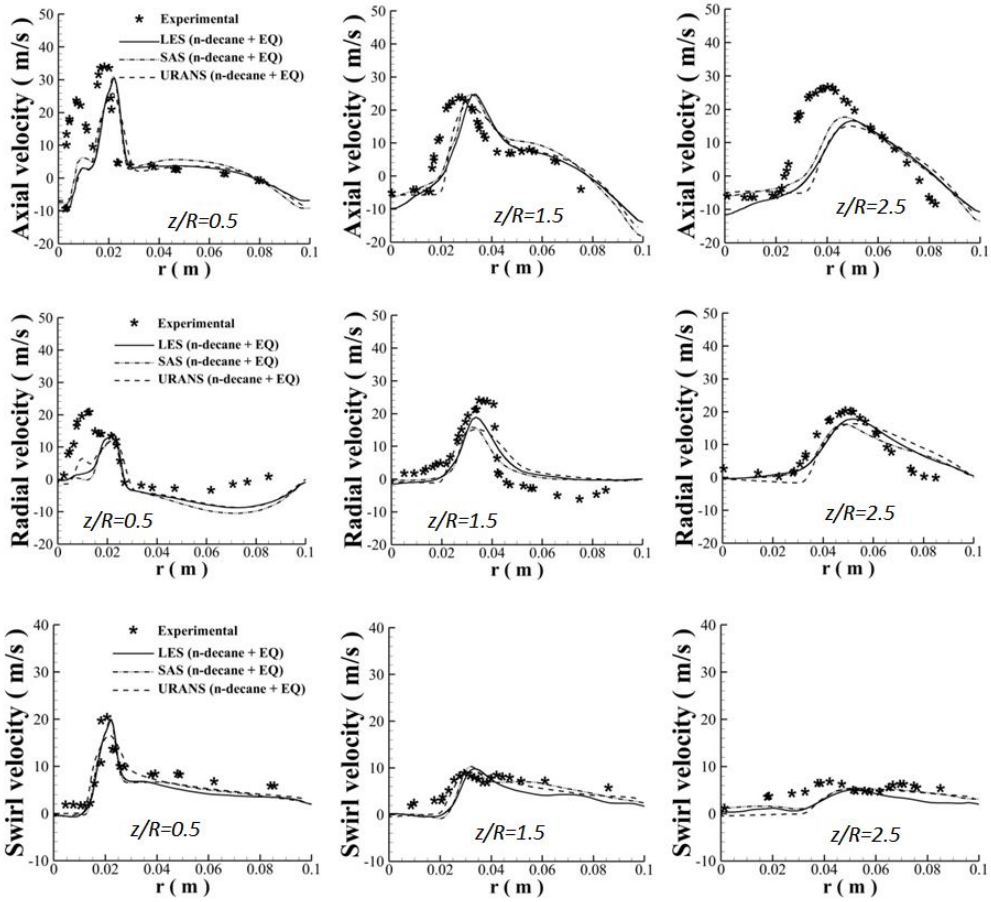

Figure 5.5: Radial profiles of the velocity components at various cross sections of the combustor. R=21 mm is the outer radius of the annular channel; z and r stand for the axial and radial coordinates, respectively

mixing is efficient because of the side recirculation zones and the relatively high velocities, as shown in Figure 5.4 and Figure 5.5. Due to the capabilities of LES and SAS to resolve part of the turbulence spectrum, they are inherently more suitable for high Reynolds number flows and consequently lead to a reasonable prediction of mixing and temperature profiles, unlike URANS. In the second part, essentially located within the central recirculation zone, some discrepancies are noted even with SAS and LES, and may be related to some drawbacks of the models used to capture turbulence-spray-chemistry interactions.

According to the prediction of major species (CO_2 and O_2) shown in Figure 5.8, in spite of some discrepancies (underprediction of CO_2 and overprediction of O_2) in the zone where $r \geq 0.03m$, it can be observed that the LES approach leads to significant improvements compared to the URANS and SAS models. A superposition of the underprediction of CO_2 to the overprediction of O_2 in the corresponding zones, as shown in Figure 5.8, allows relating the discrepancies to the fuel distribution and thus to the approximate spray parameters used. Based on this first comparative study, one can easily see that

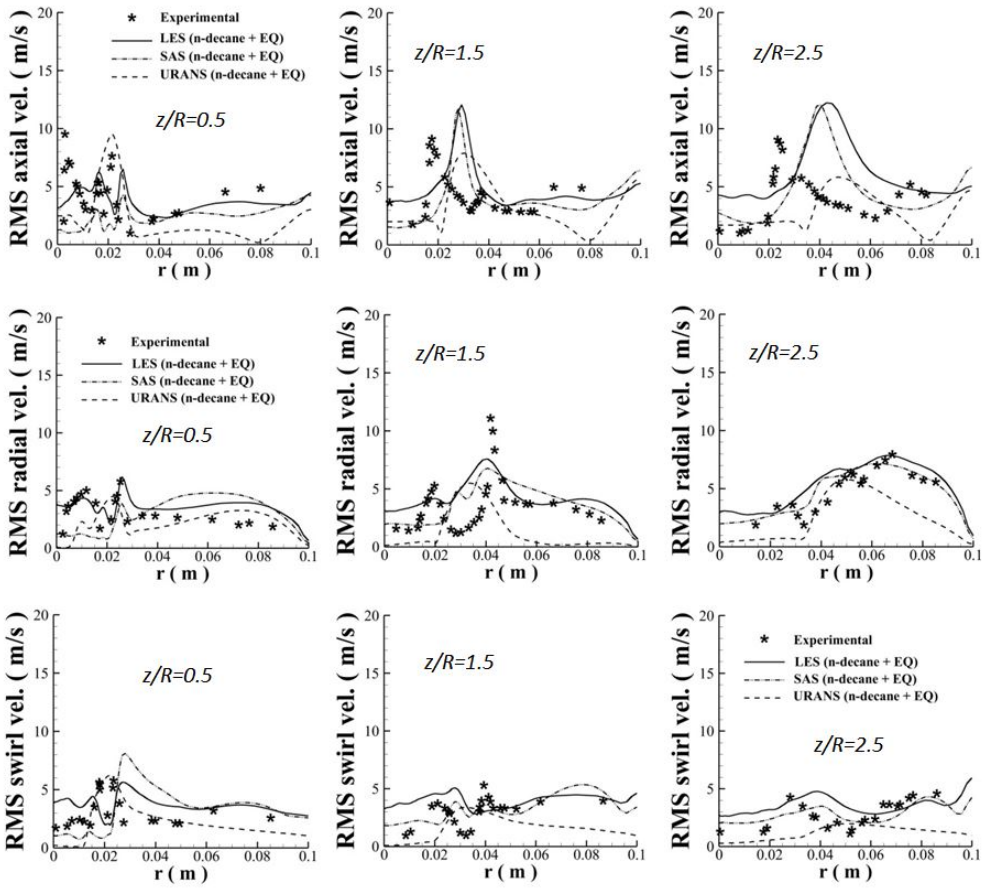

Figure 5.6: Radial profiles for the fluctuations of the velocity components at various cross sections of the combustor. R = 21 mm, is the outer radius of the annular channel.

the robustness of the turbulence model plays a relevant role in the prediction of both the aerodynamics and thermochemical state. In fact, due to the high sensitivity of the combustion processes to the fluctuations of representative scalars (in the tabulated chemistry context) on the one hand, and to the range of scales exhibited by such scalars (e.g. mixture fraction, progress variable, scalar dissipation rate, etc.) on the other hand, it is clear that the turbulence model must be robust enough to allow capturing the relevant flow features and the related scalar fluctuations. However, although the combustion processes are known to be very sensitive to the fluctuations of the representative scalars such as the mixture fraction (for non-premixed configurations), it remains that, in addition to a proper resolution of the mixing field, the global accuracy of the simulation approach based on the tabulated chemistry depends also on the suitability of the relationship between the generic scalars and the mixture fraction as well as the proper inclusion of turbulence-chemistry interactions. The partial equilibrium approach used so far fails to predict the main flame trends in the regions of the combustion chamber characterized by high strain rates such as that due to air-fuel mixing which is preponderant in the shear layer zone between the cone of spray and air. Thus, as expected, for the three turbulence models, species characterized

by low reaction rates such as CO and H_2 are significantly overpredicted in the fuel-rich zones because of the requirements for much more complex modelling of fuel partial oxidation (pyrolysis reactions) and mechanisms of soot formation. As an attempt to address this issue, the flamelet model is applied. The predictions of slow species using the three turbulence models, paired with the partial equilibrium approach, are contrasted to those obtained with the diffusion flamelet model and are discussed in the next subsection devoted to the predictions based on the finite rate chemistry assumption.

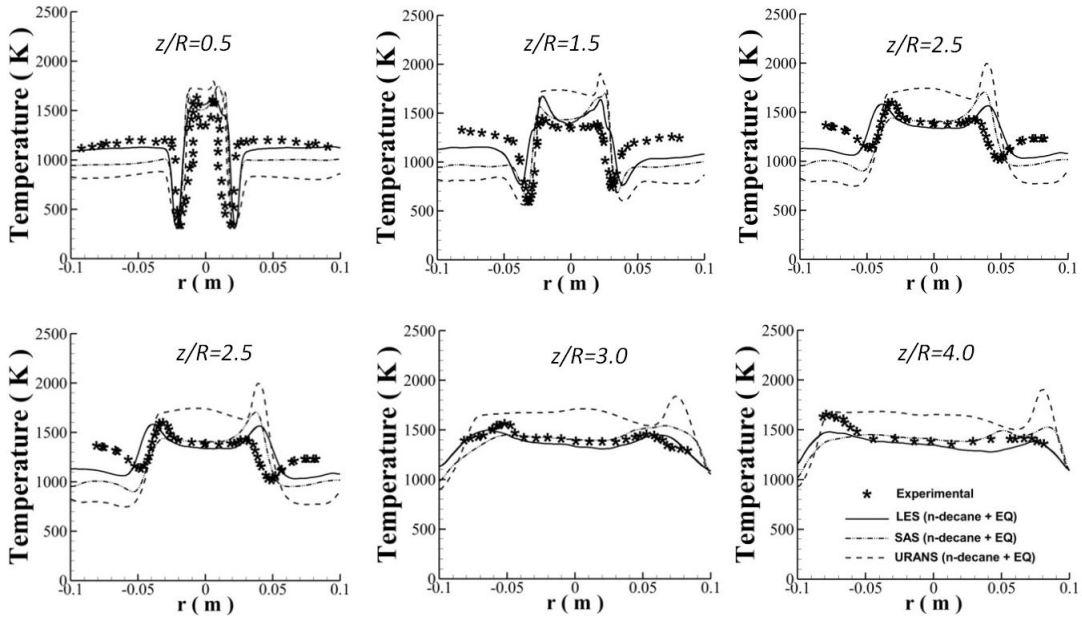

Figure 5.7: Radial profiles of the temperature at various cross sections of the combustor

5.1.3 Thermochemical state based on the finite rate chemistry assumption

To investigate the relevance of using a realistic chemistry and fuel surrogate models when simulating reacting spray flows, the three turbulence models are used in conjunction with the steady flamelet model based on one-component and two-component fuels as surrogates for Jet A-1. Simulations are performed using the same computing parameters as described in the previous sections so as to investigate separately the effects of the fuel composition and the inclusion of chemical non-equilibrium effects due to turbulent strain. To avoid overloading the graphs shown in this subsection, the results of the predictions using SAS and URANS models paired with the flamelet model are briefly reported here but are not presented since they are fully presented and discussed in [Fossi et al., 2015c] (See Appendices). Only those of the LES-predictions are presented.

The radial profiles of temperature and the corresponding fluctuations at various cross sections

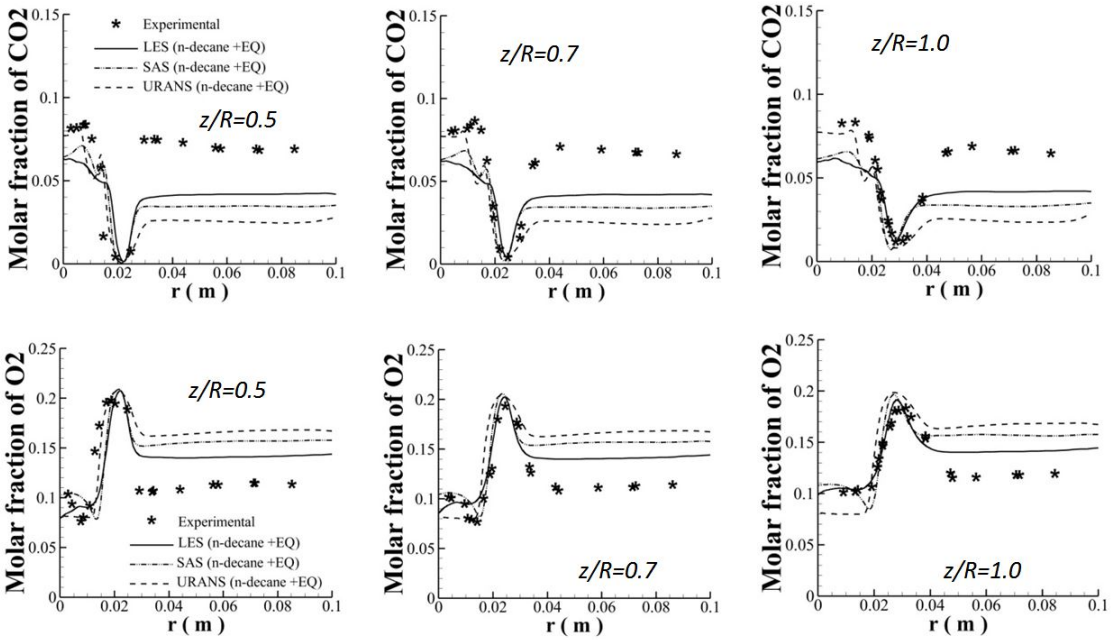

Figure 5.8: Radial profiles of the species molar fractions at various cross sections of the combustor

along the axis of the combustor are shown in Figure 5.9 and Figure 5.10. It can be observed that, in the zone close to the injector exit (i.e. $z/R \leq 10$), in the shear layers between the spray cone and air, the steady flamelet model (FM) slightly improves the prediction of the mean temperature. In fact, these shear layers correspond to zones of intense exchanges of mass, and are consequently zones of high mixture fraction gradients (i.e. high value of the scalar dissipation rate, χ, since $\chi = 2D_Z(\nabla Z.\nabla Z)$). Thus, as the classical diffusion flamelet model uses the scalar dissipation rate of the mixture fraction to parameterize the diffusion flamelet library, unlike the equilibrium approach which assumes $\chi = 0$, reaction zones featuring chemical non-equilibrium effects due to turbulent strain (e.g. flame stretching and flame wrinkling) are relatively better captured. In the remaining sections of the combustor, both simulations based on the partial equilibrium approach and those based on the flamelet model lead to almost identical results, all evolving progressively towards the equilibrium state. The same prediction trends were noted in the simulations employing URANS and SAS models as shown by the papers presented in the appendices.

The mole fractions of major species, carbon dioxide (CO_2) and oxygen (O_2), are shown in Figure 5.11. One can see that no significant improvements are yielded by the implementation of the finite rate chemistry assumption through the classical diffusion flamelet model, and the implementation of the two-component fuel surrogate. As for both URANS and SAS simulations [Fossi et al., 2015c], the two models (partial equilibrium and flamelet models) paired with the LES lead to an underprediction of CO_2 and an overprediction of O_2 in the side recirculation zones of the combustor ($\pm 0.03m \leq r \leq \pm 0.1m$). As discussed earlier, this trend is mainly due to the fuel distribution and the spray parameters extracted from the parametric study which are not as accurate as those that direct

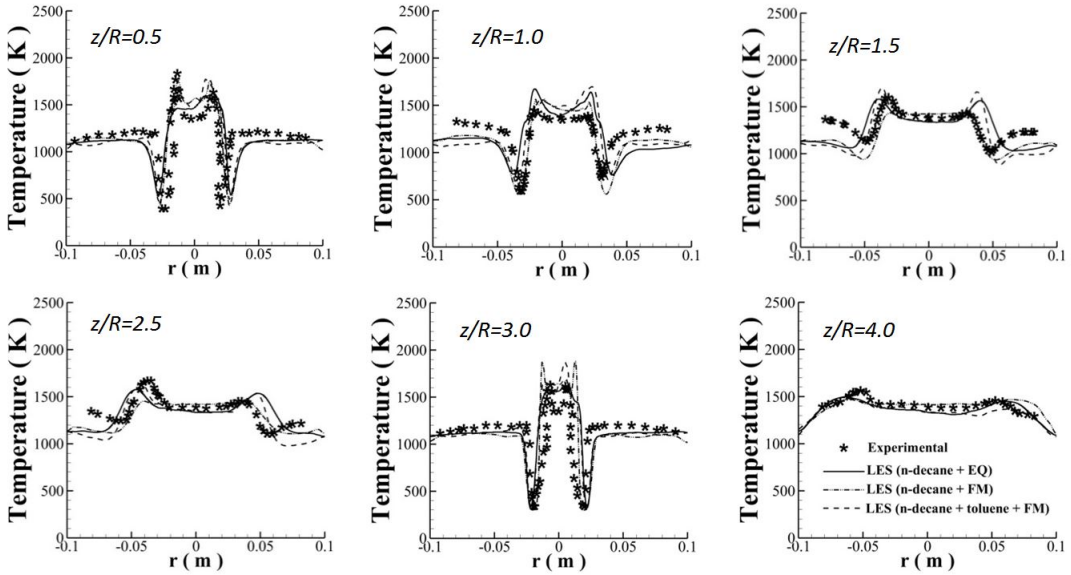

Figure 5.9: Radial profiles of the temperature at various cross sections of the combustor

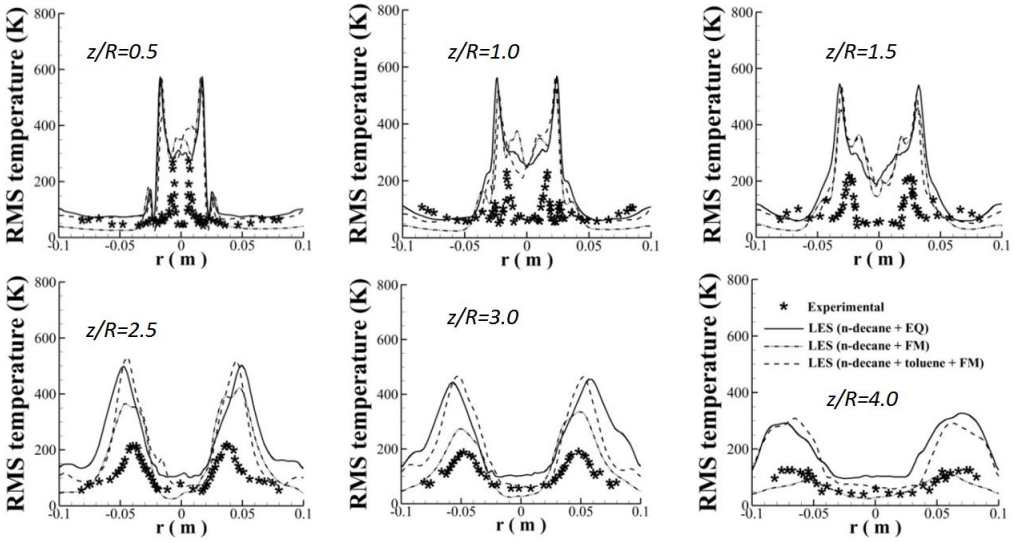

Figure 5.10: Radial profiles of the temperature fluctuations (RMS) at various cross sections of the combustor

measurements would have generated.

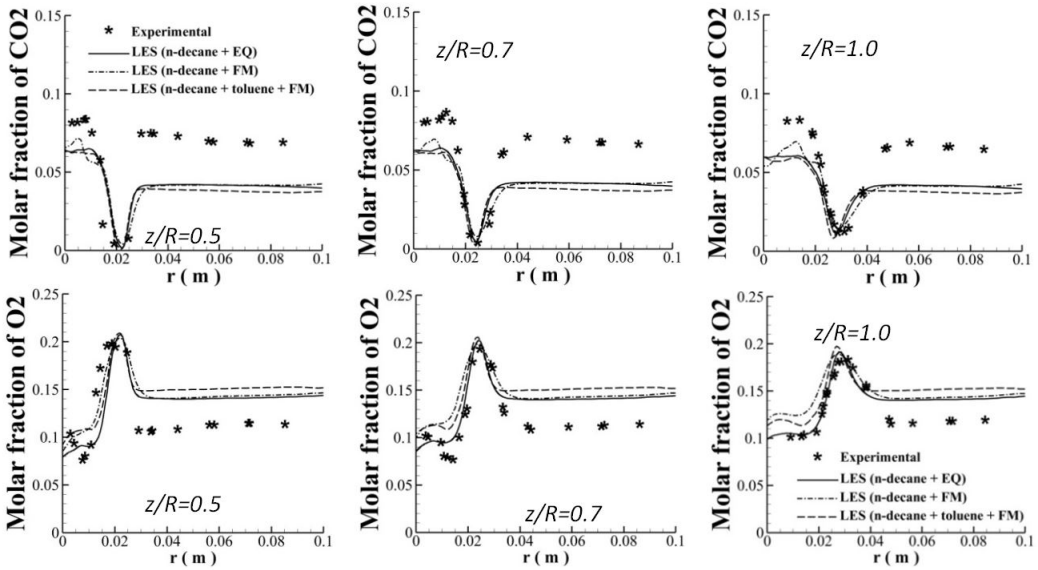

Figure 5.11: Radial profiles of major species at various cross sections of the combustor

The LES prediction of species slowly-produced such as CO and H_2 are shown in Figure 5.12. The same trends is observed in both URANS and SAS predictions. Even if both the partial equilibrium model and the diffusion flamelet model overpredict their formation, one can nevertheless note a significant improvement with diffusion flamelet model: the partial equilibrium model leads to an overprediction by a factor of 6, while the flamelet model leads to an overprediction by a factor of 2. Species such as CO and H_2 are intermediate species that are produced and/or consumed by oxidation in the post-reaction zone on slow time-scales. The flamelet model is based on the finite rate chemistry assumption, but the chemistry is still assumed to be fast (but slow compared to equilibrium approaches). In other words, the flamelet model is expected to perform well when it is applied to configurations exhibiting high Damköhler numbers, and to some extent to those featuring moderate Damköhler numbers. Plus, the unity Lewis number assumption is made for all species (i.e. the preferential and differential diffusions are neglected), and all the radiation effects are neglected. These assumptions are not always valid in most practical applications, and thus the formation of the slow species is expected to be overpredicted by each of the two combustion models. The improvements noted with the diffusion flamelet model originate from the relaxation of the infinitely-fast chemistry assumption. The discrepancies found in the prediction of slow species are related not only to the drawbacks of the diffusion flamelet model (e.g. the restrictiveness of its solution space), but also to an approximate fuel distribution as noted earlier when discussing the prediction of the major species. These discrepancies can be mitigated by implementing a multi-dimensional flamelet model (e.g. the unsteady flamelet/progress variable or its variants such as the Flamelet Generated Manifold) since the latter relies on a tabulation approach that provides a more realistic flamelet solution space [Franzelli

et al., 2013]. Indeed, in addition to the more realistic solution spaces provided by such approaches, the presence of unsteady terms in their mathematical formulation allows a more realistic modelling of the flamelet structure, and an instantaneous tracking of rapid changes of the scalar dissipation rate in the downstream direction of the reactive flow. Plus, partial premixing that may occur prior to combustion is properly captured by the progress variable, which acts also as a tracer to determine the real state of the flamelet among the possible states illustrated by the S-shaped curve. Another efficient way of solving this issue would be the implementation of a transport equation for each slow species considered in the reacting system. However, for each of these improvements, additional expenses in computing resources need to be considered.

The set of simulations conducted with the swirl-stabilized combustion chamber with the three turbu-

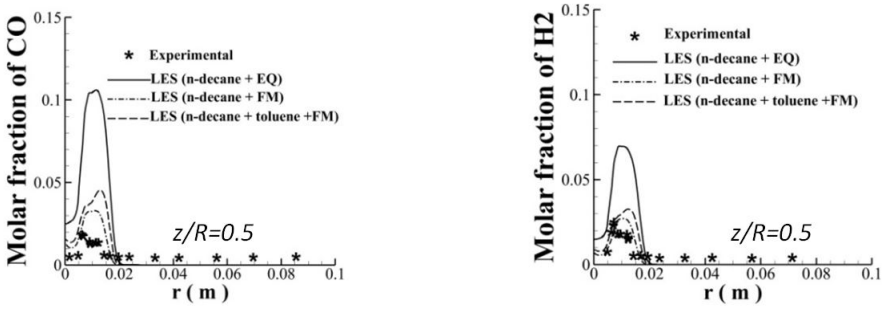

Figure 5.12: Radial profiles of slow species at various cross sections of the combustor

lence models (URANS, SAS and LES) allowed setting up a basic CFD methodology that can be used to reasonably predict the spray flow features and combustion properties governing the steady combustion regime. The resulting CFD methodology consists of LES paired with the diffusion flamelet model based on both one-component fuel and two-component fuel as the surrogates for Jet A-1. The model provides the best trade-off between the computing costs and the accuracy of the results. Indeed, for URANS simulations based on the grid consisting of 1.2 million elements, approximately 40 seconds in simulation time are required to achieve the convergence for each time step compared to 70 seconds per time step for URANS simulations based on the grid of 2.2 million elements. As pointed out earlier, the simulation results based on the two mesh densities are almost identical, and the mesh density of 1.2 million elements can then be viewed as the minimum mesh density necessary to reach the maximum accuracy with the URANS model. Hence, the computing time based on the grid having 1.2 million elements is considered as the CPU time for the URANS simulations of the investigated configuration. For the SAS and LES simulations, the average computing times required to converge each time step are approximately 64 and 70 seconds, respectively. By contrasting the improvements generated by the SAS and LES models with their corresponding computing time (see also [Fossi et al., 2015a]), one can conclude that, for the present configuration, the LES model provides the best compromise between the accuracy of the results and the computing costs. Furthermore, by using a less dense mesh (1.2 million instead of the 2.2 million hexahedral elements used in the current

LES simulation) in a previous LES simulation reported in [Fossi et al., 2015b], the LES approach led to more reasonable predictions compared to the URANS and SAS results shown in the present study, suggesting a superior performance of LES compared to the two other turbulence models.

5.2 Transient combustion regime: Spark ignition of a bluff-body stabilized burner

Transient combustion phenomena such as the spark-based ignition sequence in an aero gas turbine combustion chamber feature small scales comparable to the spark plug gap of the igniter [Eichenberger and Roberts, 1999]. As pointed out in the previous chapter, the proper resolution of the physical processes exhibiting such scales can potentially be achieved with the straightforward approach consisting of refining the local mesh of the combustion chamber near the ignition region. However, such an approach leads to a drastic increase in computational resource requirements, so that alternative approaches such as the subgrid spark-based ignition model described in the previous chapter are necessary (see Subsection 4.6 in Chapter 4). Thus, the CFD methodology initially formulated to predict the steady spray combustion regime is reconsidered, and some modifications are done to build a new CFD methodology that can capture the early stages of ignition and the resulting steady combustion regime. These modifications done on the previous CFD methodology can be viewed as an intermediate stage towards achieving the second goal of the current study, namely, the prediction of the ignition sequence and the resulting steady combustion regime. The bluff-body stabilized burner is used to appraise the ability of the new CFD methodology to predict the whole ignition sequence, and more precisely, to investigate the effect of the spark position on the ignition event success. As the burner is designed to burn gaseous fuels [Ahmed, 2007a], the modifications done in this intermediate stage consist of the following: (i) the spray module is decoupled from the previous CFD methodology (see the simulation flowchart shown in Figure 4.8, Chapter 4); (ii) the classical diffusion flamelet model is replaced by the FGM model as it provides the mixture fraction to capture fuel-air mixing, and the progress variable to track the flame front propagation (i.e. the two most relevant phenomena to be considered when investigating ignition event in non-premixed configurations); (iii) the subgrid spark-based ignition model is coupled with the turbulence and combustion models to capture the early stage of the spark kernel growth following the glow discharge phase, its propagation to ignite the neighbouring zones, and the flame stabilization following the full ignition of the burner. The part of the experimental apparatus delimited in Figure 3.5 and represented in Figure 3.4 (Chapter 3) is meshed using the structured meshing technique. To perform the mesh sensitivity study, four different mesh densities consisting of 0.7, 1.5, 2.1 and 3.2 million(s) hexahedral elements are considered. In addition, two LES modelling approaches of the eddy viscosity are considered: the Wall-Adapting Local Eddy-viscosity (WALE) and the Smagorinsky-Lilly models. In each case, the mesh is refined near the solid boundaries, and in particular around the radial fuel jet orifice to capture the partial premixing of fuel and air, and in the wake zone downstream of the bluff-body: about 50% of elements are concentrated in these zones. An illustration of the mesh structure at various domains of the burner is provided in

Figure 5.13. The suitable mesh resolution resulting from the mesh sensitivity study, and the eddy viscosity model selected from the model sensitivity study, are subsequently used to predict the aerodynamics and the mixing fields, along with the ignition events. The selection of the mesh resolution and the LES eddy viscosity model is mainly guided by the trade-off between the computational costs and the accuracy of the results. All the simulations are performed in double precision mode using a segregated solver, the Semi-Implicit Method for Pressure Linked Equations (SIMPLE) algorithm, for the pressure-velocity coupling. The transient derivatives are discretized using a second-order implicit scheme, while a bounded central differencing scheme is used for the momentum equations. The transport equations for the remaining scalars are discretized using second-order schemes. The time step used in all simulations is obtained by adopting the procedure described in the previous chapter (see the subsection devoted to the computational parameters in Chapter 4). Two kinds of simulations are performed. The first kind is based on air flow only with no fuel injection, and is mainly devoted to the mesh sensitivity study, while allowing the prediction of velocity profiles which are thereafter validated with experimental data. The second kind of simulations is based on the flow of the methane-air mixture, and is conducted to reproduce the mixture fraction distribution within the combustion domain of the burner. In both cases, simulations are initialized with a constant field of air and fuel, and are first performed over a time period equal to 10 000 time steps, which is approximately equal to 12 times the characteristic computational time. As in the previous configuration, this first stage of the simulation is devoted to eliminating the adverse effects of flow initialization, and to obtain an initial flow evolving naturally from initialization with the imposed boundary conditions. Subsequently, for the former case, the simulations are continued for 10 000 further time steps in sampling mode for statistics, and this additional number of time steps is sufficient to yield the statistical convergence; the numerical velocity profiles are thereafter extracted and compared to their experimental counterparts. In the second case, the simulations are also continued for 10 000 additional time steps, but after injecting fuel into the annular co-flowing of air. As in the cold flow simulations, this additional number of time steps is necessary to eliminate the artificial influence of the fuel stream initialization. At the end of this phase, simulations are continued for 10 000 further time steps under the sampling statistics mode to collect mean value of the mixture fraction and the corresponding fluctuations which are also compared to those provided by the experiment. Once a reasonable field of the mixture fraction is obtained, the ignition model is applied to investigate ignition events, with a particular attention paid to the effect of spark location on the ignition event success. For the hot flow simulations, a qualitative validation is done by comparing the contours of flame front tracers (e.g. reaction progress variable, temperature, etc.) with the high speed camera images of the corresponding experimental ignition events [Ahmed et al., 2007].

The experimental data used to validate the numerical predictions of aerodynamics and mixing fields are available for the mean values of the velocity components and the mixture fraction as well as their corresponding fluctuations at various cross sections of the mixing zone [Ahmed et al., 2007]. The high-speed camera images used to appraise the ability of the new CFD methodology to capture the whole ignition sequence are available for various spark locations, and allow a qualitative validation of

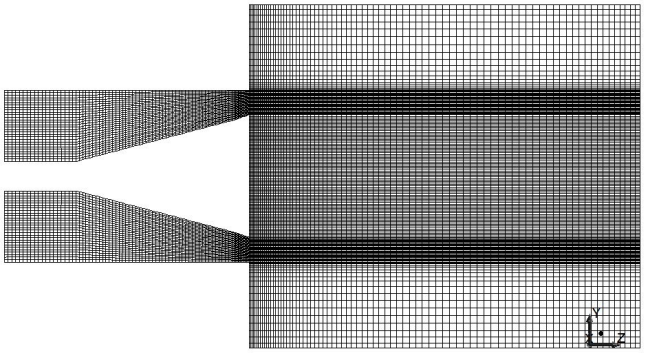

(a) global (longitudinal) symmetric plane

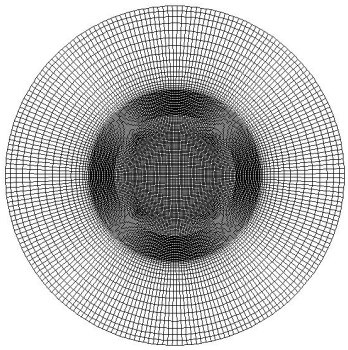

(b) Exit of the computational domain

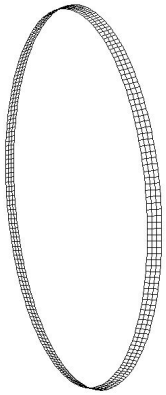

(c) Fuel Inlet

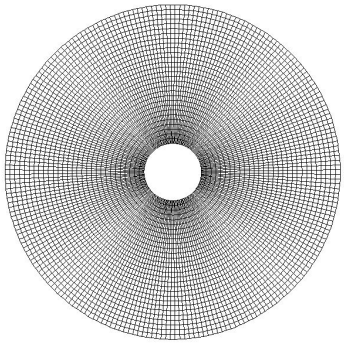

(d) Air Inlet

Figure 5.13: Grid structure at various zones of the bluff-body stabilized burner

numerical ignition events as well as the total time required to achieve the full ignition of the burner.

5.2.1 Velocity field based on the mesh and LES model sensitivity studies

Mesh sensitivity study:

Four different simulations are performed using the four mesh resolutions mentioned above. The predictions of the radial profiles of the velocity components (axial and radial velocities) along with their fluctuations for each simulation are shown in Figure 5.14.

Although the LES model is known to be intrinsically mesh dependent, one can notice that no significant improvements are found in the prediction of the velocity components when considering the more refined meshes. The numerical results generated by the four mesh resolutions are close to each other, and some of them, namely, the axial velocity at some cross sections, agrees reasonably well with the experimental results. For the radial velocity, significant discrepancies are noted, and may be related to a mismatch of the estimated radial velocity profiles at the burner inlet. In fact, as

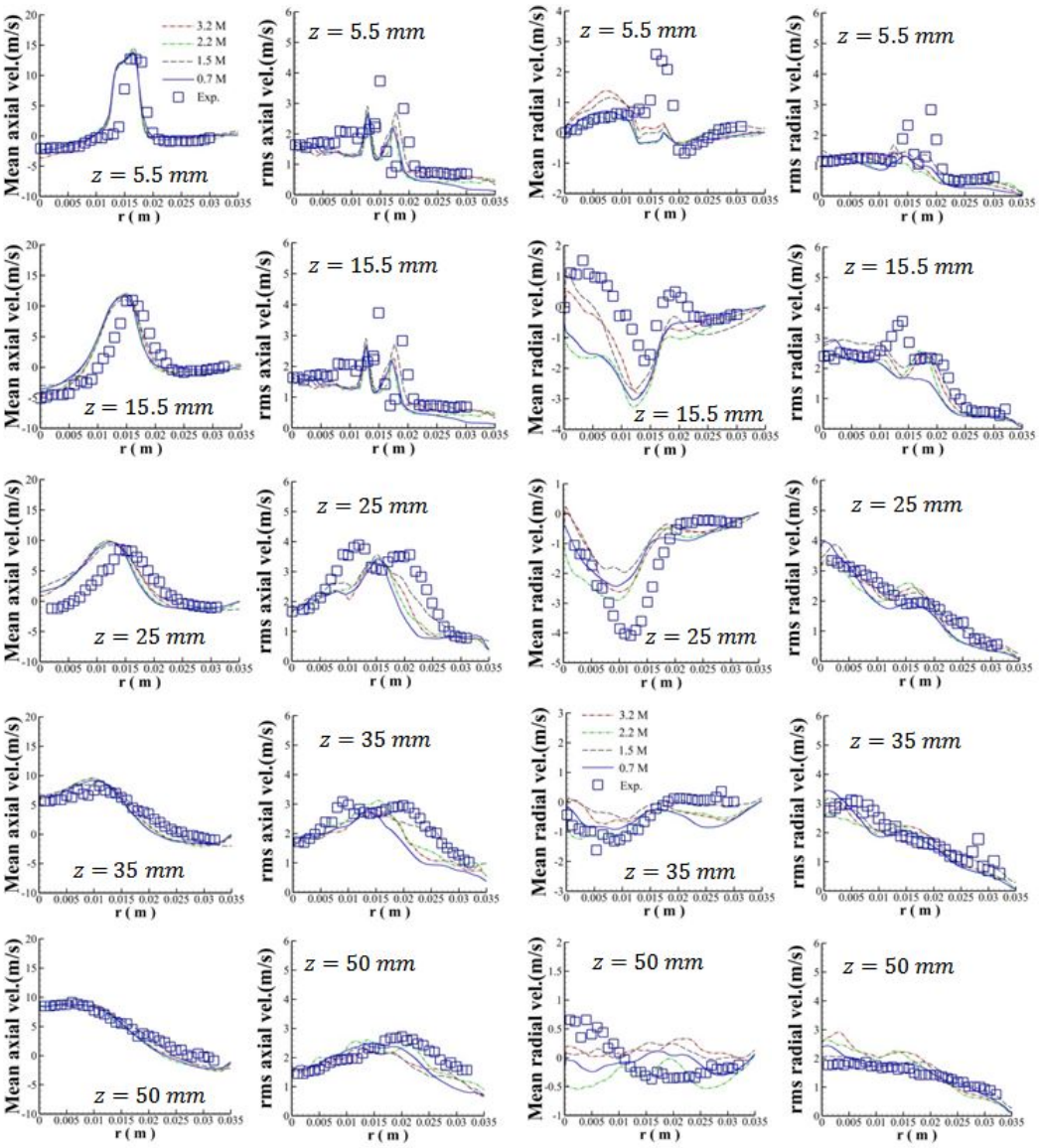

Figure 5.14: Radial profiles of axial and radial velocities and the corresponding fluctuations at various cross sections of the burner mixing zone (results based on cold flow simulation with air only).

the radial profiles of the velocity components were not experimentally recorded at the burner inlet cross section, various estimated profiles for axial and radial velocity are tested while maintaining the experimental value of the bulk velocity at the flame zone inlet. As the experimental value of the fuel velocity was measured at the exit of the circular gap which is located 2 mm just before the burner exit, a substantial part of the upstream geometry (50 mm in length) is considered, along with the flame zone in the current simulations as reported earlier and shown in Figure 3.4 (see Chapter 3). This approach is adopted to capture the partial premixing of the fuel with air in its early stage, and both axial and radial air velocities at the inlet of the burner are selected such as to match the experimental value of the equivalence ratio. The most promising results are obtained by imposing top-hat profiles of 6 m/s for both axial and radial velocities at this cross section of the burner inlet, which is located 50 mm upstream.

Sensitivity study based on the LES modelling of the eddy viscosity:

The sensitivity of the numerical results to the LES modelling of the subgrid eddy viscosity is shown in Figure 5.15, where the predictions based on the WALE and Smagorinsky-Lilly models are compared. It can be seen that, the two models lead to results which are almost identical. As the computing resources required by the two approaches are similar, the LES-WALE model is retained for subsequent simulations. This choice is also motivated by the ability of the WALE model to return a zero eddy viscosity for laminar shear flows, which is turn allows a better treatment of laminar zones in the computational domain.

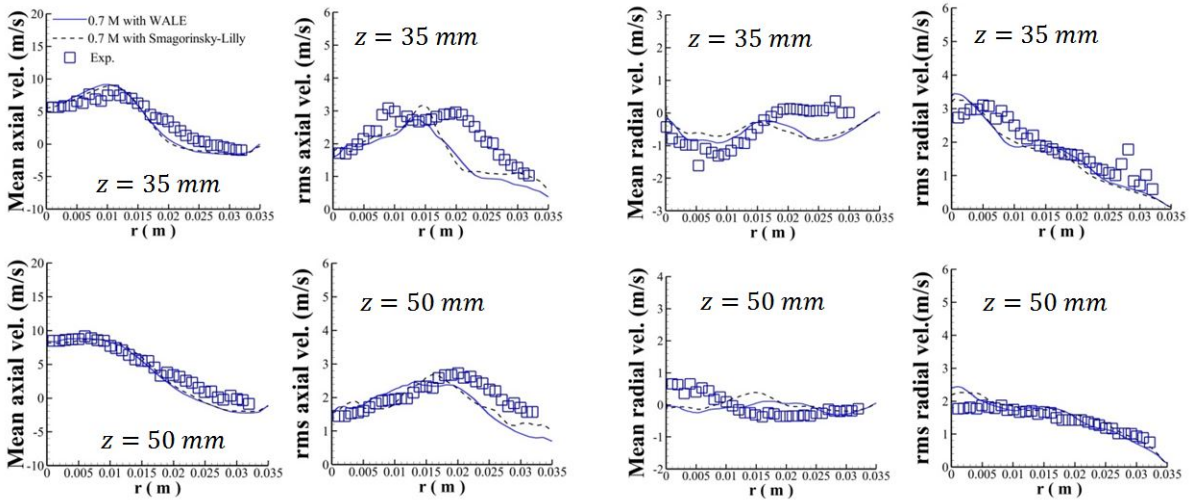

Figure 5.15: Sensitivity of the prediction to the modelling approach of the eddy viscosity for cold flow using LES

In order to select the mesh density to be used for the investigation of ignition events, two preliminary simulations based on the coarsest (0.7 M) and the more refined (3.2 M) meshes, and involving

fuel and air mixing are conducted with the aim of investigating the sensitivity of the mixture fraction field prediction to the mesh resolution. In this latter case also, no significant improvements are found, and therefore, the coarse mesh consisting of 700 000 hexahedral elements is retained to investigate all the ignition events. This choice is partly motivated by one of the main features of the ignition model, namely, its ability to track the kernel growth without requiring a fine mesh. The contours of the axial velocity and the mixture fraction fields, along with iso-contours of the temperature before the spark deposition are shown in Figure 5.16 and Figure 5.17, respectively.

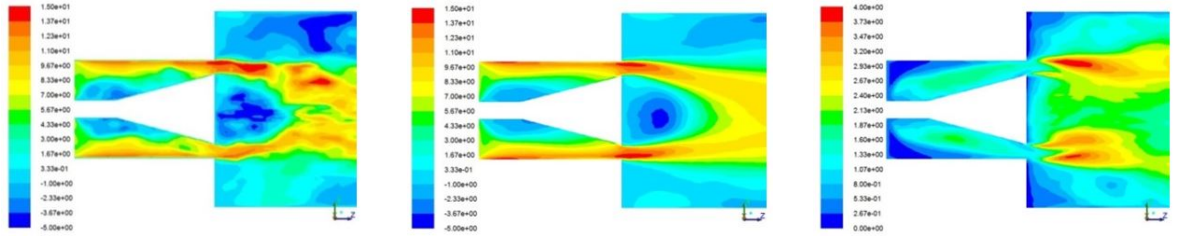

(a) Instantaneous field of the axial velocity

(b) Field of the Mean axial velocity

(c) field of the root-mean-square of the axial velocity

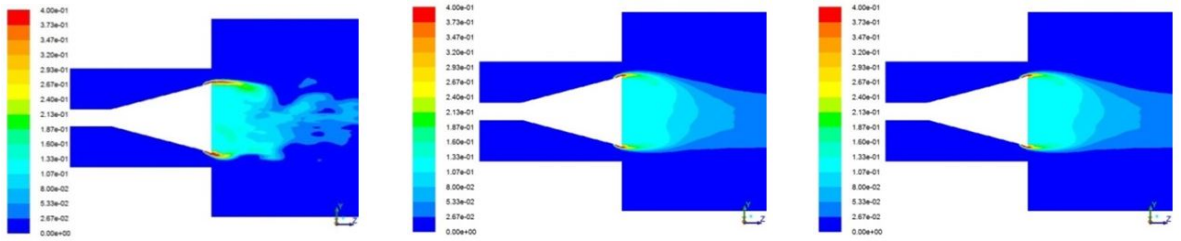

(d) Instantaneous field of the mixture fraction

(e) Field of the mean mixture fraction

(f) Field of root-mean-square of the mixture fraction

Figure 5.16: Aerodynamics and mixing fields: Contours of velocity and mixture fraction for cold flow using LES

5.2.2 Mixture fraction field

As done earlier for the velocity field, the mixture fraction field is validated by comparing the radial profiles of the mixture fraction to their experimental counterparts [Ahmed et al., 2007]. This comparison is shown in Figure 5.18. One can notice an overprediction of the mixture fraction in the zone around the bluff-body exit, which physically means an insufficient amount of air in this zone. These discrepancies may be related to the mismatch of the radial velocity component as discussed in the previous subsection. Indeed, by definition, the mixture fraction allows quantifying the mixing level as it measures the local equivalence ratio within any zone where a mixing of fuel with air occurs. According to the fundamental laws governing transport phenomena, the mixing of fuel with air is achieved through the convective and diffusive transports, and predominantly, by convective transports (also termed as bulk motion) in a turbulent environment. Thus, the axial components of the fuel and the air velocities are predominantly in charge of the fuel and air distributions in the axial direction,

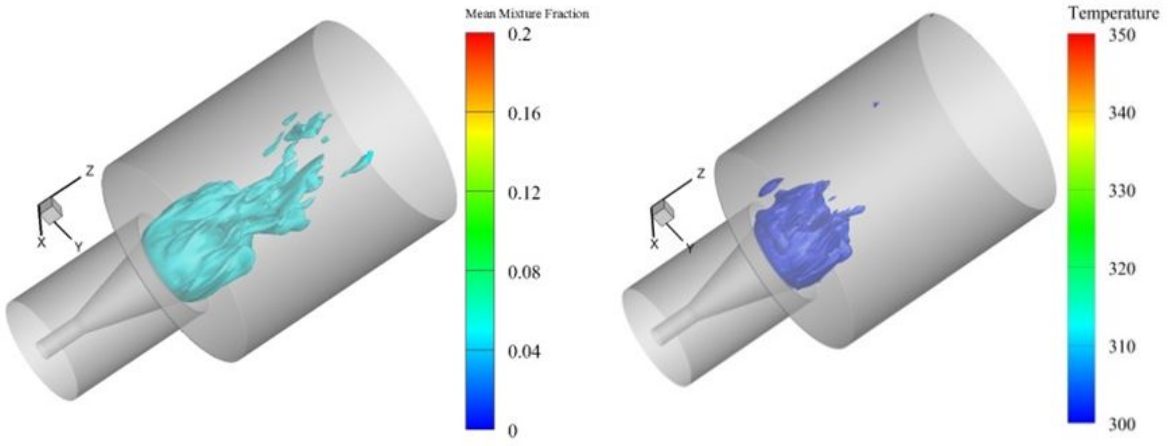

(a) Isosurfaces of the mean mixture fraction

(b) Isosurfaces of the temperature

Figure 5.17: Isosurfaces of the mixture fraction and the temperature at the moment of the spark deposition

while radial components ensure the fuel and air distributions in the radial direction (in the case of a swirling motion, the tangential component of the velocity contributes to both the axial and radial distributions of fuel and air). For the present case, the profiles of the radial velocity of air show that, the radial profiles imposed at the burner inlet lead to radial convective transports which are not strong enough to adequately supply air within the recirculation zone since the radial component of the velocity is globally underpredicted over the range of cross sections represented in Figure 5.14 (i.e. $z \in [15mm, 25mm[$).

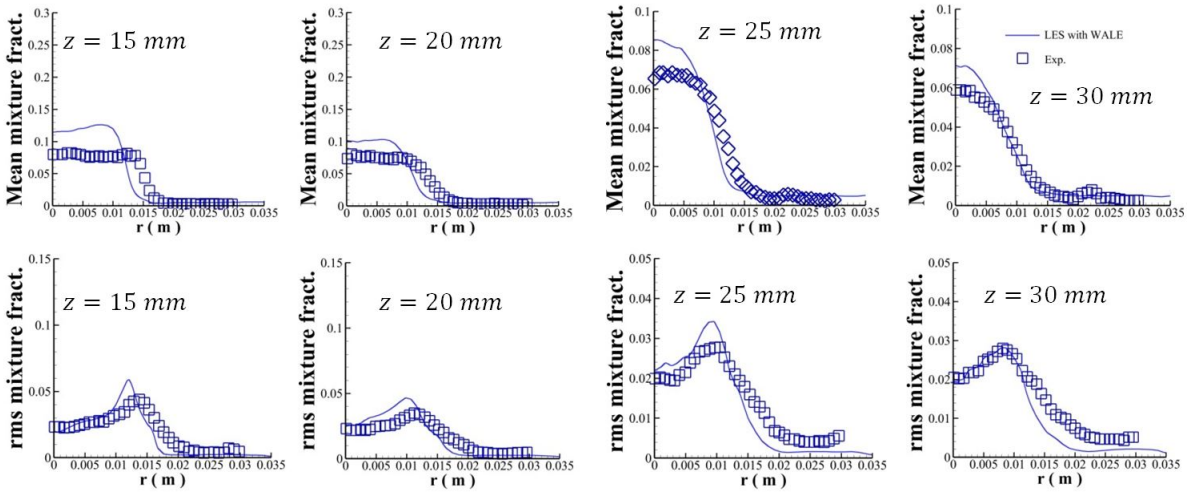

Figure 5.18: Radial profiles of the mixture fraction and the corresponding fluctuations at various cross sections of the burner for cold flow using LES

5.2.3 Visualization of ignition events

The state corresponding to the instantaneous mixing and temperature fields shown earlier in Figure 5.17 is used as the initial state to investigate the ignition event. The DPIK model described previously is used to mimic the spark energy deposition, and to capture the early stage of the spark kernel development and its propagation until the transition to the turbulent combustion model. The remaining phases governing the kernel growth until the complete flame establishment (for a successful ignition event) or the flame extinction (for a failed ignition event) are captured with the combustion model through flame front tracking parameters such as the progress variable, or any other reactive scalar (e.g. the temperature and/or the OH radical concentration). As one of the main objectives of the experimental investigation consisted in evaluating the effect of the spark location on the ignition success [Ahmed et al., 2007], two spark locations for which ignition sequences were experimentally recorded are considered, to qualitatively assess the capability of the CFD methodology to reproduce the experimental results. The experimental ignition sequences are available in terms of OH-PLIF and High-speed camera images. However, only high-speed camera images are exploited in this thesis, and the instantaneous temperature contours are therefore extracted from the simulation results for comparison. The first position is denoted "A", and is located at z=25 mm and r=0 mm, which is in the shear layer delimiting the central recirculation zone; the second position denoted "B" is located outside the central recirculation zone at z=25 mm and r=15 mm. As outlined earlier, the numerical prediction of the ignition event at each location is based on the infinitely fast and the finite rate chemistry assumptions. Thus, for each of the three simulation approaches mentioned above, the corresponding numerical ignition event is captured through the instantaneous contours of temperature, and is compared to experimental images of the ignition event provided by a high-speed camera. As mentioned earlier (Section 5.2), a successful spark ignition event consists of a flame kernel initiation, its propagation to ignite the neighbouring flammable zones, and a global flame stabilization. For this bluff-body burner configuration, experimental results show that success or failure of an ignition event can be noticed during the next 50 ms after sparking at a given location. The monitoring of the numerical ignition event is therefore restricted to the first 100 ms, and when a failed ignition event occurs with standard spark parameters, the spark strength (energy and/or duration) is increased within the allowable experimental limits. Figure 5.19 and Figure 5.20 show these comparisons for the two different spark locations mentioned above.

For each of these figures, three numerical predictions of the ignition event are shown with respect to two types of simulations: the simulations based on the finite rate chemistry (i.e. FGM tabulations populated by diffusion and premixed flamelets, respectively), and the infinitely fast chemistry (i.e. BML) assumptions. More explicitly, Figure 5.19 shows some sequences of the ignition event assuming the spark initially deposited at the location "A". One can notice that, each of the three simulation approaches leads to a successful ignition event. However, by contrasting the total time required to achieve the full ignition of the burner in the numerical predictions with the experimental results, it is found that unlike the FGM methods, the BML model predicts the full ignition of the burner earlier than

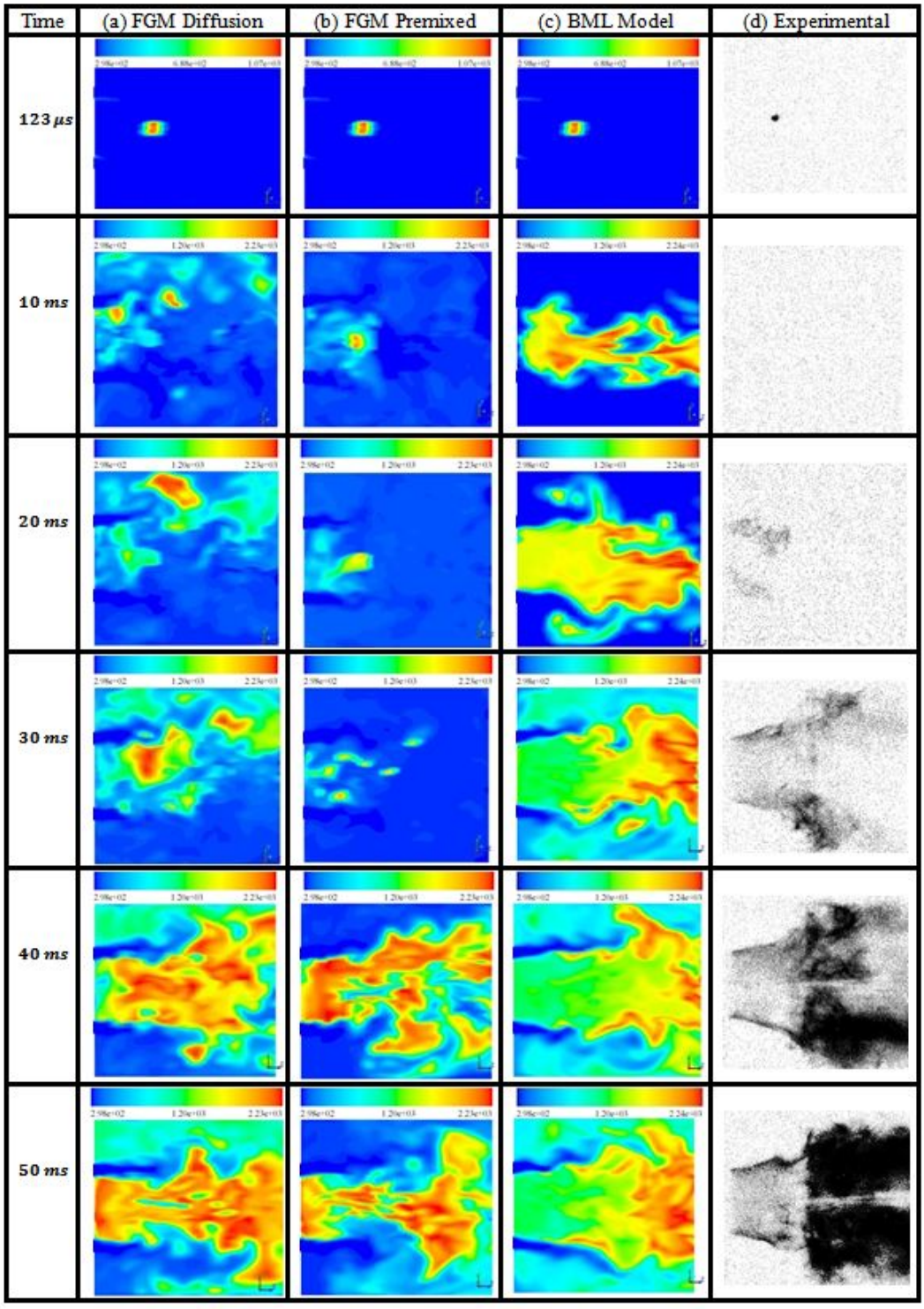

Figure 5.19: Numerical ignition events compared to the experimental ignition events provided by a high-speed camera (Ahmed et al., 2007); they are captured using the instantaneous contours of temperatures (K) for location "A"

suggested by the experiment. This may be related to the overestimation of the reaction rate caused by the infinitely thin flame assumption made in the BML formulation, especially in the zones such as flame holder wakes which feature high strain rate due to fuel-air mixing. According to predictions based on the FGM method, it can be seen that, the FGM based on premixed flamelets, even generated over a range of equivalence ratios leads to substantial discrepancies in the overall prediction of the ignition events. As outlined in the section devoted to the FGM methods, the strain rate due to fuel-air mixing as well as other relevant effects cannot be captured using premixed FGM since the diffusion of mass across iso-mixture fraction surfaces are neglected. As expected, the diffusion flamelet-based FGM method leads to a relatively reasonable prediction of the whole ignition event. This superior performance of diffusion FGM may be justified by the relative suitability of the model assumptions with the experimental configuration, and the ability of the model to account for strain rates due to fuel-air mixing and thus diffusion fluxes across iso-mixture fraction surfaces, which are more prominent in the investigated configuration. Each of the numerical ignition sequences summarized in Figure 5.19 provides a step-by-step view of the ignition event, with an initial flame front propagating towards the bluff-body, and subsequently, the propagation of the flame kernel from the zone around the bluff-body to the downstream region. This propagation behavior is related to the dynamics of recirculation zones along with those of local triple flame structures that may result from the partially-premixed combustion mode occurring in the flame zone. It can also be noticed that the experimental ignition sequence corresponding to this spark position "A" does not show any flame front during the early ignition period (i.e. $t \in [0, 20ms[$). However, the flame zone should not be viewed as extinguished. Indeed, as advocated by the experimenter, this behavior can be explained by the low heat release which prevails when the initial flame kernel reaches the rich mixture around the bluff-body so that the flame kernel dynamics are not detectable by the camera. In the second stage of the simulations, whose results are shown in Figure 5.20 and Figure 5.21, the spark energy is deposited outside the recirculation region at location "B" (i.e. z=25 mm and r=15 mm).

As reported by the experimenter, the spark deposition at this location may lead to either successful or failed ignition event depending on the flow conditions that prevail at the moment of the spark discharge. For this spark location "B", three kinds of failed ignition events were recorded in the experiment: in the first case, a spark deposition was followed by no indication of any flame kernel initiation; the second scenario showed a flame kernel initiation after the spark, followed by a flame propagation downstream from the burner that subsequently blows off; the last scenario was very close to a successful ignition event, since the spark deposition was accompanied by a kernel initiation, a flame propagation and a stabilization for a short period of time (around few milliseconds), but followed by a global flame extinction. When a spark having the characteristics mentioned earlier for the location "A" (i.e. spark duration of 500 μs, spark energy of 200 mJ and initial spark kernel size of 1 mm) is applied at location "B", all the three simulation approaches lead to the first type of failed ignition events reported earlier. By increasing the spark energy at location "B" while maintaining the spark duration (i.e. by using 400 mJ instead of 200 mJ), the second type of failed ignition event is observed for each of the three approaches (BML, premixed-FGM and diffusion-FGM) as illustrated

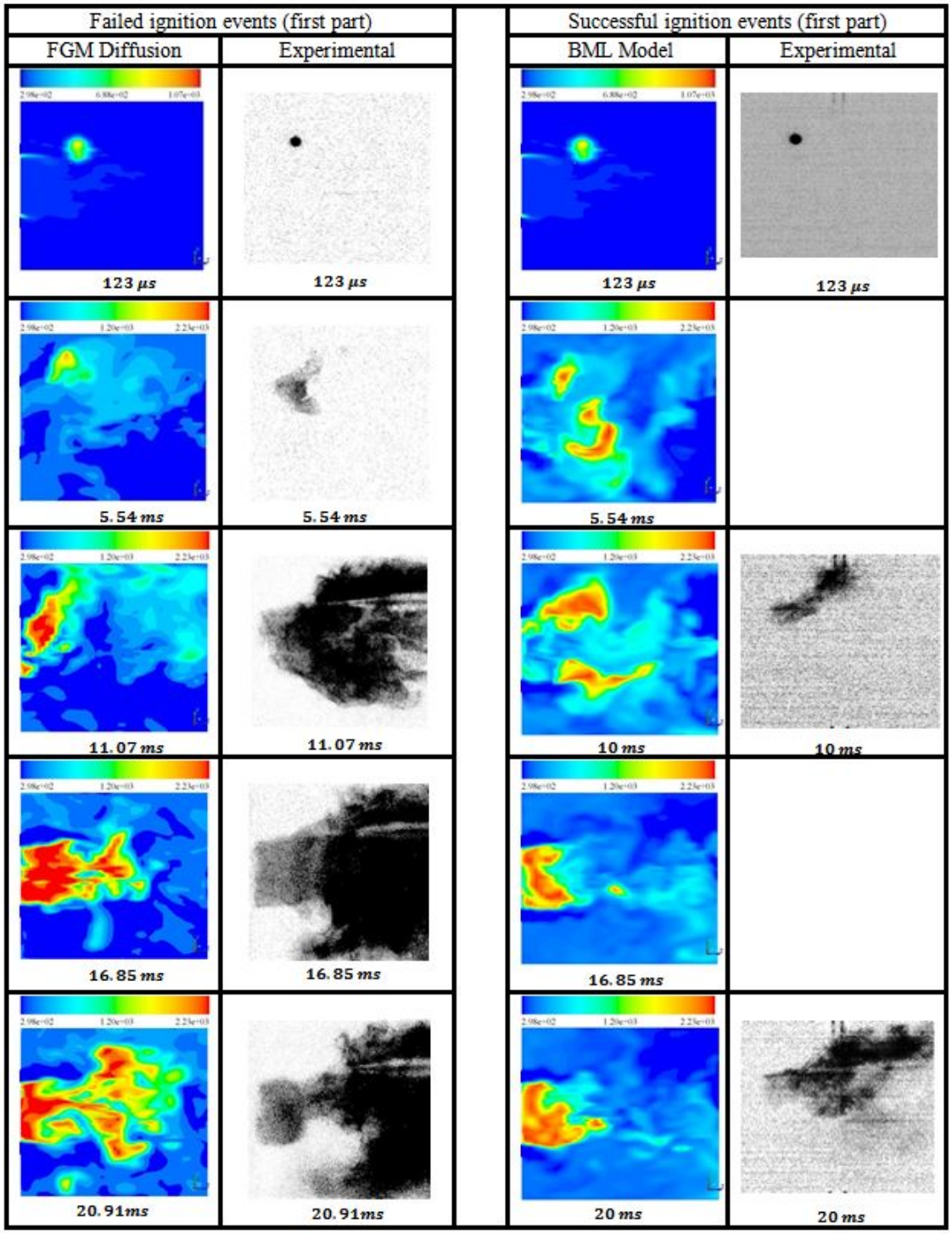

Figure 5.20: Comparison of the numerical ignition events with high-speed camera images of the ignition sequence for location "B" (Ahmed et al., 2007). The time range considered in this first part is $t \in [0, 20.91ms]$.

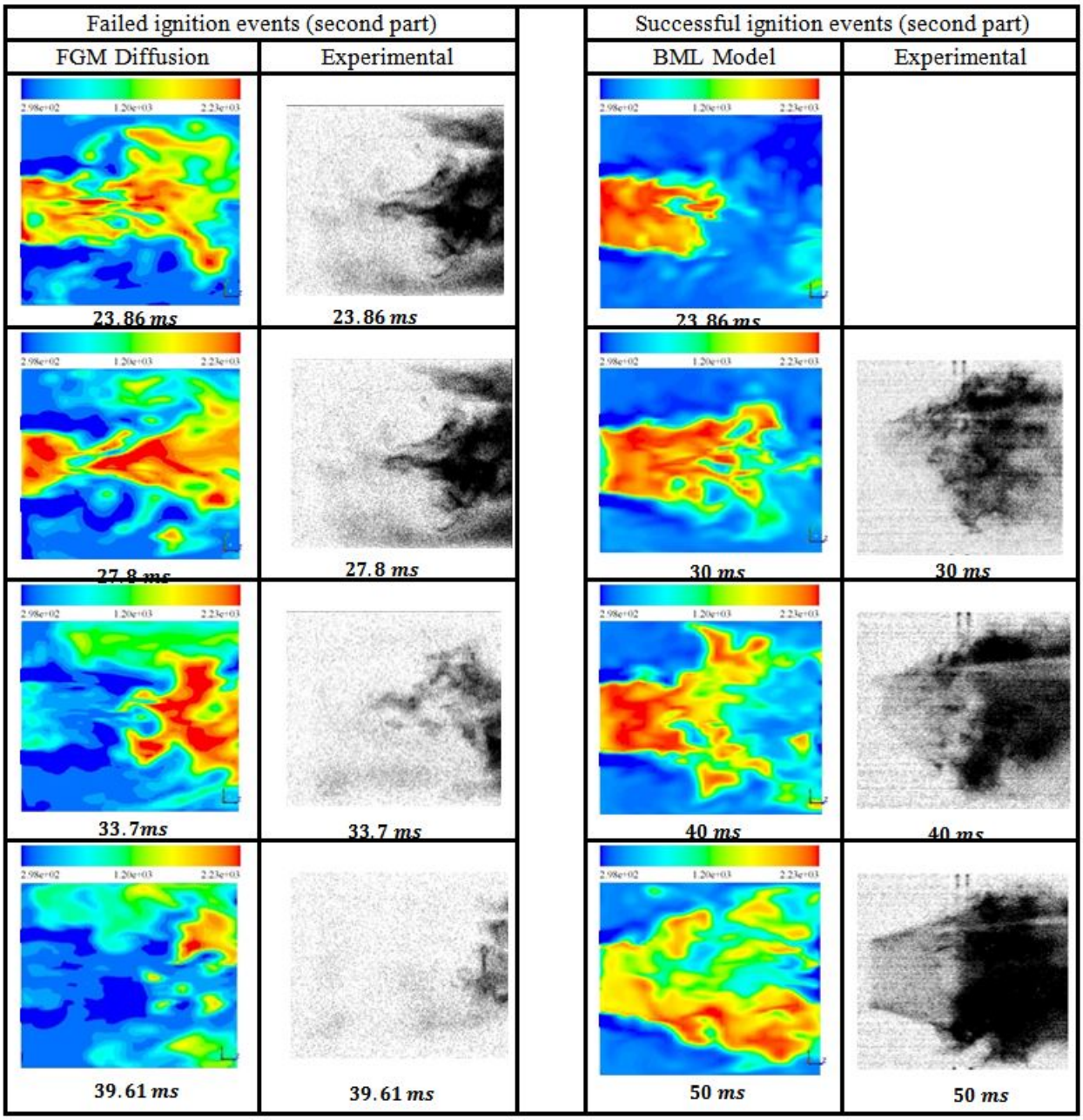

Figure 5.21: Comparison of the numerical ignition events with high-speed camera images of the ignition sequence for location "B" (Ahmed et al., 2007). The time range considered in the second part is $t \in]20.91ms, 31.61ms]$.

in the left part of Figure 5.20 and Figure 5.21 with the simulation results based on the diffusion FGM (the predictions based on premixed FGM and BML models follow the same trends). However, by further increasing the spark energy and the spark duration (i.e. using 500 mJ and a duration of 10 ms), a successful ignition event is achieved at location "B" as illustrated in the right part of Figure 5.20 and Figure 5.21 using simulations results based on the BML model (the FGM predictions follow the same trend). Based on the results corresponding to these two spark locations, it appears that, for a bluff-body stabilized burner equipped with a spark-based igniter, a successful ignition is more likely to be achieved by sparking at some specific locations within the central recirculation zone whose sizes are known to be close to the bluff-body diameter. In addition to the high ignition probability, such locations allow minimizing the ignition energy requirements as well as the spark duration.

In order to further investigate the effect of the spark location on the global ignition event, simulations based on four additional spark locations, namely, the locations "C", "D", "E" and "F" are conducted. The coordinates of these locations are explicitly given in Table 5.1, and are portrayed in Figure 5.22.

Regions of the spark location	Within the CRZ			Outside de CRZ		Shear layer delimiting the CRZ
Spark locations	A	E	C	B	D	F
Coordinates (Z;r)	(25;0)	(12.5; 0)	(20; 0)	(25; 15)	(25; 25)	(20; 12.5)

Table 5.1: Axial(z) and radial(r) coordinates of each spark locations (z and r in mm).

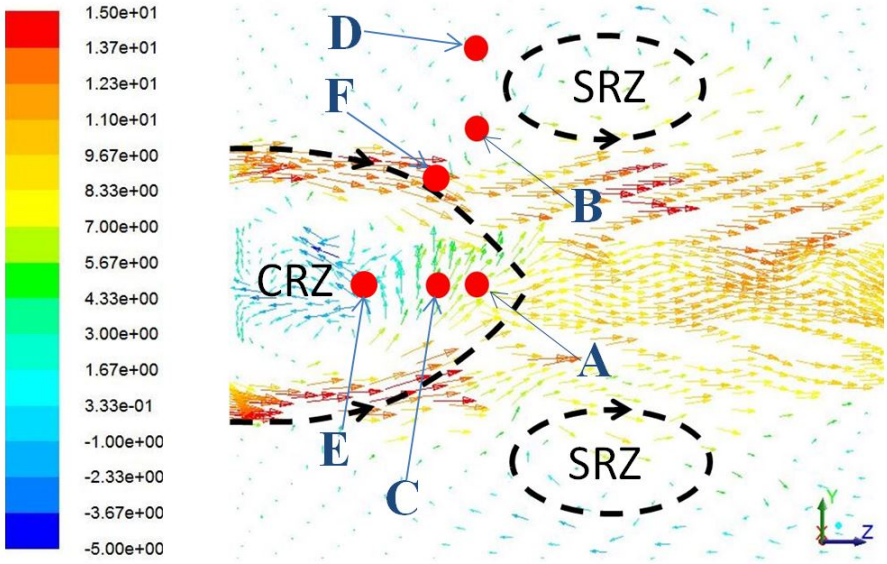

Figure 5.22: Illustration of the spark locations using the velocity field colored by the axial velocity (m/s) on the isosurface x=0. SRZ and CRZ stand for the side and central recirculation zones, respectively

The numerical ignition sequences corresponding to each of the four additional spark locations are shown in Figure 5.23. In addition to the successful numerical ignition event obtained earlier by sparking at location "A", and qualitatively validated through high-speed camera images as shown in Figure 5.19, further numerical ignition events obtained by sparking at locations "E" and "C" confirm that a successful ignition event is achieved when the spark is deposited at some specific locations of the central recirculation zone, namely, the locations of the burner mixing zone exhibiting a fuel-air mixture within the flammability limits. A successful ignition event is also achieved by sparking at another location in the shear layer bordering the central recirculation zone, namely, at location "F". Unlike other locations of the burner combustion zone, the ignition probability at this location is expected to be relatively high, as this layer features nearly stoichiometric mixtures, reduced turbulence intensity, and is therefore propitious to a successful ignition. Also, a similar behaviour in terms of ignition mechanism is noted for all these ignitable locations of the recirculation zone; the flame kernel is initiated by the spark deposition, and then propagates towards the bluff-body before expanding to ignite the remaining burnable mixture. This flame propagation trend is mainly due to the dynamics of the central recirculation zone. The numerical ignition event obtained by sparking at "D", and shown in Figure 5.23, shows that a spark deposition far outside the central recirculation zone leads to a failed ignition event regardless of the spark parameters. Indeed, by contrasting this latter result for the location "D" with those found by sparking at the location "B" (see Figure 5.20 and Figure 5.21), one can notice that, for the location "B" also, no successful ignition event is achieved with the classical spark parameters mentioned earlier. However, unlike the location "B" for which an increase in spark energy and duration may lead to a successful ignition event as shown in the right part of Figure 5.20 and Figure 5.21, the spark deposition at the location "D" leads to a failed ignition event, even with the strongest spark parameters mentioned above. For each of the three spark strengths reported earlier, the combustion zone does not show any flame kernel propagation when sparking at the location "D". Instead, as illustrated in the fourth column in Figure 5.23, a progressive diffusion of the energy supplied by the spark is observed within the burner mixing zone. This result is mainly related to the mixture characteristics at this location: unlike contours and profiles of velocity which allow deducing that aerodynamics is propitious to ignition because of the low turbulence intensity at this point, the instantaneous contour of the mixture fraction shown in Figure 5.16(d), the iso-surfaces of the mean mixture fraction shown in Figure 5.17(a), and the radial profiles of the mixture fraction shown in Figure 5.18 show that the mixture is extremely fuel-lean at this location. The value of the mixture fraction around this location is below the lean flammability limit and consequently, the flame kernel cannot propagate to ignite the whole burner.

The intermediate study conducted in the current subsection allowed formulating a CFD methodology to retrieve both transient and steady combustion regimes. The final CFD strategy is selected after testing various CFD methodologies formulated beforehand, which consist in LES-turbulence model in interaction with different combustion models paired to a subgrid spark-based ignition (DIPK) model. The prediction capability of each of the formulated CFD methodology is evaluated by using a bluff-body stabilized burner offering some various practical assets mentioned so far, namely, its ability to

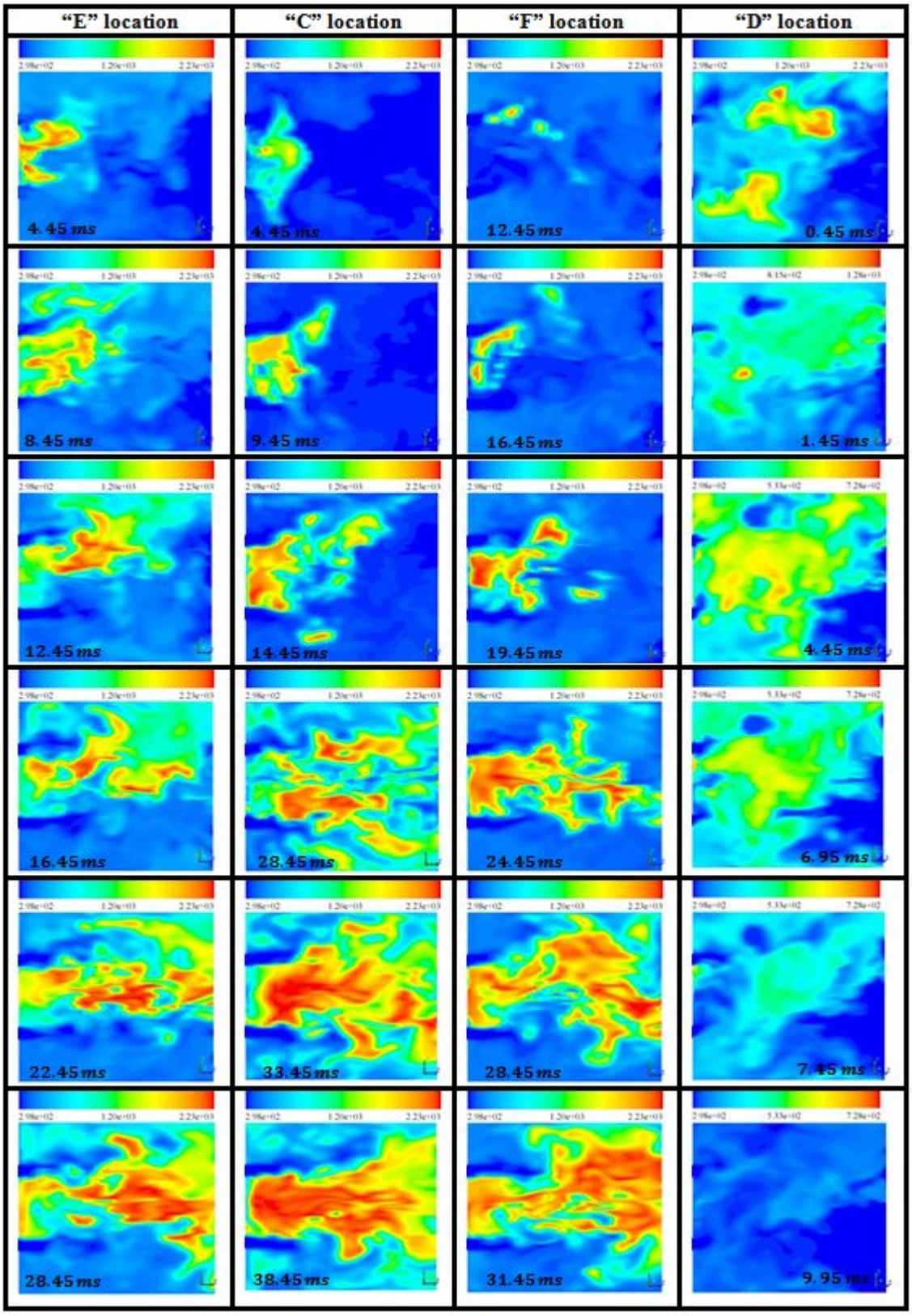

Figure 5.23: Numerical ignition events corresponding to the four additional spark locations listed in Table 5.1 and portrayed in Figure 5.22

produce flames with changing combustion features such as stability, efficiency, pollutant formation and heat transfer through variation in design and operating conditions. Plus, detailed experimental data are available to allow a step-by-step validation of the CFD methodology formulated. Based on the results discussed above, one can deduce that the CFD model consisting of the LES-turbulence model, paired with the DIPK model and a robust combustion model such as FGM, allows predicting reasonably and inexpensively the whole ignition event. Similarly to the experiment, the numerical predictions show that the ignition success resulting from a spark deposition strongly depends on the spark location, and therefore on the aerodynamics and mixing fields at the moment of the spark deposition. Also, it is found that the regions providing the highest probability for the full ignition of the burner are located in the vicinity of the shear layer delimiting the recirculation zone. This result is first illustrated by the numerical ignition events corresponding to two spark locations, and is qualitatively validated by the corresponding high-speed camera images from the experiment. Subsequently, the same result is supported by the numerical ignition events corresponding to four additional spark locations which are respectively located in the central recirculation zone, and in the shear layer delimiting the central recirculation zone. The high ignitability of such zones is mainly due to the fact that they feature mixtures within the flammability limits, and allow the flame kernel to reach a size that can sustain high strain rates. Finally, it is noticed that in each successful ignition event, the dynamics of the central recirculation zone always drives the flame kernel towards the central recirculation zone prior to the flame kernel expansion and the subsequent full ignition of the burner. Based on the promising results obtained using this burner which was designed to burn gaseous fuels, the CFD methodology is extended to spray combustion with the aim of predicting both transient and steady combustion regimes in liquid-fuelled combustion chamber; such an extension is discussed in the next section.

5.3 Transient and steady combustion regimes in a swirl-stabilized tubular combustion chamber

To extend the previous CFD methodology to spray combustion, the following modifications are made. The spray module is newly coupled to the CFD methodology used in the gaseous case (i.e. bluff-body stabilized burner), and the ignition model is slightly modified so as to match the speed of the flame kernel expansion for heavy hydrocarbons such as those found in Jet A-1 which is the fuel under investigation. The modification consists of implementing a correlation for the kerosene laminar burning rate as a function of temperature, pressure and equivalence ratio. The modified DPIK model relies on the same basic assumptions as the original version, with some additional simplifications as discussed in the previous chapter (see Subsection 4.4.6 in Chapter 4). According to the combustion model, the FGM is still retained. However, as recalled throughout the section devoted to the combustion models (see Section 1.4 in Chapter 1, or Subsection 4.4.4 in Chapter 4), the liquid-fuelled combustion chamber, as well as the previous investigated burner are predominantly non-premixed. Thus, the FGM based on diffusion flamelets is used, and the latter are generated using the reduced chemical kinetic mechanism that was previously used to investigate the steady combustion regime (i.e.

the reduced chemical kinetic mechanism consists of 1 024 elementary reactions among 139 species). The newly formulated CFD method is reapplied to the swirl-stabilized combustion chamber (see Figures 3.1 and 3.2), with the aim of predicting the ignition sequence and the resulting steady combustion regime.

When considering the transient combustion regime, in this case the prediction of the ignition sequence following the spark discharge, particular attention is paid to the ability of this new CFD method to capture the main three steps of the ignition sequence which consist of the flame kernel initiation, its propagation to fully ignite the combustion chamber, and the flame stabilization preceding the steady combustion regime. For the steady combustion regime, the ultimate goal lies in the improvement of the predictions of species characterized by low reaction rates such as CO, since an accurate prediction of such species may guarantee the ability of the CFD methodology to reasonably predict other pollutants, and thus to achieve the second objective of the current study.

For the simulation, the previous structured mesh consisting of 2.16 million hexahedral elements is used, and the same mesh adaptations are performed in order to capture reasonably the spray dynamics, the mixing process in the first instant of the evaporation phase, and both the shear layer and the boundary layer effects. As in the previous investigation based on the steady combustion regime, the mesh adaptation is motivated by the LES dependency on the mesh resolution. The grid is refined near the solid boundaries and in particular around the combustor axis and the injector exit: more precisely, about 60% of elements are located in these zones of the combustion chamber. The quality of the LES results based on the final mesh resolution is assessed through the turbulence resolution parameter defined by Pope [2004]. By using this parameter, it is found that approximately 85% of the turbulence kinetic energy is resolved with the final mesh resolution. Based on this information, a rough approximation consisting of neglecting the turbulence dispersion of the droplets is considered. According to the numerical algorithms, the Semi-Implicit Method for Pressure Linked Equations (SIMPLE) algorithm is used for the pressure-velocity coupling; the transient derivatives are discretized using the second-order implicit scheme, which is based on an iterative time-advancement algorithm; the bounded central differencing scheme is used for the momentum equation while maintaining the second-order scheme for the discretization of the transport equations for the energy and the "tracking" scalars. All the transport equations are then solved iteratively for a given time-step until the convergence criteria are met before moving on to the next time step. According to the combustion model, the diffusion-FGM whose structure is depicted in the previous chapter (see Figure 4.5 in Chapter 4) is implemented to enhance the combustion model. The Lagrangian analysis of the spray is performed using the DPM, with the coupling approach used in the previous simulations. The simulation time step is defined based on a representative convection time scale, a representative droplet residence time, and the time scale governing the spark phases. The cold simulation is started with initialized fields, and are conducted with respect to two intermediate steps: first, the computations of the unsteady non-reacting flow without coupling with the liquid phase to convergence, and second, the computations to convergence with the inclusion of the liquid phase. The two steps of the cold

flow simulations are performed over a time period equal to 1 500 time steps, which is approximately equal to 6 times the characteristic computation time. As for the previous simulations, this first phase of the simulation is devoted to eliminate the artificial effects of the flow initialization, and to obtain an initial flow evolving naturally with the imposed boundary conditions, while becoming statistically steady. Subsequently, the ignition model is coupled to the LES-spray-solver, and the simulations are continued for 4 000 additional time steps. During this second phase, the ignition sequence is recorded by monitoring the changes in reactive scalars (i.e. progress variable or temperature).

Two sparks are deposited at two different locations in the shear layer between the cone of fuel and air; the choice of these locations are oriented by the outcomes of the previous investigations based on the bluff-body stabilized burner. The energy and the duration of each spark are respectively set to 500 mJ and 10 ms, and the initial spark kernel size is set to 2 mm which corresponds to the gap between the electrodes of the spark plug. At the end of this second phase, which is characterized by the full ignition of the combustion chamber and a global flame stabilization, simulations are continued for 3 500 additional time steps under sample statistics mode to capture spray flow and combustion properties governing the steady combustion regime. This additional number of time steps is sufficient to yield the statistical convergence.

5.3.1 Ignition sequence

A qualitative overview of the whole ignition sequence in the combustion chamber is provided in Figure 5.24. For sake of clarity, the ignition sequence is timed from the instant corresponding to the end of the cold flow simulations. One can see the flame kernel initiations at the two spark locations within the shear layer formed between the spray cone and air. These flame kernel initiations are followed by their propagation as illustrated by the subsequent contours, and the global flame stabilization which occurs between 41 and 47 ms. These results of the ignition event obtained by sparking in the shear layer defined between the spray cone and air agree with the outcomes of the previous simulations devoted to the investigation of the spark locations propitious to a successful ignition event.

5.3.2 Aerodynamics of the combustion chamber predicted by the new CFD model

Figure 5.25 and Figure 5.26 show the radial profiles of the three velocity components with their corresponding fluctuations, respectively. The same prediction trends as those of previous simulations are observed for all the velocity components and the corresponding fluctuations at the various cross sections of the combustion chamber as in the previous simulations.

As mentioned when discussing the previous simulation results, the discrepancies noted for the axial and radial velocity components at some stations may be related to the dynamics of the spray which is particularly dense in this zone and consequently, more sophisticated models are necessary to accurately capture the spray dynamics. Further, some turbulence-spray interactions that need to be accounted for to properly model the turbulence-spray coupling are neglected; such interactions

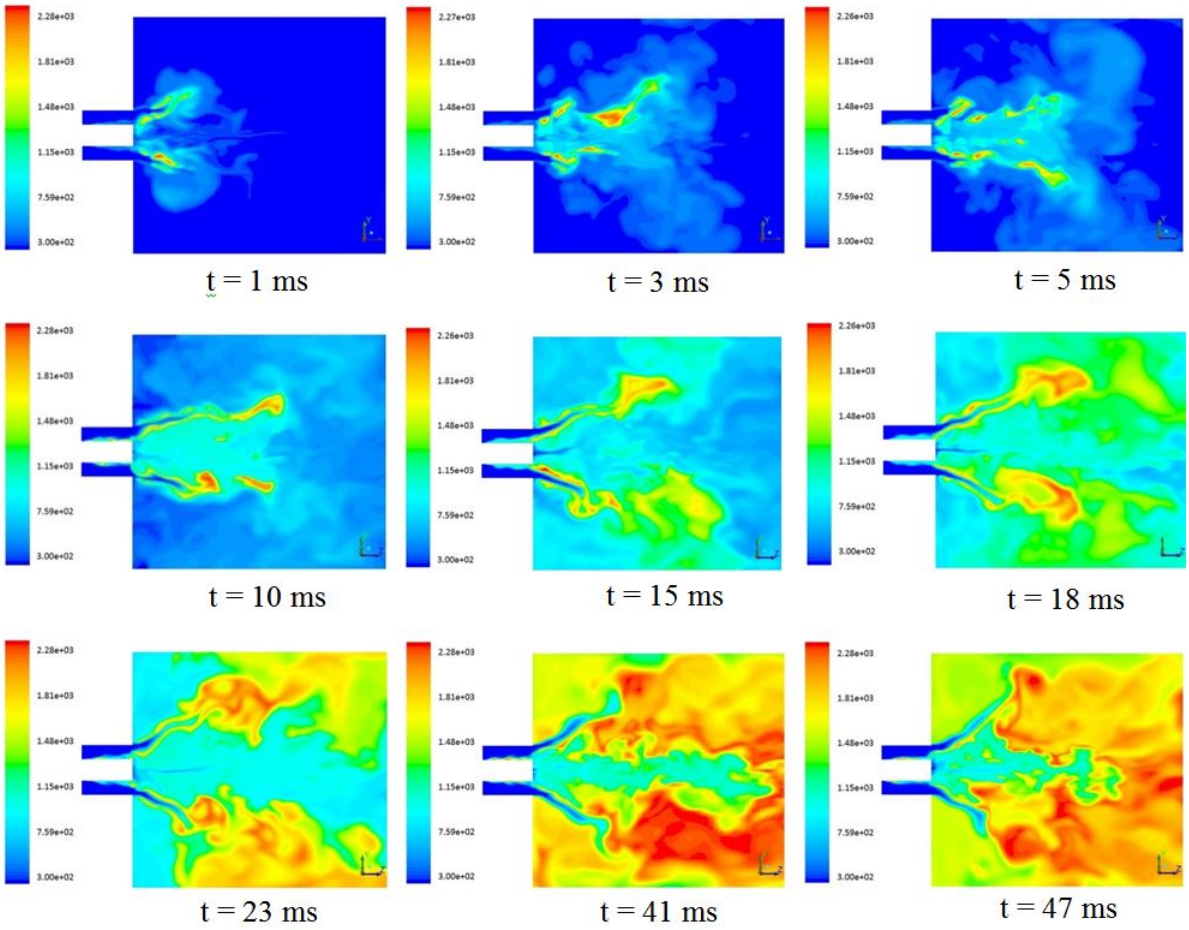

Figure 5.24: Spark-based ignition sequence in the combustion chamber. The flame front propagation is tracked through the instantaneous contours of temperature (K)

include the turbulence dispersions of the droplets. From the radial profiles of the axial velocity, the negative values of the velocity show the presence of the recirculation regions. Also, it can be seen that, the initial development of the recirculation zones is slightly delayed in the numerical prediction compared to the experiment. This delay precludes the prediction of radial velocity in the cross section close to the injector orifice (z/R=0.5), and may be partly due to the spray dynamics as noted above. A possible way of improving this prediction would be the mesh refinement, and the implementation of a model to properly capture the spray-turbulence interactions. In spite of these discrepancies, a reasonable agreement is globally obtained for the aerodynamics of the combustion chamber as in the previous simulation based on the diffusion flamelet model.

5.3.3 Thermochemical state in the combustion chamber: steady combustion regime

The radial profiles of temperature and the corresponding fluctuations at some cross-sections of the combustion chamber are show in Figure 5.27 and Figure 5.28, respectively. For radial profiles

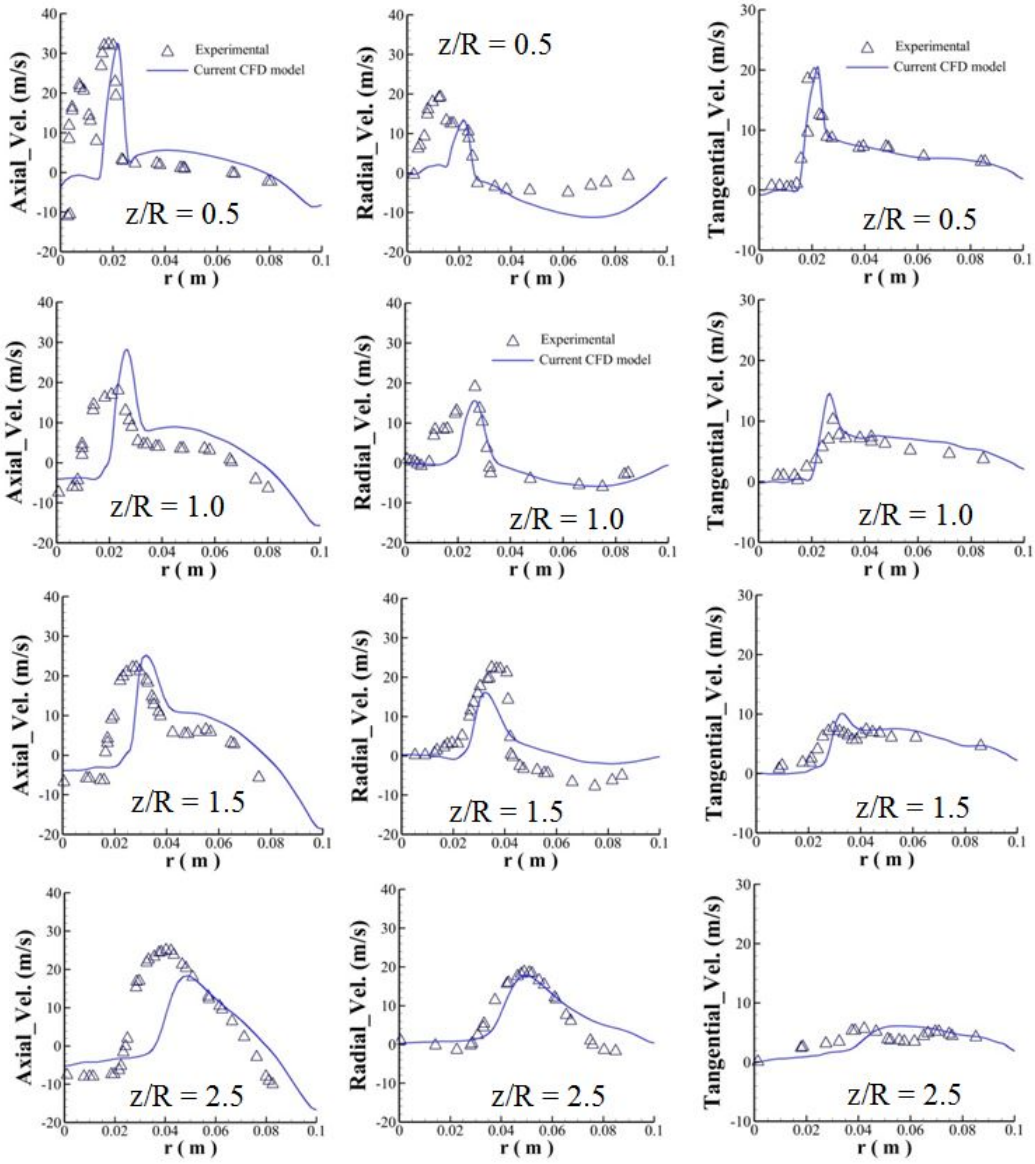

Figure 5.25: Radial profiles of the mean velocity components at various cross sections of the combustor

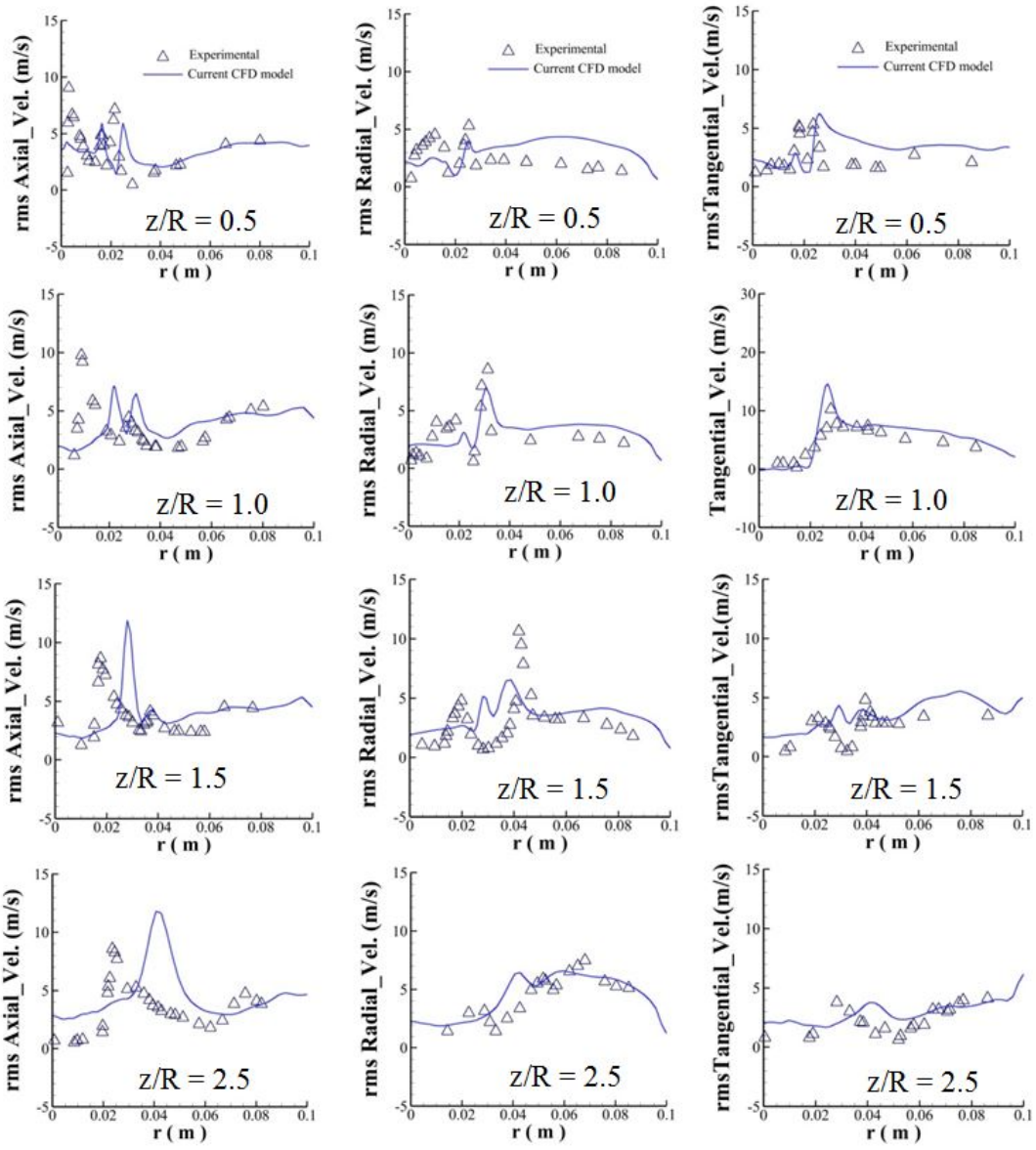

Figure 5.26: Radial profiles for the fluctuations of each velocity component at various cross sections of the combustor

of temperature in particular (see Figure 5.27), in spite of some discrepancies noted in the vicinity of the injector orifice, namely, the zone defined by $z/R \in [0.5; 2.0]$, one can see that the CFD leads to an overall reasonable agreement with experiments. The discrepancies found in the neighbourhood of the injector exit are mainly related to some drawbacks of the spray modelling approach which fails to capture accurately the spray dynamics, and especially, the spray-turbulence interactions in this zone where the spray is particularly dense. According to the temperature fluctuations shown in Figure 5.28, although the trends of the numerical results are similar to those of their experimental counterparts, it can be seen that they are over-predicted. A way to address this issue is to further increase the mesh resolution of the combustion chamber. However, such an improvement strategy would lead to additional needs in computing resources, which are not strictly justified when contrasting the computational expenses with the potential improvements in accuracy. Both numerical and experimental temperature profiles show two peaks in the vicinity of the injector exit; they emanate from the presence of the shear layer between the fuel spray cone and the entrained ambient air since such shear zones feature nearly stoichiometric mixture.

The radial profiles of major species, namely, the molar fractions of carbon dioxide and oxygen, are shown in Figure 5.29. A reasonable agreement in the zones close to the combustor axis can be noted. However, there are discrepancies in regions where the side recirculation zones are located. More explicitly, the CFD overpredicts the oxygen, and underpredicts the carbon dioxide in these regions. As discussed when investigated the steady combustion regime with the classical diffusion model, such a trend is due to the fuel distribution and therefore to the spray model and the related parameters since indicators of incomplete combustion such as carbon monoxide do not show any overprediction (see radial profiles of CO shown in Figure 5.30). Also, by contrasting the results in the regions close to the combustor axis (i.e. $r \leq 0.03$ m) with those in the regions further away in the radial direction (i.e. $r > 0.03$ m), it can be seen that an increase in mesh resolution in this zone is likely to mitigate these discrepancies.

According to the prediction of species governed by low rates such as CO, it is seen that the FGM improves remarkably their prediction. Indeed, in previous large eddy simulations of the steady combustion regime in the same configuration, namely, the LES based on the PDF method (LES-PDF) [Jones et al., 2012] and the LES based on the steady diffusion flamelet model (LES-SFM) [Fossi et al., 2015c], the biggest issue was mainly the prediction of slow species, since each of these two simulation strategies led to a reasonable prediction of the main flame trends. To provide an idea of the limitations of these previous simulation approaches in this regard, LES-PDF and LES-SFM predictions of slow species at some cross sections of the combustion chamber are extracted from each of these previous works, and are contrasted with those of the current CFD as shown in Figure 5.30. One can see a reasonable agreement with experimental data, suggesting the superior robustness of the LES-FGM approach, when considering the prohibitive computational cost incurred with the pdf-implementation of a reduced chemistry kinetic model such as the one used in the current study.

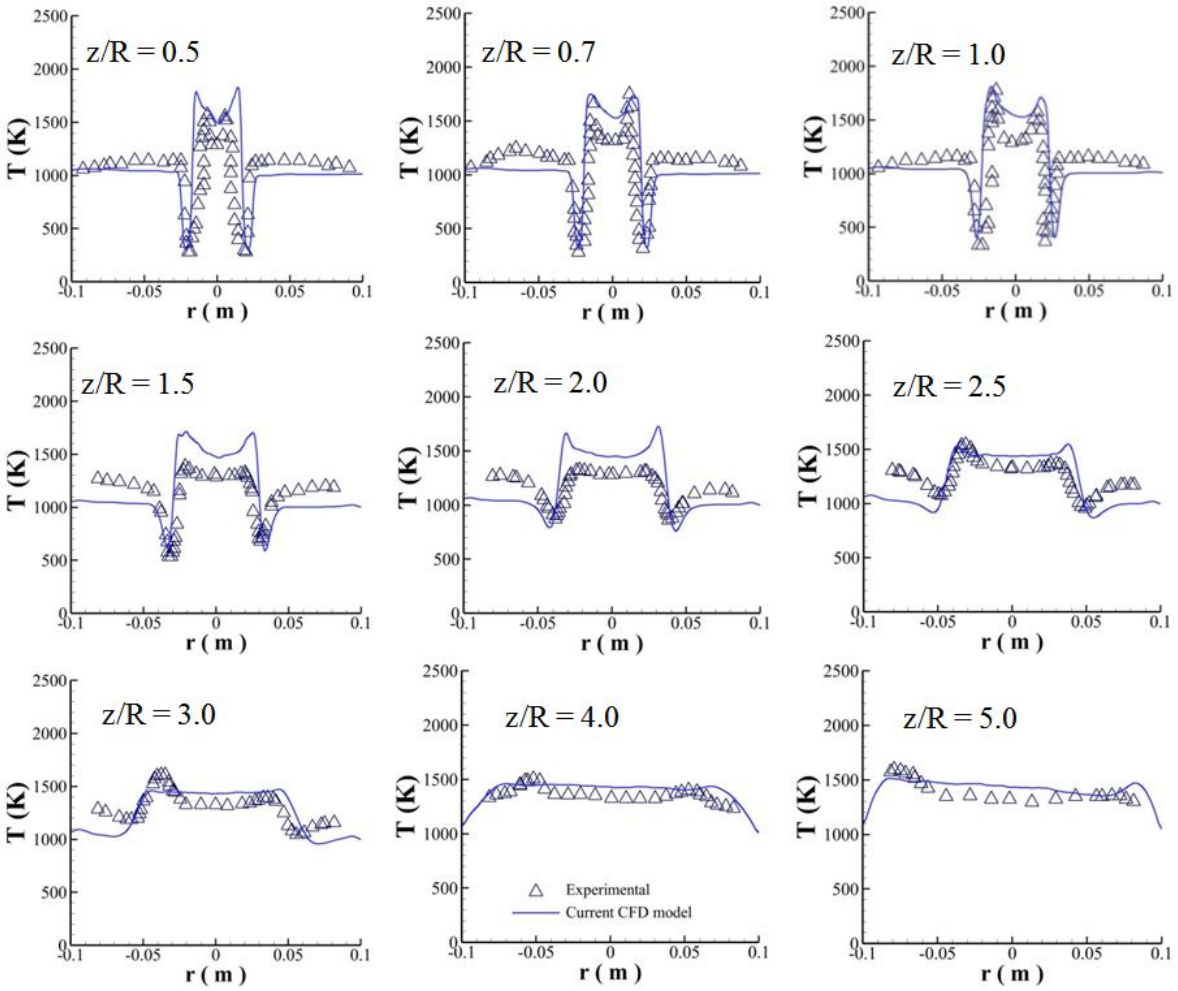

Figure 5.27: Radial profiles of the mean temperature at various cross sections of the combustion chamber

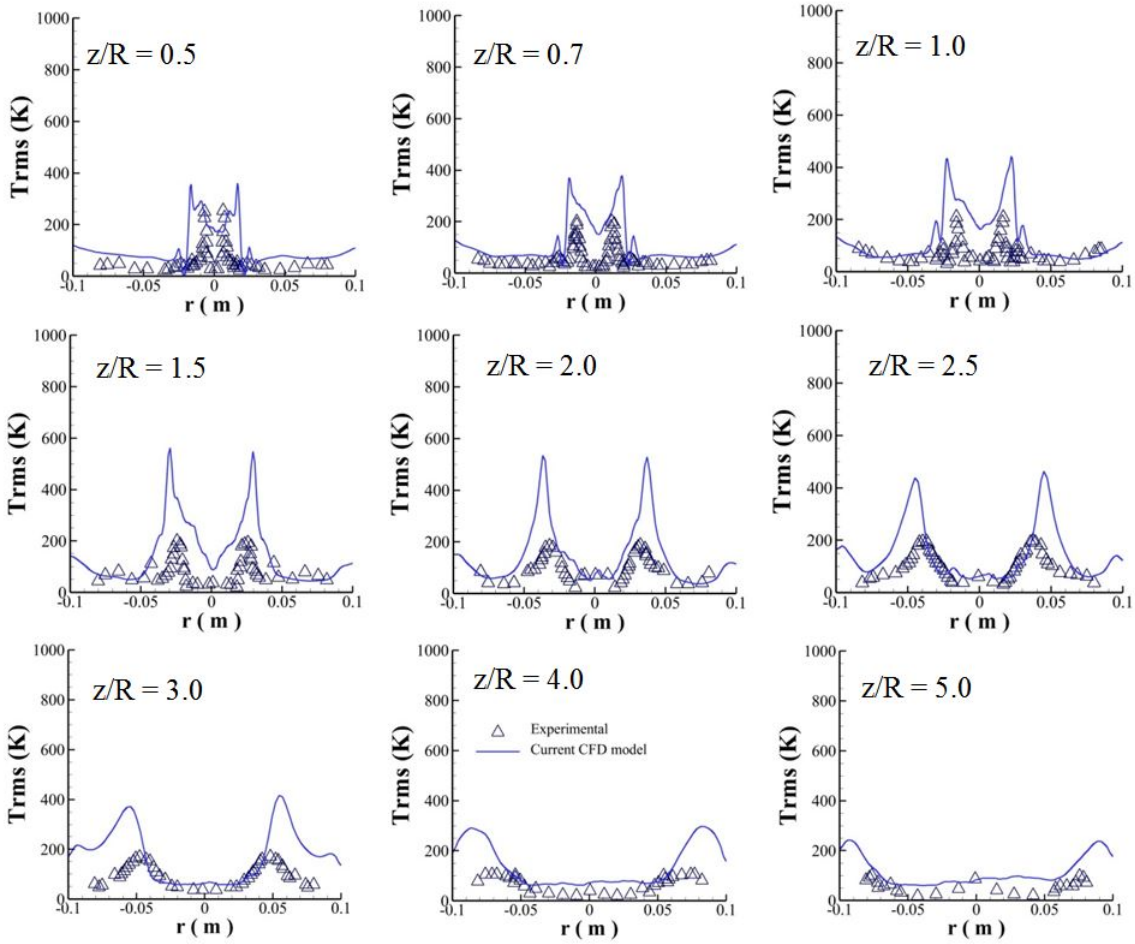

Figure 5.28: Radial profiles of the temperature fluctuations at various cross sections of the combustion chamber

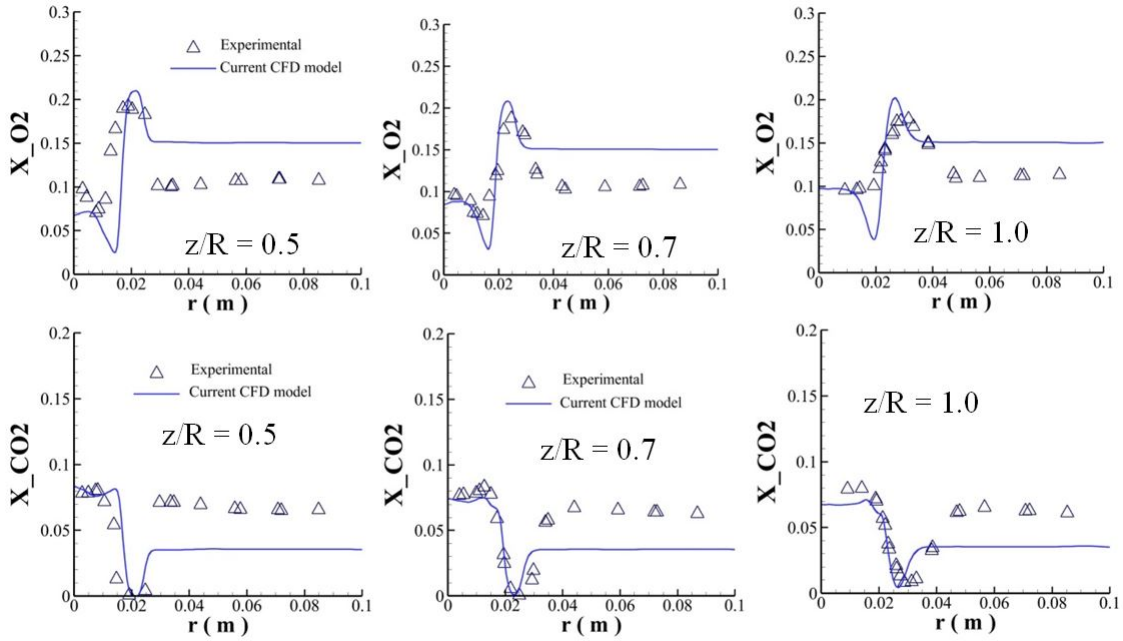

Figure 5.29: Radial profiles of the molar fractions of major species (CO_2 and O_2) at various cross sections of the combustion chamber

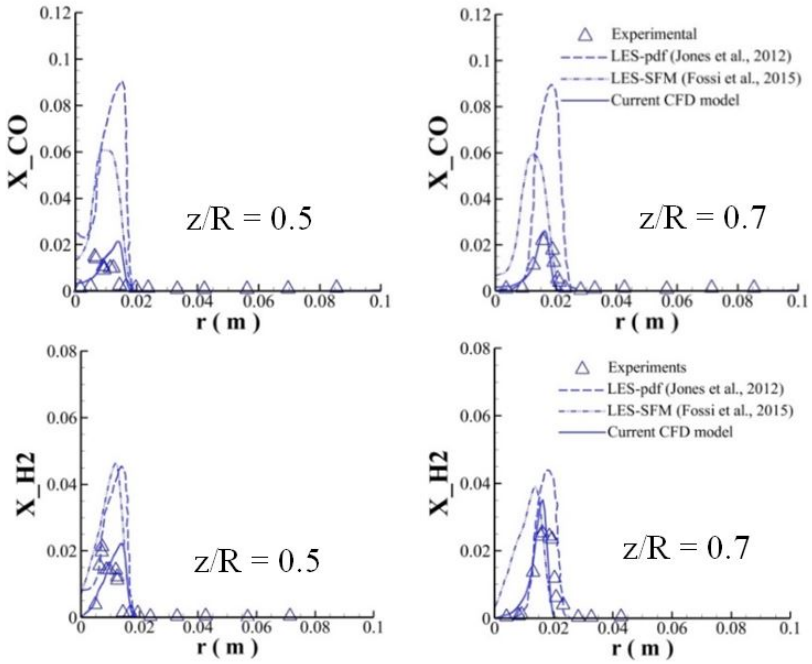

Figure 5.30: Radial profiles of the molar fractions of slow species (CO and H2) at various cross sections of the combustion chamber

5.4 Cold start and altitude relight in the P&WC scaled can combustor

This section focuses on the validation of the transient combustion regime using the third configuration presented in chapter 3 (see Figures 3.6 and 3.7). As mentioned in the previous chapter, for the cold start investigations, ten different test conditions are considered with respect to five test conditions for each of the two operating temperature selected ($T_3 = 283K$ and $T_3 = 233K$). Similarly, for the altitude relight investigations, eleven different test conditions are simulated with respect to five test conditions for the first operating altitude ($H_{al} = 15kft$) and seven test conditions for the second ($H_{al} = 35kft$). As portrayed on their corresponding experimental ignition envelope shown in Figure 5.31, Figure 5.32, Figure 5.33, and Figure 5.34, all the simulated test conditions are selected within and outside the experimental ignition envelope band. As mentioned so far, an ignition event is considered successful when the spark energy initiates a flame kernel that propagates to fully ignite the combustor, and leads to a stable flame. Each numerical ignition event is monitored over 100 ms following the spark deposit. However, to avoid overloading figures, only images corresponding to the period of time that illustrates the ignition sequence as described above are presented in each figure.

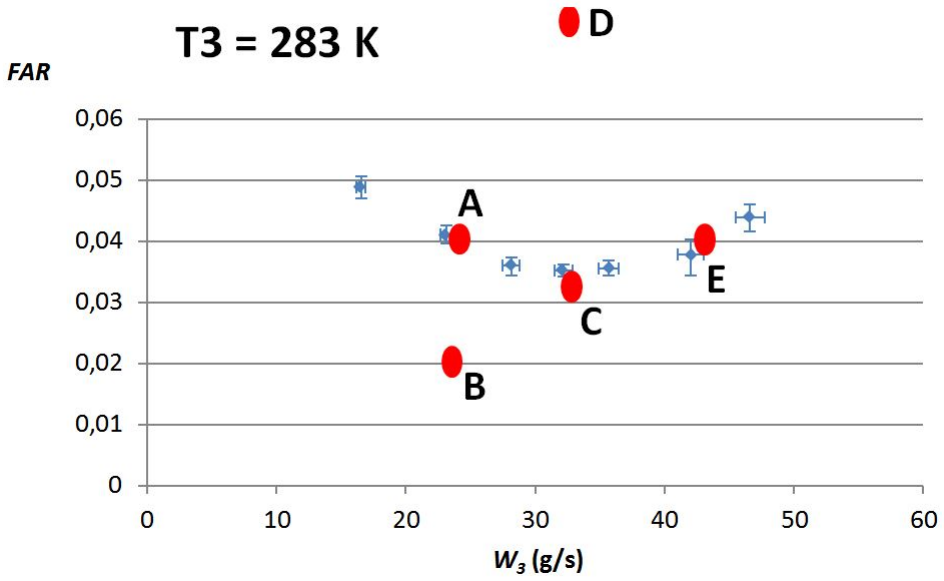

Figure 5.31: Cold start at 283 K with the simplex nozzle (Jean, 2017)

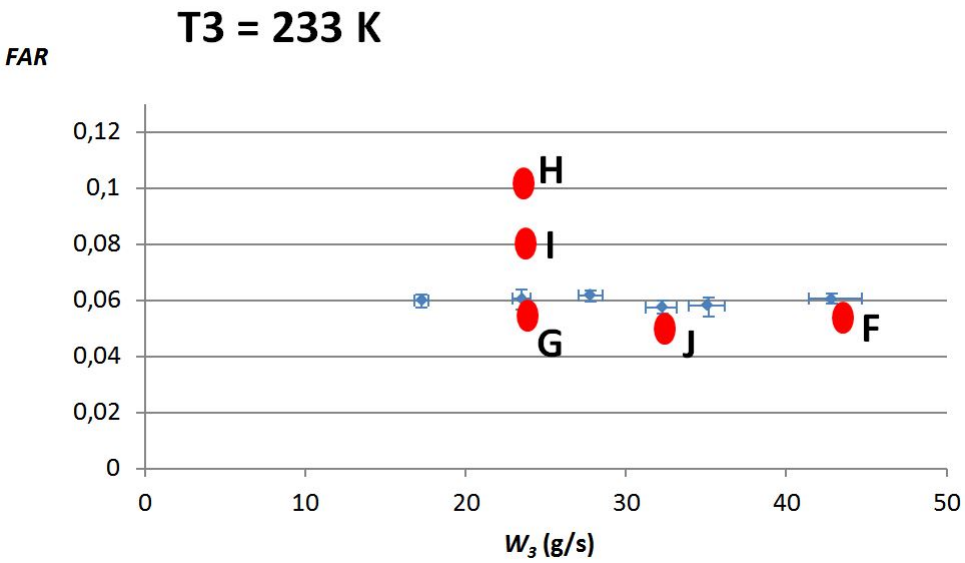

Figure 5.32: Cold start at 233 K with the simplex nozzle (Jean, 2017)

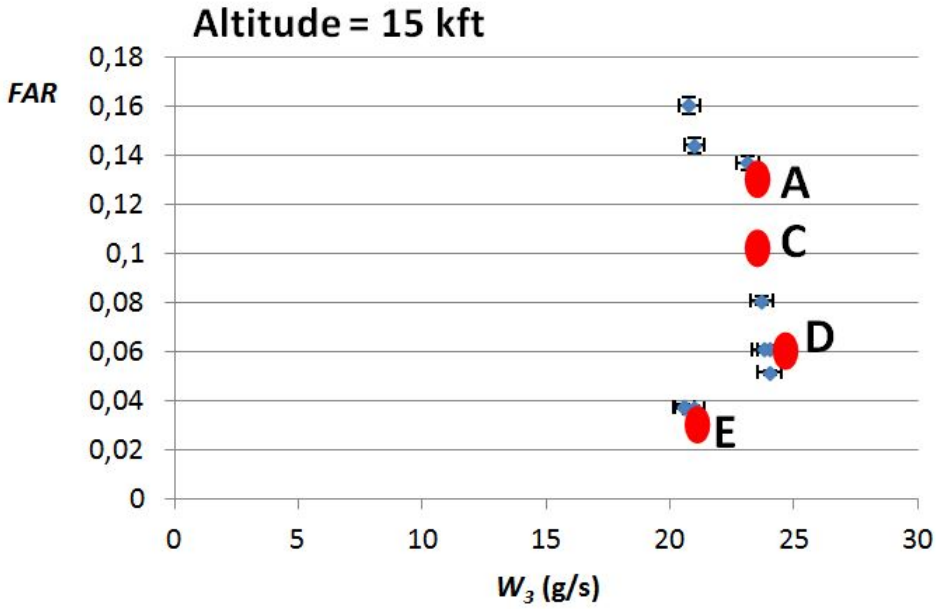

Figure 5.33: Altitude relight at 15 kft with the simplex nozzle (Jean, 2017)

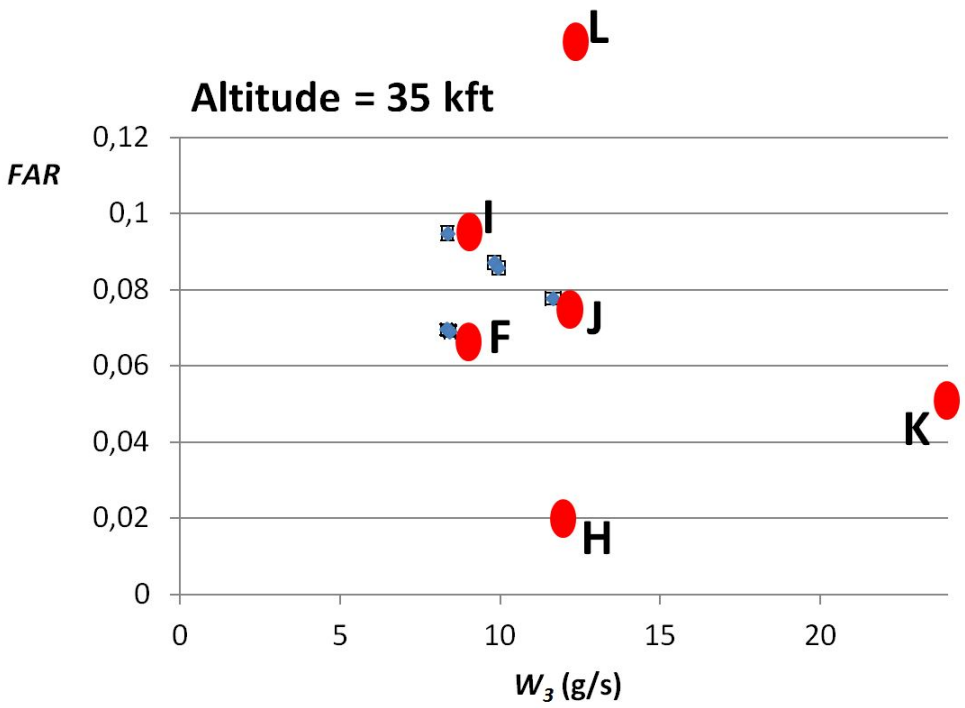

Figure 5.34: Altitude relight at 35 kft with the simplex nozzle (Jean, 2017)

5.4.1 Cold start at 283 K under various operating conditions with the simplex Injector

The CFD predictions for cold start corresponding to the test conditions "A"-"E", for an operating temperature of 283 K are shown in Figure 5.35, Figure 5.36, Figure 5.37 and Figure 5.38 through the instantaneous contours of temperature. These cold start operating conditions are explicitly given in Table 4.5 (Chapter 4), and they are portrayed in Figure 5.31.

From the results based on this first operating temperature (i.e. $283K \sim 10^oC$), the effect of the fuel-air ratio (FAR) and thus of the equivalence ratio, on the ignition event success can be identified. The test conditions "A" and "B" differ in terms of FAR only: the test condition "A" has a fuel-air ratio of 0.04, while that of the test condition B is 0.02. In order words, the test condition "B" is lean compared to the test condition "A", and the numerical prediction of the ignition sequence shows that the full ignition is delayed for the test condition "B". This delay becomes longer if the FAR is further decreased, and for some values an unsuccessful ignition event is noted, and consist of diffusion of the spark energy within the combustor without any flame kernel initiation. For the test conditions "A", "C" and "E", the mixture is sufficiently rich and the equivalence ratio lies in the flammability limits. Consequently, a successful ignition event is noted in each of these cases as shown in Figure 5.35, Figure 5.36 and Figure 5.38, respectively. However, although rich mixtures are propitious to a successful ignition event, it is worth mentioning that when the equivalence ratio exceeds a certain value, a failed

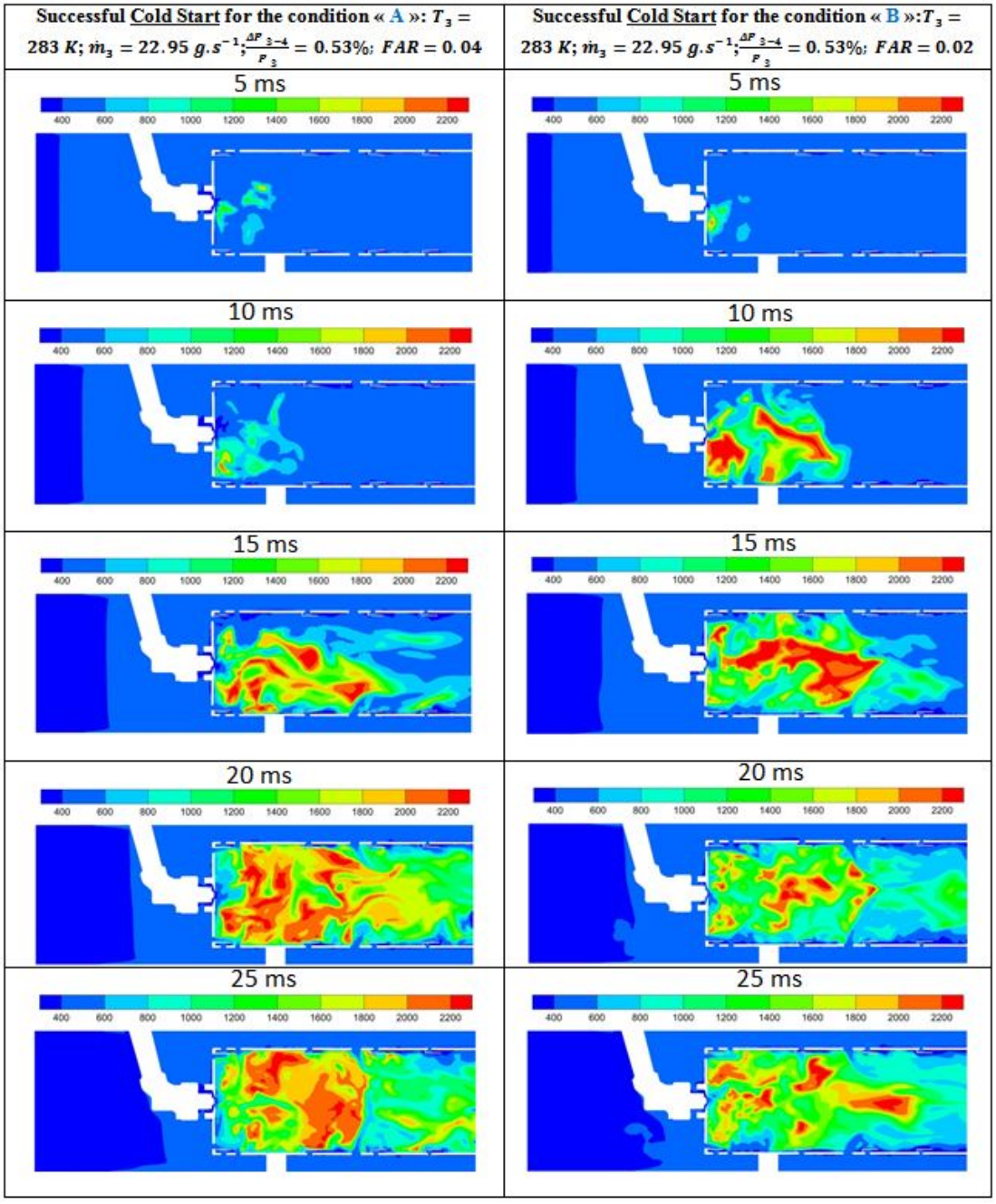

Figure 5.35: Cold start at 283 K for the operating conditions “A” and “B”. T(K)

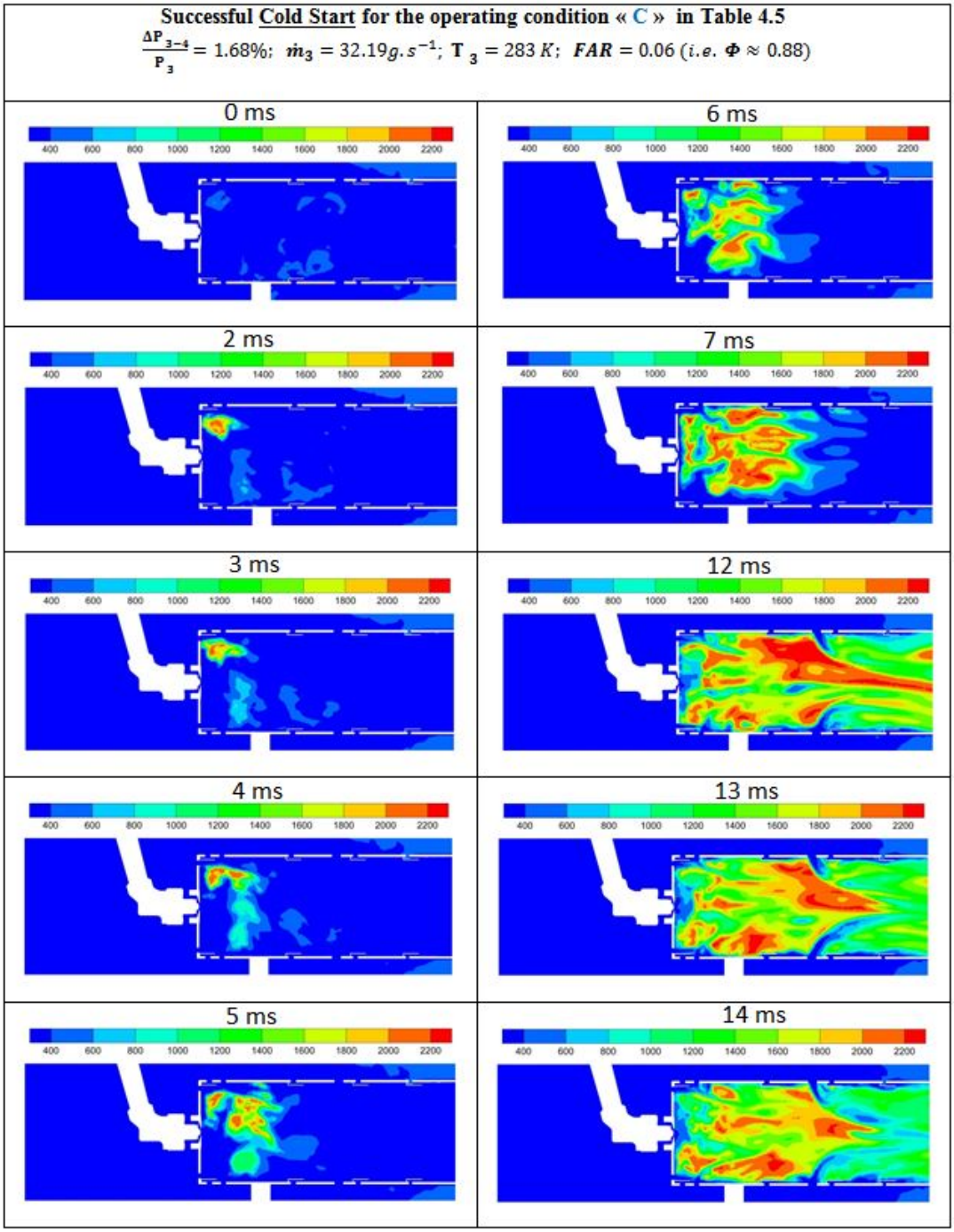

Figure 5.36: Prediction of the ground cold start at 283 K for the operating condition “C”. T(K)

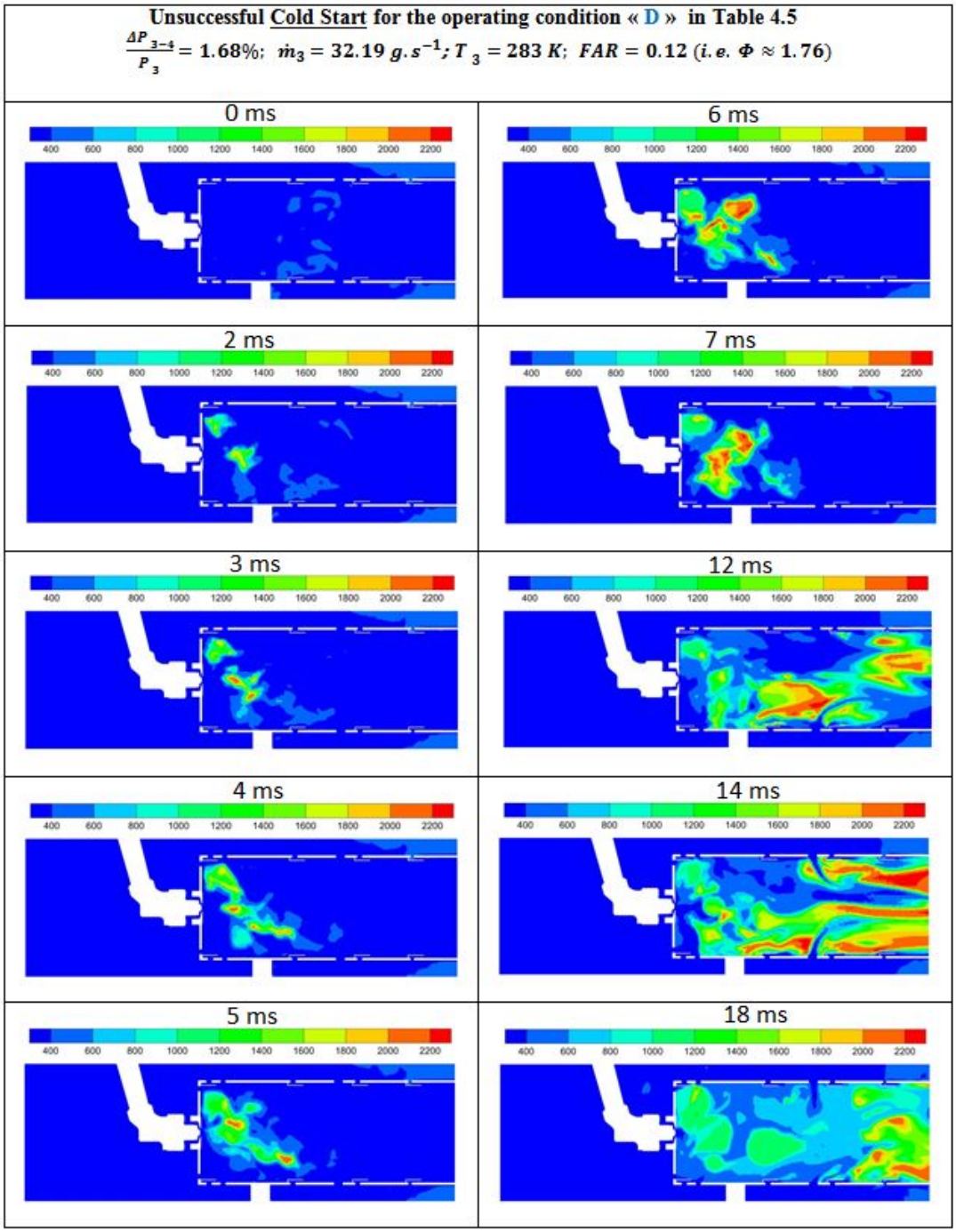

Figure 5.37: Prediction of the ground cold start at 283 K for the operating condition “D”. T(K)

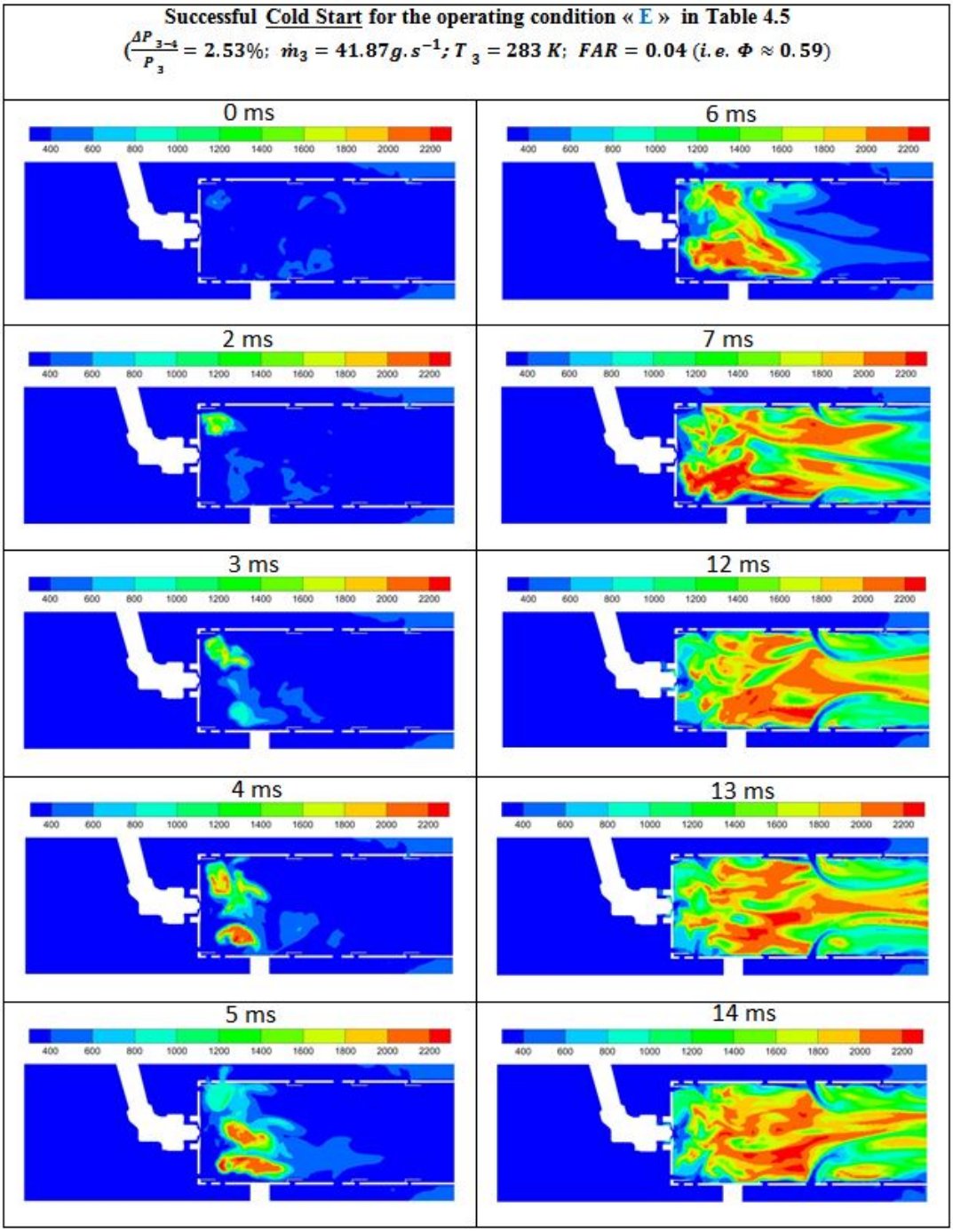

Figure 5.38: Prediction of the ground cold start at 283 K for the operating condition “E”. T(K)

ignition event is instead noted as shown in Figure 5.37 (FAR = 0.12 or $\phi = 1.76$).

5.4.2 Cold start at 233 K under various operating conditions with the simplex Injector

The test conditions "F"-"J" correspond to an operating temperature of 233 K as explicitly shown in Table 4.5 (Chapter 4), and depicted in Figure 5.32. The CFD predictions of cold start conditions are shown in Figure 5.39, Figure 5.40, Figure 5.41, Figure 5.42, and Figure 5.43 through the instantaneous contours of temperature. For this test condition also, it can be seen that, as long as the mixture is sufficiently rich, a successful ignition event is noted. By contrasting the cold start predictions corresponding to the two operating temperatures considered, 283 K ($\sim 10^oC$) and 233 K ($\sim -40^oC$), one can deduce the effect of the operating temperature on the ignition event success. For instance, the two test conditions corresponding to the ignition sequences shown in Figure 5.36 and Figure 5.39 differ mainly in terms of operating temperature (their equivalence ratios are quite identical), and it can be seen that the full ignition of the combustor at 233K takes more time to occur than at 283K. This result is expected since a substantial part of the spark energy is used in this condition to heat the air and vaporize droplets, unlike to the other case (T=283 K) for which the air temperature is high enough to initiate the droplet vaporization. In other words, the amount of spark energy required to achieve a successful ignition event increases when the operating temperature decreases. For these two operating temperatures, two kinds of failed ignition event are noted: in the first case, (see Figure 5.37, cold start at 283 K) the flame starts propagating and blows-off thereafter; for the second case (see Condition B in Figure 5.35, cold start at 283 K), the time required to achieve the full ignition of the combustion chamber is too long (more than 100 ms).

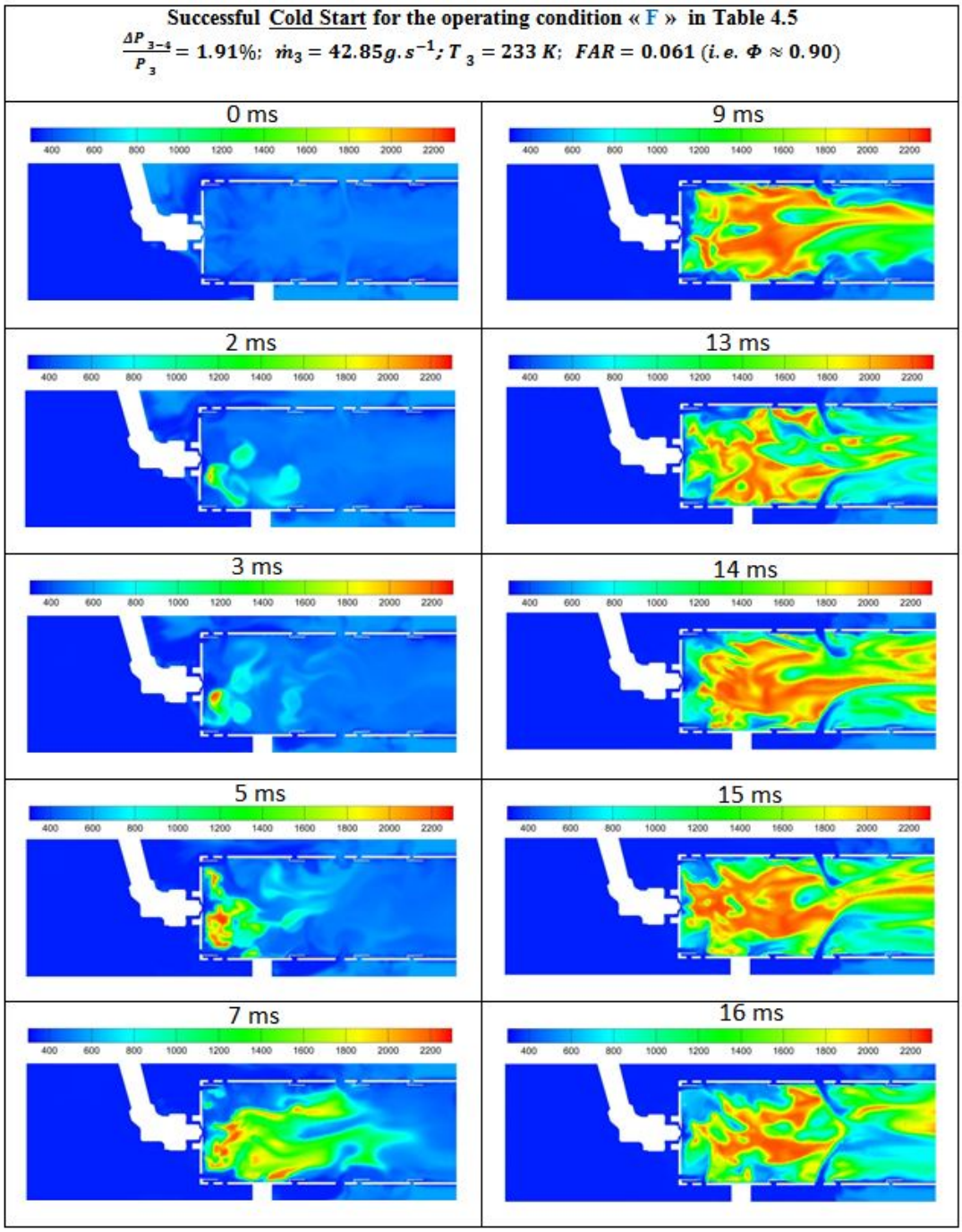

Figure 5.39: Cold start at 233 K for the operating conditions “F”. T(K)

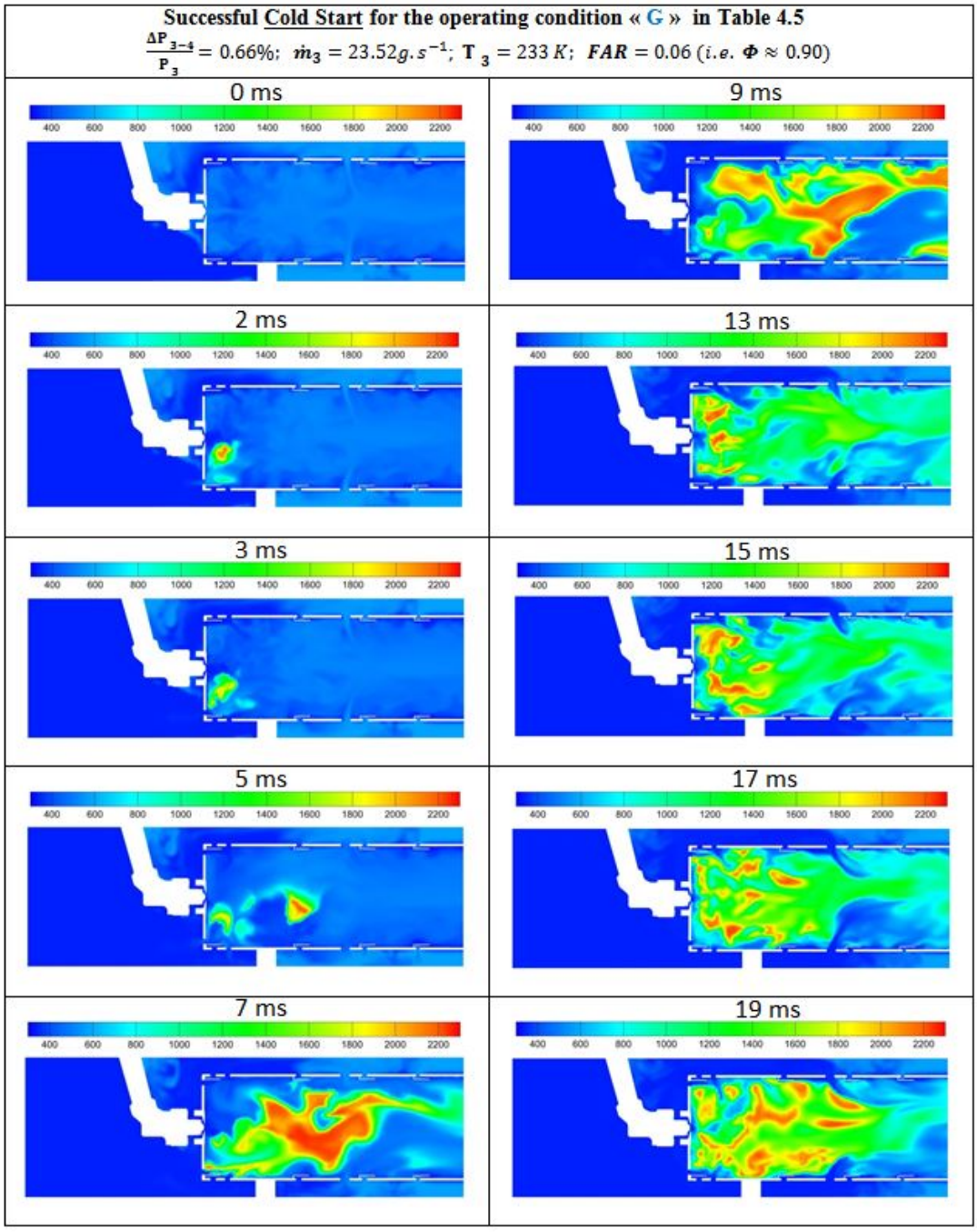

Figure 5.40: Cold start at 233 K for the operating condition “G”. T(K)

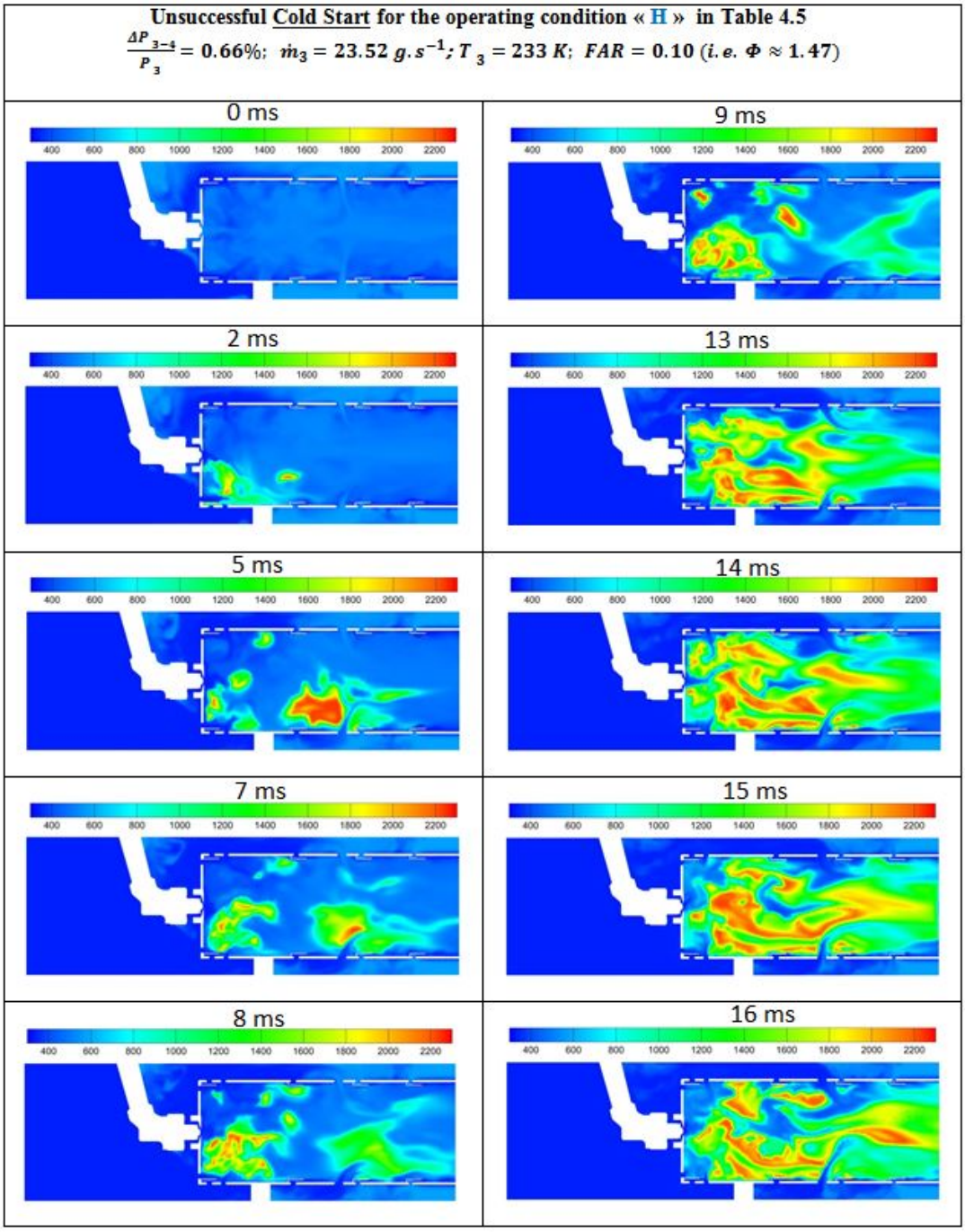

Figure 5.41: Cold start at 233 K for the operating condition “H”. T(K)

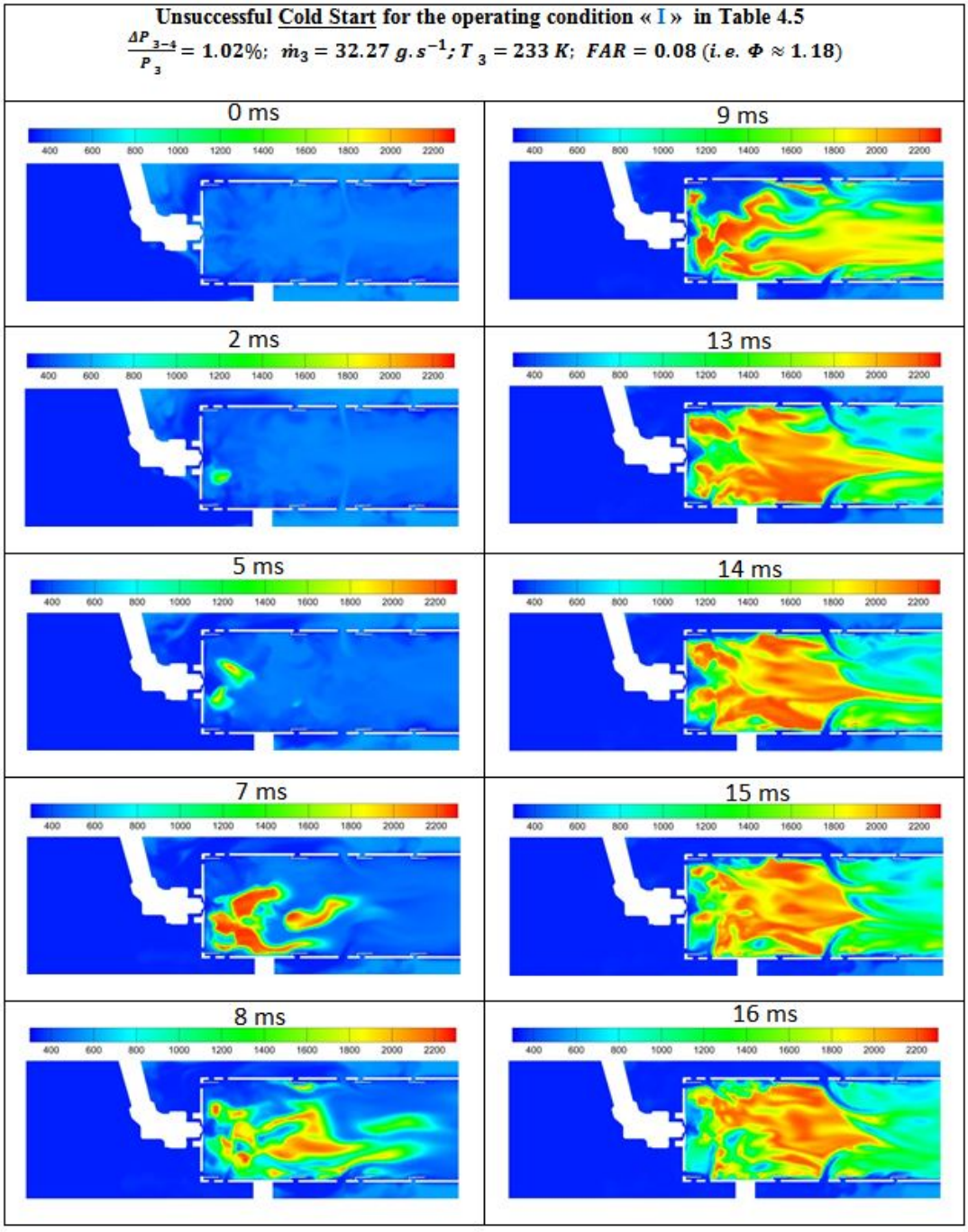

Figure 5.42: Cold start at 233 K for the operating condition “I”. T(K)

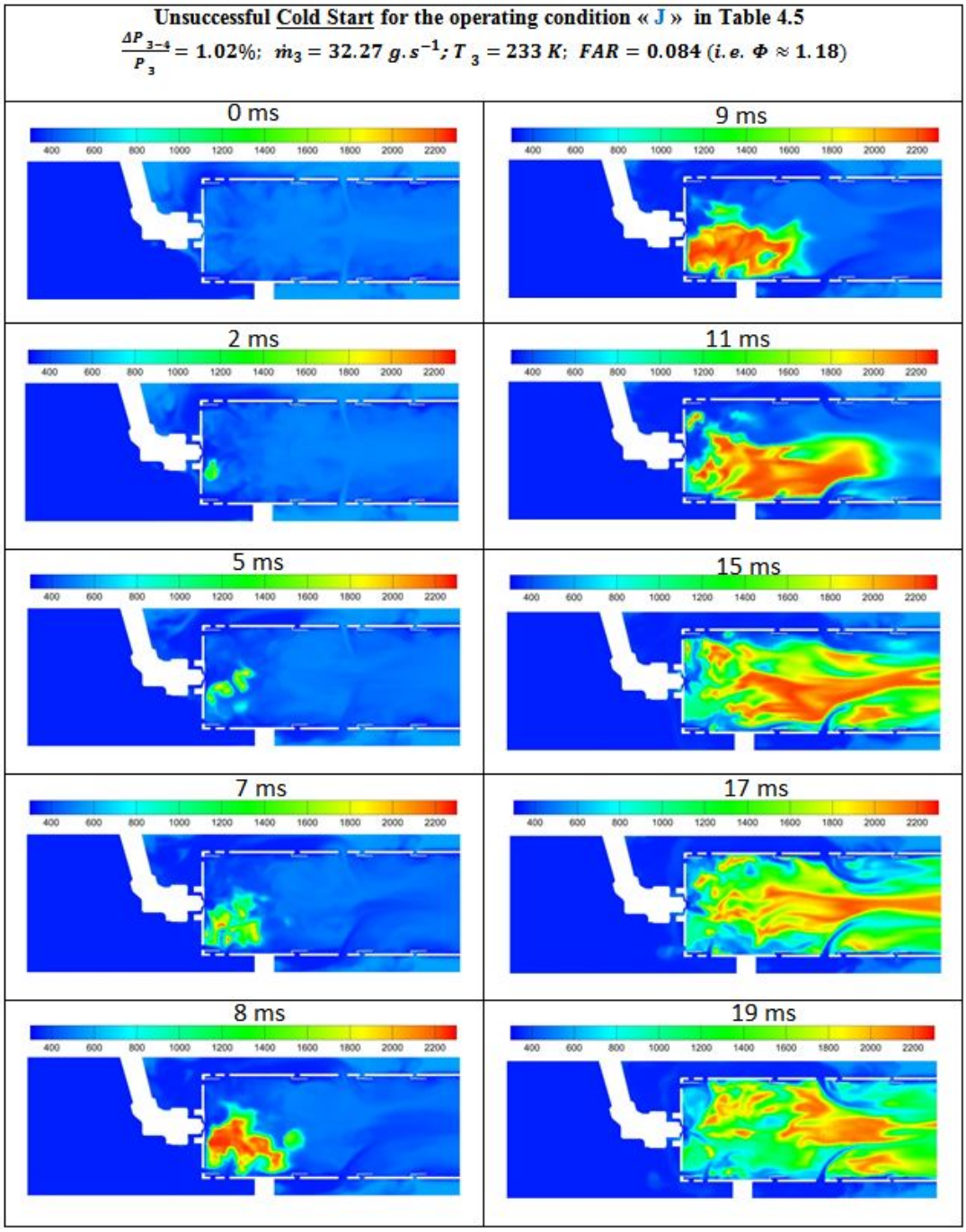

Figure 5.43: Cold start at 233 K for the operating condition “J”. T(K)

5.4.3 Altitude relight at 4 572 m (15 kft) under various operating conditions with the simplex injector

The CFD predictions of the altitude relight corresponding to the test conditions "A"-"E", for an operating altitude of 4 572 m (15 kft) are shown in Figure 5.44, Figure 5.45, Figure 5.46, Figure 5.47, and Figure 5.48 through the instantaneous contours of temperature. These altitude relight operating conditions are explicitly given in Table 4.6 (Chapter 4), and they are portrayed in Figure 5.33.

As done for the cold start simulations, the test conditions simulated are selected for a range of fuel-air ratios to assess the effect of the equivalence ratio on the ignition event success at a given operating altitude. Also, for one of the five test conditions considered, the pressure is changed to see its effect on the ignition event. The CFD model predicts an unsuccessful ignition event for the test condition "A", unlike the experiment. As shown in Figure 5.44, the flame kernel is initiated by the spark, and the latter propagates to ignite the remaining zones of the combustor. Subsequently, the flame is progressively blown off. By increasing the pressure up to the ambient pressure while maintaining the other conditions (see Figure 5.45), the same trend of results is noticed, except that the flame propagation occurs more quickly. The difference between the results corresponding to the test conditions "A" and "B" can be explained by the fact that chemical reactions of combustion are slowed at very low operating pressures, with a direct consequence of the droplet life-time which becomes longer. The majority of current experimental investigations suggests a negative pressure dependence of the laminar velocity, $S_L \propto P^n$ with $n = \simeq -0.25$ for most hydrocarbon fuels (e.g. an early experimental investigation based on light hydrocarbon fuels [Metghalchi and Keck, 1982], and a more recent experimental investigation based on for heavy hydrocarbons and jet fuels Hui and Sung [2013]). However, the minimum pressure considered in each of these investigations is 1 atm which is the maximum pressure considered in the current work. Further, as discussed in [Rallis et al., 1965], the outcomes of the investigations regarding the pressure dependence of the laminar burning velocity differ from one research group to another since positive, negative and no dependence have also been reported by various investigators.

According to the difference between the numerical and the experimental results for the test condition "A", the limitations of a fuel pump are a potential cause. In fact, the FAR of the test condition "A" is 0.14 and the mixture is therefore rich ($\phi = 2.05$). First, the equivalence ratio is close to the rich limit in the primary zone of the combustor and is potentially not propitious for the full ignition. Second, as it can be noticed through all the experimental ignition loops presented earlier, the experimental tests were mainly concentrated in the lean domain due to some limitations of the fuel pump in the high mass flow rates range. Because of these limitations, the reliability of the fuel pump in the high mass flow rate regime is not expected to be as high is in the low flow rate regime; consequently, the experimental results in the fuel-rich domain may not be as accurate as in the fuel-lean domain. Apart from this difference noticed for the test condition "A", the numerical prediction agrees with the experiment for the remaining test conditions "C", "D" and "E" (see Figure 5.33, Figure 5.46, Figure 5.47, and Figure 5.48).

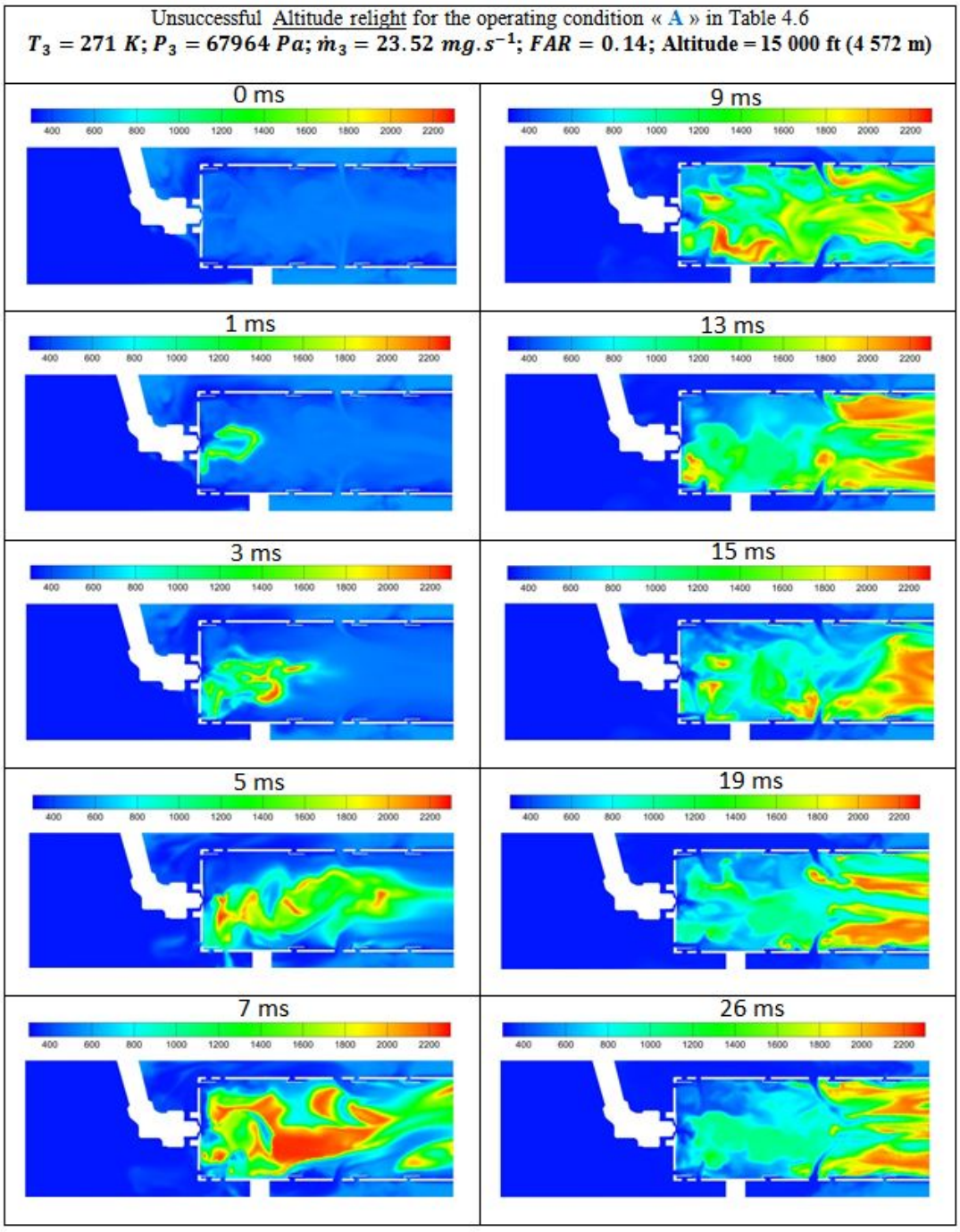

Figure 5.44: Altitude relight at 4 572 m (15 kft) for the operating condition “A”

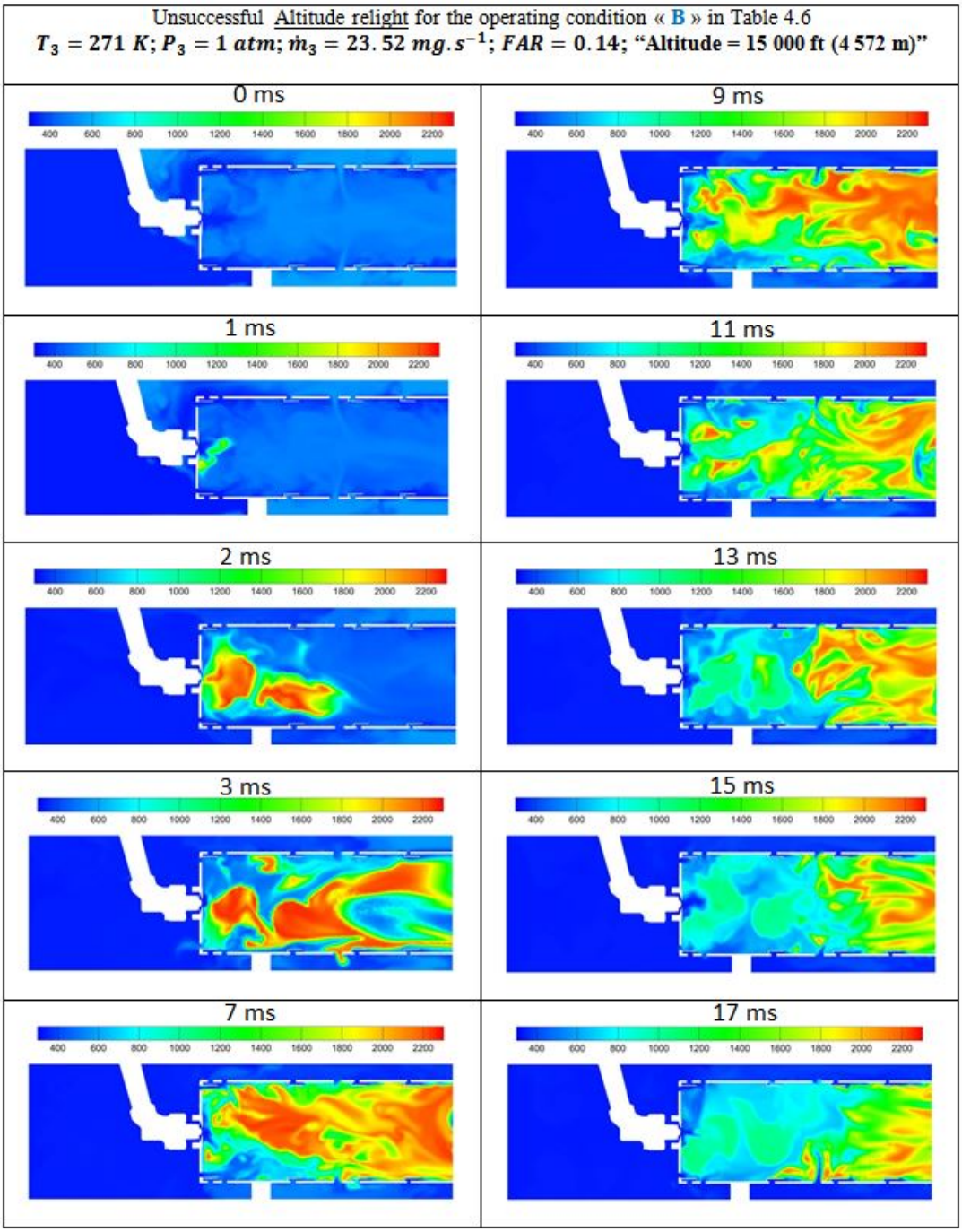

Figure 5.45: Altitude relight at 4 572 m (15 kft) for the operating condition "B"

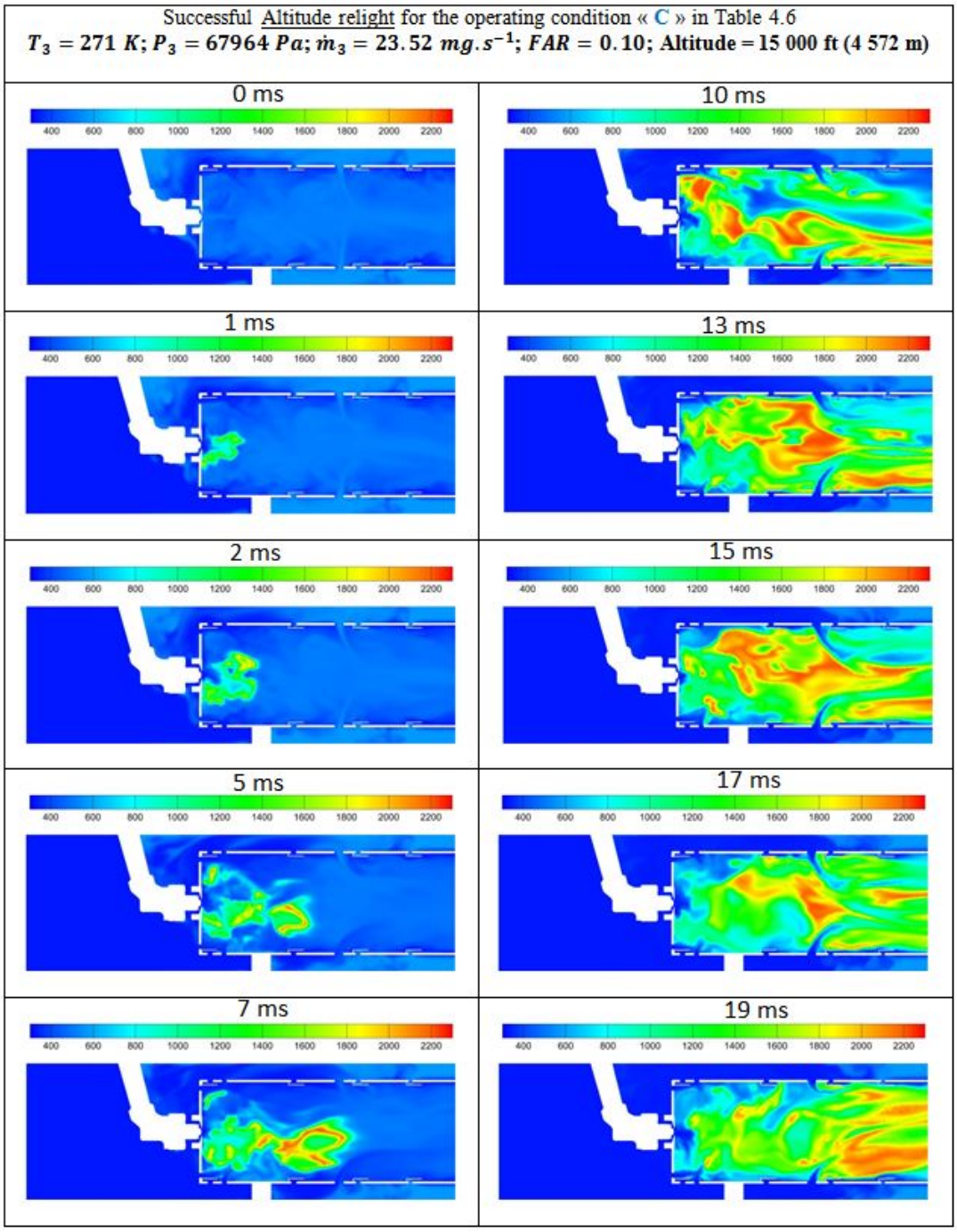

Figure 5.46: Altitude relight at 4 572 m (15 kft) for the operating condition “C”

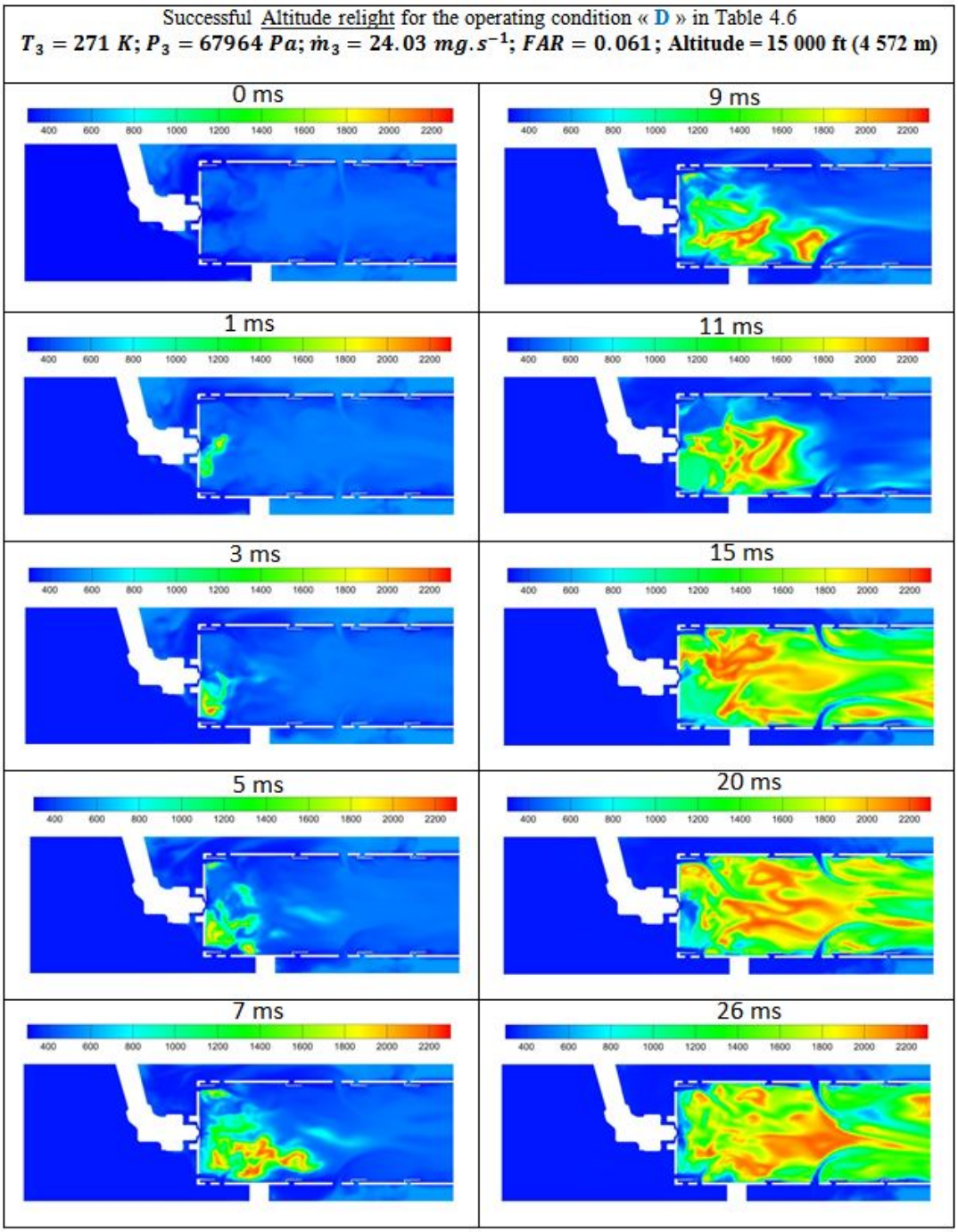

Figure 5.47: Altitude relight at 4 572 m (15 kft) for the operating condition “D”

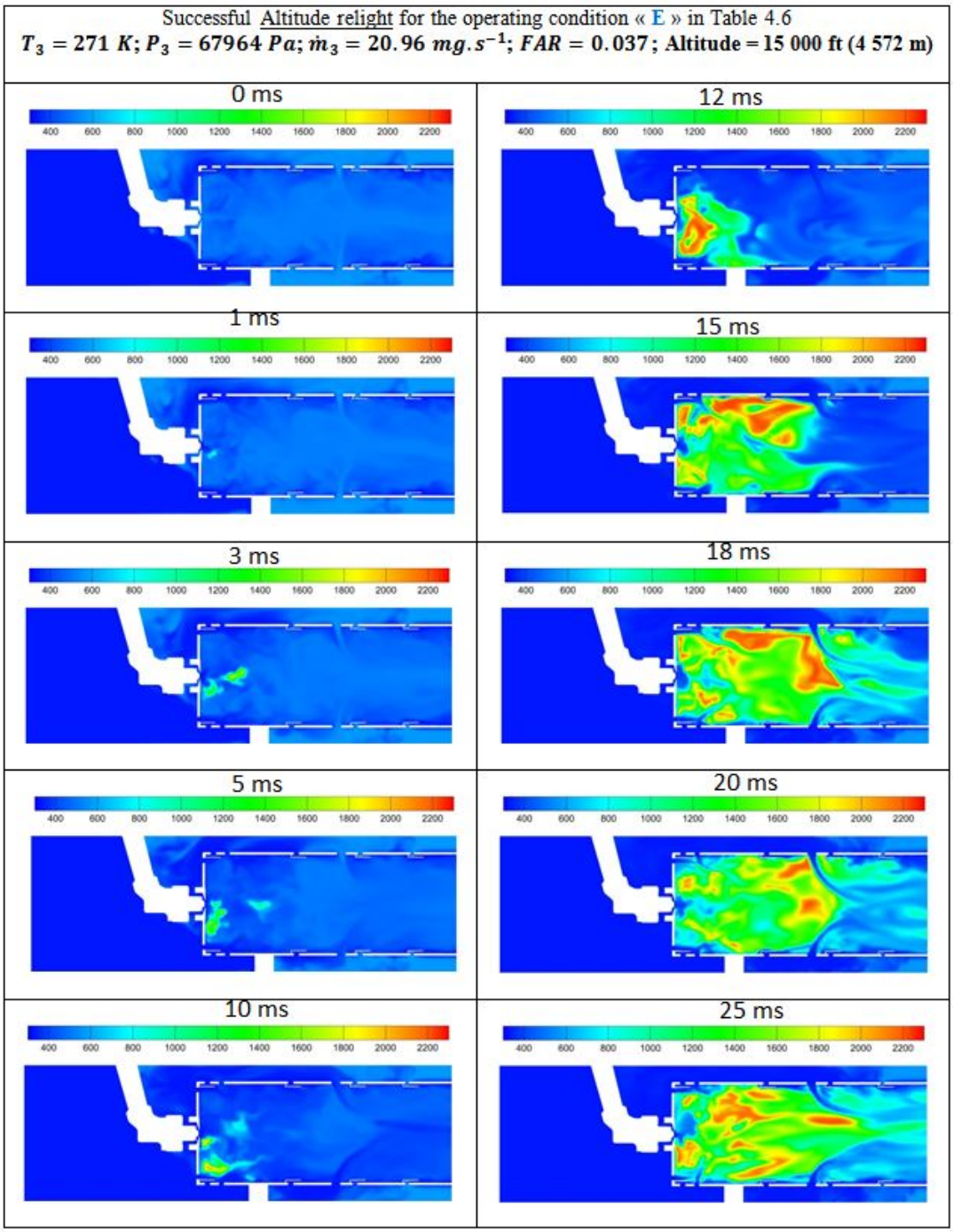

Figure 5.48: Altitude relight at 4 572 m (15 kft) for the operating condition “E”

5.4.4 Altitude relight at 10 688 m (35 kft) under various operating conditions with the simplex injector

The CFD predictions of the altitude relight corresponding to the test conditions "F"-"L", for an operating altitude of 10 688 m (35 kft) are shown in Figure 5.49, Figure 5.50, Figure 5.51, Figure 5.52, Figure 5.53 and Figure 5.53. These altitude relight operating conditions are also explicitly given in Table 4.6 (Chapter 4), and they are portrayed in Figure 5.34.

As it can be noticed from Figure 5.34, the test conditions "I", "J" and "F" are selected within the band of the experimental ignition loop, while the other test conditions "K", "L" and "H" are selected outside the experimental ignition loop. As mentioned so far, the test selection strategy allows evaluation of the ability of the CFD methodology to predict the ignition loop while revealing the operating conditions which are not propitious for a successful ignition event. For this second operating altitude also, the effect of the operating pressure is also investigated by increasing the operating pressure, while maintaining the other conditions. More precisely, the test conditions G is obtained by increasing the operating pressure up to the standard pressure (1 atm) in the test condition K. Thus, by comparing the numerical prediction of the test condition G (see Figure 5.50) to that of the test condition K (see Figure 5.54, it can newly be noticed that the low operating pressures (sub-atmospheric) have a slowing effect on the chemical reactions of combustion. For all the test conditions selected on the experimental ignition loop (see Figure 5.52, Figure 5.53, and Figure 5.49) the CFD model predicts a successful ignition event as suggested by the experiment. The time required to achieve the full ignition of the combustor is strongly influenced by the fuel-air ratio and thus by the operating equivalence ratio; this time is relatively shorter when the operating fuel-air ratio is close its stoichiometric value. The numerical results corresponding to the test condition "H" (see Figure 5.51) show an unsuccessful ignition event as expected, considering that this test condition is selected far away from the ignition loop in the lean domain. The flame kernel is initiated by the spark deposit, but due to a mixture too lean and outside the flammability limits, the flame kernel cannot propagate, and it extinguishes when the energy deposition ceases. For the test condition "L", the numerical prediction of the ignition event shown in Figure 5.52 shows an unsuccessful ignition event in which the flame kernel is initiated, propagates to ignition the whole combustion chamber and the resulting flame is subsequently blown-off. A closer look at this test condition shows that it is too fuel-rich since FAR=0.16 (i.e. $\phi = 2.35$), and is therefore not propitious to a successful ignition event. According to the third test condition selected outside the ignition loop, the corresponding ignition event is close to that of a successful ignition event: the flame kernel is initiated, propagates to ignition the whole combustion chamber. However, by contrasting this result with those corresponding the test conditions "I", "J", "F" (i.e. the test conditions selected on the experimental ignition loop), it can be notice that the flame tends to extinguish after 15 ms. This condition is thus considered as not propitious to a successful ignition event.

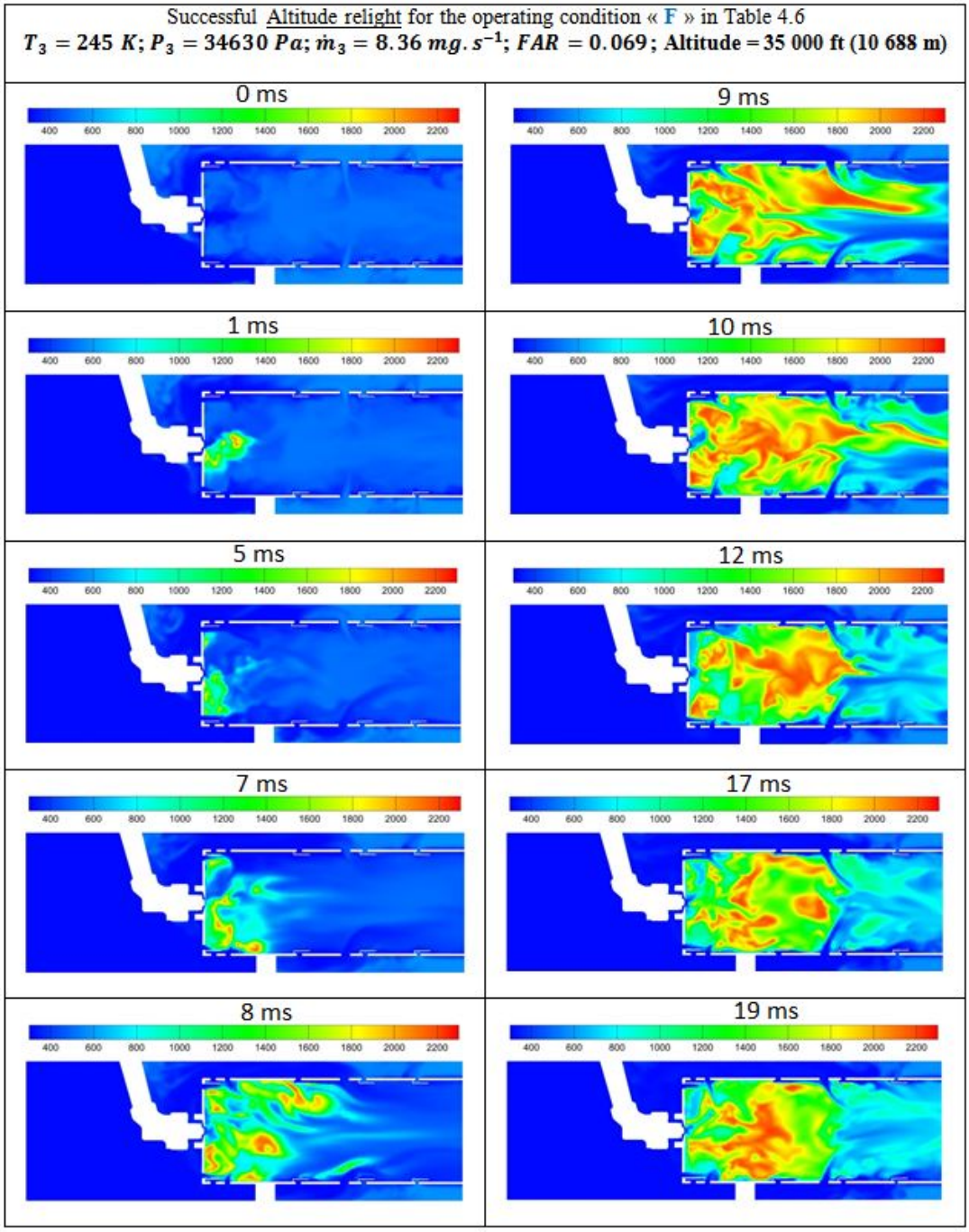

Figure 5.49: Altitude relight at 10 688 m (35 kft) for the operating condition “F”

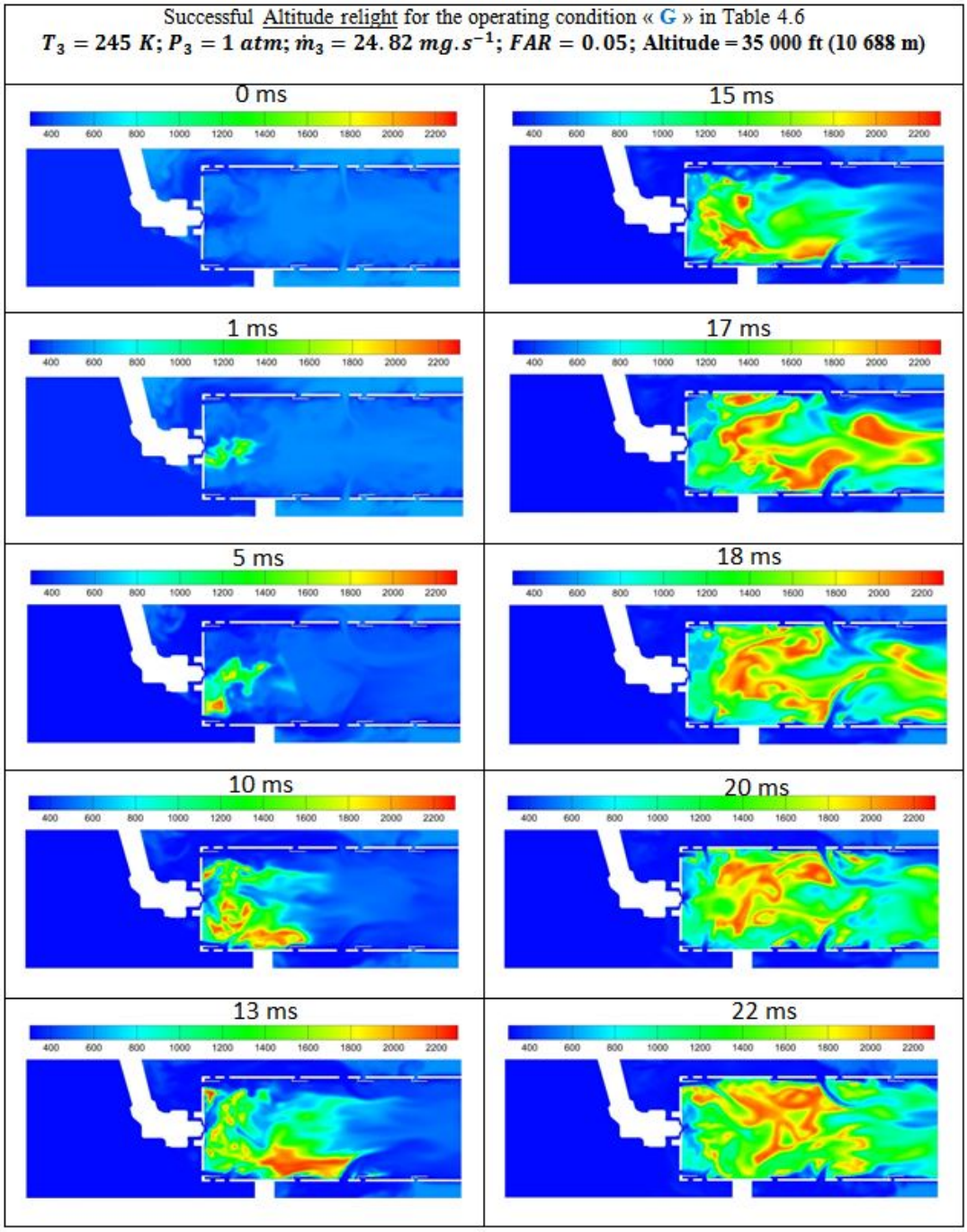

Figure 5.50: Altitude relight at 10 688 m (35 kft) for the operating condition “G”

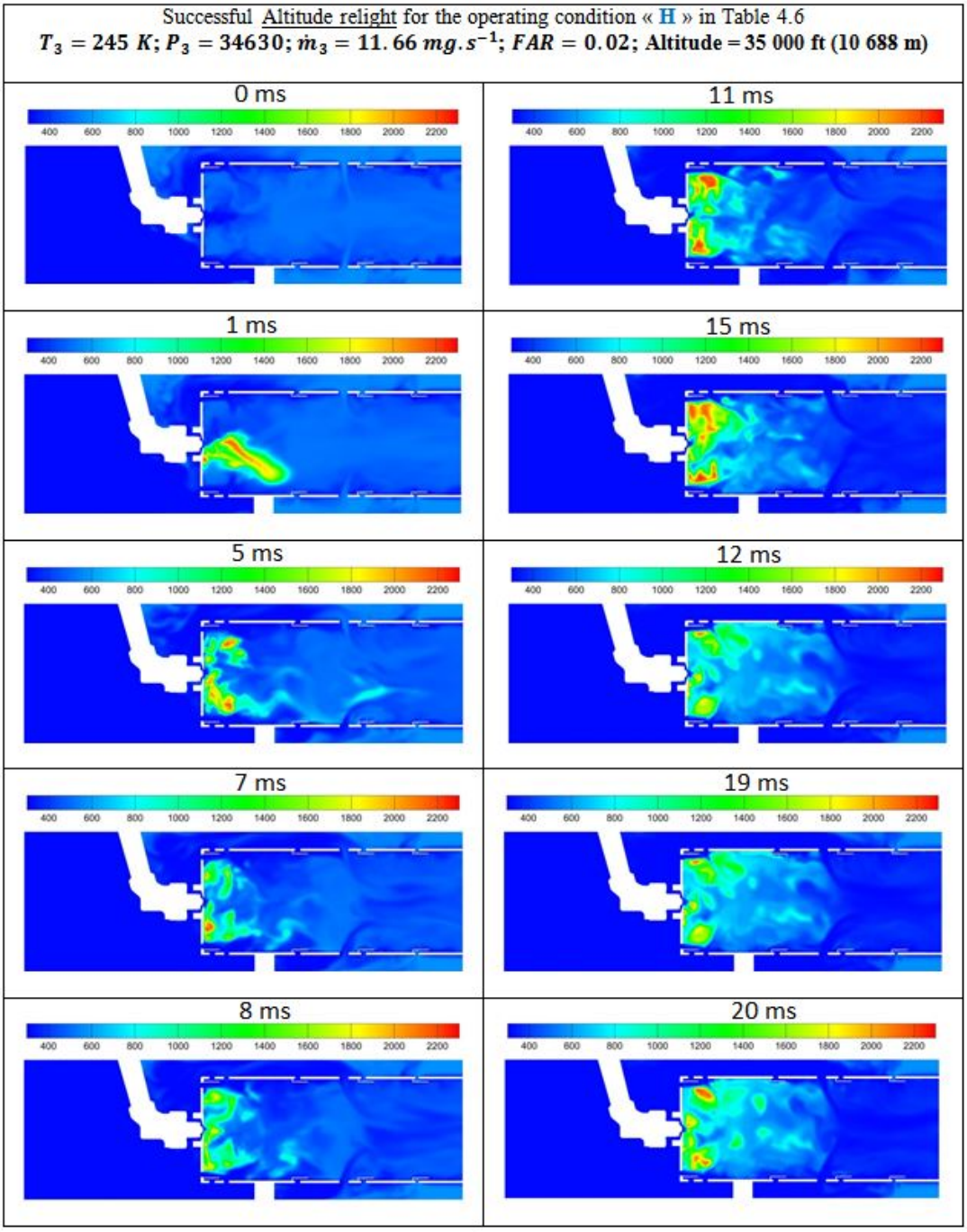

Figure 5.51: Altitude relight at 10 688 m (35 kft) for the operating condition “H”

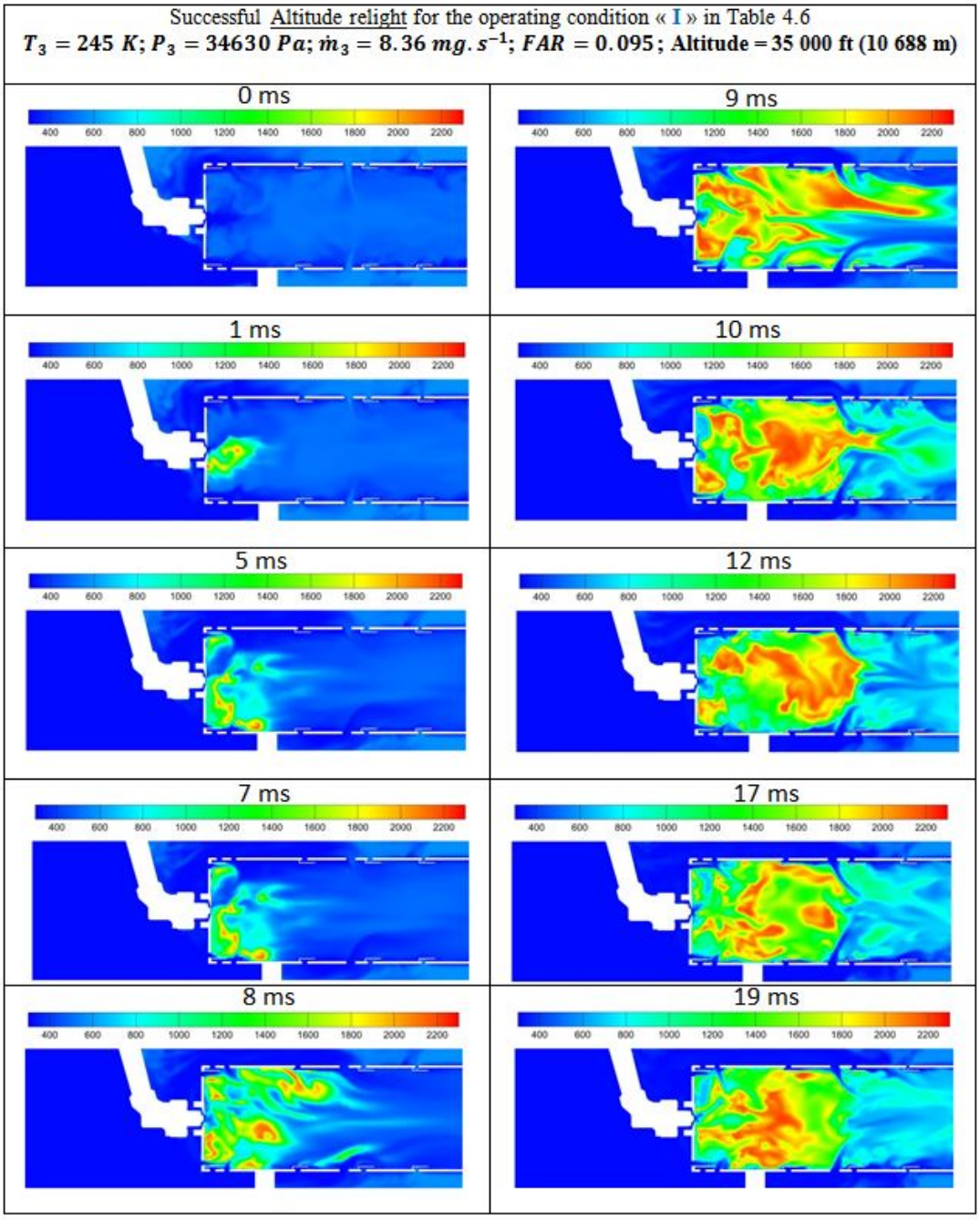

Figure 5.52: Altitude relight at 10 688 m (35 kft) for the operating condition “I”

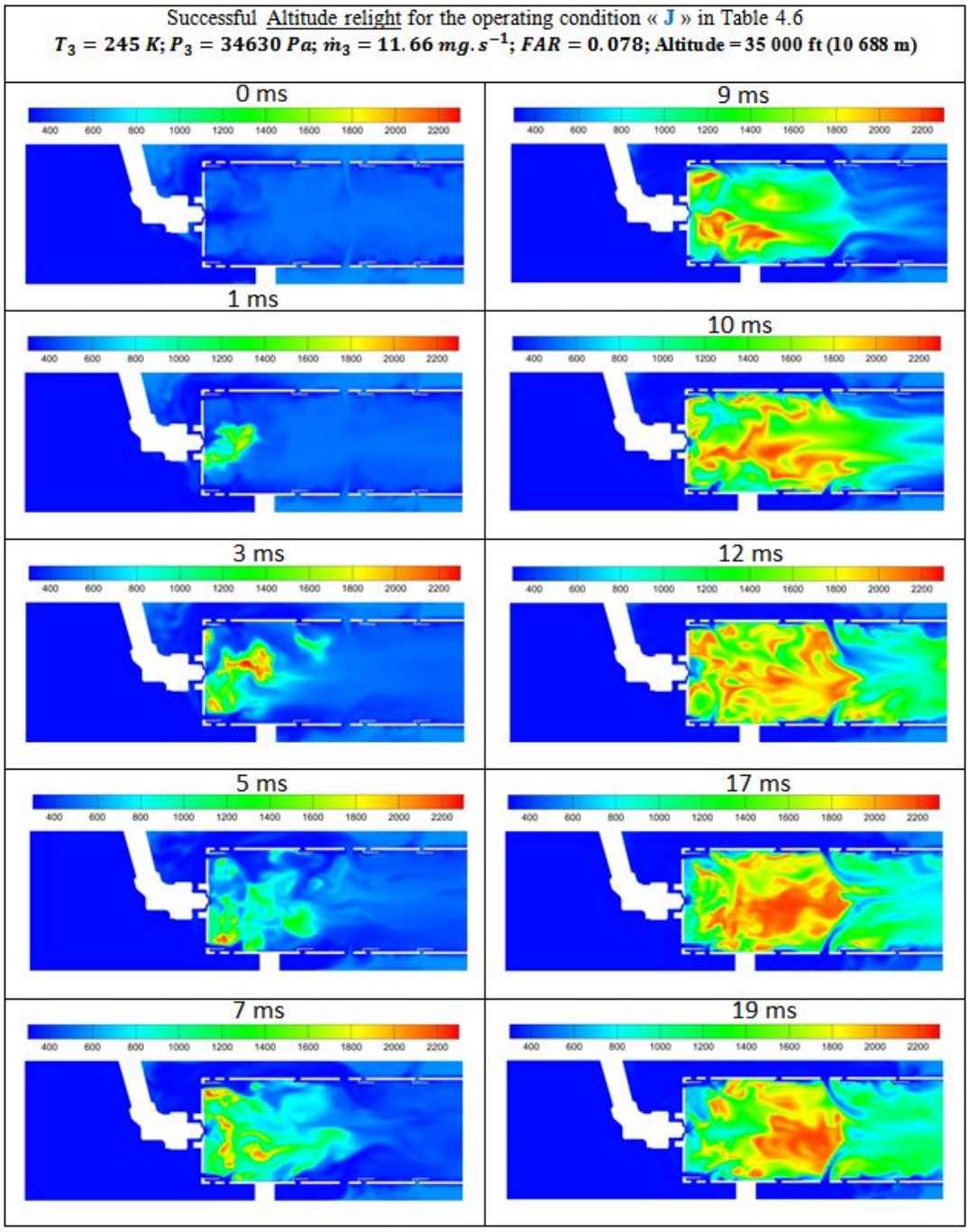

Figure 5.53: Altitude relight at 10 688 m (35 kft) for the operating condition "J"

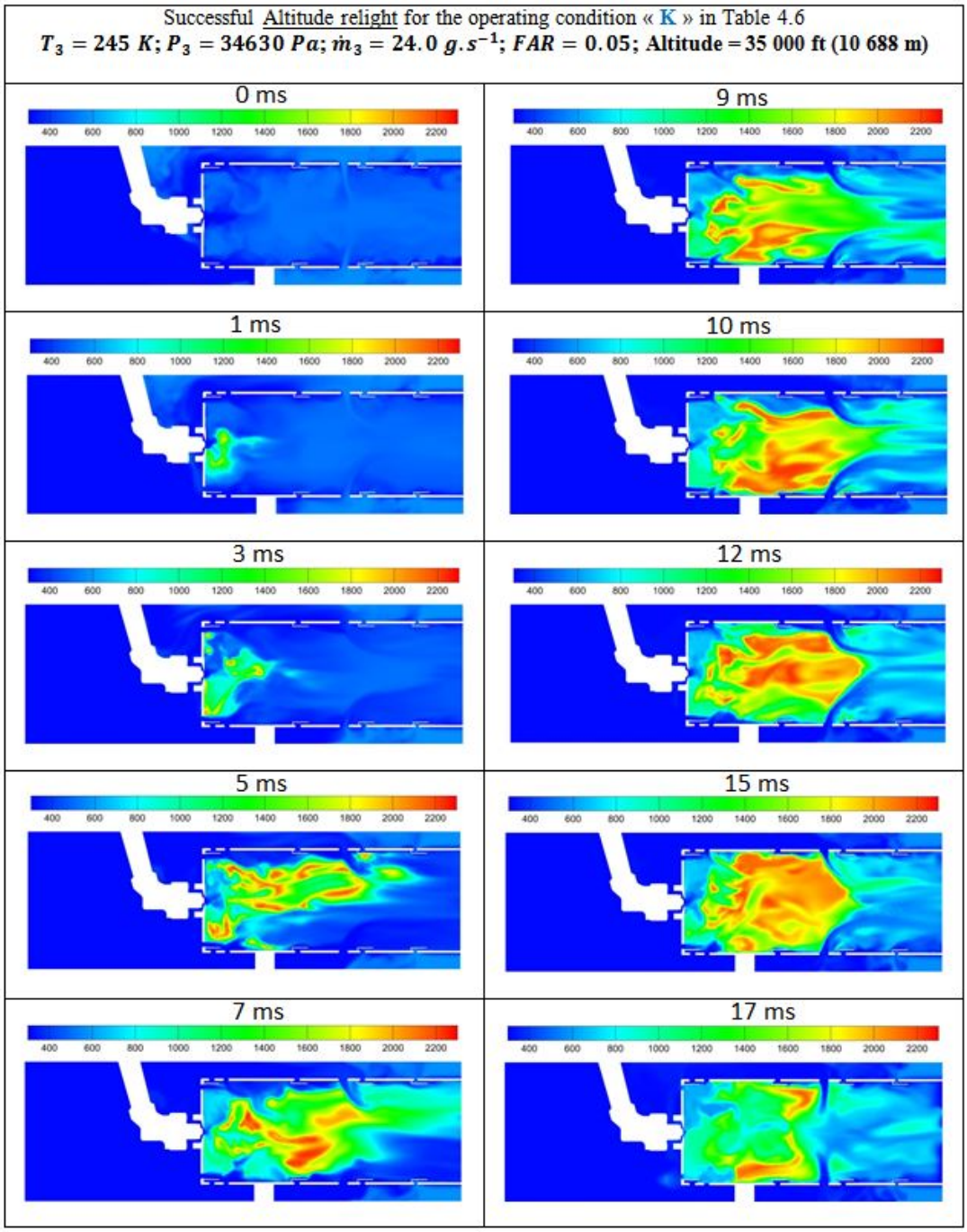

Figure 5.54: Altitude relight at 10 688 m (35 kft) for the operating condition “K”

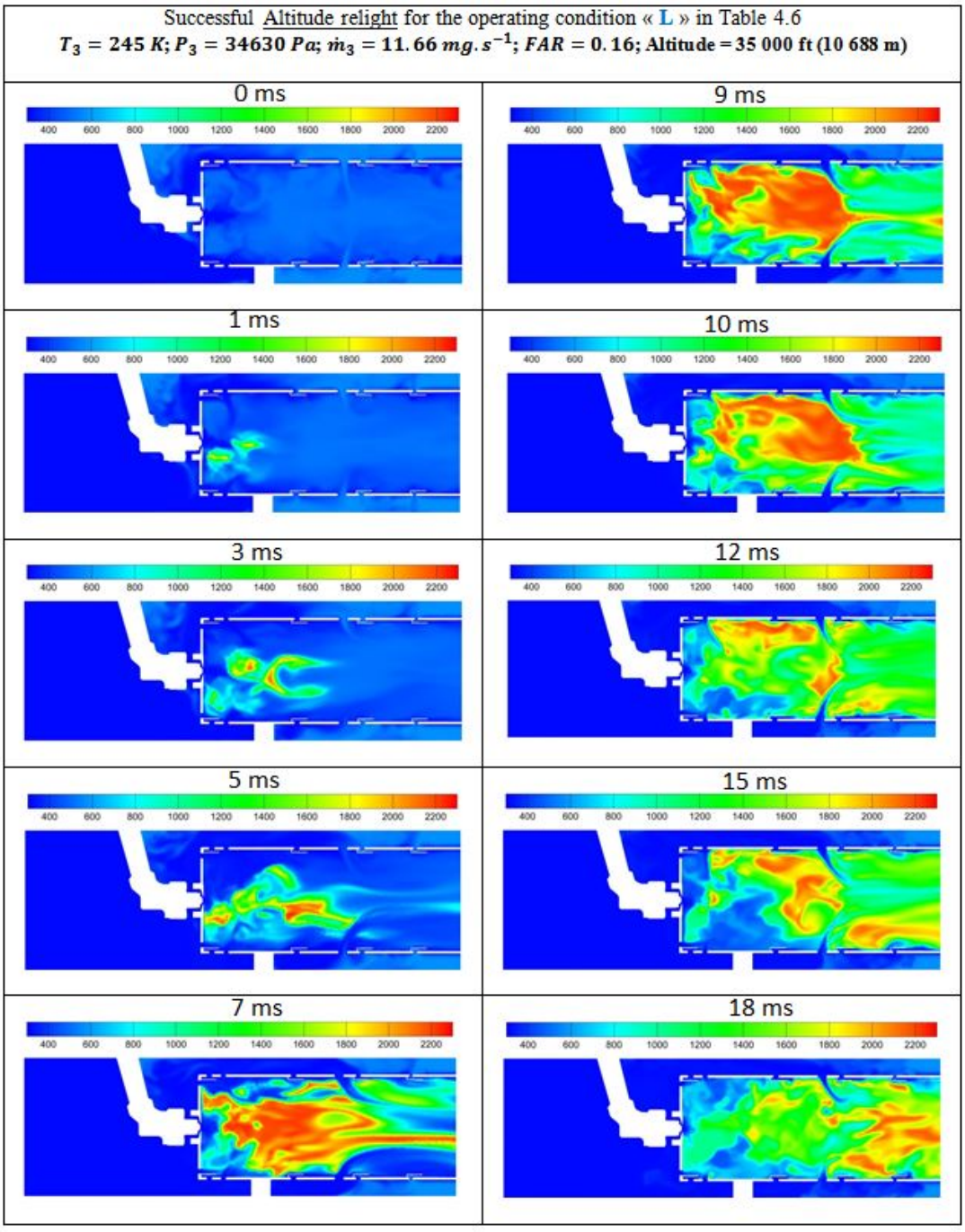

Figure 5.55: Altitude relight at 10 688 m (35 kft) for the operating condition “L”

5.4.5 High speed infrared camera images of a successful ignition event

To achieve a qualitative validation of a successful ignition event predicted by the CFD model formulated in the current study, some simulations are conducted using the duplex nozzle. The attention is particularly shifted to the test condition for which a high-speed camera (TELOPS^{TM} IR) was used to follow the whole ignition sequence. The experimental ignition sequence, represented by a set of high-speed camera images, is shown in Figure 5.56, while its numerical counterpart is shown in Figure 5.57. The test conditions considered are those shown in Table 4.4 (see Chapter 4), and they lead to results that almost identical. According to the high-speed camera images, the total time required to fully ignite the combustion chamber while achieving the steady combustion regime is found to be around 100 ms [Marcotte et al., 2013]. From the numerical prediction, it can be seen that the full ignition of the combustor occurs after 60 ms approximatively. Additional computation time might be necessary to reach the steady combustion regime since the full ignition of the combustion chamber does not necessary correspond to the steady combustion regime. By contrasting the numerical prediction (i.e. Figure 5.57) to its experimental counterpart (Figure 5.56), it can be noticed that the CFD model captures the whole ignition sequence. However, this validation is only qualitative and a rigorous comparison cannot be done since the high-speed infrared camera images do not correspond to a single cross section of the combustor (the camera was positioned is such away to detect the highest temperature over all the cross sections of the combustor); only the time required to fully ignite the combustor can be exploited to qualitatively assess the ability of the CFD model. The validation of the CFD model with respect to the prediction of the steady combustion regime in this tubular can combustor is not attempted in the current work due the lack of experimental data. However, considering the promising results obtained by applying the same CFD model to predict both transient and steady combustion regime in the previous configuration (i.e. highly swirl-stabilized combustor), this CFD model is expected to reasonably predict the main flame trends in the steady combustion regime as well.

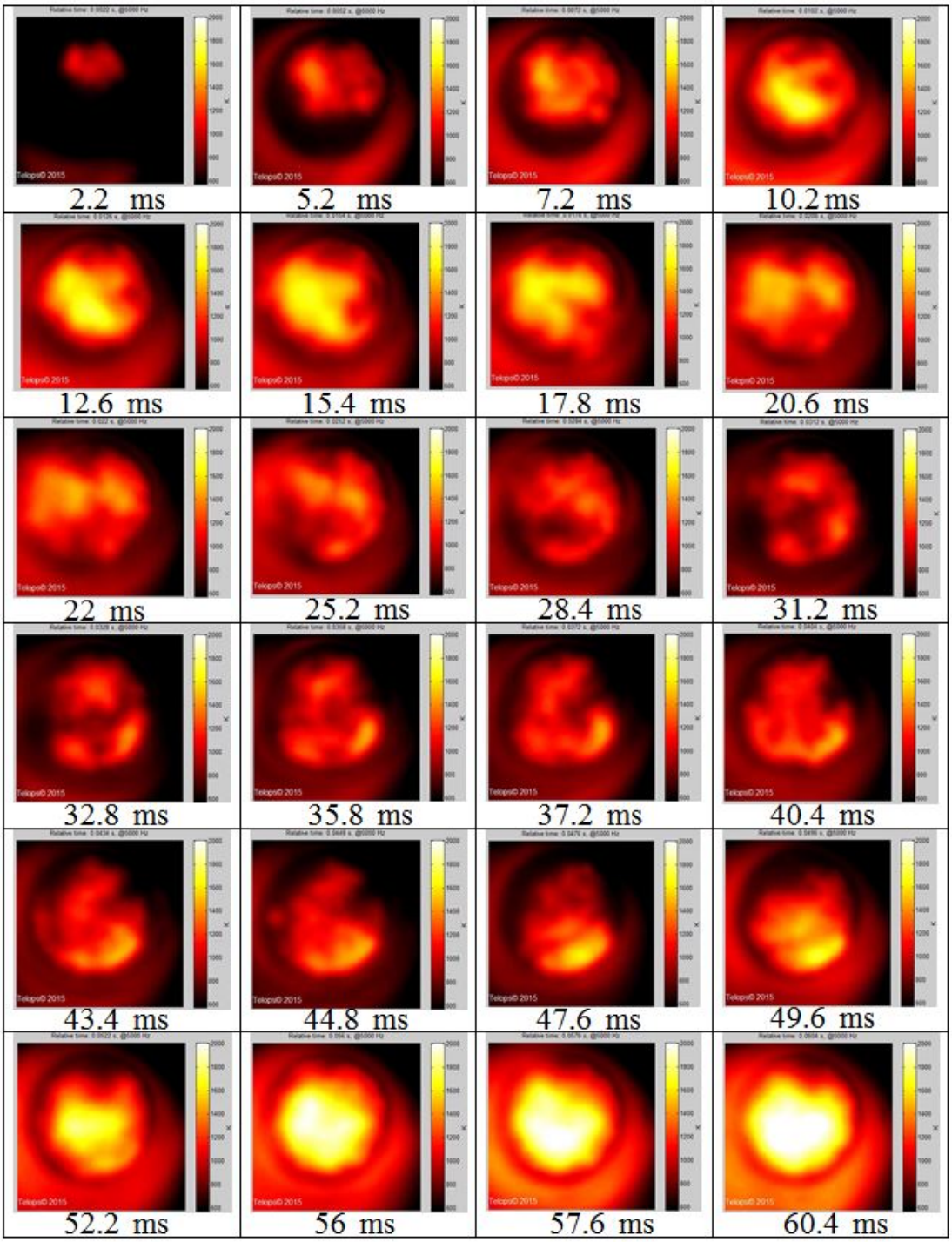

Figure 5.56: High speed camera images of a successful ignition event recorded using the TELOPS^{TM} IR camera

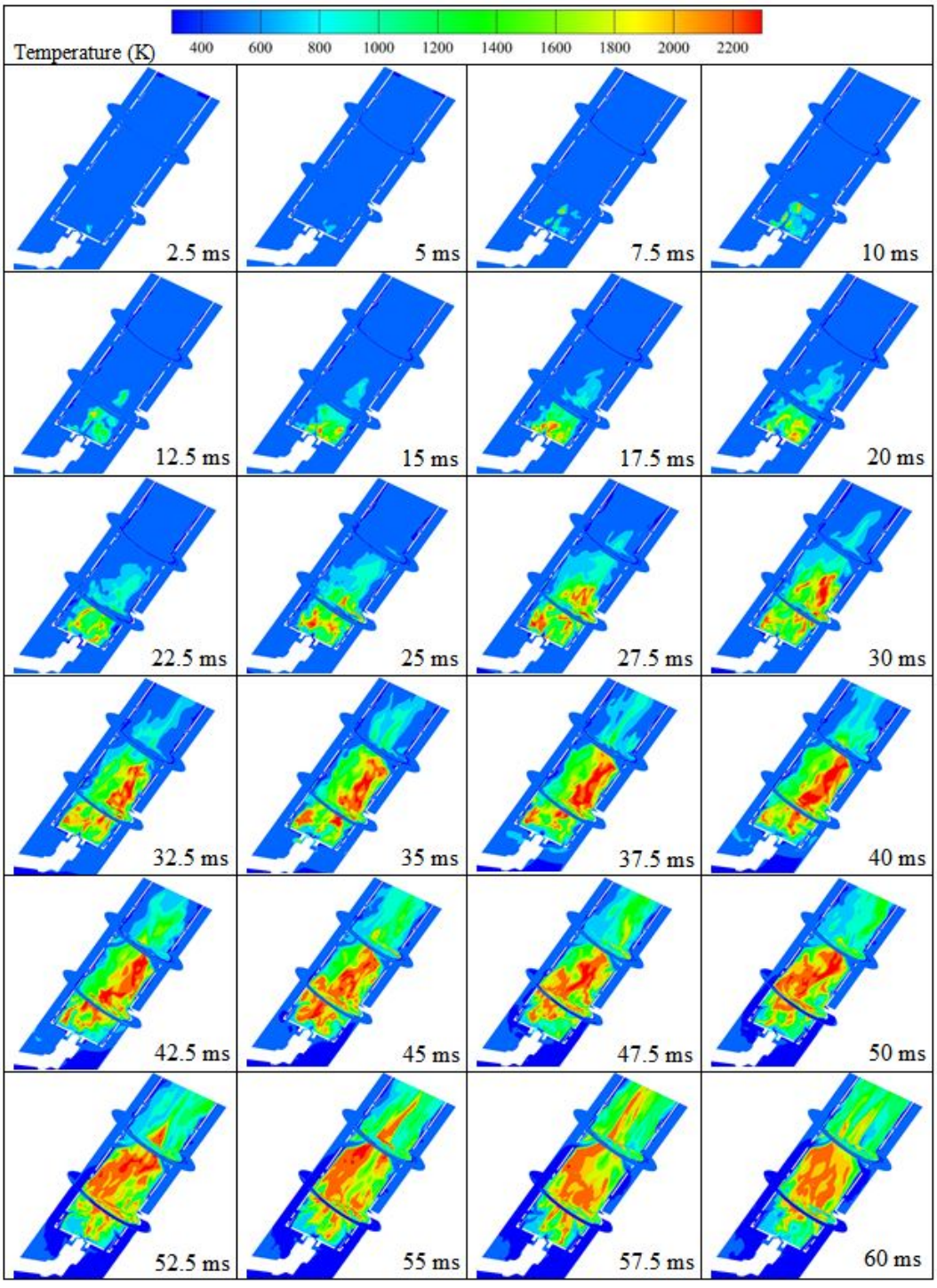

Figure 5.57: A sample of successful numerical ignition event based on the duplex injector

5.4.6 Summary

As mentioned in the introduction, three different experimental configurations were exploited to validate the new CFD methodology developed in this thesis. The experimental configurations described in Chapter 3 were selected in such a way to assist and validate each step of the CFD methodology development. This chapter discussed extensively the prediction results corresponding to each configuration, while highlighting the advantages and drawbacks of the models used to develop the CFD methodology. The main outcomes of the investigation are summarized in the next chapter followed by some suggestions for further research.

Conclusions and Suggestions for Further Research

Numerical investigations of transient and steady combustion regimes in aero gas turbine combustion chambers were conducted under various fuel-lean and fuel-rich operating conditions. The study was motivated by the need to better understand combustion processes governing these combustion regimes with the final goal of assisting the design of new aircraft engines based on the fuel-lean combustion technology. Particular attention was paid to the accuracy of the results, the computational cost and the ease of handling the numerical code from an industrial standpoint. A commercial CFD code widely used in industry was selected as the basic numerical tool. A CFD methodology was developed, and consists of advanced turbulence and combustion models paired with a subgrid spark-based ignition model that was adjusted with the final goal of predicting the whole ignition sequence under various cold start and altitude relight operating conditions, and the main flame trends in the steady combustion regime.

To assess the ability of the newly formulated CFD methodology in predicting combustion processes of both transient and steady combustion regimes, three different experimental configurations were exploited. These are, the swirl-stabilized liquid-fuelled combustion chamber, the bluff-body stabilized burner, and the tubular can combustor, with liner holes and cooling slots, provided by P&WC. An Eulerian framework was used to describe the dynamics of the gaseous phase, while that of the fuel spray was described using a Lagrangian formulation. The sensitivity of the transient combustion phenomena to the chemical kinetics was addressed by incorporating a realistic chemistry model in the CFD methodology through the tabulated flamelet-based chemistry approach. The realistic oxidation model for the fuel surrogates was represented by a reduced chemical kinetic mechanism consisting of 1 045 elementary reactions among 139 species, derived from the detailed chemical kinetic model, JetSurF 2.0, using a species sensitivity method termed Alternate Species Elimination (ASE). The effects of the fuel properties on the flame structure were accounted for by implementing empirical correlations for the various fuel physical and transport properties. A subgrid spark-based ignition model was used to capture the early stage of the ignition event as it allows circumventing the need of refining the mesh of the combustion chamber, while leading to substantial savings in computing resources.

Initially, attention was focused on the steady combustion regime. Various CFD methodologies

were formulated using three turbulence models, namely, the Unsteady Reynolds-Averaged Navier-Stokes (URANS), the Scale-Adaptive Simulation (SAS), and the Large Eddy Simulation (LES) models. To evaluate the relevance of incorporating a realistic chemical kinetics model and chemical non-equilibrium effects due to turbulent strain (e.g. flame stretching), two different assumptions were considered. These are infinitely-fast chemistry through the partial equilibrium model, and finite-rate chemistry through the diffusion flamelet model. For each of the two assumptions, both one-component and two-component fuels were considered as the surrogates for Jet A-1. The resulting CFD formulations were applied to a swirl-stabilized liquid-fuelled combustion chamber; the choice of the configuration being related to its ability to mimic complex flows typical of practical devices, and the availability of detailed experimental data including those of slow species. This first intermediate study allowed assessing the ability of each of these CFD formulations to predict the spray flow and combustion properties in the steady combustion regime, with a primary interest paid to the prediction of the main flame trends and the species characterized by low reaction rates. Subsequently, the ratios between the accuracy of the results and the computational cost of the three CFD methodologies were explicitly compared, and the CFD methodology providing the best compromise between the accuracy of the results and the computing cost was retained for the subsequent investigations.

In the second investigation, attention was focused on the transient combustion regime, namely, the ignition sequence preceding the steady combustion regime. A bluff-body stabilized burner equipped with a spark-based igniter and fuelled with a gaseous fuel was used to calibrate the newly developed CFD methodology. Although the geometry of this burner is relatively simple, it represents an important class of practical burners since flames of varying stability, efficiency, pollutant formation, and heat transfer can be produced by variations in design and operating conditions. Furthermore, it exemplifies complex flows of real configurations and can therefore provide greater understanding of complex flow fields, especially with regard to stability and ignitability. As the burner involves a partially-premixed combustion, the mixture fraction-progress variable formulation was adopted with the infinitely fast chemistry and finite rate chemistry assumptions with the Bray-Moss-Libby (BML) and Flamelet Generated Manifold (FGM) models, respectively. The subgrid ignition model was first customized by implementing a realistic correlation for the laminar burning velocity of the fuel used to feed the burner. Thereafter, the ignition model was coupled to the most robust CFD methodology obtained from the previous comparative investigation under the two above-listed chemistry reaction rate assumptions. The resulting CFD method was used to predict ignition events initiated by the spark deposition at various locations of the combustion zone of the burner, and the results were validated by comparison with their experimental counterparts.

Finally, in the third investigation, the CFD methodology was extended to spray combustion by coupling the latter to the spray module used in the first configuration, and by implementing the kerosene (Jet A-1) flame properties in the ignition model. The resulting new CFD model was first applied to the swirl-stabilized combustor investigated previously, with the aim of retrieving the whole ignition sequence and improving the previous predictions of the combustion properties in the resulting

steady combustion regime, namely, the prediction of the slow species. The final CFD methodology was also applied to a scaled can combustor (i.e. combustion chamber designed with liner and air holes to modulate combustion and wall cooling) with the aim of predicting ignition events under various cold start and altitude relight operating conditions. The ability of the CFD methodology to predict ignition events under these two ignition conditions for various environmental conditions was assessed quantitatively by contrasting various numerical ignition events with the corresponding ignition loops obtained through experimental measurements conducted in the Combustion Laboratory at Université Laval. A qualitative validation was also done by comparing one of the numerical ignition sequence to the corresponding high-speed infrared camera images of the ignition event.

In the next two sections, the main outcomes of the investigations are summarized followed by suggestions for future research.

5.5 Summary of outcomes

– The results of the numerical simulations based on the URANS and SAS turbulence models show that the mean velocity field of a swirl-stabilized reacting spray flow can reasonably be captured using each of the two turbulence models. However, a more accurate prediction is achieved by using the LES model; the LES improvements of the aerodynamics field are found to be significant in the predictions of the velocity fluctuations.

– A comparison of the URANS, SAS and LES predictions of the thermochemical field through the radial profiles of temperature and molar fraction of major species shows that the LES model paired with a combustion model based on the infinitely-fast chemistry assumption, outperforms the two other turbulence models even when the latter are paired with a combustion model relaxing the infinitely-fast chemistry assumption. In other words, when simulating a turbulent swirl-stabilized spray flame with attention paid to the main flame trends, the robustness of the turbulence model is more relevant than the assumption regarding the rate of the chemical reactions.

– The CFD methodology consisting of pairing the LES with the flamelet model is found to improve the prediction of the main flame trends, especially in the shear layer zone formed by the spray cone and air. However, outside this zone, both the partial equilibrium and flamelet models lead to identical results since the flame stretching due to fuel-air mixing is relevant in this shear layer zone, and becomes negligible elsewhere.

– For a liquid-fuelled swirl-stabilized combustion chamber, of the three turbulence models, the LES model was found to provide the best trade-off between the accuracy of the results and the

computational costs.

– The results based on the partial equilibrium and diffusion flamelet models show that these two combustion models fail to predict the formation of species characterized by low reaction rates, and therefore cannot be considered for an accurate prediction of pollutants. This common drawback to the two models is mainly related to the fast chemistry assumption. However, since the fast chemistry assumption is partly relaxed in the diffusion flamelet formulation, the discrepancies are substantially reduced when the diffusion flamelet model is applied. The improvements are particularly relevant in the shear layer between the fuel cone and air as such zones feature high straining due to fuel-air mixing.

– In spray combustion, a more accurate prediction of slow species (such as the majority of pollutants) can be achieved by using advanced flamelet models. The latter include the multidimensional Flamelet-Generated Manifold (MFGM) and all its variants (e.g. the FGM based on the mixture fraction-progress variable formulation), as they provide a proper modelling of the flamelet structure and a more realistic flamelet solution space. In addition, the progress variable and the scalar dissipation rates allow identifying the real state of the flamelet, while the presence of the unsteady terms in their mathematical formulations allows capturing the rapid changes in scalar dissipation rates throughout the combustion chamber.

– The implementation of the two-component fuel surrogate is found to provide no significant improvement of the combustion predictions in the steady combustion regime, compared to the one-component fuel. This result suggests the implementation of a two-mixture fraction definition to properly capture the contribution of the two fuel components.

– The new CFD methodology consisting of pairing LES with a FGM-based combustion model coupled to a sub-grid ignition model, is capable of predicting ignition events under various operating conditions with reasonable computing costs. The predictions from this CFD methodology led to outcomes identical to those noted in the experimental investigations conducted with the two configurations considered (the bluff-body stabilized burner used without swirl, and the scaled can combustor designed with liner and air feed holes to modulate combustion and wall cooling). For the bluff-body burner, attention was paid to the ignition event with a particular emphasis on the effect of the spark location and spark parameters on the ignition success. The following results are noted in this regard: (i) The ignition success resulting from a spark deposition strongly depends on the spark location, and therefore on the aerodynamics and mixing fields. (ii) The spark locations providing the highest ignition probability are found to be located in the vicinity of the shear layer delimiting the central recirculation region (it is worth mentioning that for the experiments conducted with the swirler, successful ignition events were found only by sparking outside the recirculation zone, but this case was not considered in the present

study); this high ignitability is mainly due to the fact that such a shear layer zone features mixtures within the flammability limits with low flow velocity, and therefore allows the flame kernel to reach a size that can sustain high strain rates. (iii) In every successful ignition event with spark initially located around the central recirculation zone, the dynamics of the recirculation region always drives the flame kernel towards the bluff-body prior to the flame kernel expansion, and the subsequent full ignition of the burner. (iv) Both the numerical and experimental investigations show that successful ignition events can also be achieved at some other locations outside the zones of highest ignition probabilities, providing that the spark is strong enough (i.e. sufficient energy and deposition time). Such successful ignition events outside the flammable region are likely related to the heat transfer due to the fluid bulk motion and the local strain rate. In order words, the ignition probability can be improved by increasing the spark energy and duration.

– Three types of failed ignition events were reported in the experiments based on the bluff-body stabilized burner. In the first case, the spark deposition was followed by no indication of the flame kernel. For the second scenario, the spark deposition was followed by the flame kernel initiation, propagation, and its subsequent extinction. In the third type of failed ignition event, the spark deposition initiates a flame kernel, the latter propagates and stabilizes for few milliseconds and, subsequently, the flame is blown out of the combustion zone. By varying the spark parameters in the subgrid spark-based ignition model, the newly formulated CFD methodology is proved capable of reproducing each of these ignition event scenarios.

The investigations based on the second configuration was mainly devoted to predict ignition events under various cold start and altitude relight operating conditions. In all the investigations related to these two ignition conditions, attention was paid to the ability of this new developed CFD methodology to predict the ignition envelope drawn with the experimental test data. Various operating conditions (temperature, fuel-air ratio and air mass flow rates) were considered for the cold start investigations, while various operating altitudes (i.e. temperature, pressure) and fuel-air ratios were considered for the altitude relight investigations.

First, unlike the swirl-stabilized combustion chamber which have no experimental data to assess the ability of the new CFD methodology developed in the present thesis with respect to the prediction of ignition events, the configuration employing the P&WC scaled can combustor provides experimental data that can help (at least partly) assessing some of its predictive capabilities. These data include experimental ignition envelopes under various operating conditions for both cold start and altitude relight. Based on the comparison of the numerical predictions with the experiment, the newly developed CFD methodology is proved capable of retrieving the whole ignition sequence under various operating conditions of cold start and altitude relight. All the successful ignition events recorded experimentally are similarly reproduced by the CFD methodology. Failed ignition events are globally obtained for the majority of conditions which are far from those corresponding to the experimental ignition loops.

– For the cold start simulations, two different operating temperatures were considered, namely, 283 K ($\sim 10^{o}C$) and 233 K ($\sim -40^{o}C$). In addition to the fuel-air ratio (and thus the equivalence ratio) which affects the ignition event success, the operating temperature is found to influence the ignition event success. As illustrated by the results based on the operating conditions "A"-"J" presented in Table 4.5 (Chapter 4) with the associated figures, for the same equivalence ratio at these two operating temperatures, a successful ignition event may not be achieved depending on the flow conditions prevailing at the instant of the spark discharge. In the case of a successful ignition event, the total ignition time for the coldest condition (233 K) is found to be longer than that corresponding to the hotter case (283 K). In other words, the amount of spark energy required to achieve a successful ignition event increases when the operating temperature decreases. For the two operating conditions considered outside the experimental ignition loop (either too fuel-rich or too fuel-lean), failed ignition events are noted. The results obtained for these test conditions show that, in addition to the operating temperature prevailing at the instant of the spark discharge, fuel-air ratios propitious to a successful ignition event belong to the fuel flammability range. For the test conditions which are too fuel-lean, the spark discharge initiates a flame kernel which does not propagate due to the lack of flammable mixture. However, for the test condition having a fuel-air ratio larger than the fuel-rich flammability limit, a flame kernel is initiated by the spark discharge. The latter starts propagating and subsequently the flame is blown out of the combustion chamber.

– According to the altitude relight investigations, two operating altitudes were simulated, namely, 4 572 m (15 000 ft) and 10 688 m (35 000 ft). Based on the predictions of the corresponding ignition sequences, the fuel-air ratio (FAR) is found to strongly influence the ignition success with the same trend noted earlier for the cold start investigations. By increasing the operating pressure in some test conditions while maintaining the other conditions, the flame propagation is found to be slower at low (sub-atmospheric) operating pressure. This effect of the pressure on the ignition is further illustrated by contrasting the prediction results at 4 572 m to those corresponding to an altitude of 10 688 m for the same values of the fuel-air ratio. Such an effect is expected considering that combustion under high pressures is thermodynamically more efficient.

The new CFD methodology developed and validated in this thesis allows a better prediction of some complex combustion phenomena while circumventing some issues faced by the combustion community, namely, the high computing cost associated to the incorporation of a sophisticated chemistry model in predicting critical phenomena such as ignition and pollutants emission. These two aspects are of high significance for flight safety and therefore a major concern for combustion engineers and aircraft operators.

5.6 Suggestions for further research

Extensive numerical simulations of transient and steady phases of combustion have so far been conducted for several academic and industrial configurations fed by various gaseous fuels. These investigations have been carried out using different turbulence and combustion models, and the more accurate results were obtained by pairing advanced turbulence models such as LES with advanced combustion models that allows a proper inclusion of chemical kinetic effects with affordable computing costs. In spite of the performance of these advanced turbulence and combustion models in gaseous combustion along with the recent efforts devoted to their extension to spray combustion, comprehensive simulations of reacting spray flows in both transient and steady regimes as well as detailed comparisons of predictions with experiments are still limited so that further investigations are necessary. Due to storage volume constraints, aircraft gas turbines are particularly concerned with liquid fuels and they should meet all the safety, performance, and environmental standards. Of these, the safety and environmental aspects in aircraft gas turbine applications were of primary interest in the current work. For the safety aspect, attention was drawn to the ignition event resulting from a spark discharge under various cold start and altitude relight operating conditions, while the environmental aspect was mainly concerned with the prediction of emissions in the steady combustion regime.

Although the CFD methodology developed in the current thesis yields promising results in the two combustion regimes, it would be interesting to further apply this simulation methodology to the combustion of various liquid fuels in similar configurations, and then, to other configurations employing different fuels under various operating conditions (e.g. fuel-air ratio, temperature, pressure, total pressure drop across the combustion chamber, etc.). Such investigations would require preliminary detailed experimental investigations that can help monitoring all the ignition event sequences corresponding to the operating conditions considered, while providing characteristic data for both the continuous and dispersed phases. Based on the results of these additional validations of the simulation methodology developed in the current work, its robustness can be further illustrated so as to supply industry with a suitable simulation methodology for a better design.

The CFD methodology developed and validated in the current work is composed of LES paired with a subgrid spark-based ignition model. The ignition model is coupled to an advanced combustion model based on the mixture fraction-progress variable formulation (FGM), and the latter allows incorporating a realistic fuel oxidation mechanism along with chemical non-equilibrium effects due to turbulent strain. The Jet A-1 flame properties is first implemented in the ignition model, and the adjusted-ignition model is used to capture the early stage of ignition until the spark kernel reaches the critical size which allows the ignition model transiting to the combustion model. In the ignition model, some simplifying assumptions were adopted, namely, the contribution of the plasma to the flame kernel expansion during the spark discharge was neglected as well as the effects of the droplet on the flame kernel propagation during the pre-breakdown and the breakdown phases of the spark discharge. The global predictive capability of the CFD methodology could be improved by taking such effects into account. Another approach that could potentially improve the predictive capability of this

CFD methodology consists of implementing a more representative correlation for the laminar burning velocity of kerosene in the ignition model instead of using that of one of its major components.

Appendix A

List of publications

Journal Publications

A. Fossi, A. DeChamplain, B. Akih-Kumgeh, "Unsteady RANS and scale adaptive simulations of a turbulent spray flame in a swirled-stabilized gas turbine model combustor using tabulated chemistry", *International Journal of Numerical Methods for Heat and Fluid Flow*, 25(5):1064-1088, (2015)

A. Fossi and A. DeChamplain, "Large Eddy Simulation of Spark-ignition of a Bluff-body Stabilized Burner using a subgrid-ignition model coupled to FGM-based combustion models", *International Journal of Numerical Methods for Heat and Fluid Flow*, (2016), Accepted.

Conference Publications

A. Fossi, A. DeChamplain, MA. Ghazlani, B. Paquet, S. Kalla, JM. Bergthorson, B. Akih-Kumgeh,"Large Eddy Simulation of a Turbulent Swirling Jet-A1 Spray Flame Incorporating chemical non-equilibrium effects through the flamelet model", *In Proceedings of the ASME Turbo Expo 2014*, (Paper GT2014-27225), June 16-21, Düsseldorf, Germany, (2014)

A. Fossi, A. DeChamplain, JM. Bergthorson, B. Paquet, S. Kalla, "Scale-Adaptive and Large Eddy Simulations of a Turbulent Spray flame in a scaled swirl-stabilized gas turbine combustor using strained flamelets", *Proceedings of the ASME Turbo Expo 2015*, (Paper GT2015-42535), June 15-19, Montreal, Canada, (2015).

In preparation

A. Fossi, A. DeChamplain, JM. Bergthorson and B. Akih-Kumgeh, "Large eddy simulation of an ignition sequence and the resulting steady combustion regime in a swirl-stabilized combustor using FGM-based tabulated chemistry" *Journal of Engineering for Gas Turbines and Power* (In Preparation)

A. Fossi, A. DeChamplain, JM. Bergthorson and B. Akih-Kumgeh, "Numerical simulation of spark ignition of an aircraft gas turbine combustion chamber under cold start and altitude relight operating conditions" *Journal of Engineering for Gas Turbines and Power* (In Preparation)

Appendix B

Appendices

Unsteady RANS and Scale Adaptive Simulations of a Turbulent Spray Flame in a Swirl-Stabilized Gas Turbine Model Combustor using Tabulated Chemistry

Alain Fossi, and **Alain deChamplain**

Department of Mechanical Engineering, Combustion Laboratory, Université Laval, Québec, Canada,

and

Benjamin Akih-Kumgeh

Department of Mechanical and Aerospace Engineering, Syracuse University, Syracuse, New York, USA

Abstract:

In this paper, the three-dimensional (3D) structure of a turbulent swirl-stabilized spray flame is numerically investigated using the commercial CFD software ANSYS FLUENT^{TM}. The first scope of the study aims to compare the predictive capabilities of two turbulence models, namely, an Unsteady RANS approach based on the Re-Normalisation Group theory (k-ε RNG model) and the Scale Adaptive Simulation (SAS) for a reasonable trade-off between accuracy of results and global computational cost when applied to simulate swirl-stabilized spray combustion. The second scope of the study is to couple chemical reactions to the turbulent flow using a realistic chemistry model and also to model the local chemical non-equilibrium effects caused by turbulent strain such as flame stretching. Standard Eulerian and Lagrangian approaches are used to describe both the gas and liquid phases, respectively. The computing method includes a two-way coupling in which phase properties and spray source terms are interchanging between the two phases within each coupling time step. The fuel used is liquid jet-A1 which is injected in the form of a polydisperse spray and the droplet evaporation rate is calculated using the infinite conductivity model. A presumed probability density function (PDF) is used to model the turbulent-chemistry interactions. The chemistry model is implemented through the tabulated flamelet-based chemistry approach. One-component (n-decane) and two-component (n-decane + toluene) fuels are used as surrogates for jet-A1. The combustion chemistry is represented through a reduced chemical kinetic mechanism (CKM) comprising 1 045 reactions among 139 species, derived from the detailed jet fuel surrogate model, JetSurf 2.0 using a sensitivity based method, Alternate Species Elimination (ASE). Numerical results of the gas velocity, the gas temperature and the species molar fractions are compared with their experimental counterparts obtained from a steady state flame available in the literature. It is observed that, SAS coupled to the tabulated flamelet-based chemistry, predicts reasonably the main flame trends, while URANS even provided with the

International Journal of Numerical Methods for Heat & Fluid Flow, Vol. 25 No. 5, 2015, pp. 1064-1088.
© Emerald Group Publishing Limited, 0961-5539, DOI 10.1108/HFF-09-2014-0272

same combustion model and computing resources, leads to a poor prediction of the global flame trends, emphasizing the significant asset of a proper resolution of mixing when simulating spray flames.

Keywords: URANS, SAS, Highly swirling flows, Turbulent spray flames, Flamelet model, Detailed chemistry, Jet-A1 surrogates

1-Introduction

Liquid fuels are widely used in many practical combustion systems including industrial liquid-fuelled furnaces, boilers, gas turbines, diesels, spark-ignition engines and liquid-fueled rockets; and they significantly contribute to the energy supply of mankind. In these systems, fuels are usually injected as a fine spray of small droplets that will evaporate and subsequently burn in the gas phase. Combustion efficiency, stability and pollutant formation which are the design and operating criteria, strongly depend on the character of the turbulent spray and chemical reactions. In the combustors of gas turbine engines, these criteria are most often achieved practically by generating swirling flows with strong recirculation regions since they enhance evaporation and mixing between the fuel and the oxidizer, while also improving the flame stabilization mechanism (Lefebvre, 1983). The design of combustors with the desired features requires an improved understanding of turbulent spray combustion systems. This understanding can be provided by experimental, or combined numerical and experimental investigations. Although they are more realistic, experimental investigations are very expensive, so that with the rapid increasing in computing resources, numerical simulations can be a more cost-effective alternative. However, the accuracy of a simulation approach does not only depend on computing resources but also on the robustness of implemented models. Modeling and simulation of turbulent spray flames is still a complex task that involves a number of phenomena which are still not well understood and quantified. These include among turbulence, heat and mass transfer, phase change and chemical reactions which are furthermore highly coupled. For instance, reliable prediction of combustor aerodynamics requires consideration of all anisotropies and unsteadiness present in the flow field while accurate prediction of emissions asks for incorporation of a realistic chemistry model which takes into account non-equilibrium effects (Poinsot and Veynante, 2005). Nowadays, different approaches are available to capture unsteady flow fields. These include the Unsteady Reynolds-Averaged Navier-Stokes (URANS), Direct Numerical Simulation (DNS), Large Eddy Simulation (LES) and hybrid URANS/LES methods. The URANS approaches commonly used in most practical applications are based on a complete statistical averaging and consequently are less accurate compared to Direct Numerical Simulation (DNS) in which the turbulent spectrum is completely resolved. The complete statistical averaging made in the URANS methods allows the prediction of time-mean or ensemble-averaged quantities for velocity, temperature and species distribution of non-reacting and reacting two-phase flow fields with an affordable computational cost, unlike DNS whose application to practical configurations still exceed capabilities of current computers. Thus, URANS enables studying additional phenomena such as those requiring a realistic chemistry model. However, experiences show that URANS approaches can lead to excess turbulent dissipation so that important flow structures might be dissipated. In order to overcome such potential URANS limitations with reasonable computing cost, Scale

International Journal of Numerical Methods for Heat & Fluid Flow, Vol. 25 No. 5, 2015, pp. 1064-1088.
© Emerald Group Publishing Limited, 0961-5539, DOI 10.1108/HFF-09-2014-0272

Resolved Simulation (SRS) approaches are increasingly used. SRS leads to the resolution of large turbulent structures and the models of the effects of small flow structures. Among SRS approaches, LES seems more appropriate to simulate gas turbine combustion systems and its potential in this field has been demonstrated by several authors in representative academic and semi-industrial combustors (Lesieur and Métais, 1996). However, due to the increased computational effort required for LES methods when applying to practical configurations, it is unclear if they will soon be widely employed in gas turbine research and development. Furthermore, some of the relevant phenomena which need further investigations in order to meet the safety requirements and to cope with the surge of environmental regulations (e.g. prediction of the ignition and the pollutants emissions) are strongly related to the chemistry model. As sophisticated chemistry models for jet fuels involve hundreds of chemical species and thousands of elementary reactions, it appears that the implementation of an accurate chemistry model leads to several additional transport equations for species and consequently to a prohibitive computational time which remains a complex task to manage with current computers. Thus, currently, for turbulent model, it is almost necessary to operate with hybrid methods which combine both LES and URANS assets, leading to a reasonable ratio between computational cost and the accuracy of the results. According to the combustion model, commonly-used approaches to overcome the restrictive computational cost of including detailed chemistry include tabulated chemistry methods based on the laminar flame structure. In this concept initially developed to incorporate a detailed chemistry in Computational Fluid Dynamic (CFD) simulation of gaseous flames, a turbulent flame is assumed to behave locally as an ensemble of laminar stretched flamelets (Pitsch and Peters, 1998; Peters, 2000). This concept whose application requires large Damköhler numbers, may be used accurately in most combustors, since in such practical systems, stable and efficient burning is obtained when chemical time scales are shorter than those of the smallest structure of turbulence (Bray *et al*., 2005). The widely separated time scales between chemistry and mixing has two consequences: the structure of the local flame sheet is fairly laminar, and the diffusive transport occurs in the direction normal to the flame front. These two consequences lead to the 1D structure of the elemental flame called flamelet. Chemistry calculations can then be decoupled from those of the mixing processes (Pitsch and Peters, 1998; Peters, 2000), such that chemistry effects are included through the mapping using the pre-calculated chemistry. Whatever the type of combustion (homogeneous or heterogeneous), the accuracy of simulations is strongly related to the adequacy between the combustion mode involved in the combustor and flamelet regime. In fact, for homogeneous combustion, the tabulated chemistry may be based on premixed and/or diffusion flamelet, and each type of flamelet library is suitable for a given combustion regime: tables of premixed and diffusion flamelets are suitable for the simulation of premixed and non-premixed combustion respectively, while flames exhibiting both premixed-like and diffusion-like reactive layers require tables of multi-regimes flamelets. For heterogeneous combustion and particularly for combustors fed by sophisticated atomizers (e.g. air-blast atomizers), in addition to the inclusion of premixing, evaporation effects should also be included (Franzelli *et al*., 2013). Despite reported success in gaseous flames simulations, tabulated chemistry applications to spray flames simulations are very limited, although this approach has the

International Journal of Numerical Methods for Heat & Fluid Flow, Vol. 25 No. 5, 2015, pp. 1064-1088.
© Emerald Group Publishing Limited, 0961-5539, DOI 10.1108/HFF-09-2014-0272

potential to reveal further details involving multiphase. In order to widen the range of applicability of the classical flamelet model, several research teams have proposed some improved versions. These versions can be divided into two main groups: the direct approach allowing the inclusion of evaporation effect in the flamelet table and the indirect approach based on gaseous flamelet table. According to (Hollman and Gutheil, 1996), the direct approach based on spray flamelet model seems more suitable for spray combustion and the consistence of this approach was established in a RANS simulation of a methanol spray flame. However, the application of the model is still demanding in computing resources namely in the pre-processing task since a set of parameters for the spray such as droplet diameter, liquid volume fraction, liquid injection velocity must be varied in order to tabulate the chemistry. On the other hand, considering the sensitivity of the combustion process to the spray characteristics and the mixture fraction fluctuations, it appears that, for a two-phase reactive flow, the reliability of a simulation approach is not related only to the chemistry tabulation approach but also to the robustness of the spray and turbulence models.

The present paper investigates the structure of a turbulent swirling jet-A1 spray flame using a tabulated flamelet-based chemistry method coupled to an URANS approach (k-ε RNG) and thereafter to an hybrid URANS/LES approach (SAS), relying on the assumption that the thermochemical state of a two-phase reactive flow can be mapped by a collection of gaseous flamelets built under the assumption of diffusion flamelets. Each laminar flamelet is then subjected to the local flow field, convecting and stretching in terms of the scalar dissipation rate at the stoichiometric condition. Particularly, in this simulation, the flamelet model based on the steady state assumption which is known as steady flamelet model (STFM) is adopted, and the main objective is to analyze the capability and the limitations of simulation approaches combining each of the turbulence models reported early to a STFM by comparing the simulation data against their experimental counterparts. The paper is organized as follows: the first section is devoted to the physical model while the second and the third section present the experimental configuration and the numerical method respectively. The results of numerical simulation as well as their related analysis are presented in the fourth section.

2- Physical model

Spray flames are commonly modeled using two different approaches (Pitsch *et al*., 2008; Sanjosé *et al*., 2011): Euler-Euler (EE) and Euler-Lagrange (EL). The former leads to spray equations which are similar to those of the gaseous phase, allowing the use of the same computer algorithm for both gas and liquid phases and then, to take full advantages of parallel computing capabilities. Despite this asset and the ability of the EE approach to manage wide range of sprays (from dilute to dense sprays), it does not allow taking into account some relevant spray features (e.g. polydispersity of the spray). In the second approach (EL), each droplet in the spray is viewed as a material point on which various transfers of mass, momentum and heat are applied during the calculation of its trajectory. As each particle is followed in EL approach, it is clear that for sprays containing a very high number of droplets (e.g. several millions and more as it is generally the case for dense sprays), the calculation of all trajectories requires computational resources very much higher than the capabilities of current computers unless the particles are clustered into small groups

International Journal of Numerical Methods for Heat & Fluid Flow, Vol. 25 No. 5, 2015, pp. 1064-1088.
© Emerald Group Publishing Limited, 0961-5539, DOI 10.1108/HFF-09-2014-0272

known as stochastic particles (i.e. groups of particles with neighboring properties) which reduce considerably their number. In this work, the liquid volume fraction is small (<10%) leading to a dilute spray and the EL approach is retained not only for its ability to account for the polydispersity of the spray, but also due to the reasonable number of droplets trajectories to be calculated. The following sections present both gaseous and liquid phases equations respectively.

2-1 Gaseous phase equations

2-1-1 Aerodynamics equations

The set of equations for the simulation of non-reacting two-phase flows includes continuity, momentum, energy and turbulence equations. The equations take the general form:

$$\frac{\partial Q}{\partial t}+\frac{\partial\left(F_j-F_{vj}\right)}{\partial x_j}+\frac{\partial F_p}{\partial x_i}=S \qquad (1) \qquad j\in\{1,2,3\},$$

where for Favre-averaged conservative quantities, $Q=\left[\bar{\rho},\bar{\rho}\tilde{u}_i,\bar{\rho}\tilde{H},\bar{\rho}\tilde{k},\bar{\rho}\tilde{\varepsilon}\right]^T$ $i\in\{1,2,3\}$ with ρ as density, u_i the velocity components, H the total specific energy and $k,\boldsymbol{\varepsilon}$ the turbulent kinetic energy and its dissipation rate respectively. F_j and F_{vj} are respectively the inviscid and the viscous fluxes in various spatial directions (x, y and z); F_p is the mechanical pressure reflecting normal stresses included in the momentum equation; S is the vector of source terms accounting for interactions with the liquid phase. The expressions of F_j, F_{vj} and S are explicitly presented in Table 1, except for those corresponding to the transport equations of $\bar{\rho}\tilde{k}$ and $\bar{\rho}\tilde{\varepsilon}$ which are presented in the next section devoted to the turbulence model.

Table 1: Expressions of F_j, F_{vj} and S

Q	F_j	F_{vj}	F_p	S
$\bar{\rho}$	$\bar{\rho}\tilde{u}_j$	0	0	$\tilde{\dot{S}}_m=\sum_{k=1}^{N_p}(n\dot{m})_{p,k}$
$\bar{\rho}\tilde{u}_i$	$\bar{\rho}\tilde{u}_i\tilde{u}_j+\overline{\boldsymbol{\rho u_i'u_j'}}$	$\mu\bar{\rho}\left(\frac{\partial\tilde{u}_i}{\partial x_j}+\frac{\partial\tilde{u}_j}{\partial x_i}-\frac{2}{3}\delta_{ij}\frac{\partial\widetilde{u_k}}{\partial x_k}\right)$	$\tilde{P}$	$\tilde{\dot{S}}_{u_i}=\sum_{k=1}^{N_p}(n\dot{m}u_i)_{p,k}$
$\bar{\rho}\tilde{H}$	$\bar{\rho}\tilde{H}\tilde{u}_j$	$\bar{\rho}D_T\frac{\partial\tilde{H}}{\partial x_j}$	0	$\tilde{\dot{S}}_H=\sum_{k=1}^{N_p}(n\dot{m}H)_{p,k}$

2-1-2 Turbulence model

In the first part of this work, the above system of partial differential equations is closed using Boussinesq hypothesis which relates Reynolds stresses to the mean velocity gradient through the turbulent viscosity. The advantage of this approach is the relatively low computing cost associated with the computation of the turbulent viscosity whatever the closure method (i.e. one or two equations models). However, closure models based on the turbulent viscosity neglect the anisotropy of the mean flow turbulence. This is not strictly true for some complex flows such as highly swirling flows. For such flow configurations, a more suitable URANS approach would be the Reynolds Stress Model (RSM) whereby a transport equation for each term in the Reynolds stress tensor is solved. As one of the main objectives of this study is to setup a simulation approach which leads to an efficient use of the available computational resources with a reasonable computing time and the accuracy of results, additional computational expenses

International Journal of Numerical Methods for Heat & Fluid Flow, Vol. 25 No. 5, 2015, pp. 1064-1088.
© Emerald Group Publishing Limited, 0961-5539, DOI 10.1108/HFF-09-2014-0272

which are not justified are avoided. Thus, instead of using the RSM to take into account some features of the investigated flow, the $k-\boldsymbol{\varepsilon}$ RNG (Yakhot *et al*., 1992) is used in the first part of the present study.

- **$k-\boldsymbol{\varepsilon}$ RNG Model**

The choice of this model is mainly related to the presence of additional term in its "$\boldsymbol{\varepsilon}$" equation which improves the accuracy for rapidly strained flows. The model also uses an analytical formula for the turbulent Prandtl number, the effect of low Reynolds number flow can be accounted for, and the effect of the swirl on the turbulence can be included through an appropriate modification of the turbulent viscosity. In order to address the highly-swirled nature of the flow, this later asset of the $\mathrm{k}-\boldsymbol{\varepsilon}$ RNG model is particularly useful in the first part of the present study. The mathematical formulation of the gradient diffusion assumption and that allowing the inclusion of the effect of the swirl in the mean flow are respectively given by equations (2) and (3).

$$-\bar{\rho}\widetilde{u_i'u_j'} = \mu_t\left(\frac{\partial\widetilde{u}_i}{\partial x_j}+\frac{\partial\widetilde{u}_j}{\partial x_i}\right)-\frac{2}{3}\left(\bar{\rho}k+\mu_t\frac{\partial\widetilde{u_k}}{\partial x_k}\right)\delta_{ij} \qquad (2)$$

$$\mu_t = \mu_{t0} f\left(a_s, \Omega, \frac{k}{\varepsilon}\right) \qquad (3)$$

where μ_t is the turbulent viscosity, μ_{t0} is the turbulent viscosity calculated without swirl modification as given by (4) where $C_\mu = 0.0845$. This value derived using the RNG theory is very close to the empirically-determined value of 0.09 used in the standard $\mathrm{k}-\boldsymbol{\varepsilon}$ model; Ω is a characteristic swirl number; a_s is a swirl constant that depends on whether the flow is swirl-dominated or only mildly swirling. The turbulent viscosity is modeled according to (3) in which k and $\boldsymbol{\varepsilon}$ are obtained by solving their transport equations respectively given by equations (5) and (6).

$$\mu_{t0} = \bar{\rho}C_\mu\frac{\tilde{k}^2}{\tilde{\varepsilon}} \qquad (4)$$

$$\frac{\partial}{\partial t}(\bar{\rho}\tilde{k})+\frac{\partial}{\partial x_j}(\bar{\rho}\tilde{k}\widetilde{u_i}) = \frac{\partial}{\partial x_j}\left(a_k\mu_{eff}\frac{\partial\tilde{k}}{\partial x_j}\right)+G_k+G_b-\bar{\rho}\tilde{\varepsilon}-Y_M+S_k \qquad (5)$$

$$\frac{\partial}{\partial t}(\bar{\rho}\tilde{\varepsilon})+\frac{\partial}{\partial x_j}(\bar{\rho}\tilde{\varepsilon}\widetilde{u_i}) = \frac{\partial}{\partial x_j}\left(a_\varepsilon\mu_{eff}\frac{\partial\tilde{\varepsilon}}{\partial x_j}\right)+C_{1k}\frac{\tilde{\varepsilon}}{\tilde{k}}(G_k+C_{3\varepsilon}G_b)-C_{2\varepsilon}\bar{\rho}\frac{\tilde{\varepsilon}^2}{\tilde{k}}-R_\varepsilon+S_\varepsilon \qquad (6)$$

G_k and G_b represent the generation of turbulence kinetic energy respectively due to the mean velocity gradients and buoyancy ($G_b \sim 0$ as the effect of the gravity is neglected in this work), Y_M represents the contribution of the fluctuating dilatation in compressible turbulence to the overall dissipation rate. The expressions of G_k and Y_M and the values of constants are evaluated as in the standard $\mathrm{k}-\boldsymbol{\varepsilon}$ model (Launder and Sharma, 1974). $S_k = \sum_{k=1}^{N_p} u_i'\left(n\dot{m}u_j\right)_{p,k}$ and $S_\varepsilon = S_k\tilde{\varepsilon}/\tilde{k}$ are the source terms used to take into account effects of the spray on the turbulence; n denotes the droplet number density, $\dot{m}$ the mass evaporation rate of particles in group k and N_p is the number of particles; $\mu_{eff} = \mu_t + \mu$, where μ_t is the effective viscosity as given by equations (2) and (3); a_k and a_ε are the effective Prandtl numbers for k and ε, determined using a formula derived analytically by the RNG theory:

International Journal of Numerical Methods for Heat & Fluid Flow, Vol. 25 No. 5, 2015, pp. 1064-1088.
© Emerald Group Publishing Limited, 0961-5539, DOI 10.1108/HFF-09-2014-0272

$$\left|\frac{a-1.3929}{a_0-1.3929}\right|^{0.6321}\left|\frac{a+2.3929}{a_0+2.3929}\right|^{0.3679}=\frac{\mu_{mol}}{\mu_{eff}} \qquad (7)$$

where $a_0 = 1.0$. In the high-Reynolds-number limit ($\mu_{mol}/\mu_{eff} \ll 1$), $a_k = a_\varepsilon \approx 1.393$; R_ε on the right-hand side of equation (6) is the additional term in the RNG version which differentiates it from the standard $\mathrm{k}-\boldsymbol{\varepsilon}$ model. By making positive and negative contributions in the regions of small and large strain rate respectively, the R_ε term makes the RNG model to be more responsive to rapid strain and streamline curvature than the standard $\mathrm{k}-\boldsymbol{\varepsilon}$ model. Despite the ability of RSM and all URANS models based on the gradient diffusion assumption to capture reasonably well relevant features of some unsteady flow fields, they are too dissipative (i.e. the resolved scales are damping relatively too quickly) and in some extent, more elaborated turbulence approaches are necessary to achieve acceptable levels of accuracy. In this light, it is proven that Scales Resolved Methods (SRM) outperform URANS approaches: as the turbulent spectrum characterized by large scales is resolved while only that corresponding to small scales is modeled. Among the SRM, the most promising is the Large Eddy Simulation (LES) which is strongly dependent upon mesh resolution since the cut-off length scale which defines the fraction of the turbulent spectrum to be resolved is proportional to the local cell size. Based on this feature for LES, it is clear that the full exploitation of the prediction capabilities of LES requires a high mesh resolution and also suitable sub-grid models (SGM) to account for interactions between sub-grid scales (SGS) and interactions between resolved scales and SGS. In order to circumvent potential high computing cost that LES would require for simulation of a given physical system as a whole, the similarity between the URANS and the LES momentum equation allows for the formulation of new models called hybrid models that can switch from URANS to LES mode, by lowering the eddy viscosity appropriately in the LES zone, without any formal change to the momentum equations. These hybrid models include Detached Eddy Simulation (DES) and Scale-Adaptive Simulation (SAS). Particularly, the second part of this work is done using SAS model whose mathematical formulation is presented in the following section.

- **Scale-Adaptive Simulation method**

Due to its ability to resolve partially the turbulent spectrum, SAS belongs to the group of SRS approaches. However, the method is viewed as a second generation of URANS method rather than a sub-grid scale modeling approach. In fact, this method does not contain any parameter related to the grid used for the resolution of transport equations as it would be the case for LES and DES for instance (Menter and Egorov, 2010). SAS was developed by (Menter and Egorov, 2010) by modifying the $k-kL$ developed by Rotta. In the modifications made to the Rotta model, a second length scale, the Von Karmann length-scale $L_{\nu K}$, is introduced to take into account the length-scale of the resolved eddies. Thus, unlike the standard turbulence models which provide a length scale proportional to the thickness of the shear layer, SAS dynamically adjusts to the length scale of the resolved structures depending on the flow situation. More explicitly, the new length-scale, $L_{\nu K}$, allows SAS model to operate in RANS-like mode in stable regions of the flow and to exhibit LES-like resolution in the unstable flow regions. The transition from RANS to SAS is initiated

International Journal of Numerical Methods for Heat & Fluid Flow, Vol. 25 No. 5, 2015, pp. 1064-1088.
© Emerald Group Publishing Limited, 0961-5539, DOI 10.1108/HFF-09-2014-0272

by the level of flow instabilities. For flow involving weak instabilities, SAS model leads to results close to those of URANS. The mathematical formulation of the SAS approach is given by equations (8) and (9).

$$\frac{\partial}{\partial t}(\bar{\rho}\tilde{k}) + \frac{\partial}{\partial x_j}(\bar{\rho}\tilde{k}\tilde{u}_i) = \frac{\partial}{\partial x_j}\left[\left(\mu + \frac{\mu_t}{\sigma_k}\right)\frac{\partial \tilde{k}}{\partial x_j}\right] - \bar{\rho}\tilde{k}\tilde{\omega}C_\mu + G_k + S_k \qquad (8)$$

$$\frac{\partial}{\partial t}(\bar{\rho}\tilde{\omega}) + \frac{\partial}{\partial x_j}(\bar{\rho}\tilde{\omega}\tilde{u}_i) = \frac{\partial}{\partial x_j}\left[\left(\mu + \frac{\mu_t}{\sigma_\omega}\right)\frac{\partial \tilde{\omega}}{\partial x_j}\right] + a\frac{\tilde{\omega}}{\tilde{k}}G_k - \bar{\rho}\beta\tilde{\omega}^2 + Q_{SAS} + (1-F_1)\frac{2\bar{\rho}}{\sigma_{\omega,2}}\frac{1}{\tilde{\omega}}\frac{\partial \tilde{k}}{\partial x_j}\frac{\partial \tilde{\omega}}{\partial x_j} + S_\varepsilon \quad (9)$$

where $\eta_2 = 3.51$, $\sigma_\Phi = 2/3$, $C = 2$, $L = \sqrt{k}/\left(C_\mu^{1/4}\tilde{\omega}\right)$, $F_1 = \frac{1}{\tilde{\omega}}\frac{\partial \tilde{\omega}}{\partial x_j}\Big/\frac{1}{\tilde{k}}\frac{\partial \tilde{k}}{\partial x_j}$ and $L_{vK} = k\frac{\partial \tilde{u}_j}{\partial y}\Big/\frac{\partial^2 u}{\partial y^2}$ (a Von Karmann length scale). The Q_{SAS} term is defined by equation (10):

$$Q_{SAS} = max\left[\bar{\rho}\eta_2 kS^2\left[\frac{L}{L_{vK}}\right]^2 - C\frac{2\bar{\rho}\tilde{k}}{\sigma_\Phi}max\left[\frac{1}{\tilde{\omega}^2}\frac{\partial \tilde{\omega}}{\partial x_j}\frac{\partial \tilde{\omega}}{\partial x_j}, \frac{1}{\tilde{k}^2}\frac{\partial \tilde{k}}{\partial x_j}\frac{\partial \tilde{k}}{\partial x_j}\right], 0\right] \qquad (10)$$

2-1-3 Combustion model

In gas turbine combustors, liquid fuels are generally injected as a spray of small droplets. Considering that chemical reactions during combustion occur in gas phase, the liquid fuel must first evaporate and mix properly with the oxidizer. Thus, spray flames can be classified as non-premixed flames or more realistically as partially-premixed flames. However, the combustor investigated in the present study is fueled by a *pressure swirl atomizer* ("simplex") which is less sophisticated compare to an *air-blast atomizer*, for example. Thus, the non-premixed combustion mode is retained for the present study. In this mode, mixing of reactants feed into the reaction zone must occur fast enough for combustion to proceed. For homogeneous (gaseous) combustion in a two-feed combustor, under the assumption of equal diffusivities, the thermochemical state of the fluid can be related to a non-reactive scalar, the mixture fraction, Z, which acts as measure of the local equivalence ratio. It is expressed by $Z = (Y_i - Y_{i.2})/(Y_{i,1} - Y_{i,2}) \equiv (\beta - \beta_2)/(\beta_1 - \beta_2)$ according to (Bilger *et al*., 1991), where subscripts 1 and 2 refer to fuel and air streams, respectively; β is a Shvab-Zeldovich function; Y_i is the elemental mass fraction of element "*i*". It is seen that $Z = 1$ from feed 1, and 0 from feed 2, and that Z may be physically interpreted as the mass fraction of material in the mixture which originated from feed 1, with $(1 - Z)$ originating from feed 2. With the assumption of equal diffusivities, the balance equations for all chemical elements are identical; there is no source term. By introducing this result in the transport equations of species, it leads to a single transport equation of the mixture fraction which includes changes due to convection and, diffusion but no chemical reactions. However, for spray combustion, the mixture fraction is no longer a conserved scale because of the evaporation of droplets (Hollman and Gutheil, 1998; Chrigui et al., 2012). In order to take into account the evaporation effects, a source term is added in the conventional transport equation for the mixture fraction, leading to the following modified Favre-averaged transport equation:

$$\frac{\partial \bar{\rho}\tilde{Z}}{\partial t} + \frac{\partial}{\partial x_j}(\bar{\rho}\tilde{u}_j\tilde{Z}) = \frac{\partial}{\partial x_j}\left[\left(\bar{\rho}D_Z + \frac{\mu_t}{\sigma_t}\right)\frac{\partial \tilde{Z}}{\partial x_j}\right] + \tilde{\dot{S}}_m \qquad (10)$$

International Journal of Numerical Methods for Heat & Fluid Flow, Vol. 25 No. 5, 2015, pp. 1064-1088.
© Emerald Group Publishing Limited, 0961-5539, DOI 10.1108/HFF-09-2014-0272

where D_Z is the mixture fraction diffusion coefficient, which is selected such that the Lewis number of the mixture Le_Z fraction is unity (*Pitsch and Peters, 1998*), σ_t is the turbulent Schmidt number, and $\tilde{\dot{S}}_m$ is the mass transfer rate due to the evaporation of droplets. This new formulation of the mixture fraction transport equation extends the conserved scalar approach to two-phase turbulent reacting systems. As such systems involve turbulence and heat transfer between both gas and liquid phases, the instantaneous fields of thermochemical variables are not only related to the mixture fraction, but also to the enthalpy. Turbulence-chemistry interactions are modeled through mixture fraction fluctuations using a presumed probability density function (PDF) which can be obtained either by presuming or by solving a balance equation. For engineering applications, a widely used, but approximate solution is to presume the shape of the PDF using simple analytical function. In this vein, the most popular shape for the presumed-PDF of the mixture fraction is the β-function which depends on two parameters, the mean mixture fraction $\tilde{Z}$ and its variance $\widetilde{Z''^2}$:

$$P(Z) = \frac{\Gamma(a+b)Z^{a-1}(1-Z)^{b-1}}{\Gamma(a)\Gamma(b)} \qquad (11)$$

where a and b are the PDF parameters calculated using the mean mixture fraction and its variance as:

$$a = \tilde{Z}\left[\frac{\tilde{Z}(1-\tilde{Z})}{\widetilde{Z''^2}} - 1\right];\ b = (1-\tilde{Z})\left[\frac{\tilde{Z}(1-\tilde{Z})}{\widetilde{Z''^2}:} - 1\right] \qquad (12)$$

Thus, in order to determine the distribution of the thermochemical variables in the combustor, an additional transport equation or a model is required for the mixture fraction variance.

$$\frac{\partial \overline{\rho}\widetilde{Z''^2}}{\partial t} + \frac{\partial}{\partial x_j}\left(\overline{\rho}\tilde{u}_j\widetilde{Z''^2}\right) = \frac{\partial}{\partial x_j}\left[\left(\overline{\rho}D_{\widetilde{Z''^2}} + \frac{\mu_t}{\sigma_t}\right)\frac{\partial \widetilde{Z''^2}}{\partial x_j}\right] + C_g\mu_t\left(\frac{\partial \tilde{Z}}{\partial x_j}\right) - \overline{\rho}\chi + \frac{\widetilde{Z''^2}(1-2\widetilde{Z''^2})}{\widetilde{Z''^2}}\tilde{S}_m \qquad (13)$$

Where $\chi = 2D_Z\left(\nabla\tilde{Z}\right)^2$ is the scalar dissipation rate which accounts for the influence of the turbulent flow field on the flame structure (e.g. flame stretching). It is modeled by $\chi = C_d\widetilde{Z''^2}\,\tilde{\varepsilon}/\tilde{k}$ (i.e. a linear function of the strain rate, $a_s = \tilde{\varepsilon}/\tilde{k}$), where $C_d \approx 2.0$. By adding the equation of state to the set of equations above and solving the resulting system, the values of the mean-mixture fraction at each point in the combustor are generated and the related mean values of thermochemical variables are obtained from a look-up database. This database is built using the PDF and the relationship between the thermochemical variables and the mixture fraction which may be based on either equilibrium (EQ) or non-equilibrium (NEQ) assumptions, depending on whether chemical NEQ effects need to be taken into account or not. The EQ model assumes that the chemistry is rapid enough for chemical equilibrium to always exist at the molecular level. An algorithm based on the minimization of Gibbs free energy is used to express the thermochemical variables as a function of Z. The EQ model is sturdy for some practical problems since it can reasonably predict some intermediate species and it does not require knowledge of detailed chemical kinetic rate data. However, in combustion chambers involving substantial chemical non-equilibrium effects, the local chemical equilibrium assumption may lead to unrealistic results. Furthermore, from a general point of view, the EQ model cannot allow the investigation of phenomena which strongly depend on the chemical kinetic

International Journal of Numerical Methods for Heat & Fluid Flow, Vol. 25 No. 5, 2015, pp. 1064-1088.
© Emerald Group Publishing Limited, 0961-5539, DOI 10.1108/HFF-09-2014-0272

scheme (e.g. ignition, pollutants emissions, etc.). In the present simulations, a realistic chemistry model is used by means of the tabulated flamelet-based chemistry approach. The tabulated chemistry derives from the simulations of one dimensional chemical structure of laminar diffusion flames. The method allows not only to implement a realistic chemical scheme, but also to include some chemical non-equilibrium effects such as those caused by the turbulent strain (e.g. flame stretching). This approach is widely used under the steady state assumption and leads to a reduced model called steady flamelet model (STFM) whereby, the flame structure is assumed to be only controlled by the balance between steady chemical reactions and steady diffusion processes. However, the STFM has some drawbacks namely the inaccurate predictions of some species involved in slow reactions, and the failure in terms of prediction of some phenomena such as flames lift-off, local ignition and re-ignition. These weaknesses of the model are related to the restrictiveness of the solution space as it is shown by the corresponding S-shaped curve. For the sake of simplicity, the STFM is retained for this work after some preliminary investigations that proved that the flame investigated lies within the diffusion-reaction regime of the Peters diagram (Peters, 2000). The investigated turbulent flame can then be viewed as an ensemble of laminar stretched flamelets. The flamelet equations can be expressed either in a physical or in a mixture fraction space. In this work, since the scalar transport equation is replaced by the mixture fraction transport equation, the flamelet equations are expressed in the mixture fraction space. This is done by applying a Crocco-type coordinate transformation on both the species and the energy equation, the new coordinate system being attached to the surface of the flame (Pitsch and Peters, 1998; Peters, 2000). By further assuming unity Lewis number, equations of the STFM can be written as follows:

$$\frac{\rho\chi}{2}\frac{\partial^2 Y_i}{\partial Z^2} + \dot{\omega}_i = 0 \quad (14)$$

$$\frac{\rho\chi}{2}\frac{\partial^2 T}{\partial Z^2} + \frac{\rho\chi}{2C_p}\frac{\partial C_p}{\partial Z}\frac{\partial T}{\partial Z} + \frac{\rho\chi}{2C_p}\sum_{i=1}^{N}\left(C_{pi}\frac{\partial Y_i}{\partial Z}\right)\frac{\partial T}{\partial Z} - \frac{1}{C_p}\sum_{i=1}^{N} h_i\dot{\omega}_i + \frac{Q_R}{C_p} = 0 \quad (15)$$

In these equations, C_p is mixture-averaged specific heat; C_{pi} specific heat of the i^{th} species; Y_i mass fraction of the i^{th} species; $\dot{\omega}_i$ net rate of production of the i^{th} species; Le_i Lewis number of the i^{th} species defined by $Le_i = \lambda/(\rho D_{im} C_p)$; D_{im} the multicomponent ordinary diffusion coefficient ; h_i enthalpy of i^{th} species; and Q_R is the radiating heat loss. The scalar dissipation rate χ is modeled through the formula proposed by Peters (Pitsch and Peters, 1998): $\chi(Z) = \chi_{st} exp\{-2[erfc^{-1}(2Z)]^2\}_s / exp\{-2[erfc^{-1}(2Z_{st})]^2\}$, where χ_{st} is the scalar dissipation rate at the stoichiometric conditions. Thus, given the boundary conditions for species and temperature at the fuel and oxidizer streams, a CKM and a profile of the scalar dissipation rate, $\chi(Z)$, equations (14) and (15) can be integrated numerically to obtain unequivocal relations between the mixture fraction and the generic scalars (also called flamelet solutions): $\Phi_i \equiv \Phi_i(Z, \chi_{st}) = \{Y_i(Z, \chi_{st}); T(Z, \chi_{st})\}$. Once flamelet solutions are obtained, they are convoluted with the PDF using equation (16) to produce the flamelet library for look-up process:

International Journal of Numerical Methods for Heat & Fluid Flow, Vol. 25 No. 5, 2015, pp. 1064-1088.
© Emerald Group Publishing Limited, 0961-5539, DOI 10.1108/HFF-09-2014-0272

$$\widetilde{\Phi}_i\left(\widetilde{Z},\widetilde{H}_s,\tilde{\chi}_{st}\right)=\int_0^1 P_a(Z,\chi_{st},H_s)\Phi_i(Z,\chi_{st},\widetilde{H}_s)dZ\ =\ \int_0^1 P(Z)\Phi_i(Z,\tilde{\chi}_{st},\widetilde{H}_s)dZ,\quad (16)$$

where H_s is the enthalpy, P_a is the joint-PDF defined by $P_a(Z,\chi,H)=P(Z)\delta(\chi_{st}-\tilde{\chi}_{st})\delta\left(H_s-\widetilde{H}_s\right)$ (i.e. turbulent fluctuations of χ_{st} and H_s are neglected, and statistical independence is assumed between variables), and $P(Z)$ is the $\boldsymbol{\beta}$-PDF defined previously.

2-2 Liquid phase equations

A Lagrangian analysis of the liquid phase leads to its description in terms of droplet position, velocity, radius and thermodynamic state; each droplet is then considered as a particle. Assuming a dilute spray of small droplets (Sauter Mean Diameter: $SMD{\sim}60\ \mu m$**)**, (i) droplet-droplet interaction and coalescence can be neglected; (ii) the effect of gravity compared to others forces acting on the droplet is considered negligible; (iii) concerning the momentum equation, only drag and thermophoretic forces are considered; (iv) effect of convection on each droplet is accounted for as well as the droplet break-up phenomenon. The position of each particle is obtained from $dX_d=V_d dt$; the acceleration of the d^{th} droplet is obtained by integrating the force balance on the particle, which is written in a Lagrangian reference frame. This force balance equates the droplet inertia with the forces acting on the droplet, and may be written as $A_d=F_D(u_i-V_d)+F_{add}$, where the drag force per unit mass F_D is defined by $F_D=18\mu/\rho_d d_d^2\ \times C_D R_e/24$, u_i is the gaseous phase velocity, V_d is the droplet velocity, μ is the molecular viscosity of the liquid, ρ is the gas density, ρ_d is the density of the droplet, d_d is the droplet diameter, R_e is the relative Reynolds number defined as $R_e=\rho d_d|u_i-V_d|/\mu$ and C_D is the droplet drag coefficient. The accurate determination of C_D is crucial for spray modeling. In this work, it is determined dynamically to account for variations which occur in the droplet shape (i.e. shape distortion experienced by an initially spherical droplet moves through a gas), $C_d=C_{d,sphere}(1+2.623y)$. Here y is the distortion coefficient, obtained by solving a second order ordinary differential equation (Liu *et al.*, 1993). The term F_{add} represents the resultant thermophoretic, Brownian and Saffman lift forces. In this work, the droplets considered are not sub-micron ($d_d>10^{-6}m$) thus one can neglect both Brownian and Saffman's Lift forces. The heat exchange between droplets and the gaseous phase are governed by inert heating, vaporization and droplet boiling. These processes are subsequent and are initiated by the vaporization temperature and the boiling temperature. Mass and heat transfers are assumed to be controlled by convective and diffusive transports and the infinite liquid-conductivity model is used for their modeling. Thus, the droplet surface temperature is assumed uniform, time-varying and equal to the temperature inside the droplet and, finite liquid thermal conductivity and droplet internal circulation are neglected (Abramzon and Sirignano, 1989). The inert heating increases the temperature of the droplets up to the "flash point". During this step, there is no exchange of mass between gaseous and liquid phases and the following relation is used to determine the change in temperature due to heat exchange with the gaseous phase: $m_{dj}c_{dj}\,dT_{dj}/dt=hS_{dj}\left(\tilde{T}_\infty-T_{dj}\right)$, neglecting radiation; during the second step, the droplet temperature reaches the vaporization temperature and the mass is transferred from the liquid phase to the

International Journal of Numerical Methods for Heat & Fluid Flow, Vol. 25 No. 5, 2015, pp. 1064-1088.
© Emerald Group Publishing Limited, 0961-5539, DOI 10.1108/HFF-09-2014-0272

gaseous phase. The vaporization rate is given by: $\dot{m}_{dj} = dm_{dj}/dt = S_{dj} k_{c,j} \rho_\infty ln\left(1 + B_{m,j}\right)$, where m_{dj} is the mass of component "*j*" in droplet; $k_{c,j}$ is the mass transfer coefficient of component "*j*" ; S_{dj} is the droplet surface area; ρ_∞ is the density of bulk gas; $B_{m,j}$ is the Spalding mass number for species "*j*" and T_{dj} is the droplet temperature. For the one-component fuel, $j = 1$ while for the two-component fuel, $j \in \{1,2\}$. In the third step, the fuel is in the boiling regime, the boiling rate is calculated by: $\dot{m}_{dj} = x_j \pi d_d k_\infty / c_{p\infty} (2.0 + 0.6 Re_d^{1/2} Sc^{1/3}) ln\left(1 + B_{T,j}\right)$, where x_j stands for the volume fraction of component "*j*" in the droplet, d_d the droplet diameter and $B_{T,j}$ is the Spalding heat transfer number for component "j" computed as: $B_{T,j} = c_{p\infty}\left(\tilde{T}_\infty - T_d\right)/h_{vap,j}$, where $h_{vap,j}$ is the latent heat of vaporization for component "*j*". Finally, the temporal change in temperature for multicomponent droplets, neglecting the radiation effect is calculated by: $m_d C_d \dot{T}_d = h S_d\left(\tilde{T}_\infty - T_d\right) + \dot{m}_d h_{fg}$, where h_{fg} is the latent heat, h is the heat convection coefficient calculated using the modified Nusselt number defined by: $Nu = h d_d / k_\infty = (2.0 + 0.6 Re_d^{1/2} Pr^{1/3}) \ln(1 + B_T)/B_T$, in which $Pr = c_g \mu / k_\infty$ is the Prandtl number. The multicomponent vaporization and boiling rates are calculated using the sum of the vaporization and boiling rates of the individual components.

3- Experimental configuration

The setup considered in the present simulation was investigated experimentally by Sheen (*Sheen, 1993*) and thereafter, numerically by (Jones *et al.*, 2012) using a four-step reaction mechanism implemented in an in-house CFD code. It consists of an annular swirling air jet flowing into a cylindrical combustion chamber. A schematic representation of the combustor is shown in Figure 1. The combustion chamber has a length of 500 mm and an internal diameter of 200 mm. The swirl is produced by an aerodynamic gas turbine type swirler with 20 equally spaced vanes with a discharge angle of 30^o to the axis. It is located in an annular duct 50 mm up-stream of the front plate of the combustor. The fuel injector ($d_{inj} = 0.25\, mm$), located at the centre of the combustor head, injects liquid jet-A1 in the form of a fine hollow cone spray into the central recirculation zone. The air and the liquid spray are not preheated ($T{\sim}300K$) and the exit of the combustor is open to the atmosphere. The co-flowing air enters the combustor axially with a tangential velocity component generated by the swirler. Given the lack of measurements of the flow upstream of the annular duct exit, an intermediate simulation step is necessary for the specification of accurate inflow boundary conditions. Top-hat profiles are used for axial and tangential components of the velocity. The values imposed at the inlet of the combustion chamber are adjusted so that the total mass flow rate of air and the swirl number at the inlet are consistent with the experimental values. The fuel mass flow rate is 0.951 g/s and the air-to-fuel ratio is 27.88. The annular pipe has an outer radius R = 21 mm which is used as a reference scale in the axial direction of the combustor. The combustor is highly swirled since its swirl number, S = 0.91 > 0.6. The correlation proposed by (Beer and Chigier, 1972) is used to deduce the swirl component of velocity.

International Journal of Numerical Methods for Heat & Fluid Flow, Vol. 25 No. 5, 2015, pp. 1064-1088.
© Emerald Group Publishing Limited, 0961-5539, DOI 10.1108/HFF-09-2014-0272

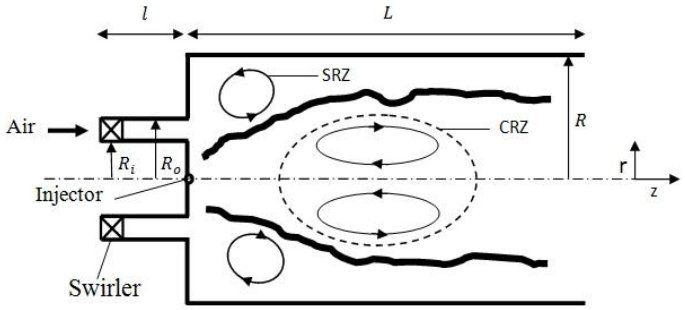

Figure 1: Sketch of the combustor. CRZ and SRZ are respectively the central and the secondary recirculation zone; $R_o = 21\,mm$ and $R_i = 11\,mm$ are the outer radius and the inner radius of the annular channel; $l = 50\,mm$ and $L = 500\,mm$ are respectively the lengths of the annular channel and the combustor.

4- Numerical model

The combustion chamber presented in Figure 1 is discretized using a structured mesh comprising 2.1 million hexahedral elements. The grid is smoothed and refined near the solid boundaries and in particular, around the combustor axis and the injector exit: approximately 60% of the elements are localized in these zones of the combustor. Simulations are performed with the double precision mode using the pressure-based solver of the finite volume-based ANSYS FLUENT CFD code (ANSYS FLUENT™ v14, 2012). The Semi-Implicit Method for Pressure Linked Equations (SIMPLE) algorithm in the A segregated solver is used for the pressure-velocity coupling. Second-order schemes are used for pressure, momentum, turbulent quantities (k and $\boldsymbol{\varepsilon}$) and interpolations of thermochemical variables (i.e. values of thermochemical variables at the cell-faces). The discretization of all diffusive terms is done using second-order accurate schemes. The temporal discretization is done using an implicit second-order scheme, which is based on an iterative time-advancement algorithm. Thus, all the transport equations are solved iteratively, for a given time-step until the convergence criteria are satisfied, before advancing to the next time step. For the SAS model, the momentum equations are discretized with a bounded central differencing scheme while transient derivatives are discretized using bounded second-order implicit scheme. In the present study, the ANSYS FLUENT flamelet solver is used to generate flamelet solutions using the skeletal chemical kinetic mechanism for the fuel surrogate. Temperature-dependent transport properties and empirical saturated vapor pressure correlation are implemented in the CFD code. The spray dynamics is described in a Lagrangian manner using the discrete phase model (DPM). The cone injection model is used to simulate the droplet distribution generated by a *Simplex atomizer*. The droplet sizes distribution is assumed to satisfy the classical Rosin-Rammler function, $f(d) = exp[-(d/d_m)^n]$, where n is the spread parameter which measures the dispersion of droplet sizes, d_m is the mean diameter of droplets. The numerical coupling between gaseous and liquid phases is performed by interchanging flow properties and particles source terms between both phases. The coupling between the two phases is accomplished using the time marching algorithm of the continuous phase because of the disparity between the fluid motion and the droplet motion, and particularly the small time scales involved in the evaporation process of droplets having diameters in

International Journal of Numerical Methods for Heat & Fluid Flow, Vol. 25 No. 5, 2015, pp. 1064-1088.
© Emerald Group Publishing Limited, 0961-5539, DOI 10.1108/HFF-09-2014-0272

the micrometer range. For each liquid-phase iteration ten gaseous phase iterations are performed, and the time step is defined using a representative convective time scale calculated from the inlet velocity and the outer radius of the annular channel. In the present study, the spread parameter (n), the droplet mean diameter (d_m) and the spray cone angle are approximated through a parametric study based on empirical data of *Simplex injectors* as reported by Lefebvre (*Lefebvre, 1989*). The inlet boundary conditions are presented in the following sections.

- *Flow boundary conditions*

Top-hat profiles based on experimental equivalence ratio, fuel mass flow rate and swirl number are used for axial and tangential components of air velocity. The calculated values are summarized in Table 2.

Table 2: Boundary conditions: Air inlet

Axial velocity (m/s)	Swirl velocity (m/s)	Air tempe-rature (K)	Air-to-fuel ratio	Swirl number	Flow Reynolds number (in the annular channel)
19.2	17.5	300	27.88	0.91	$\approx 21\,350$

- *Spray boundary conditions*

As oulined in the above section, preliminary simulations dedicated to the calibration of the injection model are performed. The set of the investigated parameters, as well as those leading to a reasonable prediction of the aerodynamics of the combustor are shown in Table 3. Thus, a total of eight simulation cases are performed to select suitable parameters for the spray model. Since, this parametric study is just an intermediate step of the current work, only results corresponding to the selected spray parameters are presented in the results section of this paper, together with their experimental counterparts.

Table 3: Spray parameters investigated for the calibration of the injection model

Set of parameters\Spray Parameters	Cone angle (α)	Mean droplet diameter (d_m)	Spread parameter (n)
Set of spray cone angles	$\alpha \in \{70^o; 80^o; 90^o\}$	$d_m = 60\ \mu m$	$n = 10$
Set of Mean droplet sizes	$\alpha = 80^o$	$d_m \in \{40\ \mu m; 50\ \mu m; 70\ \mu m\}$	$n = 10$
Set of spread parameters	$\alpha = 80^o$	$d_m = 50\ \mu m$	$n \in \{3.5\,; 10\}$
Spray parameters retained	$\alpha = 80^o$	$d_m = 50\ \mu m$	$n = 3.5$

- *Flamelet libraries and computational parameters*

The flamelet equations (Eqs.14 and 15) are solved with a flamelet solver to deliver the flamelet solution, $\emptyset_i = \emptyset_i(Z, \chi)$. For this purpose, a scheme describing properly the steps of fuel oxidation (i.e. a CKM) is required to calculate the reaction rate of each species involved in the chemical system. In the present study, the combustion chemistry is incorporated in the flamelet solution using a skeletal version of

International Journal of Numerical Methods for Heat & Fluid Flow, Vol. 25 No. 5, 2015, pp. 1064-1088.
© Emerald Group Publishing Limited, 0961-5539, DOI 10.1108/HFF-09-2014-0272

the jet fuel surrogate model, JetSurf 2.0. The JetSurf 2.0 consists of 348 species and 2168 reactions. However, most flamelet solvers have some limitations in terms of number of species and elementary reactions. Thus, in order to allow the use of detailed CKMs (DCKM) in such limited flamelet codes while keeping their full prediction capabilities, a sensitivity based method, Alternate Species Elimination (ASE) is applied to the DCKM, JetSurf 2.0. The ASE method operates by excluding some species as well as the elementrary reactions involving the excluded species from the DCKM. Particularly, in the present work, the reduced model (RCKM) derived as in (Akih-Kumgeh and Bergthorson, 2013; Munzar *et al.*, 2014) is used and consists of 1024 reactions among 139 species. It is verified that the reduced mechanism reproduces prediction of combustion properties by the detailed version as shown in Figure 2. Figures 3 (a) presents the set of flamelet solutions used in the present study for the two-component surrogate fuel model. These flamelet solutions as well as those corresponding to pure n-decane are generated over the entire range of the flow conditions quantified here by the scalar dissipation rate (χ). It is seen that, due to chemical non-equlibrium effects caused by turbulent strain (e.g. flame stretching), the maximum temperature decreases progressively from the *near-equilibrium state* ($CHI = \chi = 0.01\ s^{-1}$) towards the *quenching state* ($CHI = \chi_q = 61\ s^{-1}$) passing through intermediate states featuring finite rate chemistry with low and high strain rates. Figure 3 (b) presents the S-shaped curves corroesponding to each surrogate fuel model. Especially, only upper banches are reproduced because of the restrictiveness of the solution space under the steady state assumption. One can notice that, the quenching limit of the two-component jet-A1 surrogate is intermediate between toluene and n-decane (i.e. $\chi_{q\_toluene} < \chi_{q\_n\_decane+toluene} < \chi_{q\_n\_decane}$).

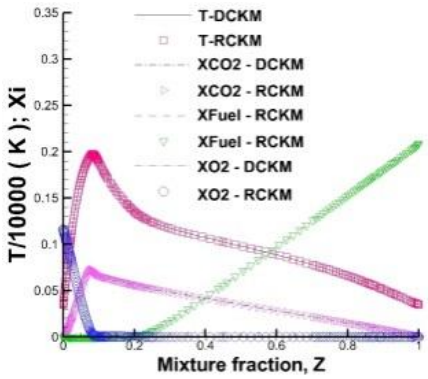

Figure 2: Validation of the reduced CKM (RCKM): thermochemical structure of a diffusion flame of 50% n-decane/50% N_2 flowing against an air stream both at 300K. **Line**: JetSurf 2.0 (DCKM), **Symbols**: Reduced CKM

International Journal of Numerical Methods for Heat & Fluid Flow, Vol. 25 No. 5, 2015, pp. 1064-1088.
© Emerald Group Publishing Limited, 0961-5539, DOI 10.1108/HFF-09-2014-0272

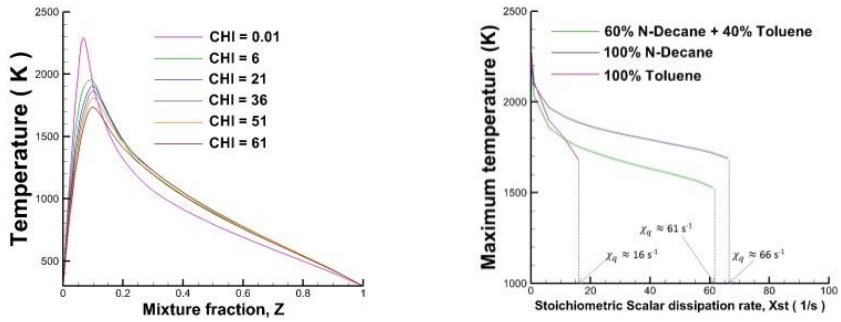

Figure 3: (a) Flamelet solution of 60% n-decane and 40% toluene (on a molar basis) for various strain rates (b) S-shaped curves corresponding to each fuel surrogate.

- *Simulation procedure*

The simulations are carried out with a grid of 2.2 million hexahedral elements generated using ANSYS ICEM meshing software. This mesh density is retained after performing a grid sensitivity study based on three structured meshes consisting of 0.7, 1.2 and 2.2 million elements. For the URANS simulations, the grid with 1.2 million elements has led to results slightly less accurate compared to those of the grid with 2.2 million elements, and this finer mesh density turned out to be sufficient to achieve the maximum accuracy with URANS. Also, for SAS simulations, the grid with 2.2 million elements were adequate to take full advantages of SAS capabilities, and further refinements were done using the mesh adaptation module of the CFD code to ensure that no further improvement of the results cannot be obtained by increasing this mesh resolution. The main steps of simulations are outlined in Figure 4. Initially, the flamelet solutions are generated with ANSYS FLUENT flamelet solver using a CKM with appropriate boundary conditions in scalar dissipation rate step of 2 s^{-1}. In processing task, the transport equations are solved using a representative convective time scale to determine the time step, $t_{ref} = L_{ref}/U_{ref}$, where the reference, $L_{ref} = R_o$ is the outer diameter of the annular duct and the reference velocity, $U_{ref} = U_{air}$ is the air bulk velocity. The reference time scale is then defined by $t_{ref} = R_o/U_{air}$ and the time step of the simulation is defined as $\Delta t = 0.1t_{ref} = 8 \times 10^{-5}\ s$. Simulations are first performed over 8000 time steps to obtain an initial flow development. Thereafter, 2000 additional time steps are taken while also implementing statistical sampling. These additional time steps are sufficient to achieve statistical convergence. All 3D unsteady calculations are performed in parallel using 8 Quad-core Intel Xeon X5560 processors on the compute Canada/Calcul Québec network supercomputer.

International Journal of Numerical Methods for Heat & Fluid Flow, Vol. 25 No. 5, 2015, pp. 1064-1088.
© Emerald Group Publishing Limited, 0961-5539, DOI 10.1108/HFF-09-2014-0272

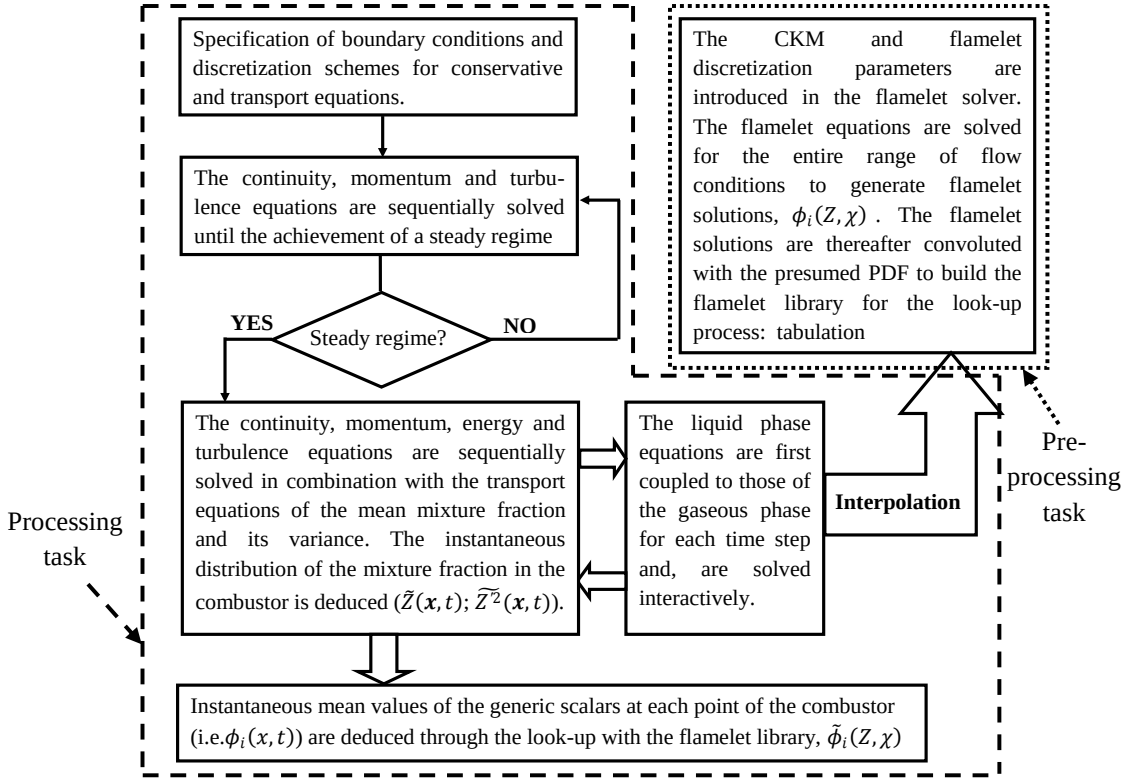

Figure 4: Flowchart of simulations

5- Results

Results of the flow field, spray dynamics and combustion properties are presented, contrasting the URANS with the SAS results.

5-1 Aerodynamics of the combustor, spray dynamics and thermochemical state

Figures 5 (a) and (b) show the aerodynamics of the combustion chamber through velocity vectors colored by the axial velocity. Central recirculation zones due to the swirl effect and the sudden expansion can be observed. Couples of side and central counter-rotating vortices are generated, which help to stabilize the flame. The counter-rotating vortices, lead to increased residence time, thereby improving mixing processes and flame stability. The SAS performs better at resolving the mixing field, so that these recirculation zones linked to mixing are more visible for SAS in Figure 5 (a). Similarly, as shown in Figures 5 (c) and (d), instantaneous distributions of the mixture fraction in the combustor provide evidence for better mixing between fuel and oxidizer in the case of the SAS model. Figures 6 (a) and (b) present the droplet dynamics through droplet size and mass distributions. The SAS and the URANS spray patterns are comparable, so that only SAS results are shown. Decreasing droplet size and droplet mass are observed and are linked to the combined effects of secondary break-up and evaporation phenomena.

Finally, an instantaneous thermochemical state at the end of the sample statistics is provided by snapshots of contours of temperature (Figures 7a and 7b) and carbon dioxide (Figures 7c and 7d). One can observe the impact of mixture fraction field prediction on the prediction of the thermochemical state. The relatively

International Journal of Numerical Methods for Heat & Fluid Flow, Vol. 25 No. 5, 2015, pp. 1064-1088.
© Emerald Group Publishing Limited, 0961-5539, DOI 10.1108/HFF-09-2014-0272

accurate prediction of the mixture fraction field provided by SAS directly correlates with the prediction of temperature and species fields.

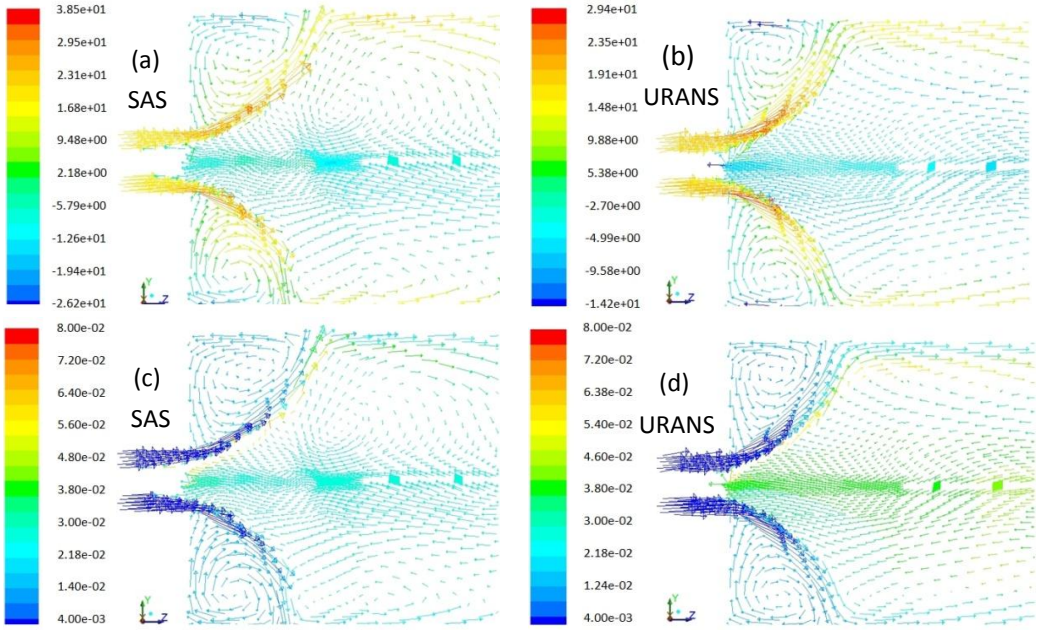

Figure 5: (a) & (b) vectors of velocity colored by axial velocity ($m.s^{-1}$); (c) & (d) vectors of velocity colored by the mixture fraction

International Journal of Numerical Methods for Heat & Fluid Flow, Vol. 25 No. 5, 2015, pp. 1064-1088.
© Emerald Group Publishing Limited, 0961-5539, DOI 10.1108/HFF-09-2014-0272

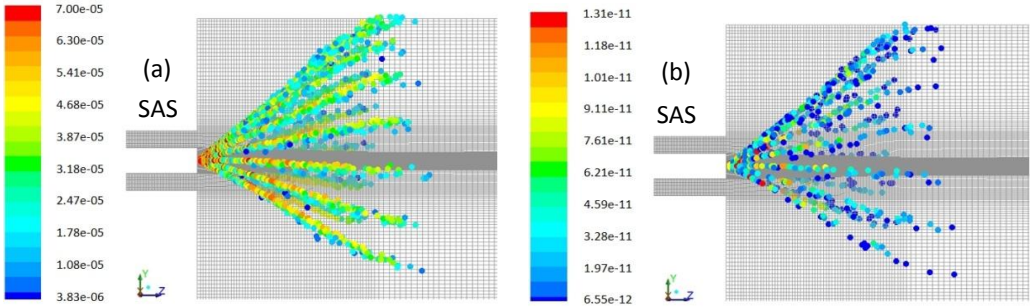

Figure 6: (a) droplet size distribution (m); (b) droplet mass distribution (kg.s^{-1})

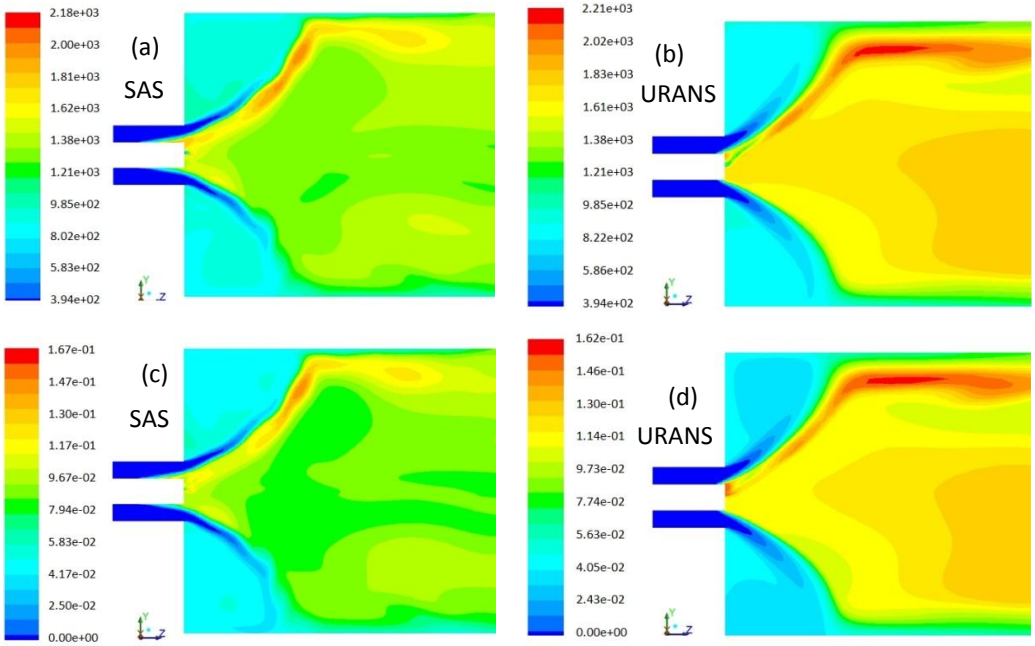

Figure 7: (a) & (b) instantaneous contours of temperature (K); (c) & (c) instantaneous contours of CO2 mass fraction.

5-2 Radial profiles of velocity components

Figure 8 presents the radial profiles of the various components of velocity and their fluctuations at given locations along the axis of the combustor. For axial and radial profiles, some discrepancies are noted in the zone close to the injector exit and the combustor axis ($z/Ro<1.0$ and $r \leq 0.015$). This could be related to the dynamics of the spray which is particularly dense in this zone and consequently, requires more elaborated models to solve both the spray dynamics and the spray-turbulence interactions accurately. Apart from this zone, reasonable agreement between the simulations and the experimental measurements is observed at each cross section of the combustor for both URANS and SAS. Further away from the combustor axis ($z/Ro \geq 1.5$), negative values of the axial velocity are observed, indicating recirculation zones. In addition to the discrepancies mentioned earlier, the axial velocity profiles show that the development of the recirculation zone is slightly delayed. This delayed development of the central

International Journal of Numerical Methods for Heat & Fluid Flow, Vol. 25 No. 5, 2015, pp. 1064-1088.
© Emerald Group Publishing Limited, 0961-5539, DOI 10.1108/HFF-09-2014-0272

recirculation zone could be related to inability of turbulence models (URANS and SAS) to capture more complex and transient local flow features. Although further mesh refinements coupled to a more advanced turbulence model such as LES could potentially improve the prediction, this is outside the scope of the present study. The reasonable prediction of the combustor aerodynamics partially confirms the suitability of the spray parameters generated by the preliminary parametric study for the present simulations.

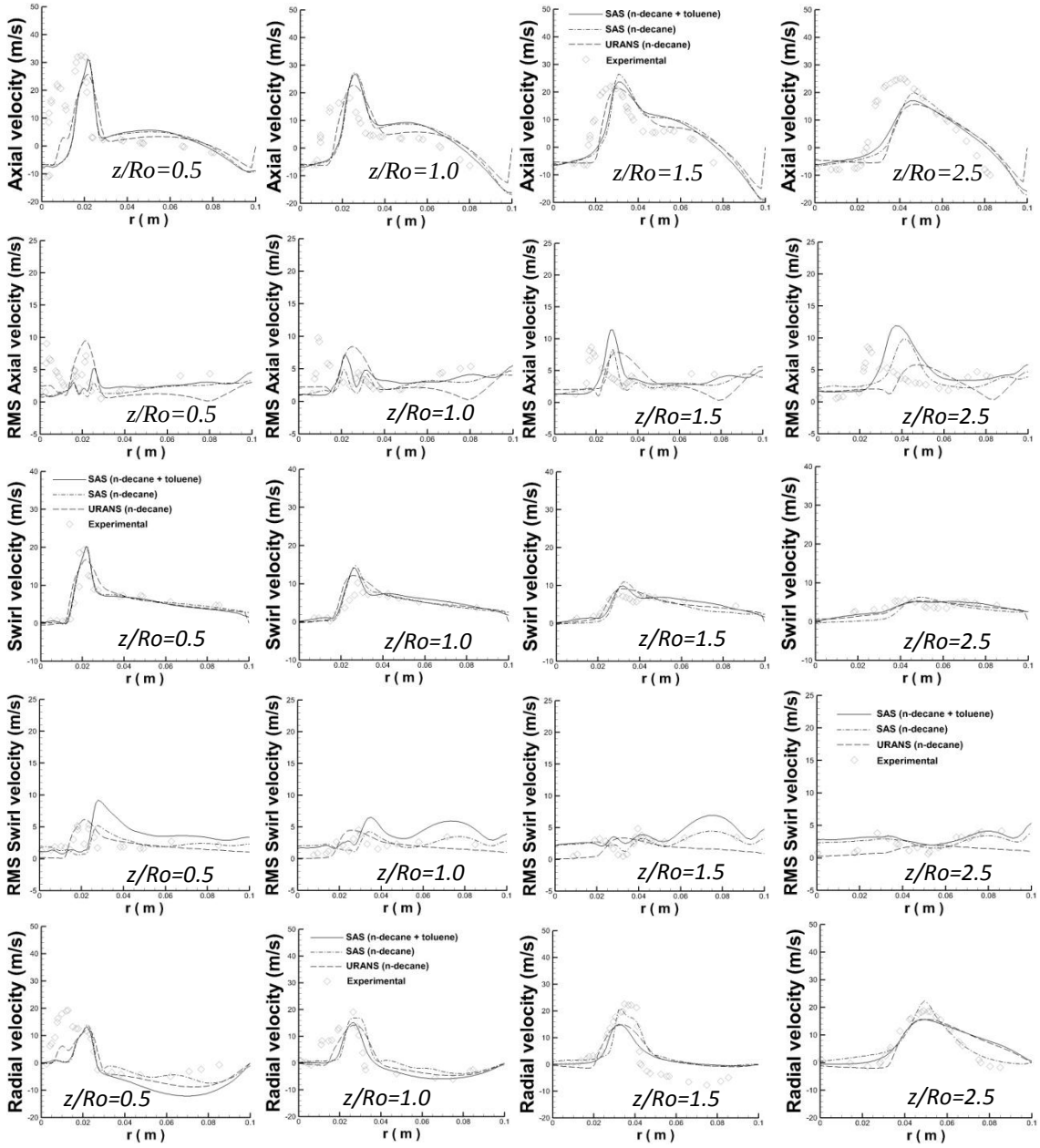

International Journal of Numerical Methods for Heat & Fluid Flow, Vol. 25 No. 5, 2015, pp. 1064-1088.
© Emerald Group Publishing Limited, 0961-5539, DOI 10.1108/HFF-09-2014-0272

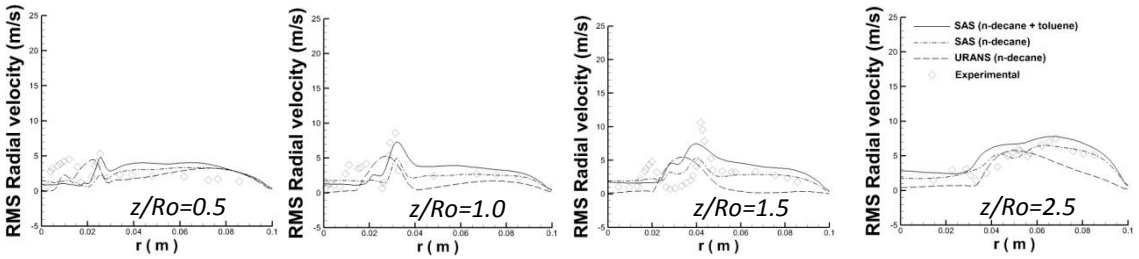

Figure 8: radial profiles of the mean velocity components at various cross sections of the combustor (*z/Ro*); "*z*" stands for the position along the combustor axis while "*R"* is the outer radius of the annular channel. *Ro=21 mm* (i.e. *z/Ro = 0.5 ⇒z = 10.5 mm*; the total length of the combutor is 500 mm)

5-3 Radial profiles of temperature

Figures 8 and 9 present the radial profiles of time-averaged temperature at each section along the axis of the combustor and the corresponding fluctuations respectively. Two peaks are observed in both experimental and numerical data: these temperature peaks may be physically explained by the presence of shear layers between the spray cone and the flowing air, resulting in zones of maximal exchange rate of mass, momentum and energy. Between the two peaks on the other hand, there is a temperature drop that may be partly related to the quenching effect of droplets. Also, one observes that SAS improves significantly the prediction of temperature profiles compared to URANS. This is linked to more accurate prediction of mixing, considering the sensitivity of combustion processes to mixture fraction fluctuations. In the zones starting at *z/Ro=3.0*, the temperature is almost at equilibrium corresponding to the experimental value for the input equivalence ratio ($\Phi = 0.53$). These experimental and numerical temperature trends of temperature attest to efficient mixing achieved with a high swirl number flow. Despite the discrepancies observed at some sections, a reasonable agreement is obtained with experimental data, showing the strengths of combined use of a better turbulence-combustion interaction based on more realistic chemistry models. Although the modelling of jet-A1 using two-component fuel consisting of paraffins (n-decane, n-dodecane, etc.) and aromatics (benzene, toluene, etc.) seems more realistic, a comparison of SAS simulation based on one-component fuel (n-decane) to SAS simulation based on two-component fuel (n-decane + toluene) shows that the main trends in the combustor flame can be reasonably predicted by only considering the one-component fuel based on the major component of jet-A1 (i.e. paraffins). However, these observations do not preclude the necessity of a representative fuel surrogate including aromatics and others more reactive fuel components when investigating phenomena which are sensitive to fuel reactivity, such as ignition.

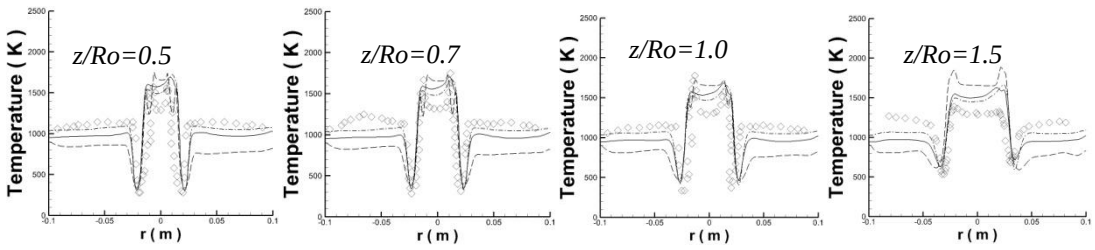

International Journal of Numerical Methods for Heat & Fluid Flow, Vol. 25 No. 5, 2015, pp. 1064-1088.
© Emerald Group Publishing Limited, 0961-5539, DOI 10.1108/HFF-09-2014-0272

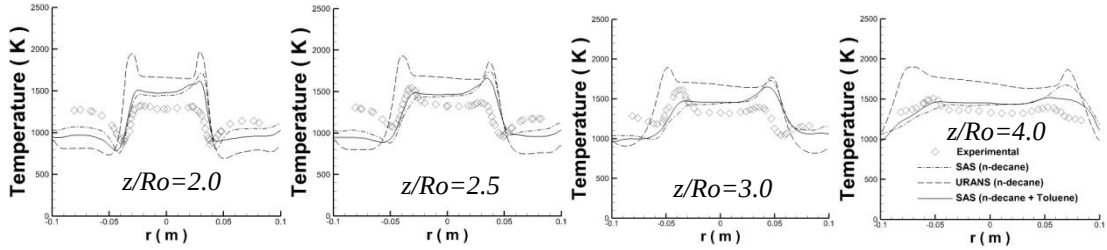

Figure 8 : radial profiles of mean static temperature at various cross sections of the combustor.

Ro=21mm (i.e. *z/Ro = 0.5 ⇒ z = 10.5 mm*; the total length of the combutor is 500 mm)

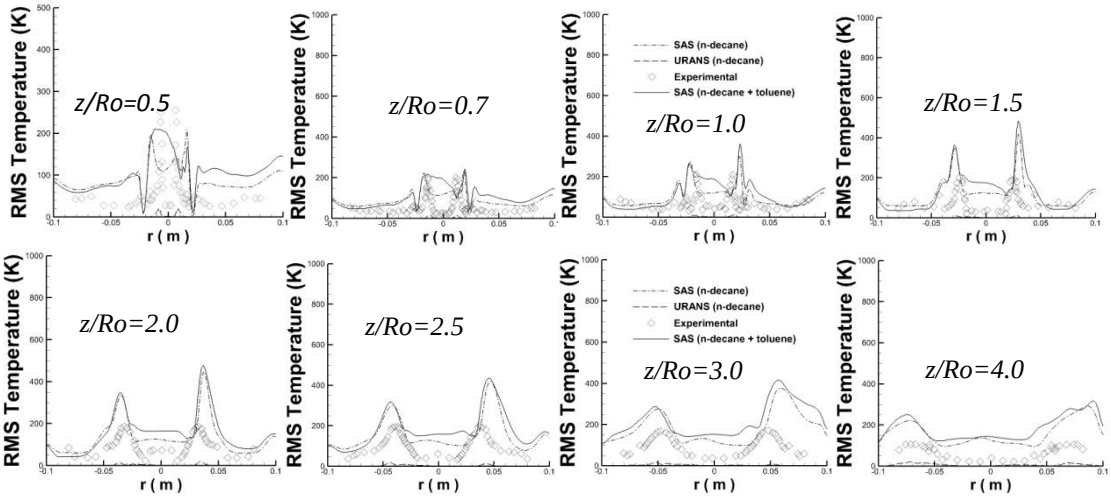

Figure 9 : radial profiles of temperature fluctuations (RMS) at various cross sections of the combustor

Ro=21mm (i.e. *z/Ro = 0.5 ⇒ z = 10.5 mm*; the total length of the combutor is 500 mm)

5-3 Radial profiles of species mole fraction

Figure 10 shows radial profiles of the mole fraction of species in the zone around the injector exit. Over-prediction of O_2 and under-prediction of carbone dioxide (CO_2) are observed in some zones of the combustor namely ($r \geq 3.0$). Physically, such trends may be explained either by an incomplete combustion or by an improper fuel distribution in the corresponding zones. However, one may relate these trends to an incomplete combustion if there is an overestimation (relative to experimental data) of unburnt fuel (e.g. CO, jet-A1, etc.) in the corresponding zones. For the present case, profiles of CO do not show an over-prediction of CO in the corresponding zones. Thus, the O_2 and CO_2 molar fraction trends are thought to be due to the fuel distribution and to some weaknesses of the turbulence model which do not facilitate capturing some relevant features. These include the spray dynamics and its interactions with turbulence, since mixture fraction fluctuations need to be accurately captured to improve the prediction of species formation and temperature. Further, unity Lewis number assumption for all species, infinite conductivity within fuel droplets and rapid mixing model for evaporation can contribute to poor performance of simulations with respect to experiments. These assumptions are not always valid since internal circulation can affect the length scale for diffusion for high vortex strengths as discussed in (Sirignano, 1999). Also,

International Journal of Numerical Methods for Heat & Fluid Flow, Vol. 25 No. 5, 2015, pp. 1064-1088.
© Emerald Group Publishing Limited, 0961-5539, DOI 10.1108/HFF-09-2014-0272

for cold droplet surface with low vapor concentration, the Lewis number is high since the molecular diffusivity of heavy hydrocarbon vapors in air is much lower than the thermal diffusivity of air. For species with low oxidation kinetics (e.g. CO and H_2), in spite of the fact that both experimental and numerical results are of the same order of magnitude, a slight under-prediction of CO is observed, and a significant under-predictions of H_2 at each station. These discrepancies are more accentuated for URANS simulations, and may be partly explained by the drawbacks of the steady flamelet assumption. In addition, the scalar dissipation rate, which quantifies the degree of departure from equilibrium, changes rapidly in the downstream direction and the flamelet model based on steady assumption cannot account for these rapid changes. Thus, in order to improve the prediction of these species, some assumptions need to be relaxed, such as those related to the steady flamelet and unity Lewis number for all species. Also, the comparison of URANS and SAS predictions highlights the relevance of a proper resolution of the mixing (i.e. a robust turbulence model) in the prediction of the thermochemical state.

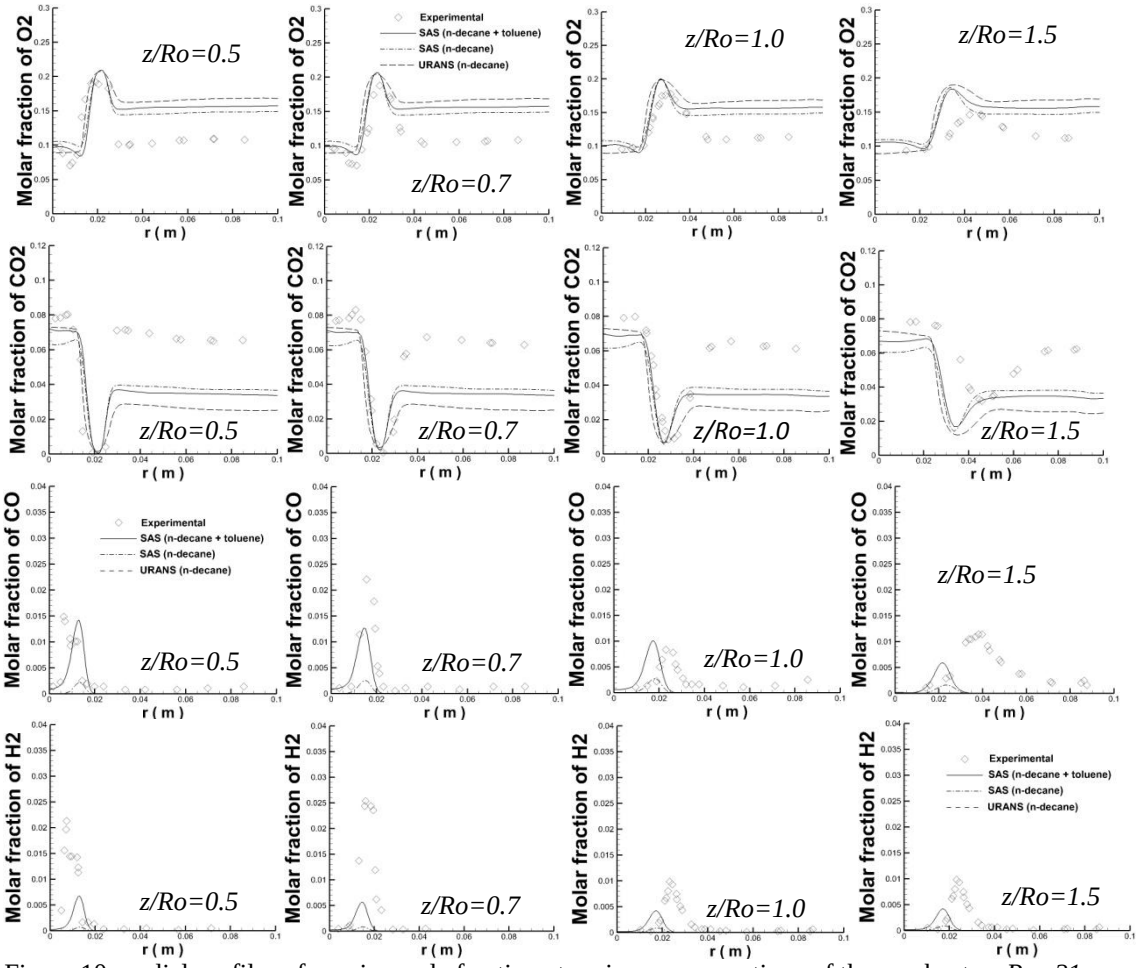

Figure 10 : radial profiles of species mole fraction at various cross sections of the combustor; *Ro=21mm* (i.e. $z/R = 0.5 \Rightarrow z = 10.5\ mm$; the total length of the combutor is 500 mm)

6-Conclusions

International Journal of Numerical Methods for Heat & Fluid Flow, Vol. 25 No. 5, 2015, pp. 1064-1088.
© Emerald Group Publishing Limited, 0961-5539, DOI 10.1108/HFF-09-2014-0272

Unsteady RANS ($k-\varepsilon RNG$) and Scale adaptive simulation (SAS) investigations of a turbulent swirling jet-A1 spray flame are carried out. High swirl number effects are used to enhance mixing and stabilize the flame. One-component (n-decane) and two-component (a mixture of 60% n-decane and 40% toluene) fuels are used as surrogates for jet-A1. Temperature dependence fuel transport properties and a realistic chemistry model implemented through the steady flamelet model coupled to a presumed Probability Density Function (PDF) are implemented. The effect of evaporation is taken into account through a source term in the transport equation of the mixture fraction. Finally, chemical non-equilibrium effects due to turbulent strain, such as flame stretching, are accounted for through the scalar dissipation rate concept in the flamelet model. The key results can be summarized as follows:

- For the investigated combustor conditions, the SAS coupled to the steady flamelet model reproduces many of the observed features of a swirling spray flames in a combustion chamber fed by a pressure swirl atomizer at reasonable computational cost.
- Although some discrepancies are observed in the species profiles, the flamelet model predicts reasonably well the temperature field. For species with slow oxidation kinetics (e.g. CO and H_2), discrepancies are more accentuated and can be related to simplifying assumptions done in the combustion model used. In fact, the steady flamelet model assumes that the flame structure is controlled by only a balance between steady chemical reactions and steady diffusion processes. In other words, the flamelet lifetime is much longer than the characteristic time scale of phenomena involved in flamelet equations and, consequently, the transient term is neglected. In addition, the preferential diffusion is neglected through the assumption of unity Lewis number for all species. This assumption is not always valid especially for slight species, such as H_2 and heavy species, such as n-decane and toluene. An accurate prediction of slow processes such as those governing the formation of CO and H_2 would require the unsteady terms of the flamelet equations.
- By comparing URANS to SAS simulations and thereafter SAS simulations with a one-component fuel to SAS simulations with a two-component fuel, one may deduce that when the major fuel components are selected as jet-A1 surrogates, the prediction of the main flame trends is more strongly affected by the turbulence model than by the fuel composition. However, the use of the two-component surrogate improves significantly the prediction of slow species (CO and H_2). This behavior suggests that by applying a more sophisticated turbulence model namely LES on a new mesh refined accordingly, one may significantly improve the global prediction. But, due to additional computing efforts and calibrations involved in such a calculation, this part will be investigated in a future work.
- This work is adding a contribution for spray flame modeling and can be seen as an extension to the significant efforts for the modelling of gaseous flames using robust turbulence models coupled with the tabulated flamelet-based chemistry approach to considerably reduce computing cost.

Acknowledgements

International Journal of Numerical Methods for Heat & Fluid Flow, Vol. 25 No. 5, 2015, pp. 1064-1088.
© Emerald Group Publishing Limited, 0961-5539, DOI 10.1108/HFF-09-2014-0272

This work received financial support from Fond Québécois de la Recherche sur la Nature et les Technologies (FQRNT) with seed funding initially provided by P&WC, CRIAQ & MDEIE. The authors wish to thank Calcul Québec/Calcul Canada for providing the required computing resources, and gratefully acknowledge Professor Jeffrey Bergthorson at McGill university for helpful discussions regarding the jet A-1 properties, its surrogates and their reaction mechanisms.

References

Abramzon, B. and Sirignano, W. A. (1989), "Droplet Vaporization Model for Spray Combustion Calculations", *Int. J. Heat Mass Transfer*, vol. 32 No 9 pp. 1605-1618.

Akih-Kumgeh, B. and Bergthorson, J. M (2013), "Skeletical kinetic Mechanisms for Syngas, Methyls Butanoate, n-heptane, and n-decane", *Energy & Fuel* vol. 10 pp. 1021.

ANSYS FLUENT™ (2012), "Fluent User's Guide", version 14.0

Beer, J. M. and Chigier, N. A. (1972), "*Combustion aerodynamics"*, Applied Science, London.

Bilger, R. W., Esler, M. B., and Starner, S. H. (1991), "Turbulent Flow with non-premixed reactant", Lecture Notes in Physics, *Springer-Verlag*, vol. 384 pp. 86.

Bray, K., Domingo, P. and Vervisch, L., (2005) "Role of the progress variable in the models for partially premixed turbulent combustion", *Combustion and Flame*, vol. 141 pp. 431-437.

Chrigui, M., Gounder, J., Sadiki, A., Masri, A.R. and Janicka, J. (2012), "Partially premixed reacting acetone spray using LES and FGM tabulated chemistry", *Combustion and flame*, vol. 159 pp. 2718-2741.

Franzelli, B., Fiorina, B. and Darabiha, N., (2013), "A tabulated chemistry method for spray combustion", *Proceedings of the combustion institute* vol. 34 pp. 1659-1666.

Hollmann, C. and Gutheil, E. (1996), "Modeling of Turbulent Spray Diffusion flames Including Detailed Chemistry", in 26th Symposium (International) on combustion, Pittsburg (1996), *The Combustion Institute*, Kansas, vol. 1 pp. 1731-1738.

Hollman, C. and Gutheil, E., (1998), "Flamelet-Modeling of Turbulent Spray Diffusion Flames Based on a Laminar Spray Flame Library", *Combust. Sci. and Tech*., vol. 135 pp. 175-192.

Jones, W.P., Lyra, S. Navarro-Martinez, S. (2012), "Numerical investigation of swirling kerosene spray flames using Large Eddy Simulation", *Combustion and Flame*, vol. 159 pp. 1539-1561.

Launder, B.E. and Sharma, B.I. (1974), "Application of Energy Dissipation Model of Turbulence to the calculation of Flow Near a spinning Disc", Letters in Heat and Mass Transfer, vol. 1 N° 2, pp. 131-138

Lefebvre, A. H. (1989), "Atomization and Sprays", *Hemisphere Publishing Corporation*.

Lefebvre, A. H. (1983), "Gas Turbine Combustion", *Taylor & Francis*.

Lesieur, M., and Métais, O. (1996), "New trends in large eddy simulations of turbulence", *Annual Review of Fluid Mechanics*, vol. 28 pp. 45-82.

Liu, A.B., Mather, D. and Reitz, R.D. (1993), "Modeling the Effects of Drop Drag and Breakup on Fuel Sprays", *SAE Technical paper* 930072. SAE.

Peters, N., (2000), "Turbulent Combustion", *Cambridge Univ. Press, Cambridge*, UK.

Pitsch, H. and Peters, N. (1998), "A Consistent Flamelet Formulation for Non-Premixed Combustion Considering Differential Diffusion Effects", *Combustion and Flame* vol. 114 pp. 26–40.

Pitsch, H., Desjardins, O., Balarac, G. and Ihme, M. (2008), "Large Eddy Simulation of turbulent reacting flow", *Prog. Aerospace Science*, vol. 44 N° 6 pp. 466-478

International Journal of Numerical Methods for Heat & Fluid Flow, Vol. 25 No. 5, 2015, pp. 1064-1088.
© Emerald Group Publishing Limited, 0961-5539, DOI 10.1108/HFF-09-2014-0272

Poinsot, T. and Veynante, D. (2005), "Theoretical and Numerical combustion", R.T. Edwards, 2nd edition.

Yakhot, V., Orszag, S.A., Thangam, S., Gatski, T.B. and Speziale, C.G. (1992), "Development of turbulence models for shear flows by a diuble expansion technique", *Physics of Fluids A*, vol. 4 N° 7 pp. 1510-1520

Menter, F.R. and Egorov, Y. (2010), "The scale-Adaptive Simulation Method for Unsteady Turbulent Flow Predictions, Part 1: theory and Model Description", *Flow Turbulence Combustion* vol. 85 pp. 113-138

Munzar, J. D., Zia, A., Versailles, P., Jimenez, R., Bergthorson J.M. and Akih-Kumgeh, B., (2014) *Comparison of Laminar Flame speeds, Extinction stretch rates and vapor pressures of Jet A-1/HRJ Biojet Fuel blends*, Proceedings of the ASME Turbo Expo 2014, paper GT2014-25951

Sanjosé, M., Senorer, J.M., Jaegle, F., Cuenot, B., Moreau, S. and Poinsot, T. (2011), "Fuel injection model for Euler-Euler and Euler-Lagrange large-eddy simulations of an evaporationg inside an aeronautical", *Int. combustor, J. Multiphase Flow* vol. 37 N°5 pp. 514-529

Sheen, D.-H. (1993), "Swirl-Stabilized Turbulent Spray Flames in an Axisymmetric Model Combustor", Ph.D. thesis, *Imperial College, University of London*.

Sirignano, W. A. (1999), "Fluid Dynamics and Transport of Droplets and Sprays", *Cambridge University Press*, Cambridge

International Journal of Numerical Methods for Heat & Fluid Flow, Vol. 25 No. 5, 2015, pp. 1064-1088.
© Emerald Group Publishing Limited, 0961-5539, DOI 10.1108/HFF-09-2014-0272

Proceedings of ASME Turbo Expo 2015: Turbine Technical Conference and Exposition
GT2015
June 15-19, 2015, Montreal, Canada

GT2015-42535

SCALE-ADAPTIVE AND LARGE EDDY SIMULATIONS OF A TURBULENT SPRAY FLAME IN A SCALED SWIRL-STABILIZED GAS TURBINE COMBUSTOR USING STRAINED FLAMELETS

Alain Fossi, Alain deChamplain*, Bernard Paquet, Smail Kalla
Combustion Laboratory
Department of Mechanical Engineering
Laval University
Québec, QC, G1V 0A6, Canada
**Email:* alain.dechamplain@gmc.ulaval.ca

Jeffrey M. Bergthorson
Alternative Fuels Laboratory
Department of Mechanical Engineering
McGill University
Montréal, QC, H3C 0C3, Canada

ABSTRACT

In this paper, the three-dimensional (3D) reacting turbulent two-phase flow field of a scaled swirl-stabilized gas turbine combustor is numerically investigated using the commercial CFD software ANSYS FLUENT™-v14. The first scope of this study aims to explicitly compare the predictive capabilities of two turbulence models namely Scale-Adaptive Simulation (SAS) and Large Eddy Simulation (LES) for a reasonable compromise between accuracy of results and global computational cost when applied to simulate swirl-stabilized spray combustion. The second scope of the study is to couple chemical reactions to the turbulent flow using a realistic chemistry model and also to model the local chemical non-equilibrium effects caused by turbulent strain. Standard Eulerian and Lagrangian formulations are used to describe both gaseous and liquid phases respectively. The fuel used is liquid jet-A1 which is injected in the form of a polydisperse spray and the droplet evaporation rate is calculated using the infinite conductivity model. One-component (n-decane) and two-component fuels (n-decane + toluene) are used as jet-A1 surrogates. The combustion model is based on the first and second moments of the mixture fraction, and a presumed-probability density function (PDF) is used to model turbulent-chemistry interactions. The instantaneous thermochemical state necessary for the chemistry tabulation is determined by using initially the partial equilibrium assumption (PEQ) and thereafter, the detailed non-equilibrium (NEQ) calculations through the laminar flamelet concept. The combustion chemistry of these surrogates is represented through a reduced chemical kinetic mechanism (CKM) comprising 1 045 reactions among 139 species, derived from the detailed jet-A1 surrogate model, JetSurf 2.0. Numerical results are compared with a set of published data for a steady spray flame. Firstly, it is observed that, by coupling the two turbulence models with a combustion model incorporating a representative chemistry to account for non-equilibrium effects with realistic fuel properties, the models predict reasonably well the main combustion trends, with a superior performance for LES in terms of trade-off between accuracy and computing time. Secondly, because of some assumptions with the combustion model, some discrepancies are found in the prediction of species slowly produced or consumed such as CO and H_2. Finally, the study emphasizes the dominant advantage of an adequate resolution of the mixing characteristics especially with the more demanding simulation of a swirl-stabilized spray flame.

INTRODUCTION

Due to substantial progress in computing resources and turbulent combustion modeling, numerical simulation plays today a significant role in the design of many combustion systems and the development of their operating criteria. More specifically, in the advanced combustion systems like those of the aeronautical industry, it may considerably speed up the development phase of new engines while helping engineers to optimise given issues under some known constraints [**1**, **2**, **3**]. In fact, considering the necessity to reduce fuel storage volumes in aircraft engines, their combustors are commonly fed with liquid fuels and consequently, detailed experimental investigation methods may become prohibitive when applied to the resulting complex systems, since they involve several phenomena mutually and continuously interacting. Furthermore, some designing and operating criteria such as combustion efficiency, combustion stability, and reduction of pollutant emissions are often practically achieved by generating swirling flows with strong recirculation regions which enhance evaporation and mixing between the fuel and the oxidizer; improve the flame stability, while also increasing the complexity of the physical system. The accurate numerical prediction of turbulent swirling spray flames is still nowadays a

challenge and should be considered with a particular care. Indeed, in addition to the swirling motion, turbulent spray flames involve a set of phenomena whose mechanisms remain complex such as turbulence, heat and mass transfers; droplets phase change and chemical reactions, which are furthermore coupled. At first, the reliable prediction of the aerodynamic of a swirl-stabilized combustor requires the consideration of an anisotropic and unsteady flow field, while the accurate prediction of emissions requires a sophisticated chemistry model with a proper inclusion of chemical non-equilibrium effects due to turbulence [2]. Three different approaches based on either Eulerian-Eulerian, Eulerian-Lagrangian or PDF formulation can be used to capture the structure of turbulent spray flames. In each of these approaches, the Eulerian treatment may be implemented with well-known turbulence models labeled as: the Unsteady Reynolds-Averaged Navier-Stokes (URANS), the Direct Numerical Simulation (DNS); the Large Eddy Simulation (LES) and recently, the hybrid URANS-LES methods such as Scale-Adaptive Simulation (SAS) and Detached Eddy Simulation (DES). The URANS approaches which are commonly used in most practical configurations are based on statistical averaging and consequently, are less accurate compared to Direct Numerical Simulation (DNS) in which the turbulent spectrum is entirely resolved, restricting thereby its application to only very simple configurations [1, 2, 4]. However, in spite of affordable computing cost associated with URANS simulations, experiences show that URANS approaches can lead to an excess of turbulent dissipation and consequently, important flow structures might be dissipated [4]. In order to cope with the URANS weaknesses while keeping computing cost at a reasonable level, Scale Resolved Simulation (SRS) approaches which consist of a partial resolution of the turbulence spectrum, are increasingly used. Among SRS approaches, LES seems more appropriate for many practical combustion systems including gas turbine combustors, and its potential in this field was demonstrated by several authors in representative academic and semi-industrial combustors [5, 6, 7, 8]. However, due to the intense computational requirements of LES, it is worth verifying before applying to industrial configurations that, it significantly outperforms all others advanced turbulence models which are theoretically less demanding (e.g. DES and SAS), for an efficient use of the available computing resources. Plus, sophisticated chemistry models which are necessary to investigate others relevant combustion phenomena involve thousands of elementary reactions among hundreds of chemical species, and consequently, require additional computing efforts. Thus, a numerical prediction with an efficient use of available computing resources is strongly related not only to the robustness of the models used, but also to the abilities of scientists and engineers to establish simulation approaches which allow circumventing non-justified sinks of computational resources which may arise when investigating some critical phenomena such as those related to turbulence-chemistry interactions. In this vein, commonly-used approaches to overcome the restrictive computational cost of including detailed chemistry include tabulated chemistry methods based on the laminar flame structure. In this concept initially developed to incorporate a detailed chemistry in Computational Fluid Dynamic (CFD) simulation of gaseous flames, a turbulent flame is assumed to behave locally as an ensemble of laminar stretched flamelets [9, 10]. This concept whose application requires large Damköhler numbers, may be used accurately in most combustors, since in such combustion systems, stable and efficient burning is obtained when chemical time and length scales are shorter than those of the smallest structures of turbulence [11]. The widely separated time scales between chemistry and mixing allow decoupling chemistry calculations from those of the mixing processes, such that chemistry effects are included through the tabulation of the pre-calculated chemistry. However, the accuracy of simulations based on this approach is also strongly related to the adequacy between the combustion mode involved in the combustor and the flamelet regime. In fact, the tabulated chemistry may be based on premixed and/or diffusion flamelets, and each type of flamelet library is suitable for a given combustion regime: tables of premixed and diffusion flamelets are suitable for the simulation of premixed and non-premixed combustion respectively, while flames exhibiting both premixed-like and diffusion-like reactive layers require table of multi-regimes flamelets. Particularly, for spray combustion, diffusion flamelets are beforehand suitable when considering injection with pressure-swirl-atomizers (e.g. *Simplex injectors*). However, for some configurations (e.g. liquid-fueled combustors equipped with sophisticated injectors such as *air-blast atomizers*), multi-regimes flamelets might be necessary to obtain realistic results [12]. Despite the reported success in turbulent gaseous flames simulations, hybrid URANS-LES turbulence models and tabulated chemistry applications to spray flames simulations are relatively very limited, although they have the potential to reveal further details involving multiphase reactive flows. In fact, the few numerical investigations of spray flames found in the literature deal either with DNS coupled to simple chemical scheme (for very simple configurations) [13, 14] or with URANS [15], and increasingly with LES associated with simple or robust combustion model including realistic chemistry schemes [16, 17, 18]. Due to the capabilities of Hybrid approaches to reproduce the main features of unsteady turbulent non-reacting flow fields in various configurations [4, 19], and the sensitivity of the combustion process to mixing fluctuations, they are likely to predict reasonably the mixing field and then, that of the thermochemical state, while keeping the computing cost at a reasonable level since a part of the turbulence spectrum is resolved. In order to validate this theoretical hypothesis, comparative studies based on the application of such approaches and classical advanced turbulence models to complex configurations are necessary. To the authors' knowledge, such a study has not been done so far, and the present paper addresses this shortcoming. Therefore, the structure of a turbulent swirling jet-A1 spray flame is numerically investigated using a hybrid URANS-LES approach (SAS), and the LES model. Each of these turbulence models is

first coupled to a combustion model based on a partial EQ assumption in order to emphasize the benefits of each turbulence model and to determine computational requirements corresponding to each model. Thereafter, the impact of the inclusion of chemical NEQ effects due to the turbulent strain (e.g. flame stretching) is highlighted by coupling one of the turbulence models mentioned earlier to a tabulated chemistry approach based on the laminar flamelet concept. Finally, the issue regarding a suitable chemical substitute for jet-A1 is explored by considering two surrogates: a one-component fuel (n-decane) and a two-component fuel (60%n-decane + 40%toluene). The paper is organized as follows: the first section is devoted to the mathematical modeling, while the second and third sections present the experimental configuration and the numerical models respectively; the computational parameters are summarized in the fourth section; the detailed findings of all numerical simulations as well as the related analyses are presented in the fifth section while salient points of the investigation are summarized in the last section.

MATHEMATICAL MODELING

In the present work, the Eulerian-Lagrangian (EL) formulation is adopted to model the structure of a swirl-stabilized turbulent jet-A1 spray flame. The Eulerian part of the model describes the behavior of the carrier gaseous phase, while the Lagrangian part replicates the dispersed liquid phase. In fact, considering its dilute nature and its small liquid volume fraction, the spray of the investigated configuration can be represented by a finite number of droplets that differ in position, velocity, temperature and size. The choice of the EL formulation is mainly justified not only by the more reasonable number of droplet trajectories to be calculated, but also by its ability to provide a straightforward implementation of relevant physical aspects, such as polydispersion of the spray, crossing trajectories, wall-droplet interaction and droplet wake combustion. However, for some practical configurations involving high droplet count as it is the case for dense sprays, the Eulerian-Eulerian formulation is more suitable as the same algorithm is used to solve both the gaseous and the liquid phases, providing therefore an almost identical parallelization. The mass transfer between the two phases influences the chemical reactions through the fuel supply, which is assumed to be controlled by convective and diffusive transports, and is quantified by the droplet evaporation rate that is calculated using the infinite conductivity model [**20**]. Thus, the droplet surface temperature is assumed to be uniform, time-varying, and equal to the uniform temperature within the droplet. The effect of the turbulent velocity fluctuations is accounted for using the Discrete Random Walk (DRW) model [**21**]. In order to take into account the chemical NEQ effects induced by turbulence, a tabulated chemistry based on strained diffusion flamelets is used to incorporate a more realistic chemistry modeling. Detailed explanations regarding the applicability of this model to the investigated configuration, and the validity of the chemical kinetic mechanism used are provided in the sections devoted to the combustion model and computing parameters respectively.

Gaseous Phase: turbulence models

Although the fuel is entirely supplied by the liquid droplets, chemical reactions are assumed to occur only in the gaseous phase, far enough from the liquid interface. The effects of the liquid phase on the gaseous phase are therefore accounted for by adding source terms in the equations governing the gaseous combustion. The structure of the gaseous flow in the combustor is obtained using two different approaches: the resolution of Favre averaged (for SAS) and Favre filtered (for LES) Navier-Stokes and scalars transport equations governing a multi-component reactive mixture. The instantaneous form of these equations and the derivation assumptions are provided in [**2, 3**] and only their averaged and filtered forms are presented in the present study to highlight the difference between the two turbulence models used.

- *Turbulence model : Scale-Adaptive Simulation (SAS)*

The SAS model is a second generation of URANS methods. In fact, the model is based on the URANS equations, and uses the turbulent viscosity to compute the turbulent stresses through a two-equation closure method, though this is not inherent to its formulation. The SAS model was formulated by Menter and Egorov [**4, 19**] through a modification of the $k-kL$ model developped by Rotta [**4**] to circumvent some drawbacks of classical URANS models such as $k-\varepsilon$ and $k-\omega$. In the modifications made to the Rotta model, a second length scale, a Von Karman length-scale L_{vK}, was introduced to account for the length scale of the resolved eddies. Thus, unlike the standard turbulence model which provide a length scale proportional to the thickness of the shear layer, the SAS model adjust dynamically to the length scales of the resolved structures depending on the flow situations and without explicit grid information. More explicitly, for unstable flows, the new length-scale L_{vK} allows the SAS model to operate in URANS-like mode in stable regions of the flow, and to exhibit LES-like resolution in the unstable flow regions. The transition from URANS to LES is initiated by the level of flow instabilities. The averaged Navier-Stokes equations used in the SAS model are similar to those of the URANS models, and are given in Eqs. (1)-(3):

$$\frac{\partial \bar{\rho}}{\partial t}+\frac{\partial}{\partial x_j}\left(\bar{\rho}\widetilde{u_j}\right)=\bar{\dot{S}}_m \qquad (1)$$

$$\frac{\partial \bar{\rho}\widetilde{u_\iota}}{\partial t}+\frac{\partial}{\partial x_j}\left(\bar{\rho}\widetilde{u_\iota}\widetilde{u_j}\right)=-\frac{\partial \bar{p}}{\partial x_i}+\frac{\partial}{\partial x_j}\left(\bar{\sigma}_{ij}-\bar{\rho}\widetilde{u_\iota''u_j''}\right)+\bar{\dot{S}}_{u_i} \qquad (2)$$

$$\frac{\partial \bar{\rho}\widetilde{\phi_\iota}}{\partial t}+\frac{\partial}{\partial x_j}\left(\bar{\rho}\widetilde{u_\iota}\widetilde{\phi_\iota}\right)=\frac{\partial}{\partial x_j}\left[\overline{\Psi}_{\phi_i}-\bar{\rho}\widetilde{u_\iota''\phi_j''}\right]+\widetilde{\dot{\omega}}_{\phi_i}+\tilde{\dot{S}}_{\phi_i} \qquad (3)$$

In these equations ρ is density, u_j is the velocity in the jth direction; and $\phi_i \in \{h_s; Y_k\}$ is ith scalar representing either the kth species mass fraction (Y_k), or the sensible enthalpy (h_s). p is the mechanical pressure which allows including normal stresses in the momentum equation, σ_{ij} is the viscous stress tensor, and $\dot{\omega}_{\phi_i} \in \left[\dot{\omega}_{Y_k}; \dot{\omega}_{h_s}\right]$ is the rate of production of species or heat.

$\dot{S}_m = \sum_{k=1}^{N}(n\dot{m})_{p,k}$, $\dot{S}_{u_i} = \sum_{k=1}^{N}(n\dot{m}u_i)_{p,k}$ and $\dot{S}_{\phi_i}$ are respectively the mass, the momentum and the scalars source terms due to the interactions with the liquid phase. Ψ_{ϕ_i} is the molecular diffusion flux of the i[th] scalar, which is modeled with the gradient diffusion assumption. Bars and tildes stand for the Reynolds and Favre averages respectively. In the SAS formulation, the turbulent stresses, $\bar{\rho}\widetilde{u_i''u_j''}$ are modeled using the turbulent viscosity. This latter is calculated with the turbulent kinetic energy, k and the turbulence eddy frequency, ω generated by the transport equations (4) and (5).

$$\frac{\partial \bar{\rho}\tilde{k}}{\partial t} + \frac{\partial}{\partial x_j}(\bar{\rho}\tilde{k}\tilde{u}_i) = \frac{\partial}{\partial x_j}\left[\left(\mu + \frac{\mu_t}{\sigma_k}\right)\frac{\partial \tilde{k}}{\partial x_j}\right] - \bar{\rho}\tilde{k}\tilde{\omega}C_\mu + G_k + S_k \quad (4)$$

$$\frac{\partial \bar{\rho}\tilde{\omega}}{\partial t} + \frac{\partial}{\partial x_j}(\bar{\rho}\tilde{\omega}\tilde{u}_i) = \frac{\partial}{\partial x_j}\left[\left(\mu + \frac{\mu_t}{\sigma_\omega}\right)\frac{\partial \tilde{\omega}}{\partial x_j}\right] + a\frac{\tilde{\omega}}{\tilde{k}}G_k - \bar{\rho}\beta\tilde{\omega}^2 + Q_{SAS} + (1-F_1)\frac{2\bar{\rho}}{\sigma_{\omega,2}}\frac{1}{\tilde{\omega}}\frac{\partial \tilde{k}}{\partial x_j}\frac{\partial \tilde{\omega}}{\partial x_j} + S_\varepsilon \quad (5)$$

where the physical term, Q_{SAS} is given by Eq. (6):

$$Q_{SAS} = max\left[\bar{\rho}\eta_2\kappa S^2\left(\frac{L}{L_{vK}}\right)^2 - C\frac{2\bar{\rho}\tilde{k}}{\sigma_\Phi}max\left[\frac{1}{\tilde{\omega}^2}\left(\frac{\partial \tilde{\omega}}{\partial x_j}\right)^2, \frac{1}{\tilde{k}^2}\left(\frac{\partial \tilde{k}}{\partial x_j}\right)^2\right], 0\right] \quad (6)$$

In these equations, $\eta_2 = 3.51$, $\sigma_\Phi = 2/3$, $\sigma_{\omega,2} = 1.168$ and $C = 2$; $L = \sqrt{k}/\left(C_\mu^{1/4}\tilde{\omega}\right)$ is the length scale of the modeled turbulence, $L_{vK} = \kappa\frac{\partial \tilde{u}_j}{\partial y}/\frac{\partial^2 \tilde{u}_j}{\partial y^2} = kS/|U''|$ is the Von-Karman length scale; $\kappa = 0.41$ is the Von Karman constant, and S is the scalar invariant of the strain rate tensor σ_{ij} : $S = \left(2\sigma_{ij}\sigma_{ij}\right)^{1/2}$ and $|U''| = \left(\sum_{(i)}\left(\partial^2\tilde{u}_j/\partial x_j^2\right)^2\right)^{1/2}$; F_1 is a model parameter.

- *Turbulence model: Large Eddy Simulation (LES)*

In the LES turbulence model, the large-scale motions are resolved, while the small-scale motions as well as their interactions with large ones are modeled. The rationality of the LES model relies on some relevant physical observations: most of the energy of turbulence is contained in large eddy motions, and the latter are problem-dependent since they are dictated by the geometry and boundary conditions of the flow involved; the small-scale motions are less geometry-dependent, they tend to be more isotropic as they are more influenced by molecular transport, and are therefore more universal in nature [**2**, **5**, **6**, **22**]. By applying a cut-off spatial filter to the conservative equations governing a multi-component reactive mixture, the following Favre-filtered conservative Eqs. (7)-(9) are derived for large-scale motions:

$$\frac{\partial \bar{\rho}}{\partial t} + \frac{\partial}{\partial x_j}\left(\bar{\rho}\tilde{u}_j\right) = \dot{\tilde{S}}_m \quad (7)$$

$$\frac{\partial \bar{\rho}\tilde{u}_i}{\partial t} + \frac{\partial}{\partial x_j}\left(\bar{\rho}\tilde{u}_i\tilde{u}_j\right) = -\frac{\partial \tilde{p}}{\partial x_i} + \frac{\partial}{\partial x_j}\left[\bar{\sigma}_{ij} - \tau_{SGS}\right] + \tilde{\dot{S}}_{u_i} \quad (8)$$

$$\frac{\partial \bar{\rho}\tilde{\phi}_i}{\partial t} + \frac{\partial}{\partial x_j}\left(\bar{\rho}\tilde{u}_i\tilde{\phi}_i\right) = \frac{\partial}{\partial x_j}\left[\overline{\Psi}_{\phi_i} - q_{SGS}^{\phi_i}\right] + \tilde{\omega}_{\phi_i} + \tilde{\dot{S}}_{\phi_i} \quad (9)$$

where $\tau_{SGS} = \bar{\rho}\left(\widetilde{u_i u_j} - \tilde{u}_i\tilde{u}_j\right)$ and $q_{SGS}^{\phi_i} = \bar{\rho}\left(\widetilde{u_i\phi_i} - \tilde{u}_i\tilde{\phi}_i\right)$. In these equations, the bars and tildes accentuations refer to Reynolds and Favre filtering. The filtered scalars laminar diffusion fluxes are modeled through the gradient diffusion assumption as in the averaged equations. The expressions of the filtered source terms of mass, momentum and scalars are formally identical to those of the averaged equations. These filtered equations are used to solve large-scale motions in both space and time, whereas the small scales are filtered out using a density-weighted function expressed as: $\bar{\rho}\widetilde{\Psi} = \int \rho\Psi(\boldsymbol{x}_i')F(\boldsymbol{x}_i - \boldsymbol{x}_i';\Delta)d\boldsymbol{x}_i'$, where $\Psi \equiv \{u_i;\phi_i\}$ is the set of unknown physical quantities, and $F(\boldsymbol{x_i};\Delta)$ is a time-invariant spatial filter function whose shape is chosen so that it approaches zero when $\boldsymbol{x_i} - \boldsymbol{x_i'}$ exceeds the filter width, Δ, and obeys the normalization law (i.e. $\int F(\boldsymbol{x_i'})d\boldsymbol{x_i'} = 1$). In the current work, a box filter was used and Δ was computed as the cubic root of the local computational cell volume ($\Delta = \sqrt[3]{V_{cell}}$); the subgrid-scale (SGS) stresses, τ_{SGS} in Eq. (10) is modelled using an eddy viscosity assumption: the SGS term is split into its isotropic and deviatoric parts; the deviatoric part is modelled using the Wall-Adapting Local Eddy (WALE) viscosity model **[23]**.

$$\tau_{SGS} = \underbrace{\tau_{ij} - 1/3\,\tau_{kk}\delta_{ij}}_{deviatoric} + \underbrace{1/3\,\tau_{kk}\delta_{ij}}_{isotropic} \quad (10)$$

The term involved in the isotropic part (τ_{kk}) can be related to the subgrid Mach number by $\tau_{kk} = \gamma Ma_{SGS}^2\tilde{P}$ where Ma_{SGS} is the subgrid Mach number. As the turbulent Mach number of the flow is small (~10^{-3}), Ma_{SGS} can be expected to be very small and consequently,

$$\tau_{SGS} \approx \underbrace{\tau_{ij} - 1/3\,\tau_{kk}\delta_{ij}}_{deviatoric} = 2\mu_t\sigma_{ij} \quad (11)$$

where $\sigma_{ij} = \frac{1}{2}\left(\frac{\partial \widetilde{u_i}}{\partial x_j} + \frac{\partial \widetilde{u_j}}{\partial x_i}\right)$. According to the WALE model, the eddy viscosity, μ_t is defined by:

$$\mu_t = \bar{\rho}L_s^2\left(S_{ij}^d S_{ij}^d\right)^{3/2}/\left[\left(\bar{\sigma}_{ij}\bar{\sigma}_{ij}\right)^{5/2} + \left(S_{ij}^d S_{ij}^d\right)^{5/4}\right] \quad (12)$$

where $L_s = \min(kd, C_w\Delta)$ is the mixing length for SGS; k is the von Karman constant; d is the distance to the closest wall; C_w is the WALE constant and its value in the current simulation is equal to 0.325; $S_{ij}^d = 1/2\left(\bar{g}_{ij}^2 + \bar{g}_{ji}^2\right) - 1/3\,\delta_{ij}\bar{g}_{kk}^2$ with $\bar{g}_{ij} = \partial\bar{u}_i/\partial x_j$. The Subgrid-scale scalar flux term, $q_{SGS}^{\phi_i}$ is also modelled using a gradient diffusion assumption: $q_{SGS}^{\phi_i} = \bar{\rho}\alpha_t\,\partial\tilde{\phi}_i/\partial x_k$, where α_t is the eddy diffusivity. For instance, the SGS enthalpy flux, $q_{SGS}^{h_s}$ is defined by: $q_{SGS}^{h_s} = \bar{\rho}\left(\mu_{SGS}/Pr_{SGS}\right)\partial\widetilde{h_s}/\partial x_k$, where μ_{SGS} is a subgrid viscosity and Pr_{SGS} is a subgrid Prandtl number equal to 0.85.

Gaseous Phase: combustion model

The thermochemical state in the combustor is explicitly governed by the scalars transport equations. As shown earlier, the Favre averaging and the Favre filtering of these equations lead to Eqs. (3) and (9) respectively. By considering the species transport equations (i.e. $\phi_i = Y_k$, where Y_k is the k[th] species

mass fraction), one can note that, in addition to unclosed terms resulting from the averaging (i.e. turbulent stresses, $\bar{\rho}\widetilde{u_i''u_j''}$ and scalars turbulent fluxes, $\bar{\rho}\widetilde{u_i''\phi_j''}$) and the filtering (i.e. SGS stresses and SGS scalars fluxes) of the transport equations which are respectively closed as described in the section devoted to SAS and LES models, the averaged and the filtered species reaction rates have to be carefully modeled. Furthermore, several research teams have so far validated the relevance of a sophisticated chemistry model in the simulation of some critical combustion phenomena such as local extinction and re-ignition, and pollutant emissions. A sophisticated chemistry model generally comprises a large number of species and elementary reactions, and these numbers become larger for jet fuels which are mixtures of several hydrocarbons. Thus, in addition to the issue regarding the modeling of the averaged (for SAS) or filtered (for LES) reaction rate of each species, several additional transport equations need to be solved. In order to mitigate the potential computing requirements of such an approach, some physical characteristics of the investigated system are exploited. In fact, because of the wide separation between chemical and mixing time scales in practical combustion systems involving stable and efficient combustion [**11**], chemistry and mixing can be calculated separately; and the thermochemical state can be deduced by resolving a transport equation for a parameter whose relationships with thermochemical variables are known. In most combustors fed with liquid fuels through less sophisticated injectors such as pressure-swirl atomizers, fuel and air are not mixed before entering the combustion chamber, and mixing must therefore bring reactants (evaporated fuel and oxidiser) into the reaction zone fast enough for combustion to proceed. Thus, the proper description of the mixing process, and therefore the robustness of the turbulence model need to be carefully considered for an accurate simulation of this kind of flames. In the present comparative investigation, the mixing is described by solving the transport equations of a non-reactive scalar, the mixture fraction, Z and the thermochemical state is deduced through the relationship between the mixture fraction and the generic scalars, $\phi_i = \{Y_k; T\}$; plus, an additional transport equation is solved for the enthalpy to capture non-adiabatic effects due to the droplets evaporation. Through its relationship with equivalence ratio, the mixture fraction can be interpreted as a normalized equivalence ratio and is defined by [**24, 25**] as a function of a conserved scalar in the form of a Shvab-Zeldovich function (β): $Z = (\beta - \beta_2)/(\beta_1 - \beta_2)$, where subscripts "1" and "2" denote the value in the first and second feed, respectively. The mixture fraction accounts for the level of mixing between the fuel and the oxidiser and change due to convection, diffusion but not reaction (for homogeneous combustion). However, for spray combustion, the mixture fraction is no longer a conserved scalar because of the evaporation of droplets dispersed in a spray [**15, 18**]. In order to take into account the evaporation effect, a source term (S_m) is introduced in the classical transport equation for Z to account for the mass transfer rate, thus partly circumventing the non-direct inclusion of droplets evaporation in the chemistry calculation. The averaged and the filtered transport equations of the mixture fraction are given in Eqs. (13) and (14) respectively.

$$\frac{\partial \bar{\rho}\tilde{Z}}{\partial t} + \frac{\partial}{\partial x_j}\left(\bar{\rho}\tilde{Z}\widetilde{u_j}\right) = \frac{\partial}{\partial x_j}\left(\bar{\Psi}_Z^{Averaged} - \bar{\rho}\widetilde{u_i''Z_j''}\right) + \tilde{\dot{S}}_m \quad (13)$$

$$\frac{\partial \bar{\rho}\tilde{Z}}{\partial t} + \frac{\partial}{\partial x_j}\left(\bar{\rho}\tilde{Z}\widetilde{u_j}\right) = \frac{\partial}{\partial x_j}\left(\bar{\Psi}_Z^{Filtered} - q_{SGS}^Z\right) + \tilde{\dot{S}}_m \quad (14)$$

where $q_{SGS}^Z = \bar{\rho}\left(\widetilde{u_i Z} - \tilde{u}_i\tilde{Z}\right)$. In Eq. (13), the averaged laminar diffusion flux of the mixture fraction is modeled using the averaged molecular diffusivity through the gradient diffusion assumption: $\bar{\Psi}_Z^{Averaged} = \bar{\rho}\bar{D}_Z\,\partial\tilde{Z}/\partial x_k$; the turbulent mixture fraction flux is modeled by: $\bar{\rho}\widetilde{u_i''Z_j''} = \mu_t/\sigma_t\,\partial\tilde{Z}/\partial x_k$; where $\sigma_t = 0.85$, and μ_t is the turbulent viscosity. In Eq. (14), the filtered laminar diffusion flux, $\bar{\Psi}_Z^{Filtered}$, and the SGS of the mixture fraction, $q_{SGS}^Z = \bar{\rho}\left(\widetilde{u_i Z} - \tilde{u}_i\tilde{Z}\right)$ are also modeled using the gradient diffusion assumption, but with filtered parameters: $\bar{\Psi}_Z^{Filtered} = \bar{\rho}\bar{D}_Z\,\partial\tilde{Z}/\partial x_k$ and $q_{SGS}^Z = \mu_{SGS}/\sigma_{SGS}\,\partial\tilde{Z}/\partial x_k$; $\bar{D}_Z$ is the filtered (for LES) or the averaged (SAS) laminar diffusion coefficient of the mixture fraction.

- *Turbulent-chemistry interactions*

In the present study, the presumed PDF formulation is retained among the two schools of thought regarding the PDF (i.e. *transported* and *presumed* PDFs). This choice is partly due to the high computing cost associated with the implementation of a detailed chemistry in the *transported PDF* model. The database for the look-up process is finally generated by convolving the presumed-PDF with a relationship between the mixture fraction and the generic scalars, Φ_i, according to the following Eq. (15):

$$\tilde{\Phi}_i = \int_0^1 PDF_{Joint}(Z,\alpha_i)\,\Phi_i(Z,\alpha_i)dZ\,\mathrm{d}\alpha_i \quad (15)$$

where α_i are additional parameters that allow including some relevant phenomena involved in the physical system (e.g. enthalpy defect due to evaporation and NEQ effects due to turbulent strain), PDF_{Joint} is the joint PDF; its shape depends on whether non-adiabatic and/or chemical NEQ effects need to be accounted for or not. In the investigated physical system, the enthalpy defect is mainly due to the vapor release and its effect on the thermochemical state should be accounted for. To this end, there are globally two approaches: an *indirect approach* proposed by Bray and Peters [**26**] whereby, a transport equation for the mean (or filtered) enthalpy with a source term added to represent the enthalpy defect due to evaporation is solved, and a second approach proposed by Carbonell and co-workers [**27**] that can be viewed as a *direct approach*, through which non-adiabatic effects can directly be included in chemistry tabulation through, $\Phi_i(Z,\alpha_i)$. For the present study, an *indirect approach* is used to include non-adiabatic effects due to the evaporation. In fact, even if *direct approach* seems more suitable for spray combustion, it is worth noting that, when generating for instance flamelet solutions in the mixture fraction space, it cannot be extended such as to include heat losses due to evaporation, since the spray distribution in the

physical space is not coupled to the mixture fraction space. The incorporation of non-adiabatic and NEQ effects leads to two additional parameters for the joint PDF namely the enthalpy and the scalar dissipation rate. The latter parameter allows measuring the departure between EQ and NEQ states, and is explicitly presented in the next section devoted to the flamelet model. Finally, with the assumption of statistically independence between Z, H_s and χ, the shape of the joint PDF may be expressed by Eq. (16):

$$PDF_{Joint}(Z,\alpha_i) \equiv PDF_{Joint}(Z,H_s,\chi) = PDF(Z).PDF(H_s).\mathrm{PDF}(\chi) \quad (16)$$

For SAS simulations, the presumed PDF of the mixture fraction, $PDF(Z)$ is modelled using the Favre-mean mixture fraction ($\tilde{Z}$) and its variance ($\widetilde{Z''^2}$) through the β-function because of its ability to change continuously from PDF shapes with one or two peaks to Gaussian shapes. For the LES simulations, the subgrid PDF ($PDF(Z)$) is modelled using the Favre filtered mixture fraction (also denoted $\tilde{Z}$) and its unresolved fluctuations (also denoted $\widetilde{Z''^2}$) through a β-function as proposed by Cook and Riley [28]. Thus, even intrinsically different in terms of physical meaning of parameters involved in their formulations, the PDFs of the mixture fraction for SAS and LES formulations have similar forms given by Eq. (17):

$$PDF(Z) = \frac{Z^{a-1}(1-Z)^{b-1}}{\int Z^{a-1}(1-Z)^{b-1}dZ} \quad (17)$$

where $a = \tilde{Z}\left[\frac{\tilde{Z}(1-\tilde{Z})}{\widetilde{Z''^2}} - 1\right]$ and $b = (1-\tilde{Z})\left[\frac{\tilde{Z}(1-\tilde{Z})}{\widetilde{Z''^2}} - 1\right]$; the fluctuations of the enthalpy and that of the scalar dissipation rate are neglected. Consequently their PDFs, $PDF(H_s)$ and $\mathrm{PDF}(\chi)$ may be approximated by delta functions: $PDF(H_s) = \delta(H_s - \widetilde{H_s})$ and $\mathrm{PDF}(\chi) = \delta(\chi - \tilde{\chi})$. Thus, based on these additional simplifications, the PDF shape retained for the present study is given in Eq. (18).

$$PDF_{Joint}(Z,H_s,\chi) = \beta_{PDF}(Z).\delta(H_s - \widetilde{H_s}).\delta(\chi - \tilde{\chi}) \quad (18)$$

- *relationship between Φ_i and Z under equilibrium (EQ) and non-equilibrium (NEQ) assumptions*

Under the full EQ assumption, the chemistry is rapid enough for chemical equilibrium to always exist at the molecular level. An algorithm based on the minimization of Gibbs free energy is used to deduce generic scalars from Z. The combustion model based on the full EQ assumption is sturdy for some practical problems since it can predict the main flame trends, and it does not require knowledge of detailed chemical kinetic rate data. However, as advocated by Peters [29], this approach based on chemical equilibrium calculations over the whole range of the mixture fraction (i.e. $Z \in [0,1]$), features some drawbacks namely a zero-prediction and an overprediction of slow species concentrations in the fuel-lean and the fuel-rich regions of the combustor respectively. In the first part of the current study, instead of using the full EQ model, a partial equilibrium (PEQ) approach is used, since complex tasks related to equilibrium calculations can be avoided in the rich regions while improving partly the predictive capabilities of the full EQ in terms of prediction of both the main flame trends and slow species formation. The entire range of the mixture fraction is then divided into two parts using a cut-off value of the mixture fraction (i.e. a rich limit, Z_{limit}). Thereafter, chemical EQ calculations are performed over a restricted range of Z ($Z \in [0, Z_{limit}]$) while the remaining range is treated with mixing calculations. Physically, this means that, in the remaining range, no combustion reaction takes place, and that unburned fuel coexists with the reacted material. In such fuel-rich zones, the composition at a given value of the mixture fraction is computed from the composition at the limiting mixture fraction (set here as Z_{limit}~1.3 $Z_{stoichiometric}$) and that corresponding to the fuel inlet stream ($Z = 1$) based on a known stoichiometry. However, in some practical combustion systems where flame stretching and/or flame wrinkling are relevant, both full EQ and PEQ approaches may lead to unrealistic results. Among these cases one can denote the modeling of the rich side of hydrocarbon flames, the prediction of the intermediate species that governs the NOx formation, the prediction of some species involved in slow reactions (e.g. CO, H_2, etc.) and the modeling of lift-off and blow-off phenomena in jet flames [7, 10, 24, 29]. For an accurate simulation of such phenomena, chemical NEQ effects need to be properly accounted for. In this vein, the flamelet model has been proposed as an efficient way to account for moderate chemical NEQ effects due to turbulence straining. In this model, the flamelet structures corresponding to various level of flame stretching are generated by solving flamelet equations either in the physical space or in the mixture fraction space. For the present study, as the species transport equations are replaced by the transport equation of the mixture fraction for both SAS and LES methods, flamelet equations are solved in the mixture fraction space. The flamelet equations are derived by performing a Crocco-type coordinate transformation on the conservative equations for species and energy, the new coordinate system being attached to the flame surface (i.e. a surface corresponding to the stoichiometric mixture fraction) [10]. With a further assumption of unity Lewis number for all species, the flamelet equations are expressed by Eqs. (19) and (20) as follows:

$$\frac{\partial Y_i}{\partial \tau} = \frac{\rho\chi}{2}\frac{\partial^2 Y_i}{\partial Z^2} + \dot{\omega}_i \quad (19)$$

$$\rho\frac{\partial T}{\partial \tau} = \frac{\rho\chi}{2}\frac{\partial^2 T}{\partial Z^2} + \frac{\rho\chi}{2C_p}\frac{\partial C_p}{\partial Z}\frac{\partial T}{\partial Z} + \frac{\rho\chi}{2C_p}\sum_{i=1}^{N}\left(C_{pi}\frac{\partial Y_i}{\partial Z}\right)\frac{\partial T}{\partial Z} - \frac{1}{C_p}\sum_{i=1}^{N}h_i\dot{\omega}_i \quad (20)$$

In these equations, T is temperature; C_p is mixture-averaged specific heat; C_{pi} specific heat of the i^{th} species; Y_i mass fraction of the i^{th} species; $\dot{\omega}_i$ net rate of production of the i^{th} species; h_i enthalpy of i^{th} species; the instantaneous scalar dissipation rate, χ is defined by $\chi \equiv \chi_Z = 2D_Z(\nabla Z.\nabla Z)$ and is modeled using the analytical approximation by [9]: $\chi(Z) \equiv \chi_{st}exp\{2[erfc^{-1}(2Z_{st})]^2 - 2[erfc^{-1}(2Z)]^2\}$.

Liquid Phase

A Lagrangian modeling of the liquid phase leads to its description in terms of droplet position, velocity, radius and thermodynamic state; each droplet is then considered as a particle. Assuming a dilute spray of small droplets (Sauter Mean Diameter, $SMD{\sim}60\ \mu m$**)**, (i) the droplet-droplet interaction and coalescence can be neglected; (ii) the effect of gravity on each droplet can also be neglected; (iii) only drag and thermophoretic forces are considered in the momentum equation; and (iv) the effect of convection on each droplet is accounted for as well as the droplet secondary break-up phenomenon. The position of each droplet is obtained from $dX_d = V_d dt$; the acceleration of the d^{th} droplet is obtained by integrating the force balance on the particle, which is written in a Lagrangian reference frame. This force balance equates the droplet inertia with the forces acting on the droplet, and may be written as in Eq. (21):

$$A_d = F_D(u_i - V_d) + F_{add}, \qquad (21)$$

where the drag force per unit mass F_D is defined by $F_D = 18\mu/\rho_d d_d^2 \times C_D R_e/24$, u_i is the gaseous phase velocity, V_d is the droplet velocity, μ is the molecular viscosity of the liquid, ρ is the gas density, ρ_d is the density of the droplet, d_d is the droplet diameter, R_e is the relative Reynolds number defined as $R_e = \rho d_d|u_i - V_d|/\mu$ and C_D is the droplet drag coefficient, which is determined dynamically to account for droplets deformation. The term F_{add} represents the resultant thermophoretic, Brownian and Saffman lift forces. As the droplets considered in the present study are not sub-micron ($d_d > 10^{-6}m$), both Brownian and Saffman Lift forces are neglected. The heat exchange between droplets and the gaseous phase are governed by inert heating, vaporization and droplet boiling. Mass and heat transfers are assumed to be controlled by convective and diffusive transports, and an infinite liquid-conductivity assumption is used for their modeling. Thus, the droplet surface temperature is assumed uniform, time-varying and equal to the temperature inside the droplet with droplets internal recirculation neglected [**20**]. For droplets temperature below the "flash point", only inert heating takes place with no exchange of mass between the gaseous and liquid phases, and the following Eq. (22) is used to determine the change in temperature due to heat exchange with the gaseous phase:

$$m_{dj} c_{dj}\, dT_{dj}/dt = hS_{dj}\left(\tilde{T}_\infty - T_{dj}\right), \qquad (22)$$

neglecting radiation. When the droplet temperature reaches the vaporization temperature, the mass is transferred from the liquid phase to the gaseous phase. The vaporization rate in a convection-diffusion medium is given by Eq. (23):

$$\dot{m}_{dj} = dm_{dj}/dt = S_{dj} k_{c,j} \rho_\infty ln\left(1 + B_{m,j}\right), \qquad (23)$$

where m_{dj} is the mass of component "j" in the droplet; $k_{c,j}$ is the mass transfer coefficient of component "j" ; S_{dj} is the droplet surface area; ρ_∞ is the density of bulk gas; $B_{m,j}$ is the Spalding mass number for species "j" and T_{dj} is the droplet temperature. For the one-component fuel, $j = 1$, while for the two-component fuel, $j \in \{1,2\}$. Once the droplet temperature reaches the boiling point, the boiling rate is calculated as:

$$\dot{m}_{dj} = x_j\, \pi d_d k_\infty / c_{p\infty} \left(2.0 + 0.6 Re_d^{\frac{1}{2}} Sc^{\frac{1}{3}}\right) ln\left(1 + B_{T,j}\right), \qquad (24)$$

where x_j stands for the volume fraction for the component "j" in droplet, d_d the droplet diameter and $B_{T,j}$ is the Spalding heat transfer number for component "j" computed as: $B_{T,j} = c_{p\infty}\left(\tilde{T}_\infty - T_d\right)/h_{vap,j}$, where $h_{vap,j}$ is the latent heat of vaporization for component "j". Furthermore, the temporal change in temperature for multicomponent droplets, neglecting the radiation effect is calculated by Eq. (25):

$$m_d C_d \dot{T}_d = hS_d\left(\tilde{T}_\infty - T_d\right) + \dot{m}_d h_{fg}, \qquad (25)$$

where h_{fg} is the latent heat, h is the heat convection coefficient calculated using the modified Nusselt number defined by:

$$Nu = hd_d/k_\infty = (2.0 + 0.6 Re_d^{1/2} Pr^{1/3}) \ln(1 + B_T)/B_T,$$

in which $Pr = c_g \mu/k_\infty$ is the Prandtl number. The multicomponent vaporization and boiling rates are calculated using the sum of the vaporization and boiling rates of the individual components.

EXPERIMENTAL CONFIGURATION

The setup considered in the present simulations was investigated experimentally by Sheen [**48**] and thereafter, numerically by [**17**], using an in-house CFD code and a four-step reaction mechanism. It consists of an annular swirling air jet flowing into a cylindrical combustion chamber. A sketch of the combustor is shown in Fig. **1**. It is made of a 500 mm long cylindrical combustion chamber with an internal diameter of 200 mm. The intense fuel and air mixing is produced by an aerodynamic gas turbine type swirler with 20 equally spaced vanes with a discharge angle of 30^o to the axis. It is located in an annular duct 50 mm up-stream of the front plate of the combustor. The fuel injector ($d_{inj} = 0.25\ mm$), located in the centre at the head of the combustor, injects liquid jet-A1 in the form of a fine hollow cone spray into the central recirculation zone. The air and the liquid spray are not preheated ($T{\sim}300K$) and the exit of the combustor is open to the atmosphere. The co-flowing air enters the combustor axially with a tangential velocity component generated by the swirler. Given the lack of measurements of the flow upstream of the annular duct exit, intermediate simulation steps are necessary for the specification of accurate inflow boundary conditions namely those characterizing the spray. Top-hat profiles are used for axial and tangential components of the velocity. The values imposed at the inlet of the combustor are adjusted so that the total mass flow rate of air and the swirl number at the inlet are consistent with the experimental values. The fuel mass flow rate is 0.951 g/s and the air-to-fuel ratio is 27.88. The annular pipe has an outer radius, R=21 mm, which is used as a reference length in the axial direction of the combustor. The combustor is highly swirled since its swirl number, S = 0.91 > 0.6. The correlation proposed by Beer and Chigier [**31**] is used to deduce the swirl component of velocity. The Reynolds number based on the annular duct radius is around 21300**.** According to the critical

Reynolds number for internal flows (Re~2100) the flow is turbulent.

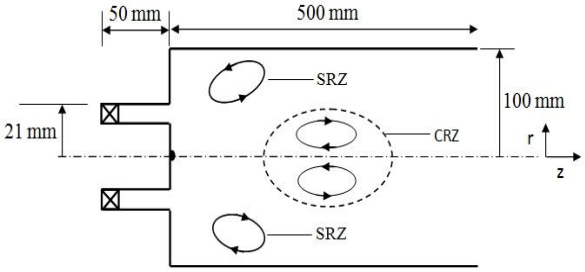

Fig.1: Sketch of the combustor

NUMERICAL IMPLEMENTATION

The set of equations governing the two-phase aerothermochemical state is solved using a commercial finite volume-based CFD code, ANSYS FLUENT^{TM} (version 14.0) [**32**]. The liquid jet fuel used in the present investigation (Jet-A1) is a mixture of several hydrocarbons that varies depending on crude source and distillation process. Thus, it is not obvious to suitably define a universal composition of this jet fuel. Several published experimental investigations [**33**, **34**, **35**, **36**, **37**] show that the most prevalent components belong to the group of n-paraffins (n-decane, n-dodecane, etc.), i-paraffins and cyclo-paraffins (iso-octane, iso-cetane, etc.), naphtalenes (cycloliphatic, methylcyclohexane, etc.) and aromatics (benzene, toluene, etc.). For instance, according to [**33**], the composition of a jet fuel on a molar basis may be approximated as follows: n-paraffins-28%, iso-paraffins-29%, cycloparaffins-20%, alkylbenzenes-18%, naphtalenes-2% and misc-3%. From this empirical composition, it appears that paraffins and aromatics are the major components for jet-A1. Thus, in this work, pure n-decane (i.e. 100% $C_{10}H_{22}$) and a mixture of n-decane and toluene (i.e. 60% $C_{10}H_{22}$ + 40% C_7H_8) are used as the surrogates for liquid jet-A1. The combustion kinetic of the evaporated jet-A1 with oxygen is described by a reduced CKM derived from the detailed JetSurf 2.0 model using the Alternative Species Elimination as in [**38**]. The detailed model (JetSurf 2.0) was validated against ignition and flame data and the reduced model for both the pure n-decane and the mixture of n-decane and toluene was verified to predict combustion properties in agreement with the detailed model and its validation targets. As illustration, a thermochemical structure of a diffusion flame computed using the two CKM models is presented in the sub-section devoted to the computing parameters (Fig. **2**a). It can be seen that the diffusion flame is reasonably well predicted by the reduced CKM model. Also, in order to strengthen the robustness of the chemistry model, realistic laws to vary fuel transport properties as a function of temperature are implemented in the CFD code for all simulations. When using the turbulent combustion model based on the NEQ assumption through the flamelet model presented earlier, an additional assumption is made to generate the flamelet solutions: the flamelet structures are assumed to be stationary, which physically means that each flamelet structure is controlled by only the balance between steady chemical reactions and steady diffusion processes.

COMPUTING PARAMETERS

- *Boundary conditions for the carrier phase*

For the air inflow, top-hat profiles based on the experimental equivalence ratio and swirl number are imposed for axial and tangential air velocity components. The potential oscillations related to this approach are mitigated by carefully setting the under-relaxation parameters. The turbulent inlet conditions are specified through the turbulent intensity and the hydraulic diameter. The turbulence intensity is estimated by using a correlation for a fully developed pipe flow at the core ($I = 0.16(Re_{D_H})^{-1/8}$~5%), where Re_{D_H} is the Reynolds number based on hydraulic diameter (D_H), Also, impermeability and no-slip boundary conditions are applied for the velocity at the wall of the combustor.

- *Boundary conditions for the liquid phase*

A pressure swirl atomizer ("*Simplex injector*") is used to atomize the liquid jet-A1 in the experimental setup. In the present simulations, a cone-type injection was used to simulate the atomization, and the droplets size distribution was assumed to follow the classical Rosin-Rammler law: $f(d) = exp[-(d/d_m)^n]$, where n and d_m are the spread parameter (dispersion of droplet sizes) and the mean diameter of droplets respectively. Due to the lack of some experimental data on the spray configuration, a parametric investigation based on the features of a *Simplex injector* as described by Lefebvre [**39**] is first conducted to the calibrate the injection through the determination of suitable parameters for the Rosin-Rammler correlation (i.e. mean diameter and spread parameter) and the spray cone angle, α. From this parametric study, the values selected for the spray parameters are the following: $n = 3.5$, $d_m = 70\mu m$ and $\alpha = 80^o$. According to the droplet-wall interaction, it is assumed that droplets rebound off the walls with a change in their momentum. This resulting change of their momentum is quantified by a restitution coefficient as described by [**40**].

- *Boundary conditions for flamelet solutions*

Flamelet solutions are generated by solving the flamelet equations presented earlier. For this purpose, CKM which describes the combustion kinetic is required. Thus, the reduced CKM model (RCKM) mentioned in the previous section is used to calculate the reaction rates of each species. But before using the RCKM, a validation test is done: its ability to predict the thermochemical structure of a diffusion flame is compared to that of the detailed CKM (DCKM) using the CHEMKIN^{TM} code [**41**] as shown in Fig. **2**(a). The calculated chemical reaction rates of species are combined to a profile of the scalar dissipation rate to close the flamelet equations in order to generate the set of flamelet solutions. The structure of flamelet solutions corresponding to the computational parameters introduced in the flamelet solver are presented in Fig. **2**(b), **2**(c) and **2**(d). Particularly, unlike premixed flamelets which feature zero-straining due to fuel-air mixing (because of the nearly

constant equivalence ratio), diffusion flamelets are more sensitive to such a straining and its effect (quantified by the scalar dissipation rate, χ_Z) on the diffusion flamelet structure is identifiable in Figs. 2(b) and 3(c). This effect is well elucidated by representing the corresponding S-shaped curve (i.e. maximum temperature as a function of stoichiometric χ) as done in Fig. 2(d). It can be first noted the restrictiveness of the solution space corresponding to the steady flamelet model, as only the upper branch of the S-shaped curve is generated; secondly, it is seen that the maximum temperature which is obtained at the stoichiometric value of the mixture fraction ($Z = Z_{st} \approx 0.08$), decreases from flow conditions close to equilibrium ($X \equiv \chi = 0.01\ s^{-1}$) to flow conditions in which the flame is strongly stretched. The highest value of the scalar dissipation rate corresponds to the extinction point and is currently denoted by χ_q. Fig. 2(d) shows that for gaseous flamelets particularly, χ_q depends on the fuel and oxidizer composition. The accuracy of the value of χ_q depends also on the discretization scheme of the flamelet equations and the numerical model implemented in the flamelet generator code. Finally, one can also notice that the value of χ_q decreases with fuel volatility (i.e. $\chi_{q\_tol.} < \chi_{q\_mixt.} < \chi_{q\_n\_dec.}$).

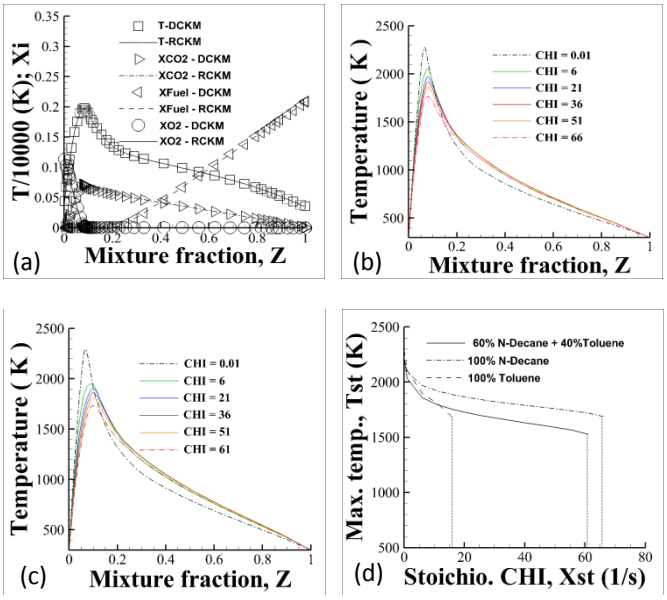

Fig. 2: CKM validation and structure of the flamelet library

- *Computing setup*

The combustor sketched in Fig. 1 was discretized using a structured mesh, and three mesh densities were considered: 0.8, 1.2 and 2.16 million hexahedral elements. After performing a mesh sensitivity study based on SAS and LES simulations, the third grid (2.16 million elements) was enough to reach the best SAS accuracy, since further mesh refinements through the mesh adaptation algorithm of the CFD did not lead to more accurate results. However, because of the inherent mesh dependence of the LES solution, the third mesh density comprising approximately 2.16 million hexahedral elements ($\sim$ 2.16 million nodes and $\sim$ 6.52 million faces) was also retained for LES simulations, and mesh adaptations were performed in order to capture properly the spray dynamics, the mixing process in the first instant of the evaporation phase, and the boundary layer effects. Thus, the grid was refined near the solid boundaries, and in particular around the combustor axis and the injector exit: about 60% of elements were localized in these zones of the combustor. The quality of the LES results based on the final mesh resolution was assessed through the turbulence resolution parameter defined by Pope [42, 43]: $M = k_{SGS}(x_j,t)/(\tilde{K}(x_j,t) + k_{SGS}(x_j,t))$, where $\tilde{K}(x_j,t)$ is the resolved kinetic energy, while $k_{SGS} = \mu_{SGS}^2/(C_m\Delta)^2$ is the SGS kinetic energy; $C_m = \sqrt{2/3}\,A/\pi K_0^{3/2}$ is a constant calculated with the Kolmogorov's constant and the Kraichman's test field model constant [43]. For the present study, $M \approx 0.19$, thus approximately 80% of the turbulent kinetic energy was resolved. The two turbulence models presented earlier are contained in the CFD code, and all the simulations were performed using the double precision mode. A segregated solver namely, the Semi-Implicit Method for Pressure Linked Equations (SIMPLE) algorithm was used for the pressure-velocity coupling. For both SAS and LES simulations, transient derivatives were discretized using a bounded second-order implicit scheme, a bounded central differencing scheme was used for the momentum equation; and second-order schemes were used for the discretization of the transport equation of the remaining variables. According to the combustion model, ANSYS FLUENT™ includes also a flamelet solver, which was used to build a flamelet library necessary for simulations including chemical NEQ effects. The Lagrangian analysis of the spray was performed using the discrete phase model (DPM) including a DRW model to take into account the effect of the turbulence on the spray dynamics (for SAS simulations). Through this model, droplets were tracked in an unsteady manner with the fluid time step and the coupling was done such as to perform 10 continuous phase iterations per DPM iteration. The investigated two-phase reactive flow is turbulent, inertial phenomena dominate viscous diffusive ones and, because every droplet features its own time scale, a time scale based on both a representative convection time scale and a representative droplet residence time was used to define the time step of the simulation: the outer diameter of the annular duct was selected as reference length ($L_{ref} = R$) while the air bulk velocity was chosen as a reference velocity $U_{ref} = U_{air}$. These two parameters were used to define a reference time scale $t_{ref} = L_{ref}/U_{ref} = R/U_{air}$. Based on a representative droplet residence time, the time step of the simulation was thereafter defined as $\Delta t = 0.1 t_{ref}$. The simulations were started with initialized fields, and were first performed over a time period equal to 8 000 time steps, which is approximately equal to 30 times the characteristic computation time (i.e. the time used by the flow to cross the computational domain in the main stream direction with the velocity equal to the bulk velocity). This first step of the

simulation was devoted to eliminate the influence of initialization, and to obtain an initial flow evolving naturally with the imposed boundary conditions, while becoming statistically steady. Subsequently, simulations were continued for 4 000 further time steps ($\sim 390 \times t_{ref}$) under sample statistics mode. This additional number of time steps turned out to be sufficient to yield the statistical convergence.

RESULTS

Aerodynamics state in the combustor

In order to provide an idea of the resolution capabilities of the two turbulence models, a vortex extraction method is applied: the iso-surfaces corresponding to $\lambda_2 = -2 \times 10^5$ flooded by the temperature and mixture fraction contours are shown in Figs. 3. The *lambda 2* (λ_2) is mathematically defined as the second real eigenvalue of the symmetric matrix, $S^2 + \Omega^2$, where S is the strain tensor, and Ω is the vorticity tensor. This parameter is related to the Navier Stokes equations and reflects the amount of strain and whirling motions in the flow field [44]. One can notice the better ability of the LES model to capture smaller turbulent structures compared to SAS. However, the two turbulence models provide mean mixture fraction fields which are almost uniform for the selected range, highlighting then the robustness of the SAS model for the mixing prediction. In Figs. 4, recirculation zones are shown using contours of velocity vectors colored by the axial velocity component; one can see side and central recirculation zones (SRZ and CRZ) generated by the combined actions of both the sudden expansion and the swirling motion. The vortex structures generated in these recirculation zones help to stabilize the flame with a lower bulk velocity. In fact considering the dynamics of each pair of generated counter-rotating vortices, their resulting effect leads to a velocity reversal increasing residence time and mixing for better flame stability. Multiple radial profiles of the three velocity components are shown in Figs. 5 for several axial positions along the axis of the combustor. It can be noticed that globally, the two turbulence models predict reasonably well the aerodynamics state. For axial and radial profiles, some discrepancies can be noted in the zone close to the injector exit near the combustor axis ($z/R \leq 1.0$).This may be related to the dynamics of the spray which is particularly dense in this zone due partly to the secondary break-up phenomenon. Such a zone requires a more elaborated model to solve accurately both the spray dynamics and its interaction with turbulence, but at a much higher computational cost. Apart from this zone, a reasonable agreement with the experimental velocity field is obtained at each cross section of the combustor. In all the represented cross sections of the combustor, one may also observe negative values of the axial velocity which evidence the presence of recirculation zones. This reasonable prediction of the aerodynamics confirms that the estimated spray parameters deduced from the parametric study mentioned earlier are quite realistic.

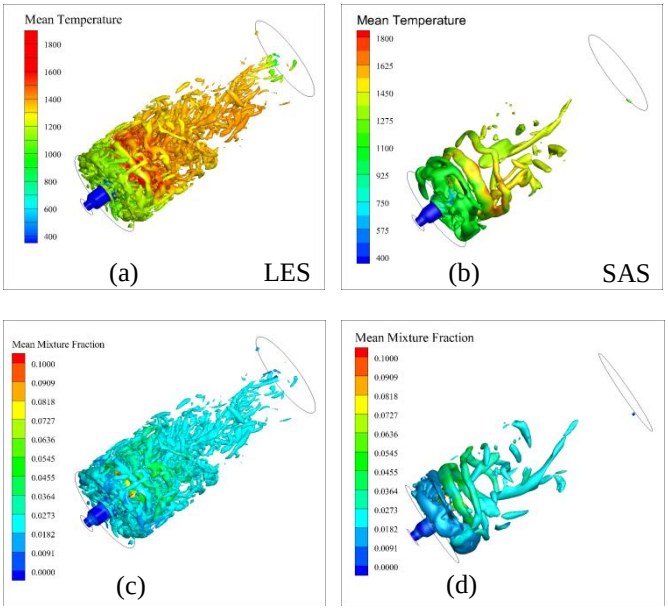

Fig. 3 Turbulent resolved structures shown by isosurfaces $\lambda_2 = -2 \times 10^5$, and flooded by: (a) & (b) temperature (K); (c) &(d) mixture fraction

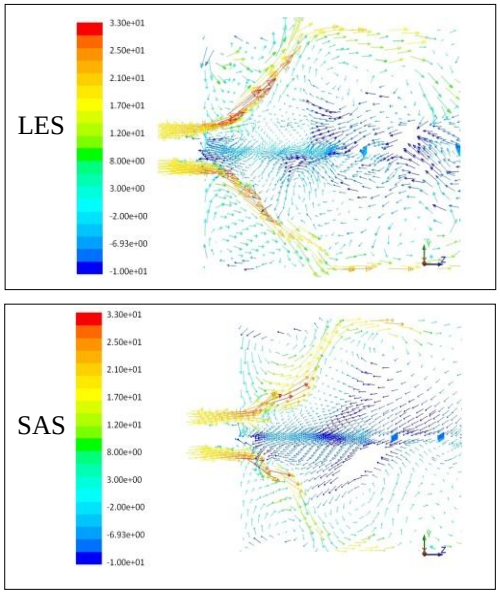

Fig. 4: Recirculation zones captured through velocity vectors colored by axial velocity (m.s^{-1})

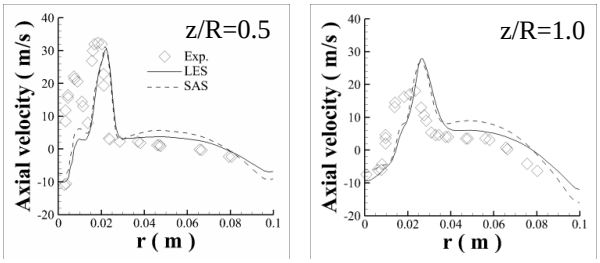

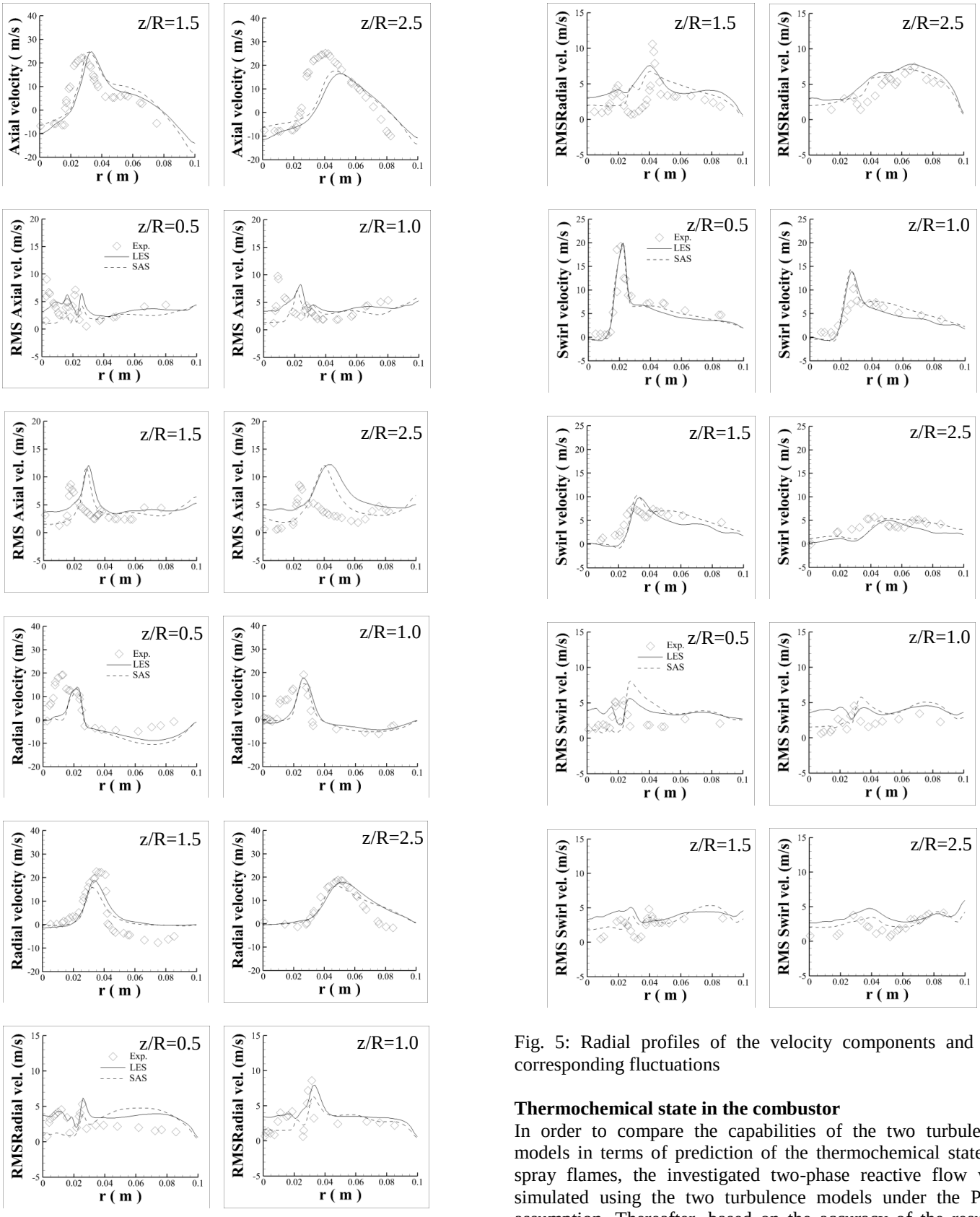

Fig. 5: Radial profiles of the velocity components and the corresponding fluctuations

Thermochemical state in the combustor

In order to compare the capabilities of the two turbulence models in terms of prediction of the thermochemical state of spray flames, the investigated two-phase reactive flow was simulated using the two turbulence models under the PEQ assumption. Thereafter, based on the accuracy of the results,

the LES model was retained to investigate both the relevance of the inclusion of chemical NEQ effects through the steady flamelet model (SFM), and the effect of the fuel composition by considering a two-component surrogate for Jet-A1. Multiple radial profiles of the mean temperature are shown in Fig.**6** corresponding to the SAS and LES simulations using the PEQ assumption coupled to the one-component surrogate for Jet-A1, and the LES simulations based on the SFM with both the one-component and the two-component jet-A1 surrogates respectively. Based on these results, it appears that the first one-fifth of the combustor (i.e. the part for which experimental data are available) can be divided into two main zones: left and right side zones ($r \in [-0.1, 0.01] \cup [0.01, 0.1]$) and a central zone directly close to the injector exit ($r \in [-0.01, +0.01]$ for $z/R \leq 3.0$). In the former zone, the mixing is efficient because of the presence of side recirculation zones and relative high velocity as shown in Figs. **3** and **4**. Because of the better abilities for LES and SAS to resolve a part of the turbulence spectrum, they are inherently more suitable for high Reynolds number flows, and consequently lead to a reasonable prediction of mixing and then, of temperature profiles with a superior performance of the LES as shown in Figs. **6**. Thus, due to the relative best trade-off between the accuracy of the LES results and the computing time, LES was retained for subsequent simulations investigating both the chemical NEQ and the fuel composition effects. In fact, for the SAS and LES simulations, the average computing times corresponding to the simulation time step were approximately 64 and 70 seconds respectively; and by contrasting the improvements generated by the LES simulations with the computing time required for each simulation, one can deduce that, for the present configuration, the LES provides the best compromise between quality of results and computing cost. This observation is particularly validated in the zones around the injector exit ($z/R \leq 3.0$), since in the downstream zones ($z/R > 3.0$), the two turbulence models lead to good agreements with experimental results. Also, by combining the same mesh adaptation approach to a less dense mesh (1.2 million instead of 2.2 million hexahedral elements) in a previous study without exceeding 1.8 million elements [**45**], the LES approach led to reasonable predictions in this zone ($z/R \leq 3.0$), unlike SAS simulations whose realistic predictions of the present configuration required a mesh density consisting at least of 2.2 million elements. Profiles shown in Figs. **6** allow also validating the relevance of the inclusion of NEQ effects due to turbulent strain. In fact, the SFM model significantly improves the prediction of temperature in the shear layer zones defined by the fuel spray cone and the co-flowing air, where the flame stretching is particularly predominant because of high mixture fraction gradients. Outside these zones, both PEQ and SFM lead to identical results as mixing becomes more uniform, and then features an almost zero-scalar dissipation rate which corresponds to the equilibrium state. For profiles of major species as shown in Figs. **8** (CO_2 and O_2), one can firstly notice that, the LES model leads to significant improvements compared to SAS; secondly, it is seen that, the implementation of the SFM and the two-component surrogates has insignificant effects on the prediction of major species compared to those of the turbulence models. For both SAS and LES simulations, on can note some discrepancies (underprediction of CO_2 and overprediction of O_2) in the zone $r \geq 0.03\ m$, which may be related to fuel distribution, and then to some inaccuracies of the spray parameters. For the two turbulence models, species characterised by low reaction rates (CO and H_2) are significantly overpredicted in fuel-rich zones when considering the PEQ model as shown in Fig. **9**. In fact, even if the combustion processes are strongly sensitive to the mixture fraction fluctuations, it remains that in addition to a proper resolution of the mixing field, the global accuracy of a predictive approach depends also on the suitability of the relationship between the generic scalars and the mixture as well as the proper inclusion of turbulence-chemistry interactions. The PEQ approach used in the first part of simulations fails to predict slow species in fuel-rich regions because of the requirements for much more complex modelling of fuel partial oxidation (pyrolysis reactions) and mechanisms of soot formation. These discrepancies are considerably reduced by incorporating the chemical NEQ effects through the SFM. However, an overprediction is still noticed when applying the SFM; this may be mainly related to simplifications done in the model. In fact, slow species such as CO and H_2 are intermediate species that are produced and/or consumed by oxidation in the post-reaction zone on time-scales that generally exceed the residence time. Since in addition to unity Lewis number assumption for all species and negligible radiation effects, the SFM assumes an infinite residence time, which is not realistic for some configurations. This drawback may be mitigated by using unsteady flamelet model (UFM) instead of SFM, because of the presence of unsteady terms which allow a more realistic modelling of flamelet structures and instantaneous tracking of rapid changes of the scalar dissipation rate in the downstream direction of the reactive flow.

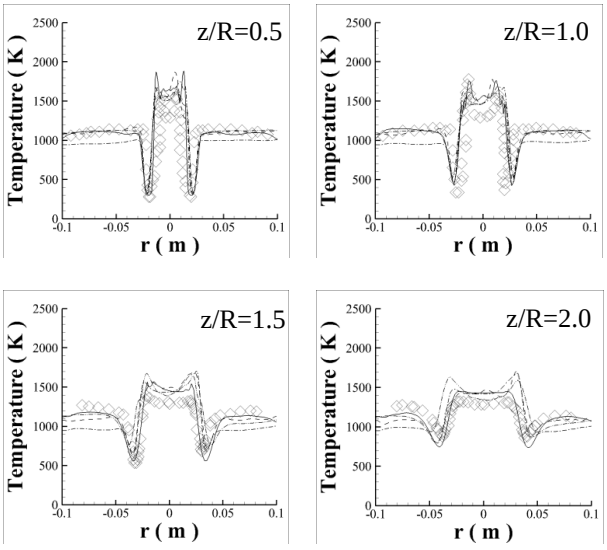

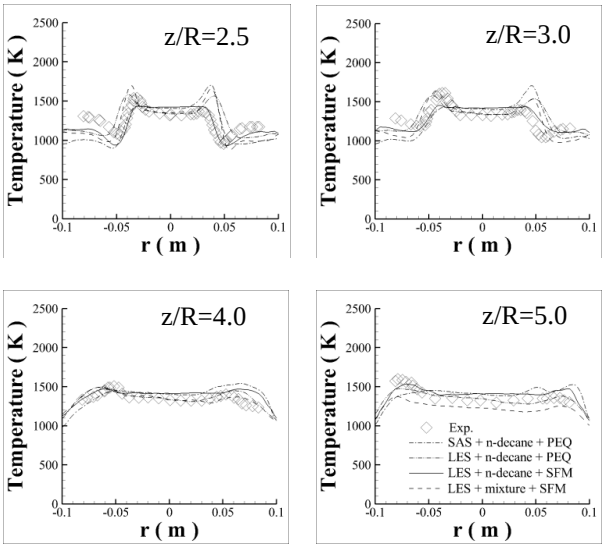

Fig. 6: Radial profiles of the mean static temperature

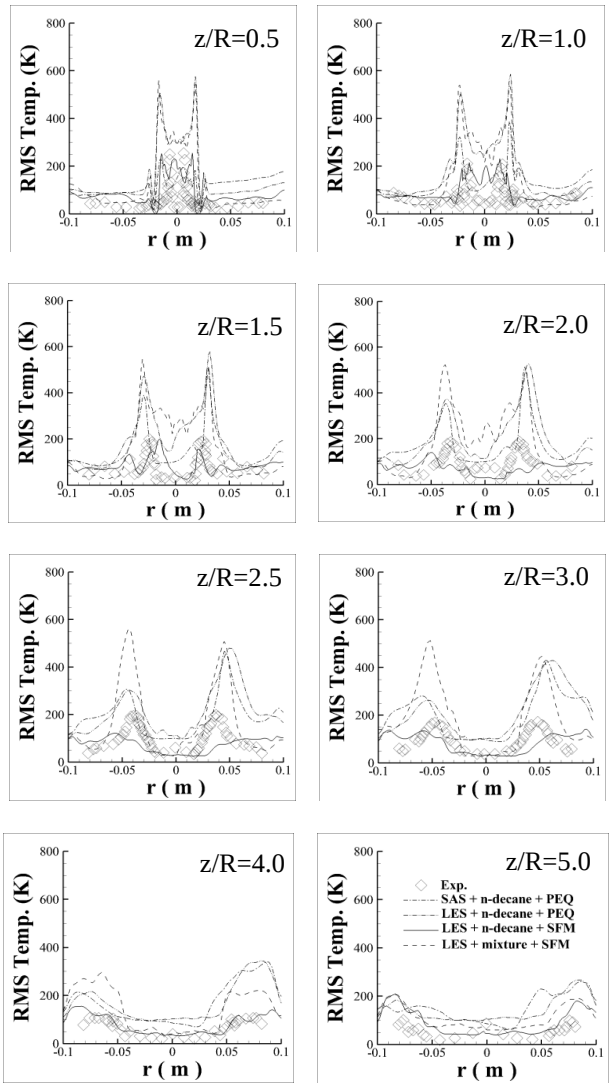

Fig. 7: Radial profiles of the RMS static temperature

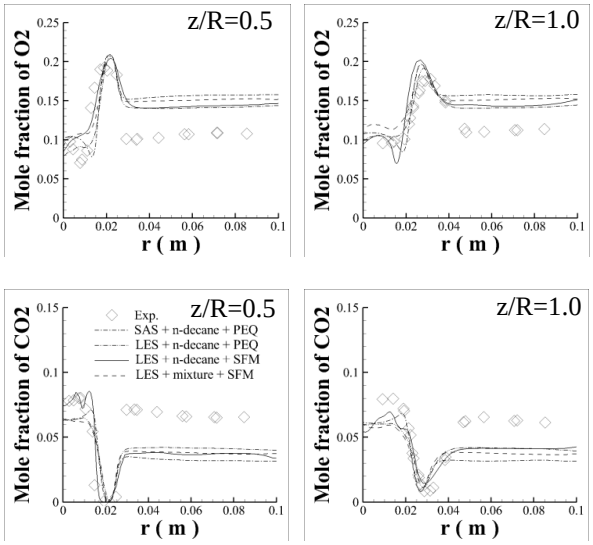

Fig. 8: Radial profiles of the mole fractions of CO_2 and O_2

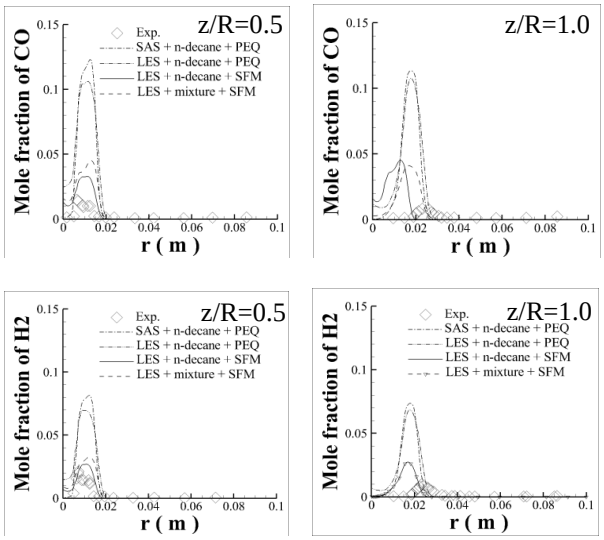

Fig. 9: Radial profiles of the mole fractions of CO and H_2

CONCLUSIONS

Numerical simulations of a turbulent jet-A1 spray flame in a swirl-stabilized gas turbine model combustor were conducted. The first part of the study was mainly devoted to the comparison of the predictive capabilities and computing resources requirements of two turbulence models namely SAS and LES considering an academic spray flame configuration. In the second part, the relevance of the inclusion of chemical non-equilibrium effects due to turbulent strain and that of fuel composition were investigated by coupling LES to a tabulated flamelet-based chemistry approach and subsequently by implementing the two-component fuel surrogate in the

chemistry tabulation. The main salient points of the study can be summarized as follows:

- For some reactive flow configurations (e.g. turbulent highly swirling spray flames), SAS and LES models can lead to a reasonable prediction of the reactive flow field, with a superior performance for LES. This superior performance of the LES is subjected to an additional computing requirement, but is substantially validated mostly in the zones around the injector exit, as these zones involve complex phenomena featuring small length scales which are relatively well captured by the LES compared to SAS, as shown in Figs. 3. The improvements generated by the LES model are more related to the LES formulation than to the mesh resolution. In fact, in the present study, the mesh resolution used for SAS simulations was selected after performing a preliminary mesh sensitivity study which showed that no significant improvements could be obtained with SAS by increasing the mesh resolution through the mesh adaptation module of the CFD code. Thereafter, the same mesh adaptation strategy was performed on the resulting optimal mesh resolution before using it for the LES simulations which turned out to produce significant improvements of the prediction with simulation times (~70 seconds per time step) not much longer than those of the SAS simulations (~64 seconds per time step). Furthermore, by performing the same mesh adaptation on a structured grid consisting of 1.2 million hexahedral elements (as shown in [**45**]) instead of 2.2 million elements of this study, the LES simulations led to reasonable prediction compared to that of the SAS around the injector exit, justifying a superior intrinsic performance of the LES model.
- The inclusion of chemical non-equilibrium effects due to turbulent strain (here the flame stretching) through the flamelet model turned out to improve the prediction of the main flame trends in the zones of high mixture fraction gradients (i.e. shear layer zones). However, an underestimation of CO_2 and an overestimation of O_2 were found on the side of the central recirculation zone of the combustor, suggesting a mismatch of spray parameters generated by the parametric investigation devoted to the calibration of the spray model. Considering the relevance of the spray parameters when modelling the injection in two-phase reactive flow simulations, this issue is likely to be solved only by using accurate spray parameters recorded in the experiment specifically for the type of injector, and these data were not available for the present study. Likely by not accounting properly the secondary breakup in the spray modelling, this further compounds for less accurate spray placement as previously reported as critical factor [**46**]. According to the prediction of species slowly produced or consumed such as CO and H_2, both the partial equilibrium (PEQ) assumption and steady flamelet model (SFM) failed to predict their formation. In fact, on the one side, the PEQ approach which is based on the pure chemical equilibrium and the mixing calculations is inadequate to model properly partial oxidation in the rich-fuel zones and mechanisms of soot formation. On the other side, even with a relative proper modelling of dissociations in the rich-fuel zones through a detailed chemical model, two assumptions preclude the robustness of the model: firstly, the assumption of infinite residence time done in SFM leads to an overprediction of slow species since the flamelet structure is not properly modelled and secondly, the rapid changes of the scalar dissipation rate cannot be followed instantaneously by the flamelet structure. A way to address this issue would be the implementation of the unsteady flamelet model. This point was not explored in the present study.

ACKNOWLEDGEMENTS

This work received financial support from Fond Québécois de la Recherche sur la Nature et les Technologies (FQRNT) with seed funding initially provided by P&WC, CRIAQ & MDEIE. The authors wish to thank Calcul Québec/Calcul Canada for providing the required computing resources and support for High Performance Computing. The authors gratefully acknowledge Dr. Navarro-Martinez at Imperial College for helpful discussions regarding the experimental configuration.

REFERENCES

[**1**] N. Swaminathan, K. N. C Bray, "*Turbulent Premixed Flames*", Cambridge University Press, Cambridge, UK, (2011).

[**2**] T. Poinsot, D. Veynante, "*Theoretical and Numerical combustion*", R.T. Edwards, Inc.; 2nd edition (2005).

[**3**] K. K. Kuo, R. Acharya, "*Fundamentals of Turbulent and Multi-Phase Combustion*", Wiley, (2012).

[**4**] F.R. Menter, Y. Egorov, "*The Scale-Adaptive Simulation Method for Unsteady Turbulent flow predictions. Part 1: Theory and Model Description"*,Flow Turbulence Combustion, 85: 113-138 (2010).

[**5**] H. Pitsch,"*Large Eddy Simulation of turbulent combustion"* Annual Review of Fluid Mechanics 38:453- 482, (2006)

[**6**] S. Som, P.K. Senecal, E. Pomraning, "*Comparison of RANS and LES Turbulence models against Constant volume Diesel experiments"*. IILAS Americas, 24th annual conference on Liquid atomization and Spray systems, San Antonio, TX, May (2012).

[**7**] M. Ihme, H. Pitsch, "*Prediction of extinction and reignition in nonpremixed turbulent flames using a flamelet/progress variable model 2. Application in LES of Sandia flames D and E*", Combustion and Flame, 155: 90-107 (2008).

[**8**] P. Domingo, L. Vervisch and D. Veynante, "*Large-Eddy Simulation of a lifted methane jet flame in a vitiated coflow*", Combustion and Flame, 152: 415-432, (2008).

[**9**] H. Pitsch, N. Peters, "*A Consistent Flamelet Formulation for Non-Premixed Combustion Considering Differential Diffusion Effects"*. Combustion and Flame 114 26–40, (1998).

[**10**] N. Peters, "*Turbulent Combustion"*. Cambridge University Press, Cambridge, UK, (2000).

[**11**] Bray, K.K, P. Domingo, L. Vervisch, "*Role of the progress variable in the models for partially premixed turbulent Combustion"*, Combust. Flame 141: 431-437, (2005).

[12] B. Franzelli, B. Fiorina, N. Darabiha, "*A tabulated chemistry method for spray combustion"*. Proceedings of the combustion institute 34:1659-1666, (2013).
[13] K. Luo, H. Pitsch, M.G. Pai, O. Desjardins, "*Direct Numerical Simulations and analysis of three dimensional n-heptane spray flames in a model swirl combustor"*. Proc. of the combustion institute 33(2):2143-2152, (2011).
[14] A. Neophytou, E. Mastorakos, R.S. Cant, "*DNS of Spark Ignition and Edge flame Propagation in Turbulent Droplet-Laden Mixing Layers"*.Combust. Flame,157:1071-1086 (2010).
[15] C. Hollman, E. Gutheil, "*Flamelet-Modeling of Turbulent Spray Diffusion Flames Based on a Laminar Spray Flame Library*", Combust. Sci. and Technology, 135:1-6 175 (1998).
[16] B. Wegner, M. Staufer, A. Sadiki, J. Janicka, *Study of Flow and mixing in a generic GT combustor using LES*", Flow Turbulence and Combustion, 79 (2007).
[17] W.P. Jones, S. Lyra, S. Navarro-Martinez, "*Numerical investigation of swirling kerosene spray flames using Large Eddy Simulation"*. Combust. Flame, 159:1539-1561, (2012).
[18] M. Chrigui, J. Gounder, A. Sadiki, A.R. Masri, J. Janicka, "*Partially premixed reacting acetone spray using LES and FGM tabulated chemistry"*. Combust. Flame159:2718-2741 (2012).
[19] Y. Egorov, F.R. Menter, R. Lechner, D. Cokljat, "*The Scale-Adaptive Simulation Method for Unsteady Turbulent flow predictions.Part 2: Applications to Complex Flows"*, Flow Turbulence Combustion, 85:139-165 (2010).
[20] B. Abramzon, W.A. Sirignano, "*Droplet Vaporization Model for Spray Combustion Calculations"*, Int. J. Heat Mass Transfer, 32 (9): 1605-1618, (1989).
[21] A. Dehbi, "*Stochastic models for turbulent particle dispersion in general inhomogeneous flows*", doctoral course, Laboratory for Thermal Hydraulics, Paul Scherrer Inst. &EPFL, Lausanne, (2008).
[22] M. Lesieur, O. Métais, "*New trends in large eddy simulations of turbulence*". Annual Review of Fluid Mechanics 28:45-82, (1996).
[23] F. Nicoud, F. Ducros, "*Subgrid-Scale modeling based on the square of the velocity gradient tensor"*, Flow Turbulence and combustion. 62:183-200 (1999).
[24] Y.R. Sivathanu, G.M. Faeth, "*Generalized State Relationships for Scalar Properties in Non-Premixed Hydrocarbon/AirFlames"*,Combust. Flame, 82:211-230 (1990).
[25] R.W. Bilger, M. B. Esler, S. H. Starner. Lecture Notes in Physics (Chap 3: "*Turbulent Flow with non premixed reactant*"). Springer-Verlag. 384:86 (1991).
[26] K.N.C Bray, N. Peters, in: P.A. Libby, F. A. Williams (Eds.), "*Turbulent Reacting Flows*", Academic, London, 63-113 (1994).
[27] D. Carbonell, C.D. Perez-Segarra, P.J. Coelho, A. Oliva, "*Flamelet Mathematical Model for non-premixed laminar Combustion"*. Combustion and Flame 156(2): 334-347 (2009).
[28] A.W. Cook, J.J. Riley, "*A subgrid model for equilibrium chemistry in turbulent flows*",Phys.FluidsA6:2868-2870 (1994).
[29] N. Peters, "Combustion theory" CEFRC Summer school, Princeton, June 28th –July 2nd (2010).
[30] D.-H. Sheen, "*Swirl-Stabilized Turbulent Spray Flames in an Axisymmentric Model Combustor"*. Ph.D. thesis, Imperial College, University of London, (1993).
[31] J. M. Beer, N.A. Chigier, "*Combustion aerodynamics*" Applied Science, London, (1972).
[32] ANSYS FLUENT, Fluent User's Guide, v. 14.0, (2012).
[33] A. Violi, S.Yan, E.G. Eddings, F. Sarofim, S. Granata, T. Faravelli, E. Ranzi, "*Experimental formulation and kinetic model for JP-8 surrogate mixtures*", Combustion Science and Technology 174: 399-417 (2002).
[34] P. Dagaut, M. Cathonnet, "*The ignition, oxidation, and combustion of kerosene: A review of Experimental and kinetic modeling*". Prog. in Energy Combust. Sci., 32:48–92(2006).
[35] H. Wang, E. Dames, B. Sirjean, D.A. Sheen, R. Tango, A. Violi, J.Y.W. Lai, F. N. Egolfopoulos, D. F. Davidson, R. K. Hanson, C.T. Bowman, C.K. Law, W. Tsang, N.P. Cernansky, D. L. Miller, R. P. Lindstedt, "*A high-temperature chemical kinetic model of n-alkane (up to n-dodecane), cyclohexane, and methyl-, ethyl-, n-propyl and n-butyl-cyclohexane oxidation at high temperatures*", JetSurF version 2.0, September 19, (2010).
[36] W.K. Metcalfe, S. Dooley, F.L. Dryer, *Comprehensive Detailed Chemical Kinetic Modeling Study of Toluene Oxidation*. Energy and Fuels, 25 (11): 4915–4936 (2011).
[37] E.Tim, Q. M. Lourdes, "*Surrogate Mixtures to Represent Complex Aviation and Rocket Fuels*". Journal of Propulsion and Power, 17(2):461-466, 01(2001).
[38] B. Akih-Kumgeh, J.M. Bergthorson, "*Skeletical kinetic Mechanisms for Syngas, Methyls Butanoate, N-heptane, and n-decane*". Energy&Fuel, 10, 1021 (2013).
[39] A.H. Lefebvre, "*Atomization and Sprays*". Hemisphere Publishing Corporation. (1989).
[40] W. Tabakoff, T. Wakeman,"*Measured particle rebound characteristics useful for erosion prediction*"ASME 82 GT-170. (1982).
[41] Chemkin-Pro 15131, Reaction Design: San Diego, (2013).
[42] S.B. Pope, "*Ten Questions Concerning the Large Eddy Simulation of Turbulent Flows*" New J. of Physics, 6 (2004).
[43] P. Sagaut, "Large Eddy Simulation for Incompressible Flows-An introduction (Springer, 2006) 3rd edition.
[44] J. Sahner, "*Extraction of Vortex Structures in 3D Flows Fields"*, Dissertation to obtain the academic degree, doctorate engineer, university of Magdeburg, (2008).
[45] A. Fossi, A. DeChamplain, J.M. Bergthorson, B. Akih-Kumgeh, A. Ghazlani, B. Paquet, S. Kalla, "Large *Eddy Simulation of a Turbulent Swirling Jet-A1 Spray Flame Incorporating chemical non-equilibrium effects through the flamelet model"*, Proceedings of the ASME Turbo Expo 2014, Paper GT2014-27225, Düsseldorf, Germany (2014).
[46] J. Odgers, D. Kretschmer, G.F. Pearce, "*The combustion of droplets within gas turbine combustors: some recent observations on combustion efficiency"*, Journal of Engineering for Gas Turbines and Power, 115 (3): 522-532 (1993).

Large Eddy Simulation of Spark-ignition of a Bluff-body Stabilized Burner using a subgrid-ignition model coupled to FGM-based combustion models

Alain Fossi, and **Alain deChamplain**

Department of Mechanical Engineering, Combustion Laboratory, Université Laval, Québec, Canada

Abstract

Safety improvement and pollutants reduction in many practical combustion systems and especially in aero-gas turbine engines require an adequate understanding of flame ignition and stabilization mechanisms. Improved software and hardware have opened up greater possibilities for translating basic knowledge and the results of experiments into better designs. The present study deals with the large eddy simulation (LES) of spark ignition of a conical shaped bluff-body stabilized burner involving a turbulent non-premixed flame, with the primary aim of studying the impact of the spark location on the ignition success. A particular attention is paid on the ease of handling of the numerical tool, the computational cost, and the accuracy of the results. The Discrete Particle Ignition Kernel (DPIK) model is used to capture the ignition kernel dynamics in its early stage of growth after the breakdown period. The ignition model is coupled to two combustion models based on the mixture fraction-progress variable formulation. An infinitely fast chemistry assumption is first done, and the turbulent fluctuations of the progress variable are captured with a bimodal probability density function (PDF) in the line of the Bray-Moss-Libby (BML) model. Thereafter, a finite rate chemistry assumption is considered through the Flamelet Generated Manifold (FGM) method. In these two assumptions, the classical beta-PDF is used to model the temporal fluctuations of the mixture fraction in the turbulent flow. To model subgrid-scales stresses and the residual scalars fluxes, the Wall-Adapting Local-Eddy (WALE) and the eddy diffusivity models are respectively used, under the low-Mach number assumption. Numerical results of velocity and mixing fields as well as the ignition sequences are validated through a comparison with their experimental counterparts. It is found that, by coupling the DPIK model to each of the two combustion models implemented in a LES-based solver, the ignition event is reasonably predicted with further improvements provided by the finite rate chemistry assumption. Finally, the locations most likely to lead to a complete ignition of the burner are found to be around the shear layer bordering the central recirculation zone, owing to the presence of mixtures within flammability limits.

Keywords: Large eddy simulation, Flamelet Generated Manifold, Bluff-body, Non-premixed flames, Spark ignition, subgrid ignition model.

1-Introduction

Ignition and flame stabilization are of great importance in many combustion systems, and especially in aircraft gas turbine engines which must satisfy cold start and high-altitude relight capabilities for wide ranges of

International Journal of Numerical Methods for Heat & Fluid Flow, Vol. 27 No. 2, 2017, pp. 400-427.
© Emerald Group Publishing Limited, 0961-5539, DOI 10.1108/HFF-07-2015-0299

environmental conditions. To improve fuel economy and to adapt to stringent emission standards, aircraft gas turbine manufacturers are increasingly interested in fuel-lean combustion mode, but this may have a detrimental effect on ignition at high altitude and combustion stability (Dunn-Rankin, 2008). Thus, there is a pressing need to accurately predict ignition dynamics at the design stage. In this regard, multidimensional modelling is increasingly adopted to investigate complex phenomena involved in such combustion systems, particularly with the exponential increase in computing resources in recent years along with the significant progress in turbulent combustion modelling (Poinsot and Veynante, 2005). However, even considering the current substantial progress in terms of computing resources, an accurate simulation of some combustion phenomena remains challenging and computationally demanding. In fact, in most practical combustion systems, stable and efficient combustion often requires rapid mixing and short combustion duration. This leads to complicated flow patterns in the combustion chamber, such as recirculation regions, swirling flows and breakdown of large-scale vortical structures (Pitsch, 2006). Therefore, an accurate prediction of time-dependent phenomena such as ignition, extinction and pollutant formation which often feature very small time scales cannot be achieved using Reynolds-Averaged Navier-Stokes (RANS) approaches, since most flow features are lost because of the averaging process. In RANS simulations, the solution to the problem of very wide range of length and time scales in turbulent flows is to solve equations for averaged variables whose minimum scales are much larger than the smallest scales of the turbulent fluctuations. Considering the prohibitive computing cost required for direct numerical simulation (DNS) of a turbulent flow at realistic Reynolds numbers, it is imperative to find alternative methods for higher accuracy at affordable computational cost. In this regard, large eddy simulation (LES) although still in a phase of rapid development, has so far demonstrated its potential in several academic and industrial investigations of reactive flows (Raman, 2005; Ihme, 2008; Chrigui *et al.*, 2013; Fossi *et al.*, 2014; Jones *et al.*, 2014). However, even if significant advances have so far been done for LES, some drawbacks still remain such as problems of modelling flow, chemistry and turbulence-chemistry interactions. In some cases, few detailed experimental data sets are available for the models validation. In spark ignition simulation, complex mechanisms governing the flame kernel initiation after the spark discharge are most often ignored and commonly, data for a pilot flame are implemented at the beginning of the simulation to mimic the flame kernel (Boileau *et al.*, 2008). An accurate prediction of the combustion process, starting from the early stage of ignition, with a reasonable computing cost depends on the ability of the numerical tools' users to implement not only robust models suitable for the investigated configurations, but also less expensive simulation methods. For instance, given the relevance of a detailed chemistry model in the prediction of most combustion phenomena (Hilbert, 2004; Fiorina *et al.*, 2005) and the need for an accurate description of the early stage of ignition for a successful prediction of the combustion initiation (Tan and Reitz, 2006), it is clear that the simulation method must include relevant features of the chemistry and those involved in the early stage of ignition. A straightforward simulation method would consist in solving all transport equations for a wide range of scales, including those needed to describe the early stage of ignition. However, in engines CFD simulations, it is not practical to resolve the process in such details for two main reasons: first, practical numerical grid sizes and time steps are most often larger than those involved in the early stage of ignition; second, the oxidation

International Journal of Numerical Methods for Heat & Fluid Flow, Vol. 27 No. 2, 2017, pp. 400-427.
© Emerald Group Publishing Limited, 0961-5539, DOI 10.1108/HFF-07-2015-0299

mechanism of hydrocarbon fuels involves hundreds of reactions and dozens of species, and these numbers become even larger for heavy hydrocarbon fuels such as jet fuels. Thus, a method consisting of solving transport equations for all the species in the mechanism, and attempting to model the filtered source term in each equation becomes prohibitively expensive. In order to circumvent the high computing cost that a fine mesh of the combustor may incur, a subgrid scale model seems appropriate to simulate the early stage of the ignition process. In this vein, Amsden (1993) suggested a simple approach in which the internal energy in specified ignition cells is increased during ignition by a specific factor for each time step. Unfortunately, this model is very sensitive to the computational mesh size. Plus, the effects of the surrounding flow and mixture conditions on the ignition process are not adequately considered. To address these drawbacks, an improved model called the Discrete Particle Ignition Kernel (DPIK) model, in which the flame kernel position is marked by particles, was proposed by Fan *et al.* (1999). In this improved model, the sensitivity of ignition prediction to the numerical grid size is minimized. This latter model was further improved by Tan and Reitz (2006) and successfully validated on two configurations, namely, a homogeneous charge combustion-chamber and a homogeneous charge propane-fueled SI engine. The model accounts for the spark discharge energy and the effects of turbulence on the kernel growth. Due to these DIPK assets, its improved version is customized and applied to the configuration investigated in the present study. For the second issue related to the implementation of a realistic chemistry model, a relevant feature of spark ignition engines is commonly exploited in the literature. According to Borghi (1988) and Peters (2000), combustion in spark ignition engines is thought to occur within the wrinkled flamelet, corrugated flamelet and thin reaction regimes of the turbulent combustion diagram. Consequently, the resulting separation between the time scales of chemistry and those of mixing allows decoupling chemistry calculations from those of mixing (Peters, 2000). Several models based on this separated time scales concept have been developed and applied successfully. These are the Bray-Moss-Libby (Bray *et al.*, 1984, 1985), the extended coherent flamelet (Poinsot and Veynante, 2005), the level-set (Peters, 2000; Tan and Reitz, 2006), the diffusion flamelet (Peters, 2000; Claramunt *et al.*, 2006; Kerschgens *et al.*, 2010; Fossi *et al.*, 2014, 2015), the flamelet generated manifold (Oijen and Goey, 2000; Fiorina *et al.*, 2005; Nguyen *et al.*, 2010; Chrigui *et al.*, 2012, 2013), and the conditional moment closure models (Bushe and Steiner, 1999; Kim and Pitsch, 2005; Triantafyllidis *et al.*, 2009). The accuracy of a simulation method based on one of these combustion models is strongly related to the level of adequacy between the model assumptions and the features of the experimental configuration. The reduced-scale model of a non-premixed bluff-body stabilized burner investigated in the present work represents an important class of practical burners. Through variation in design and operating conditions, this burner can produce flames of varying stability, efficiency, pollutants formation and heat transfer which are key parameters for fundamental investigations. Also, since this combustor exemplifies complex flows of real combustors, it can provide greater understanding of complex flow fields, especially with regard to stability and ignitability. Finally, the radial fuel injection eliminates fuel penetration of the recirculation zone and allows combustion to occur in a partially premixed mode. Therefore, at some locations within the combustor, triple flames may develop and contribute to the overall flame stabilization (Puri *et al.*, 2001; Qin *et al.*, 2004). However, although useful for the flame stabilization, partially premixed

International Journal of Numerical Methods for Heat & Fluid Flow, Vol. 27 No. 2, 2017, pp. 400-427.
© Emerald Group Publishing Limited, 0961-5539, DOI 10.1108/HFF-07-2015-0299

combustion mode leads to additional modelling difficulties as it involves mixed combustion regimes in which single regime-based combustion models can no longer hold, especially outside the inner reaction zone located in the vicinity of the stoichiometric region where premixed chemistry tabulation and diffusion combustion are almost similar (Nguyen *et al.*, 2010). On the one hand, the application of combustion modelling based on pure premixed flames to rich partially premixed or diffusion flames introduces errors when diffusive fluxes across iso-equivalence ratio surfaces dominate; on the other hand, combustion models based on pure diffusion flames cannot accurately capture the structure and consequently the propagation of premixed flame fronts (Fiorina et al., 2005). To overcome these limitations, the combustion model must then be able to capture multi-combustion regimes involved in the experimental configuration. In this regard, a multidimensional flamelet was formulated in order to naturally account for interactions between reaction zones developing at various equivalence ratios. This model was successfully validated for instance with a partially premixed methane vitiated-air combustion based on the configuration by Cabra and co-workers (Ihme and See, 2010), using the Sandia "D" and "E" flames (Ihme and Pitsch, 2008), or using an acetone spray flame (Chrigui et al., 2012).

Although a considerable amount of experimental and numerical research works have so far been carried out to study ignition in premixed flame configurations (Kravchik *et al.*, 1995; Akram and Lundgren, 1996; Reinmann and Akram, 1997), most phenomena involved in an ignition event for non-premixed flame configurations are still not fully understood, although they are critical for safe operation of combustion devices such as aero gas turbines, ramjet and turbojet afterburner systems. In addition, these combustion systems use bluff-body flame holders to stabilize flames by creating recirculation zones with shapes and sizes that are strongly dictated by various geometric and flow parameters, such as blockage ratio, cone angle, flow confinement, incoming flow velocity, and turbulent intensity of the incoming flow (Beer and Chigier, 1972). In spite of the extensive use of recirculation zones in these practical systems and especially in aero gas turbine combustors, there are still questions regarding the flame ignition in such configurations, namely, the mechanisms governing the flame kernel initiation and its propagation to form a stable flame.

In this work, an approach designed to provide a reasonable balance between computing cost, chemistry modelling and turbulence description is used to predict a forced ignition of a bluff-body stabilized burner. This configuration was experimentally investigated by Ahmed *et al.* (2007). The axial and radial components of the velocity were measured using a one-component laser Doppler velocimetry (LDV), the mixture fraction distribution was measured using acetone Planar Laser Induced Fluorescence (PLIF), and a high-speed camera was used to visualize different successful and failed ignition events. These data are used to assess the robustness of the current simulation approaches. The latter consist of a LES-solver based on a variable-density low-Mach-number formulation, and the DIPK model mentioned earlier, coupled to combustion models based on a mixture fraction-progress variable formulation. The infinitely fast chemistry assumption is first considered, and the turbulent fluctuations of the reaction progress variable are captured using a bimodal probability density function (PDF) as described in the Bray-Moss-Libby (BML) formulation. Thereafter, the finite rate chemistry assumption is considered in the line of the flamelet generated manifold (FGM) method.

International Journal of Numerical Methods for Heat & Fluid Flow, Vol. 27 No. 2, 2017, pp. 400-427.
© Emerald Group Publishing Limited, 0961-5539, DOI 10.1108/HFF-07-2015-0299

The paper is structured as follows: First, the modelling approaches of the LES and combustion models based on BML and FGM formulations are first presented in the second section, followed by a brief description of the ignition model in the third section. The experimental configuration and the computational setup including the boundary conditions are respectively presented in the fourth and the fifth sections. Analysis and discussions of the numerical results based on the comparison with experimental data are provided in the sixth section, while salient points of the investigation are summarized in the concluding section.

2-Modelling approach

As mentioned above, the turbulent flow field is captured using the LES model, the early stage of the ignition event is captured using the DPIK model, and the chemistry effects are included through a mapping of two representative scalars that are coupled to a pre-calculated chemistry. In the following subsections, the LES form of the Navier-Stokes equations is first presented followed by those of the two representative scalars and the corresponding closure models. These LES equations are all expressed in a variable-density low Mach number formulation. Finally, the key aspects of the chemistry and the ignition models used are respectively outlined in the two subsequent subsections.

2-1 LES-equations

In the LES approach, the large-scale motions are resolved, while the small-scale motions as well as their interactions with large ones are modelled. The rationality of the LES model relies on some relevant physical observations: most of the energy of turbulence is contained in large eddy motions, and the latter are problem-dependent since they are dictated by the geometry and boundary conditions of the resulting flow; the small-scale motions are less geometry-dependent, they tend to be more isotropic as they are more influenced by molecular transport, and are therefore more universal in nature (Lesieur and Métais, 2005). By applying a cut-off spatial filter to the conservative equations of mass, momentum and scalars, the following Favre-filtered conservative Eqs. (**1**)-(**3**) are derived for large-scale motions:

$$\frac{\partial \bar{\rho}}{\partial t} + \frac{\partial}{\partial x_j}\left(\bar{\rho}\tilde{u}_j\right) = 0 \qquad (1)$$

$$\frac{\partial \bar{\rho}\tilde{u}_i}{\partial t} + \frac{\partial}{\partial x_j}\left(\bar{\rho}\tilde{u}_i\tilde{u}_j\right) = -\frac{\partial \bar{p}}{\partial x_i} + \frac{\partial}{\partial x_j}\left[\bar{\sigma}_{ij} - \tau_{SGS}\right] \qquad (2)$$

$$\frac{\partial \bar{\rho}\tilde{\phi}_i}{\partial t} + \frac{\partial}{\partial x_j}\left(\bar{\rho}\tilde{u}_i\tilde{\phi}_i\right) = \frac{\partial}{\partial x_j}\left[\overline{\Psi}_{\phi_i} - q_{\phi_i}^{SGS}\right] + \widetilde{\omega}_{\phi_i} \qquad (3)$$

where $\tau_{SGS} = \bar{\rho}\left(\widetilde{u_i u_j} - \tilde{u}_i\tilde{u}_j\right)$ and $q_{\phi_i}^{SGS} = \bar{\rho}\left(\widetilde{u_i\phi_i} - \tilde{u}_i\tilde{\phi}_i\right)$ are the residual stresses for momentum, and the residual scalar fluxes respectively. The bars and tildes accentuations refer to Reynolds and Favre filtering. The residual stresses, τ_{SGS} are modelled with an eddy viscosity assumption, while the residual scalar fluxes, $q_{\phi_i}^{SGS}$, are modelled using the eddy diffusivity model. The filtered scalars for laminar diffusion fluxes are also modelled with the gradient diffusion assumption through the diffusivity of the scalar ϕ_i. In this work, the scalar ϕ_i stands for the enthalpy (H), the non reactive scalar (ϕ_{NRS}), and reactive scalar (ϕ_{RS}). The expressions of the

filtered source and subgrid terms corresponding to each scalar transport equation are given in Table **1**. In this table, Z denotes the mixture fraction, and is defined using the atomic mass fraction (Sivathanu and Faeth, 1990):

$$Z = \left(\xi_j - \xi_{j,ox}\right)/\left(\xi_{j,fuel} - \xi_{j,ox}\right) \qquad (4)$$

where ξ_j is the mass fraction for element, j; the subscripts "fuel" and "ox" denote the values at the fuel and the oxidizer stream respectively; C and Y_C are the normalized and the un-normalized reaction progress variables respectively defined as normalized and un-normalized sums of the product species mass fractions:

$$C = Y_C/Y_C^{eq} = \sum_k a_k(Y_k - Y_k^u)\Big/\sum_k a_k Y_k^{eq} \quad (5)$$

where Y_k denotes the k[th] species mass fraction, superscript u denotes the unburnt reactant, subscript "eq" denotes the chemical equilibrium, and a_k are constants that are typically zero for reactants and unity for a few product species

Table **1**: Filtered source and SGS terms for scalars transport equations

Scalars (ϕ_i)		Scalars Laminar diffusion fluxes ($\bar{\Psi}_{\phi_i}$)	SGS scalar fluxes ($q_{\phi_i}^{SGS}$)	Scalars Filtered source terms ($\widetilde{\dot{\omega}}_{\phi_i}$)
Enthalpy (H)		$\bar{\rho}\bar{D}_H\left(\partial\widetilde{H}/\partial x_j\right)$	$q_H^{SGS} = \bar{\rho}D_H^t\left(\partial\widetilde{H}/\partial x_j\right)$	0
Mixture fraction ($\phi_{NRS} \equiv Z$)		$\bar{\rho}\bar{D}_Z\left(\partial\tilde{Z}/\partial x_j\right)$	$q_Z^{SGS} = \bar{\rho}\, D_Z^t\left(\partial\widetilde{H}/\partial x_j\right)$	0
Progress variable (ϕ_{RS})	$\phi_{RS} \equiv C$	$\bar{\rho}\bar{D}\left(\partial\tilde{C}/\partial x_j\right)$	$q_C^{SGS} = \bar{\rho}\, D_C^t\left(\partial\widetilde{H}/\partial x_j\right)$	$\rho_u S_{TFS}\left\lvert\partial\tilde{C}/\partial x_j\right\rvert$
	$\phi_{RS} \equiv Y_C$	$\bar{\rho}\bar{D}\left(\partial\tilde{Y}_C/\partial x_j\right)$	$q_{Y_C}^{SGS} = \bar{\rho}\, D_C^t\left(\partial\widetilde{H}/\partial x_j\right)$	$\iint S_{FR}(Y_C,Z)P(Y_C,Z)dY_C dZ$

These filtered equations (**1**)-(**3**) are used to solve large-scale motions in both space and time, while the small scales are filtered out using a density-weighted function as follows: $\bar{\rho}\tilde{\varphi} = \int \rho\varphi(\boldsymbol{x}_i')F(\boldsymbol{x}_i - \boldsymbol{x}_i';\Delta)d\boldsymbol{x}_i'$. The parameter, $\varphi \equiv \{u_i;\phi_i\}$ stands for the set of generic physical quantities, and $F(\boldsymbol{x_i};\Delta)$ is a time-invariant spatial filter function whose shape is chosen so that it approaches zero when $\boldsymbol{x_i} - \boldsymbol{x}_i'$ exceeds the filter width, Δ, and is normalized such that $\int F(\boldsymbol{x}_i')d\boldsymbol{x}_i' = 1$. In the current work, a box filter is used, and Δ is computed as the cubic root of the local computational cell volume. For the modelling purposes, the SGS stresses, τ_{SGS} is split into its isotropic and deviatoric parts:

$$\tau_{SGS} = \underbrace{\tau_{ij} - 1/3\,\tau_{kk}\delta_{ij}}_{deviatoric} + \underbrace{1/3\,\tau_{kk}\delta_{ij}}_{isotropic} \qquad (6)$$

The isotropic part is embedded in the pressure term, while the deviatoric part is modelled by first using the classical Smagorinsky-Lilly model (Lilly, 1992), and subsequently by using the Wall-Adapting Local Eddy (WALE) viscosity model (Nicoud and Ducros, 1999).

$$\underbrace{\tau_{ij} - 1/3\,\tau_{kk}\delta_{ij}}_{deviatoric} = 2\mu_t\sigma_{ij} \qquad (7)$$

where $\sigma_{ij} = \frac{1}{2}\left(\frac{\partial\widetilde{u_i}}{\partial x_j} + \frac{\partial\widetilde{u_j}}{\partial x_i}\right)$; According to the WALE model, the eddy viscosity, μ_t is defined by:

$$\mu_t = \bar{\rho} L_s^2 \left(S_{ij}^d S_{ij}^d\right)^{3/2} / \left[\left(\bar{\sigma}_{ij}\bar{\sigma}_{ij}\right)^{5/2} + \left(S_{ij}^d S_{ij}^d\right)^{5/4}\right] \quad (8)$$

where $L_s = \min(kd, C_w\Delta)$ is the mixing length for SGS; k is the von Karman constant; d is the distance to the closest wall; C_w is the WALE constant, and its value in the current simulation is equal to 0.325; $S_{ij}^d = 1/2\left(\bar{g}_{ij}^2 + \bar{g}_{ji}^2\right) - 1/3\,\delta_{ij}\bar{g}_{kk}^2$ with $\bar{g}_{ij} = \partial\bar{u}_i/\partial x_j$. The eddy diffusivities used to calculate the SGS scalar flux terms, $D_{\phi_i}^t$ are modelled using the turbulent Schmidt number and the eddy viscosity. For instance, eddy diffusivity of the enthalpy, D_H^t is modeled by $D_{\phi_i}^t = \mu_{SGS}/Pr_{SGS}$, where μ_{SGS} is a subgrid viscosity, and Pr_{SGS} is a subgrid Prandtl number equal to 0.85.

2-2 Combustion model and turbulence-chemistry interactions

The investigated burner involves a radial injection of the fuel into an annular coaxial flow of air (see Fig. 1 in the next section). Such a configuration allows some preliminary premixing of fuel with air before the flame zone inlet, while the remaining unmixed fuel enters the combustor before being mixed with air. The combustion process can therefore be considered as occurring in partially premixed mode, as both premixed and non-premixed combustion modes are involved. Thus, for the reasons discussed earlier, combustion models based on the fully premixed or fully non-premixed theories are not exactly suitable for this burner. In the current work, as implicitly mentioned earlier through Eq. (**3**) and the closure terms shown in Table **1**, the multi-combustion regimes are accounted for using a partially-premixed combustion model based on the resolution of transport equations for two representative scalars; namely the mixture fraction and the reaction progress variable (i.e. $\phi_{RS} \in \{C;\ Y_C\}$), for the mixing and the flame front tracking, respectively. Also, the relevance of a realistic chemistry model is investigated by considering the infinitely fast chemistry and finite rate chemistry assumptions. In the infinitely fast chemistry assumption which is considered as a first approximation in the current study, transport equations are solved for the mixture fraction, and for the normalized progress variable (i.e. $\phi_{RS} = C$). The filtered source term due to chemical reactions, $\widetilde{\omega}_C$, is modelled using the turbulent flame speed closure, S_{TFS}, proposed by Zimont *et al.* (1998). This closure model of the C-transport equation is based on the assumption of equilibrium small-scale turbulence inside the laminar flame, resulting in a turbulent flame speed expression that is purely in terms of large-scale turbulent parameters. However, instead of assuming a constant laminar flame speed as it is done in the standard form of the model, the correlation by Metghalchi and Keck (1982) shown in Eq. (**9**) is implemented in the CFD code to calculate the laminar flame speed.

$$S_L = \left[s_1 - s_2\left(\phi - s_3\right)^2\right]\left(\frac{T}{298}\right)^{\alpha_1-\alpha_2(\phi-1)} \times \left(\frac{p_k}{101.3}\right)^{-\beta_1-\beta_2(\phi-1)} \quad (9)$$

This burning velocity modeling approach is more realistic as it accounts for variations of the equivalence ratio (ϕ), burnt gas pressure (p_k) and local unburned temperature (T) effects. The s_1, s_2, s_3, α_1, α_2, β_1 and β_2 quantities are the model parameters which are empirically determined.

In the finite rate chemistry assumption, a transport equation is rather solved for the un-normalized progress variable (i.e. $\Phi_{RS} = Y_C$), and the latter is defined as $Y_C = Y_{CO_2} + Y_{CO}$ (Fiorina et al., 2005). The main reason for solving the Y_C-transport equation instead of the C-transport equation as done in the BML model is that, eventual flame quenching phenomena that may occur because of the mixing of a burnt stream in chemical equilibrium

with an air jet can be modelled naturally due to a source term (in the Y_C-equation) that depends on changes in mixture fraction. To capture such phenomena when solving for the normalized progress variable (i.e. C-transport equation), additional terms involving derivatives and cross-derivatives of mixture fraction are necessary as established by Bray *et al.* (2005). As outlined in Table **1**, the filtered source term due to chemical reactions, $\widetilde{\dot{\omega}}_{Y_C}$, is modelled using the finite-rate flamelet source term, $S_{FR} \equiv \dot{\omega}_{Y_C} = \dot{\omega}_{CO_2} + \dot{\omega}_{CO}$, which is calculated and stored with the other flamelet solutions. The filtered source term, $\widetilde{\dot{\omega}}_{Y_C}$, is obtained by convoluting S_{FR} with the joint-PDF of the reaction progress variable and the mixture fraction. For the infinitely fast chemistry assumption, the relationship between the thermochemical variables (i.e. density, temperature and species mass fractions) and the "tracking" parameters is deduced from chemical equilibrium calculations; while for the finite rate chemistry assumption, this relationship is obtained using the flamelet generated manifold (FGM) method. The latter consists of solving a projection of the full system of species and energy conservation equations, in the mixture fraction-progress variable space, (Y_C, Z). In order to assess the predictive capabilities of the FGM method, two types of tabulation respectively based on the structures of premixed and diffusion flamelets are considered in the current work. In the former case, premixed laminar flamelets are generated over a range of mixture fractions (i.e. equivalence ratios) and scalar dissipation rates of the reaction progress variable, χ_{Y_C}. The equations governing the premixed-FGM are given in Eqs. (**10**) and (**11**)**,** under the assumption of negligible differential diffusion effects (Fiorina et al., 2005; Nguyen *et al.*, 2010):

$$\rho \frac{\partial Y_k}{\partial \tau} + \frac{\partial Y_k}{\partial Y_C} \dot{\omega}_{Y_C} = \rho \chi_{Y_C} \frac{\partial^2 Y_k}{\partial {Y_C}^2} + \dot{\omega}_k \qquad (10)$$

$$\rho \frac{\partial T}{\partial \tau} + \frac{\partial T}{\partial Y_C} \dot{\omega}_{Y_C} = \rho \chi_{Y_C} \frac{\partial^2 T}{\partial {Y_C}^2} + \frac{\rho \chi_{Y_C}}{C_p} \left(\frac{\partial C_p}{\partial Y_C} + \sum_{k=1}^{N} C_{pk} \frac{\partial Y_k}{\partial Y_C} \right) \frac{\partial T}{\partial Y_C} - \frac{1}{C_p} \sum_{k=1}^{N} h_k \dot{\omega}_k \qquad (11)$$

Here, the scalar dissipation rate, χ_{Y_C} at any mixture fraction, Z is modelled as proposed by Fiorina *et al.* (2005):

$$\chi_{Y_C}(Z, Y_C) = \chi_{max}^{sto} exp\left(-2\left(erfc^{-1}(Z/Z_{sto})\right)^2\right) exp\left(-2\left(erfc^{-1}\left(2\,Y_C/Y_C^{Eq}\right)\right)^2\right) \qquad (12),$$

where χ_{max}^{sto} stands for the scalar dissipation rate at the stoichiometric mixture fraction. Its value corresponds to the fuel considered as well as the operating conditions of the burner, and can be determined appropriately from physical-space premixed flamelet solution at stoichiometric mixture fraction. In the current study, χ_{max}^{sto} is set to 1000 s^{-1}, as this value matches reasonably well the solutions of freely-propagating flamelets for rich, lean and stoichiometric hydrocarbon flames at standard temperature and pressure.

However, as discussed in (Fiorina *et al.*, 2005), Eqs. (**10**) and (**11**) do not account for mass diffusion fluxes across the iso-equivalence ratio surfaces and the related straining effects, since the scalar dissipation rate of the mixture fraction, χ_Z, and the cross-scalar dissipation rate defined between the mixture fraction and the progress variable, χ_{Z,Y_C} are neglected; consequently, a tabulation based on Eqs. (**10**) and (**11**) is expected to reasonably reproduce the structure of a partially premixed flame only if the latter is predominantly premixed. Due to the radial injection of the fuel into an annular coaxial flow of air, the flame produced by the investigated burner is likely to be predominantly non-premixed. Thus, for the present configuration, although the diffusion FGM

International Journal of Numerical Methods for Heat & Fluid Flow, Vol. 27 No. 2, 2017, pp. 400-427.
© Emerald Group Publishing Limited, 0961-5539, DOI 10.1108/HFF-07-2015-0299

neglects the effect of the cross-scalar dissipation rate, it is expected to outperform the premixed-FGM. A FGM tabulation based on diffusion flamelets is then subsequently used, and the corresponding flamelet library is obtained by generating diffusion flamelet solutions over the entire range of the scalar dissipation rates until the flamelet extinction using the standard diffusion flamelet model, and thereafter, by converting the flamelet species reaction fields to a progress variable. As the strain rate increases, the flamelet chemistry departs further from chemical equilibrium and the progress variable decreases from unity towards the extinction value of the progress variable, Y_{C_ext}. The FGM between Y_{C_ext}, and the unburnt state $Y_C = 0$, is determined from the thermochemical state of the final extinguishing flamelet by switching to unsteady flamelet.

In turbulent combustion, chemical reactions and turbulence are so coupled and continually interacting that it is not realistic to discuss the former without considering the latter. In this work, the turbulence-chemistry interactions are captured by modelling the turbulent fluctuations of the representative scalars through the PDF approach. Thus, once the relationship between the representative scalars (Z and Y_C), and the generic scalars, $\Phi_{gs(i)}$, is obtained using either equilibrium calculation or FGM, it is convoluted with a joint mixture fraction-progress variable PDF to generate the database necessary for the look-up process, as shown in Eq.(**13**).

$$\widetilde{\Phi}_{gs(i)} = \int_0^1 PDF(Y_C, Z)\, \Phi_{gs(i)}(Y_C, Z) dZ \, \mathrm{d}Y_C \qquad (13)$$

The presumed-PDF formulation is used, and the two representative scalars (mixture fraction and the progress variable) are assumed to be statistically independent in each group of simulations based on the infinitely fast and finite rate chemistry assumptions (i.e. $PDF(C,Z) = PDF(Z)PDF(C)$). Because of its ability to change its shape continuously from one or two peaks to a Gaussian shape, the beta-PDF as proposed by Cook and Riley (1994) and reported in Eq. (**14**), is used to model the subgrid fluctuations of the mixture fraction.

$$PDF(Z) = \frac{Z^{a-1}(1-Z)^{b-1}}{\int Z^{a-1}(1-Z)^{b-1} dZ} \qquad (14)$$

where $a = \tilde{Z}\left[\frac{\tilde{Z}(1-\tilde{Z})}{\widetilde{Z''^2}} - 1\right]$ and $b = \left(1-\tilde{Z}\right)\left[\frac{\tilde{Z}(1-\tilde{Z})}{\widetilde{Z''^2}} - 1\right]$. $\tilde{Z}$ and $\widetilde{Z''^2}$ are the Favre filtered mixture fraction and its subgrid variance, respectively. For the simulations based on the infinitely fast chemistry assumption, a bimodal PDF is used to model the SGS fluctuations of the normalized progress variable in line with the classical BML model. According to the simulations based on the finite rate chemistry, the subgrid PDF of the un-normalized progress variable is also modelled with the beta-PDF as shown in Eq. (**14**). The subgrid variances of the mixture fraction and the progress variable are obtained through Eq. (**15**).

$$\bar{\rho}\widetilde{\phi''^2} = \bar{\rho} C_\phi L_s^2 \left(\partial\tilde{\phi}/\partial x_j\right)^2 \qquad (15)$$

2-3 Spark ignition model

When simulating a spark-based ignition event in an aero gas turbine, with the focus on its early stage of development, the model used should be able to capture phenomena featuring small scales comparable to the spark plug gap of the igniter which is generally less than a millimeter (Eichenberger and Roberts, 1999). Thus, a straightforward approach would consist in refining the computational mesh of the combustor and the surrounding areas. However, as mentioned earlier, such an approach leads to a substantial increase in computing

resources requirements and consequently, a subgrid model is more appropriate to capture the dynamics of the flame kernel initiated by the spark deposit. In the present work, the discrete particle ignition kernel (DPIK) model is applied. In this approach, the flame kernel position is marked by particles, while the flame surface density is obtained from the number density of particles in each computational cell. Thus, as fully described in (Tan and Reitz, 2006), the flame kernel growth can still be accurately tracked though the flame kernel features scales that are generally smaller than the computational size. Furthermore, the effects of the spark energy discharge and the turbulence on the kernel growth can be accounted for. The development of the DPIK model is based on a set of assumptions: (i) the phenomena involved in the pre-breakdown and the breakdown phases are neglected, and only those involved in the arc and glow discharge phases are accounted for; (ii) the kernel flame structure is not resolved, and the temperature and all reactive scalars jump from their values in the unburned mixture to the corresponding equilibrium values in the burned gas; (iii) the ignition kernel surface is assumed to be located just in front of the flame, so that, the heat transfer between the kernel and the unburned gas is negligible; (iv) the pressure is uniform inside and outside the ignition kernel, and the temperature inside the kernel is uniform. By expressing the ignition kernel mass burning rate (for a spherical-shape ignition kernel) using the effective kernel growth speed, S_{eff}, defined as the sum of turbulent flame speed, S_{TFS}, and the plasma velocity, S_{plasma} , Eq. (**16**) is derived to describe the volume expansion of the ignition kernel.

$$\frac{dr_k}{dt} = \frac{\rho_u}{\rho_k}\left(S_{TFS} + S_{plasma}\right) + \frac{V_k}{A_k}\left(\frac{1}{T_k}\frac{dT_k}{dt} - \frac{1}{p}\frac{dp}{dt}\right) \qquad (16)$$

where ρ_u is the unburnt gas density, A_k and V_k are respectively the surface area and the volume of the ignition kernel, ρ_k is the gas density, and subscript k refers to the kernel. The step-by-step derivation of the model may be found in (Tan and Reitz, 2006). For the current work, some additional assumptions and simplifications are made to reduce the model complexity: the pressure increase due to combustion is neglected, the temperature inside the kernel is assumed spatially uniform and equal to the adiabatic flame temperature of the air-fuel mixture, and the plasma contribution in the kernel growth speed is neglected. The second assumption is realistic because of the short duration of the breakdown phase (few nanoseconds) compared to both arc and glow discharge phases which last longer (of the order of milliseconds). However, considering the outcomes of a large number of investigators (Kravchik *et al.*, 1995; Herweg and Maly, 1996; Eichenberger and Roberts, 1999; Eisazadeh-Far *et al.*, 2010), it is clear that the plasma phase is present in all the three main distinct stages involved in a spark discharge process. Thus, the negligible plasma velocity assumption is expected to yield an under-prediction of the effective kernel growth speed and thus the underprediction of the rate of the flame kernel expansion, which in turn may lead to a slight overprediction of the time required to achieve the full ignition of the burner. Considering the fact that, the ignition kernel size in the early stage of the ignition process (i.e. phases corresponding to the initial kernel formation and its initial development process) is typically small compared to the turbulent integral length, the ignition flame kernel is only sensitive to the small scales of the turbulence. Therefore, for a proper modelling of the kernel expansion, the effects of the small scales of turbulence must be accounted for. In this vein, Herweg and Maly (1996) have proposed a model for the turbulent flame speed, S_{TFS}, so as to include the effects of the strain on the kernel development. This model is

International Journal of Numerical Methods for Heat & Fluid Flow, Vol. 27 No. 2, 2017, pp. 400-427.
© Emerald Group Publishing Limited, 0961-5539, DOI 10.1108/HFF-07-2015-0299

summarized in Eq. (**17**), and is used in the DPIK model; detailed explanations on the model can be found in (Herweg and Maly, 1996):

$$\frac{S_{TFS}}{S_L} = I_0 + I_0^{1/2}\left(\frac{u'}{u'+S_L}\right)^{1/2}\left(1-exp\left(-\frac{r_k}{l}\right)\right)^{1/2} \times [1-exp(-t/T_{0G})]^{1/2}\left(\frac{u'}{S_L}\right)^{5/6} \quad (17)$$

where S_L is the laminar burning velocity mentioned earlier (see Eq. (**9**)); u' is the turbulence intensity, l is the turbulence integral length scale; T_{0G} is a characteristic time scale defined by $T_{0G} = l/(u'+S_L)$, and I_0 is the stretch factor given in Eq. (**18**), which allows accounting for the effects of strain on the kernel development.

$$I_0 = 1-\left(\frac{l_F}{15l}\right)^{1/2}\left(\frac{u'}{S_L}\right)^{3/2} - 2\frac{l_F}{r_{k_2}}\frac{\rho_u}{\rho_k} \quad (18)$$

The thickness of laminar flame, l_F, is calculated using the transport properties and the laminar burning velocity: $l_F = (\lambda/c_p)_0/(\rho S_L^0)$; where the heat conductivity, λ, and the heat capacity, c_p, are evaluated at the inner layer temperature, while the density and the laminar burning velocity are evaluated in the unburned region using the model expressed in Eq. (**9**). At each time step, the kernel size is calculated using the DPIK model, and compared to a critical radius, r_{k_c}, which is related to the integral turbulent length scale, l. Once the size of the ignition kernel reaches or exceeds this critical radius of the flow field (i.e. $r_k \geq r_{k_c}$;), the ignition model switches to the combustion model described in the previous section.

3-Experimental configuration

The setup considered in the current simulations was investigated experimentally by Ahmed *et al*. (2007), and thereafter numerically by Triantafyllidis *et al.* (2009) and Subramanian *et al.* (2010), using other ignition modelling approaches and combustion models implemented in in-house CFD codes. In addition to a reasonable prediction of ignition events resulting from the spark deposition at some selected locations of the burner, with a CFD code providing an ease of handling and widely used in industries, this subsequent investigation proposes a simulation approach allowing a drastic reduction of the computing resources requirements. The setup consists of a radial injection of fuel into an annular air jet flowing into a cylindrical combustion chamber. A sketch of the burner in Fig. **1** shows its two main parts: the inlet part and the combustion zone. The inlet part consists of two circular ducts of length 400 mm. In some cases, a 60^o swirl vane was introduced to the flow at 50 mm upstream of the bluff-body surface, and the experiments were conducted for both the swirling and the non-swirling air flows. Although the current numerical investigation deals with the case without swirl only (because of the detailed measurements available), the computational domain is selected starting from this swirl vane position to capture the early stage of the partial premixing of fuel with air, unlike previous simulations (Subramanian *et al.*, 2010) where the computational domain was restricted to the combustion zone only. The inner diameter of the outer duct, D_s, is 35 mm. The inlet duct is a 6-mm-internal diameter tube having wall thickness 0.5 mm and it ends at the flame zone inlet with a conical shaped bluff-body of diameter, $D_b = 25\ mm$, giving a blockage ratio $BR = D_b^2/D_s^2 = 50\%$. The flame zone is enclosed using an 80-mm-long fused silica quartz cylinder of inner diameter 70 mm, which provides optical access for imaging and also avoid air entrainment from the surroundings. The fuel (methane having 99.96 % of purity) passes through the inner tube

all the way along the burner without mixing with the air until it reaches the bluff body. The bluff-body was designed to allow a radial fuel injection through a 0.7 mm circular gap to the annular air flow just 2 mm before the combustion zone inlet. The purpose of such a design strategy is to achieve a non-premixed flame, while avoiding penetration of the recirculation zone by the fuel jet (Ahmed *et al*. 2007). An inductive ignition system was specially designed to produce repeatable sparks whose energy and duration could be varied independently. The spark was created between two tungsten electrodes with diameter 1 mm, which are placed to ensure minimum disturbance to the flow. The spark gap was set to be 2 mm for all experiments. For most conditions, the igniter generates a $500\ \mu s$ spark with an energy of $200\ mJ$; and only approximately 30% of this energy was transferred from the spark to the mixture. Radial profiles of axial and radial velocities were measured by a one-component laser Doppler at some cross sections of the flame zone. Measurements were carried out using the air flow only, having a bulk velocity, $U_{air} = 10\ m/s$ (i.e. $R_e = 1.67 \times 10^4$, based on U_{air} and D_b). The mixture fraction distribution in the flame zone was measured using an acetone PLIF: the fuel was replaced by air having mass flow rate equal to the fuel mass flow rate in the ignition experiments, and acetone was seeded in this air stream substituting the fuel stream through a seeder with eight nozzles set at atmospheric conditions. Finally, a digital high-speed camera (Phantom V4.2) was used to visualize different successful and failed ignition events.

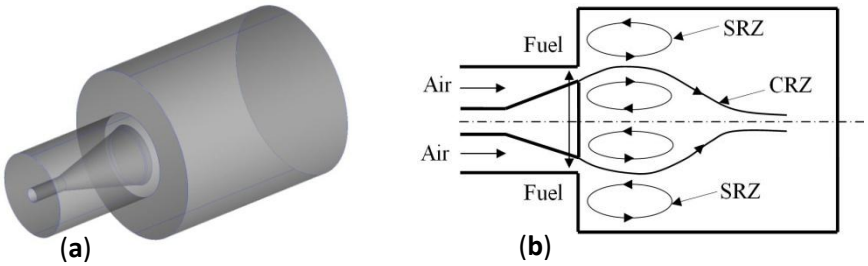

Figure **1**: Sketch of the burner: **(a)** A global 3D-view; **(b)** A close 2D-view with the radial fuel injection

4-Numerical implementation and computing parameters

The set of equations governing the whole ignition event (i.e. from the early stage following the spark breakdown period to the full ignition of the burner) is solved using the commercial finite volume-based CFD code, ANSYS FLUENT™ version 14.0 (2012). When performing simulations based on the finite rate chemistry assumption, the combustion kinetics for pure methane is described through the detailed methane-air reaction mechanism, GRI-3.0, that consists of 325 reactions with 53 species (GRI-3.0, 2014). This chemical kinetic mechanism is used in the flamelet solver included with the ANSYS FLUENT™ software package to generate the FGM tabulations based on premixed and diffusion flamelets. As mentioned earlier, when performing simulations based on the infinitely fast chemistry assumption, the turbulent flame speed model by Zimont *et al.* (1998) is coupled to the correlation by Metghalchi and Keck (1982) to calculate a local laminar flame speed in order to close the progress variable transport equation. This laminar flame speed correlation is first encoded into a C++ program, and thereafter implemented through a user defined function (UDF) module of the CFD code. For the finite-rate chemistry assumption, the progress variable equation is closed using the finite-rate flamelet source term extracted from the flamelet library as shown in Table **1**. However, when applying the DPIK ignition

model, the turbulent flame speed proposed by Herweg and Maly (1996) is used in combination with the Metghalchi and Keck (1982) model for the laminar flame speed, for the simulations based on infinitely-fast assumption, and those based on the finite-rate chemistry assumption. The boundary conditions used for all the simulations are directly extracted from the experimental configuration, and can be summarized as follows:

- *Boundary conditions for the air and fuel inflows*

Top-hat profiles based on the experimental bulk air velocity are imposed for axial and radial air velocity components. The oscillations that may arise from this approach are mitigated by carefully setting the under-relaxation parameters. The turbulent inlet conditions are specified through the turbulent intensity and the hydraulic diameter of the annular duct, D_H. The turbulence intensity is estimated by using a correlation for a fully developed pipe flow at the core ($I = 0.16(Re_{D_H})^{-1/8}$~5%), where Re_{D_H} is the Reynolds number based on D_H. Impermeability and no-slip boundary conditions are applied at the walls bounding the flame zone. The mixture fraction is set to 1 and 0 at the fuel and air inlets, respectively, while the reaction progress variable is set to 0 at the fuel and air inlets.

- *Boundary conditions for the flamelet solutions*

As noted above, the flamelet solutions are generated by solving the FGM equations based on premixed and diffusion flamelets. For this purpose, the reaction mechanism describing the combustion kinetics and the corresponding thermodynamic data are used to calculate the reaction rate of each species, while models for the mixture fraction and the progress variable scalar dissipation rates (e.g. Eq. (**12**) for premixed flamelets) are used to close the flamelet equations. When parameterizing the FGM using laminar premixed flamelets, the latter is generated over a range of mixture fraction using 64 points to discretize each dimension of the mixture fraction-progress variable space (Z, Y_C). For the FGM based on diffusion flamelets, steady diffusion flamelets are first generated over a range of scalar dissipation rates, by starting from a condition featuring nearly zero-straining due to fuel-air mixing (i.e. χ_Z=0.01 s^{-1}) and increasing this value in increments of 2 s^{-1} until the condition for which the flamelet extinguishes because of an excessive straining (i.e. $\chi_Z = \chi_q$). The diffusion FGM solutions are thereafter deduced from the diffusion laminar flamelets as described above. A sample of the structure of each type of the FGM solutions is shown in Fig. 2. One can see that for both FGM tabulation types, chemical reactions are hampered with the increase in scalar dissipation rate, χ.

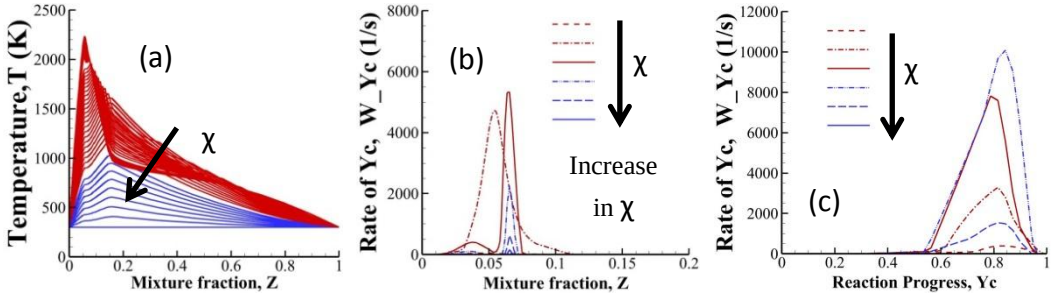

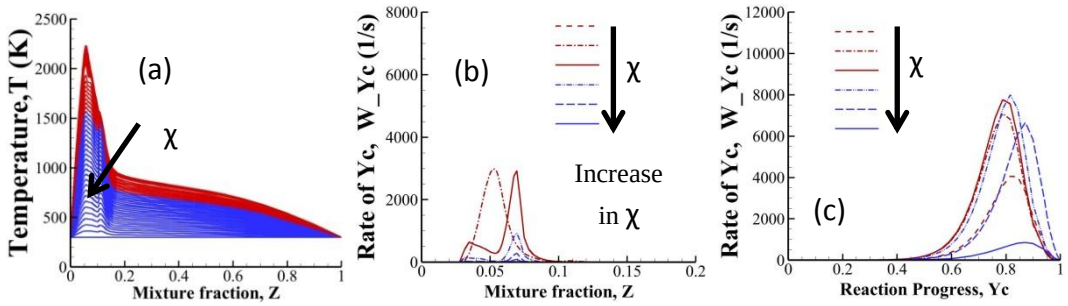

Fig. 2: Structure of the FGM solutions. (Top) Diffusion-based FGM; (Bottom) Premixed-based FGM.

- *Boundary conditions for the DPIK ignition model*

The boundary conditions used for the DPIK model are set so as to match experimental boundary conditions of the ignition device. The spark energy and the spark duration are respectively set to $200\,mJ$ and $500\,\mu s$; the initial spark kernel size is set equal to the spark gap (i.e. 2 mm). However, other spark parameters are also considered at locations where the former spark parameters lead to a failed ignition event, with the aim of appraising the sensitivity of the ignition to the spark parameters. These new spark parameters are obtained by increasing the spark energy while maintaining or increasing the spark duration.

5-Computing setup

The combustor sketched in Fig. 1 is discretized using the structured meshing technique. In order to perform a mesh sensitivity study, four mesh densities (0.7, 1.5, 2.1 and 3.2 million hexahedral elements) as well as two LES modelling approaches of the eddy viscosity are considered, namely, the WALE and the Smagorinsky-Lilly models. In each case, the mesh is refined near the solid boundaries, and in particular around the radial fuel jet orifice and the combustor axis: about 50% of elements are distributed in these zones. The suitable mesh resolution resulting from the mesh sensitivity study, and the eddy viscosity model selected from the model sensitivity study, are subsequently used to predict the aerodynamics and the mixing fields, along with the ignition events. The selection of the mesh resolution and the LES eddy viscosity model is mainly guided by the trade-off between the computational cost and the accuracy of the results. All the simulations are performed in double precision mode. A segregated solver, namely, the Semi-Implicit Method for Pressure Linked Equations (SIMPLE) algorithm is used for the pressure-velocity coupling. Transient derivatives are discretized using a second-order implicit scheme, while a bounded central differencing scheme is used for the momentum equations. The transport equations for the remaining scalars are discretized using second-order schemes. As the investigated flow is turbulent, inertial phenomena dominate viscous diffusive ones and consequently, a time scale based on a representative convective time scale is used to define the time step of the simulation: the outer radius of the annular duct is selected as the reference length ($L_{ref} = D_s/2$), while the air bulk velocity is chosen as a reference velocity ($U_{ref} = U_{air}$). These two parameters are used to define a reference time scale, $t_{ref} = L_{ref}/U_{ref} = D_s/(2U_{air})$ and based on this reference time scale, the time step of the simulation is thereafter defined as $\Delta t = 0.003 \times t_{ref} = 10^{-5}\,s$. Two kinds of simulations are performed: the first kind is based on air flow only with no fuel injection, and is mainly devoted to the mesh sensitivity study, while allowing the

prediction of velocity profiles validated with experimental data, since the latter were recorded using the air flow only as reported in (Ahmed et al., 2007). The second kind of simulations is based on the flow of the methane-air mixture, and is conducted to reproduce the mixture fraction distribution within the combustion zone. In both cases, simulations are initialized with a constant field for air and fuel, and are first performed over a time period equal to 10 000 time steps, which is approximately equal to 12 times the characteristic computation time (i.e. the time used by the flow to cross the computational domain in the stream direction with the velocity equal to the bulk velocity). This first step of the simulation is devoted to eliminate the adverse effects of initialization, and to obtain an initial flow evolving naturally from initialization with the imposed boundary conditions. Subsequently, for the former case, the simulations are continued for 10 000 further time steps ($\sim 125 \times t_{ref}$) in sampling mode for statistics, and this additional number of time steps is sufficient to yield the statistical convergence. In the second case, the simulations are also continued for 10 000 further time steps but after injecting fuel into the annular co-flowing air. As in the former case, this additional number of time steps is necessary to eliminate the artificial influence of the fuel stream initialization. At the end of this phase, simulations are continued for 10 000 further time step under the sampling statistics mode to collect the mean values of the mixture fraction and the corresponding fluctuations. Once a reasonable prediction of the mixing field is obtained, the spark-based ignition model is applied to investigate the ignition, with a particular attention paid to the effect of spark location on the ignition event.

6-Results

In order to validate the simulation approach, numerical predictions of the aerodynamics field, the mixing field, and the steps involved in the ignition event are compared to the experimental data recorded from the test rig described earlier. These experimental data are available for mean values of the velocity components and mixture fraction, along with their fluctuations, and the high-speed camera images showing the sequences of the successful and failed ignition events at different spark locations within the combustion zone.

6-1 Velocity and mixing fields based on the mesh and LES model sensitivity studies

Figures **3 (a)** and **(b)** show the radial profiles of the velocity components along with their fluctuations; for this cold flow investigation, four different simulations are performed using the four mesh resolutions mentioned above. Although the LES model is known to be intrinsically mesh dependent, one can note that no significant improvements are found in the prediction of the velocity components profiles when considering the more refined meshes. The numerical results generated by the four mesh resolutions are close each other, and some of them, namely, the axial velocity at some cross sections, agrees reasonably with the experimental results. For the radial velocity, significant discrepancies are noted, and may be related to a mismatch of the estimated radial velocity profiles at the burner inlet. In fact, as the radial profiles of the velocity components were not experimentally recorded at the burner inlet cross section, various estimated profiles for axial and radial velocity are tested while maintaining the experimental value of the bulk velocity at the flame zone inlet. Due to the fact that the experimental value of the fuel velocity was measured at the exit of the circular gap which is located 2 mm just before the burner exit, a substantial part of the upstream geometry (50 mm in length) is considered, along with the flame zone in the current simulations as reported earlier and shown on Fig. **1**. This approach is

International Journal of Numerical Methods for Heat & Fluid Flow, Vol. 27 No. 2, 2017, pp. 400-427.
© Emerald Group Publishing Limited, 0961-5539, DOI 10.1108/HFF-07-2015-0299

adopted to capture the partial premixing of the fuel with air in its early stage, and both axial and radial air velocities at the inlet of the burner are selected so as to match the experimental value for the equivalence ratio. The most promising results are obtained by imposing top-hat profiles of 6 m/s for both axial and radial velocities at this cross section of the burner inlet, which is located 50 mm upstream. Also, the WALE and the Smagorinsky-Lilly models are considered in order to investigate the sensitivity of results to the LES modelling of the subgrid eddy viscosity; some comparisons of the results generated by the two models are shown in Fig. **4.** One can see that, the two models lead to results which are almost identical. As the computing resources required by the two approaches are similar, the LES-WALE model is retained for subsequent simulations.

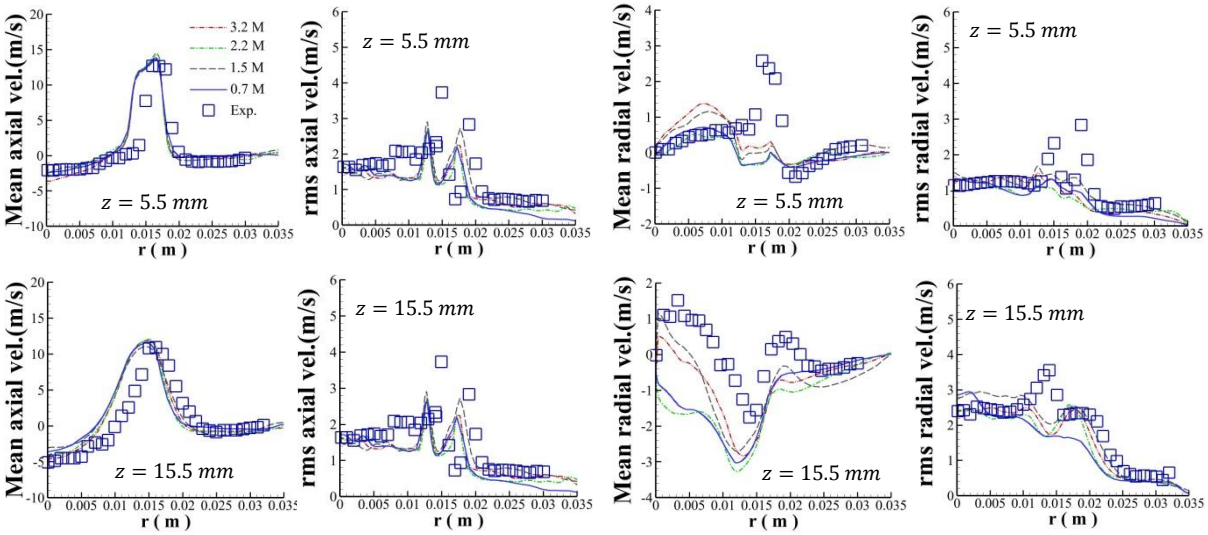

Figure **3(a)**: Radial profiles of the mean axial velocity, the mean radial velocity, and the corresponding fluctuations at various cross sections of the flame area for $z \leq 15.5\ mm$. Simulations are based on the LES-WALE model.

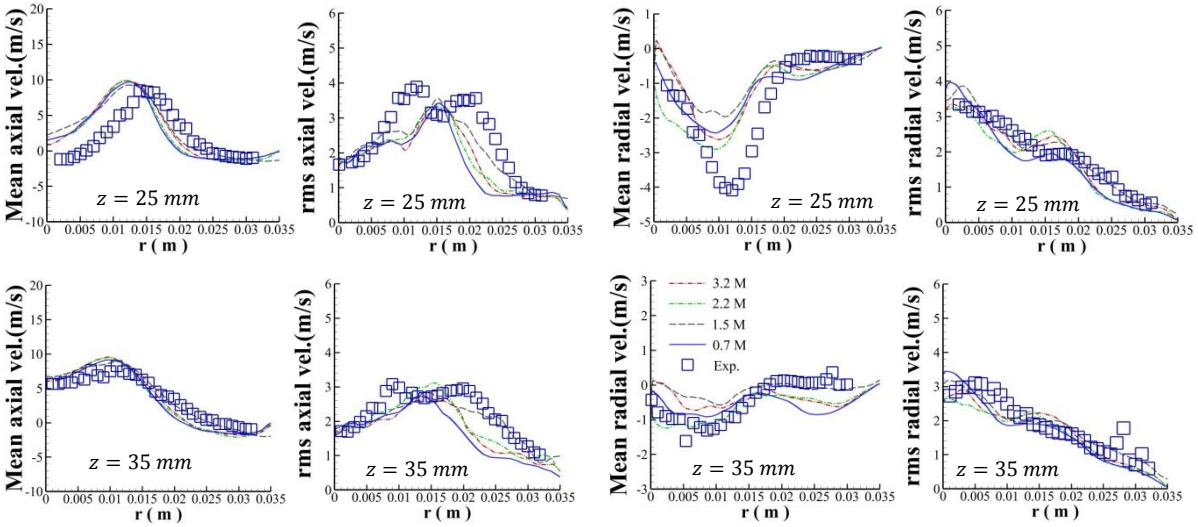

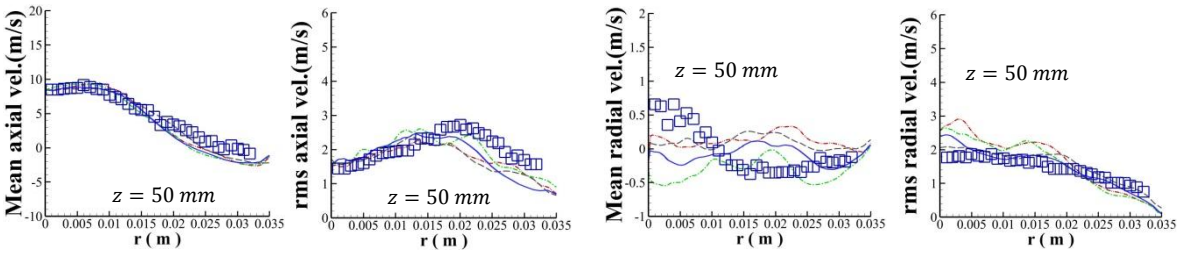

Figure 3 (b): Radial profiles of the mean axial velocity, the mean radial velocity, and the corresponding fluctuations at various cross sections of the combustion zone for $15.5\ mm \leq z \leq 50\ mm$. Simulations are based on the LES-WALE model.

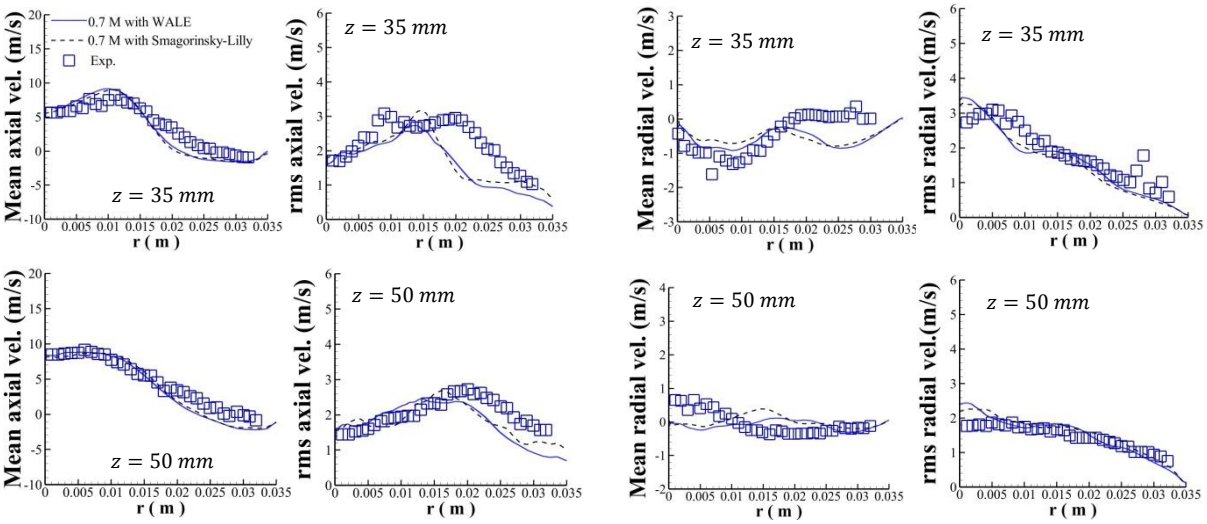

Figure 4: Radial profiles of the mean axial velocity, the mean radial velocity and the corresponding fluctuations at two cross sections of the combustion zone. Simulations are based on both LES-WALE and Smagorinsky-Lilly models.

In order to select the mesh density to be used for the investigation of ignition events, two preliminary simulations based on the coarsest (0.7 M) and the more refined (3.2 M) meshes, and involving fuel and air mixing are conducted with the aim of investigating the sensitivity of the mixture fraction field to the mesh density. In this latter case also, no significant improvements are found, and therefore, the coarse mesh consisting of 700 000 hexahedral elements is retained to investigate the ignition events. This choice is partly motivated by one of the main features of the ignition model, namely, its ability to accurately track the kernel growth without requiring a fine mesh. The contours of the axial velocity and the mixture fraction fields, along with isocontours of the temperature before the spark deposit are shown in Figs. 5 and 6. Especially, the contours of the axial velocity allow distinguishing the recirculation zones, while those of the mixture fraction allow seeing the partial premixing occurring before the inlet of the flame zone. As done earlier for the axial velocity, this mixture fraction field is validated by comparing the radial profiles of the mixture fraction to their experimental counterparts. This comparison is shown in Fig. 7; one can notice an overprediction of the mixture fraction in the zone around the bluff-body exit, which physically means a lack of air in this zone. These

discrepancies may be related to the mismatch of the radial velocity component. In fact, the mixture fraction allows quantifying the mixing level, as it measures the local equivalence ratio within a given mixing zone; the mixing of fuel with air is achieved through the convective and diffusive transports, and predominantly by convective transports in a turbulent environment. Thus, the axial components of the fuel and the air velocities are predominantly in charge of the fuel distribution in the axial direction, while radial components ensure the fuel and the air distributions in the radial direction. For the present case, the profiles of the radial velocity of air show that, radial profiles imposed at the burner inlet lead to radial convective transports which are not strong enough to adequately supply air within the recirculation zone.

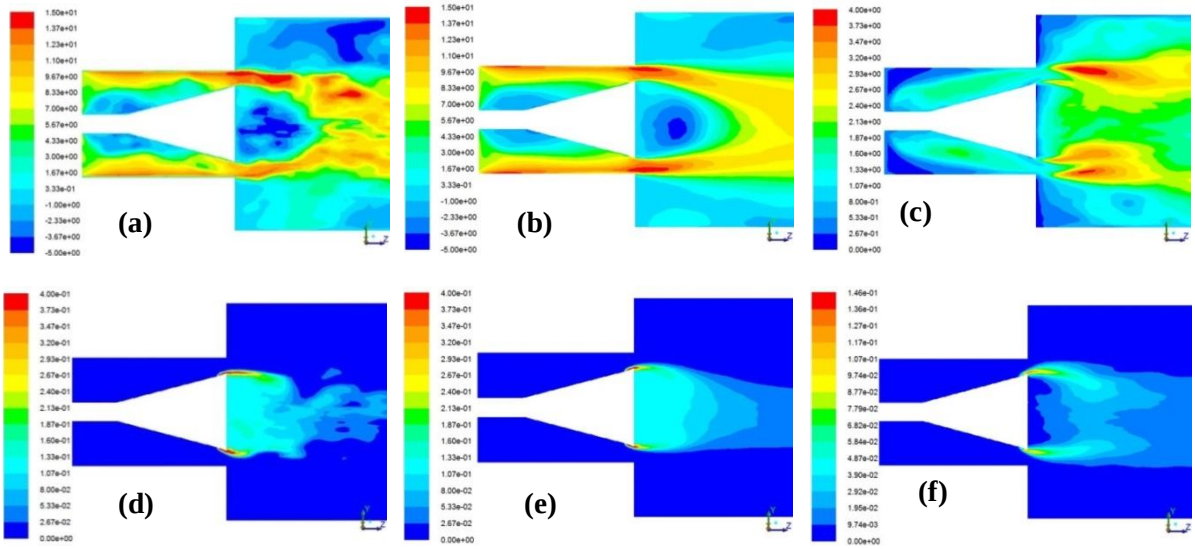

Figure 5: Contours of the velocity and the mixture fraction fields: **(a)** Instantaneous axial velocity field; **(b)** mean axial velocity field; **(c)** root-mean-square of the axial velocity; **(d)** instantaneous mixture fraction field; **(e)** mean of mixture fraction; **(f)** root-mean-square of the mixture fraction

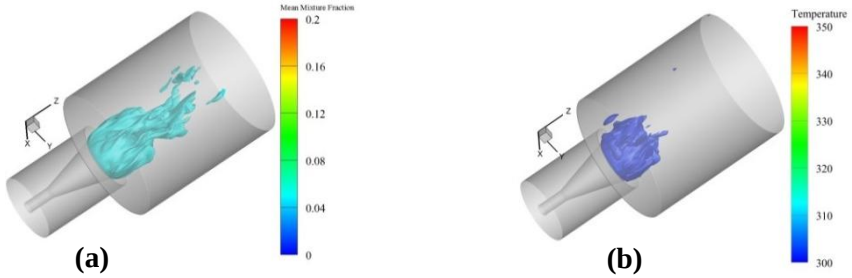

Figure **6:** Isocontours of the mean mixture fraction (**a**) and the instantaneous temperature (**b**) at the moment of the spark deposit.

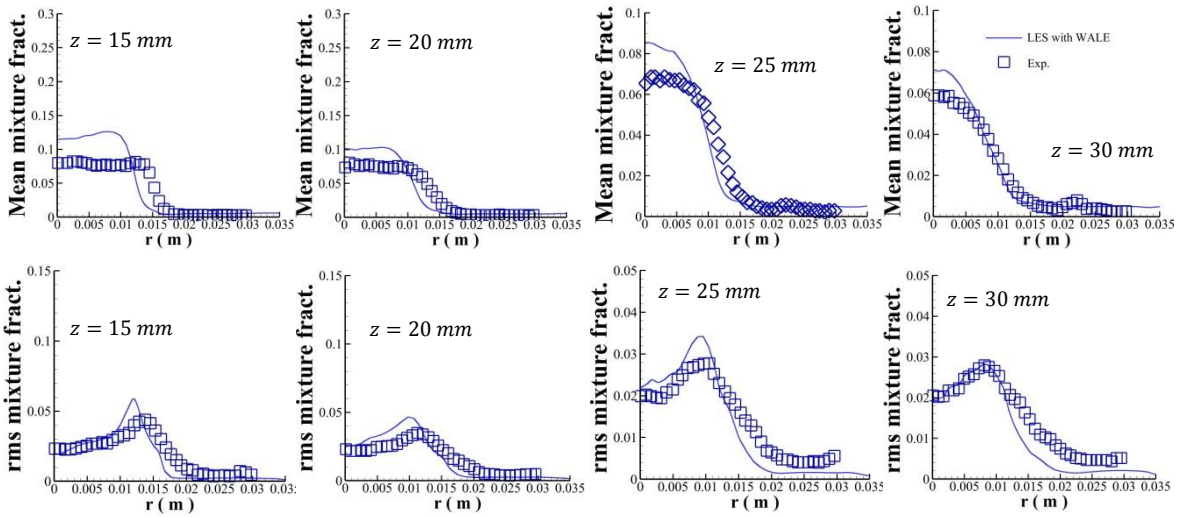

Figure 7: Radial profiles of the mixture fractions and the corresponding fluctuations at various cross sections of the combustion zone.

6-2 Visualization of ignition events

The state corresponding to the instantaneous mixing and temperature fields shown above in Figs. 5(d), 6(a) and 6(b) is used as the initial state to investigate the ignition event. The DPIK model described previously is used to mimic the spark energy deposition, and to capture the early stage of the spark kernel development and its propagation until the transition to the turbulent combustion model. The remaining phases governing the kernel growth until the complete flame establishment (for a successful ignition event) or flame extinction (for a failed ignition event) are captured with the combustion model through flame front tracking parameters such as the progress variable, the temperature and/or the OH radical concentration. As, one of the main objectives of the present work is to investigate the effect of spark location on the ignition success, two spark locations for which the images of the ignition sequence were recorded with a high-speed camera are considered. The first position is denoted "**A"**, and is located at $z = 25\ mm$ and $r = 0\ mm$, which is in the shear layer bordering the central recirculation zone; the second position denoted "**B**" is located outside the recirculation zone at $z = 25\ mm$ and $r = 15\ mm$ (see Fig. **8)**. As outlined earlier, the numerical prediction of the ignition event at each location is based on the infinitely fast and the finite rate chemistry assumptions. Thus, for each of the three simulation approaches mentioned above, the corresponding numerical ignition event is captured through the instantaneous contours of temperature, and is compared to experimental images of the ignition event provided by the high-speed camera. Figures **9** and **10** show these comparisons for the two different spark locations mentioned above. For each of these figures, three numerical predictions of the ignition event are shown with respect to two types of simulations based on the finite rate chemistry (i.e. FGM tabulations based diffusion and premixed flamelets, respectively) and the infinitely fast chemistry (i.e. BML) assumptions. More explicitly, Fig. **9** shows some sequences of the ignition event assuming the spark initially deposited at the "**A**" location; one can notice that, each of the three simulation approaches leads to a successful ignition event. However, by contrasting the total time required to achieve the full ignition of the burner in the numerical predictions with the experimental

results, it is found that unlike FGM methods, the BML model predicts the full ignition of the burner earlier than suggested by the experiment. This may be related to the overestimation of the reaction rate, especially in the zones such as flame holder wakes which feature high strain rate due to fuel-air mixing. According to predictions based on the FGM method, it can be seen that, the FGM based on premixed flamelets, even generated over a range of equivalence ratios leads to substantial discrepancies in the global prediction of the ignition event. As outlined in the section devoted to the FGM method description, the mass diffusion fluxes across iso-equivalence ratio surfaces as well as the related straining effects, cannot be captured using premixed-FGM, since the corresponding terms are neglected in premixed-FGM equations (i.e. $\chi_{Z,Y_C} = 0; \chi_Z = 0$). As expected, although the FGM based on diffusion flamelets neglects also the cross-scalar dissipation rate (i.e. $\chi_{Z,Y_C} = 0$), it leads to a relatively reasonable prediction of the whole ignition event. This superior performance of diffusion-FGM may be justified by the relative suitability of the model assumptions with the experimental configuration, and the ability of the model to account for the mass diffusion fluxes across iso-mixture fraction surfaces as well as the straining effects due to fuel-air mixing, which are more prominent in the investigated configuration. Each of the numerical ignition sequences summarized in Fig. **9** provides a step-by-step view of the ignition event, with an initial flame front propagating towards the bluff-body, and subsequently, the propagation of the flame kernel from the zone around the bluff-body to the downstream region. This propagation behavior is related to the dynamics of recirculation zones along with that of local triple flame structures that may result from the partially-premixed combustion occurring in the combustion zone. However, the experimental ignition sequence corresponding to this spark position, "**A**", does not show any flame front during the early ignition period (i.e. $t \in [0,\ 20\,ms[$) and the flame zone should not be viewed as extinguished. As advocated by the experimenter, this behavior can be explained by the low heat release which prevails when the initial flame kernel reaches the fuel-rich mixture around the bluff-body, so that the flame kernel dynamics are not detectable by the camera.

In the second group of simulations, the spark energy is deposited outside the recirculation region (i.e. at the location "**B**" mentioned above). As reported by the experimenter, the spark deposition at this location may lead to either successful or failed ignition event depending on the flow conditions prevailing during the spark deposition. For this "**B**" spark location, three kinds of failed ignition events were recorded in the experiment: in the first case, a spark deposition was followed by no indication of any flame kernel initiation; the second scenario showed a flame kernel initiation after the spark followed by a flame propagation downstream the burner that subsequently blows off; the last scenario was very close to a successful ignition event, since the spark deposition was accompanied by a flame kernel initiation, its propagation and stabilization for a short period of time (around few milliseconds), but followed by a global flame extinction. When a spark having the characteristics mentioned earlier for the location "**A**" (i.e. spark duration of $500\ \mu s$, spark energy of $200\ mJ$ and initial spark kernel size of $2\ mm$) is applied at the location "**B**", all the three simulation approaches lead to the first type of failed ignition events reported earlier. By increasing the spark energy at the location "**B**" while maintaining the spark duration (i.e. by using $400\ mJ$ instead of $200\ mJ$), the second type of failed ignition

International Journal of Numerical Methods for Heat & Fluid Flow, Vol. 27 No. 2, 2017, pp. 400-427.
© Emerald Group Publishing Limited, 0961-5539, DOI 10.1108/HFF-07-2015-0299

events is observed for each of the three approaches (i.e. BML, premixed-FGM and diffusion-FGM) as illustrated in the left part of Figs. **10**(**a**) and **10**(**b**) using simulation results based on the diffusion-FGM. However, by further increasing the spark energy and the spark duration (i.e. using $500\,mJ$ for duration of $10\,ms$), a successful ignition event is achieved at the location "**B**" with the three approaches as illustrated in the right part of Figs. **10**(**a**) and (**b**) using simulation results based on the BML model which is applied in the current study only as a first approximation. Based on these two results, it appears that, for bluff-body stabilized burners equipped with spark-based igniters, a successful ignition is more likely to be achieved by sparking at some specific locations within the recirculation zone whose sizes are known to be close to the bluff-body diameter. In addition to the high ignition probability, such locations allow minimizing the ignition energy requirements as well as the spark duration. To further investigate the effect of the spark location on the global ignition event, simulations based on four additional spark locations ("**C**", "**D**", "**E**" and "**F**") are conducted using the three combustion models (BML, premixed-FGM and diffusion-FGM); these locations are portrayed in Fig. **8**, and their coordinates are explicitly given in Table **2**.

Table **2**: Axial (z) and radial (r) coordinates of the spark locations (z and r in mm).

Regions	Within the CRZ			Outside the CRZ		shear layer bordering CRZ
Locations	**A**	**E**	**C**	**B**	**D**	**F**
Coordinates $(z; r)$	$(25;\ 0)$	$(12.5;\ 0)$	$(20;\ 0)$	$(25;\ 15)$	$(25;\ 25)$	$(20;\ 12.5)$

International Journal of Numerical Methods for Heat & Fluid Flow, Vol. 27 No. 2, 2017, pp. 400-427.
© Emerald Group Publishing Limited, 0961-5539, DOI 10.1108/HFF-07-2015-0299

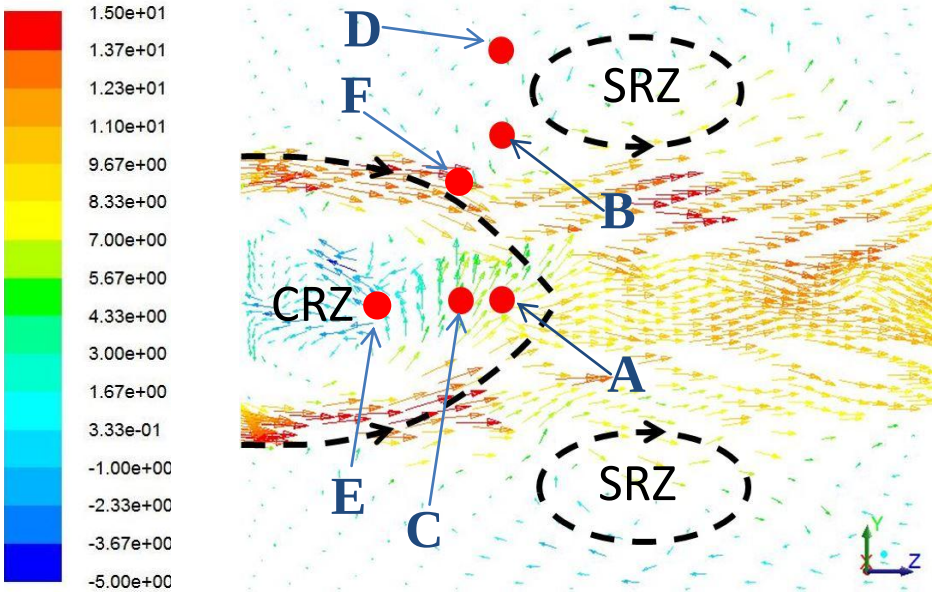

Figure **8**: Illustration of the spark locations through the velocity field colored by the axial velocity ($m.s^{-1}$) on the $x = 0$ isosurface. SRZ and CRZ stand for the side and central recirculation zones, respectively.

International Journal of Numerical Methods for Heat & Fluid Flow, Vol. 27 No. 2, 2017, pp. 400-427.
© Emerald Group Publishing Limited, 0961-5539, DOI 10.1108/HFF-07-2015-0299

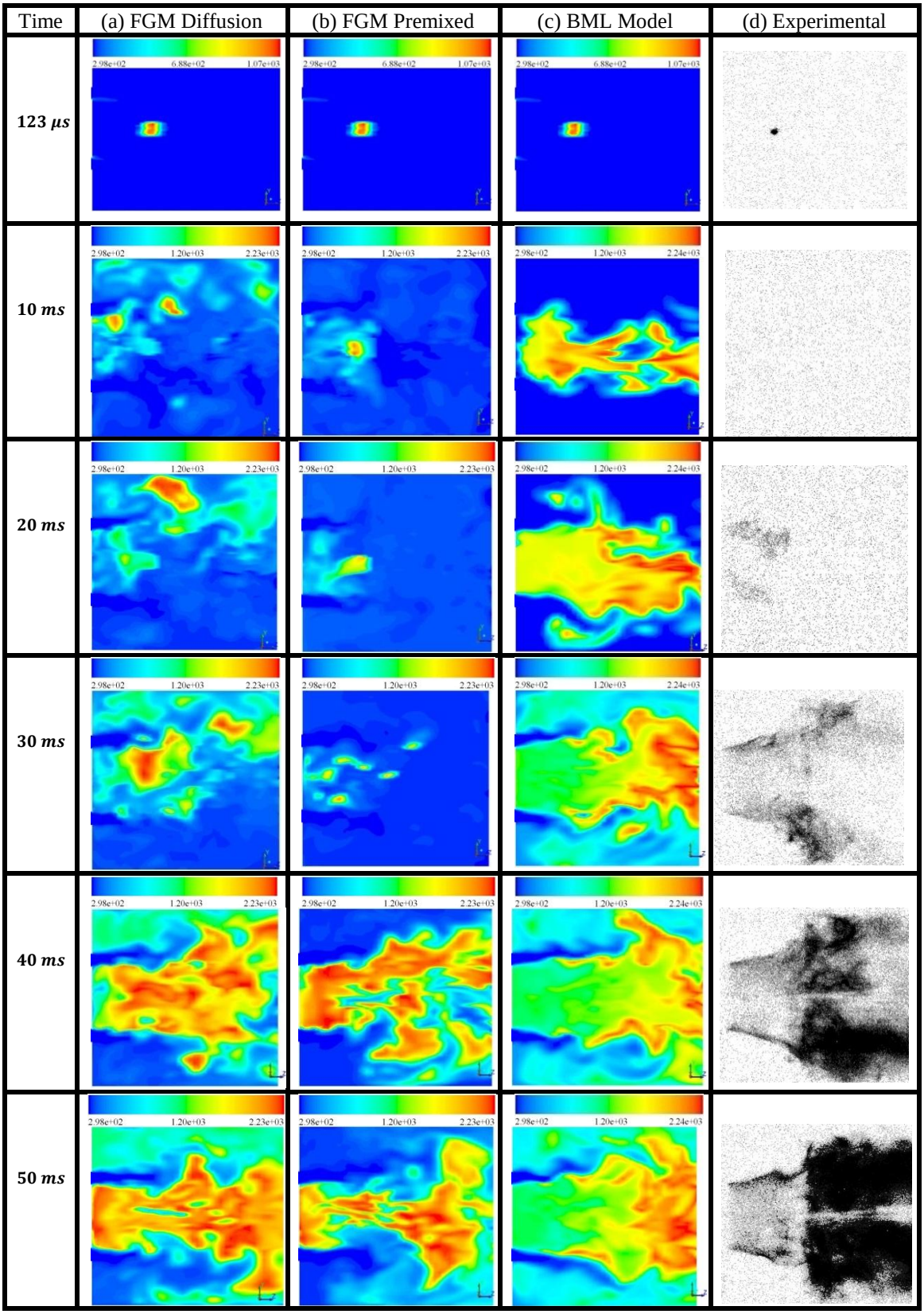

Figure **9:** Numerical ignition events compared to the experimental ignition event provided by a high-speed camera (Ahmed *et al.*, 2007); they are captured using the instantaneous contours of temperatures (K).

International Journal of Numerical Methods for Heat & Fluid Flow, Vol. 27 No. 2, 2017, pp. 400-427.
© Emerald Group Publishing Limited, 0961-5539, DOI 10.1108/HFF-07-2015-0299

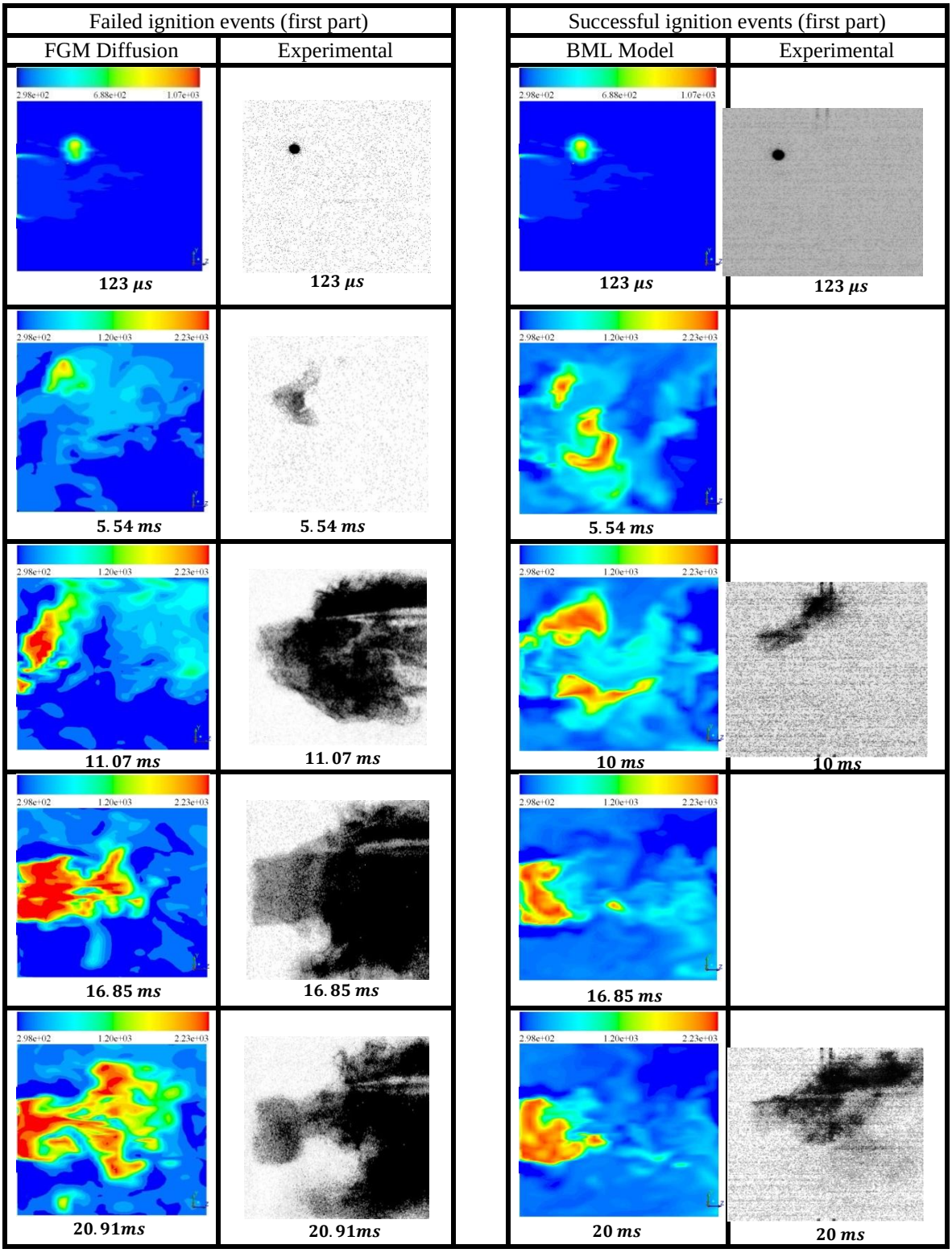

Figure **10**(**a**): Comparison of the numerical ignition events with high-speed camera images of the ignition sequence (Ahmed *et al.*, 2007). They are captured using the instantaneous contours of temperatures (K); (**a**) the time range considered in this first part is $t \in [0,\ 20.91\ ms]$. The spark is deposited at the location "**B**".

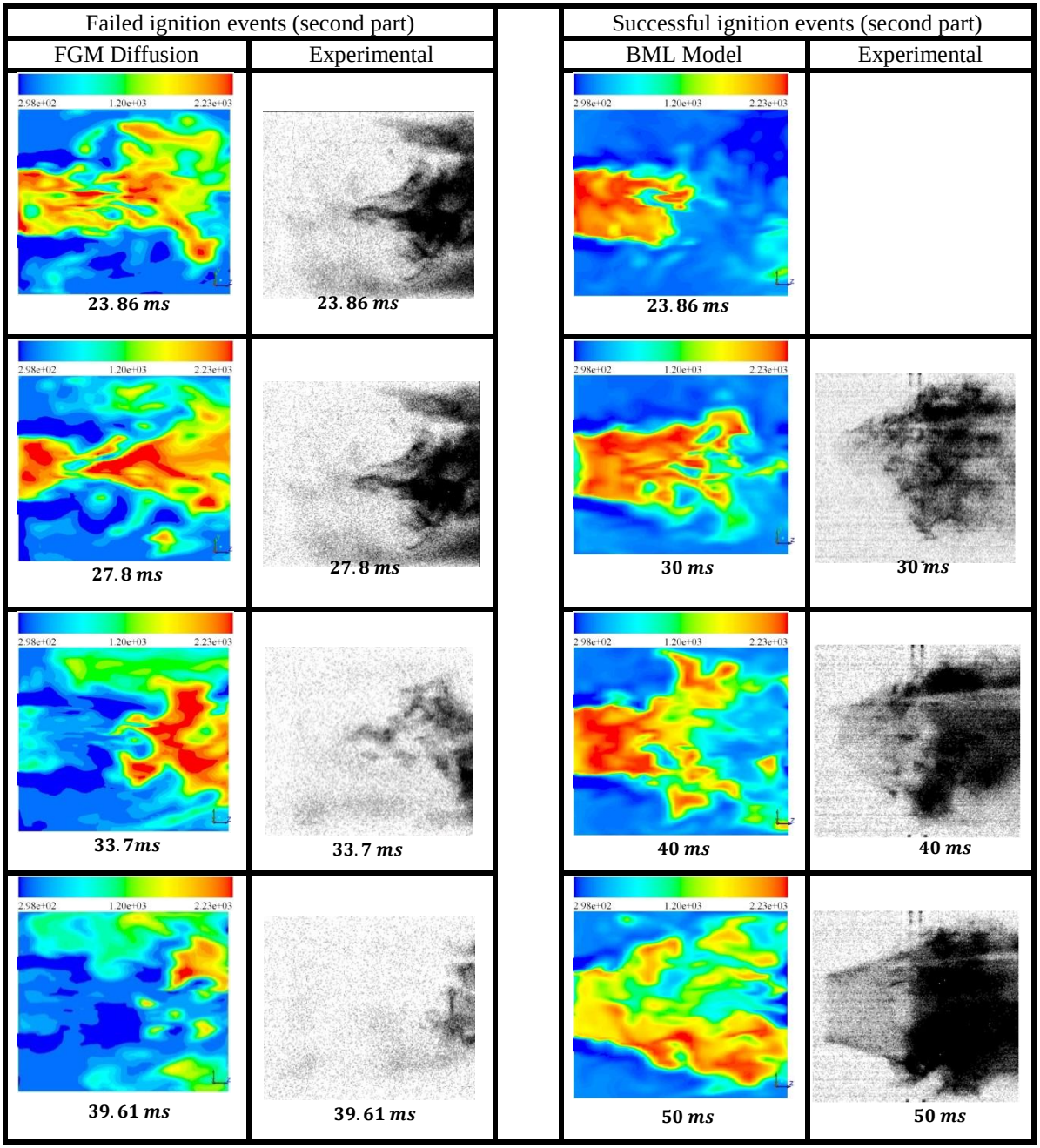

Figure **10**(**b**): Comparison of the numerical ignition events with high-speed camera images of the ignition sequence (Ahmed *et al.*, 2007). They are captured using the instantaneous contours of temperatures (K); (**b**) the time range considered in this second part is $t \in]20.91\ ms, 39.61\ ms]$. The spark is deposited at "**B**".

The numerical ignition sequences corresponding to each of the four spark locations mentioned earlier (see Table **2** and Fig. **8**) are summarized in Fig. **11**; these results are based on the diffusion-FGM model.

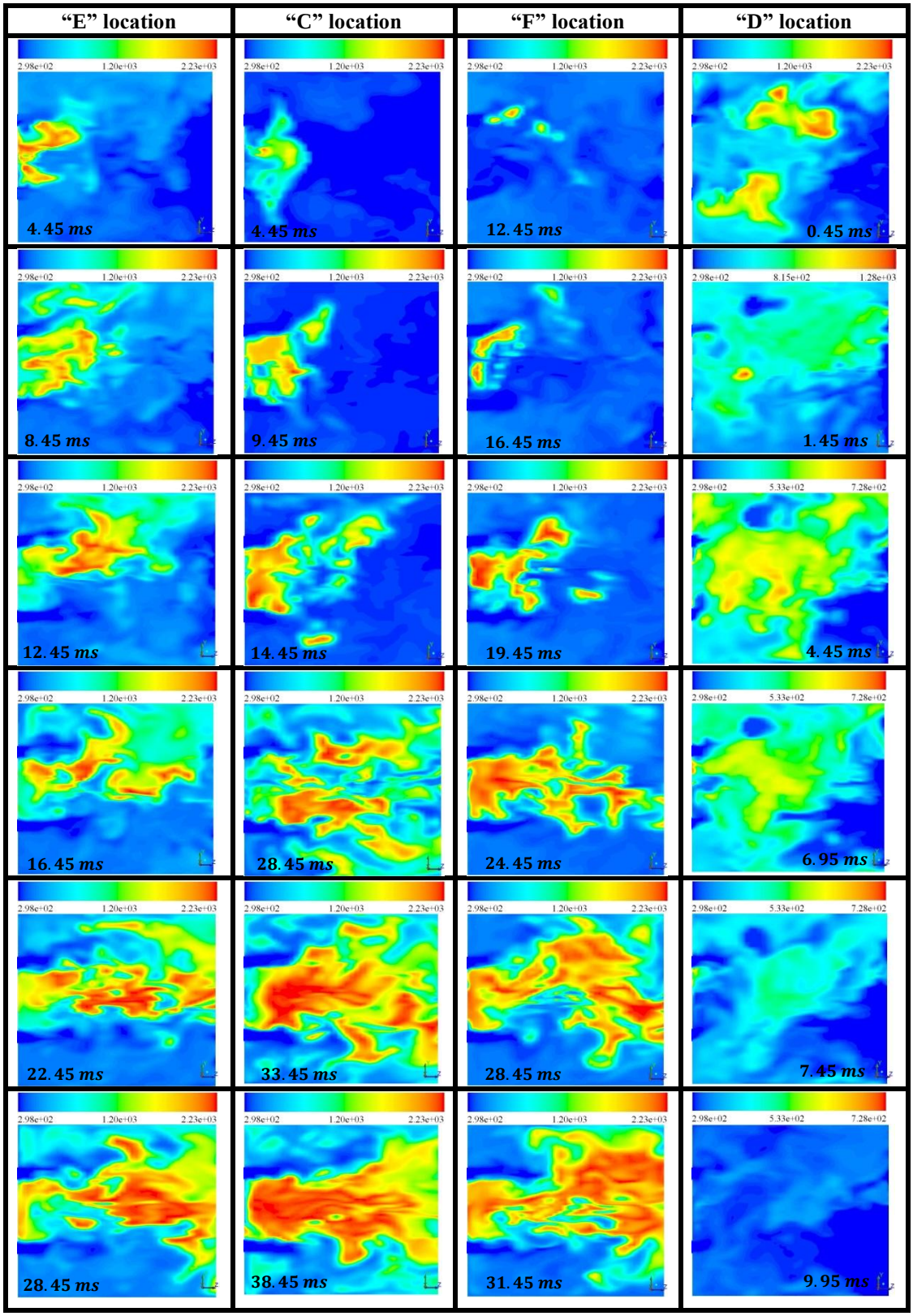

Figure 11: Numerical ignition events corresponding to spark deposited at four different locations listed in Table 2 and illustrated in Fig. 8; the results are based on the diffusion-FGM model.

International Journal of Numerical Methods for Heat & Fluid Flow, Vol. 27 No. 2, 2017, pp. 400-427.
© Emerald Group Publishing Limited, 0961-5539, DOI 10.1108/HFF-07-2015-0299

In addition to the successful numerical ignition event obtained earlier by sparking at the location "A", and qualitatively validated through high-speed camara images as shown in Fig. **9**, further numerical ignition events obtained by sparking at "E" and "C" confirm that a successful ignition event is achieved when the spark is deposited at some specific locations of the central recirculation zone where the fresh unburnt mixture is sufficiently fuel-rich, namely, when the equivalence ratio of the mixture at these locations lies within the flammability limits.

A successful ignition event is also achieved by sparking at another location in the shear layer bordering the central recirculation zone, namely, at the location "**F**". Unlike other locations of the combustion zone, the ignition probability at this location is expected to be relatively high, as this layer features nearly stoichiometric mixtures, reduced turbulence intensity, and is therefore propitious to a successful ignition event. Also, a similar behavior in terms of ignition mechanism is noted for all these ignitable locations of the recirculation zone: the flame kernel is initiated by the spark deposition, and then propagates towards the bluff-body before expanding to ignite the remaining burnable mixture. This flame propagation trend is mainly due to the dynamics of the central recirculation zone. The numerical event obtained by sparking at "**D**" as shown in Fig. **11** shows that a spark deposition far outside the recirculation zone leads to a failed ignition event regardless the spark parameters. In fact, by contrasting this latter result for the location "**D**" with those found by sparking at the location "**B**" (see Figs. **10**(**a**) and (**b**)), one can notice that, for the location "**B**" also, no successful ignition event is achieved with the classical spark parameters mentioned earlier. However, unlike the location "**B**" for which an increase in spark energy and duration may lead to a successful ignition event as shown in the right part of Figs. **10**(**a**) and (**b**), the spark deposition at the location "**D**" leads to a failed ignition event, even with the strongest spark parameters mentioned above. For each of the three spark strengths reported earlier, the combustion zone does not show any flame kernel propagation when sparking at the location "**D**". Instead, as illustrated in the fourth column in Fig. **11**, a progressive diffusion of the energy supplied by the spark is observed within the mixing zone. This result is mainly related to the mixture characteristics at this location: unlike contours and profiles of velocity which allow deducing that aerodynamics is propitious to ignition because of the low turbulence intensity at this point, the instantaneous contour of the mixture fraction shown in Fig. **5** (**d**) shows that the mixture is extremely lean, since the value of the mixture fraction around this point is below the lean flammability limit. Consequently, the flame kernel cannot propagate to ignite the whole burner.

7-Conclusions

Large eddy simulation of spark ignition of a bluff-body stabilized burner was conducted. The main interest of this configuration is related to its ability to mimic complex flows as those of practical configurations, and to produce flames with changing relevant combustion features such as stability, efficiency, pollutant formation and heat transfer, through variations in design and operating conditions. In addition to these two main assets of the experimental configuration, detailed experimental data are available so as to allow a step-by-step validation of the simulation approach. The main objective of the study was to appraise the prediction capabilities of the LES-turbulence model in interaction with different combustion models coupled to a subgrid spark-based ignition model (DPIK), to capture fully transient phenomena such as those involved in full successful or failed ignition

International Journal of Numerical Methods for Heat & Fluid Flow, Vol. 27 No. 2, 2017, pp. 400-427.
© Emerald Group Publishing Limited, 0961-5539, DOI 10.1108/HFF-07-2015-0299

events resulting from a spark deposit. A particular attention was paid to the computional cost, the robustness, and the ease of handling the numerical tools to allow reproducibility of this newly proposed simulation approach. A commercial software package widely used in industry, namely, ANSYS FLUENT^{TM}, was selected as the numerical tool. The Discrete Particle Ignition Kernel (DPIK) ignition model was first customized and implemented in the CFD code through a User Defined Function. Thereafter, the customized DPIK model was first coupled to a combustion model based on an infinitely fast chemistry through the classical Bray-Moss-Libby (BML) model, and subsequently, to a combustion model based on a finite rate chemistry in the line of the Flamelet Generated Manifold. Several spark locations were considered in order to determine locations suitable for a successful ignition event. Based on the successful and failed numerical ignition events recorded and validated qualitatively with high-speed camera images at two different locations (within and outside the central recirculation region), as well as the four additional numerical ignition events recorded inside and outside the recirculation region, the following outcomes are noted:

- When the DIPK model is coupled to the LES turbulence model paired with a robust combustion model such as FGM, it allows capturing inexpensively the early stage of the ignition event. This asset contributes substantially to a reasonable prediction of the overall ignition event with an affordable computing cost, since there is no need to deal with a very fine mesh.
- The ignition success resulting from a spark deposition strongly depends on the spark location, and therefore, on the aerodynamics and mixing fields. The regions providing the highest probability for the full ignition of the burner are found to be located in the vicinity of the shear layer delimiting the central recirculation zone. This result is first elucidated by the numerical ignition events corresponding to two spark locations, and qualitatively validated with high-speed camera images. Subsequently, this result is supported by the numerical ignition events corresponding to four other spark locations which are respectively located in the central recirculation zone, and in the shear layer delimiting the central recirculation zone. This high ignitability is mainly due to the fact that, such a shear layer zone features mixtures within the flammability limits, and allows the flame kernel to reach a size that can sustain high strain rates. In each successful ignition event with spark initially located around the central recirculation zone, the dynamics of this latter zone always drives the flame kernel towards the bluff-body prior the flame kernel expansion, and the subsequent full ignition of the burner.

The simulation approach applied in the present work provides a robust and simple way to address some ignition issues in various spark ignition-based engines, namely, the optimization of engines ignition with affordable computational costs. Based on the promising results obtained in the current work, it would be relevant to extend this simulation approach to spray combustion that is required for aircraft engines due to storage volume constraints.

Acknowledgments:

This work received financial support from Fond Québécois de la recherche sur la Nature et les Technologies (FQRNT) with seed funding initially provided by P&WC and CRIAQ&MDEIE. The authors gratefully

acknowledge Dr Ahmed for the meaningful discussions regarding the experimental configuration and Dr Linassier for helpful discussions related to the forced ignition modeling

References

Ahmed, S.F., Balachandran, R., Marchione, T. and Mastorakos E. (2007), "Spark Ignition of Turbulent Non-premixed Bluff-body Flames". *Combustion and Flame*, Vol. 151, pp. 366-385.

Akram, M. and Lundgren, E. (1996), "The evolution of spark discharge in gases: I. Macroscopic models". *Journal of Physics D: Applied Physics* Vol. 29, pp. 2129.

Amsden, A.A. (1993), "A KIVA Program with Block-Structured Mesh for Computer Geometries". *Los Alamos National Lab Report*. La-12503-MS.

ANSYS FLUENT™ (2012), *Fluent User's Guide*, versions 14.0.

Beer, J.M. and Chigier, N.A. (1972), "Combustion aerodynamics". *Applied Science*, London, UK.

Boileau, M., Staffelbach, G., Cuenot, B., Poinsot, T., Bérat, C. (2008), "Large eddy simulation of an ignition sequence in a gas turbine engine". *Combustion and Flame*, Vol. 154 No 1, pp. 2-22.

Borghi, R. (1988), "Turbulent Combustion Modeling". *Progress in Energy and Combustion Science, Vol.* 14 No 4, pp. 245-292.

Bushe, W.K. and Steiner, H. (1999), "Conditional moment closure for large eddy simulation of non-premixed turbulent reacting flows". *Physics of Fluids*, Vol. 11, pp. 1896-1906.

Bray, K.N.C, Domingo, P., Vervisch, L. (2005), "Role of the progress variable in models for partially premixed turbulent combustion". *Combustion and Flame*, Vol. 141, pp. 431-437.

Bray, K.N.C, Libby, P.A., Moss, J.B. (1984) Flamelet crossing frequencies and mean reaction rates in premixed turbulent combustion. *Combustion Science and Technology*, Vol. 41, pp. 143-172.

Bray, K.N.C, Libby, P.A., Moss, J.B., (1985), "Unified modeling approach for premixed turbulent combustion. 1. General formulation". *Combustion and Flame*, Vol. 61, pp. 87-102.

Chrigui, M., Gounder, J., Sadiki, A., Masri, A.R. and Janicka. J. (2012) "Partially premixed reacting acetone spray using LES and FGM tabulated chemistry". *Combustion and Flame*, Vol. 159, pp. 2718-2741.

Chrigui, M., Masri, A. R., Sadiki, A. and Janicka. J. (2013) "Large Eddy Simulation of a polydisperse Ethanol Spray Flame". *Flow, Turbulence and Combustion*, Vol. 90 No 4, pp. 813-832.

Claramunt, K., Cònsul, R., Carbonell, D. and Pérez-Segerra, C.D. (2006), "Analysis of the laminar flamelet concept for nonpremixed laminar flames" *Combustion and Flame*, vol.145, pp. 845-862.

Constantinescu, G., Mahesh, K., Apte, S., Iaccarino, G., Ham, F. and Moin, P. (2003), "A new paradigm for simulation of turbulent combustion in realistic gas turbine combustors using LES". *ASME-GT* 2003-38356.

Cook, A.W. and Riley, J.J. (1994) "A subgrid model for equilibrium chemistry in turbulent flows". *Physics of Fluids A*, Vol. 6 pp. 2868-2870.

Dunn-Rankin, D. (2008), "Lean Combustion: Technology and Control". *Academic Press*, Burlington.

Eichenberger, D.A. and Roberts, W.L. (1999), "Effect of unsteady stretch on-spark ignited flame kernel survival" *Combustion and Flame*, Vol. 118 No 3, pp. 469-478.

Eisazadeh-Far, K., Parsinejad, F., Metghalchi, H., Keck, J.C. (2010), "On flame kernel formation and propagation in premixed gases". *Combustion and Flame,* Vol. 157 pp. 2211-2221.

Fan, L., Li, G., Han, Z., Reitz, R.D. (1999), "Modeling Fuel Preparation and Stratified Combustion in a Gasoline Direct Injection Engine". *SAE Technical Paper* 1999- 01-0175

Fiorina, B., Gicquel, O., Vervisch, L., Carpentier, S., Darabiha, N., (2005), "Approximating the chemical structure of partially premixed and diffusion counterflow flames using FPI flamelet tabulation". *Combustion and Flame* , Vol. 140 No 3, pp. 147-160.

Fossi, A, DeChamplain, A., Bergthorson, J.M., Akih-Kumgeh, B., Ghazlani, A., Paquet, B. and Kalla, S., (2014), " Large Eddy Simulation of a Turbulent Swirling Jet-A1 Spray Flame Incorporating chemical non-equilibrium effects through the flamelet model" *Proceedings of the ASME Turbo Expo 2014*, Paper GT2014-27225, Düsseldorf, Germany.

Fossi, A, DeChamplain, A. and Akih-Kumgeh, B. (2015), "Unsteady RANS and Scale adaptive simulations of a turbulent spray flame in a swirl-stabilized gas turbine model combustion using tabulated chemistry", *International Journal of Numerical Methods for Heat & Fluid Flow*, Vol. 25 No5, pp. 1064-1088

GRI-Mech 3.0, (2014), "The Gas Research Institute", available on: http://www.me.berkeley.edu/gri_mech (Accessed in September 2014)

Hilbert, R., Tap, F., El-Rabii, H. and Thévenin, D. (2004), "Impact of detailed chemistry and transport models on turbulent combustion simulations". *Progress in Energy and Combustion Science*, Vol. 30 No 1, pp. 61-117

Herweg, R. and Maly, R.R., (1996), "A Fundamental Model for Flame Kernel Formation in S.I. Engines". *SAE 922243*, pp.1947-1976.

Ihme, M. and Pitsch, H. (2008), "Prediction of extinction and reignition in non-premixed turbulent flames using a flamelet/progress variable model; Part 2: Application in LES of Sandia flames D and E". *Combustion and Flame,* Vol. 155 Nos 1-2, pp. 90-107.

Ihme, M. and See, Y.C. (2010), "Prediction of autoignition in a lifted methane/air flame using an unsteady flamelet/progress variable model" *Combustion and Flame*, Vol. 157. pp. 1850-1862.

Jones, W. P., Marquis, A. J. and Vogiatzaki, K. (2014), "Large-eddy simulation of spray combustion in a gas turbine combustor". *Combustion and Flame*, Vol. 161 No 1, pp. 222-239.

Kerschgens, B., Gauding, M., Felsch, C., Peters, N. and Hasse C. (2010), "A Consistent Flamelet Model to Describe the Interaction of Combustion Chemistry and Mixing in the Controlled Auto Ignition Regime". *SAE Technical Paper 2010-01-0181*.

Kim, S.H. and Pitsch, H. (2005), "Conditional filtering method for large eddy simulation of turbulent non-premixed combustion. *Physics of Fluids*, Vol. 17 No10, pp.105103.

Kravchik, T., Sher, E., Heywood, J.B. (1995), "From spark ignition to flame initiation". *Combustion Science and Technology*, Vol. 108 Nos 1-3 pp. 1-30.

Lesieur, M. and Métais, O. (2005), "Large Eddy Simulations of turbulence". *Cambridge University Press*, Cambridge

International Journal of Numerical Methods for Heat & Fluid Flow, Vol. 27 No. 2, 2017, pp. 400-427.
© Emerald Group Publishing Limited, 0961-5539, DOI 10.1108/HFF-07-2015-0299

Lilly, D.K., "A proposed modification of the Germano subgrid-scale closure method" (1992). *Physics of Fluids A*, Vol. 4 No 3. Pp. 633–636.

Maly, R. (1981), "Ignition model for spark discharges and the early phase of flame front growth". *Symposium (International) on Combustion*, Vol. 18, pp. 1747-1754.

Metghalchi, M. and Keck, J.C., (1982), "Burning velocities of Mixtures of Air with Methanol, Isooctane, and Indolene at High Pressure and temperature". *Combustion and Flame*, Vol. 48, pp. 191-210.

Nguyen, P.D., Vervisch, L., Subramanian, V., Domingo, P. (2010), "Multidimensional flamelet-generated manifolds for partially premixed combustion". *Combustion and Flame*, Vol. 157 pp. 43-61.

Nicoud, F. and Ducros, F. (1999), "Subgrid-Scale modeling based on the square of the velocity gradient tensor". *Flow Turbulence and combustion*, Vol. 62, pp. 183-200.

Peters, N. (2000), "Turbulent Combustion". *Cambridge University Press*, Cambridge, UK.

Pitsch, H. (2006), "Large Eddy Simulation of turbulent combustion". *Annual Review of Fluid Mechanics* Vol. 38, pp. 453-482.

Poinsot, T. and Veynante, D. (2005), "Theoretical and Numerical combustion". *R.T. Edwards*, 2nd edition, Flourtown, PA.

Puri, I.K., Aggarwarl, S.K., Azzoni, R., Ratti, S. (2001), "On the Similitude Between Lifted and Burner-Stabilized Triple Flames: A Numerical and Experimental Investigation". *Combustion and Flame* Vol. 124 Nos 1-2, pp. 311-325.

Qin, X., Choi, C., Puri, I.K., Aggarwal, S.K. (2004), "Triple Flame Propagation and Stabilization in a laminar axisymmetric jet". *Combustion Theory and Modeling*, Vol. 8 No 2, pp. 293-314.

Raman, V. and Pitsch, H. (2005), "Large-Eddy Simulation of a Bluff-Body Stabilized Flame Using a Recursive-Refinement Procedure". *Combustion and Flame* , Vol. 142, pp. 329-347.

Reinmann, R. and Akram, M. (1997), "Temporal investigation of a fast spark discharge in chemically inert gas". Journal of Physics D: *Applied Physics*, Vol. 30 pp. 1125-1134.

Sivathanu, Y.R. and Faeth, G.M. (1990), "Generalized State Relationships for Scalar Properties in Non-Premixed Hydrocarbon/Air Flames". *Combustion and Flame*, Vol. 82, pp. 211-230.

Subramanian, V., Domingo, P., Vervisch, L. (2010), "Large eddy simulation of forced ignition of an annular bluff-body burner. *Combustion and Flame* , Vol. 157, pp. 579-601. Tan, Z., Reitz, R.D. (2006), "An ignition and combustion model based on the level-set method for spark ignition engine multidimensional modeling". *Combustion and Flame*, Vol. 145, pp. 1-15.

Triantafyllidis, A., Mastorakos, E. and Eggels, R.L.G.M. (2009), "Large eddy simulations of forced ignition of a non-premixed bluff-body methane flame with conditional moment closure". *Combustion and Flame*, Vol. 156, pp. 2328-2345. Zimont, V., Polifke, W., Bettelini, M., Weisenstein, W. (1998), "An Efficient Computational Model for Premixed Turbulent Combustion at High Reynolds Numbers Based on a Turbulent Flame Speed Closure". *Journal of Gas Turbine and Power*, Vol. (120), pp. 526-532.

International Journal of Numerical Methods for Heat & Fluid Flow, Vol. 27 No. 2, 2017, pp. 400-427.
© Emerald Group Publishing Limited, 0961-5539, DOI 10.1108/HFF-07-2015-0299

International Journal of Numerical Methods for Heat & Fluid Flow, Vol. 27 No. 2, 2017, pp. 400-427.
© Emerald Group Publishing Limited, 0961-5539, DOI 10.1108/HFF-07-2015-0299

Bibliography

B. Abramzon and WA. Sirignano. Droplet vaporization model for spray combustion calculations. *International Journal of Heat and Mass Transfer*, 32:1605–18, 1989.

SF. Ahmed. *Spark Ignition of Turbulent Non-premixed Bluff-Body Flames*. PhD thesis, Ph.D. Thesis, Cambridge University, 2007a.

SF. Ahmed, R. Balachandran, T. Marchione, and Mastorakos E. Spark Ignition of Turbulent Non-premixed Bluff-body Flames. *Combustion and Flame*, 151:366–385, 2007.

S.F.A.F.S. Ahmed. *Spark Ignition of Turblent Non-premixed Flames*. PhD thesis, Fitzwilliam College, Cambridge University, 2007b.

B. Akih-Kumgeh and JM. Bergthorson. Skeletical kinetic mechanisms for syngas, methyls bytanoate, n-heptane, and n-decane. *Energy and Fuels*, 10:1021, 2013.

SV. Apte, M. Gorokhovski, and P. Moin. Les of atomizing spray with stochastic modeling of secondary breakup. *International Journal of Multiphase Flow*, 29:1503–1522, 2003.

N. Ashgriz. *Handbook of Atomization and Sprays: Theory and Applications*. Springer, New York/Dordrecht/Heidelberg, 2011.

DL. Atkins and JS. Ervin. Experimental studies of jet fuel viscosity at low temperatures, using a rotational viscometer and an optical cell. *Energy and Fuels*, 19(5):1935–1947, 2005.

Y. Baba and R. Kurose. Analysis and flamelet modelling for spray combustion. *Journal of Fluid Mechanics*, 612:45–79, 2008.

JC. Baele and RD. Reitz. Modeling spray atomization with kelvin-helmholtz/rayleigh-taylor hybrid model. *Atomization and Sprays*, 9:623–650, 1999.

R. Balachandran. *Experimental investigation of the response of turbulent premixed flames to acoustic oscillations*. PhD thesis, Cambridge University, 2005.

RS. Barlow and CD. Carter. Raman/rayleigh/lif measurements of nitric formation in turbulent hydrogen jet flames. *Combustion and Flame*, 97(3-4):261–280, 1994.

RS. Barlow and CD. Carter. Relationships among nitric oxide, temperature, and mixture fraction in hydrogen jet flames. *Combustion and Flame*, 104(3):288–299, 1996.

LP. Bayvel and Z. Orzechowski. *Liquid and atomization*. Taylor and Francis, Washington, DC, 1993.

JC. Beale and RD. Reitz. Modelling spray atomization with the kelvin-helmholtz/rayleigh-taylor hybrid model. *Atomization and Sprays*, 9:623–650, 1999.

JM. Beer and NA. Chigier. *Combustion Aerodynamics*. Applied Science, London, 1972.

JM. Bergthorson and MJ Thomson. Combustion and emissions properties of advanced biofuels and their impact on existing and future engines. *Renewable and Sustainable Energy Reviews*, 42:1393–1417, 2015.

RW. Bilger. Conditional moment closure for turbulent reacting flow. *Physics of Fluids A*, 5(2):436–444, 1993.

M. Bini and WP. Jones. Large-eddy simulation of particle-laden turbulent flows. *Journal of Fluid Mechanics*, 614(11):207–252, 2008.

ES. Blurock. Reaction: System for modelling chemical reactions. *Journal of Chemical Information and Computer Sciences*, 35:607–616, 1995.

ES. Blurock. Generation and subsequent reduction of large detailed combustion mechanisms. *Proceedings of the combustion institute, WIP 4-D19*, page 331, 2000.

M. Boileau, G. Staffelbach, B. Cuenot, T. Poinsot, and C. Bérat. Large eddy simulation of an ignition sequence in a gas turbine engine. *Combustion and Flame*, 154:2–22, 2008.

CT. Bowman, RK. Hanson, DF. Davison, WC. Gardiner, V. Lissianski, GP. Smith, DM. Golden, M. Frenklash, and M. Goldenberg. Gri-mech home page. *University of Berkeley*, 2004.

K.N.C. Bray, P. Domingo, and L. Vervisch. Role of the progress variable in the models for partially premixed turbulent combustion. *Combustion and Flame*, 141:431–437, 2005.

JH. Burgoyne and L. Cohen. The effect of Drop Size on Flame Propagation in Liquid Aerosols. *Proceedings of the Royal Society, 225 A*, 1162:375–392, 1954.

WK. Bushe and H. Steiner. Conditional moment closure for large eddy simulation of nonpremixed turbulent reacting flows. *Physics of Fluids*, 11:1896–1906, 1999.

V. Bykov, I. Goldfarb, V. Gol'dshtein, and JB. Greenberg. Thermal explosion in hot gas mixtures with fuel droplets: a two reactants model. *Combustion Therory and Modelling*, 6:1–21, 2002.

CERFACS. Centre Européen de Recherche et de Formation Avancée en Calcul Scientifique. `https://ctr.stanford.edu`.

K. Chae. *Mass diffusion and chemical kinetic data for jet fuel surrogates*. PhD thesis, University of Michigan, 2010.

K. Chae and A. Violi. Mutual diffusion coefficients of heptane isomers in nitrogen: A molecular dynamics study. *AIP The Journal of Chemical Physics*, 134:044537, 2011.

SH. Chan, JQ. Yin, and BJ. Shi. Structure and extinction of methane-air flamelet with radiation and detailed chemical kinetic mechanism. *Combustion and Flame*, 112:445–456, 1998.

CH. Chiang, MS. Raju, and WA. Sirignano. Numerical analysis of convecting, vaporizing fuel droplet with variable properties. *International Journal of Heat and Mass Transfer*, 35:1307–24, 1992.

HH. Chiu, Y. Kim, and J. Croke. Internal group combustion of liquid droplets. *In. Proceedings of the Combustion Institute*, 19:971–980, 1982.

M. Chrigui, J. Gounder, A. Sadiki, AR. Masri, and J. Janicka. Partially premixed reacting acetone spray using les and fgm tabulated chemistry. *Combustion and Flame*, 159:2718–2741, 2012.

CITS. Center for Integrated Turbulence Simulation: the current Center for Turbulence Research (CTR). https://ctr.stanford.edu.

K. Claramunt, R. Consul, D. Carbonell, and CD. Perez-Segarra. Analysis of the Laminar Flamelet Concept for Nonpremixed Laminar Flames. *Combustion and Flame*, 145(4):845–862, 2006.

M. Colket, T. Edwards, S. Williams, NP. Cernansky, DL. Miller, F. Egolfopoulos, P. Lindstedt, K. Seshadri, FL. Dryer, CK. Law, D. Friend, DB. Lenhert, H. Pitsch, A. Sarofim, M. Smooke, and W. Tsang. Development of an experimental database and kinetic models for surrogate jet fuels. *In 45th AIAA Aerospace Sciences Meeting and Exhibit, number AIAA 2007-770. American Institute of Aeronautics and Astronautics*, 2007.

AW. Cook and JJ. Riley. A subgrid model for equilibrium chemistry in turbulent flows. *Physics of Fluids A*, 06:2868–2870, 1994.

AW. Cook and JJ. Riley. A subgrid modelling for turbulent reacting flows. *Combustion and Flame*, 112:593–606, 1998.

JA. Cooke, M. Bellucci, MD. Smooke, A. Gomez, A. Violi, T. Faravelli, and E. Ranzi. Computational and experimental study of JP-8, a surrogate, and its components in counterflow diffusion flames. *Proceedings of the Combustion Institute*, 30(1):439–446, 2005.

F. Cooper. Heat transfer from a sphere to an infinite medium. *International Journal of Heat and Mass Transfer*, 20:991–3, 1977.

CRC. *Handbook of Aviation Fuel Properties*. Society of Automotive Engineers, Inc, Warrendale, Pennsylvania, 1983.

HJ. Curran, P. Gaffuri, WJ. Pitz, and CK. Wesbrook. A comprehensive modeling of study iso-octane oxidation oxidation. *Combustion and Flame*, 129:253–80, 2002.

P. Dagaut and M. Cathonnet. The ignition, oxidation and combustion of kerosene: A review of experimental and kinetic modeling. *Progress in Energy and Combustion Science*, 32:48–92, 2006.

P. Dagaut, M. Reuillon, J. Boettner, and M. Cathonnet. Kerosene combustion at pressures up to 40 atm: Experimental study and detailed chemical kinetic modeling. *Proceedings of the Combustion Institute*, 25:919–926, 1994.

P. Dagaut, G. Pengloan, and A. Ristori. Oxidation, ignition and combustion of toluene: Experimental and detailed kinetic modeling. *Physical Chemistry Chemical Physics*, 4(10):1846–1854, 2002.

G. Damköhler. The effect of turbulence on the flame velocity in gas mixtures. *Tech. Rep. TM 1112. National Advisory Committee for Aeronautics, USA (also Z. Electrochem*, 46(28), 1940.

TE. Daubert and RP. Danner. *API tecnical data book-petroleum refining*. American Petroleum Institute, Washington DC, 1997.

Reaction Design. *CHEMKIN-PRO*. Reaction Design, San Diego.

M. Destriau and R. Borghi. *La combustion et les flammes*. Editions Technip, 1995.

M. Dianat, Z. Yang, and JJ. McGuirk. Large-eddy simulation by a two-phase plane mixing-layer. Avances in Turbulence XII. *Springer Proceedings in Physics*, 132(Part 11):775–778, 2009.

S. Dooley, SH. Won, M. Chaos, J. Heyne, YG. Ju, and FL. Dryer et al. A jet fuel surrogate formulated by real fuel properties. *Combustion and Flame*, 157:2333–9, 2010.

S. Dooley, SH. Won, J. Heyne, TI. Farouk, YG. Ju, and FR. Dryer et al. The experimental evaluation of a methodology for surrogate fuel formulation to emulate gas phase combustion kinetic phenomena. *Combustion and Flame*, 159:1444–66, 2012.

D. Dunn-Rankin. *Lean Combustion: Technology and Control*. Academic Press, Burlington, 2008.

T. Edwards and LQ. Maurice. Surrogate mixtures to represent complex aviation and rockets fuels. *Journal of Propulsion and Power*, 17(2):461–466, 2001.

T. Edwards and S. Zabarnick. Supercritical Fuel Deposition Mechanisms. *Industrial and engineering chemistry research*, 32(12):2117–3122, 1993.

G. Eggenspieler and S. Menon. Large-eddy simulation of pollutant emission in a DOE-HAT combustor. *Journal of Propulsion and Power*, 20(6):1076–85, 2004.

Y. Egorov, FR. Menter, R. Lechner, and D. Cokljat. The Scale-Adaptive Simulation Method for Unsteady Turbulent Flow Predictions. Part 2: Applications to Complex Flows. *Flow, Turbulence and Combustion*, 85:139–165, 2010.

DA. Eichenberger and WL. Roberts. Effect of unsteay stretch on spark ignited flame kernel survival. *Combustion and Flame*, 118(3):469–478, 1999.

K. Eisazadeh-Far, F. Parsinejad, H. Metghalchi, and JC. Keck. On flame kernel formulation and propagation in premixed gases. *Combustion and Flame*, 157:2211–2221, 2010.

S. Elghobashi. On predicting particle-laden turbulent flows. *Applied Scientific Research*, 42(4):309–329, 1994.

MM. Elkotb. Fuel atomization for spray modeling. *Progress in Energy and Combustion Science*, 8(1): 61–91, 1982.

Esquiva-Dano, HT. Nguyen, and D. Escudie. Influence of a bluff-body's shape on the stabilization region of non-premixed flames. *Combustion and Flame*, 127:2167–2180, 2001.

GM. Faeth, L.-H. Hsaing, and P.-K. Wu. Structure and breakup properties of sprays. *International Journal of Multiphase Flow*, 21:99–127, 1995.

CR. Ferguson and TA. Kirkpatrick. Internal combustion engines: Applied Thermosciences 2nd Edition. *Wiley*, 2000.

P. Fevrier, O. Simonin, and K. Squires. Partitioning of particle velocities in gas-solid turbulent flows into a continuous field and a spatially uncorrelated random distribution theoretical formalism and numerical study. *Journal of Fluid Mechanics*, 533:1–46, 2005.

B. Fiorina, O. Gicquel, L. Vervisch, S. Carpentier, and N. Darabiha. Approximating the chemical structure of partially premixed and diffusion counterflow flames using fpi flamelet tabulation. *Combustion and Flame*, 140(3):147–160, 2005.

A. Fossi, A. DeChamplain, and B. Akih-Kumgeh. Unsteady rans and scale adaptive simulations of a turbulent spray flame in a swirled-stabilized gas turbine model combustor using tabulated chemistry. *International Journal of Numerical Methods for Heat and Fluid Flow*, 25(5):1064–1088, 2015a.

A. Fossi, A. DeChamplain, JM. Bergthorson, B. Akih-Kumgeh, MA. Ghazlani, B. Paquet, and S. Kalla. Large eddy simulation of a turbulent swirling jet-a1 spray flame incorporating chemical non-equilibrium effects through the flamelet model. *In Proceedings of the ASME Turbo Expo 2014,*, (Paper GT2014-27225), June 16-21, Düsseldorf, Germany, 2015b.

A. Fossi, A. DeChamplain, JM. Bergthorson, B. Paquet, and S. Kalla. Scale-adaptive and large eddy simulations of a turbulent spray flame in a scaled swirl-stabilized gas turbine combustor using strained flamelets. *In Proceedings of the ASME Turbo Expo 2014,(Paper GT2015-42535), June 15-19, Montreal, Canada*, 2015c.

B. Franzelli, B. Fiorina, and N. Darabiha. A tabulated chemistry method for spray combustion. *Proceedings of The Combustion Institute*, 34:1659–1666, 2013.

RP. Fraser, P. Eisenklam, N. Dombrowski, and D. Hasson. Drop formation from rapidly moving sheets. *AIChE Journal*, 8(5):672–680, 1962.

RN. Garcia, G. Linassier, R. Lecourt, and P. Villedieu. Experimental and numerical study of high altitude ignition of a turbojet combustor. *Heat Transfer Engineering*, 32(11-12):949–956, 2011.

HW. Ge and E. Gutheil. Probablity density function (PDF) simulation of turbulent spray flows. *Atomization and Sprays*, 16(5):531–542, 2006.

M. Germano, U. Piomelli, P. Moin, and W.H. Cabot. A Dynamic subgrid-scale eddy viscosity model. *Physics of Fluids A*, 3:1760–1765, 1991.

MA. Ghazlani, A. deChamplain, B. Paquet, S. Kalla, and N. Davenport. Cfd modelling of heat soak-back phenomenon inside a gas turbine combustor. *In Proceedings of the ASME Turbo Expo 2014,(Paper GT2015-42535), June 15-19, Montreal, Canada*, 2015.

L. Gicquel, G. Staffelbach, and T. Poinsot. Large eddy simulations of gaseous flames in gas turbine combustion chambers. *Progress in Energy and Combustion Science*, 38(6):782–817, 2012.

O. Gicquel, N. Darabiha, and D. Thevenin. Laminar premixed hydrogen/air counterflow flame simulations using flame prolongation of ildm with differential diffusion. *Proceedings of The Combustion Institute*, 28:1901–1908, 2000.

I. Goldfarb, V. Gol'dshtein, G. Kuzmenko, and SS. Sazhin. Thermal radiation effect on thermal explosion in gas containing fuel droplets. *Combustion Therory and Modelling*, 3:769–787, 1999.

DG. Goodwin. An open-source, extensible software suite for cvd process simulation. *In Proceedings of CVD XVI and EuroCVD Fourteen, M Allendorf, Maury, and Teyssandier (Eds), Electrochemical Society*, pages 155–162, 2003.

M. Gratton and P. Sampath. *Alternate Fuels Combustion Research Phase II*. PRATT & WITHNEY CANADA, Mississauga, Ontario, Canada, 1983.

C. Gueret, M. Cathonnet, JC. Boettner, and F. Gaillard. Experimental Study and Modeling of Kerosene Oxidation in a Jet-Stirred Flow Reactor. *Proceedings of the Combustion Institute*, 23:211–1990, 2007.

E. Gutheil. Modeling and Simulation of Droplet and Spray Combustion. Handbook of Combustion. *Wiley-VCH Verlag GmbH and Co. KGaA*, pages 285–290, 2010.

DB. Harmon. Drop size, from low speed jets. *Journal of the Franklin Institute*, 259(6):519–522, 1955.

D. Haworth and K. Jansen. Large eddy simulation on unstructured deforming meshes: towards reciprocating IC engines. *Computers and Fluids*, 29(5):493–524, 2000.

BT. Helenbrook. Numerical studies of droplet deformation and break-up. *ILAS Americas 14th Annual Conference on Liquid Atomization and Spray Systems, Dearbon, MI, May*, 2001.

R. Herweg and RR. Maly. A fundamental model for flame kernel formation in S.I. Engines. *SAE 922243*, pages 1947–1976, 1996.

R. Hilbert, F. Tap, H. El-Rabii, and D. Thevenin. Impact of detailed chemistry and transport models on turbulent combustion simulations. *Progress in Energy and Combustion Science*, 30(1):61–117, 2004a.

R. Hilbert, F. Tap, H. El-Rabii, and D. Thévenin. Impact of detailed chemistry and transport models on turbulent combustion simulations. *Progress in Energy and Combustion Science*, 30(1):61–117, 2004b.

C. Hirsch. *Numerical Computation of Internal and External Flows*, volume 1. Wiley, 1988.

C. Hollman and E. Gutheil. Flamelet-modeling of turbulent spray diffusion flames based on a laminar spray flame library. *Combustion Science and Technology*, 135(1-6):175–192, 1998.

C. Hollmann and E. Gutheil. Flamelet-modeling of turbulent spray diffusion flames based on a laminar spray flame library. *Combustion Science and Technology*, 135(1-6):175–192, 1998.

S. Honnet, K. Seshadri, U. Niemann, and N. Peters. A surrogate fuel for kerosene. *Proceedings of the Combustion Institute*, 32:485–492, 2009.

X. Hui and CJ. Sung. Laminar flame speeds of transportation-relevant hydrocarbons and jet fuels at elevated temperatures and pressures. *Fuel*, 109:191–200, 2013.

S. Humer, A. Frassoldati, S. Granata, T. Faravelli, E. Ranzi, and R. Seiser et al. Experimental and kinetic modeling study of combustion of JP-8, its surrogates and reference components in laminar nonpremixed flows. *Proceedings of the Combustion Institute*, 31:493–400, 2007a.

S. Humer, A. Frassoldati, S. Granata, T. Faravelli, E. Ranzi, and K. Seshadri. Experimental and kinetics modeling study of combustion of jp-8, its surrogates and reference components in laminar nonpremixed flows. *Proceedings of the Combustion Institute*, 31:393–400, 2007b.

M. Ihme and H. Pitsch. Prediction of extinction and reignition in non-premixed turbulent flames using a flamelet/progress varaible model. Part 2: Application in LES of Sandia flames D and E. *Combustion and Flame*, 155(1-2):90–107, 2008.

F. Jaegle, J.-M. Senoner, M. Garcia, F. Bismes, R. Lecourt, and B. Cuenot. Eulerian and lagrangian spray simulations of an aeronautical multipoint injector. *Proceedings of the Combustion Institute*, 33(2):2099–2107, 2011.

J. Jean. Characterization of different biofuels blends for cold start and altitude relight in aeroengines, 2017.

P. Joaquim and S. Spencer. *Finite Difference, Finite Element and Finite Volume Methods for Partial Differential Equations*. Springer Netherlands, 2005.

AR. Jones. Design optimization of a large pressure-jet atomizer for power plant. *Proceedings of the 2nd International Conference on liquid Atomization and sprays, Madison Wis.*, pages 181–185, 1985.

WP. Jones and D.-H. Sheen. A probablity Density Function Method for Modelling Liquid Fuel Sprays. *Flow, Turbulence and Combustion*, 63:379–394, 1999.

WP. Jones, S. Lyra, and S. Navarro-Martinez. Numerical investigation of swirling kerosene spray flames using large eddy simulation. *Combustion and Flame*, 159(4):1539–1561, 2012.

B. Karlovitz, D. Denniston, D. Knapschaefer, and F. Wells. Studies on turbulent flames. *In 4th Symposium (International) on Combustion, William and Wilkins, Eds. The Combustion Institude, Pittsburgh*, 28:613–620, 1953.

G.E. Karniadarkis and S. Sherwin. *Spectral/hp Element Methods for CFD*. Oxford University Press, 1999.

A. Kaufmann. *Towards Eulerian-Eulerian large eddy simulationof reactive two-phase flows*. PhD thesis, Institut National Polytechnique de Toulouse, 2004.

A. Kaufmann, M. Moreau, O. Simonin, and J. Helie. Comparison between Lagrangian and Mesoscopic Eulerian modelling approaches for inertial particles suspended in decaying isotropic turbulence. *Journal of Computational Physics*, 227(13):6448–6472, 2008.

A. Kayano and T. Kamiya. Calculation of the mean size of the droplets purged from the rotating disk. *Proceedings of the 1st International Conference on Liquid Atomization and Sprays, Tokyo*, pages 133–143, 1978.

RJ. Kee, JF. Grcar, MD. Smooke, and JA. Miller. A FORTRAN Program for Modeling Steady Laminar One-Dimensional Premixed Flames. *Report No. SAND85-8240, Sandia Mational Laboratories*, 1985.

RJ. Kee, GD. Lewis, J. Warnatz, ME. Coltrin, and JA. Miller. A FORTRAN Computer Code Package for the Evaluation of Gas-Phase, Multicomponent Transport Properties. *Report No. SAND86-8246, Sandia Mational Laboratories*, 1986.

JB. Kennedy. High weber number smd correlations for pressures atomizers. *ASME Paper*, 85-GT-37, 1985.

E. Kilik. *The influence of the swirler design parameters on the aerodynamics of the downstream recirculation region*. PhD thesis, School of Mechnanical Engineering, Cranfield Institute of Technology, England, 1976.

W. Kim, S. Menon, and H. Mongia. Large-eddy simulation of a gas turbine combustor flow. *Combustion Science and Technology*, 143 (1-6):25–62, 1999.

WW. Kim and S. Menon. Application of the localized dynamic subgrid-scale model to turbulent wall-bounded flows. *Technical Report AIAA-97-0210. 35th Aerospace Sciences Meeting, Reno, NVAmerican Institute of Aeronautics and Astronautics*, January, 1997.

AY. Klimenko. Conditional moment closure and fluctuations of scalar dissipation. *Fluid Dynamics*, 28:613–637, 1993.

AY. Klimenko. On the relation between the conditional moment closure and the unsteady flamelets. *Progress in Eenergy and Combustion Science*, 5(3):275–294, 2001.

AY. Klimenko and RW. Bilger. Conditional moment closure for turbulent combustion. *Progress in Eenergy and Combustion Science*, 25:595–687, 1999.

A. Kronenburg, RW. Bilger, and JH. Kent. Second order conditional moment closure for turbulent jet diffusion flames. *Twenty-seventh Symposium (I)nternational on Combustion, The Combustion Institute, Pittsburgh, PA*, pages 1097–1104, 1998.

PK. Kundu, IM. Cohen, and DR. Dawling. *Fluid Mechanics, 5th Edition*. Elsevier, Academic Press, 2012.

A.H. Lefebvre. *Gas Turbine Combustion*. Taylor and Francis (Hemisphere Publishing Corporation), Philadelphia, 1983.

A.H. Lefebvre. *Atomization and Sprays*. Taylor and Francis(Hemisphere Publishing Corporation), New York, NY, 1989.

AH. Lefebvre and DR. Ballal. *Gas Turbine Combustion: Alternative Fuel and Emissions*. Taylor an Francis Group, Boca Raton, London, New York, 2010.

M. Lesieur and O. Metais. New Trends in Large-Eddy Simulationd of Turbulence. *Annual Review of Fluid Mechanics*, 28:45–82, 1996.

M. Lesieur, O. Metais, and P. Comte. *Large-Eddy Simulation of Turbulence*. Cambridge University Press, 2005.

L. Liang and DR. Reitz. Spark ignition engine combustion modeling using a level set method with detailed chemistry. *SAE Technical paper 930072*, 2006.

DK. Lilly. A Proposed Modification of the Germano Subgrid-Scale Closure Model. *Physics of Fluids*, 4:633–635, 1992.

RP. Lindstedt and LQ. Maurice. Detailed chemical-kinetics model for aviation fuels. *Journal of Propulsion and Power*, 16(2):187–95, 2000.

AB. Liu, D. Mather, and RD. Reitz. Modelling the Effects of Drop Drag and Breakup on Fuel Sprays. *SAE Technical Paper 930072. SAE*, 1993.

RL. Lyons. Swirl-Stabilized Turbulent Spray Flames in an Axisymmetric Model Combustor, 1985.

MC. Ma and CB. Devaud. A conditional moment closure (cmc) formulation including differential diffusion applied to a non-premixed hydrogen-air flame. *Combustion and Flame*, 162(1):144–158, 2015.

GDM. Mackay and SG. Mason. The gravity approach and coalescence of fluid droplets and liquid interfaces. *Canadian Journal of Chemical engineering*, 41:203, 1963.

BF. Magnussen. On the structure of turbulence and a generalized eddy dissipation concept for chemical reaction in turbulent flow. *Nineteenth AIAA meeting, St. Louis*, 1981.

BF. Magnussen and BH. Hjertager. On mathematical models of turbulent combustion with special emphasis on soot formation and combustion. *In 16th Symposium (International) on Combustion. The Combustion Institute*, 1976.

F. Marcotte, A. deChamplain, J. Jean, A. Fossi, and S. Ringuette. Detailed ignition sequence studied with a fast infrared camera. *In: Proceedings of Combustion Institute-Canadian Section, Spring Technical Meeting, Laval University, May 13-16*, 07:285–290, 2013.

U. Mass and SB. Pope. Simplifying Chemical Kinetics: Intrinsic Loe-Dimensional Manofolds in Composition Space. *Combustion and Flame*, 88:239–264, 1992.

HT. Mayfield. *JP-8 composition and variability. Final technical report*. Amstrong Laboratory, Environics Directorate, Environmental Research Division, AL/EQC, Tendall AFB, Florida, 1996.

FR. Menter and Y. Egorov. The Scale-adaptive Simulation Method for Unsteady Turbulent Flow Predictions. par 1: Theory and Model Description. *Flow Turbulence Combustion*, 85:113–138, 2010.

M. Metghalchi and JC. Keck. Burning velocities of mixtures of air with methanol, isooctane, and idolene at high pressure and temperature. *Combustion and Flame*, 48:191–210, 1982.

P. Moin. Advances in large eddy simulation methodology for complex flows. *International Journal for Heat and Fluid Flow*, 23(5):710–20, 2002.

P. Moin. Large eddy simulation of multi-phase turbulent flows in realistic combustors. *Progress in Computational Fluid Dynamics*, 4(3-5):237–40, 2004.

K. Morton and D. Mayers. *Numerical Solution of Partial Differential Equations*. Cambridge University Press, 1994.

JD. Munzar, B. Akih-Kumgeh, BM. Denman, A. Zia, and JM. Bergthorson. An experimental and reduced modeling study of laminar flame speed of jet fuel surrogate components. *Fuel*, 113:586–597, 2013a.

JD. Munzar, BM. Denman, R. Jimenez, A. Zia, and JM. Bergthorson. Flame speed and vapour pressure of biofuels blends. *In: Proceedings of the ASME Turbo Expo 2013, ASME paper GT2013-94650, San Antonio*, 2013b.

JD. Munzar, A. Zia, P. Versailles, R. Jimenez, B. Akih-Kumgeh, and JM. Bergthorson. Comparison of laminar flame speeds, extinction strain rates and vapour pressures of jet a-1/hrj biofuel fuel blends. *In: Proceedings of the ASME Turbo Expo 2014, ASME paper GT2014-25951, Dusseldorf, Germany*, 2014.

CV. Naik, KV. Puduppakkam, A. Modak, E. Meeks, YL. Wang, and Q Feng et al. Detailed chemical kinetic for surrogate of alternative jet fuels. *Combustion and Flame*, 158(3):434–45, 2011.

A. Neophytou, E. Mastorakos, and RS. Cant. Complex chemistry simulations of spark ignition in turbulent sprays. *Proceedings of the Combustion Institute*, 33(2):2135–2142, 2011.

F. Nicoud and F. Ducros. Subgrid-Scale Stress Modelling Based on the Square of the Velocity Gradient Tensor. *Flow, Turbulence and Combustion*, 62(3):183–200, 1999.

J. Odgers and D. Kretschmer. *Gas turbine fuels and their influence on combustion*. Abacus Press, Cambridge, MA, 1986.

JA. Van Oijen and LPH. de Goey. Modelling of premixed laminar flames using Flamelet-Generated Manifolds. *Combustion Science and Technology*, 161:113–137, 2000.

JA. Van Oijen and LPH. de Goey. A numerical simulation of confined triple flames using a Flamelet-Generated Manifolds. *Combustion Theory and Modelling*, 8(1):141–163, 2004.

OpenFOAM. OpenFOAM Foundation.

M. Orme. Experiments on droplet collisions, bounce, coalescence and disruption. *Progress in Energy and Combustion Science*, 23:65–79, 1997.

PJ. O'Rourke and AA. Amsden. The TAB method for Numerical Calculation of Spray Droplet Breakup. *SAE Technical Paper 872089. SAE*, 1987.

PJ. O'Rourke and AA. Amsden. A Spray/Wall interaction submodel for the kiva-3 wall film model. *SAE Paper*, 2000-01-0271, 2000.

MA. Patterson and RD. Reitz. Modelling the effects of fuel spray characteristics on diesel engine combustion and emission. *SAE Paper 980131*, 1998.

N. Peters. *Four Lectures on Turbulent Combustion*. ERCOFTAC Summer School, Institut für Techische Mechanik, RWTH Aachen, September 15-19, Germany, 1997.

N. Peters. *Turbulent Combustion*. Cambridge University Press, Cambridge, UK, 2000.

N. Peters. *Combustion Theory*. CEFRC Summer School, Princeton, June 28th-July 2nd, 2010.

ND. Peters, B. Akih-Kumgeh, and JM. Bergthorson. Comparative analysis of chemical kinetic models using the Alternate Species Elimination approach. *Journal of Engineering for Gas Turbine and Power*, 137(2)021505, 2014.

CD. Pierce and P. Moin. Progress-variable approach for large-eddy simulation of non-premixed turbulent combustion. *Journal of Fluid Mechanics*, 504:73–97, 2004.

H. Pitsch. Large Eddy Simulation of turbulent combustion. *Annual Review of Fluid Mechanics*, 38: 453–482, 2006.

H. Pitsch and N. Peters. A consistent flamelet formulation for non-premixed combustion considering differencial diffusion effects. *Combustion and Flame*, 114:26–40, 1998.

T. Poinsot and D. Veynante. *Teoretical and Numerical Combustion*. R.T. Edwards, 2nd Edition, Flourtown, PA, 2005.

AD. Polynin, AM. Kutepov, AV. Vyazmin, and DA. Kazenin. *Hydrodynamics, mass and heat transfer in chemical engineering*. London: Taylor and Francis; p. 149-214, 2002.

SB. Pope. Pdf methods for turbulent reactive flows. *Progress in Eenergy and Combustion Science*, 11:119–192, 1985.

S.B. Pope. Ten questions conserning the large eddy simulation of turbulent flows. *New Journal of Physics*, 6:35–59, 2004.

IK. Puri, SK. Aggarwal, R. Azzoni, and S. Ratti. On the Similitude Between Lifted and Burner-stabilized Triple Flames: A Numerical and Experimental Investigation. *Combustion and Flame*, 124 (1/2):311–325, 2001a.

IK. Puri, SK. Aggarwal, R. Azzoni, and S. Ratti. On the similitude between lifted and burner-stabilized triple flames: A numerical and experimental investigation. *Combustion and Flame*, 124(1/2):311–325, 2001b.

X. Qin, C. Choi, IK. Puri, and SK. Aggarwal. Triple Flame Propagation and Stabilization in a laminar axisymmetric jet. *Combustion Theory and Modeling*, 8(4):293–314, 2004.

NA. Ragozin. Jet Propulsion Fuels, edited by bp. mullins, International Series on Aeronatics and astronautics. *Pergamon Press, Oxford-London-New York-Paris*, 3:168, 1961.

C.J. Rallis, A.M. Garforth, and J.A. Steinz. Laminar burning velocity acetylene-air mixtures by the constant volume method: Dependence on mixture composition, pressure and temperature. *Combustion and Flame*, 9(4):345–356, 1965.

RD. Reitz. Modelling atomization processes in high-pressure vaporizing sprays. *Atomization and Spray Technology*, 3:309–337, 1993.

J. Reveillon and L. Vervisch. Anaysis of weakly turbulent dilute-spray flames. *Journal of Fluid Mechanics*, 537:317–347, 2005.

KK. Rink and AH. Lefebvre. Influence of fuel drop size and combustor operating conditions on pollutants. *SAE, Technical Paper Series*, 861541, 1986.

A. Ristori, P. Dagaut, and M. Cathonnet. The oxidation of n-hexadecane: Experimental and detailed kinetic modeling. *Combustion and Flame*, 125:1128–1137, 2001.

NK. Rizk and AH. Lefebvre. Prediction of velocity coefficient and spray cone angle for simplex swirl atomizers. *Proceedings of the 3rd International Conference on Liquid Atomization and Spray Systems, London*, pages 111C/2/1–16, 1985.

J. Sahner. *Extraction of Vortex Structures in 3D Flows Fields*. PhD thesis, Dissertation to obtain the academic degree, doctorate engineer, university of Magdeburg, 2008.

A.-L. Sanchez, J. Urzay, and A. Liman. The role of separation of scales in the description of spray combustion. *Proceedings of the Combustion Institute*, 35(2):1549–1577, 2015.

M. Sanjosé, JM. Senorer, F. Jaegle, B. Cuenot, S. Moreau, and T. Poinsot. Euler-euler euler and euler-lagrange large-eddy simulations of an evaporationg inside an aeronautical combustor. *International Journal Multiphase and Flow*, 37(5):514–529, 2011.

SS. Sazhin, G. Feng, MR. Heikal, I. Goldfarb, V. Goldshtein, and G. Kuzmenko. Thermal ignition analysis of a monodisperse spray with radiation. *Combustion and Flame*, 124:684–701, 2001.

WD. Schulz. Oxidation products of a surrogate JP-8 fuel. *ACS Petrol Chem Div Prep*, 37(2):383–92, 1991.

L. Selle, G. Lartigue, T. Poinsot, R. Koch, KU. Schildmacher, W. Krebs, B. Prade, P. Kaufmann, and D. Veynante. Compressible large eddy simulation of turbulent combustion in complex geometry on unstructured meshes. *Combustion and Flame*, 137(4):489–505, 2004.

JM. Senoner, M. Sanjosé, T. Lederlin, F. Jaegle, M. Garcia, E. Riber, B. Cuenot, L. Giquel, H. Pitsch, and T. Poinsot. Eulerian and lagrangian large-eddy simulations of an evaprating two-phase flow. *Comptes Rendus Mécanique*, 337(6-7):458–468, 2009.

DH. Sheen. *Swirl-Stabilized Turbulent Spray Flames in an Axisymmetric Model Combustor*. PhD thesis, Imperial College, London, 1993.

HJ. Sheen, WJ. Chen, SY. Jeng, and TL. Huang. Correlation of swirl number for a radial-type swirl generator. *Experimental Thermal and Fluid Science*, 12(4):444–551, 1996.

J. Shinjo, Y. Mizobuchi, and S. Ogawa. Les of unstable combustion in a gas turbine combustor. *In: Proceedings of 5th International Symposium on High Performance Computing, Spring-Verlag, Berlin/Heidelberg/New York, NY*, 2003.

B. Shotroban, KKQ. Zhang, and F. Mashayek. Improvement of particle concentration prediction in large-eddy simulation by defiltering. *International Journal of Heat and Mass Tranfer*, 50(19-20): 3728–3739, 2007.

ML. Shur, PR. Spalart, MK. Strelets, and AK. Travin. Detached-Eddy Simulation of an Airfoil at High Angle of Attack. *In. 4th International Symposium on Engineering Turbulence Modelling and Experiments, Corsica, France*, May, 1999.

ML. Shur, PR. Spalart, MK. Strelets, and AK. Travin. A Hybrid RANS-LES Approach With Delayed-DES and Wall-Modelled LES Capabilities. *International Journal of Heat and Fluid Flow*, 29(6): 1638–1649, 2008.

JM. Simmie. Detailed chemical kinetic models for the combustion of hydrocarbon fuels. *Progress in Energy and Combustion Science*, 29(6):599–634, 2003.

HC. Simmons. The prediction of sauter mean diameter for gas turbine fuel nozzles of different types. *ASME Paper 79-WA/GT-5*, 1979.

H.C. Simmons and C.F. Harding. Some effects on using water as a test fluid in fuel nozzle spray analysis. *ASME Paper*, 80-GT-90, 1980.

WA. Sirignano. *Fluid Dynamics and Transport of Droplets and Sprays*. Cambridge University Press, Cambridge, UK, 1999.

B. Sirjean, E. Dames, DA. Sheen, XQ. You, C. Sung, AT. Holley, FN. Egolfopoulos, H. Wang, SS. Vasu, DF. Davidson, RK. Hanson, H. Pitsch, CT. Bowman, A. Kelley, CK. Law, W. Tsang, NP. Cernansky, DL. Miller, A. Violi, and RP. Lindstedt. A high-temperature chemical kinetic model of n-alkane oxidation: JetSurF version 0.2, September 08, 2008. Available at. `http://melchior.usc.edu/JetSurF/JetSurF0_2/index.html`, 2008 (accessed April 19, 2016)).

B. Sirjean, E. Dames, DA. Sheen, FN. Egolfopoulos, H. Wang, DF. Davidson, RK. Hanson, H. Pitsch, CT. Bowman, CK. Law, W. Tsang, NP. Cernansky, DL. Miller, A. Violi, and RP. Lindstedt. A high-temperature chemical kinetic model of n-alkane, cyclohexane, and methyl-, ethyl-, n-propyl and n-butyl-cyclohexane oxidation at high temperature: JetSurF version 1.1, September 15, 2009. `http://melchior.usc.edu/JetSurF/JetSurF1.1/index.html`, 2009 (accessed April 19, 2016))a.

B. Sirjean, E. Dames, DA. Sheen, XQ. You, C. Sung, AT. Holley, FN. Egolfopoulos, H. Wang, SS. Vasu, DF. Davidson, RK. Hanson, H. Pitsch, CT. Bowman, A. Kelley, CK. Law, W. Tsang,

NP. Cernansky, DL. Miller, A. Violi, and RP. Lindstedt. A high-temperature chemical kinetic model of n-alkane oxidation: JetSurF version 1.0, September 15, 2009. Available at. http://web.standford.edu/group/haiwanglab/JetSurF/JetSurF1.0/index.html, 2009 (accessed April 19, 2016))b.

J. Smagorinsky. General Circulation Experiments with the Primitive Equations. *I. Tthe Basic Experiment. Monthly Weather Review*, 91:99–164, 1963.

G. Smith. *Numerical Solution of Partial Differential Equations: Finite Difference Methods*. Oxford University Press, 1985.

S. Som and SK. Aggarwal. Effect of primary breakup modeling on spray and combustion characteristics of compression ignition engines. *Combustion and Flame*, 159:1179–1193, 2010.

P. Spalart, S. Deck, ML. Shur, KD. Quires, MK. Strelets, and AK. Travin. A new version of detached-eddy simulation, resistant to ambiguous grid densities. *Theoritical and Computational Fluid Dynamics*, 20:181–195, 2006.

PR. Spalart. Detached Eddy Simulation. *Annual Review of Fluid Mechanics*, 41:181–202, 2009.

PR. Spalart and S. Allmaras. A one-equation turbulence model for aerodynamics flows. *Technical Report AIAA-92-0439, American Institute of Aeronautics and Astronautics*, 1992.

DW. Stanton and CJ. Rutland. Modeling fuel film formation and wall interaction in diesel engines. *SAE*, Paper 960628, 1996.

DW. Stanton and CJ. Rutland. Multi-dimensional modeling of thin liquid films and spray-wall interactions resulting from impinging sprays. *International Journal of Heat and Mass Transfer*, 41: 3037–3054, 1998.

C. Stone and S. Menon. Open-loop control of combustion instabilities in a model gas turbine combustor. *Journal of Turbulence*, 4(1):020, 2003.

S. Subramaniam. Lagrangian-eulerian methods for multiphase flows. *Progress in Energy and Combustion Science*, 39(2-3):215–245, 2013.

V. Subramanian, P. Domingo, and L. Vervisch. Large eddy simulation of forced ignition of an annular bluff-body burner. *Combustion and Flame*, 157:579–601, 2010.

N. Swaminthan and KNC. Bray. *Turbulent Premixed Flames*. Cambridge University Press, 2011.

W. Tabakoff and T. Wakeman. Measured particle rebound characteristics useful for erosion prediction. *ASME paper*, 82-GT-170, 1982.

L. Talbot, RK. Cheng, RW. Schefer, and DR. Willis. Thermophoretics of Particles in Heated Boundary Layer. *Journal of Fluid Mechanics*, 101(4):737–758, 1980.

Z. Tan and RD. Reitz. An ignition and combustion model based on the level-set method for spark ignition engine multidimensional modelling. *Combustion and Flame*, 145:1–15, 2006.

AMKP. Taylor and JH. Whitelaw. Velocity characteristics in the turbulent near wakes of confined axisymmetric bluff bodies. *Journal of Fluid Mechanics*, 139:391–418, 1984.

AS. Teja, M. Gude, and DJ. Rosenthal. Novel methods for measurement of the critical properties of thermally unstable fluids. *Fluid Phase Equilibria*, 57:317–26, 1989.

M. Thiele, S. Selle, U. Reidel, J. Warnatz, and U. Mass. Numerical simulat of spark ignition including ionization. *Proceedings of the Combustion Institute*, 28:1177–1185, 2000.

J. Thomas. *Numerical Partial Differential Equations: Finite Difference Methods*. Springer-Verlag, 1995.

A. Triantafyllidis, E. Mastorakos, and RLGM. Eggels. Large eddy simulation of forced ignition of a non-premixed bluff-body methane with conditional moment closure. *Combustion and Flame*, 156: 2328–2345, 2009.

MR. Turner, SS. Sazhin, JJ. Healey, C. Crua, and SB. Martynov. A breakup model for transient diesel fuel sprays. *Fuel*, 92:288–305, 2012.

J. Urzay. A revised spray-combustion diagram of diffusion-controlled burning regimes in fuel-spray clouds. *Annual Research Briefs, Center for Turbulence Research*, pages 193–198, 2011.

M. Valorani, F. Creata, DH. Goussis, HN. Najm, and JC. Lee. Chemical Kinetics Mechanism Simplification via csp. *Combustion and Flame*, 146:29–51, 2006.

A. Vié, S. Jay, B. Cuenot, and M. Massot. Accounting for Polydispersion in the Eulerian Large Eddy Simulation of the Two-Phase Flow in an Aeronautical-type Burner. *Flow, Turbulence and Combustion*, 90(3):545–581, 2013.

A. Violi, S. Yan, EG. Eddings, AF. Sarofim, S. Granata, T. Faravelli, and E. Ranzi. Experimental formulation and kinetic model for JP-8 surrogate mixtures. *Combustion Science and Technology*, 174:399–417, 2002.

S. Viswanath, K. Ghosh, H. Prasad, V. Dutt, and Y. Rani. *Correlations and estimation of pure liquid viscosity*. Springer Netherlands, 2007.

CT. Wall and P. Moin. Numerical methods for large eddy simulation of acoustic combustion instabilities. *Technical Report TF-91, Standford, CA: Stanford University*, 2005.

H. Wang. Lectures Notes: Combustion chemistry. *Combustion Summer School, CEFRC, Princeton University*, 2015.

H. Wang, X. You, AV. Joshi, SG. Davis, A. Laskin, F. Egolfopoulos, and CK. Law. Usc mech version 2. high-temperature combustion reaction model of H2 CO C1-C4 coumpounds, may 2007. available at. http://ignis.usc.edu/USB_Mech_II.htm, 2007 (accessed April 19, 2016)).

H. Wang, E. Dames, B. Sirjean, DA. Sheen, R. Tango, A. Violi, FN. Egolfopoulos, DF. Davidson, RK. Hanson, CT. Bowman, CK. Law, W. Tsang, NP. Cernansky, DL. Miller, and RP. Lindstedt. A high-temperature chemical kinetic model of n-alkane (up to n-dodecane), cyclohexane, and methyl-, ethyl-, n-propyl and n-butyl-cyclohexane oxidation at high temperatures: JetSurF version 2.0, September 19, 2010. http://web.standford.edu/group/haiwanglab/JetSurF/JetSurF2.0/index.html, 2010 (accessed April 19, 2016)).

TS. Wang. Thermophysics characterization of kerosene combustion. *Journal of Thermophysics and Heat Transfer*, 15:140–147, 2001.

XF. Wang and AH. Lefebvre. Influence of ambiant air pressure on pressure-swirl atomization, paper presented at the 32nd. *ASME International Gas Turbine Conference, Anaheim, California, June*, 1987.

CK. Westbrook, WJ. Pitz, HJ. Curran, and M. Mehl. A comprehensive detailed chemical kinetic reaction mechanism for combustion of n-alkane hydrocarbons from n-octane to n-hexane. *Combustion and Flame*, 156(1):181–99, 2009.

I. Wichterie and J. Linek. *Antoine Vapor Pressure Constants of Pure Compounds*. Academia, Prague, 1971.

DC. Wilcox. *Turbulence modelling for CFD 3rd Edition*. DCW. Industries, La Canada, California, 2006.

FA. Williams. *Combustion Theory*. Addison-Wesley Publishing Company, 1965.

O. Zienkievicz and R. Taylor. *The Finite Element Method: The basis*, volume 1. ButterWorth and Heinemann, 2000.